

A MARKOV DECISION PROCESS EMBEDDED WITH PREDICTIVE MODELING: A  
MODELING APPROACH FROM SYSTEM DYNAMICS MATHEMATICAL MODELS,  
AGENT-BASED MODELS TO A CLINICAL DECISION MAKING

by

ZHENZHEN SHI

B.S., Central South University, 2008

AN ABSTRACT OF A DISSERTATION

submitted in partial fulfillment of the requirements for the degree

DOCTOR OF PHILOSOPHY

Department of Industrial and Manufacturing Systems Engineering  
College of Engineering

KANSAS STATE UNIVERSITY  
Manhattan, Kansas

2015

## **Abstract**

Patients who suffer from sepsis or septic shock are of great concern in the healthcare system. Recent data indicate that more than 900,000 severe sepsis or septic shock cases developed in the United States with mortality rates between 20% and 80%. In the United States alone, almost \$17 billion is spent each year for the treatment of patients with sepsis. Clinical trials of treatments for sepsis have been extensively studied in the last 30 years, but there is no general agreement of the effectiveness of the proposed treatments for sepsis. Therefore, it is necessary to find accurate and effective tools that can help physicians predict the progression of disease in a patient-specific way, and then provide physicians recommendation on the treatment of sepsis to lower risk for patients dying from sepsis.

The goal of this research is to develop a risk assessment tool and a risk management tool for sepsis. In order to achieve this goal, two system dynamic mathematical models (SDMMs) are initially developed to predict dynamic patterns of sepsis progression in innate immunity and adaptive immunity. The two SDMMs are able to identify key indicators and key processes of inflammatory responses to an infection, and a sepsis progression. Second, an integrated-mathematical-multi-agent-based model (IMMABM) is developed to capture the stochastic nature embedded in the development of inflammatory responses to a sepsis. Unlike existing agent-based models, this agent-based model is enhanced by incorporating developed SDMMs and extensive experimental data. With the risk assessment tools, a Markov decision process (MDP) is proposed, as a risk management tool, to apply to clinical decision-makings on sepsis.

With extensive computational studies, the major contributions of this research are to firstly develop risk assessment tools to identify the risk of sepsis development during the

immune system responding to an infection, and secondly propose a decision-making framework to manage the risk of infected individuals dying from sepsis.

The methodology and modeling framework used in this dissertation can be expanded to other disease situations and treatment applications, and have a broad impact to the research area related to computational modeling, biology, medical decision-making, and industrial engineering.

A MARKOV DECISION PROCESS EMBEDDED WITH PREDICTIVE MODELING: A  
MODELING APPROACH FROM SYSTEM DYNAMICS MATHEMATICAL MODELS,  
AGENT-BASED MODELS TO A CLINICAL DECISION MAKING

by

ZHENZHEN SHI

B.S., Central South University, 2008

A DISSERTATION

submitted in partial fulfillment of the requirements for the degree

DOCTOR OF PHILOSOPHY

Department of Industrial and Manufacturing Systems Engineering  
College of Engineering

KANSAS STATE UNIVERSITY  
Manhattan, Kansas

2015

Approved by:

Co-Major Professor  
David Ben-Arieh

Approved by:

Co-Major Professor  
Chih-Hang Wu

# **Copyright**

ZHENZHEN SHI

2015

## **Abstract**

Patients who suffer from sepsis or septic shock are of great concern in the healthcare system. Recent data indicate that more than 900,000 severe sepsis or septic shock cases developed in the United States with mortality rates between 20% and 80%. In the United States alone, almost \$17 billion is spent each year for the treatment of patients with sepsis. Clinical trials of treatments for sepsis have been extensively studied in the last 30 years, but there is no general agreement of the effectiveness of the proposed treatments for sepsis. Therefore, it is necessary to find accurate and effective tools that can help physicians predict the progression of disease in a patient-specific way, and then provide physicians recommendation on the treatment of sepsis to lower risk for patients dying from sepsis.

The goal of this research is to develop a risk assessment tool and a risk management tool for sepsis. In order to achieve this goal, two system dynamic mathematical models (SDMMs) are initially developed to predict dynamic patterns of sepsis progression in innate immunity and adaptive immunity. The two SDMMs are able to identify key indicators and key processes of inflammatory responses to an infection, and a sepsis progression. Second, an integrated-mathematical-multi-agent-based model (IMMABM) is developed to capture the stochastic nature embedded in the development of inflammatory responses to a sepsis. Unlike existing agent-based models, this agent-based model is enhanced by incorporating developed SDMMs and extensive experimental data. With the risk assessment tools, a Markov decision process (MDP) is proposed, as a risk management tool, to apply to clinical decision-makings on sepsis.

With extensive computational studies, the major contributions of this research are to firstly develop risk assessment tools to identify the risk of sepsis development during the

immune system responding to an infection, and secondly propose a decision-making framework to manage the risk of infected individuals dying from sepsis.

The methodology and modeling framework used in this dissertation can be expanded to other disease situations and treatment applications, and have a broad impact to the research area related to computational modeling, biology, medical decision-making, and industrial engineering.

# Table of Contents

List of Figures .....	xv
List of Tables .....	xxvii
Acknowledgements.....	xxix
Chapter 1 - Research Summary .....	1
1.1 Introduction and background .....	1
1.2 Research objectives.....	4
1.3 Proposed methodologies .....	6
1.4 Research map.....	9
1.5 Outlines.....	10
Chapter 2 - Literature Review.....	11
2.1 Previous mathematical models of inflammatory responses to an infection.....	11
2.2 Agent-based model: a surging tool to simulate infectious disease in the immune system .....	12
Abstract .....	12
2.2.1 Introduction.....	13
2.2.2 Agent-based Model of Sepsis .....	14
2.2.3 Agent-based model for other types of infectious disease .....	18
2.2.4 Implementing Software Platforms for Agent-based Model.....	20
2.2.5 Advantages of agent-based modeling on infectious disease.....	25
2.2.6 Limitations of agent-based modeling of infectious disease.....	27
2.2.7 Future direction of agent-based modeling of infection.....	29



2.3 Markov Decision Process: a decision-making framework for improving quality of care in Healthcare System.....	31
Abstract.....	31
2.3.1 Introduction.....	32
2.3.2 Fundamental structures of MDP and its extended formulation .....	33
2.3.3 Fundamental algorithms of solving MDP .....	39
2.3.3.1 Backward induction algorithm.....	39
2.3.3.2 Value iteration algorithm .....	40
2.3.3.3 Policy iteration algorithm .....	41
2.3.3.4 Modified policy iteration algorithm.....	42
2.3.4 MDP applications on septic patients.....	43
2.3.5 MDP application on other types of disease.....	46
2.3.6 Future research of MDP in healthcare .....	48
Chapter 3 - Mathematical modeling of innate immunity responses of sepsis: modeling and computational studies .....	51
Abstract.....	51
3.1 Background.....	52
3.2 System dynamic mathematical model (SDMM) .....	55
3.2.1 Pathogen strain selection.....	56
3.2.2 Kupffer Cell local response model .....	57
3.2.3 Neutrophils immune response model.....	62
3.2.4 Damaged tissue model .....	68
3.2.5 Monocytes immune response model.....	70

3.2.6 Anti-inflammatory immune response model .....	73
3.2.7 Mathematical models of innate immunity of AIR .....	75
3.2.7.1 Inhibition of anti-inflammatory cytokines .....	75
3.2.7.2 Mathematical model of innate immunity of AIR.....	76
3.3 Stability analysis .....	77
3.3.1 Neutrophil subsystem stability analysis.....	78
3.3.2 Monocyte subsystem stability analysis .....	82
3.3.3 Full model stability analysis .....	83
3.4 Discussion.....	84
3.4.1 Effects of initial pathogen load on sepsis progression.....	84
3.4.1.1 Low initial load of pathogen ( $p(0)=100$ ) .....	85
3.4.1.2 Medium initial load of pathogen ( $p(0)=10000$ ) .....	86
3.4.1.3 High initial load of pathogen ( $p(0)=100000$ ).....	87
3.4.2 Effects of pro-and anti-inflammatory cytokines on sepsis progression.....	88
3.4.2.1 High effect of anti-inflammatory cytokines.....	89
3.4.2.2 Medium effect of anti-inflammatory cytokines .....	90
3.4.2.3 Low effect of anti-inflammatory cytokines .....	91
3.5 Conclusion .....	92
Chapter 4 - Mathematical Model of Innate and Adaptive Immunity of Sepsis: a Modeling and Simulation Study of Infectious Disease.....	94
Abstract.....	94
4.1 Introduction.....	95
4.2 System dynamics mathematical model development .....	97

4.2.1 Process description.....	98
4.2.2 Step 1: Kupffer Cell local response model .....	99
4.2.3 Step2: Neutrophil immune response model.....	102
4.2.4 Step3: Damaged tissue model.....	105
4.2.5 Step4: Monocyte immune response model.....	106
4.2.6 Step5: SDMM of Innate Immunity .....	108
4.2.7 Step 6: SDMM incorporated with adaptive immunity.....	110
4.3 Simulated results.....	116
4.4 Stability analysis.....	123
4.5 Discussion.....	134
4.6 Conclusion and future research.....	138
Acknowledgement .....	139
 Chapter 5 - An Autonomous Multi-Agent Simulation Model for Acute Inflammatory Response	
.....	141
Abstract.....	141
5.1 Introduction.....	142
5.2 Biological mechanism of acute inflammatory response .....	143
5.3 System dynamics modeling of AIR .....	144
5.4 An agent-based model (ABM) embedded with system dynamics mathematical model .....	146
5.5 Implementation of the agent-based model.....	151
5.6 Predictive results of the simulation model.....	152
5.6.1 Deterministic results of the simulation model .....	152

5.6.2 Stochastic results of the simulation model.....	155
5.7 Sensitivity analysis of the agent-based model .....	156
5.8 Discussion and conclusion.....	161
Chapter 6 - A Novel Agent-based Model of a Hepatic Inflammatory Response (to <i>Salmonella</i> )	
.....	164
Abstract.....	164
6.1 Introduction.....	165
6.2 Agent-based model of inflammatory responses in previous publications .....	169
6.3 Development of IMMABM for hepatic inflammatory response of a mouse.....	172
6.3.1 Simulation environment.....	173
6.3.2 Software platform .....	174
6.3.3 Simulation initial setting.....	174
6.3.4 Process of IMMABM development.....	175
6.3.4.1 Primary agent behaviors .....	177
6.3.4.2 Agent and agent complex movement.....	180
6.3.4.3 State variable updates .....	182
6.3.4.4 Mathematical equations in programming .....	183
6.3.4.5 Model calibration and parameter estimation.....	184
6.4 Simulated results and model validation .....	186
6.4.1 Statistical analysis .....	186
6.4.2 Change in selected indicator levels observed under various <i>Salmonella</i> loads	
.....	186
6.4.3 Dynamic patterns of HIR resulting from <i>Salmonella</i> infection .....	188

6.4.4 Outcome assessment .....	201
6.4.5 Biomarkers of HIR.....	208
6.5 Conclusion and discussion.....	211
6.5.1 Insights into simulated results.....	211
6.5.2 Model simplification and generalizations .....	214
6.6 Future research.....	217
Chapter 7 - A novel semi-Markov decision process for clinical decisions related to individuals with sepsis.....	219
Abstract.....	219
7.1 Introduction.....	220
7.2 Background.....	221
7.3 Previous MDPs on clinical decision makings for patients with sepsis.....	224
7.4 Model Formulation .....	226
7.4.1 Classes of MDPs .....	226
7.4.2 Basic elements of SMDP .....	228
7.4.3 Objective function of FHSMDP .....	229
7.4.4 FHSMDP data sources .....	230
7.5 Solving the FHSMDP .....	232
7.6 Computational results .....	233
7.6.1 Computational study I.....	234
7.6.2 Computational study II .....	235
7.6.3 Evaluation .....	240
7.7 Conclusion and discussion.....	241

7.8 Future research.....	244
Chapter 8 - Conclusions and Contributions .....	245
8.1 Conclusions.....	245
8.2 Contributions .....	248
References.....	250
Appendix A - Supplementary Tables for SDMMs .....	271
Appendix B - Supplementary Materials for IMMABM .....	275
Appendix C - Supplementary Material for FHSM DP .....	319

## List of Figures

Figure 1.1 Research map.....	9
Figure 2.1 Basic structure of agent changing.....	30
Figure 2.2 Relationship between states, actions, transition probabilities and rewards in MDP ...	34
Figure 3.1 Framework of the system dynamic mathematical model .....	57
Figure 3.2 (a) Concentration of <i>pathogen</i> load versus time, for three different proliferation rates of <i>Kupffer cells</i> in Kupffer local response model. (b) Concentration of <i>Kupffer cells</i> versus time, for three different proliferation rates of <i>Kupffer cells</i> in the Kupffer local response model. The horizontal axes represent the time in hours, and the vertical axes represent concentration in arbitrary units .....	61
Figure 3.3 Mechanism of cytokine release .....	63
Figure 3.4 (a) Concentration of <i>pathogen</i> versus time in neutrophil immune response model at the first 120 hours of simulation. (b) Concentration of <i>TNF-<math>\alpha</math></i> versus time in neutrophil immune response model at the first 120 hours of simulation. (c) Concentration of <i>resting neutrophils</i> versus time in neutrophil immune response model at the first 120 hours of simulation. (d) Concentration of <i>activated neutrophils</i> versus time in neutrophil immune response model at the first 120 hours of simulation. (e) Concentration of <i>pathogen</i> versus time in neutrophil immune response model at the first 240 hours of simulation. (f) Concentration of <i>TNF-<math>\alpha</math></i> versus time in neutrophil immune response model at the first 240 hours of simulation. (g) Concentration of <i>resting neutrophils</i> versus time in neutrophil immune response model at the first 240 hours of simulation. (h) Concentration of <i>activated neutrophils</i> versus time in neutrophil immune response model at the first 240 hours of	

simulation. X axes represent time (hours), and Y axes represent concentration in arbitrary unit ..... 65

Figure 3.5 Interactions between *pathogen*, *activated neutrophils*, and *TNF- $\alpha$* ..... 68

Figure 3.6 (a) Concentration of *dead hepatocytes* versus time in damaged tissue model at the first 100 hours of simulation. (b) Concentration of *dead hepatocytes* versus time in damaged tissue model at the first 240 hours of simulation. X axes represent time (in hour) and Y axes represent concentration in arbitrary unit ..... 70

Figure 3.7 (a) Concentration of *resting monocytes* versus time in monocyte immune response model at the first 240 hours of simulation. (b) Concentration of *activated monocytes* versus time in monocyte immune response model at the first 120 hours of simulation. (c) Concentration of *TNF- $\alpha$*  versus time in monocyte immune response model at the first 120 hours of simulation. (d) Concentration of *HMGB-1* versus time in monocyte immune response model at the first 120 hours of simulation. Horizontal axes represent time (in hours), and vertical axes represent concentrations in arbitrary units ..... 72

Figure 3.8 (a) Concentration of *TNF- $\alpha$*  versus time in anti-inflammatory immune response model at the first 80 hours of simulation. (b) Concentration of *HMGB-1* versus time in anti-inflammatory immune response model at the first 80 hours of simulation. (c) Concentration of *IL-10* versus time in anti-inflammatory immune response model at the first 80 hours of simulation. Horizontal axes represent time (in hours) and Vertical axes represent concentration in arbitrary unit..... 74

Figure 3.9 Mechanism of *IL-10* inhibition..... 75

Figure 3.10 (a) Computed equilibrium curve of *pathogens* in relation to system parameter  $k_{pg}$  in neutrophil subsystem. (b) Computed equilibrium curve of *pathogens* in relation to system



parameters  $r_{pn}$  in neutrophil subsystem. (c) Computed equilibrium curve of *pathogens* in relation to system parameters  $u_n$  in neutrophil subsystem. (d) Computed equilibrium curve of *pathogens* in relation to system parameters  $r_{t2max}$  in neutrophil subsystem..... 78

Figure 3.11 (a) Family of limit cycles bifurcating from the Hopf point in *TNF-a* and *pathogen* plane. (b) Family of limit cycles bifurcating from the Hopf point in  $N_f$  and *pathogen* plane. (c) Equilibria and limit cycles in ( $N_f$ , *pathogen*, and *TNF-a*)-space. (d) Period of the cycle as function of  $r_{t2max}$ ..... 80

Figure 3.12 (a) Numerical relationships between  $N_f$ , *pathogen*, and *TNF-a* in unstable neutrophil subsystem at equilibrium when  $r_{t2max}$  is equal to 6265.0029. (b) *Pathogen* diverges in unstable neutrophil subsystem at equilibrium when  $r_{t2max}$  is equal to 6265.0029. (c) *Activated Neutrophils* diverges in unstable neutrophil subsystem at equilibrium when  $r_{t2max}$  is equal to 6265.0029. (d) *TNF-as* diverges in unstable neutrophil subsystem at equilibrium when  $r_{t2max}$  is equal to 6265.0029 ..... 81

Figure 3.13 (a) Numerical relationships between  $N_f$ , *pathogen*, and *TNF-a* in stable neutrophil subsystem at equilibrium when  $r_{t2max}$  is between 5495.6394 and 6265.0029. (b) *Pathogen* converges in stable neutrophil subsystem at equilibrium when  $r_{t2max}$  is between 5495.6394 and 6265.0029. (c) *Activated Neutrophils* converges in stable neutrophil subsystem at equilibrium when  $r_{t2max}$  is between 5495.6394 and 6265.0029. (d) *TNF-a* converges in stable neutrophil subsystem at equilibrium when  $r_{t2max}$  is between 5495.6394 and 6265.0029 ..... 81

Figure 3.14 (a) Computed equilibrium curve of *pathogens* in relation to system parameter  $k_{rd}$  in monocyte subsystem. (b) Computed equilibrium curve of *pathogens* in relation to system parameters  $u_{nr}$  in monocyte subsystem. (c) Computed equilibrium curve of *pathogens* in

relation to system parameters  $u_n$  in monocyte subsystem. (d) Computed equilibrium curve of *pathogens* in relation to system parameters  $r_{t2max}$  in monocyte subsystem. (e) Computed equilibrium curve of *pathogens* in relation to system parameters  $m_{t2}$  in monocyte subsystem ..... 82

Figure 3.15 (a) Computed equilibrium curve of *pathogens* in relation to system parameter  $r_{t2max}$  if medium effect of anti-inflammatory cytokine is incorporated. (b) Computed equilibrium curve of *pathogens* in relation to system parameters  $m_{t2}$  if medium effect of anti-inflammatory cytokine is incorporated ..... 84

Figure 3.16 (a) Concentration of *pathogen* in the presence of low initial load of *pathogen*. (b) Concentration of *activated neutrophils* in the presence of low initial load of *pathogen*. (c) Concentration of *activated monocytes* in the presence of low initial load of *pathogen*. (d) Concentration of *TNF-a* in the presence of low initial load of *pathogen*. (e) Concentration of *HMGB-1* in the presence of low initial load of *pathogen*. (f) Concentration of *dead hepatocytes* in the presence of low initial load of *pathogen*. Horizontal axes represent time (in hours) and Vertical axes represent concentration in arbitrary unit..... 85

Figure 3.17 (a) Concentration of *pathogen* in the presence of medium initial load of *pathogen*. (b) Concentration of *activated neutrophils* in the presence of medium initial load of *pathogen*. (c) Concentration of *activated monocytes* in the presence of medium initial load of *pathogen*. (d) Concentration of *TNF-a* in the presence of medium initial load of *pathogen*. (e) Concentration of *HMGB-1* in the presence of medium initial load of *pathogen*. (f) Concentration of *dead hepatocytes* in the presence of medium initial load of *pathogen*. Horizontal axes represent time (in hours) and Vertical axes represent concentration in arbitrary units ..... 86

Figure 3.18 (a) Concentration of *pathogen* in the presence of high initial load of *pathogen*. (b) Concentration of *activated neutrophils* in the presence of high initial load of *pathogen*. (c) Concentration of *activated monocytes* in the presence of high initial load of *pathogen*. (d) Concentration of *TNF- $\alpha$*  in the presence of high initial load of *pathogen*. (e) Concentration of *HMGB-1* in the presence of high initial load of *pathogen*. (f) Concentration of *dead hepatocytes* in the presence of high initial load of *pathogen*. Horizontal axes represent time (in hours) and Vertical axes represent concentration in arbitrary units ..... 87

Figure 3.19 (a) Concentration of *pathogen* in the presence of high effect of *IL-10*. (b) Concentration of *activated neutrophils* in the presence of high effect of *IL-10*. (c) Concentration of *activated monocytes* in the presence of high effect of *IL-10*. (d) Concentration of *dead hepatocytes* in the presence of high effect of *IL-10*. Horizontal axes represent time (in hours) and Vertical axes represent concentration in arbitrary units ..... 89

Figure 3.20 (a) Concentration of *pathogen* in the presence of medium effect of *IL-10*. (b) Concentration of *activated neutrophils* in the presence of medium effect of *IL-10*. (c) Concentration of *activated monocytes* in the presence of medium effect of *IL-10*. (d) Concentration of *dead hepatocytes* in the presence of medium effect of *IL-10*. Horizontal axes represent time (in hours) and Vertical axes represent concentration in arbitrary units 90

Figure 3.21 (a) Concentration of *pathogen* in the presence of low effect of *IL-10*. (b) Concentration of *activated neutrophils* in the presence of low effect of *IL-10*. (c) Concentration of *activated monocytes* in the presence of low effect of *IL-10*. (d) Concentration of *dead hepatocytes* in the presence of low effect of *IL-10*. Horizontal axes represent time (in hours) and Vertical axes represent concentration in arbitrary units ..... 91

Figure 4.1 Types of indicators (cells and cytokines) and their interactions in AIR progression.  
    Italic and bold letters represent variables in our SDMM ..... 99

Figure 4.2 Mechanism of cytokine release ..... 103

Figure 4.3 A simplified mechanism of T cell activation ..... 114

Figure 4.4 Dynamic patterns of AIR progression related to various initial levels of indicators and adjustable system parameters. X-axis represents time (in hours) and Y-axis represents number of indicators (pathogen, dead hepatocyte, activated neutrophil, activated monocyte, TNF- $\alpha$ , HMGB-1, and IL-10) during AIR progression. (a) Combined dynamic patterns of indicators represent a *Healing Process* in AIR progression (pathogen initial counts = 100). (b) Combined dynamic patterns of indicators represent a *Persistent Infection* in AIR progression (pathogen initial counts = 10000). (c) Combined dynamic patterns of indicators represent *Organ Dysfunction* in AIR progression (pathogen initial counts = 100000) ..... 117

Figure 4.5 Dynamic patterns of TNF- $\alpha$ , HMGB-1, and IL-10 in mice livers during AIR generated from our SDMM. X-axis represents time (in hours) and Y-axis represents number of indicators ..... 119

Figure 4.6 An adaptive immunity influence on outcomes of sepsis progression (pathogen initial counts = 10000). X-axis represents time (in hours) and Y-axis represents number of indicators ..... 120

Figure 4.7 An adaptive immunity influence on outcomes of sepsis progression (pathogen initial counts = 100000). X-axis represents time (in hours) and Y-axis represents number of indicators ..... 121

Figure 4.8 Change in the disease free equilibrium point  **$Mkf = 12000000, P = 0, Mkb = 0$**  when  $P = 2$  and  $k_{pg}=1.2$  ..... 126

Figure 4.9 Change in the pathogen saturation equilibrium point  $\mathbf{Mkf} = \mathbf{0}, \mathbf{P} = \mathbf{P}\infty, \mathbf{Mkb} = \mathbf{0}$  when  $M_{kf} = 2$  and  $k_{mk} = 0.9$  ..... 126

Figure 4.10 (a) Computed equilibrium curve of *pathogen* in relation to system parameter  $k_{pg}$  in neutrophil immune response model. (b) Computed equilibrium curve of *pathogen* in relation to system parameter  $r_{pn}$  in neutrophil immune response model. (c) Computed equilibrium curve of *pathogen* in relation to system parameter  $u_n$  in neutrophil immune response model. (d) Computed equilibrium curve of *pathogen* in relation to system parameter  $r_{t2max}$  in neutrophil immune response model ..... 128

Figure 4.11 (a) Family of limit cycles bifurcating from the Hopf point in *TNF- $\alpha$*  and *pathogen* plane. (b) Family of limit cycles bifurcating from the Hopf point in  $N_f$  and *pathogen* plane. (c) Equilibria and limit cycles in ( $N_f$ , *pathogen*, and *TNF- $\alpha$* )-space. (d) Period of the cycle as function of  $r_{t2max}$  ..... 129

Figure 4.12 (a) *Pathogen*, *activated neutrophil* and *TNF- $\alpha$*  diverge at unstable equilibria in neutrophil immune response model when  $r_{t2max}$  is above 6265.00 (b) *Pathogen*, *activated neutrophil*, and *TNF- $\alpha$*  converge at stable equilibria in neutrophil immune response model when  $r_{t2max}$  is between 5495.64 and 6265.00 ..... 131

Figure 4.13 (a) Computed equilibrium curve of pathogen in relation to system parameter  $k_{pg}$  in the full model incorporated with adaptive immunity. (b) Computed equilibrium curve of pathogen in relation to system parameters  $r_{pn}$  in the full model incorporated with adaptive immunity. (c) Computed equilibrium curve of pathogen in relation to system parameters  $u_n$  in the full model incorporated with adaptive immunity. (d) Computed equilibrium curve of pathogen in relation to system parameters  $r_{t2max}$  in the full model incorporated with adaptive immunity ..... 133

Figure 4.14 (a) Family of limit cycles bifurcation from the Hopf point ( $K_{pg} = 2.8$ ) in $TNF-\alpha$ and $pathogen$ plane. (b) Family of limit cycles bifurcating from the Hopf point ( $K_{pg} = 2.8$ ) in $N_f$ and $pathogen$ plane. (c) Equilibria and limit cycles in ( $N_f$ , $pathogen$ , and $TNF-\alpha$ )-space. (d) Period of the cycle as function of $k_{pg}$ .....	134
Figure 5.1 Simulation results of the five equations model .....	145
Figure 5.2 Basic structure of agents changing .....	148
Figure 5.3 Comprehensive structure of the agent based model .....	149
Figure 5.4 Healthy response with low pathogen load.....	153
Figure 5.5 Severe sepsis.....	154
Figure 5.6 Persistent non-infectious inflammations .....	155
Figure 5.7 AIR response to the range of the initial pathogen load .....	156
Figure 5.8 The influence of initial load of anti-inflammatory mediator and activated phagocyte to the outcomes of AIR .....	157
Figure 6.1 Interacting behaviors among macrophages, neutrophils, and red blood cells.....	169
Figure 6.2 Simulated area of the HIR in the Netlogo interface at simulation step equal to 0 (initial status) .....	175
Figure 6.3 An overview of primary agent interactions in IMMABM .....	181
Figure 6.4 Response of different variables (agents) over the first 24 hrs after <i>Salmonella</i> infection (load) of 200 counts, 600 counts, 800 counts, and 1200 counts. Mean counts of indicators were measured at each of time points of simulation (replications =100) .....	187
Figure 6.5 Healing response after <i>Salmonella</i> infection (load) of 200. (Mean counts $\pm$ SE) of indicators were measured at each of time points of simulation (replications = 100) .....	189

Figure 6.6 Examples of the Netlogo interface at selected time points (5-240 hrs) after infection with 200 <i>Salmonella</i> . Note: 1 step is equivalent to 1 hr. post infection.....	190
Figure 6.7 (a) Persistent infection after <i>Salmonella</i> infection (load) of 600. (Mean counts $\pm$ SE) of different variables (agents) were measured at each of time points of simulation (replications = 10). (b) Persistent infection after <i>Salmonella</i> infection (load) of 600. Counts of different variables (agents) were measured at each of time points of one selected simulation.....	193
Figure 6.8 Examples of the Netlogo interface at selected time points (5-240 hrs) after infection with 600 <i>Salmonella</i> . Note: 1 step is equivalent to 1 hr. post infection.....	195
Figure 6.9 Hyperinflammatory response after <i>Salmonella</i> infection (load) of 800. (Mean counts $\pm$ SE) of indicators were measured at each of time points of simulation (replications = 10)	198
Figure 6.10 Examples of the Netlogo interface at selected time points (5-240 hrs) after infection with 800 <i>Salmonella</i> . Note: 1 step is equivalent to 1 hr. post infection.....	199
Figure 6.11 Organ dysfunction after <i>Salmonella</i> infection (load) of 1200. (Mean counts $\pm$ SE) of indicators were measured at each of time points of simulation (replications = 10) .....	200
Figure 6.12 Examples of the Netlogo interface at selected time points (5-240 hrs) after infection with 1200 <i>Salmonella</i> . Note: 1 step is equivalent to 1 hr. post infection.....	201
Figure 6.13 Four distinct patterns observed in IMMAB simulation when <i>Salmonella</i> infection (load) of 800. (Mean counts $\pm$ SE) of indicators were measured at each of time points of simulation. (a). Observed healing response (replications = 100) (b). Observed persistent infection (replications = 10) (c). Observed hyperinflammatory response. (replications = 10) (d). Observed organ dysfunction. (replications = 10).....	203

Figure 6.14 Probabilities of leading to healing response, persistent infection, hyperinflammatory response, and organ dysfunction in HIR when the Salmonella initial loads ranging from 100 counts to 1400 counts..... 207

Figure 6.15 Probabilities of leading to healing response, persistent infection, hyperinflammatory response, and organ dysfunction with the same initial Salmonella load in the HIR..... 207

Figure 6.16 Comparison of *IL-10: TNF- $\alpha$*  ratio among healing response, hyperinflammatory response, and organ dysfunction responses against various infection time. Mean values of *IL-10: TNF- $\alpha$*  ratios were measured at each of time points of simulation (replications = 10) ..... 208

Figure 6.17 Comparison of *CD4+ T Cell: CD8+ T Cell* ratio among healing response, hyperinflammatory response, and organ dysfunction responses against various infection time. Mean values of *CD4+ T cell: CD8+ T cell* ratios were measured at each of time points of simulation (replications = 10)..... 209

Figure 6.18 Comparison of *MDMII: MDMI* ratio among healing response, hyperinflammatory response, and organ dysfunction responses against various infection time. Mean values of *MDMII: MDMI* ratios were measured at each of time points of simulation (replications = 10). ..... 210

Figure 6.19 Assessment of therapy in IMMABM. Hypothetical antimicrobial agents, anti-TNF- $\alpha$  agents, and a combination of anti-TNF- $\alpha$  and anti-HMGB-1 agents were administered to determine their impact in HIR. The “Probability of survival” label represents the probability of HIR ending with a healing response. We assume 1 antimicrobial agent kills 1 CFU Salmonella, 1 anti-TNF- $\alpha$  agent degrades  $2.82 \times 10^{-5}$  pg TNF- $\alpha$ , and 1 anti-HMGB-1 agent degrades  $2.82 \times 10^{-5}$  pg HMGB-1. The administration of the treatment therapies was done



one time IMMABM starting at 0 hour to 24 hours (abscissa). 20 simulation replications were conducted for each treatment regimen (1500 simulation replications were conducted for this experiment).....	213
Figure 7.1 Classification of MDPs.....	227
Figure 7.2 Netlogo interface at selected time points (5 - 240 hrs) with hyperinflammatory response.....	231
Figure 7.3 Netlogo interface at selected time points (5 - 240 hrs) with organ dysfunction.....	231
Figure 7.4 Proposed decision-making framework .....	233
Figure 7.5 (A) Accumulated risk of an infected individual dying from sepsis from 0 - 8 hrs of hospital stays. (B) Accumulated risk of an infected individual dying from sepsis from 0 - 24 hrs of hospital stay. Treatment 1: <i>antimicrobial</i> agent, treatment 2: <i>anti-HMGB-1</i> agent, treatment 3: a combination of <i>antimicrobial</i> agent/ <i>antiHMGB-1</i> agent .....	234
Figure 7.6 Accumulated risk of infected individuals dying from sepsis (hypothetical death states) at $s_5$ from 0-24 hrs of hospital stays using various treatment strategies. Treatment 1: <i>antimicrobial</i> agent, treatment 2: <i>anti-HMGB-1</i> agent, treatment 3: a combination of <i>antimicrobial</i> agent/ <i>antiHMGB-1</i> agent .....	236
Figure 7.7 Accumulated risk of infected individuals dying from sepsis (hypothetical death states) at $s_6$ from 0-24 hrs of hospital stays using various treatment strategies. Treatment 1: <i>antimicrobial</i> agent, treatment 2: <i>anti-HMGB-1</i> agent, treatment 3: a combination of <i>antimicrobial</i> agent/ <i>antiHMGB-1</i> agent .....	237
Figure 7.8 Accumulated risk of infected individuals dying from sepsis (hypothetical death states) at $s_8$ from 0-24 hrs of hospital stays using various treatment strategies. Treatment 1:	

<i>antimicrobial</i> agent, treatment 2: <i>anti-HMGB-1</i> agent, treatment 3: a combination of <i>antimicrobial</i> agent/ <i>antiHMGB-1</i> agent .....	238
Figure 7.9 Accumulated risk of infected individuals dying from sepsis (hypothetical death states) at $s_9$ from 0-24 hrs of hospital stays using various treatment strategies. Treatment 1: <i>antimicrobial</i> agent, treatment 2: <i>anti-HMGB-1</i> agent, treatment 3: a combination of <i>antimicrobial</i> agent/ <i>antiHMGB-1</i> agent .....	239
Figure 8.1 Calibrated $P(t   s_i, a_{ik})$ from IMMABM and estimated lines for $F(t   s_i, a_{ik})$ .....	321
Figure 8.2 Calibrated $P(t   s_i, a_{ik})$ from IMMABM and estimated lines for $F(t   s_i, a_{ik})$ .....	327

## List of Tables

Table 2.1 Characteristics of various types of agent-based simulation platforms .....	24
Table 2.2 Definition of notations and their range in value .....	35
Table 5.1 Agent type and its description .....	147
Table 5.2 The sensitivity of AIR progression to the initial load of indicators.....	160
Table 5.3 The sensitivity of the AIR progression to various system parameters .....	160
Table 6.1 Relationship between dynamic patterns of hepatic inflammatory response and dynamic patterns of essential biomarkers in IMMABM .....	210
Table A.1 Definition of parameters and experimental values in Kupffer local response model	271
Table A.2 Definition of parameters and experimental values in neutrophils immune response model.....	271
Table A.3 Definition of parameters and experimental values in damaged tissue model.....	272
Table A.4 Definition of parameters and experimental values in monocytes immune response model.....	272
Table A.5 Definition of parameters and experimental values in anti-inflammatory immune response model.....	273
Table A.6 Definition of parameters and experimental values in <i>full model with adaptive immunity</i> .....	273
Table B.7 Agent Types and Agent Behaviors in IMMABM Based on Biological Behaviors (Agent types in “Agent Behavior(s)” are highlighted in <i>Italic</i> format, except terminology <i>Salmonella enterica serovar Typhimurium (Salmonella)</i> is <i>Italic</i> format in both “Biological Behavior(s)” and “Agent Behavior(s)”.....	275
Table B.8 Agent Behaviors and Agent Update Rules in IMMABM.....	289

Table B.9 Experimental data and value of system parameters in IMMABM ..... 303

## Acknowledgements

I would like to take this opportunity to express my deepest appreciation to many people who helped me to complete this dissertation.

First of all, I thank my advisor Dr. David Ben-Arieh, for recruiting me to this exciting, and challenging research project. I would like to thank him for constantly guiding me even during tough times. Sincere thanks also go to my co-major advisor, Dr. Chih-Hang (John) Wu, for giving me valuable advice on research and personal life. Dr. Wu and Dr. Ben-Arieh provided me the theoretical framework for my dissertation, and I followed this framework to complete my dissertation.

I would like to express my special thanks to Dr. Stephen K. Chapes for his generous support and continuous supervision throughout my dissertation. For approximately 2 years, Dr. Chapes guided me through the data collection and estimation process in the weekly meetings. During this process, I am always inspired and encouraged by his scientific attitude toward research.

Many thanks to my department head, Dr. Bradley A. Kramer, for serving as my committee member. I would like to thank Dr. Kramer for his constantly financial support during my PhD study. I would also like to thank Dr. H. Morgan Scott for his kindly help in serving as the outside chairperson for my final examination.

I would like to express my gratitude to faculty and staff members in my department for their help and support, including: I thank Dr. E. Stanley Lee, Dr. Shing I. Chang, Dr. Shuting Lei, Dr. Todd Easton, Dr. Jessica Heier Stamm for teaching me academic courses. I also thank Mrs. Doris Galvan, Vicky Geyer, Tina Long, Myra Peoples, and Michele Bradfield for their kind assistance.

I acknowledge my collegians in the department for their love and support during my PhD study. I would like to thank Dr. Pengfei Zhang, Dr. Qi Zhang, Dr. Na Qin, Dr. Weilong Cong, Dr. Xiaoxu Song, Dr. Meng Zhang, Mr. Songnian Zhao, Mrs. Yan Kuan to be my side when I went through tough times.

Last but not the least, this dissertation is dedicated to my parents, Youdi Shi and Shanpin Yang, for their understanding, and endless care during my PhD study. Thanks also go to my fiancé, Wenbo Wang, for his love, support and faith in me.

# Chapter 1 - Research Summary

## 1.1 Introduction and background

Sepsis, currently defined as a systemic inflammatory response (SIR) in the presence of an infectious agent or trauma, is increasingly being considered an exaggerated, poorly regulated immune response to microbial products (1, 2). The progression to severe sepsis is marked by the generalized hypotension, tissue hypoxia, and coagulation abnormality (1). Severe sepsis can further develop into septic shock under the long-lasting severe hypotension (1) and ultimately lead to the death.

Severe sepsis and septic shock during an infection are the major causes of death in an intensive care setting (3). There is an average of 250,000 deaths per year in the United States caused by sepsis (4). Among patients in intensive care units (ICUs), it ranks as the second highest cause of mortality (5) and the 10th leading cause of death overall in the US (6). Average of 750,000 sepsis cases happen annually and increasing (6). In addition, the quality of life for sepsis survivors is significantly reduced (6, 7). Care of patients with sepsis costs can be as much as \$60,000 per patient. This cost results in a significant healthcare burden of nearly \$17 billion annually in the USA alone (8). The development of sepsis in a hospitalized patient can lead to a longer length of stay in the hospital which implies stiffer financial burden.

The human immune response evolves to protect the body from infection by harmful pathogens found in the environment (9). An initial stage of a systemic inflammatory response to an infection was recognized as an acute inflammatory response (AIR). This response is characterized by the activation and mobilization of white blood cells, the release of cytokines, and the modification of the vascular and lymphoid tissue (10, 11). Unfortunately, the activation of the immune system can become dysregulated and the immune responses or AIR can become

pathogenic. Indeed, an uncontrolled AIR may lead to possible sepsis or septic shock. Whether a patient will progress to sepsis, severe sepsis, or even septic shock is determined by a cascade of immune system components.

Over the past two decades, the studies of mechanisms that lead to sepsis have made significant progress due to the discoveries of new inflammatory proteins and the interaction of host cells and pathogens. Recent data indicate that the interactions between the anti-inflammatory responses and the pro-inflammatory responses, determine the prognosis of sepsis (12, 13). TNF- $\alpha$  is a pro-inflammatory cytokine that is released from various types of immune cells (14-20). HMGB-1, recognized as a late pro-inflammatory cytokines, contributes to the release of TNF- $\alpha$ , neutrophils as well as monocytes (21). More specifically, the presence of HMGB-1, which reaches its peak concentrations around eight to twelve hours after it is induced by TNF- $\alpha$ , may be a key component during the progression of AIR. If the level of HMGB-1 remains elevated for long periods of time, the patient may at risk for more severe AIR or developing sepsis (22-24). Anti-inflammatory cytokines, such as IL-4, IL-10, IL-13, and IL-14 play crucial roles in inhibiting the production of pro-inflammatory cytokines and in turn could slow down the progression of AIR (25, 26). For example, a higher concentration of IL-10 was found in less severe sepsis, and has a correlation with a subsequent decrease in TNF- $\alpha$  concentration in a mouse model (13). Clearly, the levels of pro- and anti-inflammatory mediators are closely linked to the development of severe sepsis and septic shock. However, there is little data on the quantitative relationships of the cytokine network, which can be used to predict the progression of disease.

Clinical trials of treatments for sepsis have been extensively studied in the last 30 years (27-32), aiming at compromising the “deleterious” effects of bacteria or inflammatory cytokines.



TNF- $\alpha$  was previously recognized as a therapeutic target for sepsis infection because anti-TNF agents were tested to be early positive in some human septic shock model (33, 34). However, a large RCT found anti-TNF- $\alpha$  antibody was not effective on improving survival rates for subgroup of patients who had elevated TNF levels on the study entry (29).

Inhibition of HMGB-1 production has been observed to improve survival in sepsis models in mice (35). Also, clinical experiments have demonstrated that monoclonal antibody therapy against HMGB-1 elevation can prevent septic patients from organ damage and subsequent organ dysfunction in experimental models (36-40). Such results suggested anti-HMGB-1 antibody could be a promising candidate for treatment of septic patients (22). However, HMGB-1 antagonism has only proven to be beneficial in rodent models of sepsis, and data are needed to investigate their efficacy on higher species (41).

Empiric broad-spectrum antimicrobial agents targeting the likely cause of infection was recommended to be initiated as soon as possible when treat septic patients (42). However, antibiotics alone were not sufficient for optimal treatment of patients with sepsis (42). Current recommendations are to administer appropriate antimicrobials within 1 hour of a diagnosis of severe sepsis or septic shock (43, 44). Nevertheless, it is still unclear when it is most beneficial to administer antimicrobials because variation was observed in outcomes of sepsis after administer antimicrobials (45). Furthermore, sufficient research regarding the effects of short and prolonged duration of antimicrobial therapy on patient recovery is lacking so that it is currently difficult to make a conclusion in terms of an appropriate length of antibiotic therapy.

Biomedical researchers proposed and tested groups of treatment interventions aiming at various targets, but there is no general agreement of the effectiveness of the proposed treatments for sepsis. Only activated protein C (APC) has been approved for treatment of severe cases of

sepsis at the current stage (41). All the evidences above directed the need of developing treatment strategy for sepsis in future clinical research.

## **1.2 Research objectives**

The proposed treatments for sepsis have been disappointing based on several reasons. Firstly, it is difficult to predict the development of sepsis (46). For example, the use of anti-inflammatory mediators, such as anti-TNF- $\alpha$  antibody may be ineffective when the patients with well-established sepsis enrolled (46). In addition, patients with sepsis are highly heterogeneous based on the source of infection, site of infection, duration of illness, and current immune status (46), thus it is impossible to develop a general treatment strategy suitable for all patients (47). Furthermore, the development of sepsis involves numerous biological responses, leading to the uncertainty in the outcomes of a sepsis progression.

Riedemann *et al.* (41) stated, in their review on strategies for the treatment of sepsis, that “it is important to understand in more details the various dynamics of pathophysiological responses during sepsis that lead to hyperactive or suppressed immune and inflammatory responses”. A significant recent focus on modeling the immune response during sepsis has emerged to explore the complicated dynamic interaction of cells, tissues, and cytokines during infection (48-54). Existing mathematical/computational models that focus on inflammation provide evidence that the modeling technique is a valid approach for simulating disease progression (48-54). However, limitations to the existing models include: utilization of a small number of variables, limited control parameters, and failure to include extensive experimental data involved in real immune responses. Furthermore, Cross and Opal (32) pointed out the lack of rapid, reliable assays available to identify the stage or severity of sepsis and to monitor the use of immunomodulatory therapy. Such assays are unavailable because of the complexity of the

inflammatory response and the unpredictable nature of septic shock in individual patients; consequently increasing the difficulty of monitoring single or multiple components of inflammation with specific supportive therapies (32, 41).

The motivation of this research was inspired by the evidences and contentions above. This research is aimed to develop a non-biased, predictive model of sepsis progression, and eventually a decision making tool for the treatment of sepsis, including two main research tasks as follows:

1. **Risk assessment:** Develop predictive models to simulate the progression of sepsis.

During this task, specific tasks are as follows:

- Study the impact of cytokine network to the outcomes of inflammatory responses to an infection.
- Identify key parameters and key processes during the development of sepsis.
- Identify various dynamics of pathophysiological responses during sepsis.
- Find out a group of biomarkers during sepsis progression.
- Evaluate the effects of biomarkers to the outcomes of inflammatory responses to an infection.
- Conduct therapy-directed experiments in *silico* for infected individuals with sepsis.

2. **Risk management:** Develop a decision making tool to find out an optimal treatment bundle for treating infected individuals with sepsis. A recommendation on an optimal treatment (among a group of proposed treatments) for classified patients at various stages of hospitalization were provided.

### **1.3 Proposed methodologies**

A mathematical model currently being developed as a dynamic knowledge representation offers a promising possibility for understanding complex local and global dynamics of disease progression. Using a series of known and hypothesized kinetics of components of biological systems from the current literatures, the proposed mathematical models combined the conventional logistics dynamics, the mass-action kinetics, Michaelis-Menten kinetics, and their nonlinear transformations into ordinary differential equations. These simple, sophisticated but generalized dynamic modeling techniques can be developed into mathematical models for better describing an AIR and SIR, by measuring the steady states of various components in inflammatory responses. Mathematical models of AIR/SIR in existing literatures are limited in variable selection. This research proposed mathematical models to calibrate the global dynamics of inflammatory responses by instilling the effects of the indicators (variables) in both innate immunity and adaptive immunity. The selection of the indicators is based on the knowledge about the molecular and physiological pathways of sepsis. To initially validate the proposed mathematical models, the behaviors of the mathematical models are compared with the results from the experimental designs under specific parameter-setting. If the results don't match, the model reconfiguration will be implemented either by adjusting the relationship between the components (indicators) or fine tuning the value of parameters. After the initial validation, sensitivity analysis and stability analysis (using bifurcation theory) are conducted to identify the key parameters and the key processes in the sepsis progression, and provide insights into the appropriate ranges of the key parameters causing the uncertainty in the outcomes. This is one of the most difficult and fundamental steps since the mathematical models exhibited various outcomes, and facilitate the understanding of the complex interactions between the various

components of the AIR and SIR. Also, it is an initial modeling approach for further establishing an agent-based model (ABM) in which a careful analysis of a large amount of experimental data will be used as inputs. A detailed description of the mathematical models of inflammatory responses to an infection (*Salmonella*) is presented in Chapter 3 and Chapter 4.

ABM simulates complicated non-linear dynamic relationships between components and intuitively maps a realistic biological system by incorporating spatial effects and stochastic nature into model construction. Compared to the traditional mathematical models, ABMs are developed to simulate the behaviors of heterogeneous population (cells and cytokines) in the spatial local interactions and map intuitively to a biological system through a series of simple rules and capture its inherent stochastic nature. Key elements of ABM include agents, a collection of decision-making entities (cells and cytokines) classified into different types based on entities described in a real biological system. Each type of agents executes certain behaviors appropriate for the biological system they represent. By implementing a pre-defined set of rules, agents (cells and cytokines) move in a certain direction and arbitrarily interact with other agents (cells and cytokines) in a spatial environment. Agent behaviors are updated in various locations according to update rules executed at discrete time steps. In order to calibrate quantitative changes in agent (cells and cytokines) number, a standard logistic function is used to measure cell population increases, Michaelis-Menten kinetics is applied to calibrate cytokine release, mass-action kinetics is employed to calibrate the activation process of circulating neutrophils and monocytes, and a decay function is used to measure the natural process of apoptosis by cells or catabolism of cytokines. In addition to mathematical models, experimental data such as replication rates of cells, production rate of cytokines, killing rates of *Salmonella* by phagocytic cells, activation rates of circulating neutrophils or monocytes, and apoptotic rate of cells or

catabolism of cytokines are calibrated from existing experimental studies. These data are incorporated into ABM as system parameters. A detailed description of the agent-based models of inflammatory responses to an infection (*Salmonella*) is presented in Chapter 5 and Chapter 6.

In the absence of an analytic decision tool, physicians choose corresponding treatments for patients using heuristic strategies. Computational and artificial intelligence (AI) techniques are applied to predict optimal treatments, minimize side effects, reduce medical errors, and better integrate research and practice (55, 56). However, AI offers optimal clinical decision makings at single decision points. A decision making framework are necessary to extend optimal clinical decision makings from single decision points to multiple decision points (recognized as a decision-making horizon). Compared to AI, Markov decision process (MDP) is designed to make a sequence of optimal decisions at multiple decision epochs. Contemporary health care research has employed MDPs to solve difficult clinical decision making issues over time. For example, MDPs have been proposed to optimize sequential treatment strategies to improve quality of care (quality-adjusted life years) in clinics, or reduce the mortality rates of severe diseases. By specifying the objectives, physicians become aware of “rewards” or “costs” associated with a single treatment at specific time epochs. With a calculated transition matrix, decision makers (physicians) can calculate the total “rewards” for various treatment bundles under a certain decision making horizon, and choose the best treatment bundle. However, the biggest hindrance of a broader application of MDPs to clinical decision makings is data estimation (57). To resolve this difficulty, dynamic patterns of a disease progression were observed from ABM. The probability of one dynamic pattern (one state) transition to another dynamic pattern (another state) during a disease progression can be calculated using ABM. Those calculated transition probabilities are incorporated to a MDP as inputs. A detailed

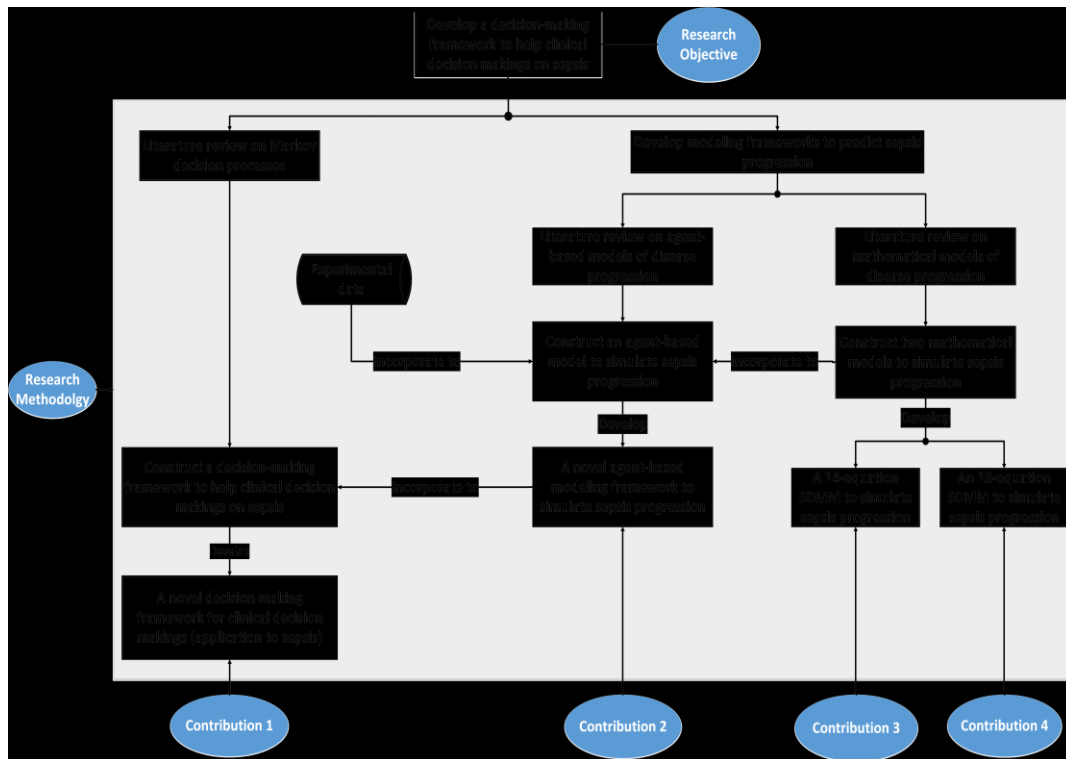
description of the novel MDP with application to a clinical decision making is presented in Chapter 7.

### 1.4 Research map

This research plans to provide scientific and effective predictive models for predicting various dynamic patterns during the development of inflammatory responses to an infection that sometimes progressed to problematic portions, known as “sepsis”. Furthermore, a decision making tool is proposed to help the clinicians treat each patient appropriately, which will significantly decrease the mortality rates of septic individuals, and reduce the huge cost of unnecessary prescription.

Figure 1.1 shows a research map that describes the research objective, research methodologies, and potential research contributions.

**Figure 1.1 Research map**



## 1.5 Outlines

The rest of dissertation is organized into seven sections: 1) Literature Review, 2) Mathematical Modeling of Innate Immunity Responses of Sepsis: Modeling and Computational Studies, 3) Mathematical Model of Innate and Adaptive Immunity of Sepsis: a Modeling and Simulation Study of Infectious Disease, 4) An Autonomous Multi-Agent Simulation Model for Acute Inflammatory Response, 5) A Novel Agent-based Model of Sepsis: a Study on the Hepatic Inflammatory Response in a Mouse infected by *Salmonella*, 6) A Novel semi-Markov decision process for Clinical Decisions Related to Individuals with Sepsis, and 7) Conclusions and Contributions.



## Chapter 2 - Literature Review

### 2.1 Previous mathematical models of inflammatory responses to an infection

In order to construct a mathematical model of sepsis, we searched literatures and found two representative system dynamics mathematical models (SDMMs) of AIR in previous studies. In 2004, Kumar *et al.* (54) presented a simplified 3-equation SDMM to describe mathematical relationships between pathogen, early pro-inflammatory mediators, and late pro-inflammatory mediators in sepsis progression. In 2006, Reynolds *et al.* (53) proposed a mathematical model for AIR that included a time-dependent, anti-inflammatory response in order to provide insights into a variety of clinically relevant scenarios associated with inflammatory response to infection.

Existing mathematical models focused on inflammation in the literature proved that mathematical modeling is a valid approach for simulating disease progression (53, 54, 58-60). However, the number of variables used, the limited control of system parameters, and the inclusion of many variables involved in real immune response were not modeled in detail. Therefore, oversimplification in AIR models (53, 59) limited AIR behaviors and biological relevance of simulated results. For example, simulated results from AIR models (53, 59) failed to capture a dampened oscillated infection in AIR progression. In addition, existing mathematical models are incomplete representations of sepsis because simulated AIR in both mathematical models (53, 59) is considered as an initial stage of sepsis progression. Therefore, to improve on current models, we propose a 14-equation SDMM and an 18-equation SDMM to incorporate the most influential variables for septic response development during innate immune response and adaptive immune response. A detailed description of two SDMMs are provided in Chapter 3 and Chapter 4.

## **2.2 Agent-based model: a surging tool to simulate infectious disease in the immune system**

Chapter 2.2 is based on the paper “Agent-Based Model: A Surging Tool to Simulate Infectious Diseases in the Immune System” published in Open Journal of Modeling and Simulation (2014), Vol. 2, No. 1, pp. 12-22.

### ***Abstract***

Agent-based models (ABMs) are capable of constructing individual system components at different levels of representation to describe non-linear relationships between those components. Compared to a traditional mathematical modeling approach, agent-based models have an inherent spatial component with which they can easily describe local interactions and environmental heterogeneity. Furthermore, agent-based model maps interactions among agents inherently to the biological phenomenon by embedding the stochastic nature and dynamics transitions, thereby demonstrating suitability for the development of complex biological processes. Recently, an abundance of literature has presented application of agent-based modeling in the biological system. This review focuses on application of agent-based modeling to progression in simulation of infectious disease in the human immune system and discusses advantages and disadvantages of agent-based modeling application. Finally, potential implementation of agent-based modeling in relation to infectious disease modeling in future research is explored.

**Keywords:** Agent-based Model; Complex Biological Processes; Progression of Infectious Disease

### ***2.2.1 Introduction***

Infectious disease, identified by clinical symptoms, is defined as the presence and growth of a various type of pathogen in an organism. Under most circumstances, intruding pathogens are eliminated by activating immune cells such as tissue macrophages and activated neutrophils in the immune system. If overwhelming immune response occurs, unbalanced responses between immune cells and cytokines lead to unexpected harmful outcomes for patients. Abundant research has recently focused on modeling immune responses to infectious disease such as sepsis or gut infection in order to explore complicated dynamic presentation of cells and cytokines in the immune system under the presence of infection. Modeling and simulation of immune responses to infectious disease could provide dynamic understanding of infectious disease progression and further acknowledge therapeutic targets for the infectious disease.

As a standard approach, mathematical modeling is currently being developed as a dynamic knowledge representation offering a promising possibility for understanding complex local and global dynamics of infectious disease (53, 54). Using a series of known and hypothesized kinetics of biologic system components from current literature, mathematical models describe infectious disease processes by measuring the steady states of various components in the immune system. However, mathematical models fail to capture inhomogeneous information of various components over the simulation space and fail to describe possible deviations of various components from their aggregated behaviors. As a powerful computational modeling technique, Agent-based model (ABM) simulates complicated non-linear dynamic relationships between components and intuitively maps a more realistic biological system by incorporating spatial effects and stochastic nature into model construction. Key elements of ABM include agents, a collection of decision-making entities classified into different

types based on entities described in a real-world system. Each type of agents executes certain behaviors appropriate for the system they represent. By implementing a pre-defined set of rules, agents move in a certain direction and arbitrarily interact with other agents in a spatial environment. Agent behaviors are updated in various locations according to update rules executed at discrete time steps. Agent-based modeling inherently captures repetitive spatial interactions between agents in a stochastic process and, therefore, is a powerful tool to render valuable information and redraw an overall picture of a biological system. Even simple implementation of ABM requires well-established technology which relies on the power of computers to explore dynamics beyond the reach of pure mathematical methods (61, 62). Because of the inherent nature in computational structure, the agent-based model can be implemented on parallel computers very efficiently (63). This review specifically investigates previous applications of agent-based modeling to infectious disease associated with failure of the immune system to respond to intruding bacteria. Subsequent article sections are organized as follows: 1) review of existing research delineating ABM implementations on infectious disease, 2) discussion of the advantages and disadvantages of ABM on modeling of infectious disease, and 3) prediction of future implementation of ABM on infectious disease and other types of disease in a broader way.

### ***2.2.2 Agent-based Model of Sepsis***

Sepsis, currently defined as a systemic inflammatory response in the presence of an infectious agent or trauma, is increasingly considered an exaggerated, poorly regulated, innate immune response to microbial products (1, 2). Progression to severe sepsis is marked by generalized hypotension, tissue hypoxia, and coagulation abnormality (1). Severe sepsis can further develop into septic shock if long-lasting severe hypotension occurs (1) and ultimately

lead to death. The first application of agent-based modeling of sepsis is employed by An (48). An has produced a very abstract ABM of Acute Inflammatory Response, an initial stage of sepsis progression. His model is built on the interface between endothelial cells and blood at the capillary level to simulate behaviors of circulating neutrophils and monocytes in the presence of injury. Neutrophils and monocytes are defined as agents and their behaviors, including rolling, sticking, diapedesis and respiratory burst, are regulated by a series of state variables which obey fundamental occurrence in AIR environment derived from literature. The variable “total oxy deficit” measures total damage caused by AIR and the state variable “End Injury Vector Number” measures accumulated infection load during AIR progression in order to reflect the characteristics of AIR progression. Using a predefined rule system, multiple independent computer programs are executed with various initial injury extents to generate three general outcomes of AIR progression, including heal, SIRS, and overwhelming infection. Furthermore, the author generates a distributed outcome of AIR progression by calibrating the “oxy” and “End Injury Vector Number” in 500 selected iterations of simulation runs under the same extent of injury. Distribution outcomes confirm that AIR progression is stochastically represented and simulates heterogeneity of a patient population. At the end of his study, An concluded that his agent-based model could not represent a real system but is helpful for understanding essential steps in the inflammatory process at the level of his proposed model. For future research, he expects to produce simulated results that can be validated based on existing experimental studies and use more sophisticated ABMs to test therapies prior to clinical trials in order to refine clinical study design in pharmacological research.

Following his previous work, An continued ABM construction to simulate and compare different therapeutic effects on the improvement of patients’ outcomes (49). The model is

developed at the cellular level and, as in the previous model, built on endothelial-blood interface. Compared to the previous model, however, he incorporated additional agents to represent sophisticated interaction between cells and pathways of immune responses in AIR progression. Positive/negative feedback relationships and interactions between agents are represented and updated using simple arithmetic relationships guided by cellular/molecular mechanisms of AIR progression. The range of initial injury which generates SIR becomes the zone of interest. Distributions of a variable “end oxy deficit (EOD) with respect to different initial injury levels in infectious and sterile models with and without antibiotics, demonstrated that survivability of patients would improve by using antibiotics. Furthermore, An generated four recognizable dynamic behavior patterns of infection, including healing, immune-compromised SIRS, hyper inflammatory SIR, and overwhelming infection under different levels of initial injury. In the end, he intended to test and compare effects of various sets of anti-cytokine therapies which originate from existing clinical trials, animal study and proposed interventions using the proposed agent-based model. Mortality rates associated with anti-cytokine therapies for a group of “patients” demonstrated that anti-cytokine sets are not statistically significant in regards to outcome improvement given design parameters of the clinical trials. Failure of the initial clinical trials, the author concluded, is because redundant pathways of innate immune response could cause therapy interventions to fail to hit the targeted pathway. An criticized the proposed agent-based model for being very abstract model, qualitatively calibrated and difficult to apply in clinics at the current level. More specific analysis, such as grouping septic patients, could account for mortality rates for specific groups of patients instead of a global mortality rate for patients as a whole. Furthermore, as a future research goal, quantitative agent-based models are expected to

calibrate patterns of inflammatory responses using basic scientific data in order to reproduce and illustrate effects of clinical interventions.

Recently, Wu *et al.* proposed an integrated ABM embedded with a mathematical model to simulate AIR progression occurring at the interface between blood vessels and cells within the tissue (64). Five of the total agents are defined in the model: pathogen, resting neutrophils, activated neutrophils, damaged tissue and anti-inflammatory cytokines. The agents' aggregated behaviors reflected characteristics of a class of cells or cytokines in AIR progression and provided biological insight into a series of immune response processes in AIR by describing intercellular interactions among the cells and cytokines. Interactions between agents obey fundamental immune response processes in the AIR environment derived from the literature, and change in the level of each type of agent is derived from ordinary differential equations. By implementing the ABM with corresponding initial profiles of the patients of interest and adjustable system parameters, behaviors of the agents and local intercellular interactions are captured by the simulated results. These results showed three different scenarios of AIR under various combinations of initial conditions: healthy response with low pathogen load, severe sepsis and persistent non-infectious inflammations. By analyzing outputs of patients (combined levels of pathogen, resting neutrophils, activated neutrophils, damaged tissue and anti-inflammatory cytokines) with variation in different initial conditions, the authors concluded that variations in initial levels of pathogen, initial levels of anti-inflammatory cytokines, system parameters associated with anti-inflammatory cytokines, as well as system parameters associated with the pathogen, primarily influenced outputs of patients. The advantage of Wu's agent-based model, compared to other agent-based models is to incorporate a dynamic mathematical

matching to recognized biological kinetics of AIR. However, experimental data incorporation as well as experimental validation is still under development.

Other than modeling interactions between cells, Dong *et al* proposed an ABM framework to model intracellular dynamics of the NF- $\kappa$ B signaling module and further illustrate subsequent intercellular interactions among macrophages and T-helper cells through up-regulation of inflammatory mediators (50). Their approach explored hypothetical scenarios of AIR and potentially improved understanding of behaviors of the molecular species which could develop and expand to emergent behavior of the overall AIR system. Simulated results include five different scenarios under various initial conditions: a self-limited response where the inflammatory stimulus was cleared, a persistent infectious response where the inflammatory stimulus such as LPS failed to be eliminated, a persistent non-infectious inflammatory response where the inflammatory stimulus was eliminated but the inflammatory response was elevated by high concentration of inflammatory stimulus, and two other scenarios associated with endotoxin tolerance and potentiation effects. The advantage of this agent-based model is integration of intracellular responses among inflammatory mediators followed by intercellular responses among immune cells. The disadvantage of this model is that it still uses a qualitative measurement of AIR and does not include experimental validation.

### ***2.2.3 Agent-based model for other types of infectious disease***

Sepsis, or acute inflammatory response, is one kind of infectious disease of primary focus in healthcare and is used to explore immune responses to other types of infectious disease. Along with sepsis, we concluded that most infectious diseases are induced by a series of unbalanced immune responses in the immune system. Agent-based models play an essential role in building interactions between immune responses and gains insight into the unbalanced infectious disease



progression. In 2007, Mi *et al.*, proposed an agent-based model to simulate underlying biological pathways, including interactions among macrophages, neutrophils, and fibroblasts and release of cytokines such as TNF- $\alpha$  and TGF- $\beta$ 1, as a cohesive whole, in diabetic foot ulcers (DFU) while also suggesting novel therapeutic approaches for treating DFU (65). The authors tested and proved that elevated TNF- $\alpha$  or reduced TGF- $\beta$ 1 result in delay of healing process compared with normal skin healing in DFU. Furthermore, they studied debridement intervention in DFU, proposed three types of therapeutic approaches for DFU, and demonstrated, using an agent-based model, that those types of therapeutic approaches could statistically suppress significant tissue damage in DFU. In 2008, Li *et al.*, proposed an agent-based model for simulating inflammation of acute vocal fold injury (66). The agent-based model quantitatively reproduced and predicted trajectories of inflammatory cytokines such as TNF- $\alpha$ , IL-1 $\beta$  and IL-10 under four-hour specific treatments, including spontaneous speech, voice rest, and resonant voice in acute vocal fold injury. Simulation results have shown theoretical individual-specific trajectories of mediator levels across treatments while revealing potential application of agent-based modeling used to design patient-specific therapies in acute vocal fold injury or expansion to other clinical domains. Also in 2008, Dancik *et al.*, proposed an agent-based model to describe natural dynamics of immune response to *L.major* infection (67). They simulated infection of macrophage by *L. major* infection as well as the recruitment of T cells in adaptive immunity response in the presence of chemokines, such as IL-8 to delineate underlying cellular mechanisms of *L.major* infection. By conducting sensitivity analysis, results indicated that strength and timing of adaptive immune response, resting macrophage speed, and transfer threshold of macrophages impact parasite load at the peak of infection. In 2011, an agent-based mode of activation of *Pseudomonas aeruginosa* virulence in the stressed gut was developed to characterize and translate information of the host

response to microbe into a behavioral rule of computational agents (68). Aggregated behavioral rules of computational agents, integrated by modular submodels, described intracellular pathways and cross-cells pathways in gut immunity. Model shows effects of initial *Pseudomonas* population on simulated host injury and measures effects of initial *Pseudomonas* population on gut flora and barrier function. Furthermore, the agent-based model is used to investigate the host-pathogen system as it responds to different experimental conditions which are not developed yet, such as transient intestinal ischemia, host stress, and phosphate depletion. Finally, the authors discussed the discrepancy between observed results in agent-based models and experimental results from animal models and illustrated hypotheses concerning the source of discrepancy. Another agent-based model concerning gut immunity was proposed by Mei *et al.*, in 2012 (69). They simulated the dynamics of gut immunity by delineating interactions among seven types of cells: epithelial cells, macrophages, dendritic cells, neutrophils, B cells, T cells and bacteria. Cell states are represented by a variable list and variable values are changed once cell states have changed. The author assigned three basic rules for changes in the states of cells: interaction with another cell, change in neighboring environment, and presence at the current state for a certain amount of time. Simulated results have shown that chemotactic movement and cytokine-induced cell-state change play critical roles in host-pathogen immune responses of gut immunity.

#### ***2.2.4 Implementing Software Platforms for Agent-based Model***

During the last decade, agent-based models are primarily used for modeling different aspects of real-world problems, such as economics, social networks, and host-pathogen interactions. Agent-based models in relation to economic and social networks deal with interactions among people and the impact of people's aggregated behaviors on complex economic or social situation (70-72). Agent-based models in relation to host-pathogen system,

otherwise, deal with interactions among cells, associated cytokines and their impact on immune system (66-69). The agent-based community has developed several agent-based toolkits, including packaged software and open source platforms to help researchers build their own agent-based model applications. In this section, we review the most commonly used agent-based toolkits and describe their applications.

In 2001, An used Starlogo to build an agent-based application to simulate AIR progression (48). Starlogo and later versions such as MacStarLogo, OpenStarLogo, and StarLogo TNG, are categorized by logo family and developed from the logo programming language. Starlogo is recognized as an educational kit for building agent-based applications. This platform emulates a parallel-processing computer, allowing for simultaneous execution of multiple independent computer programs with a high-level programming language called Starlogo. Starlogo uses a natural programming language to describe real systems, thereby, making it understandable and easy to implement without extensive programming efforts. The main user interface of Starlogo is comprised of two-dimensional grids. The agents can be divided into two categories: “patches” and “turtles.” “Patches” are fixed agents placed on background grids in the model workspace. “Turtles” are mobile agents that occupy a position or move freely on the surface of patches while executing certain functions or actions. Moreover, Starlogo offers a way to define agent set as “breed,” meaning that agent types with similar behaviors or under the control of the same mechanisms. “Breed” allows the modeler to define a class of agents with a set of common state variables and establish various functions or actions (autonomous behaviors) for agent types. Also, the modeler can generate output of a simulation and set parameters in a separate area from the Starlogo interface.

Researchers most frequently recommend and utilize the agent-based toolkit Netlogo (73). Compared with other toolkits within the logo family, Netlogo has a similar programming environment, including platform interface, agent types, and programming statements. Starlogo could easily be converted to Netlogo by adjusting certain statements. Netlogo is recognized by developers of agent-based modeling as an advanced version of Starlogo because it incorporates more agent types such as “link” and, consequently could construct more sophisticated systems (74). Furthermore, Netlogo includes a wide range of library models which could help new researchers prototype their own models. Therefore, Netlogo is recognized as the most professional platform for simulating real systems by providing a simple high-level programming language, built-in graphic interfaces, and comprehensive documentation (74).

Besides built-in, high-level programming language, agent-based platforms such as Starlogo or Netlogo, Objective-C Swarm, and its derived, Java Swarm, provide well-experienced programmers conceptual frameworks for building agent-based models. The primary advantage of Objective-C Swarm and Java Swarm is they help organize different levels of agent-based models into hierarchy and eventually integrate those small agent-based models into a complex agent-based model. This advantage plays an essential role in developing agent-based models for the immune system at the whole body level by integrating several small agent-based models at organ level. However, the disadvantages of Swam platform include lack of novice-friendly development tools, difficulty in building models because of low-level programming language, and low availability of documentation and tutorial material (74).

Recently, another popular implementing software platform for agent-based models, called Repast Symphony, is used in building agent-based simulation (75). Mei’s research group proposed an agent-based simulator called Enteric Immunity Simulator (ENISI) Visual for

modeling gut immunity (69). ENISI Visual has an interface comprised of a series of grids. Each grid has a value indicating concentration of agents, and grid background colors change as states change. The implementer could run the simulator by setting up the initial numbers of indicators, simulation speed, steps, runs, and agent movements (random or chemotactic). ENISI Visual simulator is implemented by Java language based on Repast Symphony, a popular platform for agent-based modeling (75). The homepage of Repast Symphony states that “Repast Symphony is an integrated, richly interactive, cross platform Java-based modeling system that runs under Microsoft Windows, Apple Mac OS X, and Linux. It supports the development of extremely flexible models of interacting agents for use on workstations and small computing clusters.” Specially, Repast Symphony could integrate the Netlogo model into Relogo. The interface of Repast Symphony is comprised of three main parts: the top line is the control panel, the left side is the user panel for setting initial values, and the right side is a visual window for observing agent movements and interactions. The advantage of Repast Symphony is that this software platform could highly customize agent behaviors and interaction among agents by incorporating a programming language such as Java. Few of current agent-based models have been built using Repast, but Repast could be a potential powerful agent-based toolkit with its development in functions.

Mason is recognized as a smaller and faster alternative to Repast, recently designed as a Java-based platform with a multi-agent simulation environment (74). Compared to other agent-based platforms, Mason is recognized as a less mature simulation package but having the least execution time, which is appropriate to simulate agent behavior with much iteration for experienced programmers. We have compared implementation of different agent-based platforms in the following aspects listed in Table 2.1.

**Table 2.1 Characteristics of various types of agent-based simulation platforms**

	Language	Scheduling	Generator	Grid Space	Built-in Agents	Color	Track Agents
Swam	Objective-C	Fixed/Dynamic	Mersen	Non toroidal	No	Colormap	Habitat cells
Java Swam	Java	Fixed/Dynamic		Non toroidal	No	Colormap	Habitat cells
Repast	Java/High-level	Fixed/Dynamic		toroidal	No	Built-in Java color class	Habitat cells
Mason	Java-based	Fixed/Dynamic		toroidal	No	Built-in Java color class	Habitat cells
Netlogo	High-level	Fixed/Partial Dynamic		toroidal	Yes	Color-scaling primitive	Built-in patch

Table 2.1 shows that different characteristics of five agent-based simulation platforms in seven aspects. Only Netlogo has built-in agent and built-in patches which could easily start with building interactions of agents and tracking agents' movement. Other than Netlogo and Repast, Swam, Java Swam and Mason need to write in low-level language with careful design of programming. Especially, Swam need to have a generator to build agents and does not have toroidal interface. Five agent-based toolkits have a mature color function.

When one implements an agent-based model, execution speed is crucial to determine if the agent-based platform is effective. From Railsback's implementations of 16 versions of agent-based models (74), we summarized that Mason is the fastest agent-based platform compared to nearly all versions of the agent-based model. Repast and Netlogo closely follow in results, but Swam is the slowest agent-based platform, especially when complexity increases in model structure. In conclusion, we believe that Netlogo is an appropriate toolkit for new researchers for developing agent-based applications because of its simplified programming environment, easily implemented tool sets, well-developed library model, and well-established documentation support.

### ***2.2.5 Advantages of agent-based modeling on infectious disease***

Agent-based modeling has been employed to describe numerous processes in immunology (63). Complex, nonlinear biological immune processes responding to infection require integrated information to represent interaction effects among various components rather than reconstruct those processes by linearly summarizing characteristics of each single component. Compared to traditional differential equation models, Bonabeau (76) claims that agent-based modeling (ABM) is a powerful simulation modeling technique for naturally describing nonlinear relationships between components in immune responses as a whole. The author explained that ABM could simulate more complicated individual behaviors in spatial and local environments and further exhibit individual learning and adaptation by modeling and simulating behavior of the system's constituent units and their interaction. Later, Bauer *et al.*, (63) classified multiple applications of ABM in immunology. They reviewed various ABMs relevant to host-pathogen systems and discussed contributions to understanding immunology and disease pathology. They pointed out that ABMs are closer to the description and representation of a true biological system compared to traditional modeling techniques. By suggesting directions and velocities of cell movement in simulation, ABMs could easily provide insight into spatial or localized cell interaction in host-pathogen systems while addressing limitations of traditional modeling techniques such as ordinary differential equations and partial differential equations.

A well-detailed agent-based model derived from verified research tells a story about immune system response to various insults. First, by translating basic science evidences of infectious disease into behavioral computational agents, agent-based model is intuitive and easy to understand. Secondly, agent-based model is capable of reconstructing the interactions

between cells and cytokines in relation to specific disease and therefore simulating different kinds of infectious disease. Thirdly, an agent-based model can be developed further by incorporating new types of agents or the interactions of specific types of agents with other agents, leading to greater understanding of the control mechanism for cellular behavior. Moreover, ABM is built with a random event generator, and therefore, is able to simulate the stochastic nature of immune responses to infectious disease. Analysis of various consequences of disease progression for heterogeneous patients can be accomplished by getting insight into the stochastic nature of immune responses. The randomness in an agent-based model is largely embedded in the process of agent interactions, such as one agent choosing to interact with one neighboring agent rather than another. Furthermore, agents could execute certain functions in different locations when they move or interact with other types of agents. For example, in most immune responses, neutrophils execute a series of functions such as moving rolling and adhering upon gradient to endothelial cells when they are in a blood vessel. Once they enter a nearby tissue they execute different functions and interact with various types of cytokines and immune cells. In an agent-based model, behavior of agents and the interactions of one agent with another are highly randomized and spatially-dependent which could not be described by other modeling approaches. Most importantly, in most circumstances, agent-based models are employed to support the development and design of clinical trials. By incorporating single agent-treatment or multi-agent treatment, the agent-based model could demonstrate the evidences observed in experimental design using computational results. ABM could test effects of proposed treatments, prior to clinical trials, and help in designing future potential experiments especially focused on the exploration of new therapeutic approaches. Current therapeutic experiments emphasize mediator-directed treatments. The number of



those experiments largely increases with the development of new knowledge of investigated mediators.

### ***2.2.6 Limitations of agent-based modeling of infectious disease***

Agent-based models clearly have several striking advantages; however, they also have some limitations. Firstly, an agent-based model is defined as an “instructive” tool and cannot represent real immune responses in infectious disease because it fails in one-to-one mapping of components and processes to biological systems. Biological immune responses responding to infection are recognized as a series of complex processes including both intracellular transductions (process of DNA being transferred) and intercellular pathways between cells. Those biological processes will be developed with evolved understanding and continued investigation of cellular and molecular mechanisms. Proposed agent-based models are very abstract descriptions of real systems and are still under development. The challenge of constructing an agent-based model in practice is to appropriately choose the degree of abstraction and avoid unnecessary information while incorporating essential information for recognizable results.

Also, agent behavior and interactions between agents in infectious disease are based on the understanding of basic cellular and molecular mechanisms in immune responses. However, knowledge concerning some interactions may not exist or are still under exploration (77). Furthermore, patterns of immune responses evolved from agent interactions are observed in agent-based models and, compared with results from experimental studies, serve as validation and refinement of agent-based models. However, existing experimental studies may provide contrary information to basic biological mechanisms and patterns of immune responses, which complicates building and validating an agent-based model. Various

experimental conditions, data sampling methods, and experimental designs could contribute to the conflicting results as no uniform standard exists to perform those clinical trials.

Additionally, most existing agent-based models are limited in quantitative validation of simulated results from experimental designs. Instead, they generate qualitative results to represent patterns of progression of infectious disease. However, to further validate the agent-based model, quantitative measurements are necessary to match simulated results with experimental results reported. The validation process requires a large amount of experimental data in order to incorporate or translate those data into an agent-based model. During the validation process, major difficulties occur, such as when some data is unavailable or the data format is not uniform by measurements, leading to incomplete translation of biological information into qualitative simulation.

Furthermore, an agent-based model requires high-level of computational efforts to simulate the detailed interactions among classes of agents in immune responses of infectious disease. The agent-based model is designed to describe the aggregated level of components by simulating individual agent behavior and interactions, and therefore, requires extensive computational effort and the computation efficiency is quite low. If 10 types of agents are defined in an agent-based model and each type of agent initially has 100 agents. A total of 1000 agents' behaviors need to be encoded and decoded when executing the agent-based model. In the case of overwhelming infection, the number of bacteria (one type of agent) can explode to  $10^8$  and a large amount of computational power is therefore needed to run the model.

### ***2.2.7 Future direction of agent-based modeling of infection***

Limitations of current agent-based models provide opportunities for future research. One of the initial steps needed in future research is to refine current agent-based models by adding more sophisticated cellular and molecular pathways in immune system when the immune system responding to various types of infectious disease. For instance, in simulating sepsis progression current agent-based models could be enhanced by adding anti-inflammatory pathways in both innate and adaptive immunity. The agent-based model for simulating diabetic foot ulcers could be improved by incorporating collagen contraction in the wound-healing process (50). By taking into account more molecular interactions and transductions inside cells, the agent-based models could build a bridge between intracellular mechanism and intercellular interactions. The current agent-based models primarily focus on the interface of blood borne endothelial cells as a platform to simulate the initial start of immune responses. The long-term goal of agent-based models is to construct various structures modeling different organs, eventually simulating the physiology at the organ level, and link immune responses at the organ level to systemic responses on a whole-body scale.

With the development of current biological experiments, experimental data could be obtained using experimental designs as inputs into the agent-based model, and quantitative results could be expected in future research. In addition, the existing agent-based models use simple arithmetic rules to regulate and control interactions and movement among agents. In future research, we hope to describe aggregated behaviors of agents in immune responses using well-formed and complete mathematical expressions derived from known and hypothesized kinetics of components of biologic systems.

The current agent-based models require a large computational effort. For instance, Netlogo models, one of many software platforms for the agent-based model, are limited to a few thousand agents running abstract rules on a high-performance computer (78). In particular, a large number of repetitive local interactions among agents greatly increases the running time of the agent-based model. To reduce this computational hurdle, one could use agent-owned variables (local variables) to define each type of agent (64). Values of agent-owned variables will be updated every time period predefined in the model. Similarly, the number of agent types will be updated corresponding to the change in the agent-owned variables. The relationship between the change in number of cells and change in the agent-owned variables is described in Figure 2.1.

**Figure 2.1 Basic structure of agent changing**

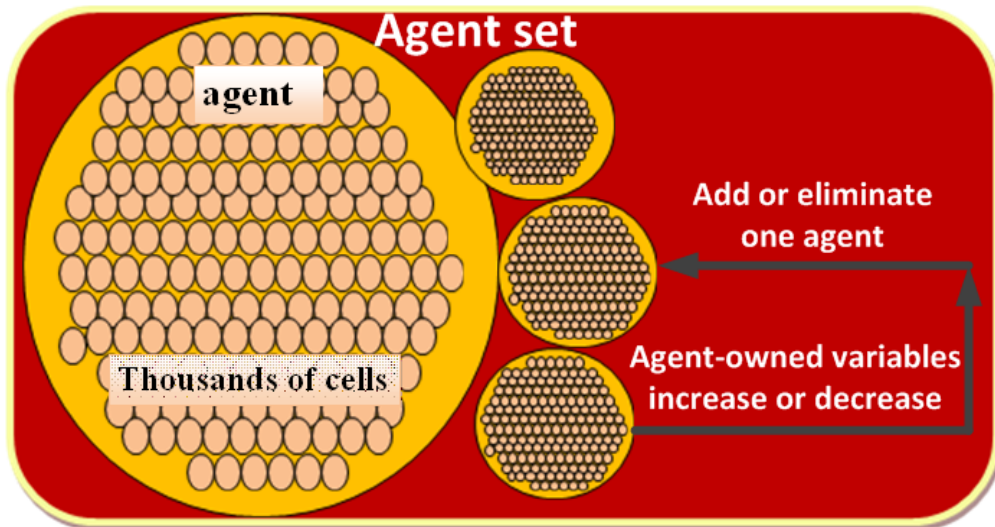


Figure 2.1 shows that agent-specific variables induce the change in the number of agents. Similarly, dynamic agent compression allows a set of homogeneous agents stored in compact bins to make the model more efficient in its use of memory and computational cycles, therefore allowing the user to scale up complexity of the model and run the model more efficiently by increasing execution speeds (79). Furthermore, the Gillespie algorithm proposed

the generation of a statistically correct trajectory for stochastic simulation and streamlining the execution of computational steps (80). More computational algorithms, as well as enhancement of computer power, are expected to implement multi-scale agent-based models. Parallel computers also have a potential to improve ABM applications in the future.

## **2.3 Markov Decision Process: a decision-making framework for improving quality of care in Healthcare System**

### *Abstract*

Since the last twenty years, Markov Decision Process (MDP) has been explored by researchers as an analytical tool with a sound theoretical base to assist hospital physicians in making sequential dynamic decisions regarding treatments. An increasing amount of treatment options to various types of diseases and unpredictable patients' responses to various treatments result in significant bias of clinical outcomes, thus hindering achievement of quality of care in the current healthcare system. Computational-based framework, such as Markov Process, was initially proposed to solve this hindrance by identifying optimal treatment strategies in clinical settings. Compared to traditional computation-based framework, such as Markov Process, MDP is more flexible and accurate, allowing decision makers to adjust treatment strategies under a variety of reasonable objectives. Such objectives can be maximizing expected quality adjusted life days of individual patients, minimizing the length of patients' hospital stay, or minimizing the risk of patients dying from a specific disease. The objective of MDP is to provide a "best" treatment plan, optimizing a particular quality of care objective. In this review, we summarize various types of MDP models and review their application for healthcare, specifically focusing on their usage in dealing with treatment strategies. Furthermore, we discuss computational algorithms for

solving categorized MDP models and provide a numerical example to illustrate an implementation of basic MDP. The paper describes the role and the challenge of MDP application in current healthcare system and propose potential directions for future research.

**Keywords:** Markov Decision Process, Treatment strategies, Healthcare

### ***2.3.1 Introduction***

Effects of medical treatments are uncertain and depend on factors such as the frequency of treatment administered, timing of the treatment, and how individual patients respond to the treatment. Therefore, physicians have difficulty making a “best” judgment on when and how to appropriately treat a patient, especially for a complicated disease with consideration of multiple clinical indicators. Recent clinical data indicates that patients receive effective diagnoses and treatments less than 50% of the time at the hospital (55), exacerbating the inefficiency and low quality of care of the current healthcare system. Since the last two decades, the Markov decision process (MDP) has been proposed as an operational, under-utilized discrete-time stochastic dynamic programming tool for discovering optimal solutions to clinical decision problems (81). Compared to other decision models such as Markov model, MDP is designed for decision-makers who make sequential decisions at multiple time epochs (57). In MDP, the decision maker can observe the state of a system they are interested in, and decide to act or not at each discrete time epoch. The time epoch at which a decision maker makes a decision is called a decision epoch. At each decision epoch, the decision maker can choose one action from an action set. Based on the action chosen, the state of the system transmits to other states according to a known probability distribution and simultaneously receives rewards related to the chosen action. Rewards are accumulated along a decision horizon and an MDP ensures an optimal total reward for a particular criterion, such as maximizing expected quality adjusted life days of individual

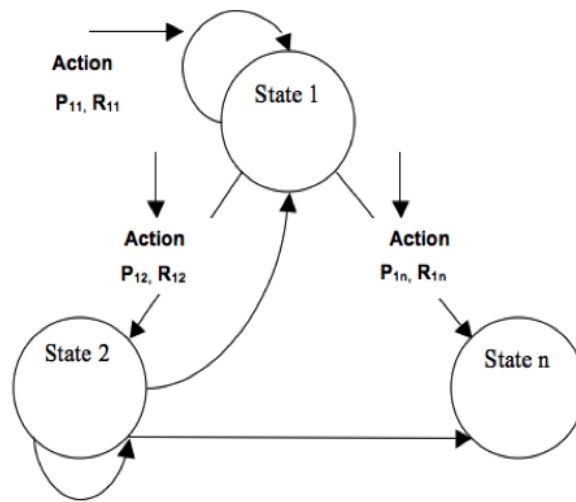
patient, if an optimal sequence of decisions is chosen. MDP is popular in medical decision problems because it can be applied to a situation in which a decision is made at multiple time epochs which is the common medical practice. Furthermore, MDP is more computationally efficient compared to traditional decision modeling, such as decision trees, and therefore more suitable to solve various types of medical decision problems with a large state space. However, MDP is limited because it requires enough quantitative data and an appropriate description of a patient's state, discussed later in this review. Subsequent article sections are organized as follows: 1) Introduction of fundamental MDP structure, 2) Summary of MDP types and related computational algorithms, 3) Review of existing literature delineating MDP application in medical research, 4) Discussion of the impact of current MDP on quality of care improvement in various clinical settings, and 5) Discussion of MDP implementation in future medical research and proposed potential technical solutions to current complications in MDP application.

### ***2.3.2 Fundamental structures of MDP and its extended formulation***

MDP consists of four basic elements: states (variable of interest), actions, transition probabilities, and rewards. For clinical decision-making, physicians care for a patient's health condition, typically utilizing conceptive terms such as healthy and ill to describe a patient's health state. These terms could be further specified by a combined level of indicators, such as pathogen level and the level of serum neutrophils, describing the current health status of a patient. Since an inherent stochastic nature exists in biological processes, individual patients respond to an action (or treatment in clinical decisions) in a variety of ways, leading to possible multiple ended-stages after the action (treatment). MDP employs transition probability to indicate the likelihood of moving from one state to another state. After a transition probability, rewards are assigned specific values to describe consequences in relation to the action

(treatment). Rewards are accumulated in a mathematical expression after a sequence of actions; with the objective of MDP to maximize the total expected rewards. MDP also attempts to find a “best” policy (sequence of actions) that maximizes total expected rewards. Figure 2.2 shows the relationship between states, actions, transition probabilities and rewards in a fundamental MDP structure.

**Figure 2.2 Relationship between states, actions, transition probabilities and rewards in MDP**



In Figure 2.2, State 1 transit to State 2 with a transit probability  $P_{12}$  under an action (treatment), obtaining a reward value  $R_{12}$ . Similarly, State 1 transit to State n with a transit probability  $P_{1n}$  under the same action (treatment), obtaining a reward  $R_{1n}$ . State 1 is recognized as a recurrent state if it retains its current state by implementing an action (treatment). State n is an absorbing state that cannot transit to another state once in an absorbing state. In clinical terms an absorbing state typically refers to a death.

MDP is categorized by length of the decision horizon. A finite-horizon MDP is defined as a MDP with a finite decision time frame, and an infinite-horizon MDP is defined as a MDP with an infinite decision time frame. Finite-horizon MDP is limited by computational intractability as problem complexity increases (82). Compared to a finite-horizon MDP, an



infinite-horizon MDP is converged and solvable in polynomial time under reasonable assumptions because the objective function of an infinite-horizon MDP can be expressed as special linear programs (83). However, decisions in clinical settings are time-concerned, and application of an infinite-horizon MDP in clinics may induce delayed optimal policy. In addition, most MDP applications we reviewed had a finite decision frame, so we presumed that a finite-horizon MDP is more applicable to medical decision than an infinite-horizon MDP. To create a uniform mathematical formulations in this review, we defined a basic MDP following Puterman's notations (84). Corresponding notations and definitions are summarized in Table 2.2.

**Table 2.2 Definition of notations and their range in value**

Not ation	Definition	Range in Value
$A$	Action set	All feasible actions
$Y_t$	An action made at $t$ th decision epoch	$Y_t \in A$
$\lambda$	Discount factor	$(0, 1]$
$A_{X_t}$	Available actions when state is $X_t$	$A_{X_t} \in A$
$S_{t+1}$	State set at $(t+1)$ th decision epoch	All feasible states
$S$	State	All feasible states
$r_{t+1}(j)$	Reward received at state $j$ at $(t+1)$ th decision epoch	All real numbers
$P_t(j X_t, Y_t)$	The probability of transmitting to state $j$ from state $X_t$ when action $Y_t$ is made at $t$ th decision epoch	$[0, 1]$
$X_t$	The state of system at $t$ th decision epoch	$X_t \in S$
$r_N(X_N)$	Reward received at state $X_N$ at $N$ th decision epoch, $N-1$ could be defined as last decision epoch in a finite-horizon MDP	All real numbers
$r_t(X_t, Y_t)$	Reward received at state $X_t$ at $t$ th decision epoch when action $Y_t$ is made	All real numbers
$r_{t+1}(j)$	Reward received at state $j$ at $(t+1)$ th decision epoch	All real numbers
$u_N^*(X_N)$	Optimal utility function when state is $X_N$ at time $N$ , $N-1$ can be defined as last decision epoch in a finite-horizon MDP	All real numbers

$u_t^*(X_t)$	Optimal utility function when state is $X_t$ at $t$ th decision epoch	All real numbers
$u_{t+1}^*(j)$	Optimal utility function when state is $j$ at $(t+1)$ th decision epoch	All real numbers
$\pi$	Policy	A sequence of actions chosen by a decision maker
$u_{t+1}^\pi(j)$	Utility function when state is $j$ at $(t+1)$ th decision epoch under a policy $\pi$	All real numbers
$m$	The predefined number of iterations within step 3 in modified policy iteration algorithm	Normally less than 10
$u_0^*(j)$	Initial optimal utility function when state is $j$ at the initial decision epoch	All real numbers
$V_t^{k+1}(X_t)$	The optimal utility function at $(k+1)$ th iteration within step 3 when state is $X_t$ at $t$ th decision epoch in modified policy iteration algorithm	All real numbers
$Y_\varepsilon(X_t)$	The optimal action when state is $X_t$ at $t$ th decision epoch in modified policy iteration algorithm	$Y_\varepsilon(X_t) \in A$

As follows, a finite-horizon MDP typically utilizes two performance criteria to discern an optimal policy.

Total expected reward in a finite-horizon MDP with discrete decision epochs:

$$v_N^\pi(s) = E_s^\pi \left\{ \sum_{t=1}^{N-1} r_t(X_t, Y_t) + \gamma_N(X_N) \right\}$$

Total discounted expected reward in a finite-horizon MDP with discrete decision epochs:

$$v_N^\pi(s) = E_s^\pi \left\{ \sum_{t=1}^{N-1} \lambda^{t-1} r_t(X_t, Y_t) + \lambda^{N-1} \gamma_N(X_N) \right\}$$

$\gamma_N(X_N)$  denotes the reward obtained at the end stage  $N$  (last stage in a finite-horizon MDP), and  $r_t(X_t, Y_t)$  is the reward obtained at time  $t$  when the state of a system at time  $t$  is  $X_t$  and the action made at time  $t$  is  $Y_t$ . The difference between the total expected reward and the

total discounted expected reward is that the total discounted expected reward is calculated with a factor  $\lambda$  ( $0 \leq \lambda < 1$ ). The factor is defined as a discount factor, and  $\lambda^{t-1}$  is accumulated along the decision horizon to represent a decaying effect of actions (treatments). The concept of a discount factor is proposed under the assumption that patients are less likely to recover from illness if they get a delayed treatment since their health conditions deteriorates with the development of the illness. In an infinite-horizon MDP, three performance criterions are applied to discern an optimal policy. The three performance criterions including total expected reward, total discounted expected reward, and average reward per stage is formulated as follows.

Total expected reward in an infinite-horizon MDP with discrete decision epochs:

$$v_N^\pi(s) = E_s^\pi \left\{ \sum_{t=1}^{N-1} r_t(X_t, Y_t) + \gamma_N(X_N) \right\}$$

$$v^\pi(s) = \lim_{N \rightarrow \infty} v_N^\pi(s)$$

Total discounted expected reward in an infinite-horizon MDP with discrete decision epochs:

$$v_N^\pi(s) = E_s^\pi \left\{ \sum_{t=1}^{N-1} \lambda^{t-1} r_t(X_t, Y_t) + \lambda^{N-1} \gamma_N(X_N) \right\}$$

$$v^\pi(s) = \lim_{N \rightarrow \infty} v_N^\pi(s)$$

Average reward per stage in an infinite-horizon MDP with discrete decision epochs:

$$v_N^\pi(s) = E_s^\pi \left\{ \frac{1}{N} \left( \sum_{t=1}^{N-1} r_t(X_t, Y_t) + \gamma_N(X_N) \right) \right\}$$

$$v^\pi(s) = \lim_{N \rightarrow \infty} v_N^\pi(s)$$

In an infinite-horizon MDP,  $v^\pi(s)$  is used to denote a reward when the decision time frame approaches infinity under different performance criterions. The objective of finite-horizon

and infinite-horizon MDPs is to find an optimal policy  $\pi^*$  (sequence of actions) which can maximize various objectives such as total expected reward, total discounted expected reward, and average reward per stage. To solve a finite-horizon MDP, a common algorithm, such as backward induction, is employed (84, 85), while a simulation-based algorithm, such as multi-stage adaptive sampling algorithm could be applied to solve an infinite-horizon MDP (86). General computational algorithms for solving various types of MDPs are discussed in the next section.

The underlying states of patients are not always perfectly observed in clinics, as for example is the pain scale of a patient. Sometimes, diagnosis to determine the current health state of patients can be applied before administering treatments, enabling physicians to treat patients more accurately and efficiently. The MDP with uncertain states is referred to as Partially Observable Markov Decision Processes (POMDP) (84, 87). POMDP is proposed to employ a general framework to model sequential clinical decisions with hidden states of patients. Total expected reward of POMDPs could be represented as a combination of linear segments solved using an exact value iteration algorithm. However, computational time of solving POMDP is exponential in actions and hidden states, resulting in computationally intractability with moderately sized state spaces (88). Therefore, heuristics algorithms or approximation techniques should be applied to generate solutions to a complicated POMDP (89-93).

A main feature of MDP is being memory-less, which means the effects of treatments in the past don't account into the states of patients in the future. However, the treatment process in clinics is typically memorialized. Under the assumption that treatment process is memorialized, treatment effects could be carried through several stages of the treatment process and future states of patients could be dependent on their current states and their previous states, including

treatment given in the past. Therefore, compared to other MDPs, a semi-MDP built on continuous decision epochs is more applicable under this assumption in a normal clinical situation. To construct a Semi-MDP, a series of concepts and notations must be introduced, as referred to Puterman's work (84).

As stated, each type of MDP approach has certain advantages and disadvantages. An infinite-horizon MDP is advantageous because of ease of implementation and computation, while a finite-horizon POMDP and Semi-MDP are more applicable in reality compared to a standard MDP. A finite-horizon POMDP with diagnosis procedures that apply to patients before treatments has ability to observe episodes of patients before transitioning to severe states. However, both finite-MDP and infinite-MDP approaches fail to consider the continuous effect of treatments. A Semi-MDP which describes continuous or delay-effects of treatments through the previous period to the next periods capture actual treatment effects in clinics. Thus, we conclude that Semi-MDP (84) is a feasible, realistic decision process for general medical decision problems.

### ***2.3.3 Fundamental algorithms of solving MDP***

A variety of computing techniques can be applied to solve MDP problems under different expectations. In this section, we focus on general algorithms, such as backward induction algorithm, value iteration, policy iteration, and modified policy iteration, whose application is dependent on the type of MDP problem. For example, backward induction algorithm is generally applied to a finite-horizon MDP.

#### ***2.3.3.1 Backward induction algorithm***

Backward induction algorithm generates an optimal solution of a MDP model by calculating the accumulated reward value from last decision epoch backwards towards the first

decision epoch. As a commonly used algorithm, backward induction algorithm is typically applied to a finite-horizon MDP. The general procedure of backward induction algorithm (84) is summarized as follows, and corresponding notations in the following procedures refer to Table 1.

Set  $t=N$ , and

$$u_N^*(X_N) = r_N(X_N) \text{ for all } X_N \in S$$

Substitute  $t-1$  for  $t$  and compute  $u_t^*(X_t)$  for each  $X_t \in S$  by

$$u_t^*(X_t) = \max_{Y_t \in A_{x_t}} \left\{ r_t(X_t, Y_t) + \sum_{j \in S_{t+1}} P_t(j|X_t, Y_t) u_{t+1}^*(j) \right\}$$

If  $t=1$ , stop. Otherwise return to step 2.

### 2.3.3.2 Value iteration algorithm

Value iteration algorithm can be applied to an infinite-horizon MDP model to identify an optimal policy. The major procedure of value iteration algorithm is to calculate the expected reward at each state by incorporating rewards from previous states in an iterative procedure until the expected rewards calculated on two successive steps are close enough (referring to step 3) or the difference between expected rewards calculated on two successive steps eventually converges (85, 94). The schematic description of value iteration algorithm is summarized as follows, and corresponding notations in the following procedures refer to Table 1.

Set  $t=1$ , and

$$u_1^*(X_1) = \max\{r_t(X_t, Y_t)\} \text{ for each state, where } Y_t \in A$$

When  $t \geq 1$

$$u_{t+1}^*(j) = \max \left\{ r_{t+1}(j) + \sum_{X_t \in S} \lambda P_t(j|X_t, Y_t) u_t^*(X_t) \right\}, \text{ for each state}$$

Stop when the following inequality holds,

$$\max_{j \in S} |u_{t+1}^*(j) - u_t^*(j)| < \varepsilon, \text{ where } \varepsilon \text{ is constant}$$

### 2.3.3.3 Policy iteration algorithm

Another common algorithm applied to an infinite-horizon MDP model is policy iteration algorithm. Compared to value iteration algorithm, policy iteration algorithm directly manipulates the policy rather than discerning it via difference calculations between two optimal value functions at each execution. For a finite-state with finite-action infinite-horizon MDP, policy iteration algorithm can be reasonably implemented since feasible policies should converge to an optimal policy in a finite number of steps. In policy iteration algorithm, the decision maker chooses an initial policy (set of actions) and calculates total expected discounted rewards at each state by executing the chosen policy. After total expected discounted rewards are calculated, the decision maker checks if improvement can occur by changing any action on states. Therefore, policy iteration is transmuted to a set of linear equations with the objective of minimizing difference between two total expected discounted rewards functions in the space of policies. Optimal policy is obtained when no improvement is observed. Schematic description of policy iteration algorithm is summarized as follows, and corresponding notations in the following procedures refer to Table 2.2.

Set initial policy  $\pi$ , and

$$u_{t+1}^\pi(j) = r_{t+1}(j) + \sum_{X_t \in S} \lambda P_t(j|X_t, Y_t) u_t^\pi(X_t), \text{ for each state}$$

When  $t \geq l$

$$u_{t+1}^*(j) = \max \left\{ r_{t+1}(j) + \sum_{Y_t \in A} \lambda P_t(j|X_t, Y_t) u_t^*(X_t) \right\}, \text{ for each state}$$

Stop when the following inequality holds,

$$\max_{j \in S} |u_{t+1}^*(j) - u_{t+1}^\pi(j)| < \varepsilon, \text{ where } \varepsilon \text{ is constant}$$

#### 2.3.3.4 Modified policy iteration algorithm

Modified Policy Iteration algorithm, a combination of value iteration algorithm and policy iteration algorithm, outperforms features of both those algorithms. The primary purpose of implementing modified policy iteration algorithm is to reduce complexity in computation when calculating utility function in value iteration algorithm and avoiding maximization over the set of decision rules in policy iteration algorithm. Convergence of modified policy iteration algorithm varies depending on different order sequences, and modified policy iteration converges at least linearly and bounded at a rate of convergence for any order sequence (84). Schematic description of modified policy iteration algorithm is summarized as follows, and corresponding notations in the following procedures refer to Table 2.2.

Set  $t = 0$ ,  $t$  is from 0 to  $N-1$ , where  $t$  represents the  $t$  th decision epoch. Specify  $u_0^*(j)$ ,  $\varepsilon$ ,  $\lambda$ , and  $m$ .  $j$  belongs to state  $S_0$  at the initial decision epoch.

Choose an action with respect to each state by

$$Y_{t+1}(X_t) \in \operatorname{argmax}_{Y_t \in A_t} \left\{ r_t(X_t, Y_t) + \sum_{j \in S_{t+1}} \lambda P_t(j|X_t, Y_t) u_t^*(j) \right\}$$

Set  $k = 0$ , where  $k$  represents the number of iterations within step 3

$$V_t^0(X_t) = \max_{Y_t \in A_t} \left\{ r_t(X_t, Y_t) + \sum_{j \in S_{t+1}} \lambda P_t(j|X_t, Y_t) u_t^*(j) \right\}$$

If

$$\|V_t^0(X_t) - u_t^*(j)\| < \varepsilon(1 - \lambda)/2\lambda$$



go to step 4. Otherwise go to (c).

If  $k = m$ , go to (e). Otherwise, compute  $V_t^{k+1}(X_t)$  by

$$V_t^{k+1}(X_t) = r_t(X_t, Y_t) + \sum_{j \in \mathcal{S}_{t+1}} \lambda P_t(j|X_t, Y_t) u_t^*(j)$$

Increment  $k$  by 1 and return to (c).

Set  $u_{t+1}^*(j) = V_t^m(X_t)$ , increment  $t$  by 1, and go to step 2.

Set  $Y_\varepsilon(X_t) = Y_{t+1}(X_t)$  and stop.

### ***2.3.4 MDP applications on septic patients***

Contemporary health care research has employed MDPs to solve difficult clinical modeling issues. For example, MDPs have been proposed to optimize sequential treatments strategies to improve quality of care in clinics or reduce the mortality rate of severe diseases. In the absence of an analytic decision tool, physicians choose corresponding treatments to patients using heuristic strategies. By implementing MDPs, physicians become aware of “rewards” or “costs” associated with a single treatment at specific time epochs. With a calculated transition matrix, decision makers (physicians) can predict the total “reward” regarding various treatment bundles, while making recommendation with respect to optimal sequence of treatment strategies. The following subsections review MDP application in various clinical settings and illustrate advantage of using MDP for clinical treatment decisions.

Sepsis, currently defined as a systemic inflammatory response in the presence of an infectious agent or trauma, is increasingly considered an exaggerated, poorly regulated innate immune response to microbial products (1, 2). The progression to severe sepsis is marked by generalized hypotension, tissue hypoxia, and coagulation abnormality (1). Severe sepsis can further develop into septic shock under long-lasting severe hypotension, ultimately leading to

death. The complex nature of the inflammatory response and the unpredictable nature of septic shock in individual patients render the effect of targeting isolated components of inflammation with supportive therapy difficult to predict (32, 41). Rangel-Frausto *et al.* (8) conducted a prospective study of 2,527 patients with systemic inflammatory response syndrome (SIRS) in a 9-month study period to predict reduction in organ dysfunction and mortality using anti-agent therapy. During the study period, Rangel-Frausto *et al.* categorized patients into five distinct states, including no SIR, SIRS, Sepsis, Severe Sepsis, and Septic Shock. Data was collected by experienced, specially trained nurses to calculate transition probability from one stage to another for a 1-, 3- and 7-day time interval. The authors computed transition rates from collected data and transformed the transition rates to transition probabilities by employing Beck and Pauker formulation (95). Based on calculated transition probabilities, Rangel-Frausto *et al.* developed a Markov matrix to describe the likelihood of change in a patient's initial states to final states at various time intervals of interest. From Markov Modeling, the author determined that patients with highest mortality rate after one day of septic shock would have lower mortality rates if their length of hospital stay increases. Furthermore, the authors calculated the probability of progression from sepsis to severe sepsis to be an average of 72%, but with use of antiseptic agent, the authors' Markov model predicted the probability of developing severe sepsis would decline to 36%. Rangel-Frausto *et al.* developed the first version of MDP application to sepsis treatment, but their application was oversimplified because it only accounted for a single abstract antiseptic agent. Previous research indicated the effectiveness of multiple treatment plans for sepsis, such as anti-TNF, BPI, activated protein-C (41, 46); therefore, a combination of treatments for sepsis could become a focus in intensive care units (ICUs) (32). Considering sepsis mortality rates differentiate among groups and races, Bäuerle *et al.* (96) developed a three-

state Markov model to predict the risk profile of various groups of patients. Kreker (97) proposed a finite-horizon MDP and POMDP to explore the influence of testing decisions on hospital discharge decisions. In Kreker's MDP approach, patients' states were ranked by total Sepsis-related Organ Failure Assessment (SOFA) scores (98) with an integer value ranging from 0 to 24, and the total 25 SOFA score values were aggregated into four patient health states: 1: {0, 1}; 2: {2, 3}; 3: {4, 5, 6, 7}; 4: {8-24}. The states changed after physicians chose to retain patients in hospital or discharge them. Using backward induction algorithm (84), the model was solved to show the existence of an optimal non-stationary policy entitled control-limit policy. Under control-limit policy, the author demonstrated fewer sick patients (health state 1 and 2) should be discharged from hospitals during the early phase of sepsis progression (1-3 days), only healthiest patients (health state 1) should be discharged from hospitals (4-6 days), and only the patients in state 4 {8-24} should remain in the hospital. Compared to the proposed MDP, patients' true health states were no longer modeled as SOFA scores, but they were represented by the value of a measured single cytokine level in the proposed POMDP. The POMDP model defined two specific states associated with patients, or two vectors pertaining to complete and partial observable health state information. Based on current observable elements or any partially observable element obtained through testing procedures at the last decision epoch, a physician must decide at each decision epoch, if they should discharge the patient from the hospital, administer continued treatment to the patient without testing, or continue treating the patient using standard treatment plus additional cytokine test. After defining and formulating POMDP, the proposed POMDP is identified as a discrete POMDP on a finite-decision horizon after admission, in which a decision was made at the end of a day. The testing cost is converted to the units of patient life days using cost-effective analysis (99); therefore, the total expected reward

value is calculated as a function of the patient's length of hospital stay. More specifically, the author defined a belief variable to demonstrate accuracy of the cytokine test. For example, the belief variable is 0.95 indicates that the probability of testing a high cytokine level in accordance with a high actual level of cytokine is 95%. Based on the optimal policy generated by POMDP, the physicians can optimize the patient's total expected length of stay by choosing one of the actions (discharge, continue standard treatment, or order a cytokine test) at the end of a day.

### ***2.3.5 MDP application on other types of disease***

In 2000, Magni (100) *et al.* proposed an MDP approach to determine optimal intervention time for mild hereditary spherocytosis (HS), a disease identified by a chronic destruction of red blood cells. Three treatments, including no surgery, cholecystectomy and splenectomy, were considered in relation to patients' gallstone state and patients' spleen state. The utility function was measured as the objective of maximizing the patient's quality-adjusted life years, and transition probabilities between states were estimated from published tables and previous studies. The author concluded that, if employing the same therapeutic protocols with static approach, the patients had a higher quality adjusted life days in MDP approach. The author also suggested that a splenectomy should not be considered for 6-year old HS children who didn't have gallstones but have spleen. Under this case, the splenectomy should be postponed until they are 15 unless gallstones are found before they are 15. Also in 2000, Hauskrecht *et al.* (89) proposed a POMDP to model and analyze the complex decision process for Ischemic Heart Disease (IHD) and discussed the advantage of POMDP over standard decision formalisms. IHD is caused by an imbalance between the supply and demand of oxygen to the heart, and progression of this disease is uncertain due to multiple factors. Patients who have IHD are defined as two states: live or dead. The states of patients are hierarchically structured, providing a detailed patient description

when the patient is known to be alive. For example, an IHD patient could be described as an alive patient with moderate coronary artery disease, severe chest pain, or positive rest EKG result. Moreover, patients' underlying states such as status of the coronary artery disease cannot be observed directly. Hauskrecht *et al.* implemented investigative actions to obtain additional information about patients' underlying states and used as medical evidence for choosing appropriate treatment action. The hierarchical structure of a patient's state decomposes the probability distribution at various levels, thereby reducing computational complexity of the model. The probability of patients evolving from one state to another is calculated or summarized from previously published data or from the suggestion of domain experts and the chance of being at an underlying state is calculated based on previous states and associated actions. The objective of POMDP is to develop a therapy plan that would minimize expected cumulative treatment cost. The authors integrated the costs associated with surgeries, costs associated with patient pain, and the costs associated with patients' states into a discounted, infinite-horizon utility function. Hauskrecht *et al.* employed revised heuristic procedures to solve their model and their recommendations, to a large extent, meet the expectation of the cardiologists even though areas for model improvement are needed. Overall, Hauskrecht *et al.* claimed that POMDP is an efficient framework to generate good medical strategies. Recently, Shechter (81) *et al.* developed the first human immunodeficiency virus (HIV) MDP model to address the question of optimal time to initiate HIV therapy, with a goal of maximizing the expected lifespan of HIV patients. The author criticized other theoretical or computational studies for possibly generating incorrect outcomes, ignoring the possibility of patient death, and underestimating stochastic progression of patient health. The proposed MDP model had a four-state space, indicating by four distinct categories of CD4 count of HIV patients. Using a least-

squares linear model and cubic smoothing spline, the author predicated HIV patients' CD4 count based on natural history data and recorded monthly CD4 counts. Each month the number of transitions from each CD4 category to the other categories was counted across all HIV patients, and the transition probability matrix of movement between CD4 categories and absorbing state of death was constructed. Using constructed transition probability matrix, the proposed MDP was simulated for the purpose of maximizing expected remaining lifetime. Their conclusion showed that maximum expected lifetime was obtained when the treatment was initiated earlier.

### ***2.3.6 Future research of MDP in healthcare***

Length of hospital stay is an essential indicator to measure quality of care in healthcare, typically measured in the number of days that patients stay in hospitals. Thus, physicians carefully monitor length of hospital stay for septic patients because the longer septic patients stay in the hospital, the higher the probability of ending with severe status and associated hospital costs (32). MDP is objectively designed to help physicians identify proper treatment interventions, thereby minimizing the length of hospital stays. Normally, various treatments could render different clinical outcomes of patients. MDP can also be used to compare the effectiveness of various treatments, using measures such as mortality rate in relation to usage of corresponding anti-therapies. Furthermore, intervention time of treatments can be easily monitored and re-planned by implementing MDP frameworks. Rather than treating patients at each decision epoch, MDP allows decision makers to reconsider sophisticated strategies based on stochastic measurements and achieve optimal goals. Inspired by previous research presented in this review, we have demonstrated that MDP is an appropriate and effective decision-aid tool to model and solve medical decision problems under various expectations.

Numerous versions of MDP implementation have been proposed since the early 1950s, but MDP framework is recognized as an essential sequential decision making tool for medical research since the last ten years, and MDP's advantages have been demonstrated in previous applications. However, a few fertile research questions in MDP are still under considerations. Details contained in the states of MDP are critical because they provide distinct information about patients' states. Currently MDP models utilize a trade-off between the model accuracy and the states detailed description considering computational complexity.

In general, the objective of MDP, formulated as a discounted utility function, has various forms due to biased rewards. Rewards are calibrated through various types of objectives such as effectiveness of treatments, costs of treatments, etc., while these estimators are subjective rather than objective scientific data. For example, the reward of receiving one treatment is categorized from level 0 to level 10, but the actual effectiveness of receiving that treatment is difficult to determine based on patient variations, clinical environments, and other factors. To remedy uncertain reward values within treatments, approach such as reinforcement learning algorithm has been proposed to track changes in rewards and achieves optimal solutions (101). However, the value of reward, typically suggested by experts in clinical domains, is difficult to obtain from solid scientific data resource.

Another difficulty is constructing an accurate transition probability matrix mostly due to lack of sufficient clinical data, and high cost of medical survey or medical experiments. In practice, transition probability that governs the likelihood of moving from one state to another must be estimated at various decision epochs for different individuals, resulting in a need for large scale medical observations and associated costs. As the number of states or feasible treatments increases, derivation of a transition probability distribution becomes more difficult

because the transition probability distribution is intractable from clinical experiments or clinical observations. Since an accurate transition probability matrix is crucial for generating an optimal treatment strategy for individual patients in MDP, the method of constructing an appropriate transition probability matrix has become an expanding research area for future research.

Insights into MDP framework limitations cause us to claim that other modeling approaches, such as mathematical modeling and computational simulation could aid in the construction of future MDPs. By implementing computational simulation such as agent-based modeling (102), practical clinical data or simulated clinical data could be retrieved and integrated into MDPs as inputs. Compared to other modeling techniques, agent-based model can map inherent intercellular interactions in disease progression to a simulation environment. This characteristic of agent-based modeling allows decision makers to retrieve a transition probability matrix in a stochastic way, potentially impacting the application of personalized treatments in future therapeutic development. In addition, an agent-based model is capable of establishing a computational experiment and testing underlying states of patients prior to clinics, consequently leading clinical research to data-concerned, pre-clinical simulation, saving costs associated with conducting clinical trials. Agent-based modeling and other types of modeling approaches could aid decision makers in acquiring valuable clinical information prior to clinical trials, and measure transition probability between patients' states. Most importantly, decision makers can construct their own transition probability matrix via computational simulation tools; and these transition probability matrixes could be updated as new clinical conditions required. With an aid of agent-based modeling, MDPs could describe heterogeneity of disease behaviors in individual patients; thereby greatly improve quality of care in future healthcare system.



## **Chapter 3 - Mathematical modeling of innate immunity responses of sepsis: modeling and computational studies**

Chapter 3 is based on the book chapter “Mathematical Modeling of Innate Immunity Responses of Sepsis: Modeling and Computational Studies” to be published in *Healthcare Analytics: From Data to Knowledge to Healthcare Improvement* (2016), ISBN-13: 978-1118919392, ISBN-10: 1118919394.

### **Abstract**

In general, sepsis is recognized as the “blood poisoning disease” because sepsis occurs when harmful chemical substances enter the blood. In clinics, sepsis is formally defined as a potentially life-threatening complication of diseases accompanied by symptoms such as high fevers, hot, flushed skin, elevated heart rate, altered mental status and so on. If sepsis progresses to severe sepsis or septic shock, organ dysfunction occurs, which leads to a high chance of death.

Patients who suffer from sepsis or septic shock are of great concern in the healthcare system. Recent data indicate that more than 900,000 severe sepsis or septic shock cases developed in the United States with mortality rates between 20% and 80%. In the United States alone, almost \$17 billion is spent each year for the treatment of patients with sepsis. Therefore, it is necessary to find an accurate and effective tool that can help physicians predict the progression of disease in a patient-specific way to prevent possible severe sepsis or septic shock to lower risk for patients.

This chapter presents a fourteen-equation system dynamics mathematical model (SDMM), which model and simulate the basic components of the innate immune response during Acute Inflammatory Response (AIR), the initial stage of sepsis. Our goal is to formally model

and provide insights into the dynamic effects of biomarkers in AIR, especially focus on interactions between pro-inflammatory and anti-inflammatory cytokines during the development of disease. Our simulated results described dynamic patterns of AIR based on patients' initial immune conditions and reveal the important but underexplored dynamic behaviors of anti-inflammatory cytokines on sepsis progression. After the initial model calibration and validation, sensitivity analysis and stability analysis was carried out using bifurcation analysis to explore the system stability during episodes of sepsis progression under various initial and boundary conditions.

We present a new SDMM in this chapter. The strength of this model is that it incorporates the interactions and interplays between pro-and anti-inflammatory cytokines and the possible pathogenesis of AIR based on the host's physiological conditions.

**Keywords:** Acute Inflammatory Response, Pro-Inflammatory Cytokines, Anti-Inflammatory Cytokines, System Dynamics Mathematical Model

### 3.1 Background

Sepsis, currently defined as a systemic inflammatory response in the presence of an infectious agent or trauma, is increasingly being considered an exaggerated, poorly regulated innate immune response to microbial products (1, 2). The progression to severe sepsis is marked by the generalized hypotension, tissue hypoxia, and coagulation abnormality (1). Severe sepsis can further develop into septic shock under the long-lasting severe hypotension (1) and ultimately lead to the death.

Severe sepsis and septic shock during an infection are the major causes of death in an intensive care setting (3). There is an average of 250,000 deaths per year in the United States caused by sepsis (4). Among patients in intensive care units (ICUs), it ranks as the second

highest cause of mortality (5) and the 10th leading cause of death overall in the US (6). Average of 750,000 sepsis cases happen annually and increasing (6). In addition, the quality of life for sepsis survivors is significantly reduced (6, 7). Care of patients with sepsis costs can be as much as \$60,000 per patient. This cost results in a significant healthcare burden of nearly \$17 billion annually in the USA alone (8). The development of sepsis in a hospitalized patient can lead to a longer length of stay in the hospital which implies stiffer financial burden. Cross *et al.* in their research (32) pointed out “the availability of rapid and reliable assays that could be used to quickly identify the stage or severity of sepsis and to monitor therapy may optimize the use of immunomodulatory therapy”. However, no such assays are available because the complex nature of the inflammatory response and the unpredictable nature of septic shock in individual patients render the effect of targeting isolated components of inflammation with supportive therapy difficult to predict (32, 41).

The human immune response evolves to protect the body from infection by harmful pathogens found in the environment (9). This response is characterized by the activation and mobilization of white blood cells, the release of cytokines, and the modification of the vascular and lymphoid tissue (10, 11). Unfortunately, the activation of the immune system can become dysregulated and the immune responses or Acute Inflammatory Responses (AIR) can become pathogenic. Indeed, an uncontrolled AIR may lead to possible sepsis or septic shock. Whether a patient will progress to sepsis, severe sepsis, or even septic shock is determined by a cascade of immune system components. These include, pro-inflammatory cytokines such as tumor necrosis factor- $\alpha$  (TNF- $\alpha$ ), interferon gamma (IFN- $\gamma$ ), interleukins (IL)-1, IL-6, IL-8, and high motility group box-1 (HMGB-1) (32, 103). These cytokines are released to recruit more activated phagocytes to the location of infection to help eliminate the causal pathogen(s). Unfortunately,

this process likely causes tissue damage (104). In addition, anti-inflammatory cytokines such as IL-1ra, IL-4, IL-10, IL-6, and Transforming Growth Factor- $\beta$  (TGF- $\beta$ ) are also released to serve as negative regulators of the response (12, 104).

Recent data indicate that the interactions between the anti-inflammatory responses and the pro-inflammatory responses, determine the prognosis of AIR (13, 104). More specifically, the presence of HMGB-1, which reaches its peak concentrations around eight to twelve hours after it is induced by TNF- $\alpha$ , may be a key component in the progression of AIR. If the level of HMGB-1 remains elevated for long periods of time, the patient may at risk for more severe AIR or developing sepsis (22-24). Also, clinical experiments have demonstrated that monoclonal antibody therapy against HMGB-1 elevation can prevent septic patients from organ damage and subsequent organ dysfunction in both animals and humans trials (36-40). Anti-inflammatory cytokines, such as IL-4, IL-10, IL-13, and IL-14 also play crucial roles in inhibiting the production of pro-inflammatory cytokines and in turn slowing down the progression of AIR (25, 26). For example, circulating levels of IL-6 can be used to predict the severity of acute respiratory distress syndrome, sepsis, and the associated acute pancreatitis (105). Clearly, the levels of pro- and anti-inflammatory mediators are closely linked to the development of severe sepsis and septic shock.

As mentioned above, the levels of cytokines and their presence over time play very important roles in AIR and the development of sepsis; however, there is little data on the quantitative relationships of the cytokine network, which can be used to predict the progression of disease. Kumar *et al.* (54) presented a simplified three-equation SDMM to describe mathematical relationships between pathogen, early pro-inflammatory mediators, and late pro-inflammatory mediators, respectively. However, the model is overly simplified and fails to

represent the overall prognosis of AIR. It lacks several key components including phagocytes, anti-inflammatory cytokines, and the resultant tissue damage. Later, Reynolds *et al.* (53) proposed a mathematical model for AIR that included a time-dependent, anti-inflammatory response in attempt to provide insights into a variety of clinically relevant scenarios associated with the inflammatory response to infection. However, this model missed essential mathematical expression of early and late pro-inflammatory mediators (TNF- $\alpha$ ) and (HMGB-1) that are important biomarkers used in the progression of sepsis during treatments.

The collective disadvantage of current existing mathematical models is that they are incomplete. They only represent some of the essential factors in AIR. Therefore, to improve on current models, we have developed a fourteen-equation SDMM in an attempt to incorporate the most critical variables involved in the development of the septic response and the innate immune system during the AIR. In particular, we have included equations to represent pathogen load, phagocyte (including neutrophils and monocytes) activation, early and late pro-inflammatory cytokine mediators, tissue damage, and anti-inflammatory cytokine mediators.

### **3.2 System dynamic mathematical model (SDMM)**

A mathematical model currently being developed as a dynamic knowledge representation may be a powerful tool to help understand the complex local and global dynamics of AIR and the development of sepsis. Using a series of known and hypothesized kinetics of biochemical and immunological components from the existing literature, this approach provides a comprehensive attempt to model the progression of sepsis. This method combines conventional Logistics dynamics, the laws of Mass-action, Michaelis-Menton kinetics, and their nonlinear transformations into ordinary differential equations. We propose this modeling technique to

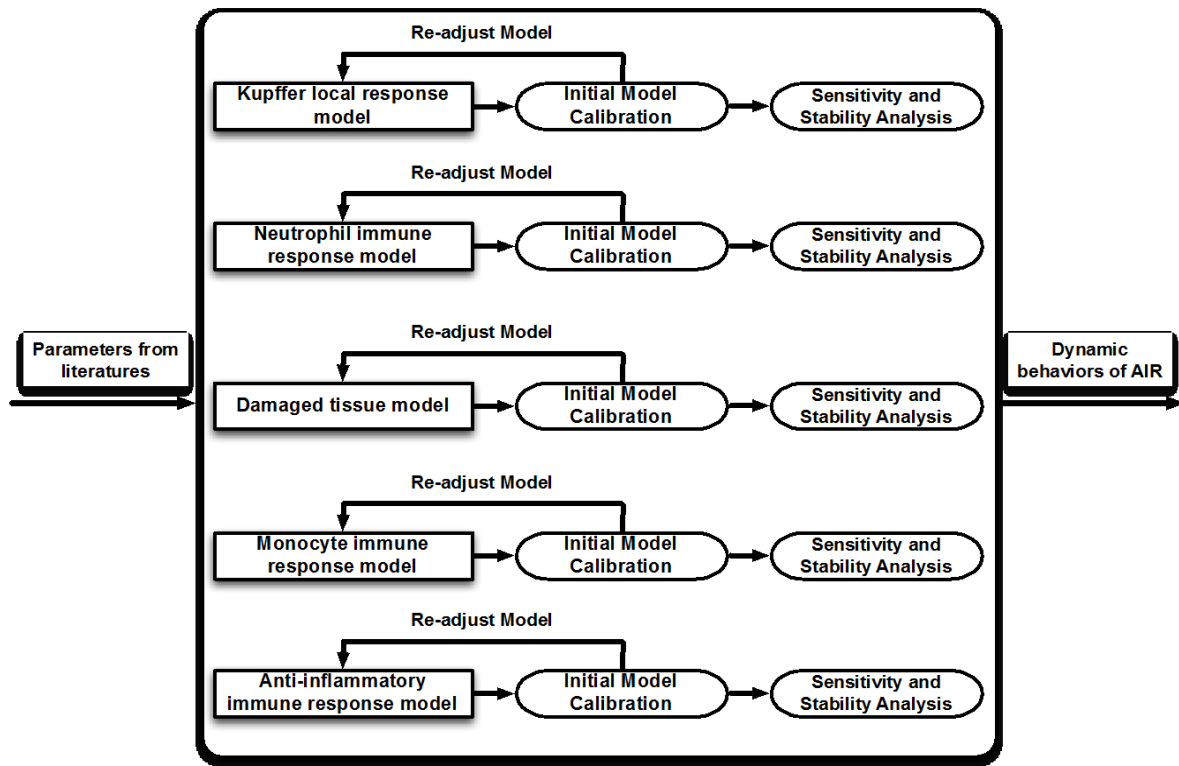
describe AIR and the Systemic Inflammatory Response (SIR) processes by measuring either the steady state or changes of the various components during simulated inflammatory responses.

The first step in our analysis was to create a mathematical model to reflect the global dynamics of sepsis. The variables were selected based on what is known about the molecular and physiological mediators that are important to the development of sepsis. We initially validated the mathematical model by comparing the model outcomes to data from actual experiments. If the results didn't match, equations were rewritten or the model was reconfigured to adjust relationships between the components (indicators). After the initial validation, we conducted sensitivity and stability analyses (based on bifurcation theory). The goal was to identify which parameters and processes were critical in influencing modeled outcomes. We believe that construction of the mathematical model for exhibiting various outcomes and facilitating the understanding of complex interactions between various components in AIR and SIR response, will be one of the most difficult and fundamental steps of using the mathematical model in the future as a platform to generate experimental-dependent results by incorporating a large amount of experimental data. In order to help on reading, we have summarized a framework of the mathematical model in Figure 3.1.

### ***3.2.1 Pathogen strain selection***

We chose *Salmonella* as a “targeted” pathogen strain in our mathematical model and simulated immune responses to *Salmonella* in the liver of mice. We chose *Salmonella* because it is Gram-negative bacteria and *Salmonella* sepsis widely impacts developing countries, commonly occurred in young children (106). Furthermore, immune responses to *Salmonella* sepsis have been investigated in mice's experiments for past several years (107-112) and hence it is effective for us to get either data or evidence support for our mathematical model.

**Figure 3.1 Framework of the system dynamic mathematical model**



### 3.2.2 Kupffer Cell local response model

Macrophages are one of first lines of the innate host defense system against bacterial pathogens. They are important because they are not only antimicrobial cells but also they play a role in the initiation of the adaptive immune response (113). Therefore, macrophages often determine the outcomes of an infection (113). In septic responses, the liver frequently plays a major role in host defense (114). Furthermore, hepatic macrophages (also known as Kupffer cells or resident liver macrophages) constitute 80%-90% of tissue resident macrophages in the body and significantly influence the propagation of liver inflammation (115, 116). Majority of bacteria that enter the blood stream are taken up and eliminated by Kupffer cells within the liver (117).

During the initial stage of an acute inflammatory response, Kupffer cells will eliminate the pathogens, specifically *Salmonella*, during the local immune responses.

The Kupffer cell-related local immune response was defined as the interactions between the pathogen and Kupffer cells (115) and was modeled as follows:

$$\frac{dP}{dt} = k_{pg}P \left(1 - \frac{P}{P_\infty}\right) - r_{pmk} \frac{[P^n]}{[P^n + k_{c1}^n]} M_{kf} P^* \quad (3.1)$$

$$\frac{dM_{kf}}{dt} = k_{mk}M_{kf} \left(1 - \frac{M_{kf}}{K_\infty}\right) + k_{mkub}M_{kb} - \frac{[P^n]}{[P^n + k_{c1}^n]} M_{kf} P^* - u_{mk}M_{kf} \quad (3.2)$$

$$\frac{dM_{kb}}{dt} = \frac{[P^n]}{[P^n + k_{c1}^n]} M_{kf} P^* - k_{mkub}M_{kb} \quad (3.3)$$

In Eq. (3.1),  $P$  denotes the pathogen load.  $k_{pg}$  represents a constant growth rate for pathogens and  $P_\infty$  represents maximum carrying capacity of the pathogen. The parameter  $r_{pmk}$  represents phagocytosis rate of Kupffer cells when Kupffer cells start to engulf pathogens. Although phagocytosis rate is dependent on time in a slow-S-shape curve (118), the phagocytosis rate changes only slightly per hour if we assume the phagocytosis rate versus time is linear, and therefore we relaxed this condition in our model and assumed it was constant (118). Eq. (3.2) represents the changes of the Kupffer cells over a unit time period, and  $M_{kf}$  denotes the amount of Kupffer cells resided in liver available for pathogen binding. The parameter term,  $k_{mk}$ , represents a constant proliferation (replenishment) rate for Kupffer cell population and  $K_\infty$  represents maximum carrying capacity of Kupffer cells. The parameter term,  $k_{mkub}$ , represents the unbinding rate of binding Kupffer cells and  $u_{mk}$  represents the killing rate of free Kupffer cells induced by binding to intruding pathogens.

Here, a standard logistic function is used to model the pathogen population growth with limited maximal carrying capacity, which is the first term ( $k_{pg}P \left(1 - \frac{P}{P_\infty}\right)$ ) in Eq. (3.1) (119). The second term of Eq. (3.1) models the local Kupffer cell responses, the decrease in pathogen



population phagocytized by initial tissue resident macrophages (Kupffer cells). This process includes two steps: pathogen-ligand binding to the receptors of Kupffer cells and the actual phagocytosis by Kupffer cells. We used a Hill-type function and receptor-ligand kinetics to model the two basic steps (109, 113, 115, 120-122). First, we define the rate of pathogen binding to Kupffer cells as a Hill-type function  $(\frac{[P^n]}{[P^n+k_{c1}^n]})$ . Here,  $n$  represents a strong affinity of pathogen binding to Kupffer cells and  $k_{c1}$  is the pathogen concentration occupying half of Kupffer cell receptors. Second, we modeled pathogen to Kupffer cell receptors using receptor-ligand kinetics  $(\frac{[P^n]}{[P^n+k_{c1}^n]}M_{kf}P^*)$ , where  $P^*$  represents pathogen concentration. We determined the pathogen concentration using the number of pathogens divided by the maximum carrying capacity of pathogen ( $10^8$  cells in mouse (112)). The final variable to determine the pathogen is the phagocytosis rate of pathogens by Kupffer cells (represented by  $r_{pmk}$ ) times the portion of pathogens binding to Kupffer cells  $(\frac{[P^n]}{[P^n+k_{c1}^n]}M_{kf}P^*)$ .

We assumed that Kupffer cells population growth followed a standard logistic growth pattern with a constant proliferation (replenishment) rate denoted as  $k_{mk}$ , and a maximal carrying limit,  $K_\infty$ , represented by the first term  $(k_{mk}M_{kf}(1 - \frac{M_{kf}}{M_\infty}))$  in Eq. (3.2). Since the binding of a pathogen did not preclude the phagocytosis of additional bacterial after the completion of phagocytosis, we used receptor-ligand kinetics to model the release of Kupffer cells from the binding-complex, which is represented by the second term  $(k_{mkub}M_{kb})$  in Eq. (3.2) and  $k_{mkub}$  represents the rate of the motile enterobacteria (i.e., *Salmonella*) are phagocytosed by the free Kupffer cells and made available for additional interactions with motile enterobacteria. The decreasing number of free Kupffer cells is due to two things: the free Kupffer cells binding to pathogen, which is described by the third term  $(\frac{[P^n]}{[P^n+k_{c1}^n]}M_{kf}P^*)$ , also the natural decay of free

Kupffer cells represented by the fourth term ( $u_{mk}M_{kf}$ ) in Eq. (3.2). The free Kupffer cells become binding Kupffer cells once they bind to pathogen, which is described by the first term ( $\frac{[P^n]}{[P^n+k_{c1}^n]}M_{kf}P^*$ ) in Eq. (3.3). The second term ( $k_{mkub}M_{kb}$ ) in Eq. (3.3) measures decreasing (releasing) portion of binding Kupffer cells. The definition of parameters and corresponding experimental data for each system parameter in Kupffer local response model are summarized in Table A.1.

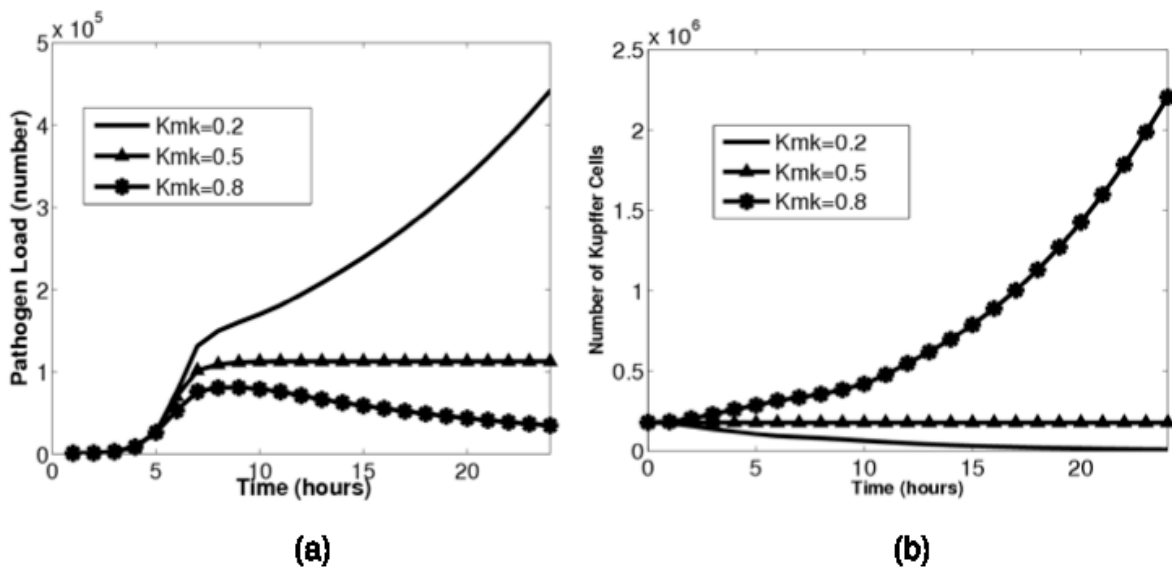
Experimental results show that 50% *Salmonella* are phagocytosed by Kupffer cells in liver, and we used this fact to determine the number of Kupffer cells that phagocytoses half of *Salmonella* equal to the number of Kupffer cells in the liver (110). Experimental data also show that *Salmonella* ingestion can kill macrophages, and such macrophages will no longer return to the active state for pathogen binding if they are killed (111). Our assumption was that the “dissociation” rate of Kupffer cells is equivalent to 1-infected rate of Kupffer cells. This is based on data showing Kupffer cell activity could range from 0.1 to 0.77 from known infection rates (111). Other parameters are either directly derived from published observations in literature or will be estimated from our model. Our sensitivity analysis revealed that this system is highly sensitive to the proliferation (replenishment) rate of Kupffer cells ( $k_{mk}$ ).

The data are represented by plotting the number of motile enterobacteria and Kupffer cells (arbitrary units) versus time (hours) based on the variation in the proliferation rate (including the growth rate of Kupffer cells, as well as the recruitment rate of monocytes from the blood vessels) of Kupffer cells ( $k_{mk}$ ) in Figure 3.2 (a) and (b).

Figure 3.2 indicates that Kupffer cells alone are not able to resolve an infection when the “proliferation rate” of Kupffer cells is less than 0.5/h. In this simulation, all Kupffer cells are phagocytosing pathogens and there are no Kupffer cells available to phagocytose additional

motile enterobacteria, and hence phagocytosis fails to continue. However, the pathogen could be cleared completely if Kupffer proliferation rate is set relatively high. In our model, we assume the proliferation rate of Kupffer cells in liver comprises two parts: the natural growth rate of Kupffer cells and the recruiting rate of monocytes from the nearby blood vessels. The results of the experimental studies show that the local growth rate of Kupffer cells is low and stable with 0.015/h (123, 124). Therefore, we conclude that the increase in proliferation rate of Kupffer cells is due to the increasing recruitment rate of monocytes from blood vessels, with those recruited monocytes contributing to the clearance of local infection. Based on our simulation results, we could further inference that Kupffer cells are not a major responder to resolve an overwhelming acute inflammatory response episode, which allows us to model the effects of other immune cells during AIR such as neutrophils and monocytes.

**Figure 3.2 (a) Concentration of *pathogen* load versus time, for three different proliferation rates of *Kupffer cells* in Kupffer local response model. (b) Concentration of *Kupffer cells* versus time, for three different proliferation rates of *Kupffer cells* in the Kupffer local response model. The horizontal axes represent the time in hours, and the vertical axes represent concentration in arbitrary units**

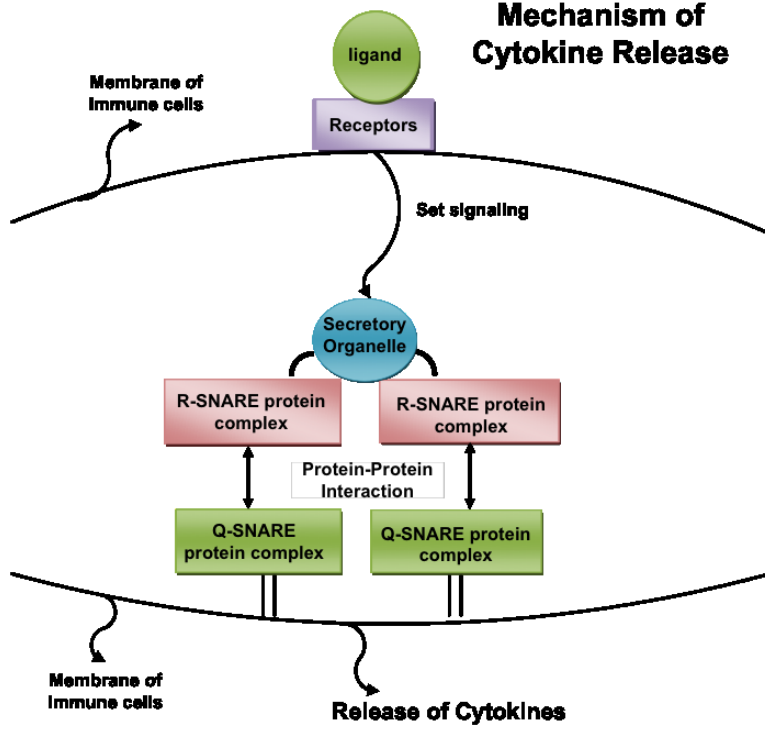


### ***3.2.3 Neutrophils immune response model***

The results in the Kupffer immune response model show that Kupffer cells may not be sufficient to eliminate the infection, especially when the local infection is overwhelming. The Kupffer cells in local immune response release pro-inflammatory cytokines such as TNF- $\alpha$ , which contribute to the recruitment of neutrophils in the circulation and accumulation of neutrophils in the liver (transmigration) (125-127). The transmigration can be mediated by a chemokine gradient (e.g., TNF- $\alpha$ , IL-1, CXC chemokines, and PAF) established towards the hepatic parenchyma which generally involves the adhesion molecules on neutrophils ( $\beta_2$  integrins) and on endothelial cells (intracellular adhesion molecules, ICAM-1). After transmigration, neutrophils adhere to distressed hepatocytes through their  $\beta_2$  integrins and ICAM-1 expressed on hepatocytes. Neutrophils contact with hepatocytes mediate oxidative killing of hepatocytes by initiation of respiratory burst and neutrophil degranulation leading to hepatocellular oncotoc necrosis. Neutrophils, as a double-effect mediator, will either phagocytose pathogens or induce tissue damages by killing distressed hepatocytes (127). Furthermore, activated neutrophils (priming) will release TNF- $\alpha$  and therefore recruit even more neutrophils to the site of infection (128). The release of cytokines follows trafficking machinery and the cytokines are released via protein-protein interactions initiated by the ligand binding to the receptors (129, 130). The mechanism of cytokine release is depicted in Figure 3.3.

During the process of cytokine release, R-SNARE protein complex on the membrane of the secretory organelle will interact with Q-SNARE protein complex on the membranes of different types of immune cells, which allows membrane fusion and extrusion of cytokines from the granule interior (129). We model a protein-protein interaction as Michaelis-Menten kinetics (131) and derive our neutrophil immune response model as follows:

Figure 3.3 Mechanism of cytokine release



$$\frac{dP}{dt} = k_{pg}P \left(1 - \frac{P}{P_\infty}\right) - r_{pmk} \frac{[P^n]}{[P^n + k_{c1}^n]} M_{kf} P^* - r_{pn} \frac{[P^n]}{[P^n + k_{c2}^n]} (N_f + N_b) P^* \quad (3.4)$$

$$\frac{dM_{kf}}{dt} = k_{mk} M_{kf} \left(1 - \frac{M_{kf}}{K_\infty}\right) + k_{mkub} M_{kb} - \frac{[P^n]}{[P^n + k_{c1}^n]} M_{kf} P^* - u_{mk} M_{kf} \quad (3.5)$$

$$\frac{dM_{kb}}{dt} = \frac{[P^n]}{[P^n + k_{c1}^n]} M_{kf} P^* - k_{mkub} M_{kb} \quad (3.6)$$

$$\frac{dT}{dt} = \left(\frac{r_{1\max} M_{kb}}{m_{t1} + M_{kb}}\right) M_{kb} + \left(\frac{r_{2\max} N_b}{m_{t2} + N_b}\right) N_b - u_t T \quad (3.7)$$

$$\frac{dN_R}{dt} = k_{rd} N_R \left(1 - \frac{N_R}{N_S}\right) - r_1 N_R (T + P)^* - u_{nr} N_R \quad (3.8)$$

$$\frac{dN_f}{dt} = r_1 N_R (T + P)^* + k_{nub} N_b - \frac{[P^n]}{[P^n + k_{c2}^n]} N_f P^* - u_n N_f \quad (3.9)$$

$$\frac{dN_b}{dt} = \frac{[P^n]}{[P^n + k_{c2}^n]} N_f P^* - k_{nub} N_b \quad (3.10)$$

$$\frac{dr_1}{dt} = k_{r1} (1 + \tanh(N_f^*)) - u_{r1} r_1 \quad (3.11)$$

Eq. (3.4) is further derived from Eq. (3.1) in the Kupffer local immune response by incorporating the phagocytotic effects of neutrophils, which is represented by term  $r_{pn} \frac{[P^n]}{[P^n + k_c^n]} (N_f + N_b) P^*$ . Details about parameters are defined in Table A. 2. Eq. (3.5) and Eq. (3.6) are cited from Eq. (3.2) and Eq. (3.3).

Eq. (3.7) represents the changes of the pro-inflammatory cytokines (denoted by  $T$ ) such as TNF- $\alpha$ , released by both binding tissue resident Kupffer cells ( $M_{kb}$ ) and binding activated Neutrophils ( $N_b$ ) along with a constant degradation rate ( $u_t$ ). Since TNF- $\alpha$  was released after pathogens binding to the receptors of tissue resident macrophages or neutrophils, we model the process of TNF- $\alpha$  release as a combination of Michaelis–Menten kinetics and receptor-ligand kinetics (10). In Eq. (3.7), the release of TNF- $\alpha$  from Kupffer cells is initiated by a receptor-ligand kinetics and secondly following enzymatic kinetics (Michaelis-Menten) represented by the term  $\left( \frac{r_{t1max} M_{kb}}{m_{t1} + M_{kb}} \right)$  where  $r_{t1max}$  represents the maximal production rate of TNF- $\alpha$  by binding Kupffer cells. It is well known that the release of TNF- $\alpha$  is a combined effect of both receptor-ligand kinetics and enzymatic kinetics, and therefore, we incorporate both terms together  $\left( \frac{r_{t1max} M_{kb}}{m_{t1} + M_{kb}} \right) M_{kb}$  in the model to represent the combined effects of the TNF- $\alpha$  releasing processes. Similarly, we use the same principle to model the release of TNF- $\alpha$  contributed by activated neutrophils in the second term in Eq. (3.7). The third term in Eq. (3.7),  $u_t T$ , measures the degradation of TNF- $\alpha$ , with  $u_t$  representing the degradation rate of TNF- $\alpha$ .

In Eq. (3.8), the first term  $k_{rd} N_R \left(1 - \frac{N_R}{N_S}\right)$  is a standard logistic function to measure the increase in number of resting neutrophils per time unit (hour), which is represented by the influx of neutrophils into blood vessel per hour. The second term  $r_1 N_R (T + P)^*$  describes that the decrease in number of resting neutrophils per time unit is due to neutrophils activation process

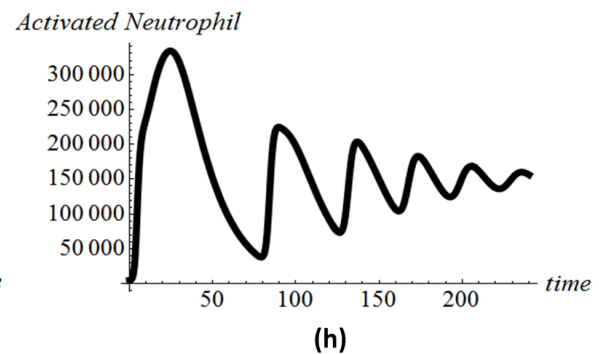
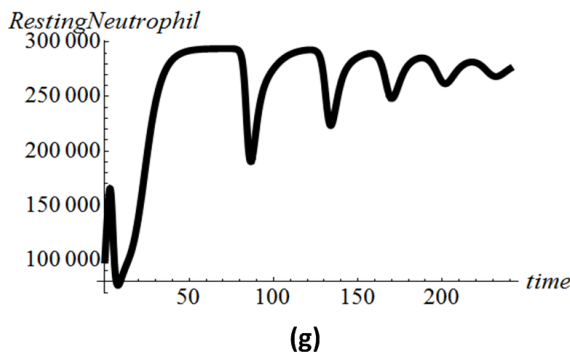
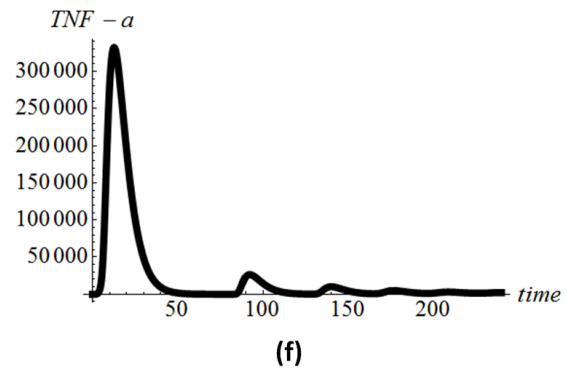
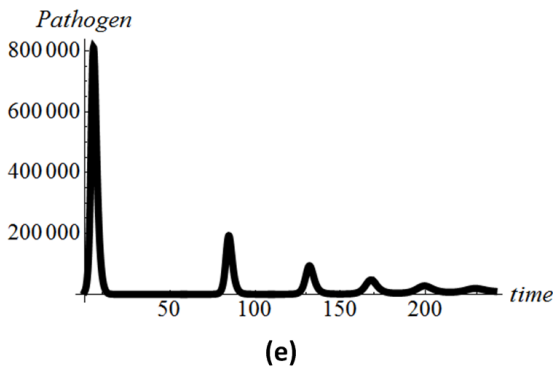
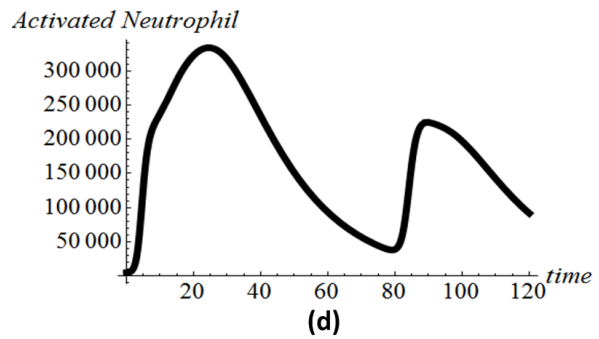
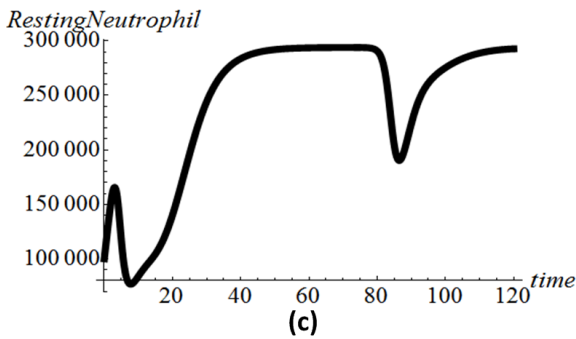
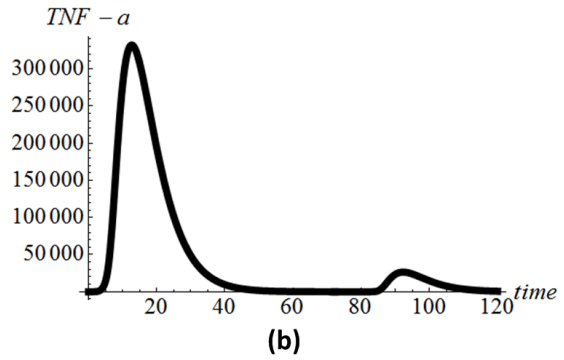
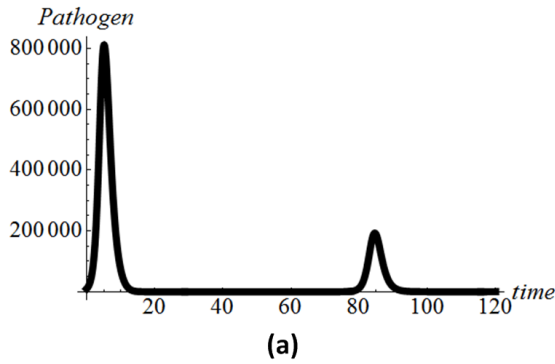
promoted by pro-inflammatory mediator  $TNF-\alpha$  where  $T^*$  denotes the concentration of  $TNF-\alpha$ , and  $P^*$  denotes the concentration of pathogens (126-128). The third term in Eq. (3.8)  $\mu_{nr}N_R$  represents the natural decay of resting neutrophils and  $u_{nr}$  is defined as the apoptotic rate of resting neutrophils per time unit in hours. In Eq. (3.9), the first term exactly equals to the second term in Eq. (3.8) since the increase population of activated neutrophils results directly from the population of resting neutrophils being activated. The second term of Eq. (3.9), used mass action kinetics ( $k_{nub}N_b$ ) to model the release of activated phagocytes from the binding-complex and make activated phagocytes available for additional interaction with pathogens, where  $N_b$  represents the binding-complex and  $k_{nub}$  represents the rate of activated phagocytes releasing from the binding-complex. The third term of Eq. (3.9), similar to the third term in Eq. (3.8) modeling the natural apoptosis of activated neutrophils.

Eq. (3.10) is similar to the derivation of Eq. (3.3) in Kupffer local response model. We used a hyperbolic tangent function in Eq. (3.11) to represent a slow-saturation influx rate of neutrophils into hepatic parenchyma and therefore represent the rate of resting neutrophils being activated. The definition and corresponding experimental data for newly added system parameters in neutrophils immune response model are summarized in Table A. 2.

By substituting the above experimental data into our neutrophil immune response model, we plot the pathogen loads,  $TNF-\alpha$ , resting neutrophils, activated neutrophils versus time (hours) using mathematica, and the computed results are shown in Figure 3.4 (a), (b), (c), and (d).

**Figure 3.4 (a) Concentration of *pathogen* versus time in neutrophil immune response model at the first 120 hours of simulation. (b) Concentration of *TNF- $\alpha$*  versus time in neutrophil immune response model at the first 120 hours of simulation. (c) Concentration of *resting neutrophils* versus time in neutrophil immune response model at the first 120 hours of simulation. (d) Concentration of *activated neutrophils* versus time in neutrophil immune response model at the first 120 hours of simulation. (e) Concentration of *pathogen* versus time in neutrophil immune response model at the first 240 hours of simulation. (f) Concentration of *TNF- $\alpha$*  versus time in neutrophil immune response model at the first 240**

hours of simulation. (g) Concentration of *resting neutrophils* versus time in neutrophil immune response model at the first 240 hours of simulation. (h) Concentration of *activated neutrophils* versus time in neutrophil immune response model at the first 240 hours of simulation. X axes represent time (hours), and Y axes represent concentration in arbitrary unit



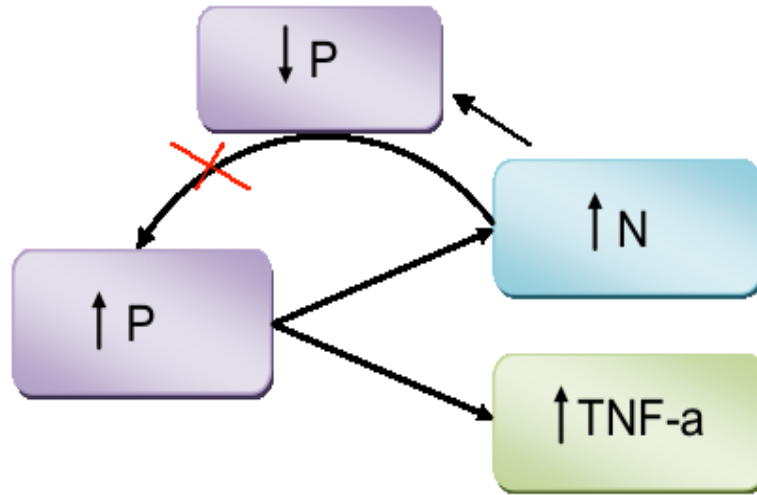


Compared to the result in Figure 3.2 (a), the result in Figure 3.4 (a) shows that pathogen load peaks out and decreases significantly in a short time period (around 10 hours from our neutrophil immune response model) if the effects of neutrophils are incorporated. Regardless of the overall effects of immune cells in the liver, experimental studies have shown that mice at 6 hours after infection exhibit a large decrease ( $0.6\log_{10}$ ) in bacteria correlating with the influx of neutrophils (117). The bulk of clearance of bacteria or pathogen is largely due to influx of neutrophils and their programmed mechanism to ingest bacteria and other harmful microorganisms (132). Being one of the major immune cells arrived early at the site of infection; neutrophils play an essential role in the initial stage of AIR and further influence the downstream progression of AIR. Also, previously activated neutrophils release pro-inflammatory cytokines such as TNF- $\alpha$ , and newly released TNF- $\alpha$  helps to recruit more neutrophils from blood vessels to the site of infection. Our neutrophil immune response model recapitulates the patterns of TNF- $\alpha$  reported in literature that TNF- $\alpha$  concentration in the liver increases to a peak at 6 hour after infection and trends down toward baseline by 24 hour (Figure 3.4 (b)) (133). The peak level of activated neutrophils occurs around 10 hours after infection, later than occurrence of TNF- $\alpha$ 's peak level, and trends down toward the baseline in 3 days (72 hours) after infection from our simulation results (Figure 3.4 (d)). Furthermore, we observed infection is "oscillated" during first 500 hours of simulation in Figure 3.4 (e), (f), (g) and (h), which matches to biological experimental data in literature (132). The relationships among pathogen, TNF- $\alpha$ , and activated neutrophils, shown in Figure 3.5, are interconnected with each other, based on our model.

Figure 3.5 provides a simple logistic chart to illustrate the interactions between each component in our neutrophil immune response model. An increase in pathogen (denoted as P in Figure 3.5) will induce the production of TNF- $\alpha$  and further help to recruit more activated

neutrophils (denoted as  $N$  in Figure 3.5), which contribute to the decrease in pathogen load. We conclude that the clearance of pathogen is more dependent on the effects of infiltrating neutrophils in liver than on the Kupffer Cells in liver after comparing the results from both models.

**Figure 3.5 Interactions between *pathogen*, *activated neutrophils*, and *TNF- $\alpha$***



### 3.2.4 Damaged tissue model

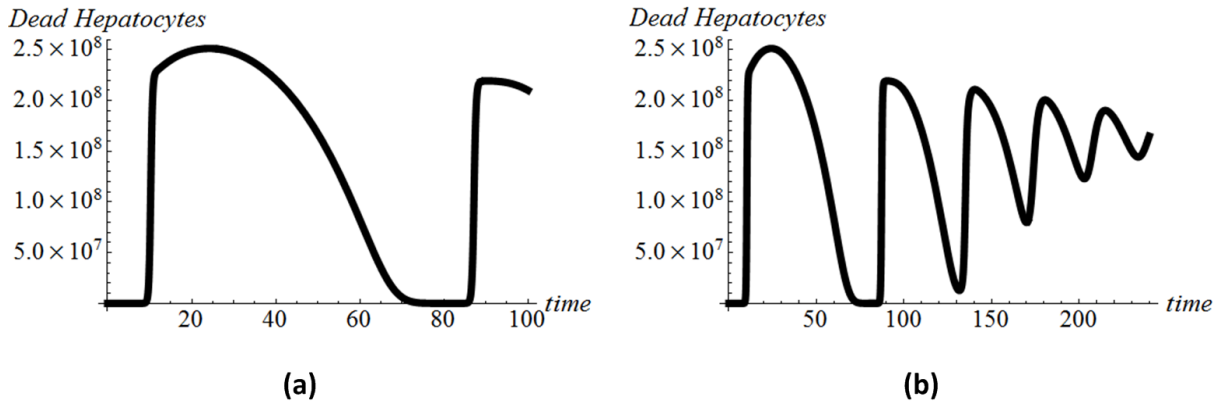
The complexity in AIR is due to the multiple effects induced by inflammatory cells. We show that the recruitment of neutrophils helps to clear local pathogen level; however, those inflammatory cells are harmful at the same time because they release toxic molecules such as reactive oxygen species (ROS), which could cause damage to the host tissue (127, 128). Recent experimental results show neutrophils'  $\beta_2$  integrins adhere to the ICAM-1 receptors of hepatocytes and accelerate the killing process of distressed hepatocytes (134). We assume the binding process of neutrophils to hepatocytes also follows ligand-receptor kinetics and derive the following damaged tissue model.

$$\frac{dD}{dt} = r_{hn} \left( \frac{D^n}{D^n + k_{c3}^n} \right) N_f D^* \left( 1 - \frac{D}{A_\infty} \right) - r_{ah} D \quad (3.12)$$

In Eq. (3.12),  $D$  denotes the number of apoptotic hepatocytes or dead hepatocytes) and  $r_{hn}$  represents the rate of apoptotic hepatocytes killed by activated neutrophils and  $r_{ah}$  represents the recovery rate of apoptotic hepatocytes. The ligand-receptor kinetics  $\frac{[D^n]}{[D^n+k_{c3}^n]}N_fD^*$  is used to represent the amount of apoptotic hepatocytes that bind to activated neutrophils, with the binding rate being modeled as a Hill-type function  $\frac{[D^n]}{[D^n+k_{c3}^n]}$ . The activated neutrophils have recently been found to kill the apoptotic hepatocytes (134). After neutrophil adhered to apoptotic hepatocytes, the neutrophils release reactive oxygen species and proteases, which accelerate the death of apoptotic hepatocytes (134, 135). Multiplying  $\frac{[D^n]}{[D^n+k_{c3}^n]}N_fD^*$  by  $r_{hn}$ , the entire first term in Eq. (3.12) represents the number of apoptotic hepatocytes killed by activated neutrophils per hour, which is the total number of dead hepatocytes per hour. The maximal number of apoptotic or dead hepatocytes will not exceed the total number of hepatocytes in liver (represents by  $A_\infty$ ). In addition, we use  $r_{ah}$  to represent the recovery rate of apoptotic hepatocytes and the second term in Eq. (3.12) is defined as the amount of recovering apoptotic hepatocytes. The definition of parameters and corresponding experimental data in damaged tissue model are summarized in Table A.3, and Figure 3.6 shows the concentration of dead hepatocytes versus time (hours).

Our simulation result shows that the population of dead hepatocytes significantly increases by 12 hours. The dead hepatocytes are defined as accumulated apoptotic hepatocytes over time. In the Gal/ET shock model (135), neutrophils extravasate in response to 15–20% of hepatocytes undergoing apoptosis at 6 hour and the neutrophil attack expands the tissue damage to 40–50% of hepatocytes by 7 hour. Our simulation results correspond to the evidence that about 15% of hepatocytes are undergoing apoptosis at 9 hours and the tissue damage is expanding to around 40% of hepatocytes by 10 hours with the attack of neutrophils.

**Figure 3.6 (a) Concentration of *dead hepatocytes* versus time in damaged tissue model at the first 100 hours of simulation. (b) Concentration of *dead hepatocytes* versus time in damaged tissue model at the first 240 hours of simulation. X axes represent time (in hour) and Y axes represent concentration in arbitrary unit**



### 3.2.5 Monocytes immune response model

Recent biological experiments from the literatures (136, 137) have shown that monocyte, recruited by the presence of HMGB-1, plays an essential role in the liver inflammation and liver fibrosis. Upon liver injury, the inflammatory Ly6cC (Gr1C) monocyte subset as precursors of tissue macrophages in blood vessel near the infected site will be attracted and recruited to the injured liver via CCR2-dependent bone marrow egress. The chemokine receptor CCR2 and its ligand MCP-1/CCL2 promote monocyte subset infiltration upon liver injury and further promote the progression of liver fibrosis (115, 138). Since evidence showed that tumor necrosis factor (TNF- $\alpha$ ) induced a marked increase in CCL2/MCP-1 production in dose- and time-dependent manners (139), we assume the influx of monocytes from the blood vessel to liver is induced by effects of both HMGB-1 and TNF- $\alpha$  and model the influx of monocytes similar to the kinetics of neutrophils influx. According to existing literature, HMGB-1 is released by necrotic cells and activated monocytes in response to TNF- $\alpha$  stimulation (24, 139, 140). Hence, we model the release of HMGB-1 using receptor-ligand kinetics as well as enzymatic kinetics, similar to the release of TNF- $\alpha$ , by incorporating the effects of necrotic cells and activated monocytes.

$$\frac{dP}{dt} = k_{pg}P \left(1 - \frac{P}{P_\infty}\right) - r_{pmk} \frac{[P^n]}{[P^n + k_{c1}^n]} M_{kf} P^* - r_{pn} \frac{[P^n]}{[P^n + k_{c2}^n]} (N_f + N_b) P^* - r_{pm} \frac{[P^n]}{[P^n + k_{c4}^n]} (M_f + M_b) P^* \quad (3.13)$$

$$\frac{dN_b}{dt} = \frac{[P^n]}{[P^n + k_{c2}^n]} N_f P^* - u_{mn} N_b M_f^* - k_{nub} N_b \quad (3.14)$$

$$\frac{dM_R}{dt} = k_{mr} M_R \left(1 - \frac{M_R}{M_S}\right) - r_2 M_R (H + T)^* - u_{mr} M_R \quad (3.15)$$

$$\frac{dM_f}{dt} = r_2 M_R (H + T)^* + k_{umb} M_b - \frac{[P^n]}{[P^n + k_{c4}^n]} M_f P^* - u_m M_f \quad (3.16)$$

$$\frac{dM_b}{dt} = \frac{[P^n]}{[P^n + k_{c4}^n]} M_f P^* - k_{umb} M_b \quad (3.17)$$

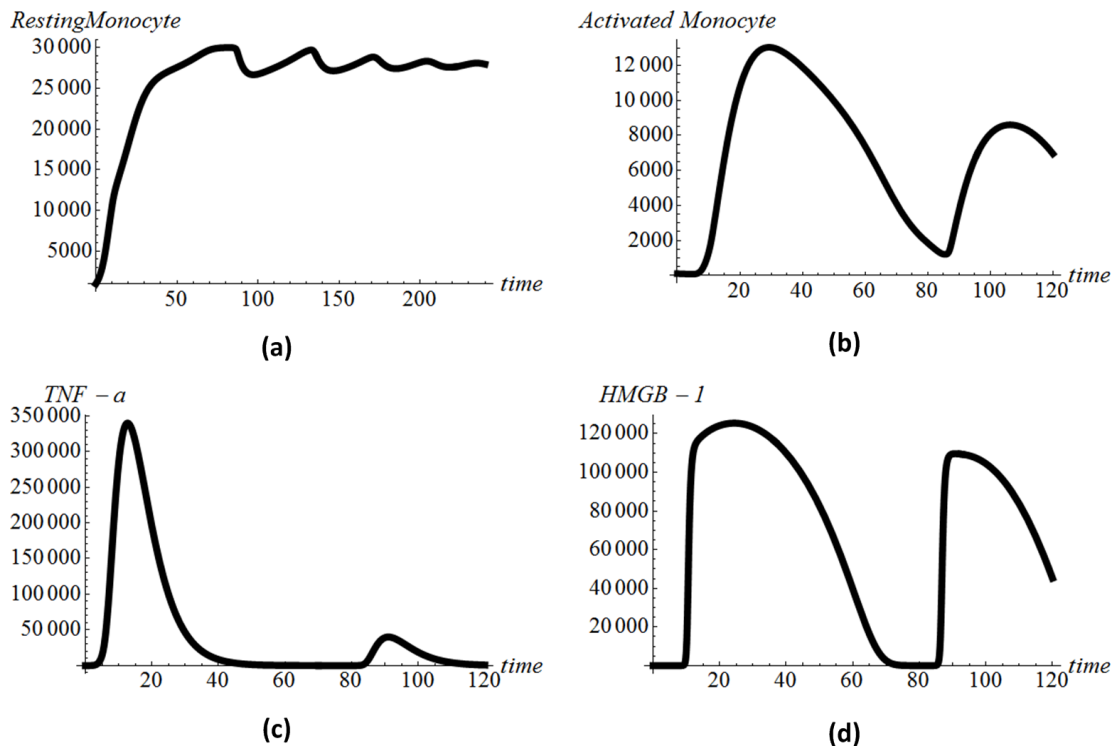
$$\frac{dH}{dt} = \left( \frac{r_{h1\max} (M_b + D)}{mh_1 + M_b + D} \right) (M_b + D) - u_h H \quad (3.18)$$

In Eq. (3.13), we incorporate the effect of phagocytosis by monocytes into Eq. (3.4) since monocytes phagocytose Gram-negative bacteria by a CD14-dependent mechanism (141). We recall hill-type function Equation  $\left(\frac{[P^n]}{[P^n + k_{c4}^n]}\right)$  to represent the receptor-ligand binding kinetics between pathogens and activated monocytes. Since binding activated neutrophils are engulfed by infiltrating monocytes (142), we use  $u_{mn} N_b M_f^*$  to calibrate the killing process of binding activated neutrophils by activated monocytes, which modify Eq. (3.10) to Eq. (3.14). Eq. (3.15), Eq. (3.16), and Eq. (3.17) describe the activation and migration of resting monocytes from blood vessel to infected tissue. In Eq. (3.15), Eq. (3.16), and Eq. (3.17),  $M_R$ ,  $M_f$ , and  $M_b$  represents the resting monocytes, free activated monocytes, and binding activated monocytes, respectively. The principles used to build those three equations are similar to the principle used to build Eq. (3.8), Eq. (3.9), and (3.10) for the neutrophil immune response model. Eq. (3.18) calibrates the release of HMGB-1 per hour by activated monocytes (monocytes-derived macrophage) and apoptotic hepatocytes, and the process of releasing HMGB-1 is similar to the process of releasing TNF- $\alpha$ . Most experiments in the literatures have shown that HMGB-1 is a delayed pro-inflammatory

cytokine and is released late in the course of AIR (23, 24, 143). The definition of parameters and corresponding experimental data in the monocyte immune response model are summarized in Table A. 4.

We plot the population size of resting monocytes in blood vessel, activated monocytes in liver and concentration of TNF- $\alpha$ , and HMGB-1 versus time (hours) in Figure 3.7 (a), (b), (c) and (d).

**Figure 3.7 (a) Concentration of *resting monocytes* versus time in monocyte immune response model at the first 240 hours of simulation. (b) Concentration of *activated monocytes* versus time in monocyte immune response model at the first 120 hours of simulation. (c) Concentration of *TNF- $\alpha$*  versus time in monocyte immune response model at the first 120 hours of simulation. (d) Concentration of *HMGB-1* versus time in monocyte immune response model at the first 120 hours of simulation. Horizontal axes represent time (in hours), and vertical axes represent concentrations in arbitrary units**



From Figure 3.7 (b), the recruitment of monocytes to liver reaches its maximal level around 40 hours after the introduced infection in our model, compared with 3 days in an experimental model (144), which demonstrates that monocytes arrive later to the site of

infection, following the recruitment of neutrophils. Our simulation results correspond to the evidence from experimental study that serum HMGB1 levels were not significantly altered for the first 10 hours and then significantly increased at 18 hours after the introduced infection as shown in Figure 3.7 (d) (23, 36). Comparing the peak level of HMGB-1 with the peak level of TNF- $\alpha$ , the peak level of HMGB1 is smaller and the release time of HMGB-1 is slower than the release time of TNF- $\alpha$  (10 hours vs. 6 hours post-infection). Furthermore, our simulation results show that HMGB-1 is readily detectable at 10 hours and is maintained at peak, plateau levels from 18 to 32 hours after infection, which is similar to the results from experimental studies (23). Our simulation results suggest that HMGB-1, as a late pro-inflammatory cytokine, down-regulates the AIR induced by TNF- $\alpha$  production.

### 3.2.6 *Anti-inflammatory immune response model*

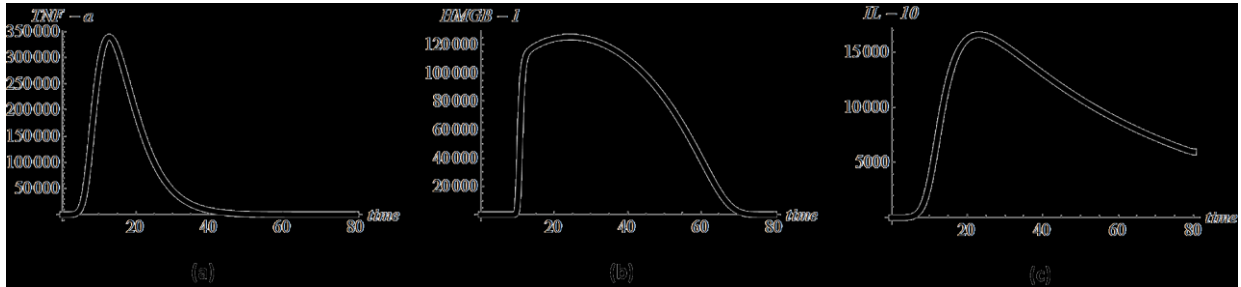
IL-10 is an anti-inflammatory cytokine. Plasma levels are elevated in animal models of endotoxemia and inhibit the release of pro-inflammatory cytokine (TNF- $\alpha$ , IL-1 $\beta$ , and IL-6) from monocytes/macrophages, thus preventing subsequent tissue damage (145). This anti-inflammatory mediator is produced by macrophages, dendritic cells (DC), B cells, and various subsets of CD4 and CD8\_T cells (146) and follows the same mechanism as pro-inflammatory (TNF- $\alpha$  and HMGB-1) release. Since our main focus in this paper is to model the innate immune responses, we ignore the release of IL-10 by B cells and T cells during the adaptive immune responses. Hence, we model the release of IL-10 in a similar way as pro-inflammatory cytokine release.

$$\frac{dC_A}{dt} = \left( \frac{r_{ca \max} M_b}{C_{Ah} + M_b} \right) M_b^{-u_{ca}} C_A \quad (3.19)$$

In Eq. (3.19),  $C_A$  represents the concentration of anti-inflammatory cytokine (IL-10) during AIR.  $\left(\frac{r_{camax}M_b}{C_{Ah}+M_b}\right)$  represents the release rate of anti-inflammatory cytokine (IL-10) by activated monocytes, derived from enzymatic kinetics. The first term in Eq. (3.19) calibrates the increase in number of anti-inflammatory cytokines every hour and the second term  $u_{ca}C_A$  calibrates the decrease in number of anti-inflammatory cytokines every hour due to a natural degradation. The corresponding parameters and their values are defined in Table A.5.

We plot the concentration of TNF- $\alpha$ , HMGB-1, and IL-10 versus time (hours) in Figure 3.8 (a), (b) and (c).

**Figure 3.8 (a) Concentration of *TNF- $\alpha$*  versus time in anti-inflammatory immune response model at the first 80 hours of simulation. (b) Concentration of *HMGB-1* versus time in anti-inflammatory immune response model at the first 80 hours of simulation. (c) Concentration of *IL-10* versus time in anti-inflammatory immune response model at the first 80 hours of simulation. Horizontal axes represent time (in hours) and Vertical axes represent concentration in arbitrary unit**



Experimental studies in mice have shown that early predominance of pro-inflammatory cytokines transitions to anti-inflammatory predominance at 24 h (13, 133). Figure 3.8 (a), (b) and (c) shows that the time to approach the peak levels of TNF- $\alpha$ , HMGB-1, and IL-10 are 6 hours, 18 hours, and 24 hours respectively and demonstrates that anti-inflammatory responses will follow pro-inflammatory responses and play a role in the later phase of AIR. In the following section, we will discuss the inhibiting effects of anti-inflammatory cytokines and the comprehensive structure of our mathematical model of innate immunity in the AIR.

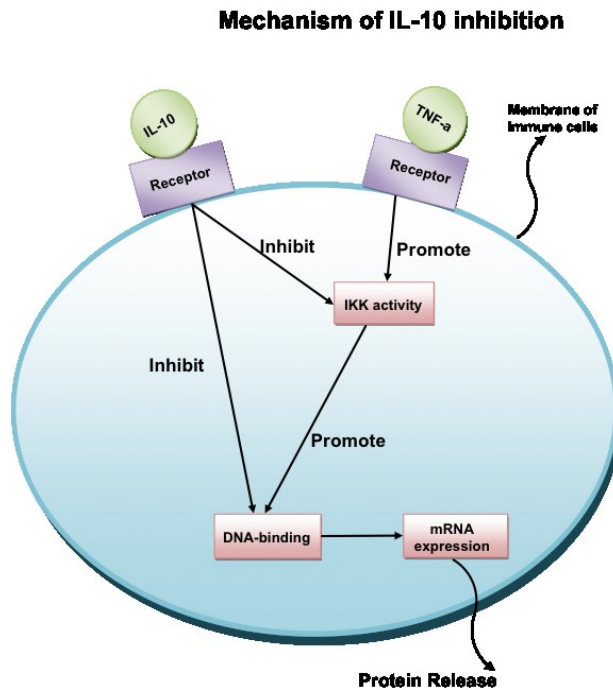


### 3.2.7 Mathematical models of innate immunity of AIR

#### 3.2.7.1 Inhibition of anti-inflammatory cytokines

Before we incorporate mathematical models of subsystems into a comprehensive mathematical model of innate immunity in AIR, we will review the mechanism of inhibition of anti-inflammatory cytokines to the course of infection. IL-10 was found to inhibit protein kinase activation (IKK activity) induced by LPS binding to the CD14 receptor and to consequently block the downstream Ras signaling pathway (147). Furthermore, IL-10 inhibits both TNF- $\alpha$  and LPS-induced NF- $\kappa$ B DNA binding, gene transcription, and cytokine synthesis (148-150). The mechanism of IL-10 inhibition of protein production is shown in Figure 3.9.

**Figure 3.9 Mechanism of *IL-10* inhibition**



By IKK activity, NF- $\kappa$ B as a protein complex is released from cytoplasm into the cell nucleus and binds to DNA in order to accomplish NF- $\kappa$ B-dependent DNA transcription (151).

We assume the NF- $\kappa$ B protein complex binding to DNA as an enzyme-kinetics, since DNA-binding proteins, such as transcription factors, have recently been found to exhibit enzymatic activity during the process of transcription (152). Furthermore, we assume and model IL-10 inhibition as an enzyme inhibition process, since IL-10 inhibits the process of DNA-protein binding, as well as transcription. The mathematical formation of IL-10 inhibition will, therefore, follow simplified competitive enzyme kinetics ( $\alpha$  denoted as adjustment) as follows.

$$f(C_A, x) = \frac{\alpha x}{\left(1 + \frac{C_A}{C_\infty}\right)} \quad (3.20)$$

After incorporating the inhibition function of IL-10, we derive a comprehensive mathematical model for innate immunity of AIR, and  $C_\infty$  represents the dissociation rate of IL-10 with initial estimated value equivalent to 0.02.

### 3.2.7.2 Mathematical model of innate immunity of AIR

$$\frac{dP}{dt} = k_{pg}P \left(1 - \frac{P}{P_\infty}\right) - r_{pmk} \frac{[P^n]}{[P^n + k_{c1}^n]} M_{kf} P^* - r_{pn} \frac{[P^n]}{[P^n + k_{c2}^n]} (N_f + N_b) P^* - r_{pm} \frac{[P^n]}{[P^n + k_{c4}^n]} (M_f + M_b) P^* \quad (3.21)$$

$$\frac{dM_{kf}}{dt} = k_{mk} M_{kf} \left(1 - \frac{M_{kf}}{K_\infty}\right) + k_{mkub} M_{kb} - \frac{[P^n]}{[P^n + k_{c1}^n]} M_{kf} P^* - u_{mk} M_{kf} \quad (3.22)$$

$$\frac{dM_{kb}}{dt} = \frac{[P^n]}{[P^n + k_{c1}^n]} M_{kf} P^* - k_{mkub} M_{kb} \quad (3.23)$$

$$\frac{dT}{dt} = \left(\frac{r_{t1\max} M_{kb}}{m_{t1} + M_{kb}}\right) M_{kb} + \left(\frac{r_{t2\max} N_b}{m_{t2} + N_b}\right) N_b - u_t T \quad (3.24)$$

$$\frac{dN_R}{dt} = k_{rd} N_R \left(1 - \frac{N_R}{N_S}\right) - r_1 N_R (T + P)^* - u_{nr} N_R \quad (3.25)$$

$$\frac{dN_f}{dt} = \frac{r_1 N_R (T + P)^*}{\left(1 + \frac{C_A}{C_\infty}\right)} + k_{nub} N_b - \frac{[P^n]}{[P^n + k_{c2}^n]} N_f P^* - u_n N_f \quad (3.26)$$

$$\frac{dN_b}{dt} = \frac{[P^n]}{[P^n + k_{c2}^n]} N_f P^* - u_{mn} N_b M_f^* - k_{nub} N_b \quad (3.27)$$

$$\frac{dr_1}{dt} = k_{r1} \left(1 + \tanh(N_f^*)\right) - u_{r1} r_1 \quad (3.28)$$

$$\frac{dD}{dt} = r_{hn} \left( \frac{D^n}{D^n + k_{c3}^n} \right) N_f D^* \left(1 - \frac{D}{A_\infty}\right) - r_{ah} D \quad (3.29)$$

$$\frac{dM_R}{dt} = k_{mr} M_R \left(1 - \frac{M_R}{M_S}\right) - r_2 M_R (H + T)^* - u_{mr} M_R \quad (3.30)$$

$$\frac{dM_f}{dt} = \frac{r_2 M_R (H + T)^*}{\left(1 + \frac{C_A}{C_\infty}\right)} + k_{umb} M_b - \frac{[P^n]}{[P^n + k_{c4}^n]} M_f P^* - u_m M_f \quad (3.31)$$

$$\frac{dM_b}{dt} = \frac{[P^n]}{[P^n + k_{c4}^n]} M_f P^* - k_{umb} M_b \quad (3.32)$$

$$\frac{dH}{dt} = \left( \frac{r_{h1 \max} (M_b + D)}{mh_1 + M_b + D} \right) (M_b + D) - u_h H \quad (3.33)$$

$$\frac{dC_A}{dt} = \left( \frac{r_{ca \max} M_b}{C_{Ah} + M_b} \right) M_b - u_{ca} C_A \quad (3.34)$$

### 3.3 Stability analysis

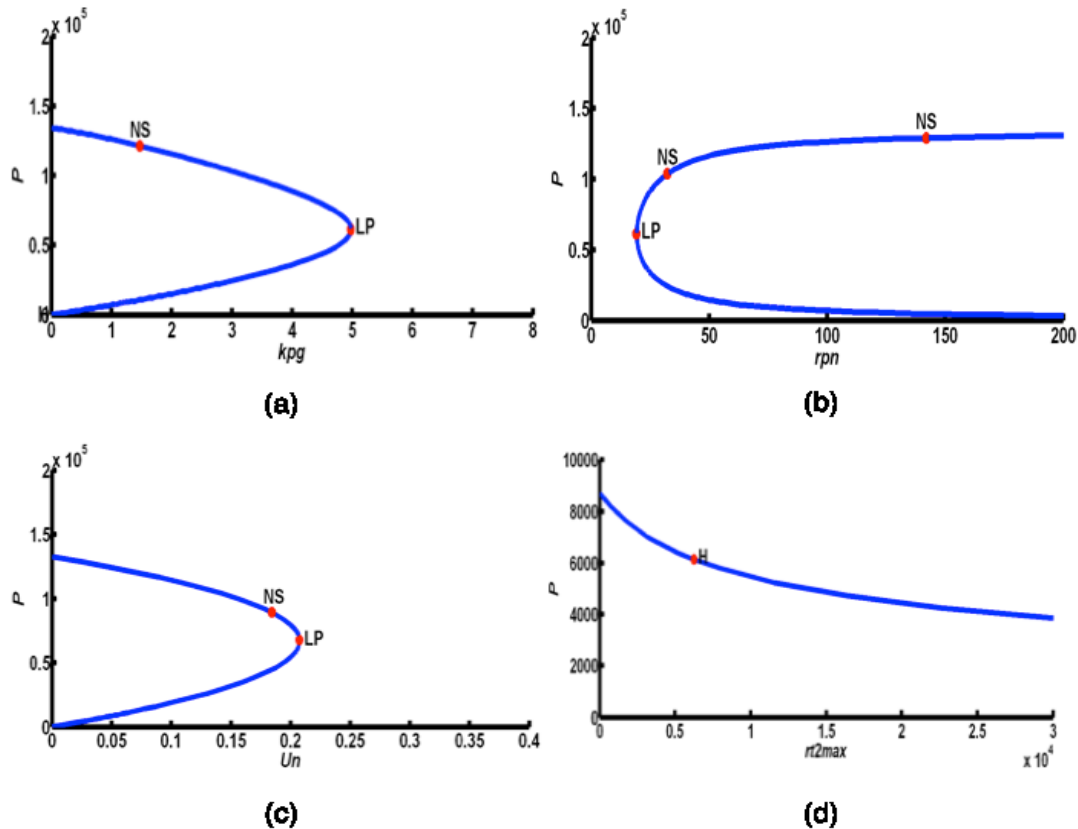
To study the model behaviors under various parameter settings and initial conditions, stability analysis are conducted for each subsystem during model construction using bifurcation diagrams. Bifurcation diagrams are graphical tools to visualize the behaviors of dynamic system change with parameters, which are generated by Matcont in this paper. Matcont is a Matlab continuation package with a graphic user interface (GUI) for the interactive numerical study of parameterized nonlinear ODEs. It allows to compute curves of equilibria, limit points, Hopf point, limit cycles, fold, torus, and branch point bifurcation of limit cycles and so on (153).

In bifurcation diagrams, Y-axis represents equilibrium of state variable and X-axis represents value of system parameter that generates equilibrium. Therefore, bifurcation diagrams reflect change in equilibrium of dynamic system (either change in number of equilibrium or change in numerical value of equilibrium) in relation to the change in numerical value of system parameter. We analyzed stability of dynamic system by identifying types of bifurcation point in

bifurcation diagrams since bifurcation points are defined as points where stability changes from stable to unstable. In our bifurcation diagrams, there are two typical bifurcation points: limit point (marked as “LP” in Matcont) and Hopf point (marked as “H” in Matcont). Neutral Saddle Point is marked as “NS” in bifurcation diagram, however it is not a bifurcation point for the equilibrium since it is identified as a hyperbolic saddle. Figure 10 shows stability of equilibria of state variable *pathogens* change in relation to system parameters change in neutrophil subsystem.

### 3.3.1 Neutrophil subsystem stability analysis

Figure 3.10 (a) Computed equilibrium curve of *pathogens* in relation to system parameter  $k_{pg}$  in neutrophil subsystem. (b) Computed equilibrium curve of *pathogens* in relation to system parameters  $r_{pn}$  in neutrophil subsystem. (c) Computed equilibrium curve of *pathogens* in relation to system parameters  $u_n$  in neutrophil subsystem. (d) Computed equilibrium curve of *pathogens* in relation to system parameters  $r_{t2max}$  in neutrophil subsystem



LPs in bifurcation diagrams of neutrophil subsystem appear when two equilibria merge into one equilibrium, and thus, the number of equilibrium of dynamic system changes when LPs are detected. LPs are also turning points at which dynamic system changes from stability to instability. In Figure 3.10 (a), there is stable equilibrium of *pathogen* when system parameter  $k_{pg}$  increases from 0 to 4.93, when  $k_{pg}$  equals to 4.93, LP is identified and unstable equilibrium of *pathogen* is generated as  $k_{pg}$  decreases from 4.93 to 0. Therefore, equilibrium of *pathogen* of our neutrophil subsystem is bistable when  $k_{pg}$  is from 0 to 4.93. Similarly, equilibrium of *pathogen* in Figure 3.10 (b) is bistable when system parameter  $r_{pn}$  is from 25 to 200. In Figure 3.10 (c), equilibrium of *pathogen* before LP is stable, and the equilibrium is bistable when  $u_n$  is from 0.05 to 0.21.

A Hopf bifurcation, identified in Figure 3.10 (d), is a periodic bifurcation in which a new limit cycle is born from a stationary solution. Hopf Point is a point is a turning point for periodic orbits, and Hopf Point is detected when system parameter  $r_{t2max}$  changes. The detected Hopf Point in Figure 3.10 (d) is used to start a limit cycle continuation, where two cycles collide and disappear. Since the first Lyapunov coefficient (154) is positive, there exists an unstable limit cycle, bifurcating from this equilibrium. Figure 3.11 (a) and (b) shows the family of limit cycles bifurcating from detected Hopf Point in Figure 3.10 (d). The family of limit cycles is represented using limit cycle planes such as *TNF-a-pathogen plane* and *N<sub>f</sub>-pathogen plane*. Figure 3.11 (c) shows a limit cycle sphere represented by a *TNF-a*, *N<sub>f</sub>*, and *pathogen Plane*. Figure 3.11 (d) indicates the presence of two limit cycles occurs when  $r_{t2max}$  equal to 5495.6394 or 6265.0029.

In Figure 3.11 (c), the first family of limit cycle (a red small cycle in the center of sphere) spiral outward as system parameter  $r_{t2max}$  decreases, and the second family of limit cycle appears when  $r_{t2max}$  decreases to 5495.6394 (a red cycle line appears). As  $r_{t2max}$  increases from

5495.6394, the second family of limit cycle spiral outward again, when  $r_{t2max}$  increases to 6265.0029, an unstable equilibrium is detected in Figure 3.12. If value of  $r_{t2max}$  is between 5495.6394 and 6265.0029, the equilibria of neutrophil subsystem are stable and converged shown by Figure 3.13.

To conclude, we have detected system parameters  $k_{pg}$ ,  $r_{pn}$ , and  $r_{t2max}$  contributing to bistability of our neutrophil subsystem. Furthermore, we observe system parameter  $r_{t2max}$  (the maximum release rate of TNF-a by activated neutrophils) is essential for generating a closed trajectory of neutrophil subsystem. A significant unstable infection oscillation occurs when  $r_{t2max}$  increases to 6265.0029.

**Figure 3.11 (a) Family of limit cycles bifurcating from the Hopf point in *TNF-a* and *pathogen* plane. (b) Family of limit cycles bifurcating from the Hopf point in *N<sub>f</sub>* and *pathogen* plane. (c) Equilibria and limit cycles in (*N<sub>f</sub>*, *pathogen*, and *TNF-a*)-space. (d) Period of the cycle as function of  $r_{t2max}$**

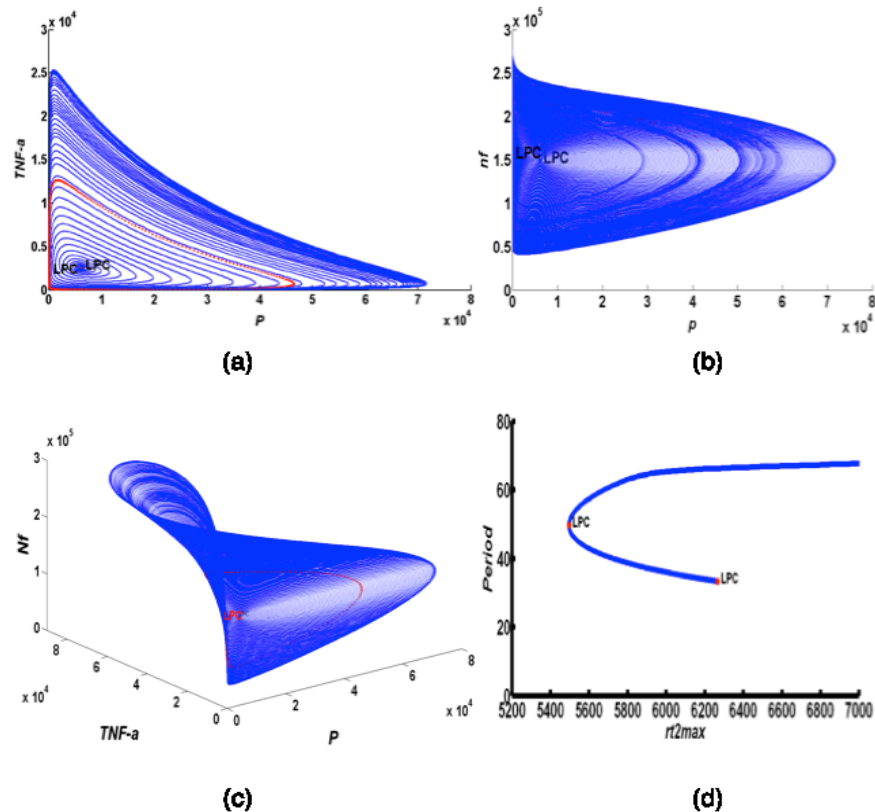


Figure 3.12 (a) Numerical relationships between  $N_f$ , *pathogen*, and *TNF-a* in unstable neutrophil subsystem at equilibrium when  $r_{t2max}$  is equal to 6265.0029. (b) *Pathogen* diverges in unstable neutrophil subsystem at equilibrium when  $r_{t2max}$  is equal to 6265.0029. (c) *Activated Neutrophils* diverges in unstable neutrophil subsystem at equilibrium when  $r_{t2max}$  is equal to 6265.0029. (d) *TNF-as* diverges in unstable neutrophil subsystem at equilibrium when  $r_{t2max}$  is equal to 6265.0029

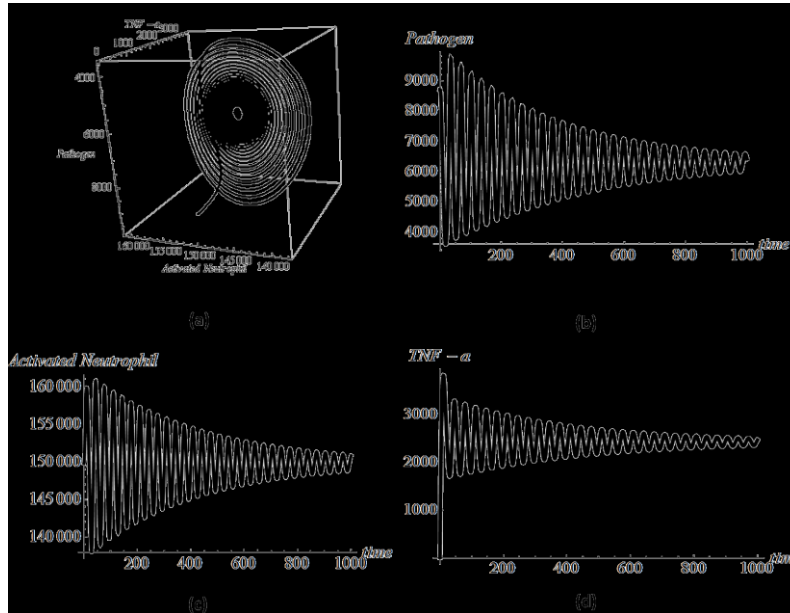
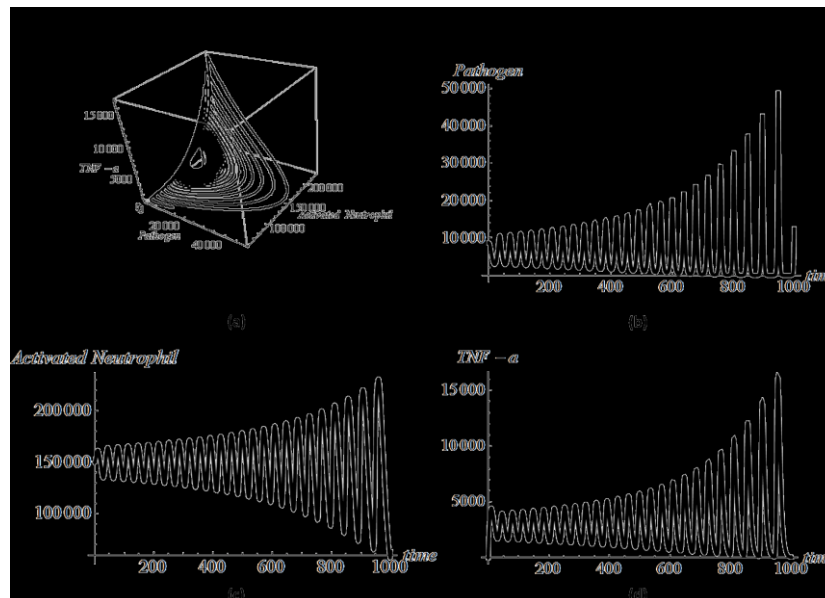
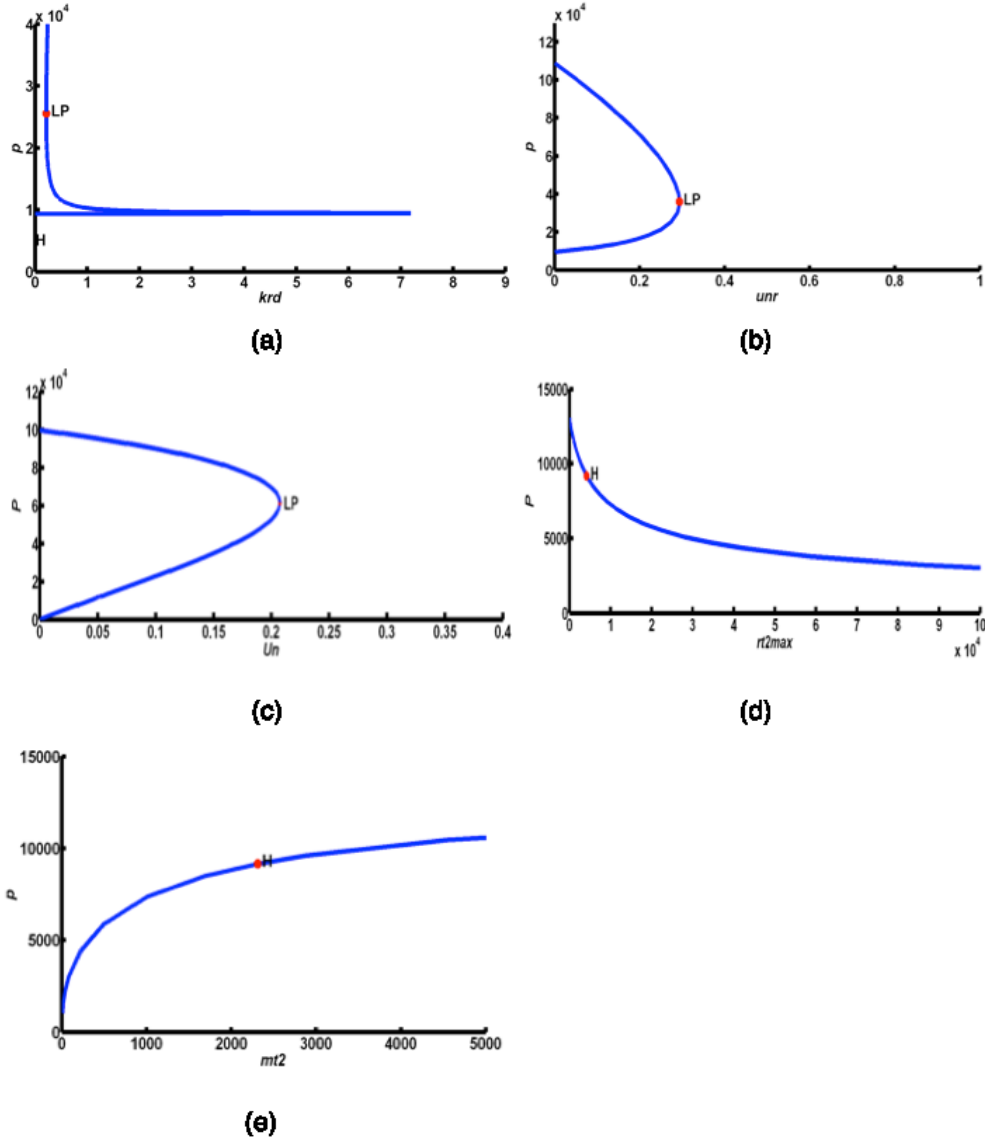


Figure 3.13 (a) Numerical relationships between  $N_f$ , *pathogen*, and *TNF-a* in stable neutrophil subsystem at equilibrium when  $r_{t2max}$  is between 5495.6394 and 6265.0029. (b) *Pathogen* converges in stable neutrophil subsystem at equilibrium when  $r_{t2max}$  is between 5495.6394 and 6265.0029. (c) *Activated Neutrophils* converges in stable neutrophil subsystem at equilibrium when  $r_{t2max}$  is between 5495.6394 and 6265.0029. (d) *TNF-a* converges in stable neutrophil subsystem at equilibrium when  $r_{t2max}$  is between 5495.6394 and 6265.0029



### 3.3.2 Monocyte subsystem stability analysis

Figure 3.14 (a) Computed equilibrium curve of *pathogens* in relation to system parameter  $k_{rd}$  in monocyte subsystem. (b) Computed equilibrium curve of *pathogens* in relation to system parameters  $u_{nr}$  in monocyte subsystem. (c) Computed equilibrium curve of *pathogens* in relation to system parameters  $u_n$  in monocyte subsystem. (d) Computed equilibrium curve of *pathogens* in relation to system parameters  $r_{t2max}$  in monocyte subsystem. (e) Computed equilibrium curve of *pathogens* in relation to system parameters  $m_{t2}$  in monocyte subsystem



Continue stability analysis on monocyte subsystem indicates change in system parameters  $k_{rd}$ ,  $u_{nr}$ , and  $u_n$  induce bistability of monocyte subsystem. From Figure 3.14 (a), (b), and (c), we know monocyte subsystem is bistable if at least one of the three conditions meets:  $k_{rd}$



is between 0 to 0.32,  $u_{nr}$  is between 0 to 0.28, and  $u_n$  is between 0 to 0.21. Specifically, we have observed  $r_{t2max}$  (the maximum release rate of TNF- $\alpha$  by activated neutrophils) and  $m_{t2}$  (the number of activated neutrophils releasing half of TNF- $\alpha$ ) are essential for oscillated monocyte subsystem. Limit cycles are bifurcating from Hopf point, shown in Figure 3.14 (d) and (e), similar to neutrophil subsystem. Therefore, we conclude that the oscillated infection is significantly dependent on the amount of released TNF- $\alpha$  and further recruited neutrophils in AIR. However, the released monocytes and associated cytokines such as HMGB-1, playing no roles in contributing to oscillation in AIR progression.

### ***3.3.3 Full model stability analysis***

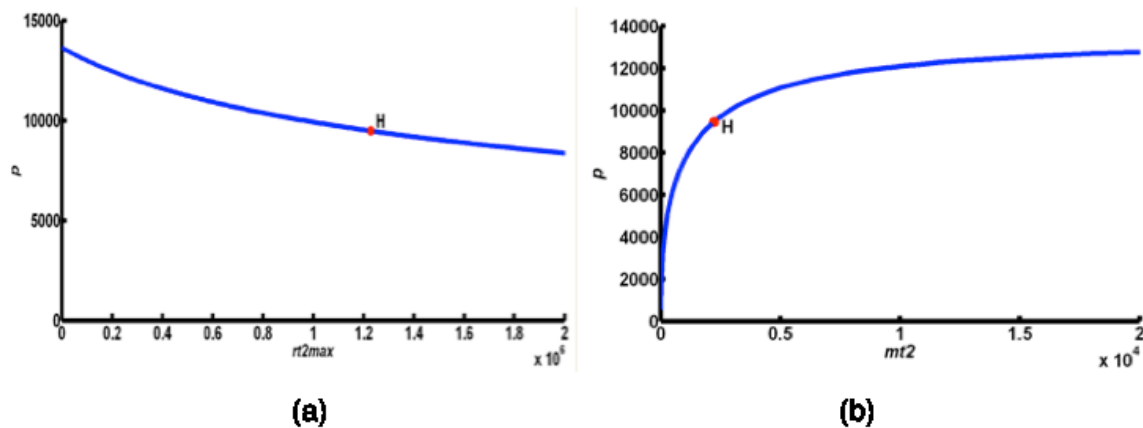
Built upon monocyte subsystem, our full model incorporate the effect of anti-inflammatory cytokines and our stability analysis show the stability of our full model is significantly dependent on the effect of anti-inflammatory cytokines, especially when medium effect of anti-inflammatory cytokines are incorporated (dissociation rate of IL-10 equal to logarithm 4). Our stability analysis, in Figure 3.15, shows the Hopf Points move forward as  $r_{t2max}$  and  $m_{t2}$  increases when medium effect of anti-inflammatory cytokines is incorporated.

Medium effect of anti-inflammatory cytokines:

In Figure 3.15 (a) and (b), comparing to Figure 3.14 (d) and (e), we see the Hopf Point is detected when  $r_{t2max}$  and  $m_{t2}$  increases to a bigger value since the anti-inflammatory cytokines inhibit the activation of phagocytic cells (neutrophils and monocytes). This trend indicates the infection oscillation requires, with the medium effect of anti-inflammatory cytokines, more pro-inflammation (including TNF- $\alpha$  and activated neutrophils) compared to our monocyte subsystem without including the effect of anti-inflammatory cytokines. The strengthened (increased  $r_{t2max}$  and  $m_{t2}$ ) pro-inflammatory immune responses could also induce stable or unstable equilibria, and

therefore leads to a dampened oscillated infection or diverged infection, similar to our observations in Figure 3.12 and Figure 3.13. However, we have observed our AIR progression, if high effect of anti-inflammatory cytokine is incorporated (dissociation rate equal to logarithm 6) at the beginning of infection, will induce a stable overwhelming pathogen load. These observations inspire us the effects of anti-inflammatory cytokines play a vital role in AIR progression and could be either positive or negative to AIR progression dependent on levels of anti-inflammatory cytokines.

**Figure 3.15 (a) Computed equilibrium curve of *pathogens* in relation to system parameter  $r_{12max}$  if medium effect of anti-inflammatory cytokine is incorporated. (b) Computed equilibrium curve of *pathogens* in relation to system parameters  $m_{12}$  if medium effect of anti-inflammatory cytokine is incorporated**



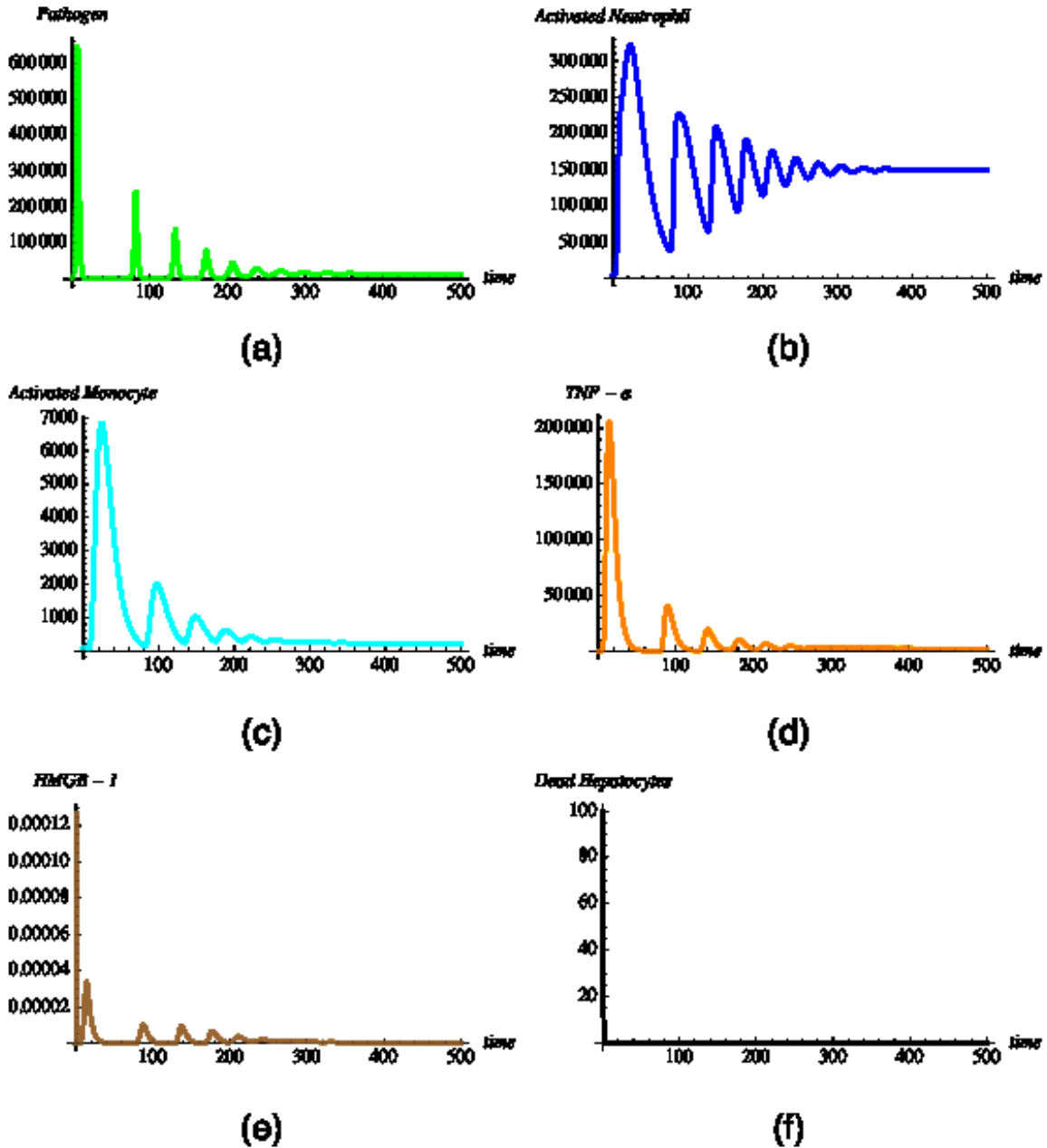
### 3.4 Discussion

#### 3.4.1 Effects of initial pathogen load on sepsis progression

Using our system dynamic mathematical model, we analyzed the impact of effect of bacteria load on phagocytic cells, inflammatory cytokines, and damaged tissue at low, medium, and high level during innate immunity of AIR. The computed results are shown in Figure 3.16, 3.17, and 3.18.

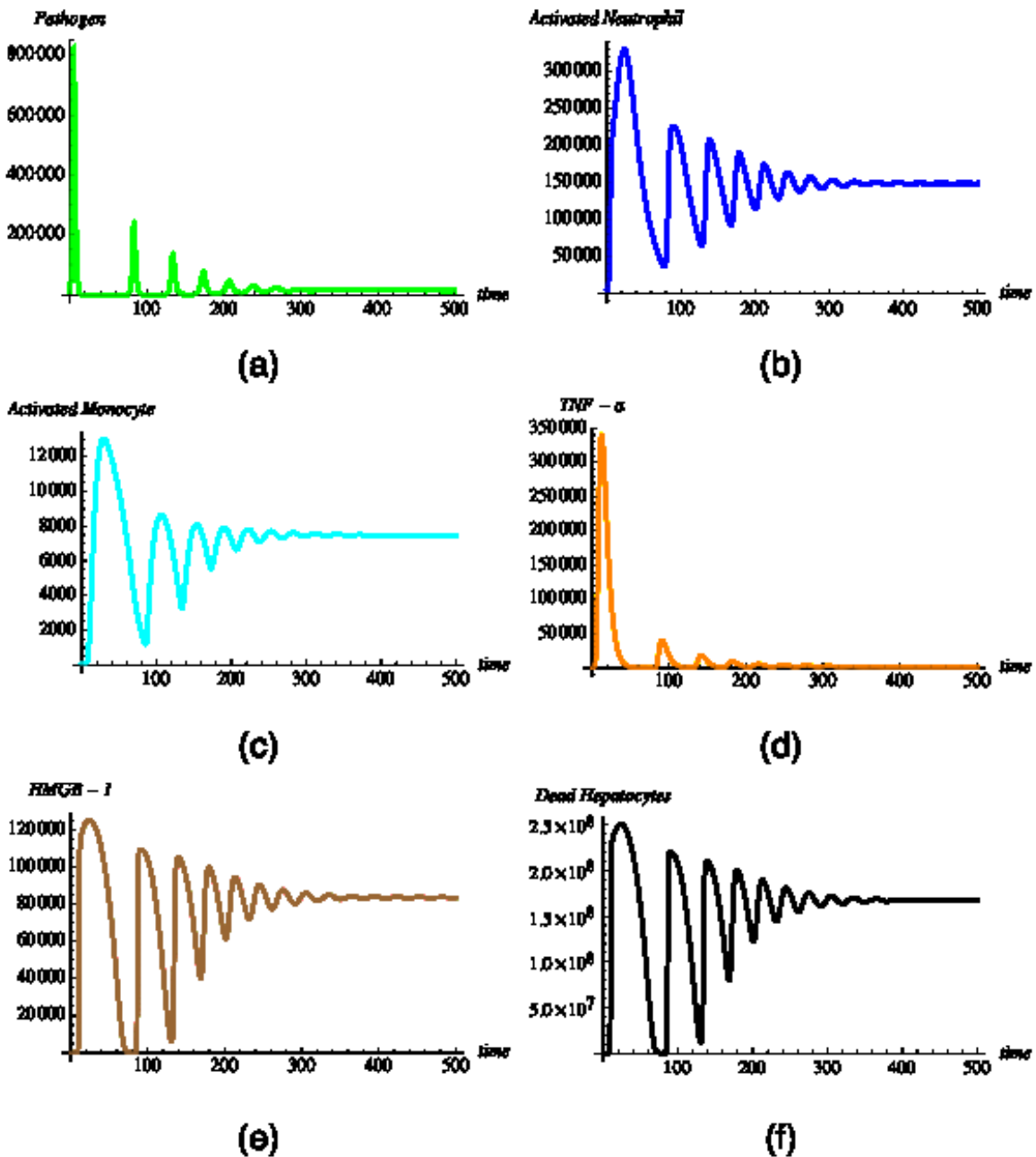
3.4.1.1 Low initial load of pathogen ( $p(0)=100$ )

Figure 3.16 (a) Concentration of *pathogen* in the presence of low initial load of *pathogen*. (b) Concentration of *activated neutrophils* in the presence of low initial load of *pathogen*. (c) Concentration of *activated monocytes* in the presence of low initial load of *pathogen*. (d) Concentration of *TNF- $\alpha$*  in the presence of low initial load of *pathogen*. (e) Concentration of *HMGB-1* in the presence of low initial load of *pathogen*. (f) Concentration of *dead hepatocytes* in the presence of low initial load of *pathogen*. Horizontal axes represent time (in hours) and Vertical axes represent concentration in arbitrary unit



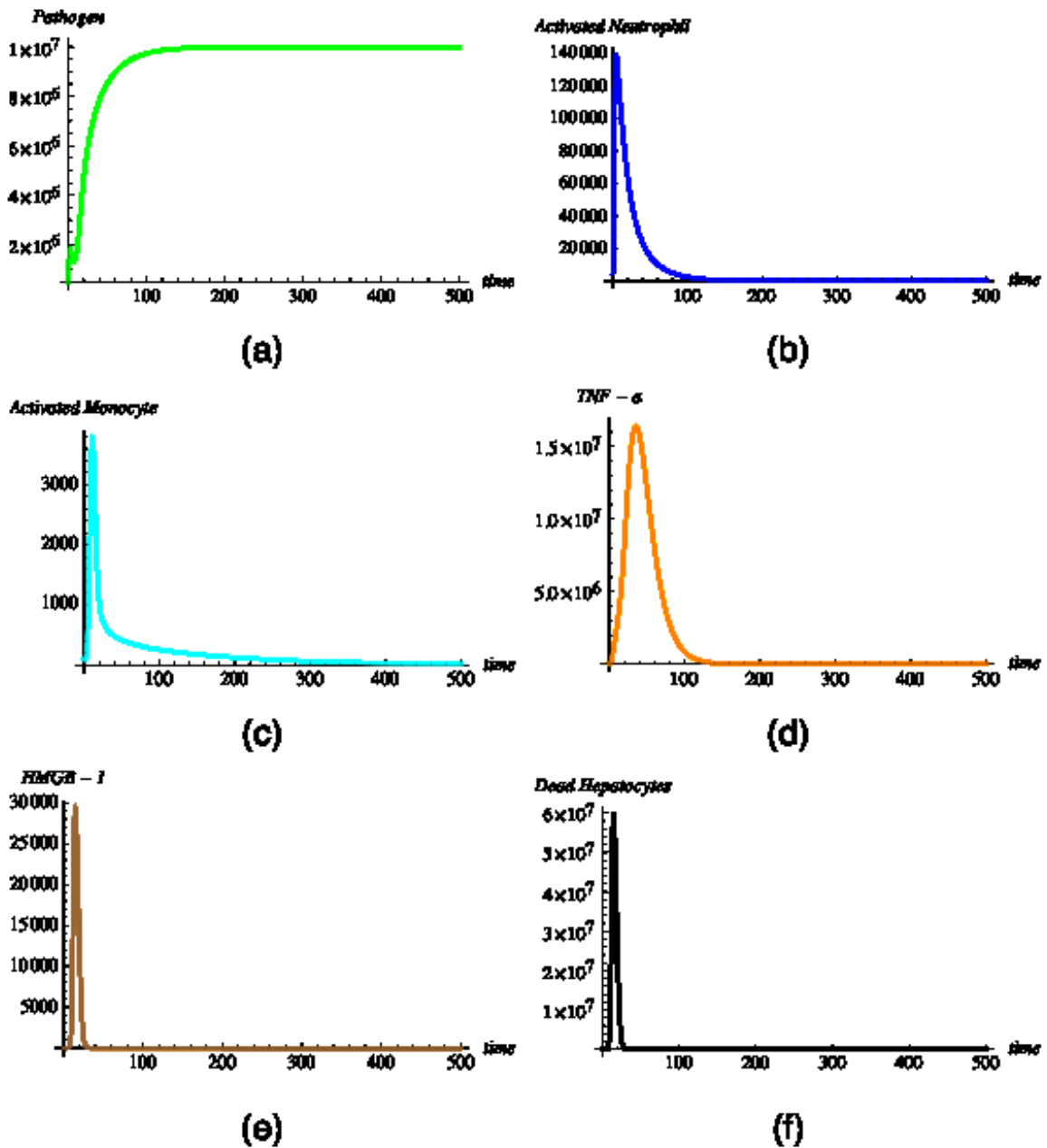
3.4.1.2 Medium initial load of pathogen ( $p(0)=10000$ )

Figure 3.17 (a) Concentration of *pathogen* in the presence of medium initial load of *pathogen*. (b) Concentration of *activated neutrophils* in the presence of medium initial load of *pathogen*. (c) Concentration of *activated monocytes* in the presence of medium initial load of *pathogen*. (d) Concentration of *TNF- $\alpha$*  in the presence of medium initial load of *pathogen*. (e) Concentration of *HMGB-1* in the presence of medium initial load of *pathogen*. (f) Concentration of *dead hepatocytes* in the presence of medium initial load of *pathogen*. Horizontal axes represent time (in hours) and Vertical axes represent concentration in arbitrary units



3.4.1.3 High initial load of pathogen ( $p(0)=100000$ )

Figure 3.18 (a) Concentration of *pathogen* in the presence of high initial load of *pathogen*. (b) Concentration of *activated neutrophils* in the presence of high initial load of *pathogen*. (c) Concentration of *activated monocytes* in the presence of high initial load of *pathogen*. (d) Concentration of *TNF- $\alpha$*  in the presence of high initial load of *pathogen*. (e) Concentration of *HMGB-1* in the presence of high initial load of *pathogen*. (f) Concentration of *dead hepatocytes* in the presence of high initial load of *pathogen*. Horizontal axes represent time (in hours) and Vertical axes represent concentration in arbitrary units



Based on our computed results, we conclude a resolved healthy state, pathogen falls below threshold during the oscillation as well as other phagocytic cells and inflammatory cytokines, when initial pathogen load is low. We recognize a persistent infection pattern happening, when initial pathogen load is medium, if inflammatory responses are still active (damaged tissue oscillates during infection). If initial pathogen load is high, an overwhelming bacteria load occurs eventually and leading to a high risk of death.

### ***3.4.2 Effects of pro-and anti-inflammatory cytokines on sepsis progression***

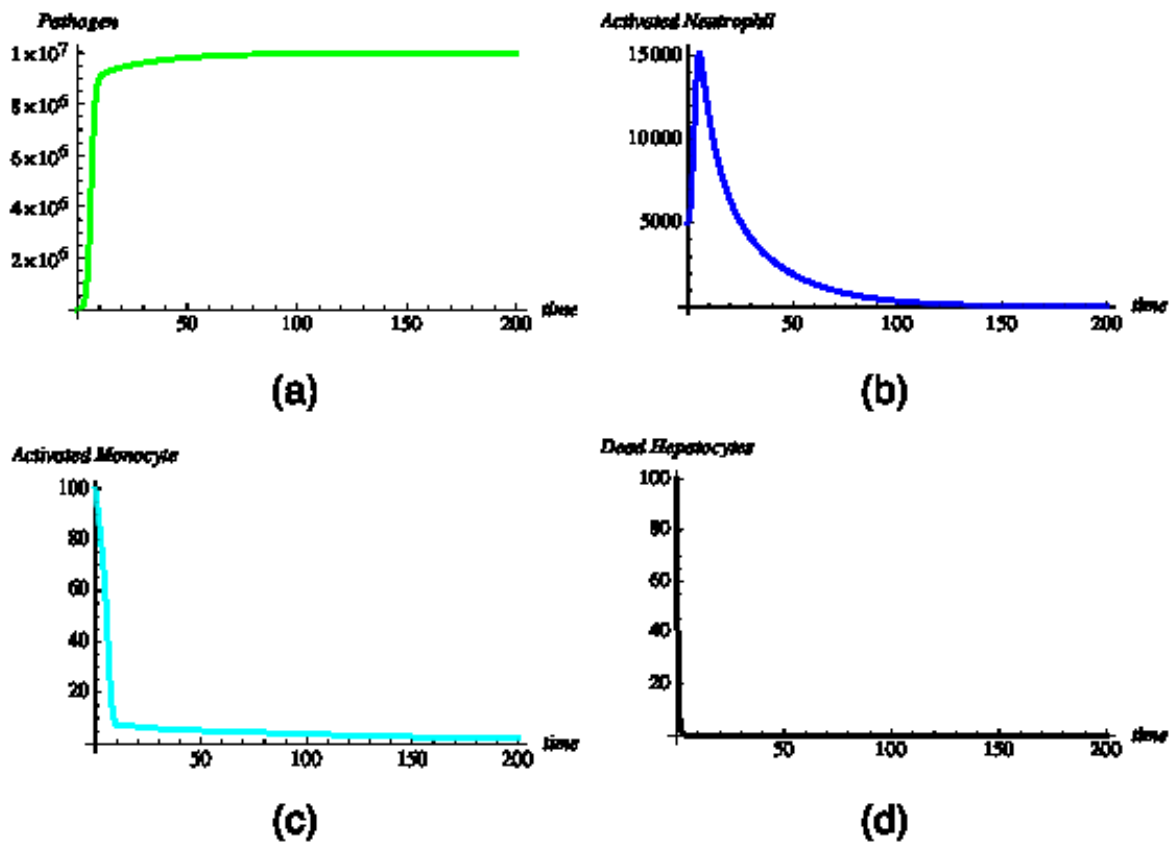
Interactions and balances between pro-inflammatory cytokines and anti-inflammatory cytokines are essential to the progression of the AIR. Previous experiments on mice (13) have found a close link between severity of sepsis and the balance and time course of inflammatory cytokines. Experiments from existing literature showed that excess production of pro-inflammatory cytokines has been associated with multiple organ-system dysfunction (severe sepsis), post-fluid resuscitation hypertension (septic shock), and mortality (12). Based on our simulation results, the response of TNF- $\alpha$  is maximal at an early stage of AIR. Following TNF- $\alpha$ , the late pro-inflammatory HMGB-1 and the anti-inflammatory IL-10 will typically dominate AIR progression and ultimately determine the possible outcomes of AIR. Therefore, local TNF- $\alpha$  level elevation may not end with multiple organ-system dysfunctions and anti-TNF- $\alpha$  treatment alone could be ineffective in the early stages of AIR, consistent with clinical trials (145).

Biological results show that effect with IL-10 increases mortality in the murine model (133). In general, effectiveness of IL-10 on sepsis progression is inconsistent in experimental studies. A group of experimental studies showed that IL-10 improved the outcome of mice undergoing cecal ligation and puncture (CLP), while antibody against IL-10 contributed to worsened outcome or even mortality (13, 155). In contrast, other investigators failed to confirm

the improvement by showing no difference on survival rate between pretreatment with IL-10 and non-pretreatment with IL-10 in mice after CLP (156). Using our system dynamic mathematical model, we analyzed the impact of effect of IL-10 (measured by system parameter  $C_A$ ) on bacteria load, phagocytic cells, and damaged tissue at high, medium, and low level during innate immunity of AIR. The computed results are shown in Figure 3.19, 3.20, and 3.21.

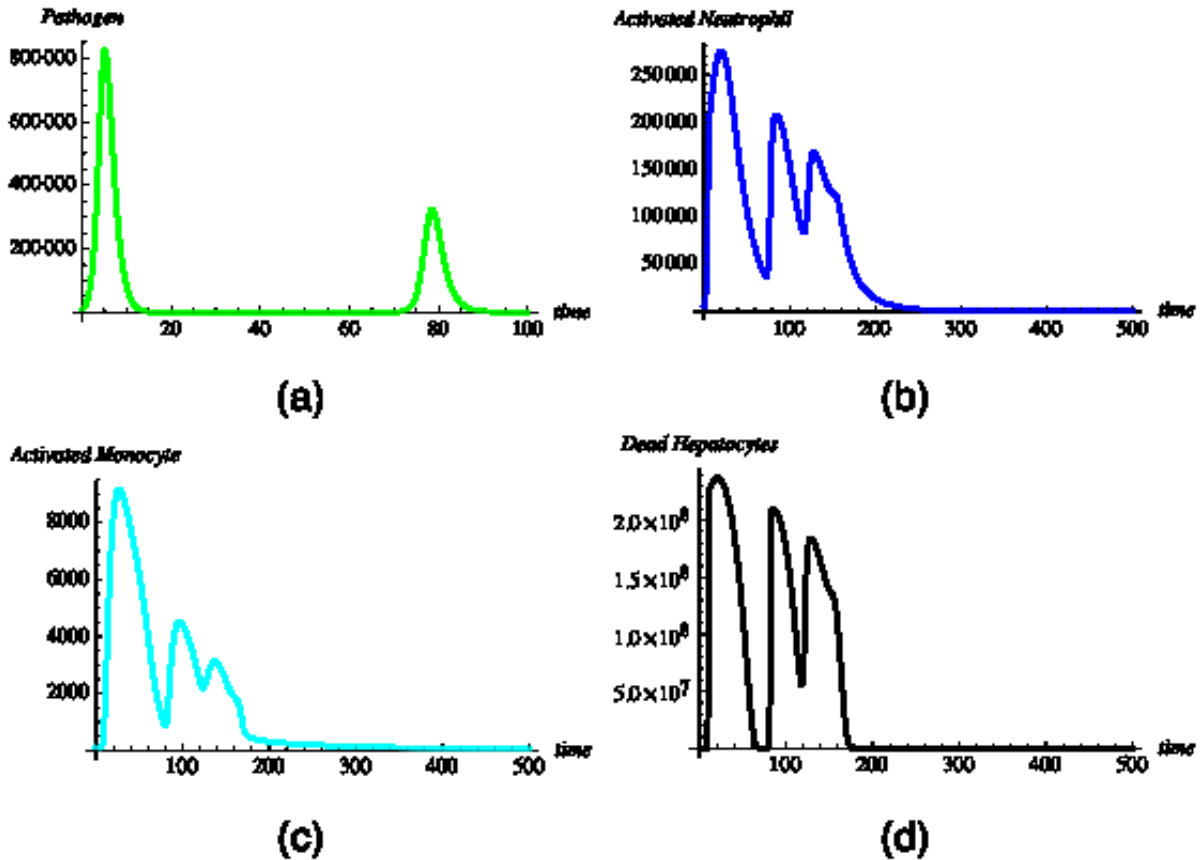
### 3.4.2.1 High effect of anti-inflammatory cytokines

**Figure 3.19** (a) Concentration of *pathogen* in the presence of high effect of *IL-10*. (b) Concentration of *activated neutrophils* in the presence of high effect of *IL-10*. (c) Concentration of *activated monocytes* in the presence of high effect of *IL-10*. (d) Concentration of *dead hepatocytes* in the presence of high effect of *IL-10*. Horizontal axes represent time (in hours) and Vertical axes represent concentration in arbitrary units



### 3.4.2.2 Medium effect of anti-inflammatory cytokines

Figure 3.20 (a) Concentration of *pathogen* in the presence of medium effect of *IL-10*. (b) Concentration of *activated neutrophils* in the presence of medium effect of *IL-10*. (c) Concentration of *activated monocytes* in the presence of medium effect of *IL-10*. (d) Concentration of *dead hepatocytes* in the presence of medium effect of *IL-10*. Horizontal axes represent time (in hours) and Vertical axes represent concentration in arbitrary units



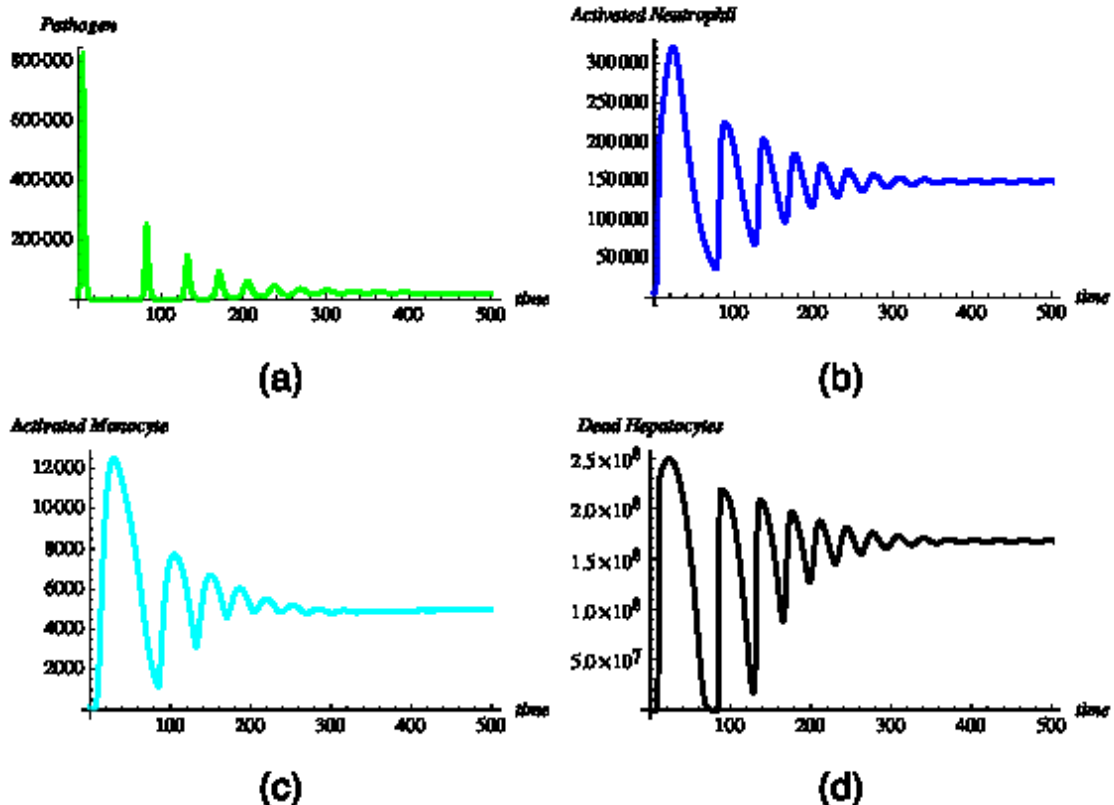
Our simulation results have shown that the high effect of anti-inflammatory cytokine (*IL-10*) inhibits the release of activated immune cells (activated neutrophils and activated monocytes) as well as subsequent cytokine production. The levels of damaged tissue significantly decrease with the presence of the anti-inflammatory cytokine, which in turn moderates the progression of the AIR and reduces the risks of the sepsis development. Our quantitative results are supported by an abundance of experimental studies in the literatures, which have shown that *IL-10* down-regulates the production of secreted cytokines by inhibiting



the various behaviors of activated immune cells (25, 26, 157). Moreover, existing experimental results have suggested that anti-inflammatory mediator inhibits the activation of phagocytes and reduces the ability of activated phagocytes to attack pathogen (39) and therefore is associated with mortality and severity of infection in sepsis (133, 158). Based on the above evidence, our computed results suggest that the high effect of anti-inflammatory cytokines is a “double edged-sword” for AIR since it would either decrease the mortality associated with tissue damage or increase the mortality associated with high load of bacteria.

### 3.4.2.3 Low effect of anti-inflammatory cytokines

Figure 3.21 (a) Concentration of *pathogen* in the presence of low effect of *IL-10*. (b) Concentration of *activated neutrophils* in the presence of low effect of *IL-10*. (c) Concentration of *activated monocytes* in the presence of low effect of *IL-10*. (d) Concentration of *dead hepatocytes* in the presence of low effect of *IL-10*. Horizontal axes represent time (in hours) and Vertical axes represent concentration in arbitrary units



With the low effect of anti-inflammatory cytokines, our computed results have shown low effect of anti-inflammatory cytokine (*IL-10*) fails to inhibit the release of activated immune cells (activated neutrophils and activated monocytes) as well as subsequent cytokine production. The levels of damaged tissue significantly accumulate during the first 500 hours (about 20 days) of infection. In the presence of low effect of the anti-inflammatory cytokine, AIR is at a high risk of development to organ dysfunction and eventually progression to septic shock.

To further investigate the effects of anti-inflammatory cytokines, we simulate a medium effect of anti-inflammatory cytokines and compare simulated results to both high effect of anti-inflammatory cytokines and low effect of anti-inflammatory cytokines. Our computed results show bacteria load decreases during the first 100 hours of infection, together with the total amount of dead hepatocytes. Furthermore, we have observed the production of both activated neutrophils and activated monocytes declines to baseline near 0 at the end of simulation, which indicates a positive trend of sepsis progression to a healthy pattern. Thus, we conclude that the level of anti-inflammatory cytokines plays a vital role in determining the direction of sepsis progression, and the levels of anti-inflammatory cytokines and the time of intervention of anti-inflammatory cytokines will largely influence the outcomes of AIR.

### **3.5 Conclusion**

In this chapter, we propose a system dynamic mathematical model and show that the model has significant potential to help predict the possible pathogenesis of AIR based on a patient's physiological conditions. Also, we show that the model is able to give insight into the innate immunity of sepsis progression by exploring various combinations of levels of phagocytes and cytokines. Our focus is especially on the effects of anti-inflammatory cytokines on pathogen load, phagocytic cells, and tissue damage. We observed that the outcomes of sepsis progression

could be improved by in presence with IL-10 at a medium level at an early stage of infection. Furthermore, our model quantitatively measures the levels of phagocytes (neutrophils and monocytes), compared with existing mathematical models, which provide qualitative estimates.

One of the assumptions of our model is that we currently only include innate immunity, and therefore the results of our model could only represent an early stage of AIR. Adaptive immunity occurs following the innate immune response and includes B-cells, T-cells, and antibodies released from B-cells, which contribute to pathogen clearance (77). IL-10 is known to be released by various subsets of T-cells, which may lead to overproduction of the anti-inflammatory cytokines by the compensatory anti-inflammatory response and, eventually, an increased risk of secondary infection and poor prognosis (77, 146). For further research, we expect to explore the prominent effects of anti-inflammatory mediators on the outcomes of AIR progression by incorporating adaptive immunity and its effects on anti-inflammatory cytokine. Also, we will propose an agent-based model of sepsis progression and compare the results from the system dynamic mathematical model and the agent-based model.

The system dynamic mathematical model proposed in this chapter is a robust and accurate representation of the comprehensive innate immune responses within an AIR/Sepsis episode. This underlining model is general enough and flexible enough that it can be further used to predict the possible outcomes and prognosis for different patient demographics with different model parameters using the experimental data from the literature.

## **Chapter 4 - Mathematical Model of Innate and Adaptive Immunity of Sepsis: a Modeling and Simulation Study of Infectious Disease**

Chapter 4 is based on the paper “Mathematical Model of Innate and Adaptive Immunity of Sepsis: A Modeling and Simulation Study of Infectious Disease” published in BioMed Research International (2015), in press.

### **Abstract**

Sepsis is a systemic inflammatory response (SIR) to infection. In this work, a system dynamics mathematical model (SDMM) is examined to describe the basic components of SIR and sepsis progression. Both innate and adaptive immunities are included, and simulated results *in silico* have shown that adaptive immunity has significant impacts on the outcomes of sepsis progression. Further investigation has found that the intervention timing, intensity of anti-inflammatory cytokines, and initial pathogen load are highly predictive of outcomes of a sepsis episode. Sensitivity and stability analysis were carried out using bifurcation analysis to explore system stability with various initial and boundary conditions. The stability analysis suggested that the system could diverge at an unstable equilibrium after perturbations if  $r_{t2max}$  (maximum release rate of Tumor Necrosis Factor (TNF)- $\alpha$  by neutrophil) falls below a certain level. This finding conforms to clinical findings and existing literature regarding the lack of efficacy of anti-TNF antibody therapy.

**Keywords:** System Dynamics Mathematical Model, Sepsis, Stability Analysis, Bifurcation, Healthcare

## 4.1 Introduction

Sepsis, currently defined as a systemic inflammatory response (SIR) to an infectious agent or trauma, is increasingly considered an exaggerated, poorly regulated innate immune response to microbial products (1, 2). Under health conditions, intruding pathogens are eliminated by immune cells in the immune system. If overwhelming immune response occurs, unbalanced responses between immune cells lead to unexpected harmful patient outcomes such as high fevers, flushed skin, and elevated heart rate, resulting in sepsis. Possible progression to severe sepsis is marked by generalized hypotension, tissue hypoxia, and organ dysfunction (2). Severe sepsis can further develop into septic shock under long-lasting severe hypotension (159), ultimately leading to death.

Severe sepsis and septic shock during an infection are the primary causes of death in intensive care settings (3). On average, sepsis causes 250,000 deaths per year in the United States (4). Among patients in intensive care units (ICUs), sepsis is the second highest cause of mortality (5) and the 10<sup>th</sup> leading cause of death overall in the United States (6). An average of 750,000 sepsis cases occur annually, and this number continues to increase each year (5). Care of patients with sepsis can cost as much as \$60,000 per patient, resulting in a significant healthcare *burden* of nearly \$17 billion annually in the United States (7, 8). Sepsis development in a hospitalized patient can lead to extended hospital stays and consequently increase financial burdens. Cross and Opal (32) pointed out the lack of rapid, reliable assays that could be used to identify the stage or severity of sepsis and to monitor the use of immunomodulatory therapy. However, no such assays are available because complexity of the inflammatory response and the unpredictable nature of septic shock in individual patients render the effect of targeting isolated components of inflammation with supportive therapy difficult to predict (32, 41).

Development of a non-biased, predictive model and model-derived policies that prevent patients from experiencing severe consequences of sepsis (*e.g.*, organ dysfunction) is critical for improving ICU patient care. As studies of mechanisms leading to sepsis development significantly progress due to discoveries of new inflammatory proteins and increased knowledge of the interaction of host cells and pathogens, mathematical models have been developed as dynamic knowledge representation of complicated biological processes. Specifically, the models have been used to simulate dynamic patterns of selected essential indicators in disease progression by integrating cellular and molecular pathways in an immune system. These mathematical models offer potential for understanding complex dynamic systems and, therefore, are used by researchers from various fields to simulate immune response to specific disease (53, 54, 58, 59). Development of modeling techniques could allow novel strategies for disease treatment, oriented at compromising harmful effects of inflammatory responses, to be proposed or tested in model simulations.

In order to construct a mathematical model of sepsis, we searched literatures and found two representative system dynamics mathematical models (SDMMs) of Acute Inflammatory Response (AIR) in previous studies. In 2004, Kumar *et al.* (54) presented a simplified 3-equation SDMM to describe mathematical relationships between pathogen, early pro-inflammatory mediators, and late pro-inflammatory mediators in sepsis progression. In 2006, Reynolds *et al.* (53) proposed a mathematical model for AIR that included a time-dependent, anti-inflammatory response in order to provide insights into a variety of clinically relevant scenarios associated with inflammatory response to infection.

## 4.2 System dynamics mathematical model development

Existing mathematical models focused on inflammation in the literature proved that mathematical modeling is a valid approach for simulating disease progression (53, 54, 58-60). However, the number of variables used, the limited control of system parameters, and the inclusion of many variables involved in real immune response were not modeled in detail. Therefore, oversimplification in AIR models (53, 59) limited AIR behaviors and biological relevance of simulated results. For example, simulated results from AIR models (53, 59) failed to capture a dampened oscillated infection in AIR progression. In addition, existing mathematical models are incomplete representations of sepsis because simulated AIR in both mathematical models (53, 59) is considered as an initial stage of sepsis progression. Therefore, to improve on current models, we developed an 18-equation SDMM to incorporate the most influential variables for septic response development during innate immune response and adaptive immune response. We included equations to represent pathogen load, phagocyte (including neutrophil and monocyte) activation, early and late pro-inflammatory cytokine release, tissue damage, anti-inflammatory cytokine release, CD4+ T cell activation, CD8+ T cell activation, B cell activation, and antibody release. Indicator selection was based on knowledge of cellular and molecular pathways of sepsis from experts in the field and extensive literature review (3, 12, 24, 103, 108, 113, 117, 118, 127, 132, 138, 142, 157). We chose *Salmonella* as a “targeted” pathogen strain in our mathematical model and simulated immune responses to *Salmonella* in the liver of mice. Immune responses to *Salmonella* infections have been investigated extensively in (107-112); therefore, an abundance of data exists for accurate incorporation of relationships among variables to support our SDMM. We used a series of known and hypothesized kinetics of biological system components, including conventional logistics function, law of mass action, and

Michaelis-Menten kinetics to build SDMM from subsystems and mimic interactions between indicators. We combined these formulated but generalized dynamic modeling techniques into a comprehensive SDMM framework to describe sepsis progression, by measuring the steady state of various components in inflammatory responses. In the following seven subsections, we present a detailed description of mathematical construction for each subsystem in a mouse hepatic inflammatory response during SDMM development.

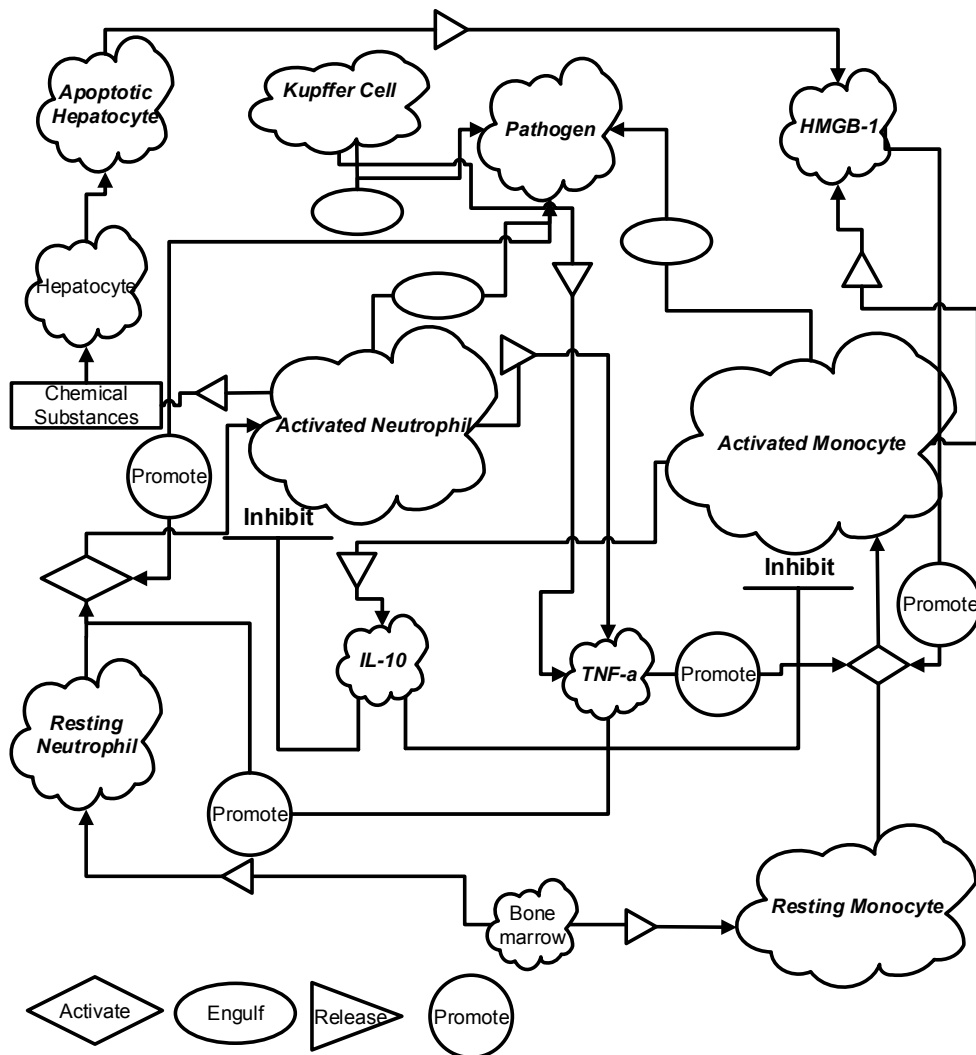
#### ***4.2.1 Process description***

AIR typically occurs when immune cells, such as tissue macrophage, detect intruding pathogens or existing tissue damage and emit a signal to resting phagocytes, such as neutrophil and monocyte (two types of immune cells), in the blood vessels near the infected tissue. Resting phagocytes are activated and migrate towards the site of pathogens or damaged tissue that have recognizable proteins on surface similar to proteins of immune cells. Once activated phagocytes reach the infection site, they engulf and consume the pathogens. Meanwhile, these activated phagocyte cells release pro-inflammatory cytokines such as Tumor Necrosis Factor- $\alpha$  (TNF- $\alpha$ ), Interleukins (IL)-1, Interleukins (IL)-6, Interleukins (IL)-8, and High-Mobility Group Protein B1 (HMGB-1) that activate and recruit additional resting phagocytes from circulation to the infection site. All activated phagocytes eliminate pathogens and secrete substances that accelerate the killing of healthy cells and induce inflammation in the initial process of inflammatory response. In the later stage of AIR progression, several types of anti-inflammatory mediators, such as Interleukins (IL)-10, are released by activated phagocytes (primarily monocyte-derived-macrophage). These anti-inflammatory cytokines inhibit the production of pro-inflammatory cytokines, consequently inhibiting further recruitment of resting phagocytes.



We translated biological processes of AIR to a logical chart, as shown in Figure 1. An explicit description for each biological process is presented in the following six subsections.

**Figure 4.1** Types of indicators (cells and cytokines) and their interactions in AIR progression. *Italic and bold letters represent variables in our SDMM*



#### ***4.2.2 Step 1: Kupffer Cell local response model***

Macrophages, one of the innate host’s first lines of defense against bacterial pathogens, are antimicrobial cells that often determine outcomes of an infection (113). Furthermore, hepatic macrophages (also known as Kupffer Cells or resident liver macrophages) constitute 80%-90% of tissue resident macrophages in the body and significantly influence propagation of

liver inflammation (115, 116). Kupffer Cells within the liver trap and eliminate a majority of bacteria that enter the blood stream (117). During the initial stage of AIR, Kupffer Cells eliminate pathogens, specifically *Salmonella*, during local immune responses.

We developed a Kupffer Cell local response model, defined as interactions between the pathogen and Kupffer Cell (115), consisting of the following:

$$\frac{dP}{dt} = k_{pg}P \left(1 - \frac{P}{P_\infty}\right) - r_{pmk} \frac{[p^n]}{[p^n + k_{c1}^n]} M_{kf} P^* \quad (4.1)$$

$$\frac{dM_{kf}}{dt} = k_{mk} M_{kf} \left(1 - \frac{M_{kf}}{K_\infty}\right) + k_{mkub} M_{kb} - \frac{[p^n]}{[p^n + k_{c1}^n]} M_{kf} P^* - u_{mk} M_{kf} \quad (4.2)$$

$$\frac{dM_{kb}}{dt} = \frac{[p^n]}{[p^n + k_{c1}^n]} M_{kf} P^* - k_{mkub} M_{kb} \quad (4.3)$$

In Eq. (4.1),  $P$  denotes pathogen load,  $k_{pg}$  represents a constant growth rate for pathogens, and  $P_\infty$  represents maximum carrying capacity of the pathogen. Parameter  $r_{pmk}$  represents phagocytosis (killing) rate of Kupffer Cells when Kupffer Cells begin to kill pathogens. Although phagocytosis rate is dependent on time in a slow-S-shape curve (118), the phagocytosis rate does not change if the phagocytosis rate versus time is assumed to be linear. Therefore, we relaxed the condition that phagocytosis rate is constant in our model and assumed  $r_{pmk}$  was constant (118). Eq. (4.2) represents changes of Kupffer Cells over a unit of time, and  $M_{kf}$  denotes the amount of Kupffer Cells in the liver that is available for pathogen binding. Parameter term  $k_{mk}$  represents a constant proliferation (replenishment) rate for Kupffer Cell population, and  $K_\infty$  represents maximum carrying capacity of Kupffer Cells in the liver of mice. Parameter term  $k_{mkub}$  represents the unbinding rate of binding Kupffer Cells and  $u_{mk}$  represents the killing rate of free Kupffer Cells induced by binding to intruding pathogens.

A standard logistic function was used to model pathogen population growth with limited maximum carrying capacity, identified as the first term ( $k_{pg}P \left(1 - \frac{P}{P_\infty}\right)$ ) in Eq. (4.1) (119). The

second term of Eq. (4.1) models local Kupffer Cell responses, or decrease in pathogen population phagocytized by initial tissue resident macrophages (Kupffer Cells). The process of phagocytosis includes two steps: pathogen-ligand binding to receptors of Kupffer Cells and phagocytosis by Kupffer Cells. We used a Hill-type function and receptor-ligand kinetics to model the two basic steps (109, 113, 115, 120-122). First, we defined the rate of pathogen binding to Kupffer Cells as a Hill-type function  $(\frac{[P^n]}{[P^n+k_{c1}^n]})$  in which  $n$  represents a strong affinity of pathogen binding to Kupffer Cells and  $k_{c1}$  is Kupffer Cell concentration that phagocytoses half the pathogens. Second, we modeled pathogen to Kupffer Cell receptors using receptor-ligand kinetics  $(\frac{[P^n]}{[P^n+k_{c1}^n]}M_{kf}P^*)$ , where  $P^*$  represents pathogen concentration. We determined pathogen concentration using the number of pathogens divided by maximum carrying capacity of the pathogen ( $10^8$  cells in the liver of mouse (112)). The final variable to determine pathogen decrease was the phagocytosis rate of pathogens by Kupffer Cells (represented by  $r_{pmk}$ ) times the portion of pathogens binding to Kupffer Cells  $(\frac{[P^n]}{[P^n+k_{c1}^n]}M_{kf}P^*)$ .

We assumed that Kupffer Cells population growth followed a standard logistic growth pattern with a constant proliferation (replenishment) rate, denoted as  $k_{mk}$ , and a maximum carrying limit,  $K_\infty$ , represented by the first term  $(k_{mk}M_{kf}(1 - \frac{M_{kf}}{K_\infty}))$  in Eq. (4.2). Because pathogen binding did not preclude phagocytosis of additional pathogens after completion of phagocytosis, we used receptor-ligand kinetics to model the release of Kupffer Cells from the binding-complex, represented by the second term  $(k_{mkub}M_{kb})$  in Eq. (4.2);  $k_{mkub}$  represents the rate *Salmonella* are phagocytosed by free Kupffer Cells and made available for additional interactions with *Salmonella*. The decreasing number of free Kupffer Cells was due to free Kupffer Cells binding to pathogen, described by the third term  $(\frac{[P^n]}{[P^n+k_{c1}^n]}M_{kf}P^*)$ , and the natural

decay of free Kupffer Cells represented by the fourth term ( $u_{mk}M_{kf}$ ) in Eq. (4.2). Free Kupffer Cells become binding Kupffer Cells once they bind to pathogen, as described by the first term ( $\frac{[P^n]}{[P^n+k_{c1}^n]}M_{kf}P^*$ ) in Eq. (4.3). The second term ( $k_{mkub}M_{kb}$ ) in Eq. (4.3) measures decreasing (releasing) portion of binding Kupffer Cells. The definition of parameters and corresponding experimental data for each system parameter in Kupffer Cell local response model are summarized in Table A.1 (refer to Appendix A).

### 4.2.3 Step2: Neutrophil immune response model

Simulated results (data not shown) from our Kupffer Cell local response model indicated that Kupffer Cells may not sufficiently eliminate infection, especially when the local infection is overwhelming. Furthermore, evidences in biological studies have shown that recruitment of neutrophils (one type of immune cells) from circulation to the infection site significantly contributes to AIR progression because neutrophils is capable to kill pathogens. Neutrophils accumulation is induced by a pro-inflammatory cytokine called “TNF- $\alpha$ ” that is released by Kupffer Cells or activated neutrophils in the tissue. Release of cytokines follows trafficking machinery, and cytokines are released via protein-protein interactions initiated by ligand binding to receptors (129, 130). The mechanism of cytokine release is depicted in Figure 4.2.

We modeled a protein-protein interaction as Michaelis-Menten kinetics (131) and derived our neutrophil immune response model as follows:

$$\frac{dP}{dt} = k_{pg}P \left(1 - \frac{P}{P_\infty}\right) - r_{pmk} \frac{[P^n]}{[P^n + k_{c1}^n]} M_{kf} P^* - r_{pn} \frac{[P^n]}{[P^n + k_{c2}^n]} (N_f + N_b) P^* \quad (4.4)$$

$$\frac{dM_{kf}}{dt} = k_{mk} M_{kf} \left(1 - \frac{M_{kf}}{K_\infty}\right) + k_{mkub} M_{kb} - \frac{[P^n]}{[P^n + k_{c1}^n]} M_{kf} P^* - u_{mk} M_{kf} \quad (4.5)$$

$$\frac{dM_{kb}}{dt} = \frac{[P^n]}{[P^n + k_{c1}^n]} M_{kf} P^* - k_{mkub} M_{kb} \quad (4.6)$$

$$\frac{dT}{dt} = \left( \frac{r_{t1\max} M_{kb}}{m_{t1} + M_{kb}} \right) M_{kb} + \left( \frac{r_{t2\max} N_b}{m_{t2} + N_b} \right) N_b - u_t T \quad (4.7)$$

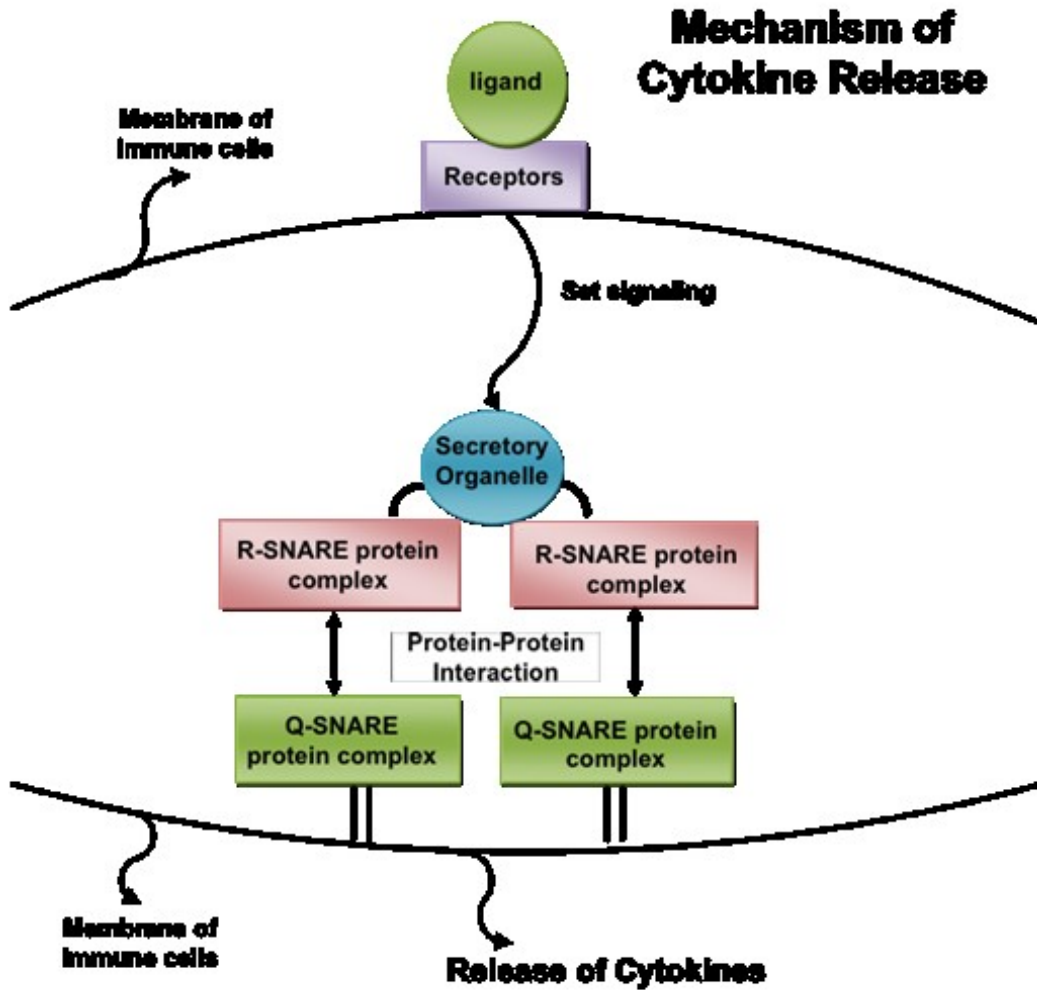
$$\frac{dN_R}{dt} = k_{rd} N_R \left( 1 - \frac{N_R}{N_S} \right) - r_1 N_R (T + P)^* - u_{nr} N_R \quad (4.8)$$

$$\frac{dN_f}{dt} = r_1 N_R (T + P)^* + k_{nub} N_b - \frac{[P^n]}{[P^n + k_{c2}^n]} N_f P^* - u_n N_f \quad (4.9)$$

$$\frac{dN_b}{dt} = \frac{[P^n]}{[P^n + k_{c2}^n]} N_f P^* - k_{nub} N_b \quad (4.10)$$

$$\frac{dr_1}{dt} = k_{r1} (1 + \tanh(N_f^*)) - u_{r1} r_1 \quad (4.11)$$

Figure 4.2 Mechanism of cytokine release



Eq. (4.4) was further derived from Eq. (4.1) in the Kupffer local immune response by incorporating phagocytic effects of neutrophils, represented by term  $r_{pn} \frac{[P^n]}{[P^n + k_{c2}^n]} (N_f + N_b) P^*$ . Eq. (4.5) and Eq. (4.6) are cited from Eq. (4.2) and Eq. (4.3).

Eq. (4.7) represents changes of pro-inflammatory cytokines (denoted by  $T$ ), such as TNF- $\alpha$ , released by binding tissue resident Kupffer Cells ( $M_{kb}$ ) and binding activated neutrophils ( $N_b$ ). Because TNF- $\alpha$  was released after pathogens bound to receptors of tissue resident Kupffer Cells or activated neutrophils, we modeled the process of TNF- $\alpha$  release as a combination of Michaelis–Menten kinetics and receptor-ligand kinetics (10). In Eq. (4.7), the release of TNF- $\alpha$  from Kupffer Cells was initiated by receptor-ligand kinetics, followed by enzymatic kinetics (Michaelis-Menten), represented by the term  $\left(\frac{r_{t1max}M_{kb}}{m_{t1}+M_{kb}}\right)$  where  $r_{t1max}$  represents the maximum production rate of TNF- $\alpha$  by binding Kupffer Cells. The release of TNF- $\alpha$  is a combined effect of receptor-ligand kinetics and enzymatic kinetics; therefore, we incorporated both terms  $\left(\frac{r_{t1max}M_{kb}}{m_{t1}+M_{kb}}\right) M_{kb}$  in the model to represent combined effects of TNF- $\alpha$  releasing processes. Similarly, we used receptor-ligand kinetics and Michaelis-Menten kinetics to model the release of TNF- $\alpha$  from binding activated neutrophils in the second term of Eq. (4.7). The third term in Eq. (4.7),  $u_t T$ , measures degradation of TNF- $\alpha$ , with  $u_t$  representing the degradation rate of TNF- $\alpha$  per hour.

In Eq. (4.8), the first term  $k_{rd} N_R \left(1 - \frac{N_R}{N_S}\right)$  is a standard logistic function to measure increase in the number of resting neutrophils per time unit (hour), represented by the influx of neutrophils into blood vessels per hour. The second term  $r_1 N_R (T + P)^*$  indicates that the decrease in number of resting neutrophils per time unit is due to the neutrophils activation process promoted by pathogen and pro-inflammatory cytokine TNF- $\alpha$ , where  $T^*$  denotes

concentration of TNF- $\alpha$  and  $P^*$  denotes concentration of pathogens (126-128). The third term in Eq. (4.8),  $\mu_{nr}N_R$ , represents the natural decay of resting neutrophils;  $u_{nr}$  is defined as the apoptotic rate of resting neutrophils per time unit in hours. In Eq. (4.9), the first term exactly equals the second term in Eq. (4.8) because the increased population of activated neutrophils directly resulted from activation of the population of resting neutrophils. The second term of Eq. (4.9) used mass action kinetics ( $k_{nub}N_b$ ) to model the release of activated neutrophils from the binding-complex and make activated neutrophils available for additional interaction with pathogens, where  $N_b$  represents the binding-complex and  $k_{nub}$  represents the rate of activated neutrophils released from the binding-complex. Similar to the third term in Eq. (4.8), the third term of Eq. (4.9) models natural apoptosis of activated neutrophils. Eq. (4.10) is similar to the derivation of Eq. (4.3) in the Kupffer local response model. We used a hyperbolic tangent function in Eq. (4.11) to represent a slow-saturation influx rate of neutrophils into hepatic parenchyma, thereby representing the rate of activated resting neutrophils. The definition and corresponding experimental data for newly added system parameters in the neutrophil immune response model are summarized in Table A. 2 (refer to Appendix A).

#### ***4.2.4 Step3: Damaged tissue model***

Complexity in AIR progression is due to multiple effects induced by inflammatory cells. Recruitment of neutrophils helps clear local pathogen levels; however, those inflammatory cells are harmful because they release toxic molecules such as reactive oxygen species (ROS), that can damage host tissue (127, 128). Recent experimental results have shown that neutrophils'  $\beta_2$  integrins adhere to ICAM-1 receptors of hepatocytes and accelerate the killing process of distressed hepatocytes (134).

We assumed the binding process of neutrophils to hepatocytes (healthy liver cells) also followed ligand-receptor kinetics; therefore, we derived the following damaged tissue model:

$$\frac{dD}{dt} = r_{hn} \left( \frac{D^n}{D^n + k_{c3}^n} \right) N_f D^* \left( 1 - \frac{D}{A_\infty} \right) - r_{ah} D \quad (4.12)$$

In Eq. (4.12),  $D$  denotes the number of apoptotic hepatocytes or dead hepatocytes,  $r_{hn}$  represents the rate of apoptotic hepatocytes killed by activated neutrophils, and  $r_{ah}$  represents the recovery rate of apoptotic hepatocytes. Ligand-receptor kinetics  $\frac{[D^n]}{[D^n + k_{c3}^n]} N_f D^*$  represents the amount of apoptotic hepatocytes that bind to activated neutrophils, with binding rate modeled as a Hill-type function  $\frac{[D^n]}{[D^n + k_{c3}^n]}$ . Activated neutrophils have recently been found to kill apoptotic hepatocytes (134). After neutrophils adhere to apoptotic hepatocytes, neutrophils release harmful chemical substances such as reactive oxygen species and proteases that accelerate death of apoptotic hepatocytes (134, 135). When multiplying  $\frac{[D^n]}{[D^n + k_{c3}^n]} N_f D^*$  by  $r_{hn}$ , the entire first term in Eq. (4.12) represents the number of apoptotic hepatocytes killed by activated neutrophils per hour, which is the total number of dead hepatocytes per hour. The maximum number of apoptotic or dead hepatocytes does not exceed the total number of hepatocytes in the liver (represented by  $A_\infty$ ). In addition,  $r_{ah}$  represents the recovery rate of apoptotic hepatocytes, and the second term in Eq. (4.12) is defined as the amount of recovering apoptotic hepatocytes. The definition of parameters and corresponding experimental data for newly added system parameters in damaged tissue model are summarized in Table A.3 (refer to Appendix A).

#### **4.2.5 Step4: Monocyte immune response model**

Recent biological experiments from the literature (136, 137) have shown that monocyte, recruited by the presence of HMGB-1, significantly impacts liver inflammation and liver



fibrosis. Upon liver injury, inflammatory Ly6cC (Gr1C) monocyte subset, as precursors of tissue macrophages in blood vessels near the infected site are attracted and recruited to the injured liver via CCR2-dependent bone marrow egress. The chemokine receptor CCR2 and its ligand MCP-1/CCL2 promote monocyte subset infiltration upon liver injury and further promote the progression of liver fibrosis (134, 138). Because evidence has shown that tumor necrosis factor TNF- $\alpha$  induces a marked increase in CCL2/MCP-1 production in dose- and time-dependent manners (139), we assumed the influx of monocytes from blood vessels to liver is induced by effects of HMGB-1 and TNF- $\alpha$ . Therefore, we modeled the influx of monocytes similarly to kinetics of neutrophils influx. According to existing literature, HMGB-1 is released by necrotic cells and activated monocytes (117, 139, 140). Therefore, we modeled the release of HMGB-1 using receptor-ligand kinetics and enzymatic kinetics, similar to the release of TNF- $\alpha$ , by incorporating effects of necrotic cells and activated monocytes.

$$\frac{dP}{dt} = k_{pg}P \left(1 - \frac{P}{P_\infty}\right) - r_{pmk} \frac{[P^n]}{[P^n + k_{c1}^n]} M_{kf} P^* - r_{pn} \frac{[P^n]}{[P^n + k_{c2}^n]} (N_f + N_b) P^* - r_{pm} \frac{[P^n]}{[P^n + k_{c4}^n]} (M_f + M_b) P^* \quad (4.13)$$

$$\frac{dN_b}{dt} = \frac{[P^n]}{[P^n + k_{c2}^n]} N_f P^* - u_{mn} N_b M_f^* - k_{nub} N_b \quad (4.14)$$

$$\frac{dM_R}{dt} = k_{mr} M_R \left(1 - \frac{M_R}{M_S}\right) - r_2 M_R (H + T)^* - u_{mr} M_R \quad (4.15)$$

$$\frac{dM_f}{dt} = r_2 M_R (H + T)^* + k_{umb} M_b - \frac{[P^n]}{[P^n + k_{c4}^n]} M_f P^* - u_m M_f \quad (4.16)$$

$$\frac{dM_b}{dt} = \frac{[P^n]}{[P^n + k_{c4}^n]} M_f P^* - k_{umb} M_b \quad (4.17)$$

$$\frac{dH}{dt} = \left( \frac{r_{h1\max} (M_b + D)}{mh_1 + M_b + D} \right) (M_b + D) - u_h H \quad (4.18)$$

In Eq. (4.13), we incorporate the effect of phagocytosis by monocytes into Eq. (4.4) because monocytes phagocytose pathogen by a CD14-dependent mechanism (141). We recalled

the Hill-type function equation  $\left(\frac{[P^n]}{[P^n+k_{c4}^n]}\right)$  to represent receptor-ligand binding kinetics between pathogens and activated monocytes. Because binding activated neutrophils are engulfed by infiltrating monocytes (142), we used  $u_{mn}N_bM_f^*$  to calibrate the killing process of binding activated neutrophils by activated monocytes, thereby modifying Eq. (4.10) to Eq. (4.14). Eq. (4.15), Eq. (4.16), and Eq. (4.17) describe activation and migration of resting monocytes from blood vessels to infected tissue. In Eq. (4.15), Eq. (4.16), and Eq. (4.17),  $M_R$ ,  $M_f$ , and  $M_b$  represent resting monocytes, free activated monocytes, and binding activated monocytes, respectively. Principles used to build those three equations are similar to the principle used to build Eq. (4.8), Eq. (4.9), and (4.10) for the neutrophil immune response model. Eq. (4.9) calibrates the release of HMGB-1 per hour by activated monocytes and apoptotic hepatocytes. The process of releasing HMGB-1 is similar to the process of releasing TNF- $\alpha$ . The definition of parameters and corresponding experimental data for newly added system parameters in the monocyte immune response model are summarized in Table A. 4 (refer to Appendix A).

#### ***4.2.6 Step5: SDMM of Innate Immunity***

As one type of anti-inflammatory cytokines, IL-10 was found to prevent subsequent tissue damage by inhibiting activation of phagocytes, including neutrophils and monocytes (145). This anti-inflammatory mediator, produced by macrophages, dendritic cells (DC), B cells, and various subsets of CD4+ and CD8+T cells (146), follows the same mechanism as pro-inflammatory (TNF- $\alpha$  and HMGB-1) release. Because our main focus in this paper was to model innate immune responses, we ignored the release of IL-10 by B cells and T cells during adaptive immune responses; therefore, we modeled the release of IL-10 similarly to pro-inflammatory cytokine release:

$$\frac{dC_A}{dt} = \left( \frac{r_{ca \max} M_b}{C_{Ah} + M_b} \right) M_b - u_{ca} C_A \quad (4.19)$$

In Eq. (4.19),  $C_A$  represents the number of anti-inflammatory cytokine (IL-10) during AIR, and  $\left( \frac{r_{camax} M_b}{C_{Ah} + M_b} \right)$  represents the release rate of anti-inflammatory cytokine (IL-10) by activated monocytes, derived from enzymatic kinetics. The first term in Eq. (4.19) calibrates the increase in the number of anti-inflammatory cytokines every hour and the second term  $u_{ca} C_A$  calibrates the decrease in the number of anti-inflammatory cytokines every hour due to natural degradation. Corresponding parameters and their values are defined in Table A.5 (refer to Appendix A). After incorporating  $(C_A, x) = \frac{x}{(1 + \frac{C_A}{C_\infty})}$ , the inhibition function of IL-10, we derived a comprehensive mathematical model for innate immunity of AIR as follows.  $C_\infty$  represents the dissociation rate of IL-10 with initial estimated value equivalent to 0.02.

$$\frac{dP}{dt} = k_{pg} P \left( 1 - \frac{P}{P_\infty} \right) - r_{pmk} \frac{[P^n]}{[P^n + k_{c1}^n]} M_{kf} P^* - r_{pn} \frac{[P^n]}{[P^n + k_{c2}^n]} (N_f + N_b) P^* - r_{pm} \frac{[P^n]}{[P^n + k_{c4}^n]} (M_f + M_b) P^* \quad (4.20)$$

$$\frac{dM_{kf}}{dt} = k_{mk} M_{kf} \left( 1 - \frac{M_{kf}}{K_\infty} \right) + k_{mkub} M_{kb} - \frac{[P^n]}{[P^n + k_{c1}^n]} M_{kf} P^* - u_{mk} M_{kf} \quad (4.21)$$

$$\frac{dM_{kb}}{dt} = \frac{[P^n]}{[P^n + k_{c1}^n]} M_{kf} P^* - k_{mkub} M_{kb} \quad (4.22)$$

$$\frac{dT}{dt} = \left( \frac{r_{t1 \max} M_{kb}}{m_{t1} + M_{kb}} \right) M_{kb} + \left( \frac{r_{t2 \max} N_b}{m_{t2} + N_b} \right) N_b - u_t T \quad (4.23)$$

$$\frac{dN_R}{dt} = k_{rd} N_R \left( 1 - \frac{N_R}{N_S} \right) - r_1 N_R (T + P)^* - u_{nr} N_R \quad (4.24)$$

$$\frac{dN_f}{dt} = \frac{r_1 N_R (T + P)^*}{\left( 1 + \frac{C_A}{C_\infty} \right)} + k_{nub} N_b - \frac{[P^n]}{[P^n + k_{c2}^n]} N_f P^* - u_n N_f \quad (4.25)$$

$$\frac{dN_b}{dt} = \frac{[P^n]}{[P^n + k_{c2}^n]} N_f P^* - u_{mn} N_b M_f^* - k_{nub} N_b \quad (4.26)$$

$$\frac{dr_1}{dt} = k_{r1} \left( 1 + \tanh(N_f^*) \right) - u_{r1} r_1 \quad (4.27)$$

$$\frac{dD}{dt} = r_{hn} \left( \frac{D^n}{D^n + k_{c3}^n} \right) N_f D^* \left( 1 - \frac{D}{A_\infty} \right) - r_{ah} D \quad (4.28)$$

$$\frac{dM_R}{dt} = k_{mr} M_R \left( 1 - \frac{M_R}{M_S} \right) - r_2 M_R (H + T)^* - u_{mr} M_R \quad (4.29)$$

$$\frac{dM_f}{dt} = \frac{r_2 M_R (H + T)^*}{\left( 1 + \frac{C_A}{C_\infty} \right)} + k_{umb} M_b - \frac{[P^n]}{[P^n + k_{c4}^n]} M_f P^* - u_m M_f \quad (4.30)$$

$$\frac{dM_b}{dt} = \frac{[P^n]}{[P^n + k_{c4}^n]} M_f P^* - k_{umb} M_b \quad (4.31)$$

$$\frac{dH}{dt} = \left( \frac{r_{h1\max} (M_b + D)}{mh_1 + M_b + D} \right) (M_b + D) - u_h H \quad (4.32)$$

$$\frac{dC_A}{dt} = \left( \frac{r_{ca\max} M_b}{C_{Ah} + M_b} \right) M_b - u_{ca} C_A \quad (4.33)$$

In this 14-equation SDMM, variables  $P$ ,  $M_{kf}$ ,  $M_{kb}$ ,  $T$ ,  $N_R$ ,  $N_f$ ,  $N_b$ ,  $r_l$ ,  $D$ ,  $M_R$ ,  $M_f$ ,  $M_b$ ,  $H$ , and  $C_A$  represent levels of pathogen, free Kupffer Cell, binded Kupffer Cell, TNF- $\alpha$ , resting neutrophil, free activated neutrophil, binded activated neutrophil, rate of resting neutrophil activated under infection, damaged tissue, resting monocyte, free activated monocytes, binded activated monocytes, HMGB-1, and IL-10, respectively. These variables are identified and selected as essential indicators in AIR. All system parameters ( $k_{pg}$  *et al.*), which reflect the strength of the host's immune system, are adjustable during model simulation. Detailed description of system parameters is presented in the Appendix A.

#### 4.2.7 Step 6: SDMM incorporated with adaptive immunity

Innate immunity plays a significant role in regulating pathogen clearance through multiple types of cell interactions, providing the first line of defense during early stages of inflammation. Compared to innate immunity, adaptive immunity is typically recognized as a late stage of immune response to infection activated by antigen-presenting cells (APCs) (11). The

nature of adaptive immune response is more complicated than innate immune responses and involves numerous interactions among cells and cytokines. To simplify adaptive immunity, we selected four representative cells including CD4+ T cells, CD8+ T cells, B cells, and antibodies, to simulate a series of immune responses during pathogenic inflammation. The 18-equation SDMM incorporated with adaptive immunity is presented as follows:

$$\frac{dP}{dt} = k_{pg}P \left(1 - \frac{P}{P_\infty}\right) - r_{pmk} \frac{[P^n]}{[P^n + k_{c1}^n]} M_{kf} P^* - r_{pn} \frac{[P^n]}{[P^n + k_{c2}^n]} (N_f + N_b) P^* - r_{pm} \frac{[P^n]}{[P^n + k_{c4}^n]} (M_f + M_b) P^* - r_{pAb} \frac{[P^n]}{[P^n + k_{c5}^n]} A P^* - r_{pcd4} \frac{[P^n]}{[P^n + k_{c6}^n]} T_{CD4} P^* \quad (4.34)$$

$$\frac{dM_{kf}}{dt} = k_{mk} M_{kf} \left(1 - \frac{M_{kf}}{K_\infty}\right) + k_{mkub} M_{kb} - \frac{[P^n]}{[P^n + k_{c1}^n]} M_{kf} P^* - u_{mk} M_{kf} \quad (4.35)$$

$$\frac{dM_{kb}}{dt} = \frac{[P^n]}{[P^n + k_{c1}^n]} M_{kf} P^* - k_{mkub} M_{kb} - r_{Mkbcd8} \frac{[M_{kb}^n]}{[M_{kb}^n + k_{c7}^n]} T_{CD8} M_{kb}^* \quad (4.36)$$

$$\frac{dT}{dt} = \left(\frac{r_{t1\max} M_{kb}}{m_{t1} + M_{kb}}\right) M_{kb} + \left(\frac{r_{t2\max} N_b}{m_{t2} + N_b}\right) N_b - u_t T \quad (4.37)$$

$$\frac{dN_R}{dt} = k_{rd} N_R \left(1 - \frac{N_R}{N_S}\right) - \frac{r_1 N_R (T + P)^*}{\left(1 + \frac{C_A}{C_\infty}\right)} - u_{nr} N_R \quad (4.38)$$

$$\frac{dN_f}{dt} = \frac{r_1 N_R (T + P)^*}{\left(1 + \frac{C_A}{C_\infty}\right)} + k_{nub} N_b - \frac{[P^n]}{[P^n + k_{c2}^n]} N_f P^* - u_n N_f \quad (4.39)$$

$$\frac{dN_b}{dt} = \frac{[P^n]}{[P^n + k_{c2}^n]} N_f P^* - u_{mn} N_b M_f^* - k_{nub} N_b - r_{Nbcd8} \frac{[N_b^n]}{[N_b^n + k_{c7}^n]} T_{CD8} N_b^* \quad (4.40)$$

$$\frac{dr_1}{dt} = k_{r1} (1 + \tanh(N_f^*)) - u_{r1} r_1 \quad (4.41)$$

$$\frac{dD}{dt} = r_{hn} \left(\frac{D^n}{D^n + k_{c3}^n}\right) N_f D^* \left(1 - \frac{D}{A_\infty}\right) - r_{ah} D \quad (4.42)$$

$$\frac{dM_R}{dt} = k_{mr} M_R \left(1 - \frac{M_R}{M_S}\right) - \frac{r_2 M_R (H + T + T_{CD4} + T_{CD8})^*}{\left(1 + \frac{C_A}{C_\infty}\right)} - u_{mr} M_R \quad (4.43)$$

$$\frac{dM_f}{dt} = \frac{r_2 M_R (H + T + T_{CD4} + T_{CD8})^*}{\left(1 + \frac{C_A}{C_\infty}\right)} + k_{umb} M_b - \frac{[P^n]}{[P^n + k_{c4}^n]} M_f P^* - u_m M_f \quad (4.44)$$

$$\frac{dM_b}{dt} = \frac{[P^n]}{[P^n + k_{c4}^n]} M_f P^* - k_{umb} M_b - r_{Mbcd8} \frac{[M_b^n]}{[M_b^n + k_{c7}^n]} T_{CD8} M_b^* \quad (4.45)$$

$$\frac{dH}{dt} = \left( \frac{r_{h1\max} (M_b + D)}{mh_1 + M_b + D} \right) (M_b + D) - u_h H \quad (4.46)$$

$$\frac{dC_A}{dt} = \left( \frac{r_{ca\max} M_b}{C_{Ah} + M_b} \right) M_b - u_{ca} C_A \quad (4.47)$$

$$\frac{dT_{CD4}}{dt} = k_{cd4} T_{CD4} \left( 1 - \frac{T_{CD4}}{T_{cd4\infty}} \right) + r_{cd4Mb} \frac{[M_b^n]}{[M_b^n + k_{c8}^n]} M_b^* T_{CD4} - k_{cd4M} \frac{[T_{cd4}^n]}{[T_{cd4}^n + k_{c10}^n]} T_{CD4}^* (M_b + M_f) - u_{cd4} T_{CD4} \quad (4.48)$$

$$\frac{dT_{CD8}}{dt} = k_{cd8} T_{CD8} \left( 1 - \frac{T_{CD8}}{T_{cd8\infty}} \right) + r_{cd8Mb} \frac{[M_b^n]}{[M_b^n + k_{c8}^n]} M_b^* T_{CD8} - k_{cd8M} \frac{[T_{cd8}^n]}{[T_{cd8}^n + k_{c10}^n]} T_{CD8}^* (M_b + M_f) - u_{cd8} T_{CD8} \quad (4.49)$$

$$\frac{dB}{dt} = k_B B \left( 1 - \frac{B}{B_\infty} \right) + r_{Bt} \frac{[B^n]}{[B^n + k_{c9}^n]} B^* T_{cd4} - u_B B \quad (4.50)$$

$$\frac{dA}{dt} = \left( \frac{r_{Ab\max} B}{m_{Ab} + B} \right) B - u_{Ab} A \quad (4.51)$$

Eq. (4.48) describes the recruiting process of CD4+ T cells during adaptive immunity.

The first term  $k_{cd4} T_{CD4} \left( 1 - \frac{T_{CD4}}{T_{cd4\infty}} \right)$  in Eq. (4.48) is a standard logistic function to describe the natural migration process of CD4+ T cells to the site of infection, and  $k_{cd4}$  is a constant parameter to define the recruitment rate of CD4+ T cells from lymph node to the site of infection under undefined mechanisms in our SDMM. Activated monocytes that are phagocytizing pathogens were recognized as one type of APCs; APCs display major histocompatibility complex class II (MHCII) peptide on the surface available for binding to T cell antigen-specific receptor (TCR) (*160*). APCs also activate the TCR on CD4+ T cells and enhance CD4+ T cell migration to the site of infection through a TCR-MCHII receptor-ligand response (*11*), represented by the second term,  $r_{cd4Mb} \left( \frac{M_b^n}{M_b^n + k_{c8}^n} \right) M_b^* T_{CD4}$ . Similar to the receptor-ligand response we modeled in innate immunity, we used a Hill-type  $\left( \frac{M_b^n}{M_b^n + k_{c8}^n} \right)$  function to model the binding rate of activated monocytes to CD4+ T cells. Receptor-ligand kinetics

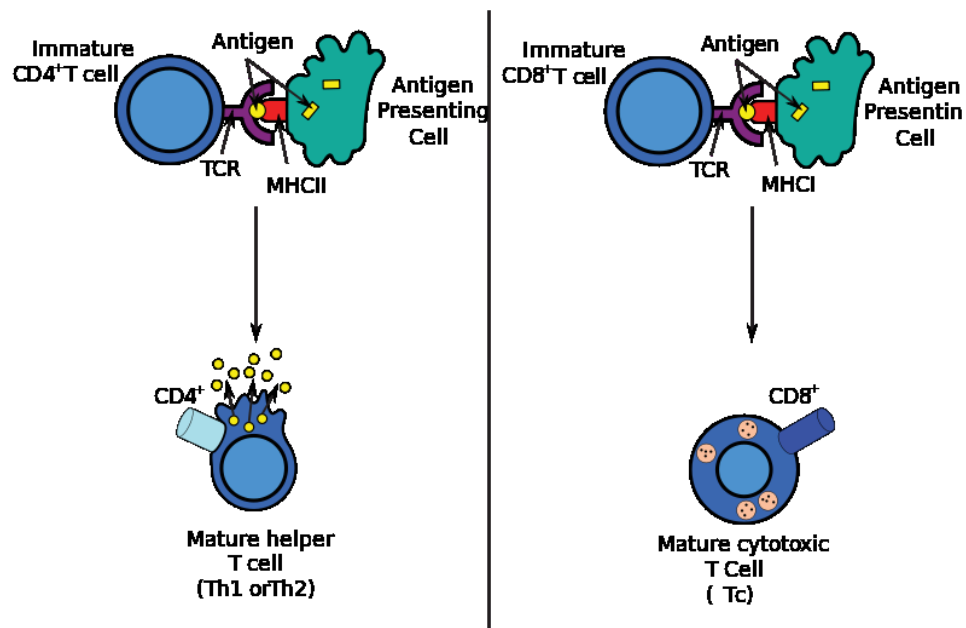
$r_{cd4Mb} \left( \frac{M_b^n}{M_b^n + k_{c8}^n} \right) M_b^* T_{CD4}$  represent the amount of CD4+ T cells activated by activated monocytes. Our model assumes that T cells become activated under TCR-MCHII receptor-ligand response; however, we recognize that the activation process of T cells is much more complicated than we modeled because T cell activation requires at least two signals in order to become fully activated (160-163). CD4+ T cells that undergo apoptotic are phagocytized by activated monocytes (164), represented by the third term in Eq. (4.48). We assume that free activated monocytes and binding activated monocytes phagocytize binding CD4+ T cells, represented by a receptor-ligand response  $k_{cd4M} \frac{[T_{cd4}^n]}{[T_{cd4}^n + k_{c10}^n]} T_{CD4}^* (M_b + M_f)$ , with the binding rate equal to  $k_{cd4M} \frac{[T_{cd4}^n]}{[T_{cd4}^n + k_{c10}^n]}$  and the phagocytosis rate equal to  $k_{cd4M}$ . The fourth term,  $u_{cd4} T_{CD4}$ , in Eq. (4.48) describes a natural apoptosis process of CD4+ T cell during migration and activation processes.

Similar to Eq. (4.48), Eq. (4.49) describes the recruitment process of CD8+ T cells during adaptive immunity. The activation process of CD8+ T cells through a major histocompatibility complex class I peptide (MHCI)-TCR mechanism follows similar receptor-ligand kinetics of CD4+ T cells, represented by the second term,  $r_{cd8Mb} \left( \frac{M_b^n}{M_b^n + k_{c8}^n} \right) M_b^* T_{CD4}$ , in Eq. (4.49). The activation process of CD4+ T cells and CD8+ T cells is depicted in Figure. 4.3.

CD4+ T and CD8+ T cells mediate the host response to sepsis in various ways. Experimental studies have shown that T<sub>H1</sub> effector cells proliferated by CD4+ T cells can improve the phagocytosis rate of Kupffer Cells, activated neutrophils, and activated monocytes through a receptor-ligand response (165). To simplify our SDMM, we used CD4+ T cell population to substitute for T<sub>H1</sub> effector cell population, and we measured a decrease in the amount of pathogens via CD4+ T cell-dependent interactions using receptor-ligand kinetics,

represented by the sixth term  $r_{pcd4} \frac{[P^n]}{[P^n + k_{c6}^n]} T_{CD4} P^*$  in Eq. (4.34). CD8<sup>+</sup> T cells are cytotoxic cells because their primary function is to kill infected target cells (165, 166). Therefore, we incorporated receptor-ligand kinetics into the third term in Eq. (4.35), the fourth term in Eq. (4.40), and the third term in Eq. (4.45) to measure the decrease in binding Kupffer Cells, binding activated neutrophils, and binding activated monocytes. In SDMM, we used the population of binding Kupffer Cells, binding activated neutrophils, and binding activated monocytes to represent the population of infected cells under the assumption that binding cells bind to pathogens. Therefore, the population of binding cells was also used to represent the population of APCs in our SDMM.

**Figure 4.3** A simplified mechanism of T cell activation



Macrophage activation is related to IFN-gamma released by T cells (167-169). Because we did not calibrate INF-gamma in our SDMM, we calculated the monocyte activation process using CD4<sup>+</sup> T cell and CD8<sup>+</sup> T cell populations instead of interferon-gamma (IFN-gamma)



population for simplicity. Under this assumption, we revised the second term in Eq. (4.43) and the first term in Eq. (4.44) to  $\frac{r_2 M_R (H+T+T_{CD4}+T_{CD8})^*}{(1+\frac{C_A}{C_\infty})}$ . The newly revised term,  $\frac{r_2 M_R (H+T+T_{CD4}+T_{CD8})^*}{(1+\frac{C_A}{C_\infty})}$ , incorporates the CD4+ T cell and CD8+ T cell populations to reflect the role of CD4+ T cells and CD8+ T cells in the resting monocyte activation process.

T<sub>h1</sub> or T<sub>h2</sub> effector cells activate B cells to release antibodies (11). Eq. (4.50) describes the activation process of B cells by the CD4+ T cell population under the assumption that the CD4+ T cell population can represent T<sub>h1</sub> and T<sub>h2</sub> effector cell populations due to model simplification. The first term  $k_B B \left(1 - \frac{B}{B_\infty}\right)$  in Eq. (4.50) measures the migration process of B cells from lymph nodes to the site of infection, which is derived from a standard logistic function. Derivation of the second term,  $r_{Bt} \frac{[B^n]}{[B^n+k_{c9}^n]} B^* T_{cd4}$ , in Eq. (4.50) is similar to derivation of the second terms in Eq. (4.48) and Eq. (4.49), following a receptor-ligand kinetics. Decrease in B cell population was induced by natural apoptosis, represented by the third term,  $u_B B$ , in Eq. (4.50). Plasma cells secrete antibodies (11), but we did not incorporate this specific mechanism into our SDMM. Instead, we modeled that antibodies were released by B cells. In Eq. (4.51), the release of antibodies from B cells is represented by the first term,  $\left(\frac{r_{Abmax} B}{m_{Ab} + B}\right) B$ , following receptor-ligand kinetics and enzymatic kinetics (Michaelis-Menten), similar to TNF- $\alpha$ , HMGB-1, IL-10 release process described in innate immunity. The second term,  $u_{Ab} A$ , in Eq. (4.51) describes the natural catabolism of antibodies. When antibodies are released from plasmas cells, T<sub>H</sub> cells define the isotype of the antibody (11); we did not model specific isotype of antibodies in our model. Antibodies can opsonize pathogen and contribute to further pathogen clearance at the late stage of inflammation (11, 165), as represented by the fifth term,  $r_{pAb} \frac{[P^n]}{[P^n+k_{c5}^n]} AP^*$ , in Eq.

(4.34). The definition and corresponding experimental data for newly added system parameters in SDMM incorporated with adaptive immunity are summarized in Table A. 6 (refer to the Appendix A).

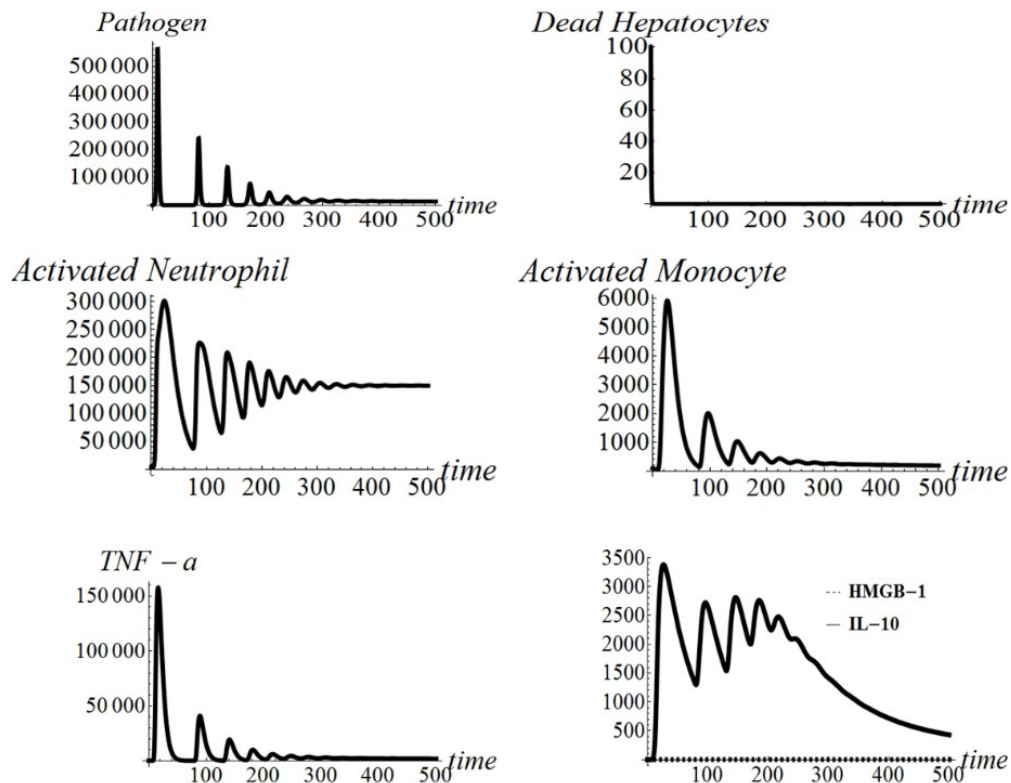
### 4.3 Simulated results

Using SDMM, we identified three distinct dynamic patterns of indicators that represent three states of AIR progression: *Healing Process*, *Persistent Infection*, and *Organ Dysfunction*. Based on our computed results, we concluded that a *Healing Process* occurs when the level of pathogens, level of phagocytic cells (neutrophils and monocytes), and level of inflammatory cytokines (TNF- $\alpha$ , HMGB-1, and IL-10) oscillates below threshold during infection. We recognized that a *Persistent Infection* occurs if inflammatory responses are active (damaged tissue oscillates above threshold during infection). We also recognized that *Organ Dysfunction* occurs if an overwhelming load of bacteria is observed. Computed results are shown in Figure 4.4.

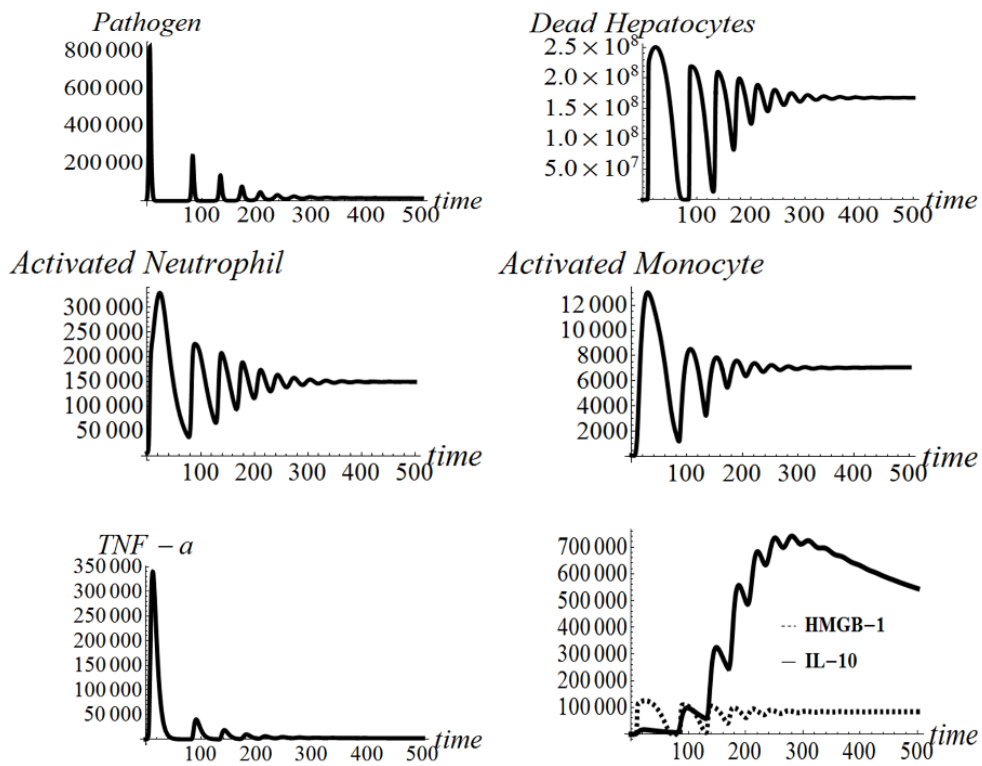
In order to initially validate our SDMM, model behaviors were compared to results from experimental designs under specific parameter-settings. If results did not match, model reconfiguration was implemented by adjusting the relationship between components (indicators) or fine-tuning parameter values. We compared our simulated results to experimental results (170) and simulated results from a latest version of an AIR progression mathematical model (53). We observed that our simulated results had better agreement with experimental results compared to simulated results from the previous mathematical model because our simulated results captured a dampened oscillated infection. We recognized that this improvement of simulation accuracy is a result of additional cellular and molecular pathways of AIR progression incorporated into our SDMM compared to previous mathematical models (53, 54). For example,

we simulated the effect of monocytes in our SDMM by incorporating interactions of monocytes with other cells and cytokines. In contrast, previous mathematical models simulated the combined effect of neutrophils and monocytes with the limitation of oversimplification of AIR progression. Our simulated results indicated that time required for peak levels of TNF- $\alpha$ , HMGB-1, and IL-10 is approximately 12 hrs, 18 hrs, and 24 hrs, respectively. These results are consistent with results from clinical trials (157), as shown in Figure 4.5.

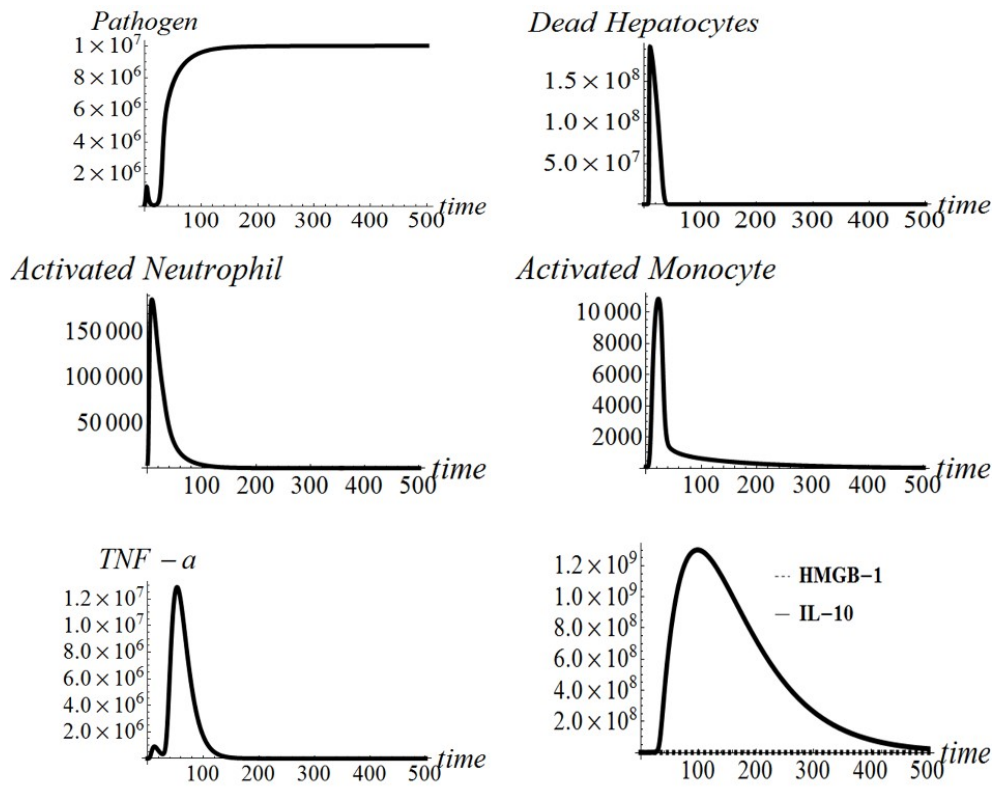
**Figure 4.4 Dynamic patterns of AIR progression related to various initial levels of indicators and adjustable system parameters. X-axis represents time (in hours) and Y-axis represents number of indicators (pathogen, dead hepatocyte, activated neutrophil, activated monocyte, TNF- $\alpha$ , HMGB-1, and IL-10) during AIR progression. (a) Combined dynamic patterns of indicators represent a *Healing Process* in AIR progression (pathogen initial counts = 100). (b) Combined dynamic patterns of indicators represent a *Persistent Infection* in AIR progression (pathogen initial counts = 10000). (c) Combined dynamic patterns of indicators represent *Organ Dysfunction* in AIR progression (pathogen initial counts = 100000)**



(a)

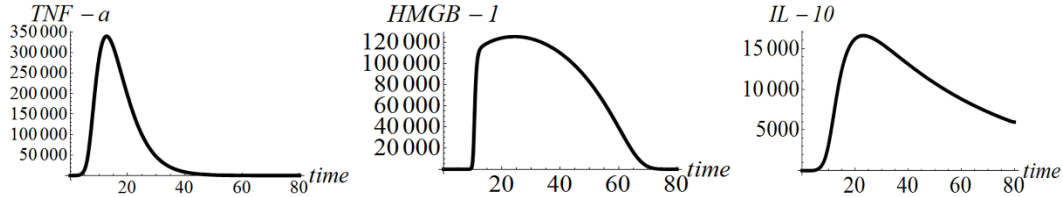


(b)



(c)

**Figure 4.5 Dynamic patterns of TNF- $\alpha$ , HMGB-1, and IL-10 in mice livers during AIR generated from our SDMM. X-axis represents time (in hours) and Y-axis represents number of indicators**



We also explored the impact of pathogen initial load on phagocytic cells, inflammatory cytokines, and damaged tissue at low, medium, and high levels during AIR progression. We found that dynamic patterns of AIR progression were identified as “*Healing Process*” if the initial number of pathogens was set below 3.2 (result was transformed to a base-10 logarithm) in simulation; dynamic patterns of AIR progression were identified as “*Persistent Infection*” if the initial number of pathogens was set between 3.2 and 5.9 (result was transformed to a base-10 logarithm) in simulation; and dynamic patterns of AIR progression were identified as “*Organ Dysfunction*” if the initial number of pathogens was set above 5.9 (result was transformed to a base-10 logarithm) in simulation. During some simulation replications, our findings are inconsistent with evidences found from experimental studies (171-173) that indicated outcomes of AIR progression are more likely to lead to a healthy state with a low-dose of pathogens, which will be further illustrated in the discussion section.

By incorporating adaptive immunity to SDMM, we generated dynamic patterns of pathogen count, dead hepatocyte count, activated neutrophil count, activated monocyte count, TNF- $\alpha$ , HMGB-1, IL-10, CD4+ T cell, CD+ 8 T cell, B cell, and antibodies using Mathematica (Wolfram Mathematica 9.0). Computed results are shown in Figure 4.6, 4.7.

**Figure 4.6 An adaptive immunity influence on outcomes of sepsis progression (pathogen initial counts = 10000). X-axis represents time (in hours) and Y-axis represents number of indicators**

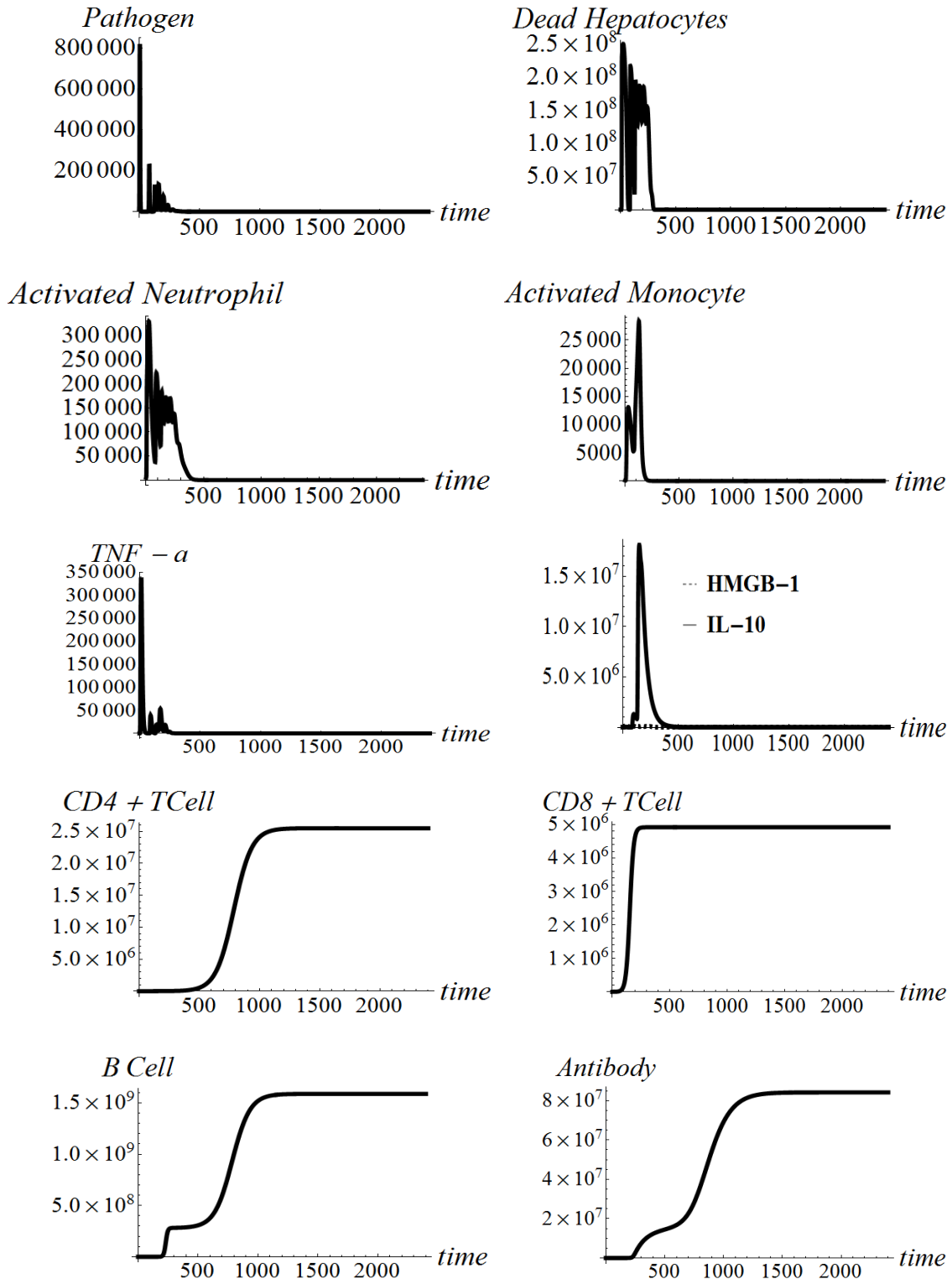
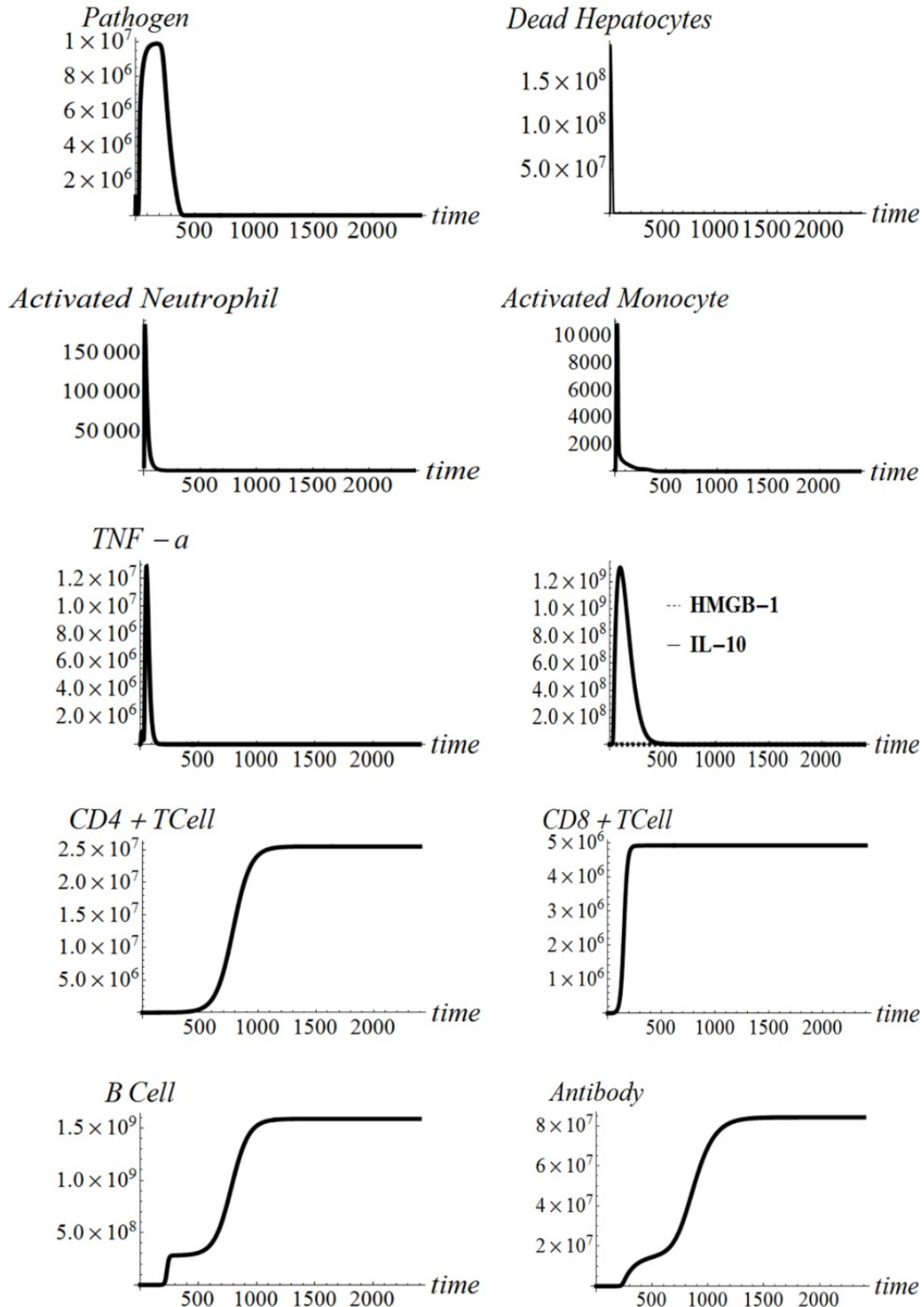


**Figure 4.7 An adaptive immunity influence on outcomes of sepsis progression (pathogen initial counts = 100000). X-axis represents time (in hours) and Y-axis represents number of indicators**



Based on our computed results, we observed pathogen count converged toward 0 at approximately 14 days (336 hrs) post infection during a **Persistent Infection** when the effect of adaptive immunity was incorporated into the full model. Compared to **Persistent Infection** observed in innate immunity (shown in Figure 4.4 (b)), the activated neutrophil count and HMGB-1 count converged toward 0 at approximately 25 days (600 hrs) post infection. Convergence in TNF- $\alpha$  count occurred at approximately 14 days post infection, earlier than convergence in HMGB-1 count in innate immunity. The peak level of activated monocytes increased to 26000, which was 2 times higher than the peak level of activated monocytes observed in innate immunity. No additional dead hepatocytes were observed after 25 days (600 hrs) post infection because cells (activated neutrophils and activated monocytes) and cytokines (TNF- $\alpha$ , HMGB-1, and IL-10) associated with further tissue damage converged toward 0, indicating adaptive immunity positively impacted outcomes of sepsis progression.

By incorporating CD4+ T cells, CD8+ T cells, B cells and antibodies into innate immunity, we observed that elevated pathogen count during **Organ Dysfunction** began to drop at approximately 20 days post infection (500 hrs), and the process of pathogen clearance induced by adaptive immunity persisted approximately 5 days post infection. Pathogen count returned to 0 at 25 days post infection (720 hrs). Cells (activated neutrophils and activated monocytes) and cytokines (TNF- $\alpha$ , HMGB-1, and IL-10) associated with innate immunity dropped significantly during simulation, but CD4+ T cells, CD8+ T cells, and B cells persistently elevated after 500 hrs post infection, indicating adaptive immunity's contribution to pathogen clearance during the late stage of sepsis progression. A mice model infected with a high dose of *Escherichia coli* (174) showed that the number of CD4+ T cells, CD8+ T cells, and B cells persisted throughout 7



days, thereby conforming to dynamic patterns of CD4+ T cells, CD8+ T cells, and B cells observed in our SDMM.

#### 4.4 Stability analysis

In order to study model behaviors under various parameter settings and initial conditions, bifurcation diagrams were used to conduct stability analysis for each subsystem during model construction. The objective of stability analysis was to identify key parameters or key processes in sepsis episodes. Numerical analysis that we used is similar to the previous study (60).

We started with stability analysis by calculating equilibrium points in Kupffer Cell local response model. The equilibrium points were derived by setting equations in Kupffer Cell local response model free of the time (time is denoted by  $t$  in equations), which imply that:

$$k_{pg}\bar{P}\left(1 - \frac{\bar{P}}{P_\infty}\right) - r_{pmk} \frac{[\bar{P}^n]}{[\bar{P}^n + k_{c1}^n]} \bar{M}_{kf} \bar{P}^* = 0 \quad (4.52)$$

$$k_{mk} \bar{M}_{kf} \left(1 - \frac{\bar{M}_{kf}}{K_\infty}\right) + k_{mkub} \bar{M}_{kb} - \frac{[\bar{P}^n]}{[\bar{P}^n + k_{c1}^n]} \bar{M}_{kf} \bar{P}^* - u_{mk} \bar{M}_{kf} = 0 \quad (4.53)$$

$$\frac{[\bar{P}^n]}{[\bar{P}^n + k_{c1}^n]} \bar{M}_{kf} \bar{P}^* - k_{mkub} \bar{M}_{kb} = 0 \quad (4.54)$$

To solve Eq. (4.52), Eq. (4.53), and Eq. (4.54), we firstly added Eq. (4.53) to Eq. (4.54), which eliminate the Eq. (4.53) and Eq. (4.54) to Eq. (4.55):

$$k_{mk} \bar{M}_{kf} \left(1 - \frac{\bar{M}_{kf}}{K_\infty}\right) - u_{mk} \bar{M}_{kf} = 0 \quad (4.55)$$

By solving Eq. (4.52) and Eq. (4.55) together, we could obtain the following feasible equilibrium points:

If  $k_{mkub} \neq 0$ ,

$$(\bar{M}_{kf} = 0, \bar{P} = 0, \bar{M}_{kb} = 0) \text{ or } (\bar{M}_{kf} = 0, \bar{P} = P_\infty, \bar{M}_{kb} = 0) \text{ or } \left(\bar{M}_{kf} = \frac{k_\infty(k_{mk} - \mu_{mk})}{k_{mk}}, \bar{P} = 0, \bar{M}_{kb} = 0\right)$$

The above equilibrium points are valid if the following conditions are satisfied:

$$k_\infty \neq 0, P_\infty \neq 0, k_{c1} \neq 0, n > 0$$

From the derived feasible equilibrium points, we obtained two disease free equilibrium points given as:

$$(\overline{M}_{kf} = 0, \overline{P} = 0, \overline{M}_{kb} = 0) \text{ or } \left( \overline{M}_{kf} = \frac{k_{\infty}(k_{mk} - \mu_{mk})}{k_{mk}}, \overline{P} = 0, \overline{M}_{kb} = 0 \right)$$

We further calculated the associated Jacobian matrix to determine stability of the disease free equilibrium points, the Jacobian matrix was given as follows:

$$\begin{bmatrix} k_{pg} - \frac{2k_{pg}\overline{P}}{P_{\infty}} - \frac{r_{pmk}\overline{M}_{kf}\sigma}{P_{\infty}}, & -r_{pmk} \frac{\overline{P}^{n+1}}{(\overline{P}^n + k_{c1}^n)P_{\infty}}, & \mathbf{0} \\ -\frac{\overline{M}_{kf}\sigma}{P_{\infty}}, & (k_{mk} - u_{mk}) - \frac{2k_{mk}\overline{M}_{kf}}{K_{\infty}} - \frac{\overline{P}^{n+1}}{(\overline{P}^n + k_{c1}^n)P_{\infty}}, & k_{mkub} \\ \frac{\overline{M}_{kf}\sigma}{P_{\infty}}, & \frac{\overline{P}^{n+1}}{(\overline{P}^n + k_{c1}^n)P_{\infty}}, & -k_{mkub} \end{bmatrix} \quad (4.56)$$

Where,  $\sigma = \frac{n\overline{P}^{2n} - n\overline{P}^n(\overline{P}^n + k_{c1}^n)}{(\overline{P}^n + k_{c1}^n)^2}$

Replacing the first disease free equilibrium point  $(\overline{M}_{kf} = 0, \overline{P} = 0, \overline{M}_{kb} = 0)$  into the Jacobian matrix above (Eq. (4.56)), we can further derive the following Jacobian matrix:

$$J_1 = \begin{bmatrix} k_{pg} & \mathbf{0} & \mathbf{0} \\ \mathbf{0} & k_{mk} - u_{mk} & k_{mkub} \\ \mathbf{0} & \mathbf{0} & -k_{mkub} \end{bmatrix} \quad (4.57)$$

In order to find the associated eigenvalues with (4.57), we solved the following equation:

$$\det(J_1 - \lambda I) = \begin{bmatrix} k_{pg} - \lambda & \mathbf{0} & \mathbf{0} \\ \mathbf{0} & k_{mk} - u_{mk} - \lambda & k_{mkub} \\ \mathbf{0} & \mathbf{0} & -k_{mkub} - \lambda \end{bmatrix} = \mathbf{0} \quad (4.58)$$

Using Mathematica (Wolfram Mathematica 9.0), we obtained the eigenvalues of Eq. (4.58) as follows:

$$\lambda_{11} = -k_{mkub}, \lambda_{21} = k_{pg}, \lambda_{31} = k_{mk} - u_{mk}$$

Thus, we concluded that the first disease free equilibrium point is stable if and only if the following conditions are satisfied:

$$k_{mkub} > 0 \text{ and } k_{pg} < 0 \text{ and } k_{mk} < u_{mk}$$

Following a similar procedure above, we replaced the second disease free equilibrium point  $(\overline{M}_{kf} = \frac{k_{\infty}(k_{mk} - \mu_{mk})}{k_{mk}}, \overline{P} = 0, \overline{M}_{kb} = 0)$  into the Jacobian matrix in Eq. (4.56).

The Jacobian matrix associated with the second disease free equilibrium point was revised to:

$$J_2 = \begin{bmatrix} k_{pg} & 0 & 0 \\ 0 & u_{mk} - k_{mk} & k_{mkub} \\ 0 & 0 & -k_{mkub} \end{bmatrix} \quad (4.59)$$

Again, by solving Eq. (4.60):

$$\det(J_2 - \lambda I) = \begin{bmatrix} k_{pg} - \lambda & 0 & 0 \\ 0 & u_{mk} - k_{mk} - \lambda & k_{mkub} \\ 0 & 0 & -k_{mkub} - \lambda \end{bmatrix} = 0 \quad (4.60)$$

We obtained the eigenvalues associated with the second disease free equilibrium point, and the eigenvalues were expressed as follows:

$$\lambda_{12} = -k_{mkub}, \lambda_{22} = k_{pg}, \lambda_{32} = u_{mk} - k_{mk}$$

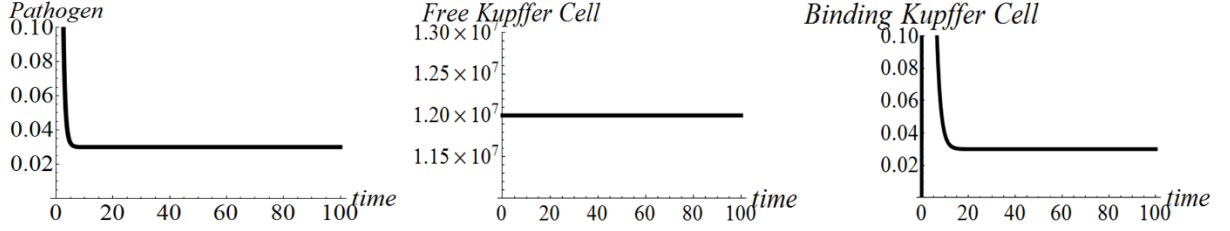
Thus, the stability of the second disease free equilibrium can be achieved if and only if the following conditions are satisfied:

$$k_{mkub} > 0 \text{ and } k_{pg} < 0 \text{ and } k_{mk} > u_{mk}$$

Because  $k_{pg}$  (the growth rate of pathogen) was assumed to be always larger than 0, we concluded that the disease free equilibrium points for Kupffer Cell local response model are always unstable.

In order to verify our conclusion, we did a numerical study on the second disease free equilibrium point  $(\overline{M}_{kf} = 12000000, \overline{P} = 0, \overline{M}_{kb} = 0)$ . We found the disease free equilibrium point  $(\overline{M}_{kf} = 12000000, \overline{P} = 0, \overline{M}_{kb} = 0)$  changed if pathogen load was changed from 0 to 2 at equilibria (a small perturbation was given), the simulated results of change in the disease free equilibrium point  $(\overline{M}_{kf} = 12000000, \overline{P} = 0, \overline{M}_{kb} = 0)$  are shown in Figure 4.8.

**Figure 4.8 Change in the disease free equilibrium point ( $\overline{M}_{kf} = 12000000, \overline{P} = 0, \overline{M}_{kb} = 0$ ) when  $P = 2$  and  $k_{pg}=1.2$**

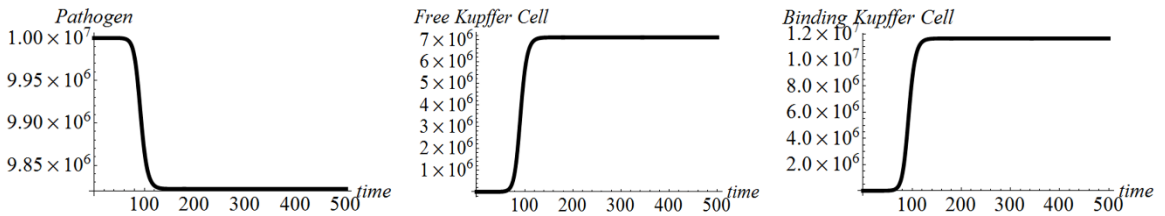


We also analyzed stability of the pathogen saturation equilibrium point ( $\overline{M}_{kf} = 0, \overline{P} = P_\infty, \overline{M}_{kb} = 0$ ). By numerical analysis, we concluded that the pathogen saturation equilibrium point ( $\overline{M}_{kf} = 0, \overline{P} = P_\infty, \overline{M}_{kb} = 0$ ) is stable if the following conditions are satisfied:

$$k_{mk} < 0.5 \text{ and } u_{mk} > 0.2$$

When  $k_{mk} > 0.5$ , the pathogen saturation equilibrium point ( $\overline{M}_{kf} = 0, \overline{P} = P_\infty, \overline{M}_{kb} = 0$ ) became unstable. Simulated results of change in the pathogen saturation equilibrium point ( $\overline{M}_{kf} = 0, \overline{P} = P_\infty, \overline{M}_{kb} = 0$ ) are shown in Figure 4.9.

**Figure 4.9 Change in the pathogen saturation equilibrium point ( $\overline{M}_{kf} = 0, \overline{P} = P_\infty, \overline{M}_{kb} = 0$ ) when  $M_{kf} = 2$  and  $k_{mk} = 0.9$**



Stability analysis of equilibrium points in Kupffer Cell local response model indicated that Kupffer Cell local response model is not a stable system. The disease free equilibrium point ( $\overline{M}_{kf} = 12000000, \overline{P} = 0, \overline{M}_{kb} = 0$ ) changed when the second infection occurred ( $P$  was

changed from 0 to 2). However, recruiting more Kupffer Cells positively contributed to the pathogen clearance after a saturated infection ( $P = P_\infty$ ), as shown in Figure 4.9.

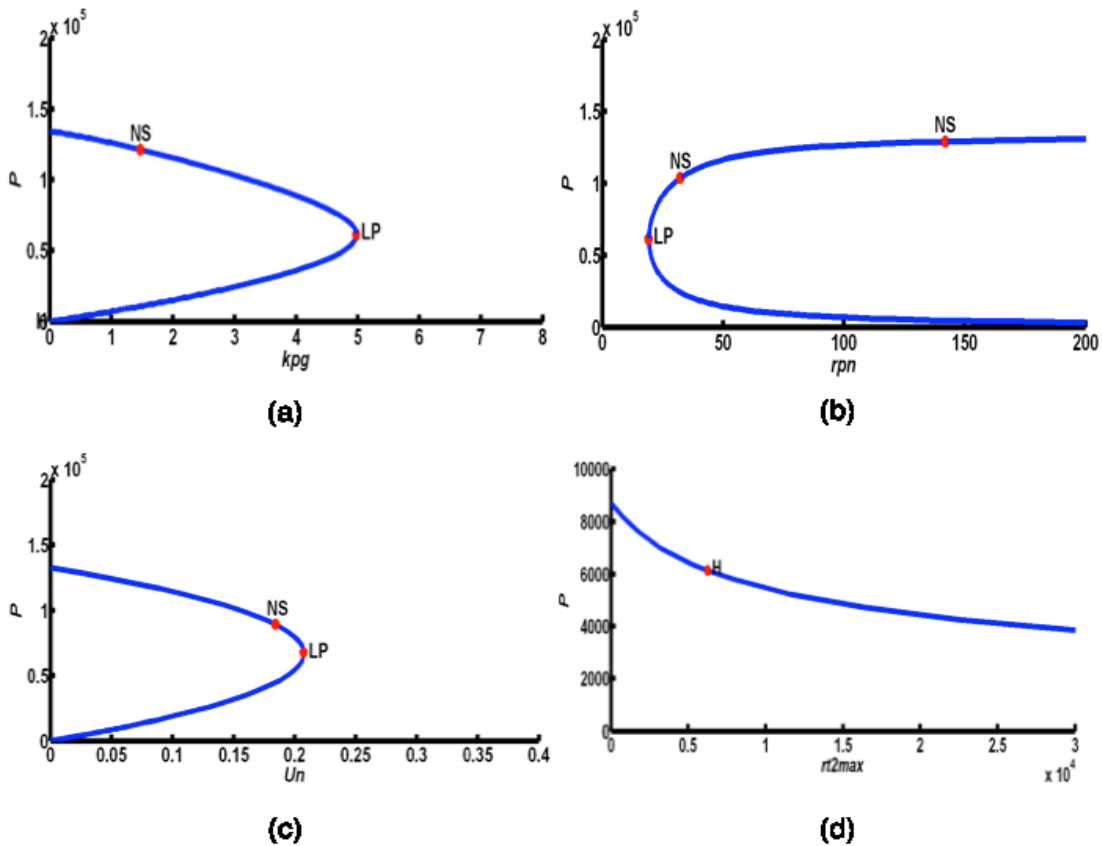
Bifurcation diagrams are graphical tools to visualize dynamic system behavior changes with parameters. In this paper, we used Matcont to generate bifurcation diagrams. Matcont, a Matlab continuation package with a graphic user interface (GUI) for interactive numerical study of parameterized nonlinear ordinary differential equations (ODEs), computes curves of equilibria, limit points, Hopf point, limit cycles, fold, torus, and branch point bifurcation of limit cycles (153).

In bifurcation diagrams, Y-axis represents equilibria of state variable and X-axis represents value of system parameter that generates equilibria. Therefore, bifurcation diagrams reflect change in equilibria of dynamic systems (change in number of equilibria or change in numerical value of equilibria) in relation to change in numerical value of system parameters. We analyzed stability of dynamic systems by identifying types of bifurcation points in bifurcation diagrams because bifurcation points are defined as points at which stability changes from stable to unstable. Two typical bifurcation points were evident in our bifurcation diagrams: limit point (marked as “LP” in Matcont) and Hopf point (marked as “H” in Matcont). Neutral Saddle point was marked as “NS” in the bifurcation diagram, but it is not a bifurcation point for equilibrium because it is identified as a hyperbolic saddle. Figure 4.10 shows that change in equilibria of state variable *pathogen* is related to change in system parameters in the neutrophil immune response model.

LPs in bifurcation diagrams of neutrophil immune response model appeared when two equilibria merged into one equilibrium; the number of equilibria of dynamic systems changed when LPs were detected. LPs are also turning points at which dynamic systems change from

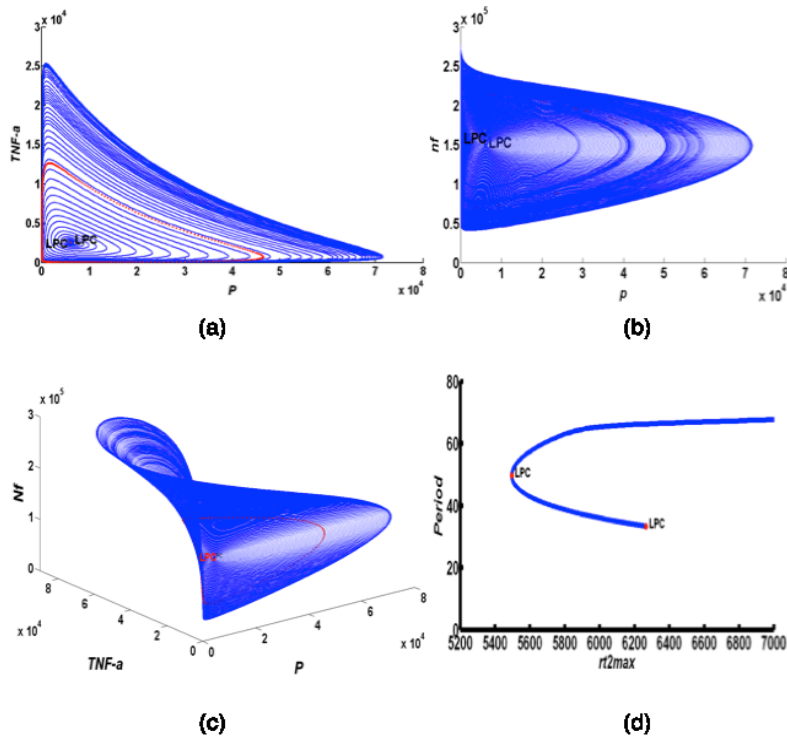
stability to instability. In Figure 4.10 (a), stable equilibria of *pathogen* are observed when system parameter  $k_{pg}$  increases from 0 to 4.93. When  $k_{pg}$  equals 4.93, LP is identified and unstable equilibria of *pathogen* are generated as  $k_{pg}$  decreases from 4.93 to 0. Therefore, equilibria of *pathogen* of our neutrophil immune response model are bistable when  $k_{pg}$  ranges from 0 to 4.93. Similarly, equilibria of *pathogen* in Figure 4.10 (b) are bistable when system parameter  $r_{pn}$  ranges from 25 to 200. In Figure 4.10 (c), equilibria of *pathogen* are bistable when  $u_n$  ranges from 0 to 0.21.

**Figure 4.10 (a) Computed equilibrium curve of *pathogen* in relation to system parameter  $k_{pg}$  in neutrophil immune response model. (b) Computed equilibrium curve of *pathogen* in relation to system parameter  $r_{pn}$  in neutrophil immune response model. (c) Computed equilibrium curve of *pathogen* in relation to system parameter  $u_n$  in neutrophil immune response model. (d) Computed equilibrium curve of *pathogen* in relation to system parameter  $r_{t2max}$  in neutrophil immune response model**



A Hopf bifurcation, identified in Figure 4.10 (d), is a periodic bifurcation in which a new limit cycle is born from a stationary solution. Hopf point, a turning point for periodic orbits, is detected when system parameter  $r_{t2max}$  changes. The detected Hopf point in Figure 4.10 (d) begins a limit cycle continuation in which two cycles collide and disappear. Because the first Lyapunov coefficient (154) is positive, an unstable limit cycle exists, bifurcating from this equilibrium. Figure 4.11 (a) and (b) show the family of limit cycles bifurcating from detected Hopf point in Figure 4.10 (d). The family of limit cycles is represented using limit cycle planes, such as  $TNF-a$ - $pathogen$  plane and  $N_f$ - $pathogen$  plane. Figure 4.11 (c) shows a limit cycle sphere represented by a  $TNF-a$ ,  $N_f$ , and  $pathogen$  plane. Figure 4.11 (d) indicates that two limit cycles occur when  $r_{t2max}$  equals 5495.64 or 6265.00.

**Figure 4.11 (a) Family of limit cycles bifurcating from the Hopf point in  $TNF-a$  and  $pathogen$  plane. (b) Family of limit cycles bifurcating from the Hopf point in  $N_f$  and  $pathogen$  plane. (c) Equilibria and limit cycles in  $(N_f, pathogen, and TNF-a)$ -space. (d) Period of the cycle as function of  $r_{t2max}$**



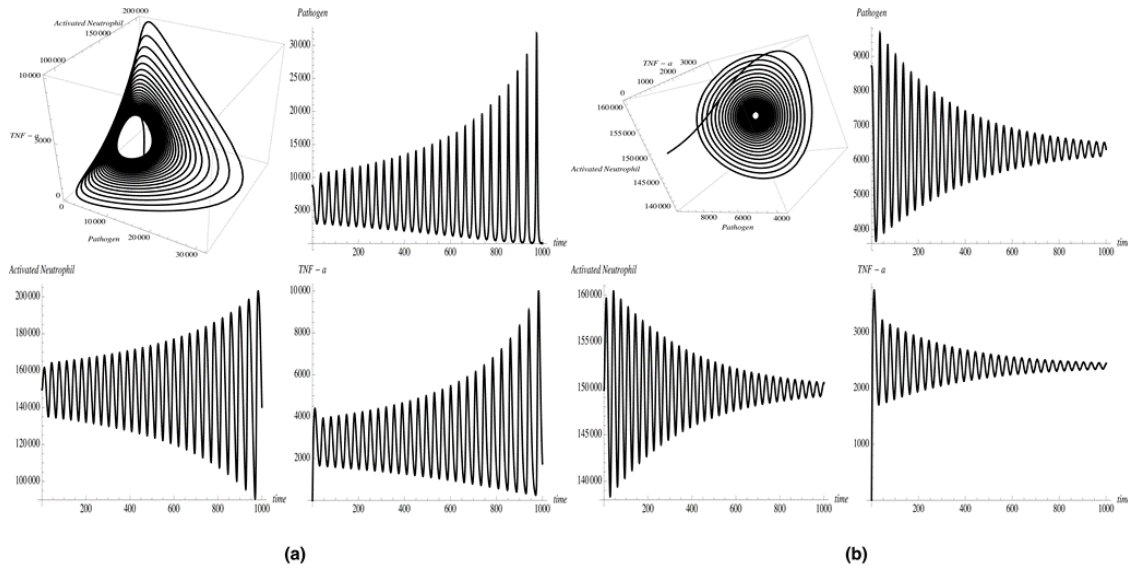
In Figure 4.11 (c), the first family of limit cycle (small red cycle in the center of the sphere) spirals outward as system parameter  $r_{t2max}$  decreases, and the second family of limit cycle appears when  $r_{t2max}$  decreases to 5495.64 (a red cycle line appears). As  $r_{t2max}$  increases from 5495.64, the second family of limit cycle spirals outward again. When  $r_{t2max}$  increases to 6265.00, an unstable equilibrium is detected, as depicted in Figure 4.12 (a). If value of  $r_{t2max}$  is between 5495.64 and 6265.00, equilibria of the neutrophil immune response model are stable and converged, as shown in Figure 4.12 (b). This finding infers either a high release rate of TNF- $\alpha$  ( $r_{t2max}$  is above 6265.00) or a low release rate of TNF- $\alpha$  ( $r_{t2max}$  is below 5495.64), thereby inducing generation of unstable equilibria in the neutrophil immune response model. From a biological response perspective, high release rate of TNF- $\alpha$  indicates overproduction of pro-inflammatory cytokines related to overwhelming pro-inflammation; low release rate of TNF- $\alpha$  leads to failure to recruit a sufficient amount of neutrophils related to infection clearance. Based on our stability analysis, we found that the release rate of TNF- $\alpha$  can positively or negatively influence outcomes of AIR progression, thereby conforming to experimental perturbation findings regarding effectiveness of anti-TNF- $\alpha$  therapies (46, 47, 175).

Continued stability analysis on the monocyte immune response model indicated that change in system parameters  $k_{rd}$ ,  $u_{nr}$ , and  $u_n$  induces bistability of the monocyte immune response model. We observed that the monocyte immune response model was bistable if at least one of the following three conditions was met:  $k_{rd}$  was between 0 to 0.32,  $u_{nr}$  was between 0 to 0.28, or  $u_n$  was between 0 to 0.21. Specifically, we observed that  $r_{t2max}$  (maximum release rate of TNF- $\alpha$  by activated neutrophil) and  $m_{t2}$  (number of activated neutrophils at which the reaction rate is half of the maximum production rate) are essential for oscillated monocyte immune response model. Similar to the neutrophil immune response model, limit cycles bifurcate from



Hopf point, Therefore, we conclude that the oscillated infection is dependent on the amount of released  $TNF-\alpha$  and recruited neutrophils in AIR progression. However, released monocytes and associated cytokines such as HMGB-1 do not contribute to oscillation in AIR progression.

**Figure 4.12 (a) Pathogen, activated neutrophil and  $TNF-\alpha$  diverge at unstable equilibria in neutrophil immune response model when  $r_{t2max}$  is above 6265.00 (b) Pathogen, activated neutrophil, and  $TNF-\alpha$  converge at stable equilibria in neutrophil immune response model when  $r_{t2max}$  is between 5495.64 and 6265.00**



Building upon the monocyte immune response model, we incorporated the effect of anti-inflammatory cytokine (IL-10) into the full model. We observed that Hopf point was detected when  $r_{t2max}$  increased to 128000 because anti-inflammatory cytokine inhibited activation of phagocytic cells (neutrophils and monocytes). This trend indicates that infection oscillation (harmful outcomes) requires additional pro-inflammation activated by neutrophils in the full model, compared to monocyte immune response model without including the effect of anti-inflammatory cytokine. Therefore, our simulated results demonstrated that AIR progression is more likely to end with *healing process* if the effect of anti-inflammatory cytokine is incorporated.

Strengthened (increased  $r_{t2max}$  and  $m_{t2}$ ) pro-inflammatory immune responses could also induce stable or unstable equilibria, leading to a dampened oscillated infection or diverged infection, similar to our observations in Figure 4.12. However, we observed that if high effect of anti-inflammatory cytokine was incorporated (dissociation rate equal to a base-10 logarithm 8) at the beginning of infection, AIR progression resulted in an unstable overwhelming pathogen load at equilibria (refer to Figure 4.12(a)). However, a stable dampened oscillated pathogen load at equilibria (refer to Figure 4.12(b)) was observed if medium effect of anti-inflammatory cytokine (dissociation rate equal to a base-10 logarithm 5) was incorporated. These observations confirmed that effects of anti-inflammatory cytokine can be positive or negative to AIR progression depending on levels of anti-inflammatory cytokine.

We conducted bifurcation analysis for the model incorporated with adaptive immunity, similar to bifurcation analysis we conducted in the neutrophil subsystem, monocytes subsystem, and full model. We selected four bifurcation diagrams as shown in Figure 4.13.

As shown in Figure 4.13 (a), two Hopf bifurcations were detected at  $k_{pg} = 2.8$  and  $k_{pg} = 4.1$ . Similarly, Hopf bifurcations were also detected in Figure 4.13 (b) and Figure 4.13 (c) when  $r_{pn} = 17$ ,  $r_{pn} = 38$ , or  $u_n = 0.047$ . Compared to innate immunity, incorporation of adaptive immunity induced a further stabilized limit cycles, bifurcation from the equilibrium. Our stability analysis shown in Figure 4.13 (d) illustrates that the Hopf bifurcation move to lower  $r_{t2max}$  value compared to Hopf bifurcation detected in innate immunity. The change in bifurcations indicated the contribution of adaptive immunity to sepsis progression.

In Figure 4.14 (a), (b), and (c), the first family of limit cycle (small red cycle in the center of the sphere, marked as LPC) spiral outward as system parameter  $k_{pg}$  decreases, and the second family of limit cycle appears when  $k_{pg}$  decreases to 2.4 (a red cycle line appears). As  $k_{pg}$  increases

from 2.4, the second family of limit cycle spirals outward again. A period doubling is detected when  $k_{pg}$  increases to 3, marked as PD in Figure 4.14. Because the first Lyapunov coefficient is negative, limit cycle bifurcations from the equilibrium are stable compared to unstable limit cycles detected in the neutrophil subsystem.

**Figure 4.13 (a) Computed equilibrium curve of pathogen in relation to system parameter  $k_{pg}$  in the full model incorporated with adaptive immunity. (b) Computed equilibrium curve of pathogen in relation to system parameters  $r_{pn}$  in the full model incorporated with adaptive immunity. (c) Computed equilibrium curve of pathogen in relation to system parameters  $u_n$  in the full model incorporated with adaptive immunity. (d) Computed equilibrium curve of pathogen in relation to system parameters  $rt_{2max}$  in the full model incorporated with adaptive immunity**

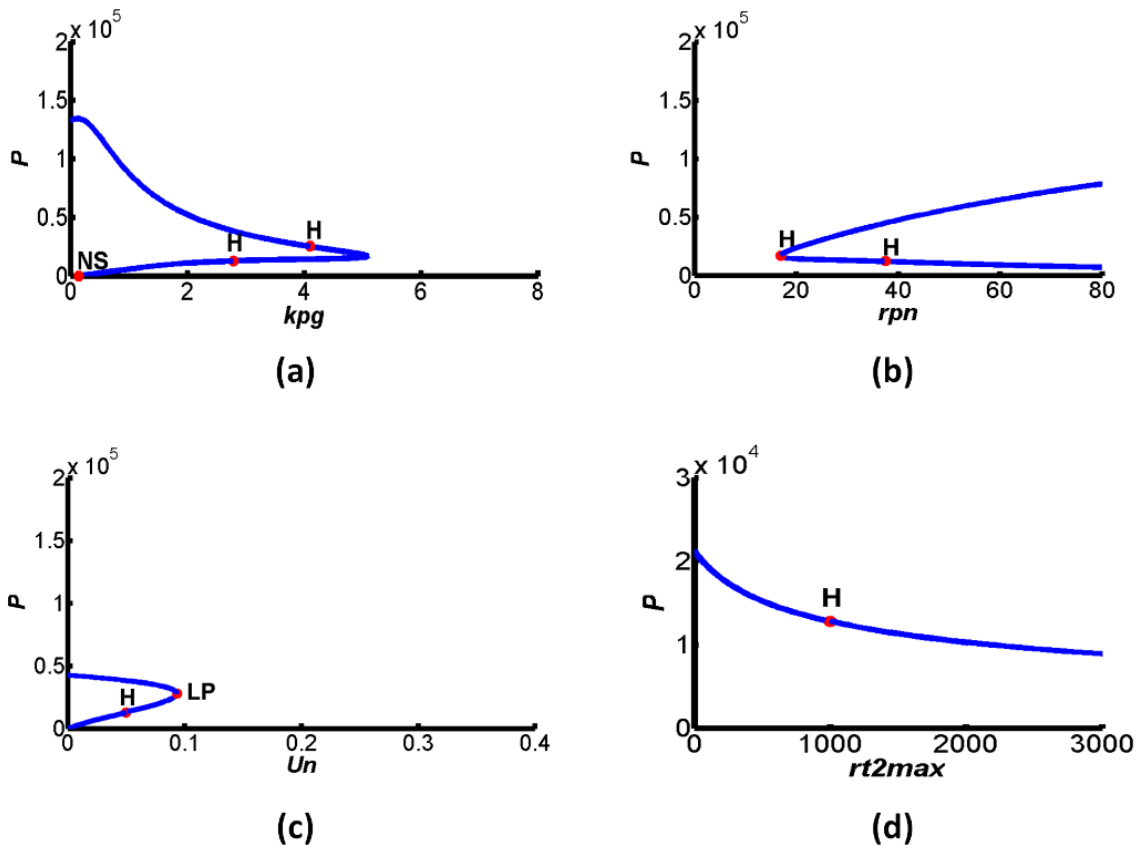
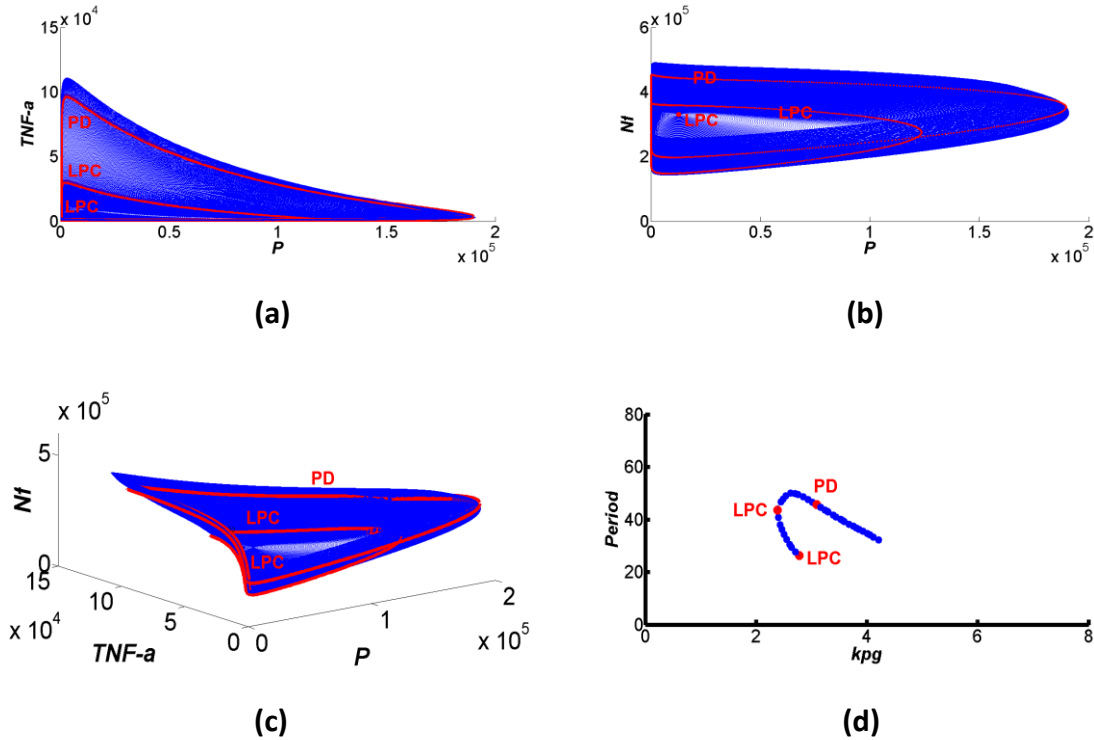


**Figure 4.14** (a) Family of limit cycles bifurcation from the Hopf point ( $K_{pg} = 2.8$ ) in  $TNF-\alpha$  and pathogen plane. (b) Family of limit cycles bifurcating from the Hopf point ( $K_{pg} = 2.8$ ) in  $N_f$  and pathogen plane. (c) Equilibria and limit cycles in ( $N_f$ , pathogen, and  $TNF-\alpha$ )-space. (d) Period of the cycle as function of  $k_{pg}$



## 4.5 Discussion

Experimental results in literature have suggested that anti-inflammatory mediator inhibits activation of phagocytes and reduces the ability of activated phagocytes to attack pathogen (39), consequently related to mortality and severity of infection in sepsis (133, 158). However, other experimental studies have shown that anti-inflammatory cytokine down-regulates production of secreted cytokines by inhibiting various behaviors of activated immune cells, thereby reducing the risk of tissue damage (25, 26, 157). Our computed results from SDMM suggested that the effect of anti-inflammatory cytokines could be a “double-edged sword” for AIR because anti-inflammatory cytokine would either decrease mortality associated with tissue damage or increase

mortality associated with high load of bacteria. With a low effect of anti-inflammatory cytokine (dissociation rate equal to a base-10 logarithm 2), our computed results showed that anti-inflammatory cytokine fails to inhibit the release of activated immune cells (activated neutrophils and activated monocytes) and subsequent cytokine production. Levels of damaged tissue significantly accumulated during the first 500 hours (approximately 20 days) of simulation. With the high effect of anti-inflammatory cytokine (dissociation rate equal to a base-10 logarithm 8), our simulated results and stability analysis demonstrated that sepsis progression leads to increased chance of death caused by overwhelming pathogen load at the end of simulation.

To further investigate effects of anti-inflammatory cytokines, we simulated a medium effect of anti-inflammatory cytokine (dissociation rate equal to a base-10 logarithm 5) and compared simulated results to high effect of anti-inflammatory cytokine and low effect of anti-inflammatory cytokine. Our computed results showed that pathogen load decreases during the first 100 hours of infection in combination with the total amount of dead hepatocytes. Furthermore, we observed that production of activated neutrophils and activated monocytes declined to baseline near 0 at the end of simulation, indicating a positive trend of sepsis progression to a healthy pattern. Therefore, we conclude that the level of anti-inflammatory cytokines significantly impacts direction of sepsis progression. We also conclude that levels of anti-inflammatory cytokine and time of intervention of anti-inflammatory cytokines determine outcomes of AIR under specific system configuration. Based on simulated results from our SDMM, we inferred that the survival rate of the host (chance of ending with a *Healing Process*) could be improved if a medium level of IL-10 injection was set between 3 hrs and 6 hrs after infection.

We assert that care must be taken when applying simulated results to clinics before the implementer fully understands the underlying setting of the simulation. Because it was difficult to simultaneously incorporate every intermediate biological process of inflammatory response, reasonable assumptions must be made when building a mathematical model. In our SDMM, we did not model *Salmonella* replicating within neutrophils. However, experimental study (176) asserted that neutrophils and macrophages were the primary sites for *Salmonella* proliferation in a mouse. Therefore, *Salmonella* replication could be considered in the future model if additional literature supported this fact. Various T cell types were reported to be able to express IL-10 under various conditions (177). Therefore, IL-10 production estimation is difficult because IL-10 levels produced by T cells were various due to stimuli type or the strength of stimuli. In our model, we did not differentiate helper T cells to specific types that are identified in biological process. Plasma cells secrete antibodies (11), but we did not incorporate this specific mechanism in our SDMM. Instead, we modeled that B cells released antibodies. When antibodies are released from plasmas cells, T<sub>H</sub> cells define the isotype of the antibody (11); however, we also did not model specific isotype of antibody in our model. Furthermore, we ignored the fact that antibody opsonization induces stimulation of cytokine release when they are phagocytized by inflammatory cells. For example, we ignored the fact that cytokine release from the processes that antibody-opsonized *Salmonella* are phagocytized by neutrophils and macrophages (11). Also, we ignored effects of other pro-inflammatory cytokines such as IL-1, IL-12, and IL-8 in our SDMM. Biological immune responses responding to infection are recognized as a series of complex processes including intracellular transductions (transfer of DNA) and intercellular pathways between cells. These biological processes will be developed with evolved understanding and continued investigation of cellular and molecular mechanisms (115), which

could be further research interests in the field. In our SDMM, we used numerical count, or the number of indicators in the simulation, as the estimate of cell or cytokine number in AIR. In practice, physicians must translate data to measurable units of indicators similar to how we translated clinical data to simulation data. Furthermore, our conclusion regarding IL-10 was drawn based on specific simulation settings including setting system parameters and initial loads of indicators. Initial system setting must be fully understood before considering application of IL-10 level for per-clinic experiments.

Based on our simulated results regarding anti-inflammatory cytokine, we propose a hypothesis testing: If medium levels of anti-inflammatory antibody were injected into the host with sepsis between 3 hrs and 6 hrs would survival rates of the host improve under hyperinflammation? The purpose of this hypothesis testing is to detect effective zones of the anti-inflammatory antibody related to *Healing Process* of AIR in order to help develop therapeutic agents in pre-clinical trials.

According to our simulation study, we found that initial levels of pathogen significantly impact dynamic patterns of AIR progression. However, inconsistency in observations between our simulated results and existing experimental studies force us to propose another hypothesis testing: What is the range of initial loads in pathogen with a maximum likelihood of leading to a *Healing Process*? After discussing with experts in the field, our initial assumption is that if the initial load of pathogen is low, AIR progression have a chance to end with a *Persistent Infection* because immune responses fail to be fully activated at the beginning of infection. However, if the initial load of pathogen is high, the immune system fails to control and regulate infection that could also lead to *Organ Dysfunction*. The purpose of this hypothesis testing is to detect

dangerous zones of initial loads in pathogens in order to develop effective therapeutic targets in pre-clinical trials.

Mathematical modeling, at various levels, could regulate individual components of inflammation and provide insights into biological interactions in order to understand complex inflammatory processes during sepsis progression. However, the traditional mathematical model has unique disadvantages. First, the model fails to capture stochastic process for heterogeneous populations. Second, the model fails to describe local interactions between heterogeneous populations, such as the movement of tissue macrophage towards the local pathogen in the infected area. In order to improve simulation accuracy and overcome disadvantages of the mathematical model, a hybrid modeling framework may be used to model and simulate sepsis progression in future research (102).

#### **4.6 Conclusion and future research**

We proposed an 18-equation system dynamic mathematical model and showed that the model has significant potential to predict possible pathogenesis of sepsis based on the host's physiological conditions. Also, we showed that the model provides essential biological insight into innate immunity and adaptive immunity of sepsis episodes by exploring various combinations of phagocyte and cytokine levels. We focused primarily on the combined effects of pathogen load, phagocytic cells, tissue damage, anti-inflammatory cytokine, CD4+ T cell, CD8+ T cell, B cell, and antibodies by adding cellular pathways during sepsis progression. We observed that outcomes of sepsis progression could be improved with IL-10 at a medium level in an early stage of infection (between the first 3 hrs and the first 6 hrs after infection). Furthermore, our model quantitatively measured levels of phagocytes (neutrophils and



monocytes) and captured a *dampened oscillated infection* in AIR progression, compared to existing mathematical models that provide more accurate qualitative estimates.

Adaptive immunity contributes to further pathogen clearance after innate immunity because it includes B cells, T cells, and antibodies released from B cells (77). We conducted an initial study of adaptive immunity during sepsis progression by incorporating CD4+ T cells, CD8+ T cells, B cells, and antibodies to the SDMM. We observed that CD4+ T cell count, CD8+ T cell count, B cell count, and antibody count were persistently elevated, which contributed to the pathogen clearance during a late stage of sepsis progression. Because we did not specify T cell type during SDMM, IL-10 production by T cells was not considered in the current SDMM. IL-10 production by T cells potentially leads to overproduction of anti-inflammatory cytokines by compensatory anti-inflammatory response and eventually increases risk of secondary infection and inaccurate prognosis (77, 146). For further research, we expect to explore prominent effects of anti-inflammatory mediators secreted by T cells as they relate to outcomes of sepsis progression.

The system dynamic mathematical model proposed in this paper is a robust, accurate representation of comprehensive immune responses within a sepsis episode. This underlying model is general and flexible to be used to predict possible outcomes and prognosis for various hosts' initial conditions with various model parameters using experimental data from the literature. In addition, hypothesis testing proposed based on our simulated results could be a reference to help reduce unnecessary clinical trials and focus on essential processes of sepsis.

### **Acknowledgement**

This work was financially supported by China Scholarship Council and KC AV Medical Center. I would like to thank Dr. Stephen Chapes from the Department of Biology at Kansas State

University and Dr. Steven Simpson from the University of Kansas Medical Center for helping develop the biological models. Publication of this article was funded in part by the Kansas State University Open Access Publishing Fund.

## **Chapter 5 - An Autonomous Multi-Agent Simulation Model for Acute Inflammatory Response**

Chapter 5 is based on the paper “An Autonomous Multi-Agent Simulation Model for Acute Inflammatory Response” published in International Journal of Artificial Life Research (2011), Vol. 2, No. 2, pp. 105-121.

### **Abstract**

This research proposes an agent-based simulation model combined with the strength of systemic dynamic mathematical model, providing a new modeling and simulation approach of the pathogenesis of AIR. AIR is the initial stage of typical sepsis episode, often leading to severe sepsis or septic shocks. The process of AIR has been in the focal point affecting more than 750,000 patients annually in the United States alone. Based on the agent-based model presented herein, clinicians can predict the sepsis pathogenesis for patients using the prognostic indicators from the simulation results, planning the proper therapeutic interventions accordingly. Impressively, the modeling approach presented creates a friendly user-interface allowing physicians to visualize and capture the potential AIR progression patterns. Based on the computational studies, the simulated behavior of the agent-based model conforms to the mechanisms described by the system dynamics mathematical models established in previous research.

**Keywords:** Acute Inflammatory Mediator, Agent-based Model System, Dynamic Model, Multi-agent Simulation Model, Simulation Model

## 5.1 Introduction

The function of the human immune system is to respond to intruding pathogens or damage tissues (e.g., trauma) and to prevent them from spreading to the entire body by producing warning chemical signals, activating relevant immune cells in the blood circulation system near the infected area, and then killing the intruded pathogen or microbial organisms. The process to protect the human body from further infection by harmful stimuli is commonly referred as the immune responses or acute inflammatory responses. However, an uncontrolled series of Acute Immune Responses (AIR) may lead to possible sepsis, severe sepsis or sepsis shocks since the immune cells and their released cytokines eliminate pathogens and microbial organisms but which also kill neighboring healthy cells. Recent census found that more than 750,000 severe sepsis or sepsis shock cases developed from sepsis in the US (4) with mortality rates between 20% and 80% (28). In the United States alone, almost \$17 billion is spent each year, treating patients with sepsis (4). Therefore, it is necessary to find an effective methodology that can help physicians predict the outcomes of an AIR, prevent possible severe sepsis or septic shocks, and control the involved risks for patients, which is the focus of this research.

This article presents a new modeling approach to predict the evolution of the Acute Inflammatory Response (AIR) which is the initial stage of sepsis pathogenesis. This predictive agent-based model (ABM) uses the system dynamics model developed by Reynolds *et al.* (53) as a benchmark.

The organization of this paper is as follows: first we present the basic biological process of AIR, using a system dynamics model developed in previous research. Next, the agent-based model embedded with an existing system dynamics model is presented while its implementation detail is discussed. Outcomes of the agent based simulation are demonstrated and a sensitivity

analysis is presented. Finally, conclusions and potential applications of the proposed model are discussed.

## **5.2 Biological mechanism of acute inflammatory response**

The Acute Inflammatory Response, which can be the initial stage of sepsis, usually occurs when the human immune system detects intruding pathogens or existing tissue damages and sends out a signal (e.g., Interleukin-8 (IL-8) and C5a, the process is referred to as the chemotaxis) to the resting phagocyte cells such as the neutrophils initially and followed by the monocytes (two typical immune cells in the human body) in the blood vessel near the infected tissue. The resting phagocyte cells are activated and start to migrate towards the pathogens or damaged tissue whose recognizable protein on the surface is similar to those of the immune cells. Once the activated phagocyte cells reach the infection site, they start to engulf and consume the pathogens. Meanwhile, these activated phagocyte cells release pro-inflammatory cytokines such as Tumor Necrosis Factor (TNF), Interleukins (IL-1), IL-6, IL-8 and High Mortality Group Box-1 (HMGB-1) that activate more phagocyte cells and recruit them to the infection site. All those activated phagocyte cells not only eliminate the pathogens but also secrete substances which contribute to killing healthy cells and induce more inflammation in the initial progression of sepsis. Almost at the same time, several types of anti-inflammatory mediators such as IL-6, IL-10, soluble TNF receptors (sTNFRs) and IL-1 receptor antagonist (IL-1ra) are also released by the activated phagocyte cells in this stage. These anti-inflammatory mediators inhibit the production of pro-inflammatory mediators and therefore inhibit recruiting more phagocyte cells (12).

### 5.3 System dynamics modeling of AIR

Undoubtedly, the complex mechanism of the AIR allows various possibilities of sepsis progression which may lead to a healthy response or a septic shock. Thus, based on insights into the biological mechanism of AIR a three equation system dynamics model was developed by Kumar *et al.* (54). In the three equations model, pathogen level, early pro-inflammatory mediator, and late pro-inflammatory mediators were defined respectively. Moreover, those three essential indicators in AIR were measured by three individual equations. However, considering many other important indicators involved in AIR, a more complete system dynamics model based on five equations was developed by Reynolds *et al.* (53). This model is shown next:

$$\frac{dP}{dt} = K_{pg}P \left( 1 - \frac{P}{P_\infty} \right) - \frac{K_{pm}S_m P}{i_m + K_{mp}P} - K_{pn}f(N^*)P \quad (5.1)$$

$$\frac{dN_R}{dt} = S_{nr} - R_1 N_R - i_{nr} N_R \quad (5.2)$$

$$\frac{dN^*}{dt} = R_1 N_R - i_n N^* \quad (5.3)$$

$$\frac{dD}{dt} = K_{dn}f_s(f(N^*)) - i_d D \quad (5.4)$$

$$\frac{dC_A}{dt} = s_c + \frac{K_{cn}f(N^* + K_{cnd}D)}{1 + f(N^* + K_{cnd}D)} - i_C C_A \quad (5.5)$$

Where

$$R_1 = f(K_{nn}N^* + K_{np}P + K_{nd}D)$$

$$f(V) = V / (1 + (C_A / C_\infty)^2)$$

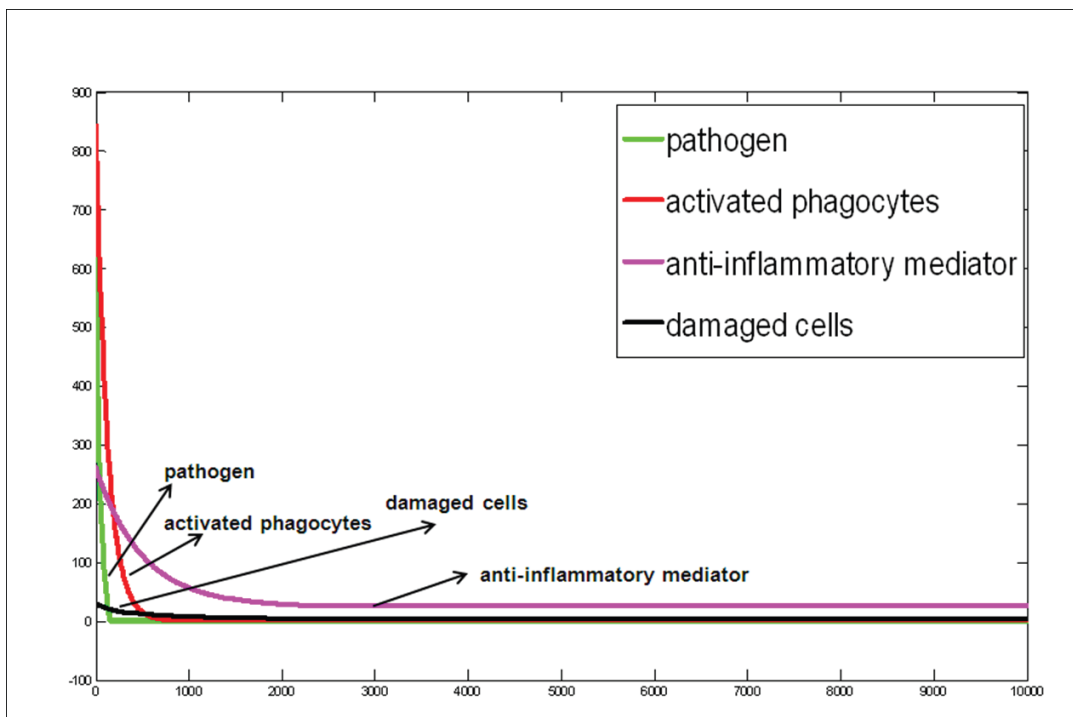
$$f_s(V) = V^6 / (x_{dn}^6 + V^6)$$

In this five equations model, the variables  $P$ ,  $N_R$ ,  $N^*$ ,  $D$  and  $C_A$  represent pathogen level, resting phagocyte cells, activated phagocyte cells, damaged tissue and anti-inflammatory

mediators respectively. All the system parameters (*K<sub>nn</sub> et al.*) reflect the strength of the immune system but their detailed description is beyond the scope of this paper.

The measurements in both mathematical models are based on time-based rates, so their function is to calibrate the change in number of indicators in AIR with the progress of time. Since the change in number of indicators in the next time unit depends on the previous number of indicators, the mathematical models alone are not convenient to automatically calibrate the indicators during the development of acute inflammatory response. Thus, two Simulink models in MatLab were implemented to separately simulate both mathematical models. The results from the simulation reflect the progression of acute inflammatory responses since it measures the corresponding changes in the number of pathological and physiological markers during the acute inflammatory response. One of the results from the Simulink model of five equations system dynamics model is shown in Figure 5.1 to demonstrate the feasibility of measurement.

**Figure 5.1 Simulation results of the five equations model**



In Figure 5.1, the Y axis represents the change of pathological indicators in AIR, and the X axis represents the simulation time corresponding to the progression of AIR. Thus the models established are capable of reflecting the progression of AIR.

Both mathematical models provided a high level review of the AIR progression by defining the changes in the number of indicators which react with the cells or in the blood circulation system. However, the actual immune system response is much more complicated and is highly stochastic in nature. For example, the strength of immune response differs among the organs of the patient. Thus, the system dynamics models presented so far have limited ability of capturing these variations since they use deterministic scalar parameters. In order to model the important stochastic nature of the biological system in focus and allow the ability to include the correct boundary conditions we expand the modeling method to an agent based modeling approach as shown next.

#### **5.4 An agent-based model (ABM) embedded with system dynamics mathematical model**

The agent-based model employs agents representing the various indicators in the progression of AIR. With each type of agent defined based on the variables described in the system dynamics model, it constructs the link between the system dynamics models and a real AIR environment. Moreover, agents can have autonomous and probabilistic behaviors, and therefore, provide improved modeling capability capturing the stochastic nature of the AIR progression episode. Compared to system dynamics models, the agent-based modeling approach is more flexible and more realistic. Furthermore, our ABM embedded with system dynamics models is applied at the intercellular level and expands to the tissue level, an improvement over the agent-based models previous established (48, 49, 178). Thus, this ABM embedded with



system dynamics mathematical models has advantages of both system dynamics and traditional ABM models.

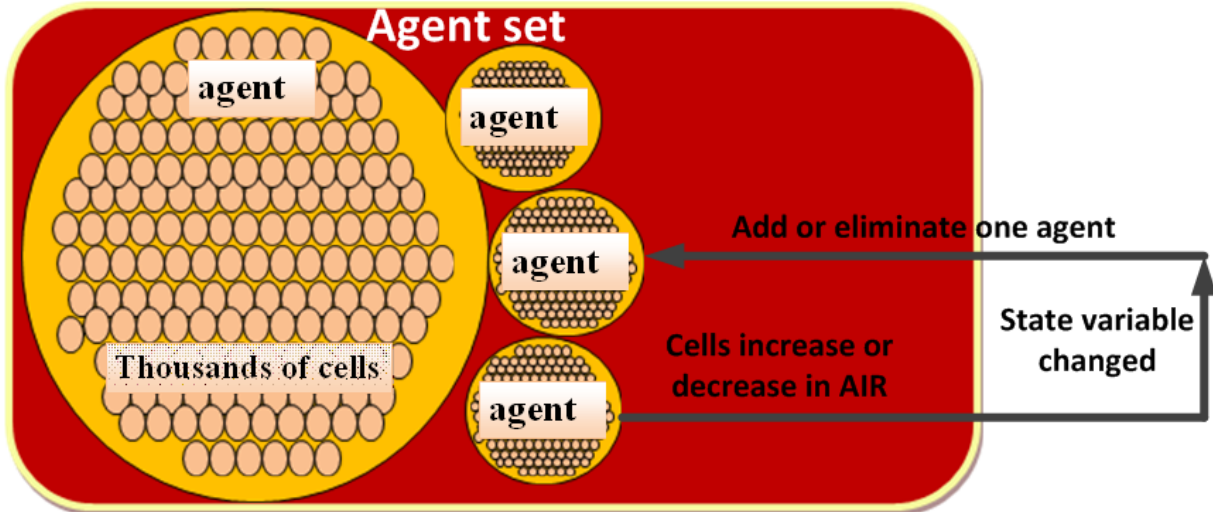
In this modeling approach, there are nine agent types: (1) *pathogen*, (2) *resting phagocytes*, (3) *activated phagocytes*, (4) *damaged cells*, (5) *IL-10s*, (6) *TNF- $\alpha$ s*, (7) *IL-1s*, (8) *HMGB-1s*, and (9) *IL-6s*. Since the damaged tissue in the system dynamics model is hard to calibrate, we use *damaged cells* agent in our agent-based model as a representation of the extent of tissue damaged. The agent types and their description are shown in Table 5.1.

**Table 5.1 Agent type and its description**

<b>Agent Type</b>	<b>Description</b>
<i>Pathogen</i>	Instigator of AIR; AIR starts when pathogen intrude into body
<i>Resting Phagocytes</i>	Inactive immune cells such as neutrophils and macrophages existing in the blood vessel
<i>Activated Phagocytes</i>	Activate immune cells that respond with intruding pathogen and secrete corresponding cytokines such as <i>TNF-<math>\alpha</math>s</i> , <i>IL-1s</i> etc
<i>Damaged Cells</i>	Normal cells damaged by intruding pathogen or cytokines released by the activated phagocytes
<i>IL-10s</i>	Anti-inflammatory mediator released by the activated phagocytes
<i>TNF-<math>\alpha</math>s</i>	Early pro-inflammatory mediator released by the activated phagocytes
<i>IL-1s</i>	Early pro-inflammatory mediator released by the activated phagocytes
<i>HMGB-1s</i>	Late pro-inflammatory mediator released by the activated phagocytes
<i>IL-6s</i>	Late pro-inflammatory mediator released by the activated phagocytes

Each type of agent is defined as a homogeneous set of agents that may contain thousands of body cells, microorganisms or microbial antagonisms. For instance, the pathogen agent set contains pathogen agents, each consisting of thousands of pathogens. Figure 5.2 shows the logical structure of the agent set in the agent-based model.

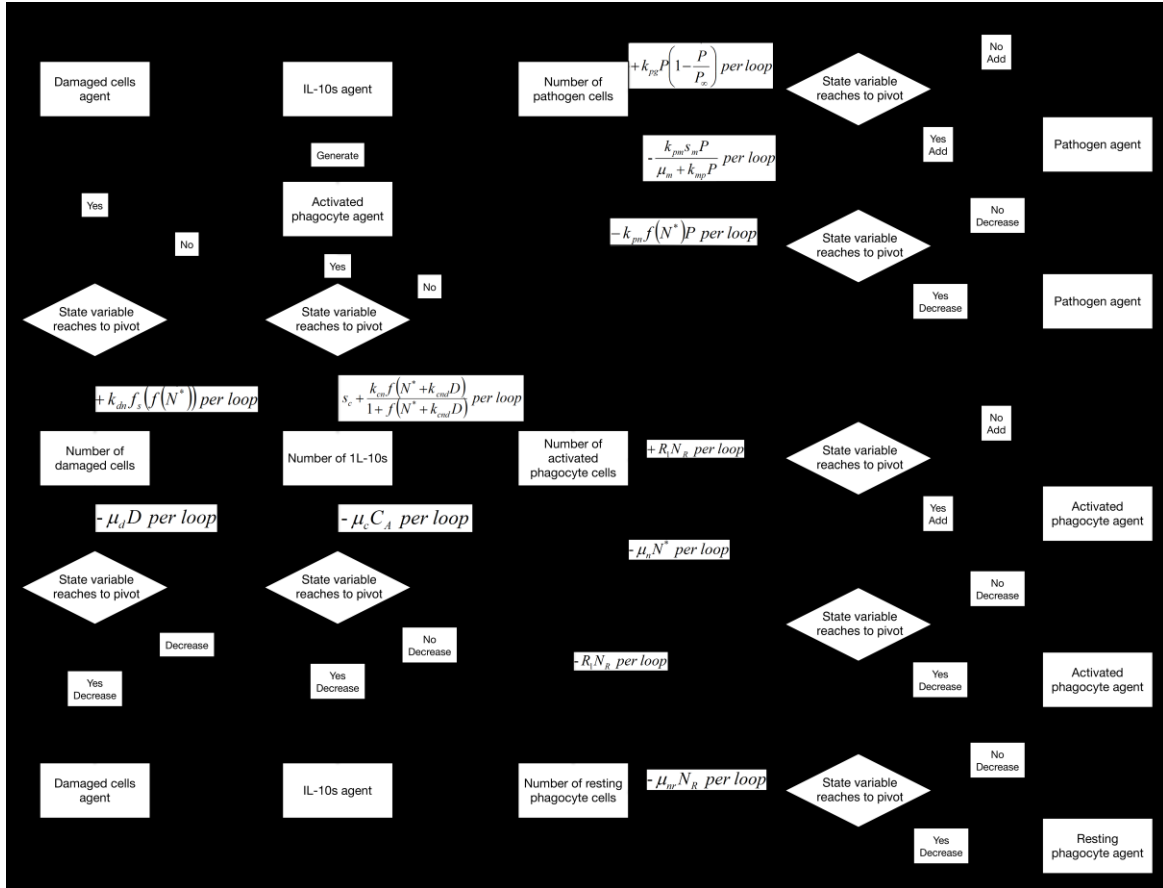
**Figure 5.2 Basic structure of agents changing**



As increase or decrease (e.g., creation, death or transformation) in the number of cells for a particular type of agent is executed by changing the current states of that agent in the agent set, and the current state of any agent is tracked by a set of pre-defined state variables. Since the ABM is implemented as loops and each loop is corresponding to one simulation time unit, the amount of changes in state variables follows a deterministic behavior similar to the systemic dynamic Eq. (5.1), (5.2), (5.3), (5.4), (5.5). In our agent based model, *pathogen*, *resting phagocytes*, *activated phagocytes*, *damaged tissue* and *IL-10s* are the five main agents whose state changes are defined by the system dynamics model (i.e., Eqs. (5.1) - (5.5)). Each positive mathematical term in the equations such as  $K_{pg}P\left(1 - \frac{P}{P_{\infty}}\right)$  contributes to define the increase of

cells in one agent while negative terms are used to define the decrease process. Figure 5.3 shows a comprehensive structure of the agent based model.

**Figure 5.3 Comprehensive structure of the agent based model**



As an example, one of the state variables defined in the agent based model is called “increased-number-of-pathogen-cells-in-one-agent”. This state variable measures the increased number of pathogen cells in one *pathogen* agent and it will keep increasing by  $+K_{pg}P\left(1-\frac{P}{P_{\infty}}\right)$  per loop when the agent based model evolves. When the cell population in a *pathogen* agent grows beyond a predefined boundary condition, (maximal number of cells in a *pathogen* agent), the total number of *pathogen* agents will increase by one and the value of this state variable in

newly generated *pathogen* agent is set to its proper level. Also often, one agent will turn into another agent or generate other types of agents depending on the real physiological behaviors patterns modeled in the ABM. Therefore, the proposed ABM is quite flexible and functional in modeling the microbial pathogenesis of the AIR.

In addition, the stochastic behaviors of the agents are included in the ABM to enhance the probabilistic nature of agents' creation, deaths and transformations. Once the state of the agent reaches a point of change (defined as the boundary conditions of the system), the agent will choose one of four possibilities: keep the original agents population, increase it population, be eliminated, or transform into another type of agent. For example, pathogen agent will be eliminated when the pathogen dosages in the agent turns to 0. The resting phagocytes will transform into activated phagocytes during the chemotaxis process when pathogens exist in the surrounding environment. The states of one type of agent s can be changed by other agents either of the same type or of different types, allowing interaction between various types of agents. Moreover, the possibility of those creations, deaths and transformation is easier to define as the probability distribution in the ABM. For instance, the growth rate of pathogens could be assigned as normal distribution with mean equal to 0.1 and deviation equal to 0.01. Thus, the proposed autonomous multiagent-based model effectively describes the processes of acute inflammatory response, quantitatively defining the relationships among the various indicators (e.g. pathogen, resting phagocyte cells, activated phagocyte cells, damaged tissue, pro-inflammatory mediators and anti-inflammatory mediators) and capturing the complex and stochastic interactions among the pathological or physiological indicators.

Unlike the mathematical model, the ABM computer simulation allows the implementers and users to simulate and observe the interactions among different agents, thus it is more

intuitive and flexible than the traditional mathematical models (this will be further demonstrated in the next section). However, the ABM approaches generally require large amount of computing resources for a precise simulation of complex behaviors. The use of large agent populations results in more accurate system behaviors but could require large amount of computer memory, and a detailed simulation may be time consuming.

The novel ABM approach presented above permits us to implement the simulation models on microcomputers platforms with moderate configuration. Such simulation experiments were completed within few minutes.

### **5.5 Implementation of the agent-based model**

The ABM presented in the previous section, as a methodology, is well-suited for modeling the complicated relationships and behaviors in the progression of acute inflammatory response. However, the implementation needs a certain type of computer simulation tool. In this research, we used Netlogo 4.0.4 (179), a Java based modeling platform for implementing the proposed agent-based model. This tool allows modelers to specify the behaviors of hundreds or thousands of “agents”, which makes it possible to explore the connections between the microbial agent behaviors and the macro-level patterns that emerge from the interactions of multiple autonomous agents.

The main user interface of Netlogo is made up two-dimensional grids. The agents can be divided into two categories: “patches” and “turtles”. The “patches” are fixed agents placed on the background grids in the model workspace. The “turtles” are mobile agents who could occupy a position or move freely on the surface of patches and execute certain functions or actions. In the AIR agent-based model, the *damaged cell* agents are defined as patches because they simulate the tissue or artery cells, which are not movable. All the other eight agent types are defined as

“turtle”. Moreover, Netlogo offers a way to define agent set as “breed” which means agent types whose behaviors are similar or controlled by the same mechanisms. This allows the modeler to define a class of agents with a set of common state variables and establish various functions or actions (autonomous behaviors) for agent types. Also, the modeler can generate the output of a simulation and set parameters in a special area of the Netlogo interface.

## **5.6 Predictive results of the simulation model**

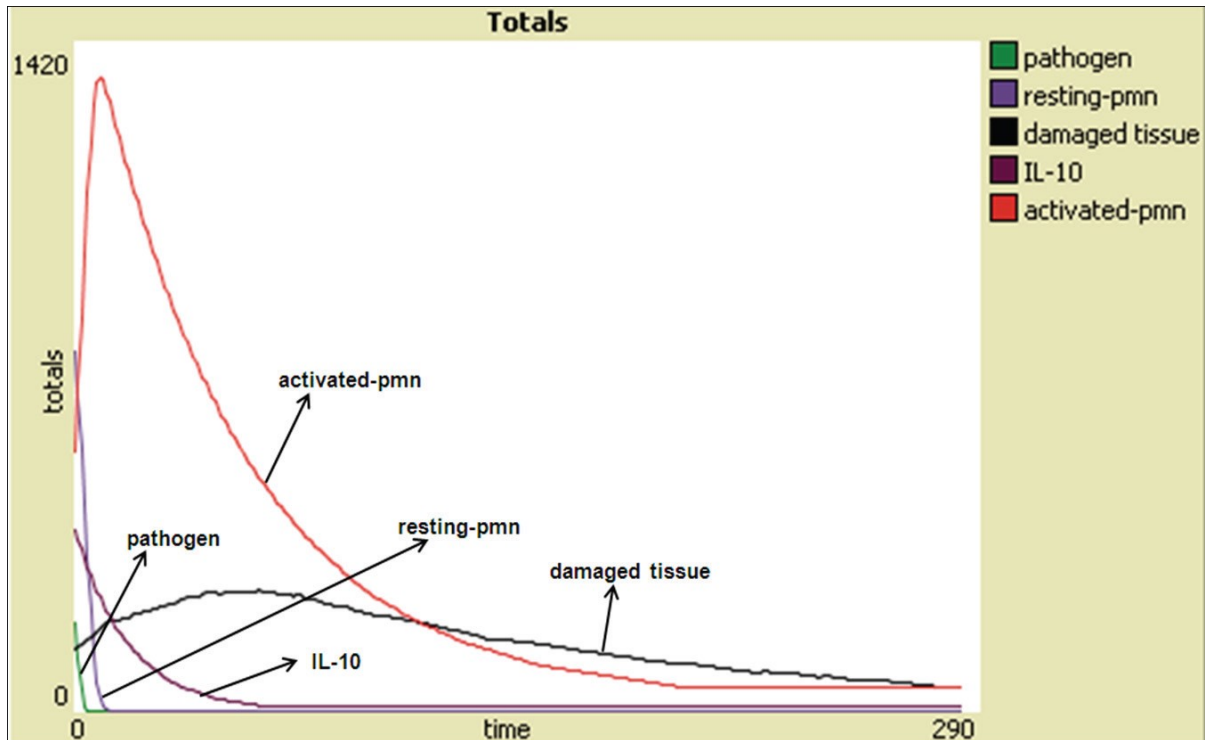
### ***5.6.1 Deterministic results of the simulation model***

In this section, the simulation tool developed is used as a predictive model for the prognosis of AIR. The predictive model is a useful tool to assess patients with different initial pathogens load levels or physiological conditions. To predict the pathogenesis of acute inflammatory response, the simulation model is run with the corresponding initial profiles of the patients of interest and a combination of adjustable system parameters, resulting is the behavior shown, for example, in Figure 5.4.

In Figure 5.4, the trajectories of all the indicators show that a patient with a low-level initial pathogen load is more likely to recover from an acute inflammatory response episode. Here all the indicators (pathogens, resting phagocyte cells, activated phagocyte cells, damaged tissue and anti-inflammatory mediators) return to a relatively low level and stay in stable state after a moderately long period of simulation. Furthermore, the mechanism of acute inflammatory response could be explained by the predicted outcomes from the ABM simulation. That is, the activated immune cells could quickly eliminate a low-level pathogen load at the early stage of the episode. Without more pathogens recruited, the activated immune cells will then gradually decrease. The anti-inflammatory mediators (depicted as the IL-10 level) will decrease as well

with the lack of production of activated immune cells. It is clear that the damaged tissue will increase initially with the effect of activated immune cells; however, they smoothly recover from the damaged status to normal cells under the tissue regeneration process.

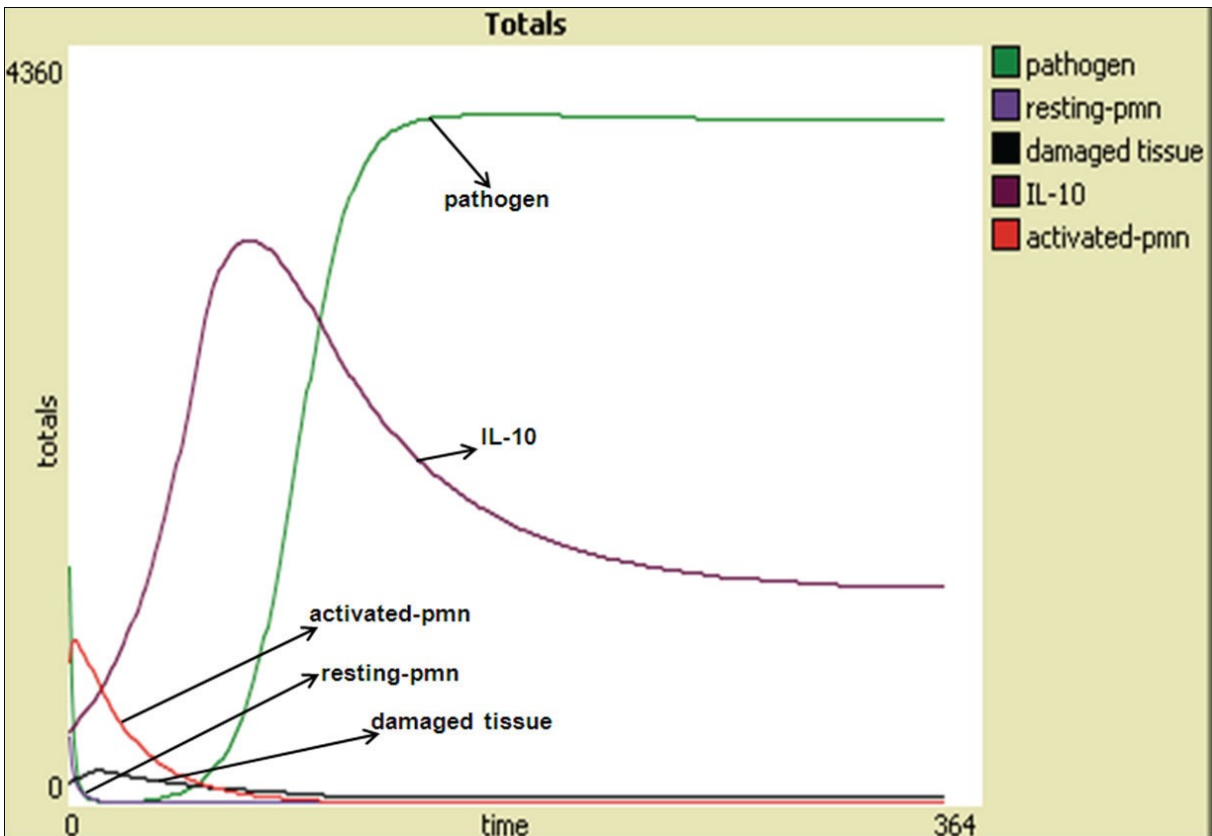
**Figure 5.4 Healthy response with low pathogen load**



In contrast, Figure 5.5 depicts a different prognosis of AIR. The predictive ABM demonstrates that the pathogens will initially decrease rapidly and then sharply increase to saturation level if the initial load of pathogens is elevated. Meanwhile, the value of system parameter  $K_{pn}$  (180) of the predictive ABM decreases from 0.01 to 0.005 responding to the relatively-high initial load of pathogens. The system parameter  $K_{pn}$  represents the efficiency of pathogens elimination by activated phagocyte cells ( $K_{pn} = 0.01$  means 1 percent of pathogens will be consumed by 1 measure unit of activated phagocytes cells per hour). The change of its value shows that the effectiveness of the immune system of a hypothetical patient who had a high initial load of pathogens decreases with time. Thus, the pathogens could not be entirely

eliminated at the acute initial stage of the episode. After the number of activated immune cells decrease to a relatively low level (depicted as the activated PMN granulocyte), the pathogens elevate in a logistic growth form. This situation is frequently referred as a possible prognosis of a septic shock.

**Figure 5.5 Severe sepsis**

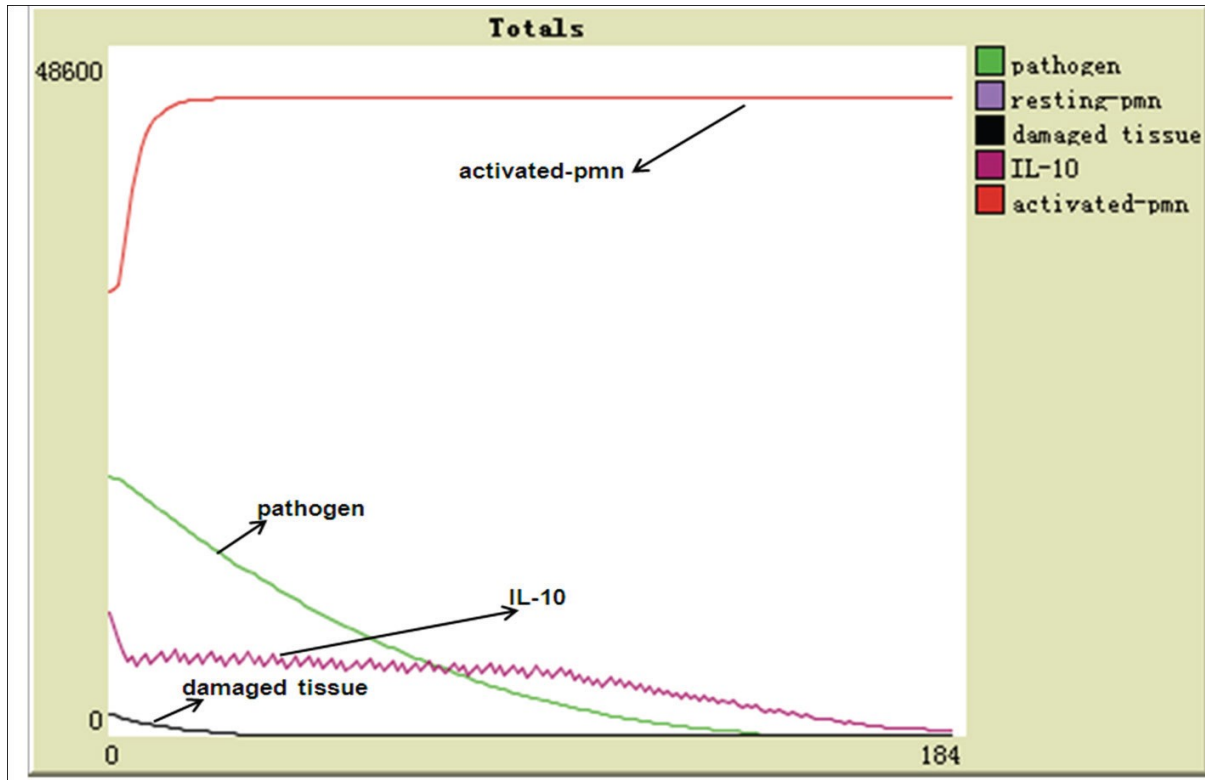


Moreover, the persistent non-infectious inflammation could happen if the number of activated phagocyte goes to saturation, which is shown in Figure 5.6.

Under this condition, a patient could die from further inflammation reactions caused by the persistent pro-inflammatory cytokines released by the activated phagocyte even though the level of pathogens vanishes. Thus, it would eventually lead to multiple organ failure and death (181).



**Figure 5.6 Persistent non-infectious inflammations**



### ***5.6.2 Stochastic results of the simulation model***

Our agent-based model has the special ability of modeling the stochastic process of AIR. In this case, the change of indicators follows a certain distribution since randomization exists when indicators interact with each other. For example, the growth rate of pathogen is not deterministic but having a normal distribution with mean and variance. This situation is common especially when the inner environment of cells varies corresponding to different individual patients.

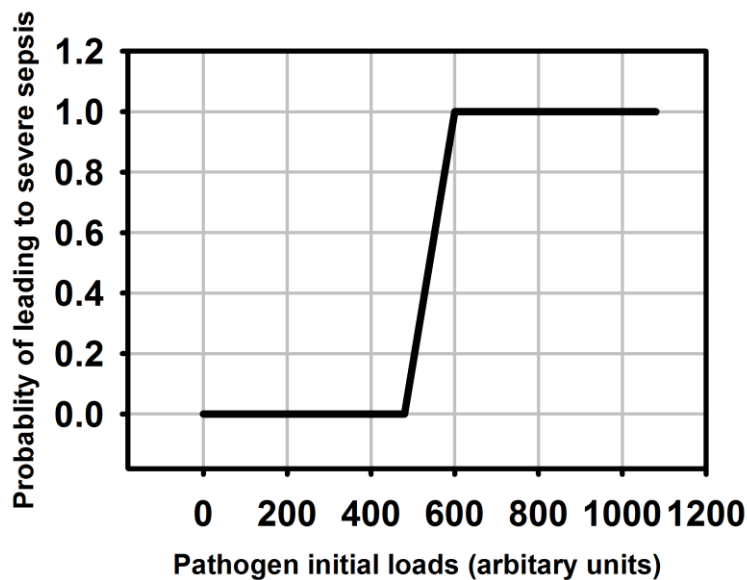
When the pathogen growth has a normal distribution of (0.25, 0.04) for mean and variance, the progression of the episode can be observed (52). After running the simulation 20 times, it is found that the curve of those indicators such as activated-pmns, IL-10s have a

narrower gap between maximum number and minimum number (52). While, the pathogen with probabilistic growth rate has the bigger deviation over multiple replications (52).

### 5.7 Sensitivity analysis of the agent-based model

Predictive results show that the pathogenesis of AIR did have a strong relationship with the threshold of pathogen level. However, the range of initial pathogen loads leading to a healthy response or towards an undesired acute inflammatory response is not clear. Thus, this section explores the sensitivity of the AIR episode to different initial loads of pathogen dosage. Figure 5.7 illustrates the impacts of the initial pathogen loads and shows that the model is quite sensitive to the pathogenesis of AIR while the influence of anti-inflammatory mediators is kept at a relatively low level.

**Figure 5.7 AIR response to the range of the initial pathogen load**

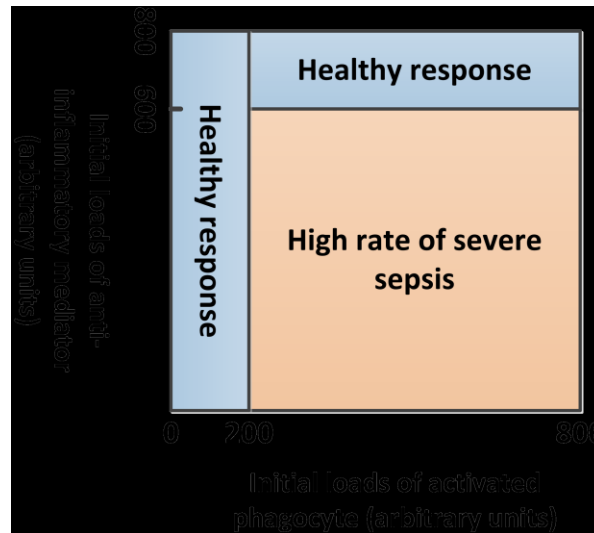


In Figure 5.7, the initial load of pathogens (the X-axis) starts from 0 and is increased by 120 for each simulation run. The Y-axis ranges from 0 to 1 representing the state of AIR, with a value of 0 presenting a healthy acute inflammatory response and 1 represents a possible severe sepsis outcome. It is clearly seen that under an initial pathogen load below 480 the progression of

AIR leads to a healthy response. Statistically, the initial value of pathogens which cause the different prognosis of AIR is  $480 \pm 2.56$  with 95% confidence interval after multiple simulation experiments.

This result is achieved under a low anti-inflammatory mediator environment. Our simulated prognosis experiments suggest that the initial anti-inflammatory mediator or the system parameters controlling the change of anti-inflammatory mediators are sensitive to the AIR pathogenesis. Thus, next we tested the influences of anti-inflammatory mediator on the progression of AIR. A set of simulation runs using different combinations of initial loads of anti-inflammatory mediator (IL-10s), and initial loads of activated phagocytes, under the condition of low initial load of pathogen (range from 0 to 480), were executed. The results are shown in Figure 5.8.

**Figure 5.8 The influence of initial load of anti-inflammatory mediator and activated phagocyte to the outcomes of AIR**



This experiment shows that there are two essential pivot points for a change of the AIR prognosis. One relates to the initial number of anti-inflammatory mediator, and the other to the initial level of activated phagocytes. When the initial load of activated phagocyte ranges from 0 to 200 the AIR episode is stable and healthy regardless the initial value of anti-inflammatory

mediator. An initial load of activated phagocyte higher than 200 cells will expose patients to an elevated risk for severe sepsis when initial load of anti-inflammatory mediator is lower than 600. This means that an uncontrolled AIR episode in which overly activated immune cells lacking proper self-generated or medicated anti-inflammatory controls could develop, even with a low initial pathogen load.

Based on the analysis, one can realize that patient still experience different AIR outcomes due to the variation in their immune systems, even though they have the same threshold of pathogen induction. Since the initial value of system parameters in ABM are associated with the initial conditions of patients, it is necessary to consider the relationships between the initial values of physiological indicators and the system parameters as defined in the system dynamics mathematical model.

First we consider the influence of system parameter  $K_{nn}$  and  $K_{np}$  on the AIR in equation (5.1). The reduction of the pathogens is assumed to follow the standard competitive enzyme inhibition effects among the three agents namely, the *activated phagocytes*, *current pathogen load*, and *damaged tissue* (182). The  $K_{nn}$  represents the ability of activated phagocyte cells to recruit more resting phagocytes to the infectious location, and the  $K_{np}$  calibrates the number of resting phagocyte cells to be activated in order to eliminate the existing pathogens. Based on three different initial pathogen loads, our simulation results have shown that there is a certain relationship between these two system parameters contributing to a stable ultimate state of AIR. That is, the numbers of activated phagocytes needs to be balanced in order to achieve a healthy AIR response. Otherwise, the acute inflammatory response will turn out to be a persistent non-infectious or septic shocks episode.

Our simulated result showed that if  $K_{np}$  decreased and  $K_{nn}$  increased (the number of activated phagocytes induced by pathogens could be supplemented by previously activated phagocytes), the patient can still be on track for a healthy response. However, since the boundary of activation rate of resting phagocytes by previously activated phagocytes is much lower than activation rate of resting phagocytes by pathogens, the patients with a relatively low activation rate of resting phagocytes by pathogens under the condition of previously suffering infection or trauma still could not recovery from sepsis by increasing the value of  $K_{nn}$ . This explains why patient populations such as HIV infected patients or those with organ transplant are more likely to suffer immune-deficiency after AIR (54).

To conclude, we summarize the sensitivity of the other system parameters in our ABM simulation. The test of sensitivity of our system parameters is based on the observation of curve-changing of indicators. It is believed that one parameter is sensitive to the AIR progression if the curve of indicators goes to different directions when this specific parameter interested changes and others fix. The results are shown in Tables 5.2 , and 5.3.

These tables provide insights for various indicators and system parameters which are sensitive to the AIR progression and are essential for a better understanding of the pathogenesis of the AIR. The potential benefits of this research include helping physicians plan proper medication interventions for patients who develop AIR. Moreover, a greater benefit to clinicians will be provided if some of the essential system parameters could be converted or translated into the patient's physiological indicators, which will create an individualized predication of the AIR progression.

**Table 5.2 The sensitivity of AIR progression to the initial load of indicators**

Initial value of indicators in the AIR progression	If it is sensitive to the AIR progression
<b>Pathogen</b>	Very sensitive
<b>Activated Phagocytes</b>	Sensitive under certain condition
<b>Damaged cells</b>	Not quite sensitive
<b>Anti-inflammatory mediator</b>	Very sensitive specially when the initial load of pathogen is low

**Table 5.3 The sensitivity of the AIR progression to various system parameters**

Pathogen system parameters	If it is sensitive to the AIR progression
$K_{pg}$ (183)	Very sensitive
$K_{pm}, S_m, S, i_m, (10, 184) K_{mp}$	Not quite
$K_{pn}$	Sensitive
<b>Activated phagocyte system parameters</b>	
$K_{nn}, K_{np}, K_{nd}$	Sensitive
$i_n$ (185)	Very sensitive
<b>Damaged cells system parameters</b>	
$K_{dn}, i_d$ (23)	Not quite
<b>IL-10s system parameters</b>	
$K_{cn}, i_c$ (40, 180, 186, 187)	Sensitive
$K_{cd}, S_c$ (39)	Not quite

## 5.8 Discussion and conclusion

Systemic inflammation and multiple organ dysfunctions are two of the major causes of mortality today (188, 189). With the advent and improvement of antibiotics and organ support therapy, these conditions have become increasingly relevant (1). The incidences of systemic inflammation are also expected to increase with further advancement of medical technology and the aging of our population (4). The application of system dynamics equations proposed in the existing literature is limited by the lack of modeling stochastic phenomena such as an AIR episode and difficulty in measuring the required parameters. An agent-based model is presented herein, capable of synthesizing the information acquired from the biological process (interaction between indicators) into a modeling/calibrating process while preserving the complexity of the acute inflammatory response process.

Thus, the proposed agent-based model combined the strength of the system dynamics models with that of the simpler agent-based model, decomposing the dynamics model into multiple autonomous agents and capturing the stochastic nature of a biological system.

In order to validate the ABM simulation we compared results from the DNA-Neumococo Study Group with our simulation. This group sampled 353 patients with community –acquired pneumonia and found that bacterial load is highly correlated with the outcomes in patients with pneumonia. The bacterial load of  $\geq 10^3$  copies per milliliter occurred in 29.0% of patients (27 of 93 patients; 95% CI, 20.8 to 38.9%) being associated with a statistically significant higher risk of septic shocks, the need for mechanical ventilation, and hospital mortality (190). Our simulated prognosis experiments also have shown that the initial pathogen load is highly associated with prognosis of AIR pathogenesis.

In addition, maintenance of elevated levels of anti-inflammatory mediators or the transient administration of the anti-inflammatory mediator in patients who would otherwise survive or evolve to septic death is needed (53). This finding corresponds to the simulated results from our model that either AIR turns to healthy response or high rate of severe sepsis when the initial load of anti-inflammatory mediator is elevated. Thus, the proper management of anti-inflammatory mediators plays an important role in the acute phase of infection. The fact that a significant body of recent clinical evidence suggests that low-dose immune-suppression with an anti-inflammatory mediator may in fact improve outcomes in patients with severe infection, particularly in patients with an insufficient anti-inflammatory response (191) is also illustrated by the outcome of our model.

The major strength of the proposed agent-based modeling and simulation approach is that it can help to predict the possible pathogenesis of acute inflammatory response based on the patients' initial physiological conditions. Furthermore, the new approach it is more flexible, visible and more accurate than existing of mathematical models. Even with the complex non-deterministic system presented herein, the proposed ABM uses only few types of agents in the simulation, and it is modular, more flexible and applicable for the development of more complex and accurate models for simulating disease progression.

For further research, we expect to use real clinical data such as the measurement of pathogen load, activated immune cells, resting immune cells as well as the measurement representing damaged tissue as input to this model. This will allow applying this predictive agent-based model towards real clinical environments after a proper calibration. Furthermore, even though the system's parameters could be predicted by the model, these parameters are difficult to measure clinically in practice. Thus our next step is to convert the current system



parameters into physiological indicator such as temperature, blood pressure, CD14 markers, etc. that are easier to measure. These parameters will be used then to model the progression of a sepsis pathogenesis for different patients using patient specific physiological markers.

# Chapter 6 - A Novel Agent-based Model of a Hepatic Inflammatory Response (to *Salmonella*)

## Abstract

Sepsis is defined as a systemic inflammatory response syndrome caused by an infection, primarily bacteria. Sepsis accompanied by organ dysfunction, defined as severe sepsis, can progress with persistently low blood pressure and intravascular coagulation, eventually resulting in septic shock. Severe sepsis and septic shock have a mortality rate of approximately 40% to 60%, and the increasing incidences of sepsis translate to a large financial burden on the healthcare system. Sepsis is a complicated process that involves numerous interactions among cells, cytokines, and tissues. The complexity of sepsis results in various dynamic patterns manifested in unique ways for each patient; however, computational techniques such as modeling complicated interactions among cells and cytokines *in silico* allow observation of those individual patterns. This paper presents a novel integrated-mathematical-multi-agent-based model (IMMABM) to simulate a hepatic inflammatory response (HIR) in a mouse infected by *Salmonella* that progressed to problematic proportions, known as “sepsis progression,” in some circumstances. This IMMABM incorporated experimental HIR data into a computational model. To our knowledge, this IMMABM is the first version of an agent-based model that measures quantitative indicator levels in HIR by incorporating extensive experimental data. Based on over 200 published studies, this IMMABM describes interactions among 23 agents and incorporates 226 system parameters to simulate a mouse HIR *in silico*. Under model assumptions, our simulated results reproduced dynamic patterns of HIR reported in existing experimental studies. We identified four distinct patterns in HIR, including a healing response, persistent infection, a

hyperinflammatory response, and organ dysfunction. As shown *in vivo*, our model also demonstrated that the initial infection dose of *Salmonella* significantly impacted HIR outcomes. In addition, the course of HIR varied when the initial *Salmonella* dose ranged from 300 counts to 1300 “counts” (the *in silico* equivalent to colony forming units, CFU). The occurrence of a healing response, persistent infection, hyperinflammatory response, or organ dysfunction was also highly related with the initial *Salmonella* dose. We determined that high mobility group box-1 (HMGB-1), C-reactive protein (CRP), and the interleukin-10: tumor necrosis factor- $\alpha$  (IL-10/TNF- $\alpha$ ) ratio, and CD4+ T cell: CD8+ T cell ratio, all recognized as biomarkers during HIR, significantly correlated with outcomes of HIR. Therefore, this novel IMMABM links underlying biological processes to computational simulation and begins to enable quantitative simulation and prediction of sepsis progression *in silico*.

### **Keywords**

IMMABM, Mouse Hepatic Inflammatory Response, *Salmonella*, Complex Biological Processes, Sepsis

## **6.1 Introduction**

Sepsis is initially activated by the presence and growth of pathogens in an organism. Under normal healthy circumstances, intruding pathogens are eliminated by the activation of immune cells, such as tissue macrophages and activated neutrophils, in the immune system (192, 193). If an overwhelming immune response occurs, an unbalanced response between immune cells and cytokines may lead to unexpected harmful outcomes for patients, resulting in sepsis. In clinics, sepsis is defined as a potentially life-threatening complication of disease accompanied by symptoms such as high fevers, elevated heart rate, and altered mental status. If sepsis progresses to severe sepsis or septic shock, organ dysfunction occurs, leading to a high chance of death (1).

Severe sepsis and septic shock during an infection are the major causes of death in intensive care settings (3). An average of 250,000 deaths per year in the United States (US) are caused by sepsis (4). Among patients in intensive care units (ICUs), sepsis ranks as the second highest cause of mortality (5) and the 10th leading cause of death overall in the US (6). An average of 750,000 sepsis cases occur annually, and this number continues to increase (5). Care of patients with sepsis can cost as much as \$60,000 per patient, resulting in a significant healthcare burden of nearly \$17 billion annually in the US (7, 8). Sepsis in a hospitalized patient can lead to extended hospital stays and subsequently increase financial burdens. Cross and Opal (32) discussed the lack of rapid, reliable assays available to identify the stage or severity of sepsis and to monitor the use of immunomodulatory therapy. Such assays are unavailable because of the complexity of the inflammatory response and the unpredictable nature of septic shock in individual patients; consequently increasing the difficulty of monitoring single or multiple components of inflammation with specific supportive therapies (32, 41).

A significant recent focus on modeling immune responses during sepsis has emerged in an effort to explore the complicated dynamic presentation of cells, tissues, and cytokines during infection. In 2004, Kumar *et al.* (54) presented a simplified 3-equation system dynamics mathematical model (SDMM) to describe mathematical relationships between pathogen, early pro-inflammatory mediators, and late pro-inflammatory mediators in sepsis progression. In 2006, Reynolds *et al.* (53) proposed a mathematical model for acute inflammatory response (AIR) that included a time-dependent, anti-inflammatory response in order to provide insights into a variety of clinically relevant scenarios associated with inflammatory response to infection. Modeling and simulation of immune responses to sepsis could provide a dynamic understanding of the infectious disease process and may reveal targets for therapeutic intervention. Mathematical

modeling may be refined to allow additional understanding of complex local and systemic dynamics of infectious disease (53, 54). Using a series of known and hypothesized kinetics of biological system components from the literature, current mathematical models describe infectious disease processes by measuring steady states of various components in the immune system. Unfortunately, these models fail to capture heterogeneous information of various components in the simulations and fail to account for deviations from various components' aggregated behaviors (194).

The agent-based model (ABM), a powerful computational modeling technique, simulates complicated nonlinear dynamic relationships between components and intuitively maps a realistic biological system by incorporating spatial effects and the stochastic nature of the immune response into model construction (76, 195). One key element of ABM includes agents, a collection of decision-making entities classified into types based on components described in the real-world system. Each type of agent executes behaviors that can mimic the system they represent when aggregated. Implementation of a predefined set of rules allows agents to move in a designed direction and arbitrarily interact with other agents in a spatial environment. Agent behaviors are updated in various locations according to update rules executed at discrete time steps. ABM inherently captures repetitive spatial interactions between agents in a stochastic process or under a known probability distribution, making it a powerful tool to render valuable information and simulate a biological system. Implementation of ABM requires well-established technology that relies on computers to explore dynamics beyond the reach of pure mathematical methods (61, 62). The inherent nature of computational structure allows ABM to be efficiently implemented on parallel computers (63).

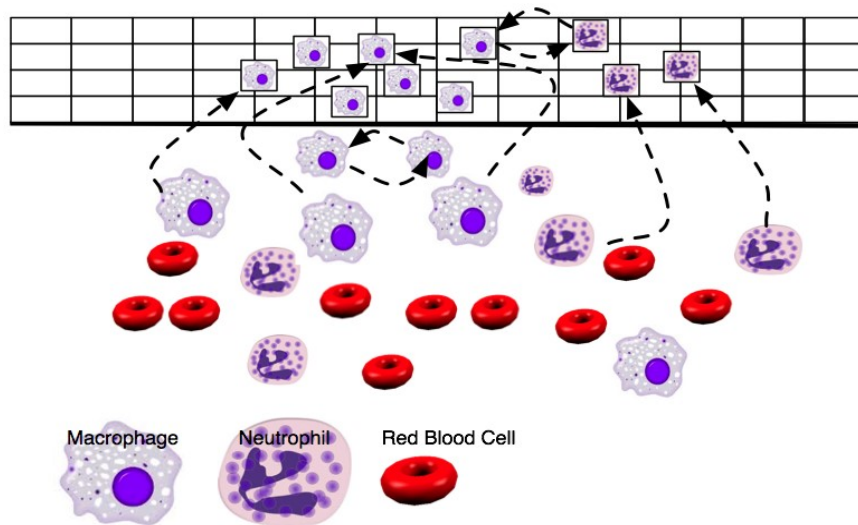
This paper presents a novel integrated-mathematical-multi-agent-based model (IMMABM) of an inflammatory response and possible sepsis progression. The paper specifically focuses on IMMABM implementation into complicated cellular and molecular pathways during a mouse hepatic inflammatory response (HIR) stimulated by *Salmonella*. This IMMABM was constructed based on interactions between 23 selected agents and 226 incorporated system parameters summarized over 200 publications. System parameters were calibrated from various *in vivo* experimental models, using as much data as possible from actual *Salmonella* infections observed in mouse systems. Corresponding citations are available in the reference section and supplementary material. Simulated results from IMMABM showed that four distinct dynamic patterns emerge during mouse HIR: a healing response, persistent infection, a hyperinflammatory response, and organ dysfunction. Emerging simulations were verified through a pattern-oriented analysis found in available mouse experimental studies. Furthermore, simulated results from IMMABM determined that expression of high mobility group protein 1 (HMGB-1), C-reactive protein (CRP), interleukin 10 (IL-10): Tumor necrosis factor alpha (TNF- $\alpha$ ) ratio, and the CD4<sup>+</sup> T cell: CD8<sup>+</sup> T cell ratio are highly correlated with the outcomes of mouse HIR. We also correlated mouse HIR to the initial *Salmonella* challenge level during IMMABM simulation.

This paper is organized into five sections to present details of IMMABM construction and corresponding simulated results: 1) previously published examples of agent-based models, 2) development of this IMMABM for mouse HIR, 3) simulated results and model validation, 4) our conclusions and discussion, and 5) future research.

## 6.2 Agent-based model of inflammatory responses in previous publications

An (48) described the first application of ABM of sepsis in which he produced a very abstract ABM of an acute inflammatory response (AIR), an initial stage of sepsis. His model was built on the interface between endothelial cells and blood at the capillary level in order to simulate behaviors of circulating neutrophils and monocytes in the presence of injury. Neutrophil and monocyte behaviors, including rolling, sticking, diapedesis, and respiratory burst, were regulated by a series of state variables, and obeyed fundamental observations in an AIR environment derived from the literature. Figure 6.1 shows interacting behaviors of macrophages, neutrophils, and red blood cells in An's ABM.

**Figure 6.1 Interacting behaviors among macrophages, neutrophils, and red blood cells**



As shown in the Figure 6.1, each square represents a specific intercellular location near the infection site in an ABM model (48). Macrophages and neutrophils were recruited from blood vessels to the location of infection based on known biological mechanisms. State variables related to macrophages and neutrophils varied from location to location when the agent-based

simulation was executed. The accumulated value of macrophage and neutrophil-dependent state variables was used to calibrate global variables such as “total oxy deficit” and “End Injury Vector Number.” “Total oxy deficit” measured total damage caused by AIR, and “End Injury Vector Number” measured accumulated infection load during AIR progression in order to reflect characteristics of AIR progression. This particular model generated a distributed outcome of AIR progression by calibrating the “oxy” and “End Injury Vector Number” in 500 iterations of simulation runs under identical extent of injury parameters. Distribution outcomes simulated heterogeneity of a patient population and confirmed that ABM could represent stochastic characteristics of AIR progression (48).

An (48) concluded that his ABM could not represent a real system but that his approach increased understanding of complex steps in the inflammatory process at the sophistication level of his model. Subsequent efforts by An (49) continued use of ABM to simulate and compare various therapeutic effects for improvement of patient outcomes. The next-generation model (49) was developed at the cellular level and, as in the previous effort, built on the endothelial-blood interface. The second-generation ABM incorporated additional agents to represent the interaction between cells and pathways of immune responses in AIR progression. Positive/negative feedback relationships and interactions between agents were represented and updated using arithmetic relationships guided by cellular/molecular mechanisms of AIR progression. The range of initial injury generating a systemic inflammatory response (SIR) became the “zone of interest”. Distributions of a variable “end oxy deficit (EOD)” related to initial injury levels in infectious and sterile models with and without antibiotics and demonstrated that patient survivability improved with the use of antibiotics. An suggested that the second-generation ABM was difficult to apply in clinics because the proposed ABM had limitations such as being



extremely abstract”, having a “lack of experimental validation” and had “limited mathematical matching to recognized kinetics (49).

In 2011, Wu *et al.* (52), proposed an integrated ABM embedded with a mathematical model to simulate AIR progression at the interface between blood vessels and cells within a hypothetical generalized organ. Five total agents were defined in the model: pathogen, resting neutrophils, activated neutrophils, damaged tissue, and anti-inflammatory cytokines. Implementation of the ABM with corresponding initial profiles of patients of interest and adjustable system parameters allowed simulation of agent behaviors and local intercellular interactions. The ABM in Wu *et al.* (52) is advantageous compared to other ABMs because it incorporates ordinary differential equations into recognized biological kinetics of AIR. However, experimental data incorporation and experimental validation were not included.

Recently, Dutta-Moscato *et al.* (51) proposed a multi-scale agent-based *silico* model of liver fibrosis using an ABM to simulate an HIR. The authors simulated key cellular and molecular processes by incorporating interplays between agents such as TNF- $\alpha$ , TGF- $\beta$ 1, and Kupffer Cells. The authors found that the pattern of collagen deposition during liver inflammation conformed well to the known patterns of collagen deposition during inflammation in rat livers treated with Chemokine ligand 4 (CCL4). However, the authors claimed their version of ABM was limited because it sacrificed detailed mechanisms of the HIR and it was not calibrated against an *in vivo* time course of liver injury (51).

In addition to modeling interactions between cells, Dong *et al.* (50) proposed an ABM framework to model intracellular dynamics of the NF- $\kappa$ B signaling cascade, illustrating subsequent intercellular interactions among macrophages and T-helper cells through the up-regulation of inflammatory mediators. Their approach explored hypothetical scenarios of AIR

and potentially improved understanding of molecular behaviors that could develop and expand to emergent behavior of the entire AIR system. This ABM provided unprecedented integration of molecular interactions involved in signaling cascades activated in response to lipopolysaccharide (LPS) stimulation. The disadvantages of this ABM were that it utilized a qualitative AIR measurement and did not include experimental validation.

### **6.3 Development of IMMABM for hepatic inflammatory response of a mouse**

Existing ABMs that focus on inflammation provide evidence that agent-based modeling is a valid approach for simulating disease progression (48-52). However, limitations to the existing models include: utilization of a small number of agent types, limited control system parameters, and failure to include many critical variables (agents) involved in real immune responses. Furthermore, previous ABMs focused on a general modeling approach of inflammatory responses. However, because outcomes of an inflammatory response vary due to the source of infection, the relevant species, or various strains of one species, a general modeling framework of inflammatory response cannot accurately model sepsis progression. In addition, a general ABM framework may cause difficulty in model validation due to discrepancies in modeling platforms and differences in experimental models.

In an effort to improve existing ABMs, we proposed an IMMABM to simulate mouse HIR caused by *Salmonella* at the tissue level. By specifying the infected species, source of infection, and site of infection, the scope of the IMMABM allowed us to improve modeling approach accuracy without loss of generality. This IMMABM is also the first ABM to simulate mouse HIR stimulated by *Salmonella*. This ABM required that each interaction incorporated into the model was based on actual data from observations made during experimental infections *in vivo* or measurements made *ex vivo* or *in vitro*, thereby resulting in an incorporation of data from

210 publications related to mouse hepatic inflammation induced by *Salmonella*. When data were not available, we extrapolated from related Gram-negative bacteria or other pathogens, keeping in mind that fidelity to actual *Salmonella* infections was necessary. Therefore, we summarized interactions among cells, tissues, and cytokines during mouse HIR and we calibrated quantitative changes in the HIR with experimental data and necessary mathematical expressions for agent modeling. Consequently, this approach is superior because previous ABMs were limited in incorporating essential molecular and cellular interactions of the inflammatory response, resulting in simulation inaccuracies. In addition, results generated from most existing ABMs are limited in the lack of realistic units (qualitative calibration), thereby increasing the difficulty of matching simulated results with real experimental results during model validation. We attempted to calibrate variables based on unit relationships observed in the experimental systems.

### ***6.3.1 Simulation environment***

This IMMABM attempted to simulate a *Salmonella* infection at the level of the mouse liver. The liver, enriched with resident tissue macrophages (Kupffer Cells), is recognized as a key organ of the immune system that is vital for elimination of a *Salmonella* infection (15, 176). We chose *Salmonella* as a “targeted” pathogen strain because it is responsible for millions of deaths in developing countries every year (106). Furthermore, immune responses to *Salmonella* infections have been investigated extensively (107-112). Therefore, an abundance of data is available for accurate incorporation of relationships among variables (agents) in order to support our IMMABM.

### ***6.3.2 Software platform***

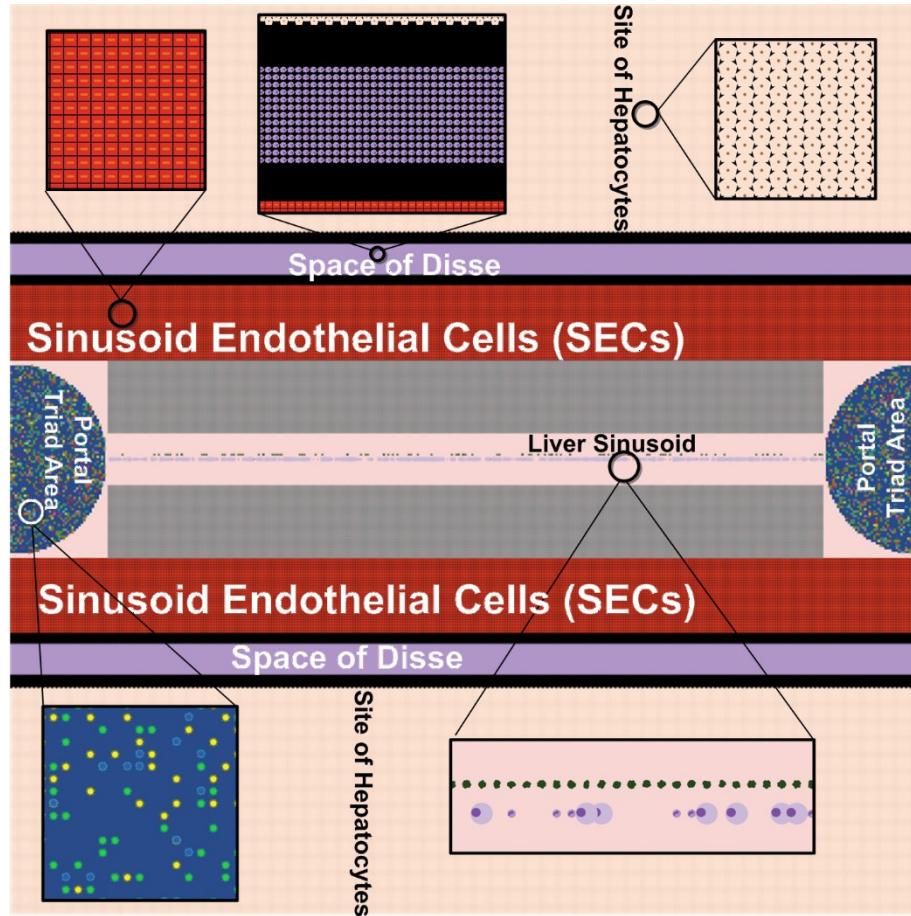
We used Netlogo, a platform with a simplified programming environment, easily implemented tool sets, and well-established documentation support, in order to implement the IMMABM (102). The primary user interface of Netlogo is comprised of two-dimensional (2D) grids, and agents can be divided into two categories: “patches” and “turtles.” “Patches” are fixed agents placed on background grids in the model workspace. “Turtles” are mobile agents that occupy a position or move freely on the surface of patches and execute certain functions or actions regulated by the simulated system. In our IMMABM, we defined all agents as “turtles” because all agents in our simulation were movable. Netlogo also applies a class called “breed” to define agent types with similar behaviors or types that are controlled by the same mechanism. The concept of “breed” allows the modeler to define a class of agents with a set of common state variables and establish various functions or actions (autonomous behaviors) for agent types. The interface of Netlogo allows the modeler to set initial parameters and observe simulation results.

### ***6.3.3 Simulation initial setting***

We generated a  $200 \times 200$  2D grid in Netlogo as the simulation interface, designed to simulate a 2D reflection of a mouse liver. We divided the entire interface of Netlogo into five regions to represent the liver sinusoid, sinusoid endothelial cells (SECs), the space of Disse, the site of hepatocytes, and portal triad in the liver (14). The initialized interface of Netlogo is shown in Figure 6.2. Kupffer Cell numbers are approximately one-fourth the number of hepatocytes in the liver (196). SEC numbers are approximately one-third the number of hepatocytes, and approximately one-eighth the number of mast cells exist compared to the number of hepatocytes (196, 197). The initial number of hepatocytes was determined by an automated process of filling the region with hepatocytes in a  $200 \times 200$  2D grid. The hepatocytes filled each patch in the

hepatocyte region, as shown in Figure 6.2). For simulation size presented in this paper, the number of hepatocytes was initialized to 80,200. Considering the numeric proportion between hepatocytes, Kupffer Cells, SECs, and mast cells, we set the initial number of Kupffer Cells to 20,160, SECs to 26,466, and mast cells to 10,426.

**Figure 6.2 Simulated area of the HIR in the Netlogo interface at simulation step equal to 0 (initial status)**



### 6.3.4 Process of IMMABM development

IMMABM was developed as an agent-oriented computer program to describe agent rules and behaviors. Each agent type was defined as “breed” in Netlogo, and each “breed” in IMMABM had specific state variables. By assigning 0 or 1 to the state variables, the agents were regulated to execute a series of functions based on various locations and interfaces. Interactions

between agents were highly stochastic, and we incorporated mathematical expressions such as logistic growth function, mass-action kinetics, Michaelis-Menten kinetics, and decay functions to quantitatively measure complicated biological processes. Furthermore, the process of writing computer codes for IMMABM strictly followed conditional statement “if-then” rules, conforming to biological mechanisms of HIR.

The primary objective of our IMMABM was to incorporate available experimental data into computational simulation. Data such as infiltration time of immune cells, replication rate of *Salmonella*, and degradation rate of associated mediators allowed us to advance ABM application by mapping biological processes that occur during HIR to our IMMABM. By integrating experimental data and mathematical expressions derived from hypothesized kinetics, we attempted to quantitatively simulate dynamic patterns of HIR. In addition, a global variable defined as “Infection Time” in IMMABM reflected simulation execution time and mimicked kinetic associations between a series of responses. In our simulation, 1 tick (representing 1 simulation step in the simulation software) represented 1 hr in an actual biological process, and numeric counts of an agent were updated per tick to correspond to the biological response time in the experiments.

Incorporation of data from 210 publications and our experience with *Salmonella* infections and infectious disease processes motivated us to select a total of 23 essential cells and cytokines as agent types in this IMMABM. In this paper, we use italic format to highlight agent type for convenience. Each agent type, further defined as “breed”, could contain multiple entities. Among the 23 types of agent, we defined 20 primary agent types: *Hepatocyte*, *Hepatocyte Debris*, *Kupffer Cell*, *Salmonella*, *Mast Cell*, *Resting Neutrophil*, *Activated Neutrophil*, *Resting Monocyte*, *MDMI (monocyte-derived type 1 macrophage)*, *MDMII*

(monocyte-derived type 2 macrophage), *TNF- $\alpha$*  (tumor necrosis factor- $\alpha$ ), *HMGB-1* (high mobility group box-1), *IL-10* (interleukin-10), *CD4 T Cell*, *CD8 T Cell*, *B Cell*, *Antibody*, *CRP* (C-reactive protein), *NET* (neutrophil extracellular traps), and *Histamine*. We also defined three auxiliary agent types: *SEC* (sinusoidal endothelial cell), *Signal*, or *Anti-Signal*. The rule system for these agents was based on the literature. A sequence of interactions among primary agents and primary agent behaviors during interactions are introduced in Section 6.3.4.1.

#### **6.3.4.1 Primary agent behaviors**

*Salmonella*, a “trigger” to begin HIR, was the first agent to move and interact with *Kupffer Cells*, thereby initializing HIR. The percentage of *Salmonella* killed by *Kupffer Cells* was set from 15% to 16% of the total *Salmonella* population per hour because 90% to 95% of *Salmonella* were phagocytosed (engulfed) by *Kupffer Cells* in 6 hrs (198). *Salmonella* that survived in *Kupffer Cells* turned *Kupffer Cells* into an “apoptotic” state and “proliferated” within *Kupffer Cells* (172, 173). “Die” in Netlogo occurs when an agent in the simulation is forced to disappear, but “proliferate” is defined as new agent generation in the simulation. State variables associated with agent type were used to define various states of individual agents. Implementation of state variables is introduced in Section 6.3.4.3. The maximum number of *Salmonella* that “proliferate” within one *Kupffer Cell* was limited to 50 (176). The newly generated *Salmonella* were released to liver tissue after “apoptotic” *Kupffer Cells* “died” between 6 and 14 hrs (172). These released *Salmonella* were assigned to a state variable “salmonellaNewlyReleasedFromKupfferCell” in order to express aborted interaction with *Kupffer Cells* and prepare for “proliferation” in surrounding *Hepatocytes* or *SECs* (176, 199). When *Activated Neutrophils* or *MDMIs* were recruited to the site of infection, *Neutrophils* or *MDMIs* “killed” *Salmonella* (172, 198, 200, 201). Experimental data showed that every

neutrophil phagocytized approximately 3 to 13 *Salmonella* per hour, and every *MDMI* phagocytized approximately 1 to 7 *Salmonella* per hour (202). In addition to immune cells, *CRP* released from *Hepatocytes* and *Antibody* released from *B Cells* also contributed to the “killing” of *Salmonella* (10, 203-206).

*Hepatocytes* account for approximately 60% of the total number of cells in the liver (196). In our IMMABM, *Hepatocytes* were primary locations for *Salmonella* “proliferation”, and the *Hepatocytes* become “apoptotic” once they interacted with *Salmonella* or *TNF- $\alpha$*  (15, 198, 199). “Apoptotic” *Hepatocytes* released acute stress proteins such as *CRP*, or cytokines such as *TNF- $\alpha$* , and *HMGB-1* (203, 204, 207, 208). In addition, “Apoptotic” *Hepatocytes* could undergo a natural aging process or interact with infiltrating *Activated Neutrophils* (127, 209, 210). “Apoptotic” *Hepatocytes* that interacted with *Activated Neutrophils* “died” immediately and released their interacted *Salmonella* to the liver tissue (198). Alternatively, “Apoptotic” *Hepatocytes* underwent natural aging and became *Hepatocyte Debris* after 2 or 3 hrs (211). In addition to death, *Hepatocyte* was also regenerated at a rate of  $1.32 \times 10^{-3}$  to  $6.80 \times 10^{-3}$  per hour to simulate proliferation of *Hepatocyte* in a mouse’s liver (212).

We modeled five primary phagocytic cells in our IMMABM, including *Kupffer Cell*, *Mast Cell*, *Activated Neutrophil*, *MDMI*, and *MDMII*. *Kupffer Cells* reside principally within the lumen of liver sinusoids, adherent to *SECs* that comprise blood vessel walls (14). The first phagocytic cells that interacted with *Salmonella* in the liver (113, 115, 116) were *Kupffer Cells* that killed approximately 90% to 95% of the *Salmonella* population in 6 hrs; however, 5% to 10% of *Kupffer Cells* were killed by *Salmonella* during the same time period (198). *Kupffer Cells* released cytokines such as *TNF- $\alpha$*  which helped recruit other phagocytic cells such as *Activated Neutrophils* to the site of infection or incurs further damage to *Hepatocytes* (15, 171). *Kupffer*



*Cells* also released *IL-10*. *IL-10* represents anti-inflammatory cytokines in this model and is capable of inhibiting the release of  $TNF-\alpha$ . As typical phagocytic cells, *Kupffer Cells* “killed” various types of cell debris such as hepatocyte debris (to represent their scavenging or “clean up” function), *Antibody*-opsonized *Salmonella*, and *CRP*-opsonized cell debris (10, 205). The apoptosis of *Kupffer Cells* occurs at a rate of  $4.20 \times 10^{-3}$  to  $3.20 \times 10^{-2}$  per hour (123). Replenishment of *Kupffer Cells* came from *MDMIs* and *MDMIIs* at a rate of  $6.30 \times 10^{-3}$  to  $7.90 \times 10^{-3}$  per hour (123). Similar to *Kupffer Cells*, *Activated neutrophils* also “killed” *Salmonella*, *Antibody*-opsonized *Salmonella*, *CRP*-opsonized cell debris, and released cytokines such as  $TNF-\alpha$  or *IL-10* (10, 17, 205, 213). Biologically, *Activated Neutrophils* were recently recognized to release *NETs* to eliminate *Salmonella* (214, 215). *Activated Neutrophils* underwent natural aging or were “killed” by *Kupffer Cells* (14). “Apoptotic” *Activated neutrophils* underwent apoptosis, indicated by a state variable labeled “apoptotic.” The “apoptotic” *Activated Neutrophils* were killed by *MDMIs* (216). *MDMIs* were activated from *Monocytes* between 6 hrs to 24 hrs post-infection (137, 138). The activation level of *Monocytes* was dependent on the existing number of *Salmonella*,  $TNF-\alpha$ , *HMGB-1*, “apoptotic” *Activated neutrophil*, *CD4 T cell*, and *CD8 T cell*. The activation amount was calculated based on Michaelis-Menten kinetics, as discussed in Section 6.3.4.4. Upon activation, *Monocyte* became *MDMI* or *MDMII* (216). *MDMI* “killed” *Salmonella* and released  $TNF-\alpha$  (216), while *MDMII* “killed” “apoptotic” *Activated Neutrophils* and released *HMGB-1* and *IL-10* as mediators to resolve the inflammation (142, 216). *MDMI* and *MDMII* helped activate T cell recruitment (164), and both *MDMI* and *MDMII* released *IL-10* when they “killed” apoptotic *CD4 T Cell* or *CD8 T Cell* (166).

*CD4 T Cell*, *CD8 T Cell*, and *B Cell* occupied spaces in the portal triad (10, 11). Activation of *CD4 T Cell*, *CD8 T Cell*, or *B Cell* occurred when *MDMI* or *MDMII* were detected (164), at which point the activated *CD4 T Cell*, *CD8 T Cell*, or *B Cell* moved from the portal triad to the liver sinusoid (217). *CD4 T Cell* released *TNF- $\alpha$*  or *IL-10* when they interacted with phagocytic cells interacting with *Salmonella*, and *CD 4 T Cell* improved the phagocytic rate of phagocytic cells (206). *CD8 T Cell* “killed” phagocytic cells that interacted with *Salmonella* (10, 206). *CD4 T Cell* and *CD8 T Cell* underwent natural apoptosis, and both “apoptotic” *CD4 T Cell* and *CD8 T Cell* were “killed” by *MDMI* or *MDMII* (166). *B Cell* released *Antibody* to form an *Antibody-Salmonella* complex, and the *Antibody-Salmonella* complex was killed by phagocytic cells, simulating opsonization (206). The binding process is described in Section 6.3.4.2.

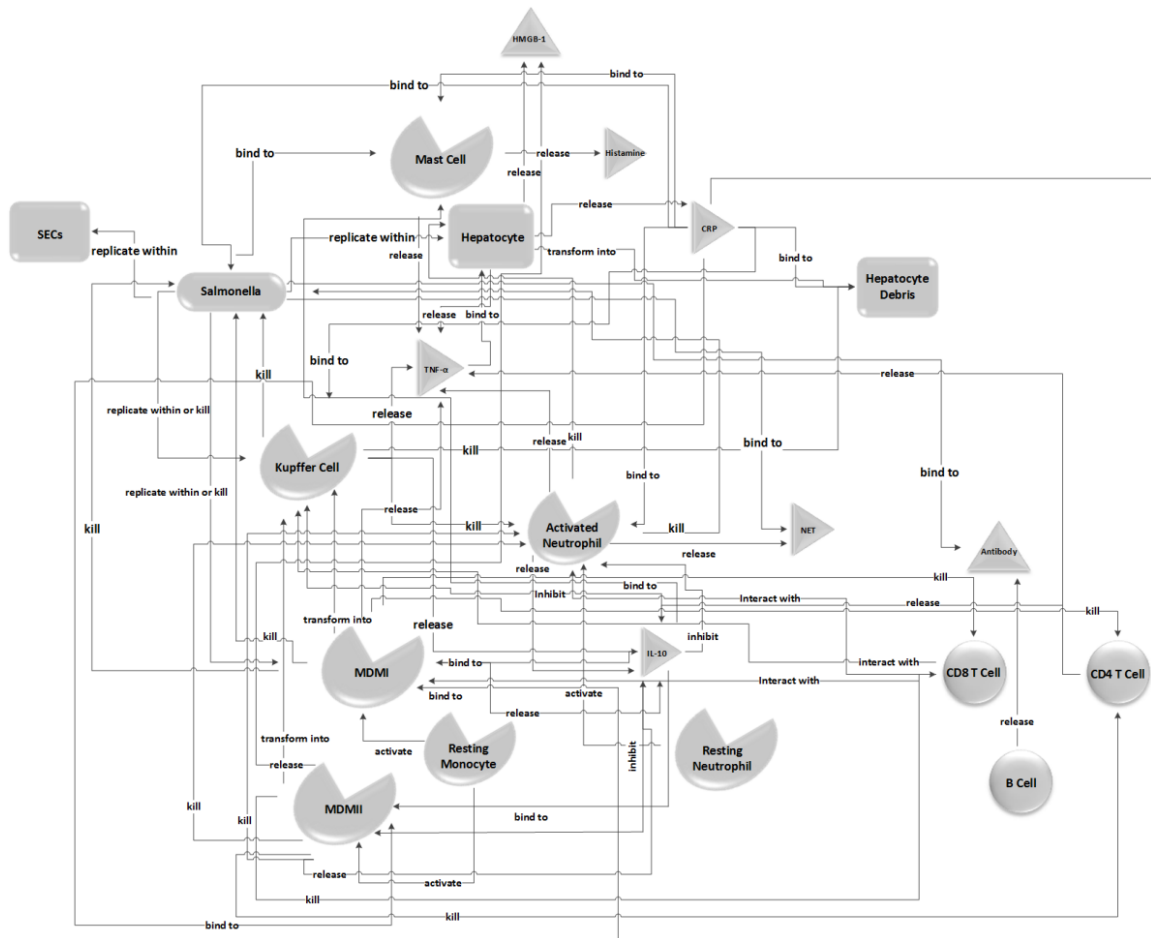
*TNF- $\alpha$* , *HMGB-1*, and *IL-10* are cytokines released from phagocytic cells. *TNF- $\alpha$*  was released from *Kupffer Cell*, *Mast Cell*, “apoptotic” *Activated Neutrophil*, *MDMI*, and *Hepatocyte* (14-20, 216). *TNF- $\alpha$*  caused *Hepatocyte* to become “apoptotic” (15). *HMGB-1* was released from *MDMII* and “apoptotic” *Hepatocyte* (24, 139, 218), and *IL-10* was released from *Activated Neutrophil*, *MDMII*, and *CD4 T Cell* (16, 77, 213, 216, 218, 219). *IL-10* prevented secretion of *TNF- $\alpha$* , *HMGB-1*, and *IL-10* from interacting with phagocytic cells or T cells (147-150, 219, 220). Procedurally, *TNF- $\alpha$* , *HMGB-1*, and *IL-10* “died” to reflect their clearance away from the simulation. Interactions among and between 21 agents in the IMMABM are shown in Figure 6.3 (anti-signals and signals were not included), and a comprehensive description of agent behaviors is presented in Table B.7.

#### **6.3.4.2 Agent and agent complex movement**

Agent movement in IMMABM was determined by agent behaviors described in Section 6.3.4.1. For example, *Resting Neutrophils* or *Resting Monocytes* moving to *SECs* were driven by

Signals released from cytokines or cells (24, 127, 171, 206, 216, 221-223). When Signals appeared on SECs, Resting Neutrophils or Resting Monocytes moved to SEC locations. Mass-action kinetics determined the number of moving Resting Neutrophils or Resting Monocytes, as described in Section 6.3.4.4. Biological interaction between two agents occurred in IMMABM simulation if two agents occupied the same patch.

**Figure 6.3 An overview of primary agent interactions in IMMABM**



*Salmonella* that replicated within *Kupffer Cells*, *MDMIs*, *SECs*, and *Hepatocytes* (172, 173, 176, 199, 216) were released to nearby patches when infected cells “died”. Released *Salmonella* randomly moved to the nearest *Hepatocytes* and damaged those *Hepatocytes*.

We used a “link” breed to model movements of the *Antibody-Salmonella* complex or *CRP*-cell complexes because the two components of the complex need to move simultaneously.

For example, when an *Antibody-Salmonella* complex moved to one phagocytic cell, *Antibody* and *Salmonella* moved in the same direction for the same distance (10). The *Antibody-Salmonella* complex's killing process using the phagocytic cell occurred when the distance between the complex and the phagocytic cell was less than one patch-size.

#### **6.3.4.3 State variable updates**

Each agent type had its own state variables in IMMABM. These state variables helped differentiate individual agents in the same agent type in order to allow individual agents to execute various behaviors based on agent rules. The value of state variables was either 0 or 1, and the function of a state variable was similar to a switch: 0 represented “off”, and 1 represented “on”. If a state variable was equal to 1, individual agents that had that state variable would express specific attributes or execute biological functions. For example, *Kupffer Cell* had a state variable named “kupfferCellBindToIL10”. The value of the state variable was equal to 1 when *Kupffer Cell* interacted with *IL-10*, and individual *Kupffer Cells* that had the state variable “kupfferCellBindToIL10” equal to 1 did not release *TNF- $\alpha$* . *Salmonella* that proliferated within *Kupffer Cell* had a state variable named “salmonellaReplicateWithinKupfferCell” equal to 1; *Salmonella* that had “salmonellaReplicateWithinKupfferCell” equal to 1 generated new agents until the state variable “salmonellaReplicateWithinKupfferCell” was reset to 0. *Kupffer Cell* was assigned to a state variable named “kupfferCellKillBySalmonella” equal to 1 when *Kupffer Cells* interacted with *Salmonella* that had the state variable “salmonellaReplicateWithinKupfferCell” equal to 1. *Kupffer Cells* had the state variable “kupfferCellKillBySalmonella” equal to 1 “die” after 6 simulation ticks, and the state variable “salmonellaReplicateWithinKupfferCell” of interacted *Salmonella* was reset to 0. *Resting neutrophil* were activated in order to move to *SECs* in response to signaling by *TNF- $\alpha$* , *HMGB-1*, or *Salmonella* signaling, consequently becoming

*Activated neutrophil*. *Activated neutrophil* moved to the “apoptotic” *Hepatocytes* with a state variable labeled “hepatocyteUndergoApoptosis” equal to 1. “Apoptotic” *Hepatocytes* that interacted with *Activated neutrophils* “died” immediately due to the killing process of “apoptotic” *Hepatocyte* by *Activated neutrophil* (137, 200). A comprehensive description of agent rule updates is presented in Table B.8.

#### 6.3.4.4 Mathematical equations in programming

In order to calibrate quantitative changes in agent number during HIR, we used a standard logistic function to measure cell population increases, Michaelis-Menten kinetics to calibrate cytokine release, mass-action kinetics to calibrate the activation process of circulating neutrophils and monocytes, and a decay function to measure the natural process of apoptosis by cells or catabolism of cytokines.

For example, we calibrated the *Salmonella* population to increase using a standard logistic growth function (119) as follows:

$$\frac{dP}{dt} = k_{pg} P \left( 1 - \frac{P}{P_{\infty}} \right) \quad (6.1)$$

In Equation (6.1),  $P$  represents the *Salmonella* count,  $K_{pg}$  represents a constant growth rate for *Salmonella*, and  $P_{\infty}$  represents maximum carrying capacity of the *Salmonella*. Growth rates and carrying capacities of *Salmonella* varied when *Salmonella* replicated within various cells. Corresponding experimental data is presented in Table B.9.

The activation process of circulating neutrophils was promoted by the pro-inflammatory mediator TNF- $\alpha$ , *Salmonella*, and HMGB-1 (24, 127, 171, 206, 221). We used a mass-action kinetics equation (224) to calibrate the activation process of circulating neutrophils as follows:

$$\frac{dN}{dt} = rN_R (T^* + P^* + H^*) \quad (6.2)$$

In Equation (6.2),  $N$  represents *Activated Neutrophil* count and  $N_R$  represents *Resting Neutrophil* count.  $T^*$  denotes concentration of TNF- $\alpha$ ,  $P^*$  denotes concentration of *Salmonella*, and  $H^*$  denotes concentration of HMGB-1.

The release of cytokines obeyed trafficking machinery, and cytokines were released via protein-protein interactions initiated by ligand binding to receptors (129, 130). Therefore, we used Michaelis-Menten kinetics (131) to calibrate the cytokine release process as follows:

$$\frac{dC}{dt} = \frac{K_{max} Cell}{Cell_{half} + Cell} \quad (6.3)$$

In Equation (6.3),  $C$  represents cytokine count and  $K_{max}$  represents the maximum production rate of cytokines secretion by the cell.  $Cell$  denotes current numbers of the cell intending to release the cytokine and  $Cell_{half}$  denotes cell numbers when half the maximum production rate of the cytokine was reached in the IMMABM.

Natural cell apoptosis or cytokine catabolism occurred at every tick; thus, we assumed that the decrease in cell or cytokine counts followed a simple decay function as follows:

$$\frac{dC}{dt} = K_c C \quad (6.4)$$

In Equation (6.4),  $C$  represents cell or cytokine count and  $K_c$  represents a constant decay rate for cells or cytokines.

#### **6.3.4.5 Model calibration and parameter estimation**

In addition to mathematical models, we calibrated experimental data such as replication rates of cells, production rate of cytokines, killing rates of *Salmonella* by phagocytic cells, activation rates of circulating neutrophils or monocytes, and apoptotic rate of cells or catabolism of cytokines from existing experimental studies. These data were incorporated into IMMABM as system parameters. We collected experimental data from studies that were most similar to our

simulation setting. We also estimated parameters during simulation if data were not available from experimental studies. For example, we estimated that the CRP-opsonized debris moved to inflammatory cells (e.g. Kupffer Cell, mast cell, neutrophils, MDMI, and MDMII) with an equal chance of 0.2. All experimental data (including calibrated and estimated data) and corresponding system parameters are presented in Table B.9.

In IMMABM, we used agent count to represent cell number with the awareness that cytokine production rate has a unique experimental unit compared to cell number. Thereby, cytokine production rate had to be transformed into an agent number in order to make the experimental data consistent in IMMABM. Therefore, we used one agent count to represent one real experimental unit. For example, we estimated that one phagocytic cell can bind  $1.23 \times 10^{-17}$  g IL-10 from experimental data (225). Therefore, we used one IL-10 agent count to represent  $1.23 \times 10^{-17}$  g IL-10 in real experiments. Similarly, we calibrated that  $1.25 \times 10^{-5}$   $\mu$ g CRP could bind to one phagocytic cell (226). Thus, we used one CRP agent count to represent  $1.25 \times 10^{-5}$   $\mu$ g CRP in real experiments. Data showed that  $2.82 \times 10^{-5}$  pg TNF- $\alpha$  damaged one hepatocyte per hour (227), so we used one TNF- $\alpha$  agent count to represent  $2.82 \times 10^{-5}$  pg TNF- $\alpha$  in order to transform experimental units into the agent count. Unfortunately, however, *NET* structure is fragile, thereby making it difficult to quantify *NETs* in experiments (228). The rate at which *NETs* kill *Salmonella* was also difficult to establish (229). Therefore, since neutrophil elastase (NE) is required for *NET* formation and NE is an essential component of *NET* (214), we used the rate at which NE kill *Salmonella* to substitute for the rate at which *NETs* kill *Salmonella*.

## 6.4 Simulated results and model validation

### 6.4.1 Statistical analysis

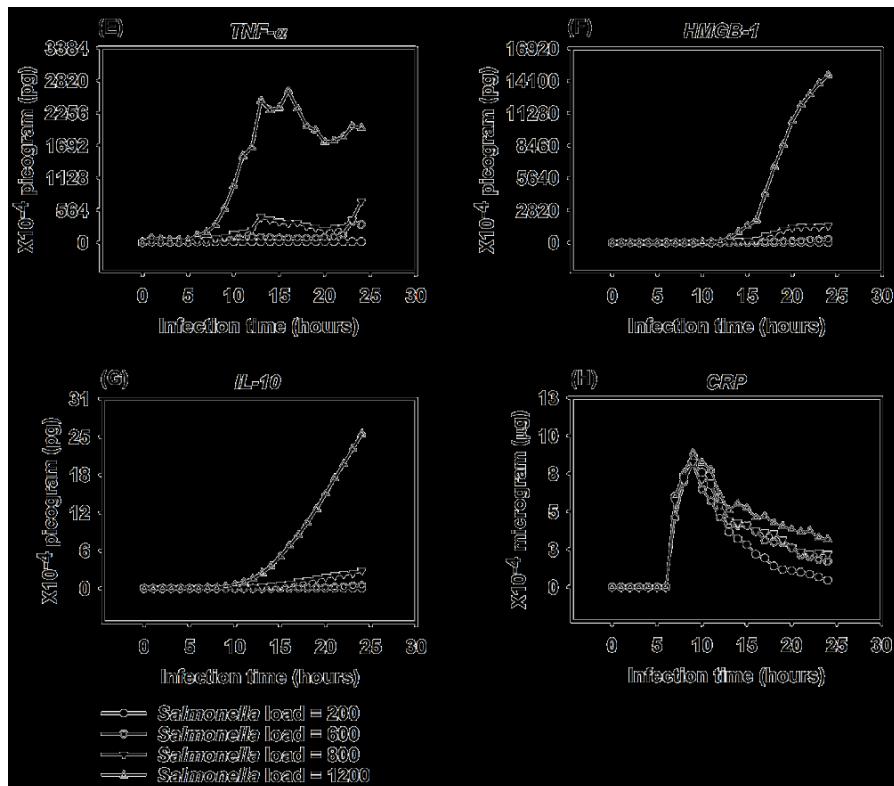
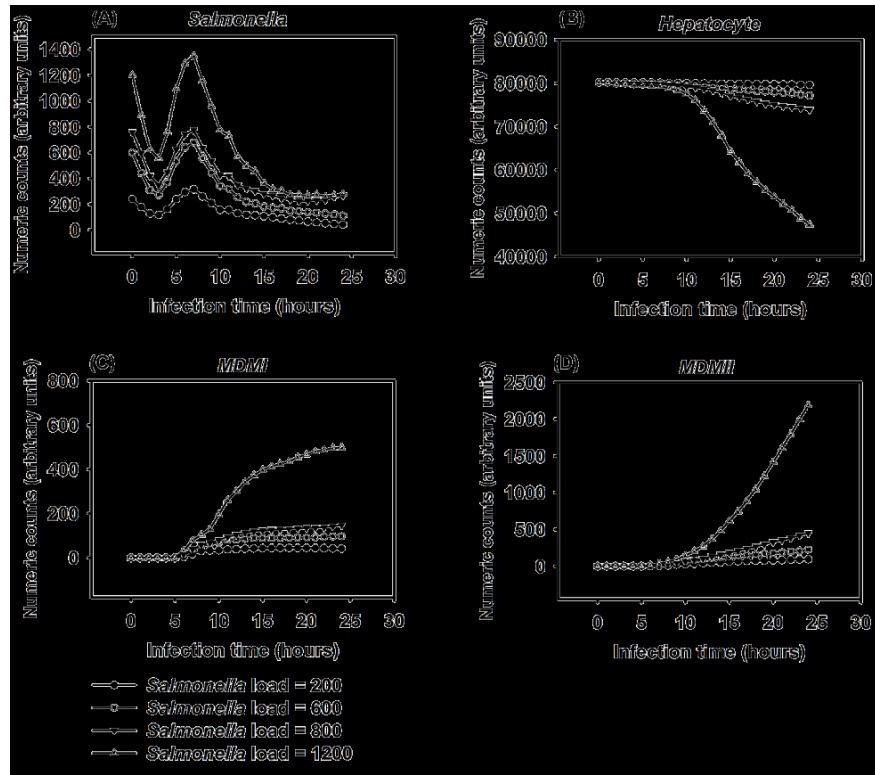
Results are expressed as mean  $\pm$  standard error (SE). Data normality was checked using both histogram and quantile-quantile (Q-Q) plot. For normally distributed data, group comparisons were performed using one-way analysis of variance (ANOVA). For non-normally distributed data, Mann-Whitney  $U$  tests were conducted to compare groups. All tests were performed using R 3.1.2. (230). A  $P < 0.05$  was considered statistically significant at the significance level  $\alpha=0.05$ .

### 6.4.2 Change in selected indicator levels observed under various *Salmonella* loads

The IMMABM generated quantitative results by running simulations with various initial *Salmonella* counts (equivalent to infection dose). The input data, converted as described to mathematical expressions and incorporated into the computer code, assembled cellular and molecular variables in order to generate a hypothetical immune response. Clinical and experimental data showed that the risk of patients dying from sepsis is significantly correlated to the initial dose of pathogen (231). Therefore, we hypothesized that HIR would have a higher likelihood of progressing to septic shock and death if the infection was initially high. To test this hypothesis, we ran our simulations using *Salmonella* doses of 200 counts, 600 counts, 800 counts, and 1200 counts, and we ran 100 replications for each proposed *Salmonella* dose. Results from these simulations were initially generated to identify dynamic patterns of indicators in HIR with various initial *Salmonella* doses, as shown in Figure 6.4.



Figure 6.4 Response of different variables (agents) over the first 24 hrs after Salmonella infection (load) of 200 counts, 600 counts, 800 counts, and 1200 counts. Mean counts of indicators were measured at each of time points of simulation (replications =100)



We observed that *Salmonella* counts, phagocytic cell (*MDMI* and *MDMII*) counts, and inflammatory cytokine (*TNF- $\alpha$* , *HMGB-1* and *IL-10*) counts increased as *Salmonella* infection (load) increased. Specifically, the number of phagocytic cells and the concentration of inflammatory cytokines significantly increased (based on one-way ANOVA tests with significance level  $\alpha = 0.05$  and  $P < 0.05$ ) when *Salmonella* infection (load) increased from 800 counts to 1200 counts. A significant decrease (based on one-way ANOVA tests with significance level  $\alpha = 0.05$  and  $P < 0.05$ ) in hepatocyte counts was also observed when *Salmonella* infection (load) increased from 800 counts to 1200 counts. The dose-response hypothesis test initially indicated that the HIR was correlated to *Salmonella* infection, which was consistent with experimental data (231).

#### **6.4.3 Dynamic patterns of HIR resulting from *Salmonella* infection**

We found four identifiable patterns in simulated HIR, as shown in Figures 6.5, 6.7, 6.9, and 6.11, respectively. Corresponding changes in the interface of Netlogo simulation were captured and are shown in Figures 6.6, 6.8, 6.10, and 6.12.

When the initial infection with *Salmonella* was 200 counts, the number of *Hepatocyte Debris* and *CRP* increased for the first 18 hrs of simulation but then progressively decreased to 0, demonstrating no additional pathology at later stages of the simulation. The *Salmonella* counts, *Activated Neutrophil*, *NET*, *TNF- $\alpha$* , *HMGB-1*, *MDMI*, and *MDMII* levels in the simulation sharply increased at the beginning of the infection but progressively decreased as the infection progressed. We inferred that this combination of variables is similar to a host curing an infection, so we referred to it as a healing process (Figure 6.5). We detected that a small number of hepatocytes (less than 0.3% of total hepatocyte counts) were damaged at simulation step 15 (Figure 6.5: Hepatocyte Count). We also found that only a few neutrophils and monocytes (less

than 200 cell counts) were activated when the initial *Salmonella* infection was 200. Ultimately, damaged hepatocytes were replaced with new (healthy) hepatocytes as the simulation proceeded (Figure 6.6).

**Figure 6.5 Healing response after *Salmonella* infection (load) of 200. (Mean counts  $\pm$  SE) of indicators were measured at each of time points of simulation (replications = 100)**

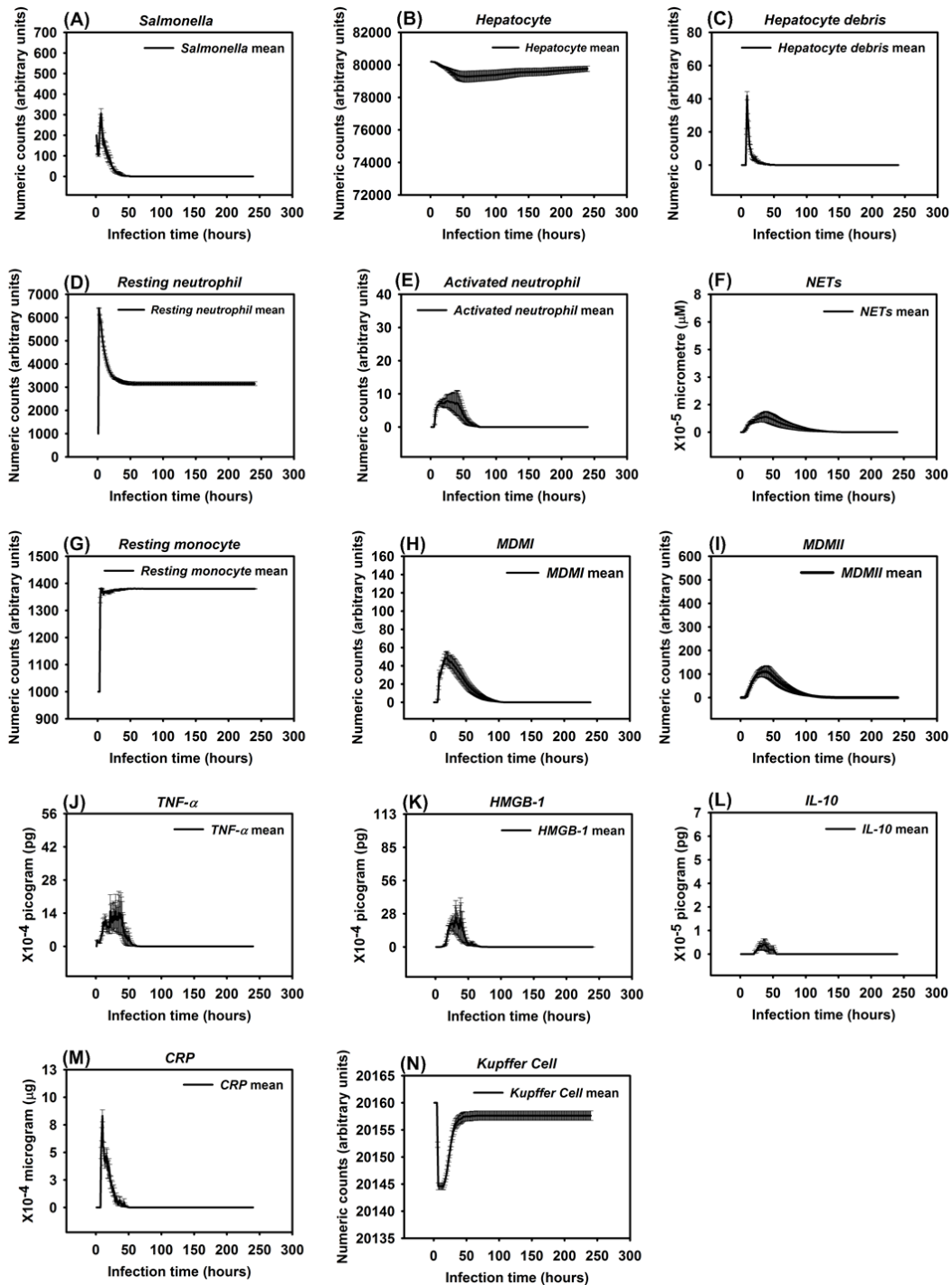
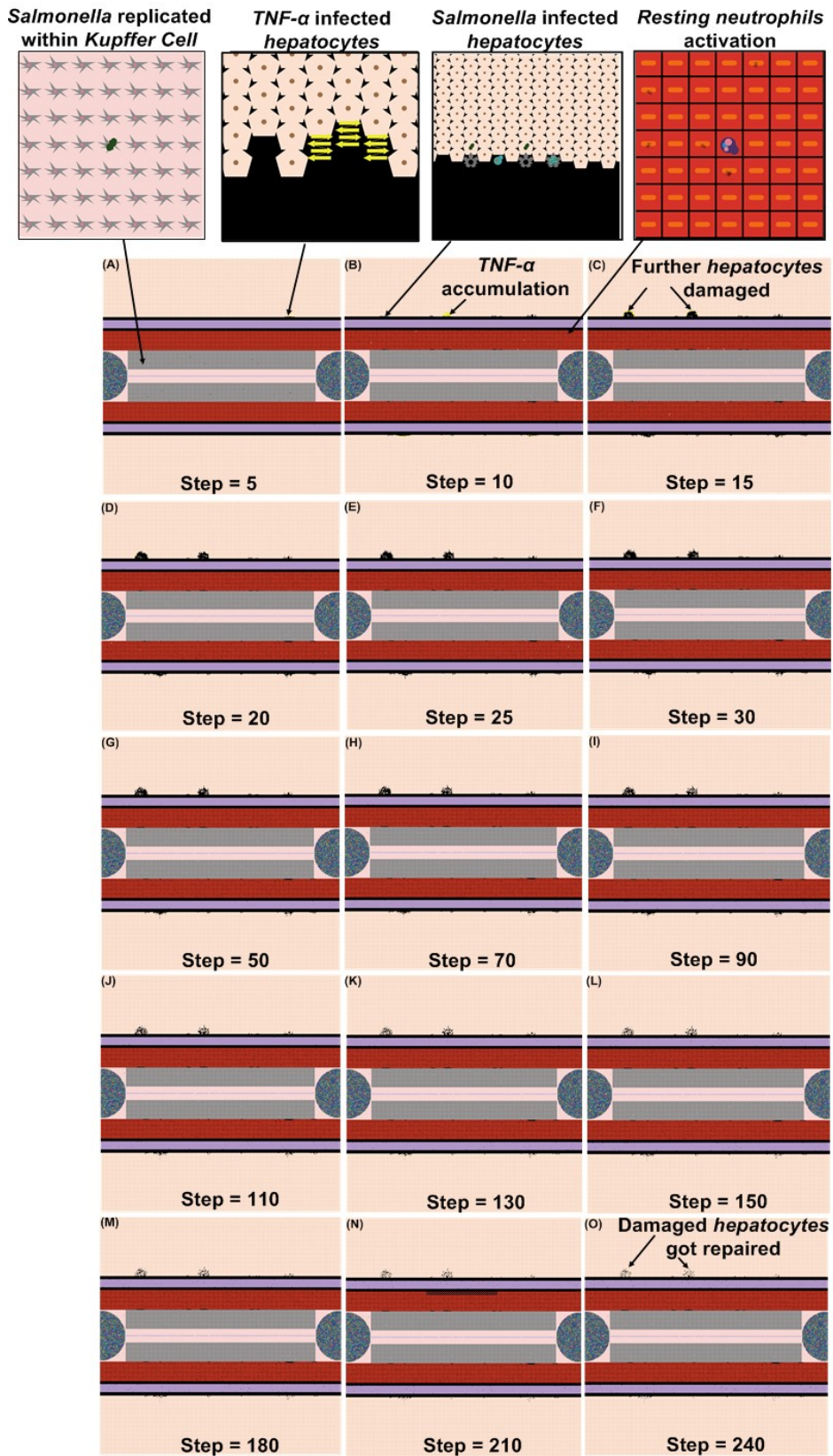


**Figure 6.6 Examples of the Netlogo interface at selected time points (5-240 hrs) after infection with 200 *Salmonella*. Note: 1 step is equivalent to 1 hr. post infection**



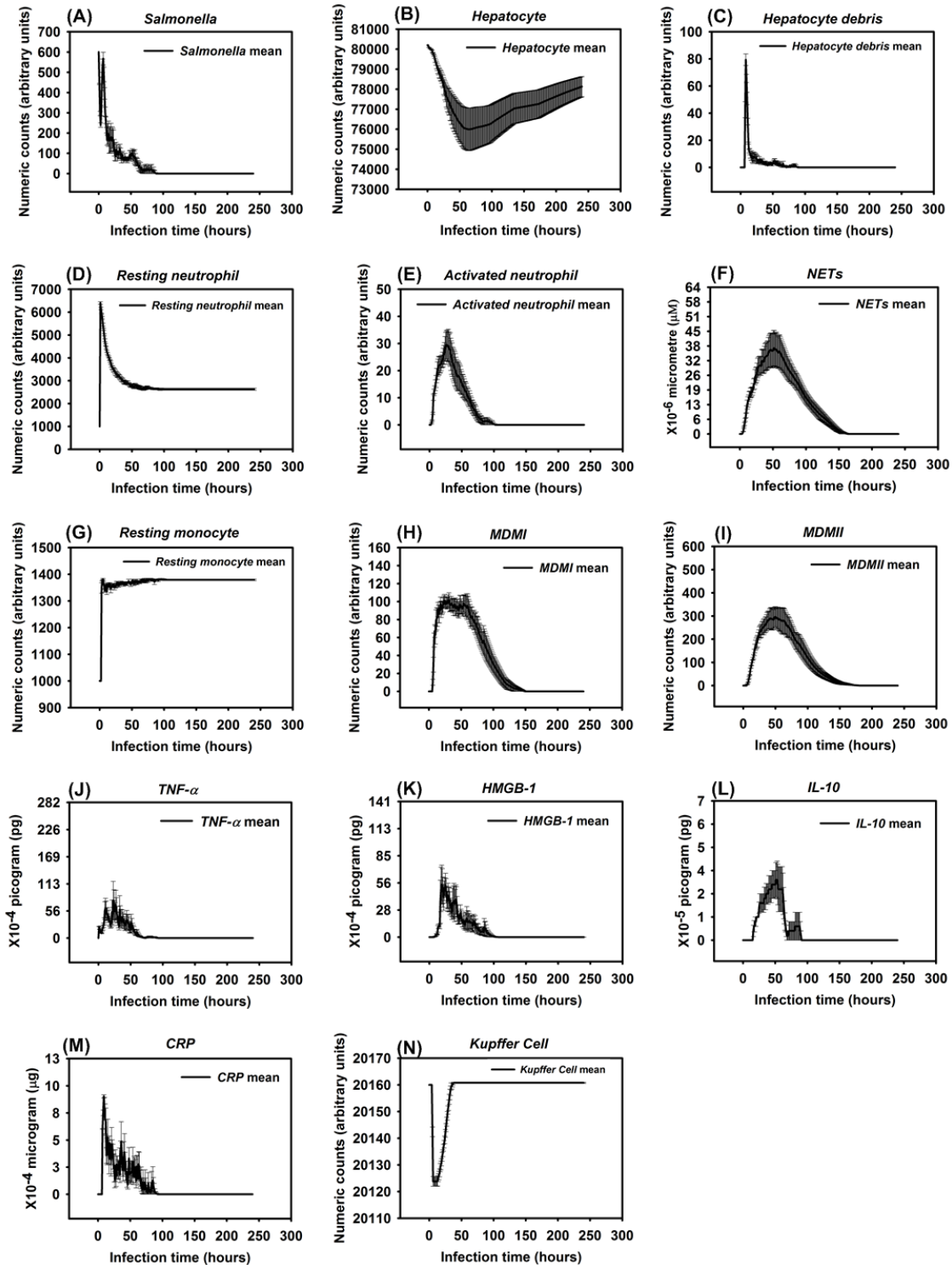
Experimental studies in mice have shown early expression of pro-inflammatory cytokines in response to *Salmonella* infection (13). A comparison of the peak level of *HMGB-1* to the peak level of *TNF- $\alpha$*  reveals that the peak level of *HMGB-1* is lower and that the time required to reach maximum concentrations of *TNF- $\alpha$*  was less than the time required for *HMGB-1* (average of 9 hrs versus 24 hrs post infection) (13, 18, 23). Our simulated results recapitulated this *TNF- $\alpha$*  and *HMGB-1* pattern. We found that the peak level of *TNF- $\alpha$*  ranged from  $1.40 \times 10^{-3}$  to  $2.64 \times 10^{-3}$  pg. Because we modeled liver dimensions based on the model size ( $200 \times 200$  2-D grid), we assumed that *TNF- $\alpha$*  secretion was proportional to the model size and that intensity of *TNF- $\alpha$*  secretion was proportional to the initial challenge of *Salmonella* dose. Under those two assumptions, this response paralleled *TNF- $\alpha$*  levels (160 to 210 pg) found in a mouse model responding to  $10^7$  CFU *Escherichia coli* (a medium dose) (18, 176). Similarly, the kinetics and amounts of secreted *HMGB-1* correlated with the peak level of an *HMGB-1* response seen in experimental observations if model size was taken into account (23). We observed that the increase in *HMGB-1* levels began later in our model (approximately 16 hrs; Figures 6.4, 6.6, 6.8, and 6.10) compared to production kinetics observed in *in vitro* stimulation assays (23). However, kinetics of our model were consistent with the delayed contribution *HMGB-1* is proposed to have during sepsis (232).

Recruitment of monocytes to the liver rose sharply around 24 hrs after infection in our model, which is consistent to approximately 1 day in an actual experimental system (144). Approximately 50% *Salmonella* decreased within 6 hrs after initiation of HIR (Figure 6.5: *Salmonella* Count), paralleling kinetics previously observed in mice (117). During actual infections, the decrease in bacterial load correlated with the influx of neutrophils (117). We observed a similar trend in the simulation (Figure 6.6). We used *CRP* levels and *Hepatocyte*

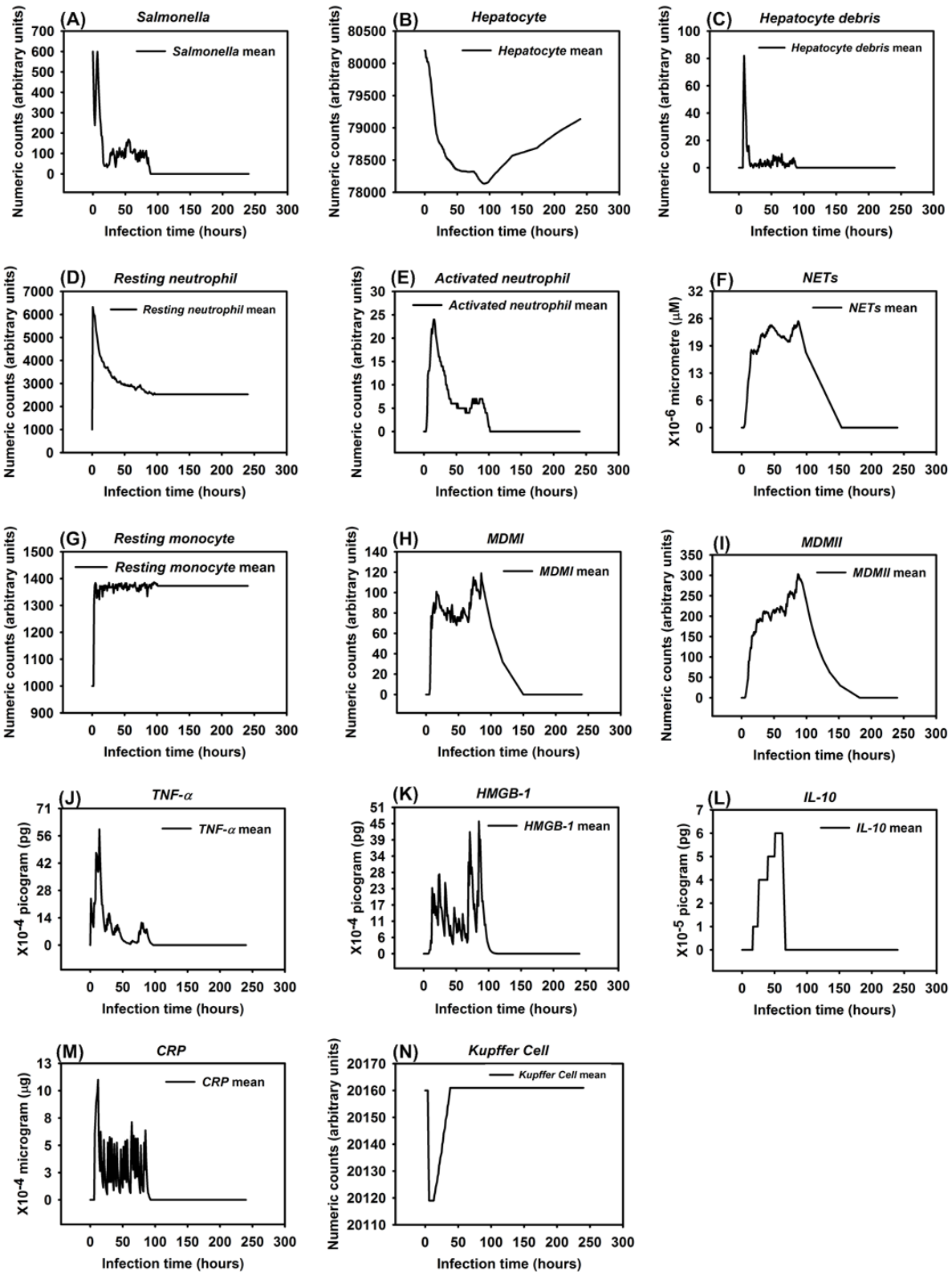
*Debris* to reflect the level of tissue damage that occurred after infection. *CRP* is released by the liver in response to stress, infection, and/or damage (203, 205, 233), and the debris simulates dead and dying hepatocytes. Our simulated results showed that *CRP* rose initially after infection, but *CRP* concentration fell sharply after the infection was cured as part of the “Healing Response”. A similar pattern of *CRP* concentrations was identified in healthy patients infected by bacteria in clinical cases (234).

In some simulation replications, when the initial *Salmonella* infection was 600, the outcome more closely resembled a persistent infection, defined as the state in which *Hepatocyte Debris*, *CRP*, and *Salmonella* levels initially declined but subsequently increased to much higher levels before the infection was resolved at approximately 90 hrs. (Figure 6.7 (b)). Under this condition, *Activated Neutrophil* numbers declined along with the decline in bacterial numbers and *NET* values did not return to baseline for approximately 50 more hrs. We also observed oscillations in levels of cytokine mediators *TNF- $\alpha$*  and *HMGB-1* as the infection was resolved (Figure 6.7 (b)). Moreover, this resolution correlated with oscillating *Salmonella* numbers during the waning 25 to 60 hrs of the infection. Others have observed oscillatory patterns in host responses to other types of bacteria in mouse infections (170). Therefore, we were reassured that the simulation captured the essence of a real infection. The *CRP* pattern during persistent infection (Figure 6.7 (a)) was significantly distinct from the *CRP* pattern observed in the healing response (Figure 6.5). As shown in Figure 6.7 (a), the *CRP* level rose initially after the infection and waxed and waned for another 2 to 3 days. On the 4<sup>th</sup> day after infection, *CRP* levels diminished sharply and damaged hepatocytes began their recovery, similar to the *CRP* pattern reported in a clinical study (234).

**Figure 6.7 (a) Persistent infection after *Salmonella* infection (load) of 600. (Mean counts  $\pm$  SE) of different variables (agents) were measured at each of time points of simulation (replications = 10). (b) Persistent infection after *Salmonella* infection (load) of 600. Counts of different variables (agents) were measured at each of time points of one selected simulation**



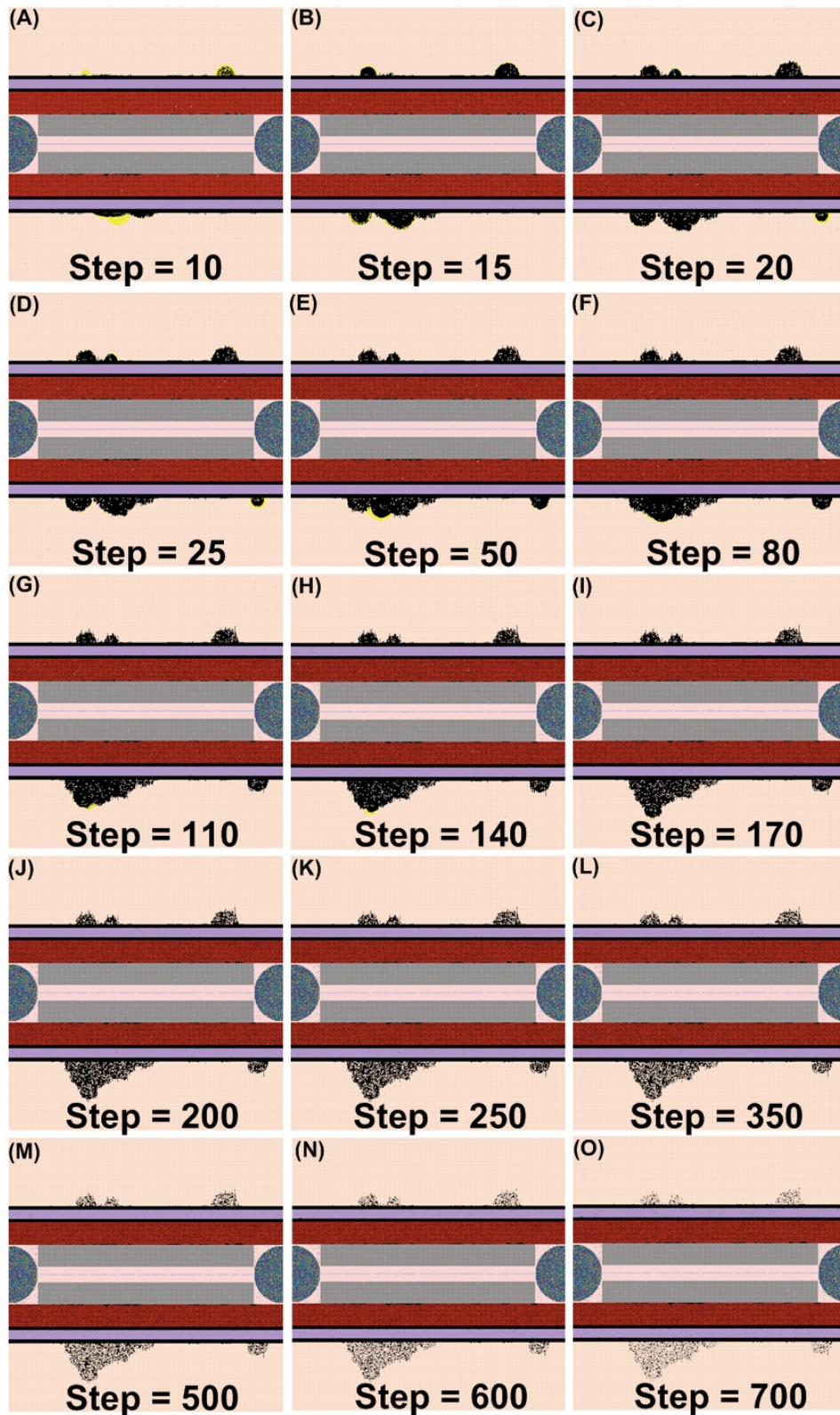
(a)



(b)



Figure 6.8 Examples of the Netlogo interface at selected time points (5-240 hrs) after infection with 600 *Salmonella*. Note: 1 step is equivalent to 1 hr. post infection



Detectable hepatocyte damage began at simulation step 10 (10 hrs post infection), and a significant increase in hepatocyte damage was observed beginning at stimulation step 15 (15 hrs post infection). Hepatocyte damage was persistently observed for 7 days. As the persistent infection proceeded, a large area of hepatocyte damage, which would translate to liver damage in an animal model, was observed (Figure 6.8). Our simulated results paralleled hepatocyte damage seen in vivo after experimental infections where recovery (or “healing”) of hepatocytes was detected after 7 days and continued for approximately 30 days (235). These data are consistent with the idea that a persistent infection will induce a higher mortality rate compared to a healing response because acute tissue damage is more detrimental to the host (Figure 6.7 (a): Hepatocyte Count). Remarkably, we observed that oscillations in agent counts were damped when calculated mean values of the agent counts for simulation replications (Figure 6.7 (a)). The oscillations we observed in a single simulation run (Figure 6.7 (b)) of IMMABM indicate that the individuals with persistent infection could have identifiable oscillated patterns during HIR.

HIR could also result in a pattern we termed as a hyperinflammatory response (Figure 6.9 and Figure 6.10). During this type of response, *Salmonella* counts dropped within the first 24 hrs of HIR (Figure 6.9: *Salmonella* Count). However, a significant elevation in phagocytic cells (Figure 6.9: *Activated Neutrophil* Count, *MDMI* Count, *MDMII* Count) and inflammatory cytokines was observed (Figure 6.9: *TNF- $\alpha$* , *HMGB-1* and *IL-10*) compared to the healing and the persistent infection responses, causing severe hepatocyte damage that could lead to death (Figure 6.9: *Hepatocyte* Count). Interestingly, we observed that the ranges of agent counts in the hyperinflammatory response (Figure 6.9) were more variable compared to the healing and persistent infection responses (Figure 6.5 and Figure 6.7). This made it difficult to accurately predict outcomes in this type of HIR. However, we suggest that when the mean values of *TNF-*

$\alpha$ , *HMGB-1* and *IL-10* exceeded the mean values identified in the hyperinflammatory response (Figure 6.9: *TNF- $\alpha$*  Count, *HMGB-1* Count and *IL-10* Count), this serves as a warning signal of HIR progression to a hypothetical death status as the simulation proceeded. In a few simulation replications, we observed that all the hepatocytes were killed or damaged (*Hepatocyte* count = 0) within the first 48 hrs of infection during HIR characterized as hyperinflammatory (data not shown). These data suggest that a hyperinflammatory response could lead to a higher mortality rate compared to a persistent infection because of the acute and severely damaged hepatocytes observed.

The last pattern of HIR that we observed was characterized by progressively increasing *Salmonella* counts. Under this condition, *Salmonella* and inflammatory cytokines continued to rise as the simulation proceeded. Therefore, we classified the combined pattern of increasing *Salmonella* counts and inflammatory cytokine counts (*TNF- $\alpha$* , *HMGB-1*, and *IL-10*) as “organ dysfunction”, as shown in Figure 6.11 and Figure 6.12. Organ dysfunction appeared to be so problematic because in HIR the liver contained less than 1/4 of the healthy hepatocytes after 24 hrs compared to the number present at the time of the initial infection (Figure 6.11). Specifically, the simulation stopped under the condition that no more healthy hepatocytes existed. We only calibrated the data of organ dysfunction for the first 24 hrs of HIR because healthy hepatocytes died out at 24 hrs of simulation in some replications. According to our simulations, a sign of organ dysfunction might be characterized by continued increases in *Salmonella*, *TNF- $\alpha$*  and, *HMGB-1* counts and continued high levels of CRP. The acute rise and a slow decrease in *CRP* levels observed in our model were consistent with *CRP* concentration patterns identified in patients with septic shock (236). This adds validity to the simulated results from our IMMABM.

**Figure 6.9** Hyperinflammatory response after *Salmonella* infection (load) of 800. (Mean counts  $\pm$  SE) of indicators were measured at each of time points of simulation (replications = 10)

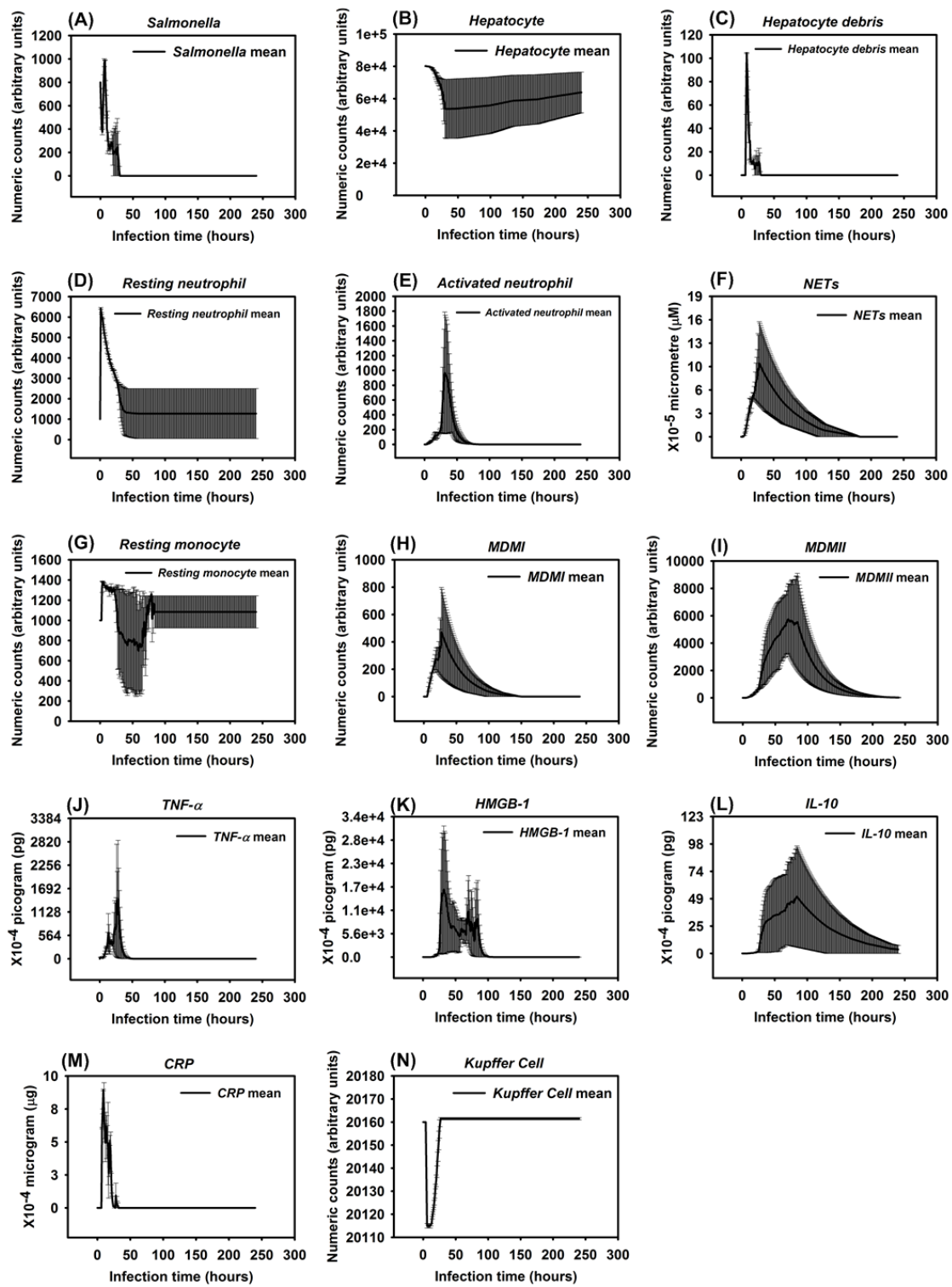
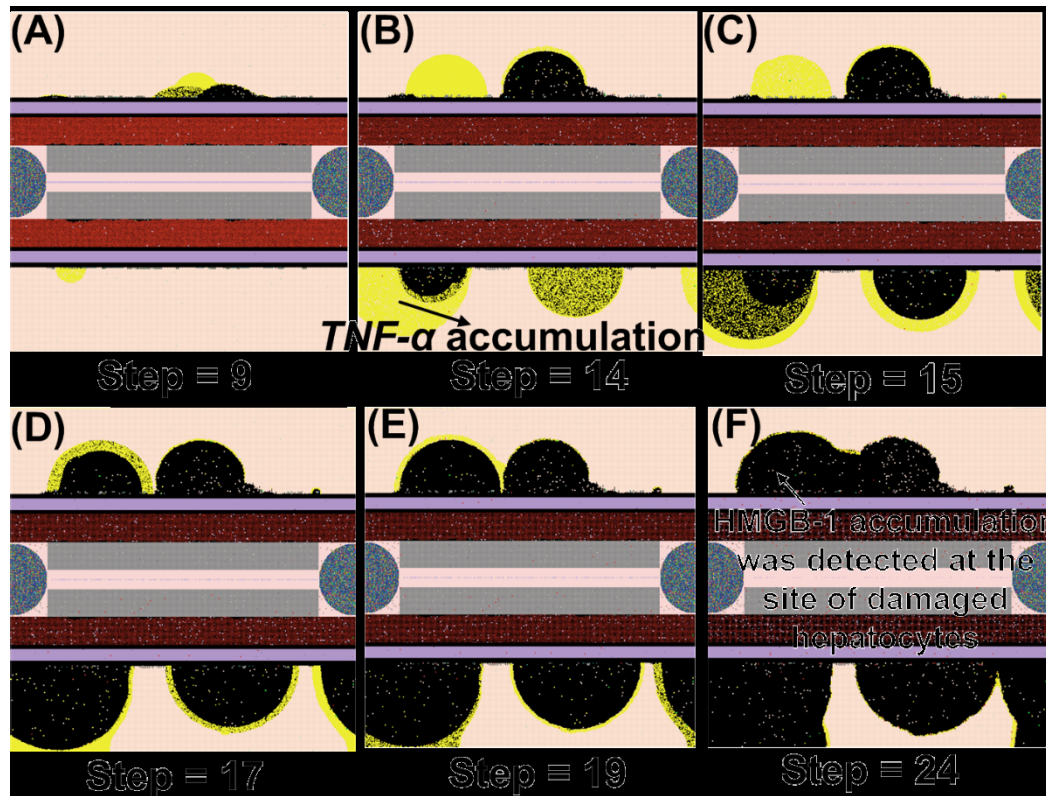


**Figure 6.10** Examples of the Netlogo interface at selected time points (5-240 hrs) after infection with 800 *Salmonella*. Note: 1 step is equivalent to 1 hr. post infection



To conclude, we found that a healing response, where *Salmonella*, other phagocytic cells, and inflammatory cytokines quickly fell below threshold levels, was more likely to occur when the initial *Salmonella* load was low. We identified a persistent infection pattern if inflammatory responses were active (characterized as when *Salmonella* and inflammatory cell levels oscillate during infection). However, if the initial *Salmonella* load was high, a hyperinflammatory response or organ dysfunction was most likely to occur, leading to the death of infected individuals. In addition, when these simulated results were compared to experimental data, the simulations paralleled indicator patterns reported in actual mouse experiments (13, 23, 117, 144, 170, 234, 235). It also became clear that predicting a final outcome from the emerging dynamic patterns of HIR became more difficult when initial *Salmonella* loads were above 500 counts (See Section 6.4.4).

**Figure 6.11 Organ dysfunction after *Salmonella* infection (load) of 1200. (Mean counts  $\pm$  SE) of indicators were measured at each of time points of simulation (replications = 10)**

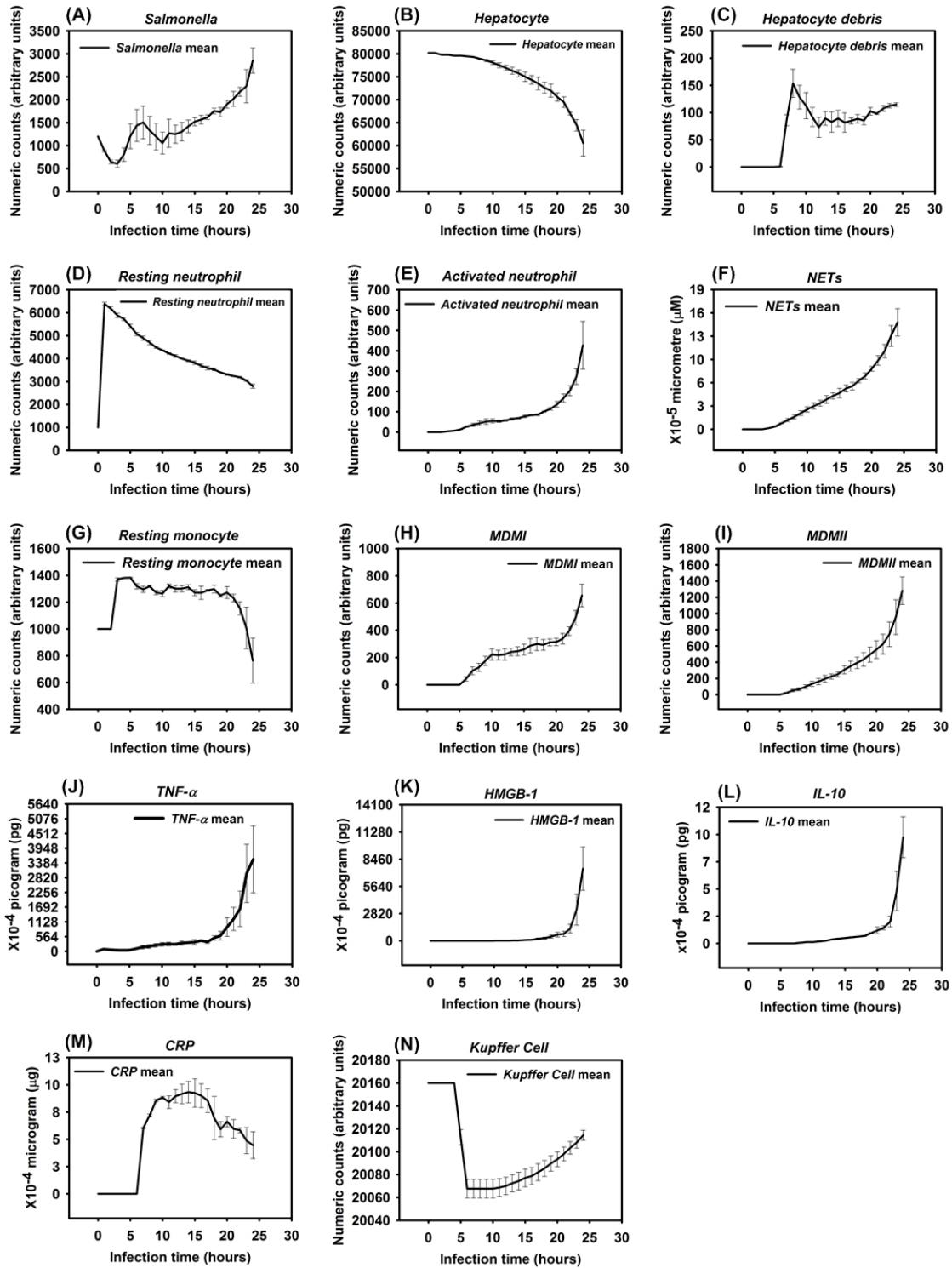
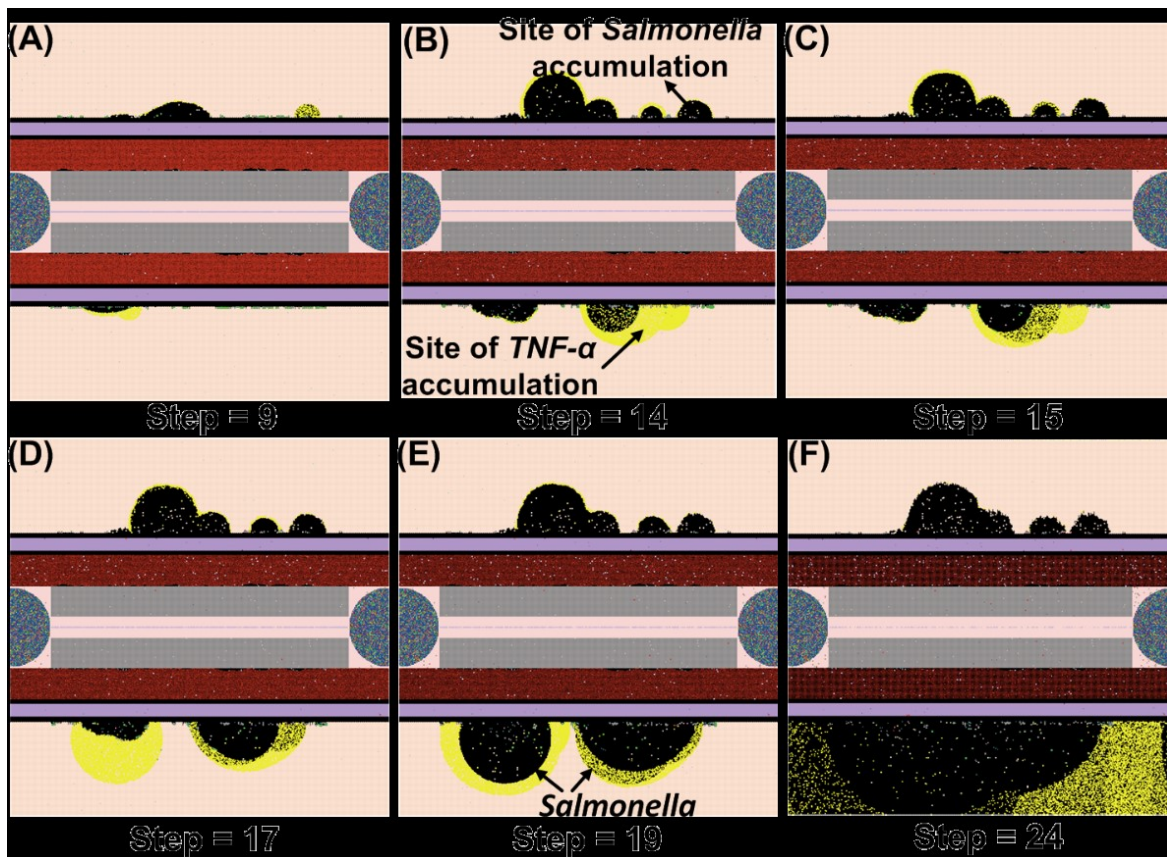


**Figure 6.12** Examples of the Netlogo interface at selected time points (5-240 hrs) after infection with 1200 *Salmonella*. Note: 1 step is equivalent to 1 hr. post infection



#### 6.4.4 Outcome assessment

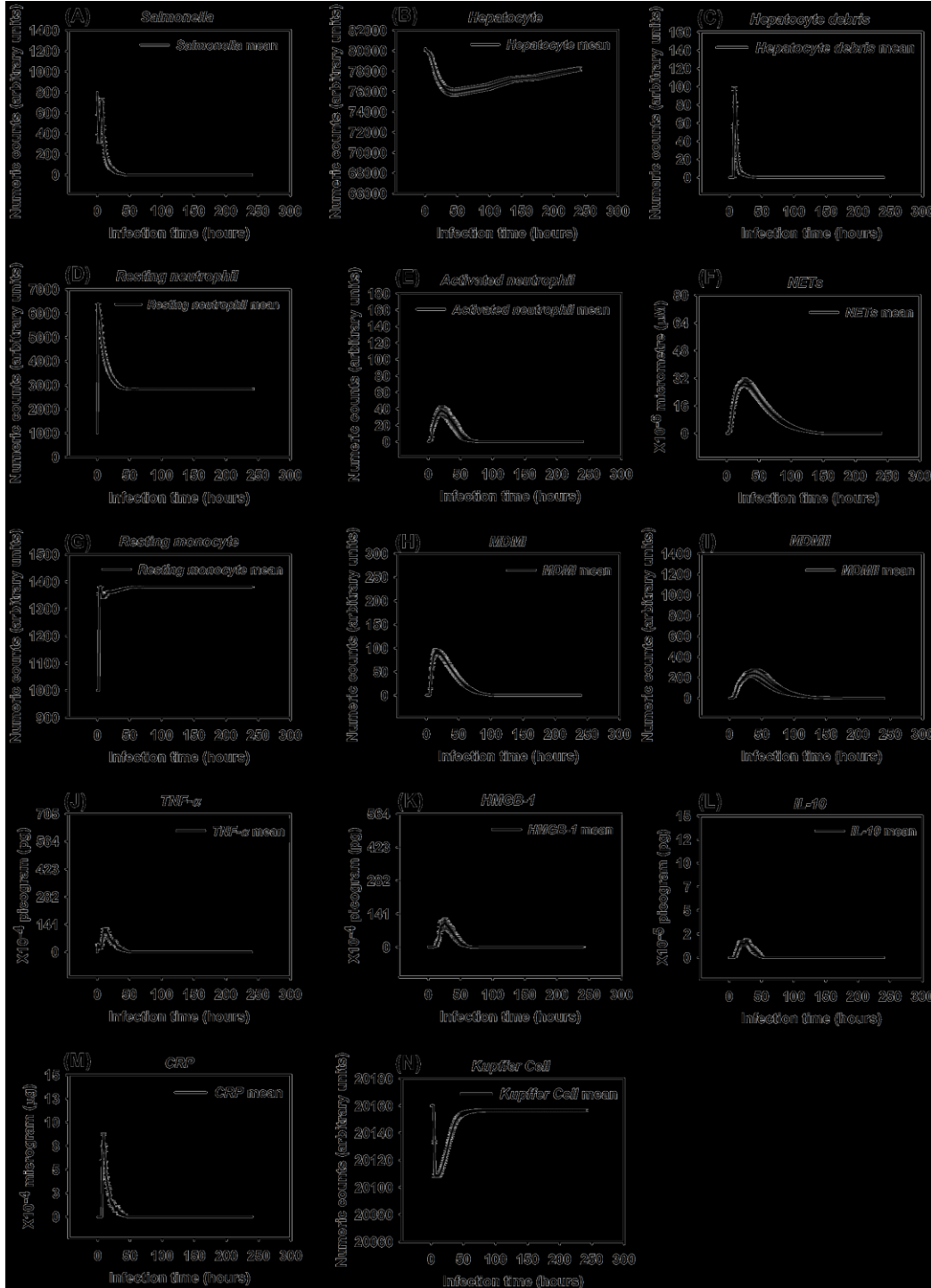
We ran simulations using initial *Salmonella* doses ranging from 100 counts to 1400 counts in increments of 100 counts with 100 replications per dose for a total of 1400 replications in the IMMABM. HIR outcomes clearly skewed toward a healing response at doses less than 500 counts. However, as the initial *Salmonella* doses increased, it became clear that the dynamic patterns of HIR could diverge in the health outcomes (healing response vs. persistent infection vs. hyperinflammatory response vs. organ dysfunction). For example, when the initial *Salmonella* load was 800 counts, all four dynamic patterns of HIR could emerge (Figure 6.13). Nevertheless, when initial *Salmonella* counts were below 500, the healing response was identified over 98% of the time. However, when the initial *Salmonella* count exceeded 1300 counts, only hypothetical

death status (hyperinflammatory response or organ dysfunction) was identified from IMMABM simulation (Figure 6.14). In order to compare potential survival and mortality rates of HIR under various initial *Salmonella* challenge loads, we generated a probability distribution that ended with the healing response, persistent infection, hyperinflammatory response, or organ dysfunction of HIR against various *Salmonella* initial loads (Figure 6.14 and 6.15). The probability of HIR ending in each possible outcome clearly changes as the dose increases from 100 counts to 1400 counts (Figure 6.14).

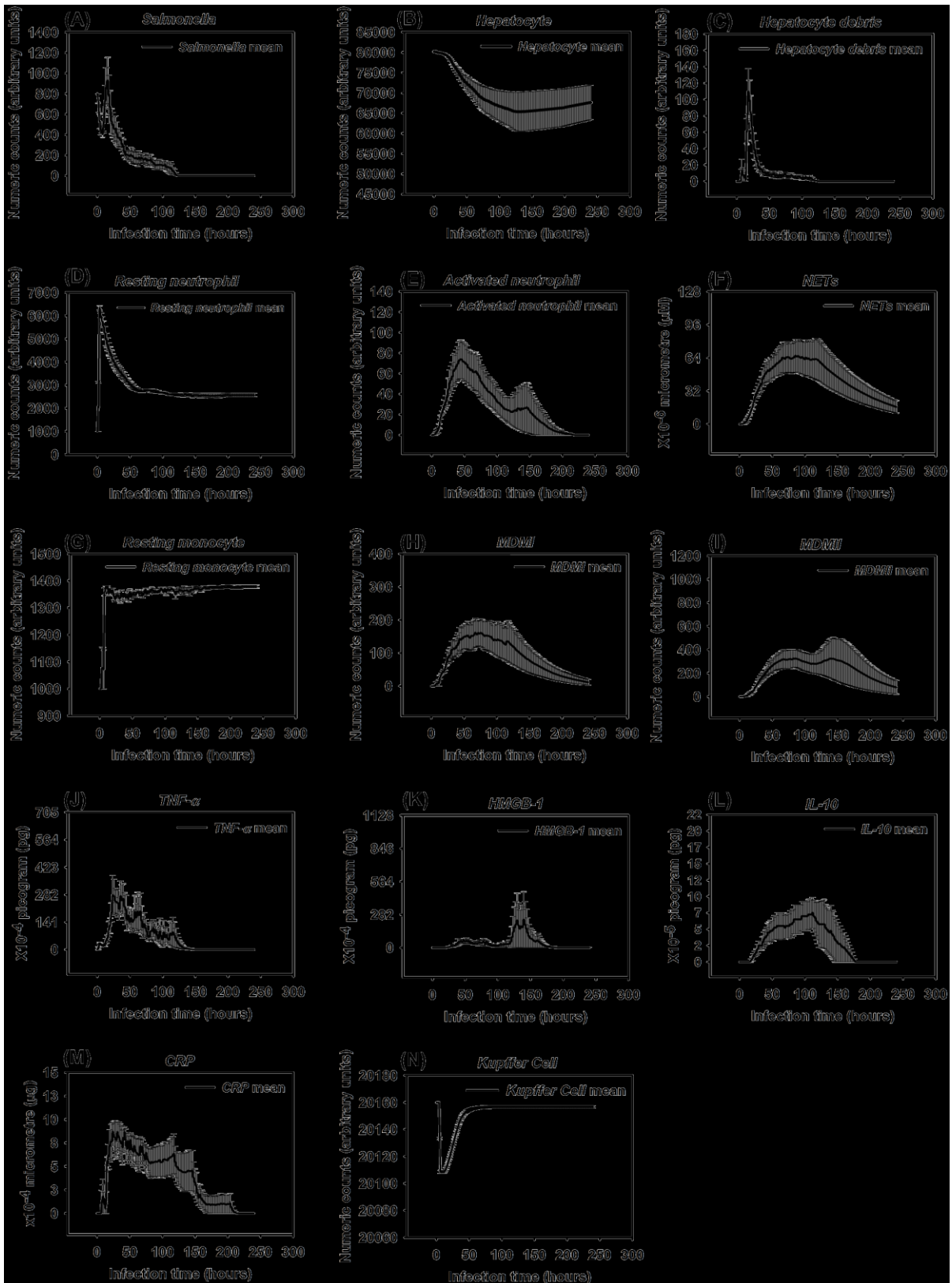
Experimental data and stochastic processes embedded in IMMABM were essential in order to map HIR to a computational simulation because HIR is an inherently stochastic process. Experimental studies proved that cellular and soluble mediator interactions and numerical changes in their levels were dependent on location and time. For example, the *Salmonella* killing rate by one neutrophil can range from 2.94 to 12.94 *Salmonella*/per neutrophil/hr according to a human model (202). The data illustrated in Figure 6.14 suggests that IMMABM was able to capture the stochastic nature of the host response during HIR by showing that interactions among agents and the outcomes of the simulations varied for each run. Consistent with its embedded stochastic nature, the IMMABM allowed us to determine the probability of each possible outcome in individuals, thereby allowing reasonable predictions of HIR outcomes. For example, the simulated results in Figure 6.15 demonstrated as *Salmonella* initial loads increased, the probability increased that HIR would end with hyperinflammatory response or organ dysfunction. In contrast, lower initial challenge doses were more likely to be identified as healing response or persistent infection.



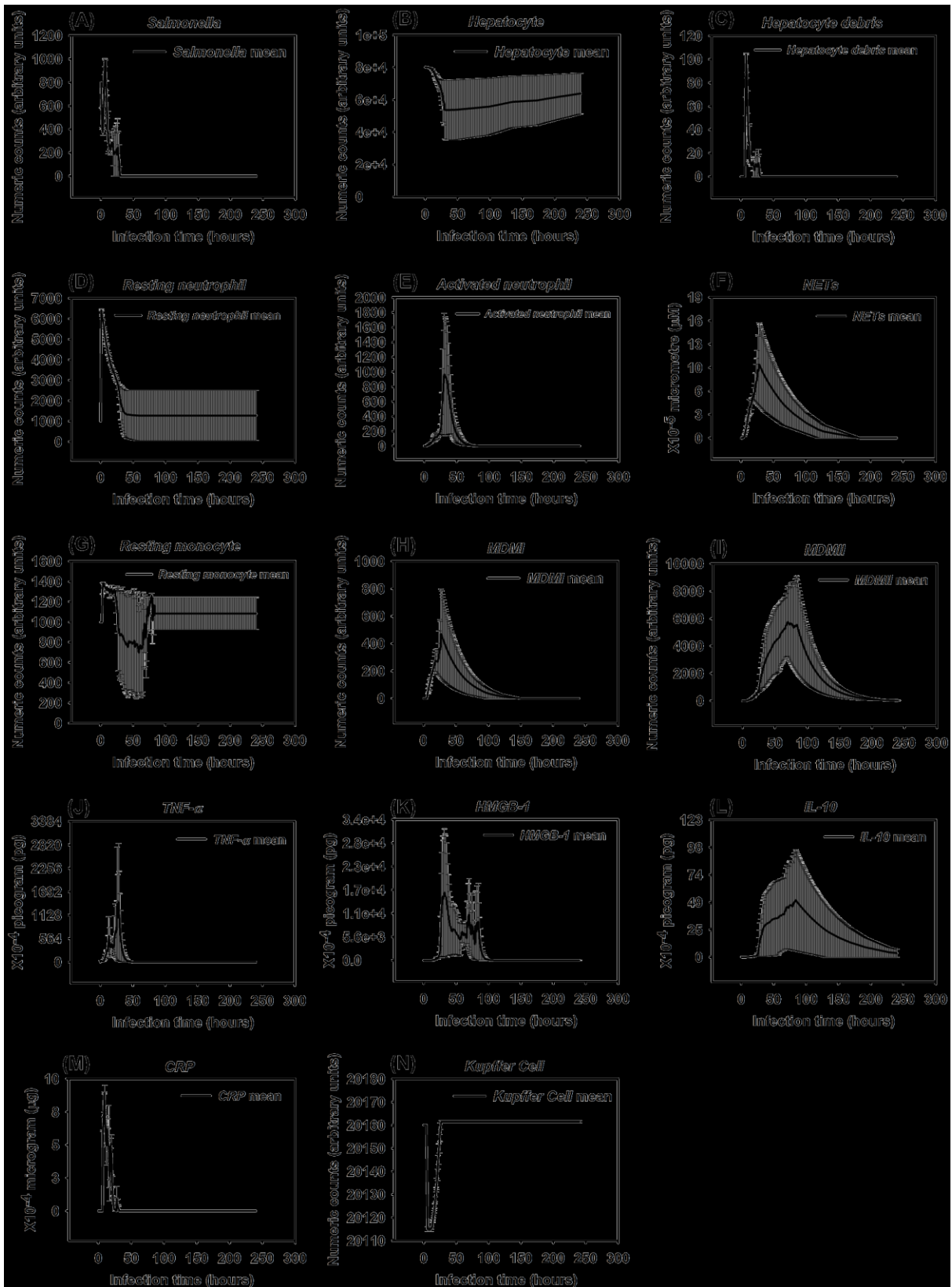
**Figure 6.13** Four distinct patterns observed in IMMAB simulation when Salmonella infection (load) of 800. (Mean counts  $\pm$  SE) of indicators were measured at each of time points of simulation. (a). Observed healing response (replications = 100) (b). Observed persistent infection (replications = 10) (c). Observed hyperinflammatory response. (replications = 10) (d). Observed organ dysfunction. (replications = 10)



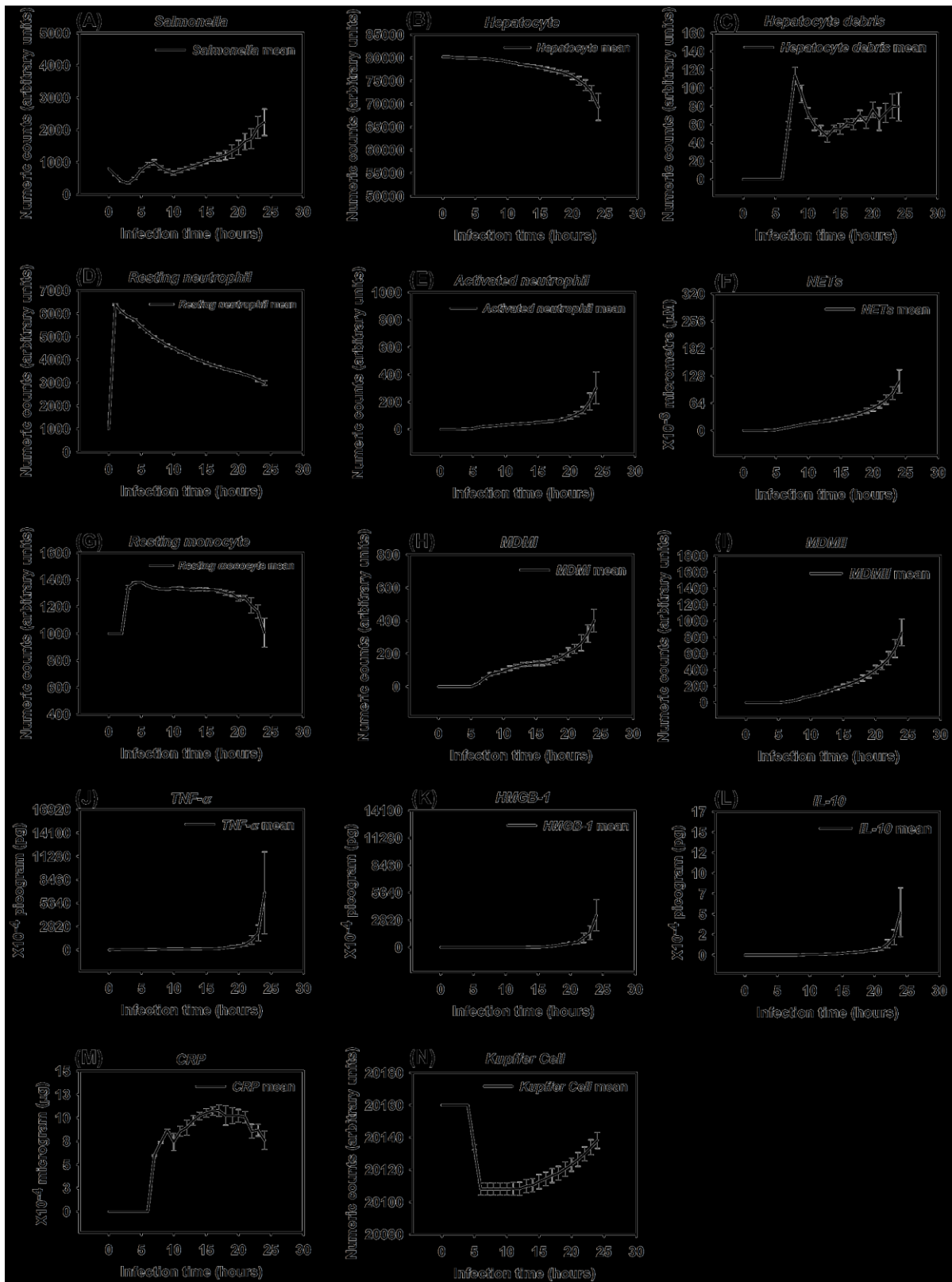
(a)



(b)



(c)



(d)

**Figure 6.14** Probabilities of leading to healing response, persistent infection, hyperinflammatory response, and organ dysfunction in HIR when the Salmonella initial loads ranging from 100 counts to 1400 counts

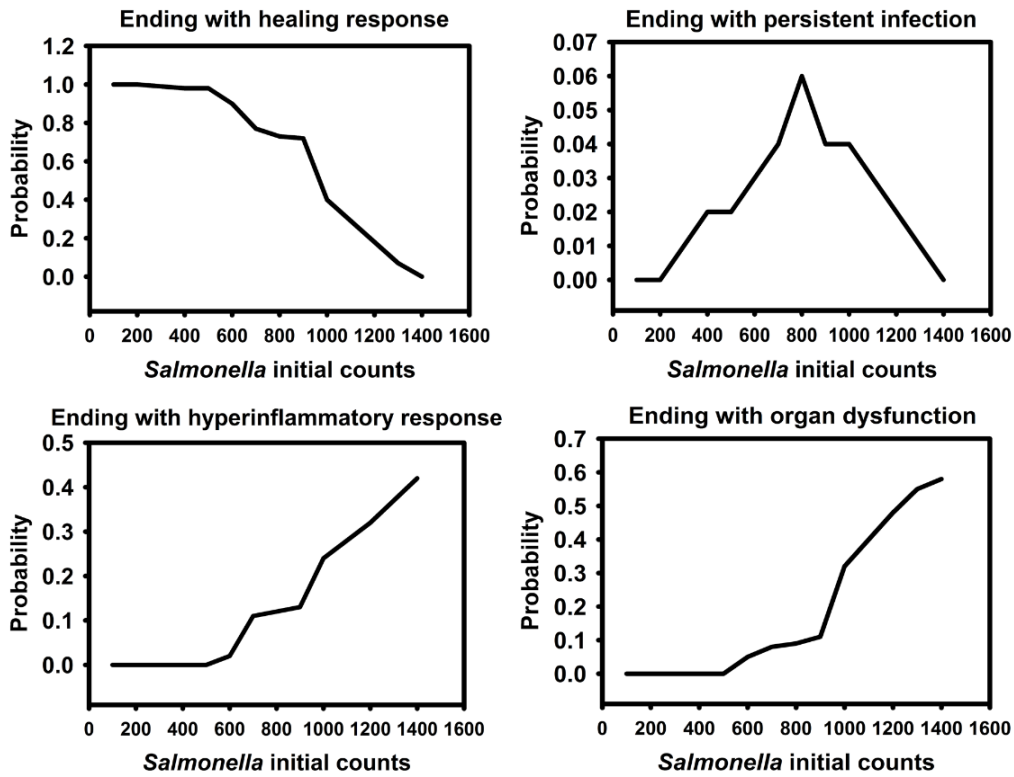
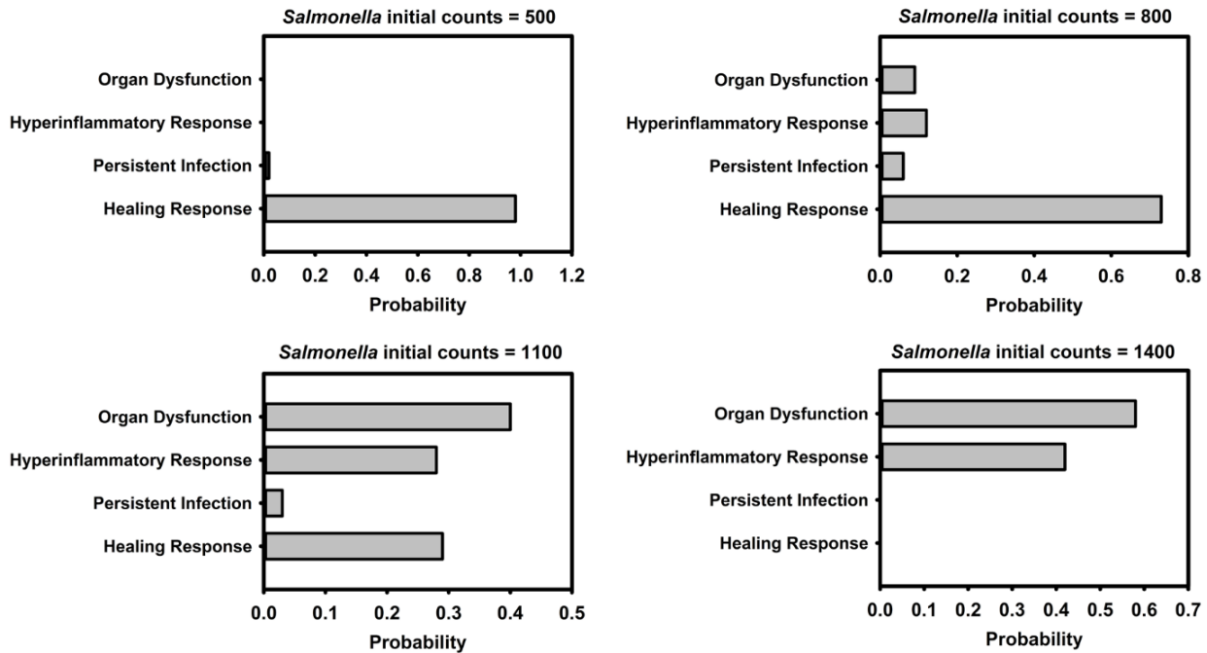


**Figure 6.15** Probabilities of leading to healing response, persistent infection, hyperinflammatory response, and organ dysfunction with the same initial Salmonella load in the HIR

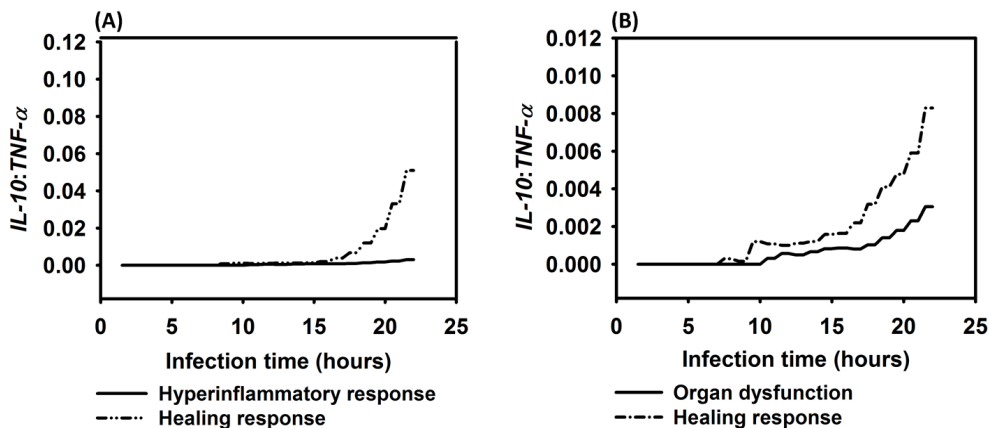


### 6.4.5 Biomarkers of HIR

As described in Section 6.4.2, *HMGB-1* and *CRP* emerged as biomarkers for HIR because their expression patterns closely correlated to HIR outcomes. Our simulated results showed that *CRP* and *HMGB-1* were significantly elevated during hyperinflammatory and organ dysfunction responses compared to the healing response (Figures 6.6 vs. Figures 6.9 and 6.11). Similar to our simulated results, persistent elevation of *HMGB-1* and *CRP* was also observed in experimental studies (22, 236, 237).

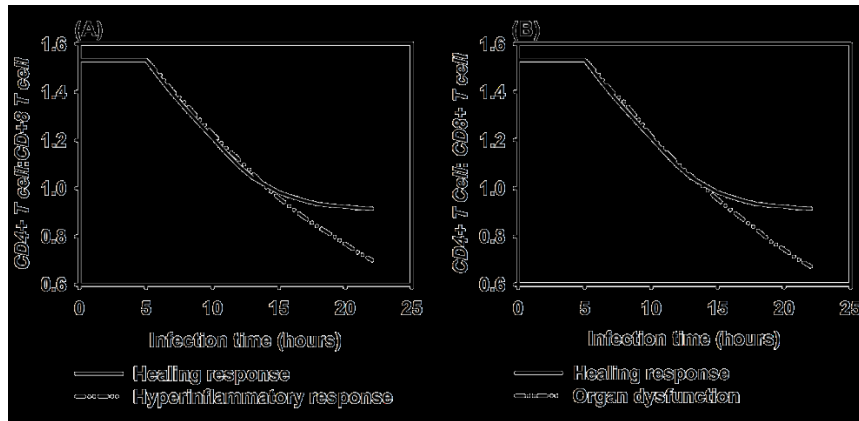
In clinical practice, the *IL-10: TNF- $\alpha$*  ratio is one recommended biomarker used to monitor sepsis progression (238, 239). Therefore, we calculated the average *IL-10: TNF- $\alpha$*  ratio for a healing response, a hyperinflammatory response, and organ dysfunction during infection in 10 simulation runs. Using Mann-Whitney *U* tests, we found that the average *IL-10: TNF- $\alpha$*  ratios in both the hyperinflammatory and organ dysfunction were significantly lower compared to the healing response ( $P = 0.0061$  and  $P = 0.0152$ ) (Figure 6.16). We infer that the *IL-10: TNF- $\alpha$*  ratio in the IMMABM accurately captures that elevated *IL-10: TNF- $\alpha$*  ratio were associated with patients' healing process (12).

**Figure 6.16 Comparison of *IL-10: TNF- $\alpha$*  ratio among healing response, hyperinflammatory response, and organ dysfunction responses against various infection time. Mean values of *IL-10: TNF- $\alpha$*  ratios were measured at each of time points of simulation (replications = 10)**



The  $CD4^+$  T cell:  $CD8^+$  T cell ratio is relatively lower in patients with sepsis, compared to control groups (non-sepsis patients) (240, 241). Simulated results from IMMABM reported that there is a significant lower  $CD4^+$  T cell:  $CD8^+$  T cell ratio when HIR has progressed to hyperinflammatory ( $P = 0.0083$ ) or organ dysfunction responses ( $P = 0.0041$ ) after 15 hrs of infection (Figure 6.17). Therefore, these T cells also appear to be accurately reflected in the IMMABM compared to the clinical studies (240, 241).

**Figure 6.17 Comparison of  $CD4^+$  T Cell:  $CD8^+$  T Cell ratio among healing response, hyperinflammatory response, and organ dysfunction responses against various infection time. Mean values of  $CD4^+$  T cell:  $CD8^+$  T cell ratios were measured at each of time points of simulation (replications = 10)**



Our simulated results showed that the  $MDMII$ :  $MDMI$  ratio was less significantly correlated to the outcomes of HIR as compared to the  $IL-10$ :  $TNF-\alpha$  ratio and the  $CD4^+$  T cell:  $CD8^+$  T cell ratio. During the healing response, the  $MDMII$ :  $MDMI$  ratio was not significantly higher ( $P = 0.2623$ ) than the ratio during hyperinflammatory response but it was significantly elevated ( $P = 0.0019$ ) compared to the ratio in organ dysfunction (Figure 6.18). Although it is clear that  $MDMI$  polarization is common in bacterial infections (242), it is less clear if that kind of polarization is associated with host dysfunctional responses. Therefore, it is possible that our simulated data reflect the *in vivo* ambiguity. Alternatively,  $MDMII$ :  $MDMI$  ratio may not be appropriate in the liver compartment. Refinement of the model will be necessary to help resolve

this. In spite of this, the IMMABM in its current format, has identified some biomarkers that reflect the *in vivo* situation (Table 6.1). This suggest that the IMMABM is beginning to function in a useful manner by paralleling actual host responses.

**Figure 6.18 Comparison of *MDMI:MDMI* ratio among healing response, hyperinflammatory response, and organ dysfunction responses against various infection time. Mean values of *MDMI:MDMI* ratios were measured at each of time points of simulation (replications = 10).**

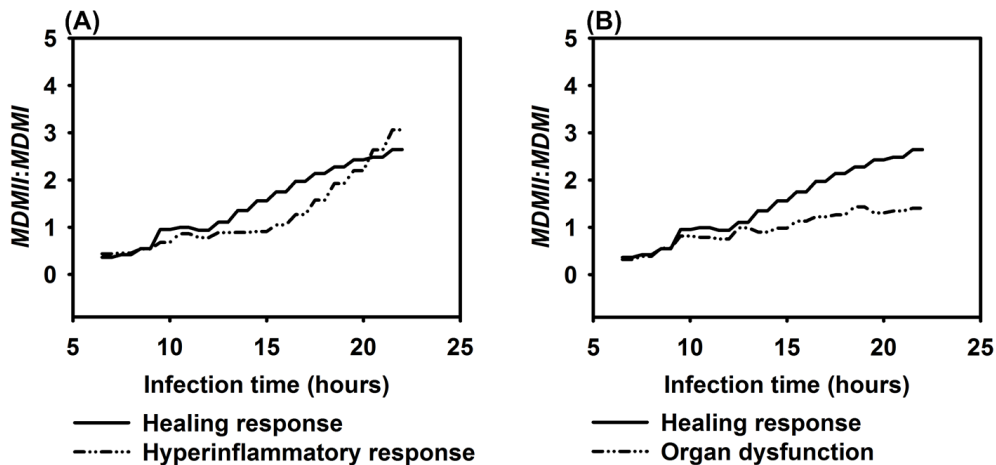


**Table 6.1 Relationship between dynamic patterns of hepatic inflammatory response and dynamic patterns of essential biomarkers in IMMABM**

Dynamic patterns of hepatic inflammatory response	Dynamic patterns of <i>CRP</i>	Dynamic patterns of <i>HMGB-1</i>	<i>IL-10: TNF-<math>\alpha</math></i> (ratio)	<i>CD4+ T cell: CD8+ T cell</i> (ratio)
<b>Healing Response</b>	Sharply increase and smoothly decay	Smoothly decay	Low	High
<b>Persistent Infection</b>	Oscillating decay	Oscillating decay	Medium	High
<b>Hyperinflammatory Response</b>	Sharply increase and smooth decay	Significantly elevated and decay	High	Low
<b>Organ Dysfunction</b>	Sharply increase and slow decay	Significantly elevated	High	Low



## 6.5 Conclusion and discussion

This paper describes a novel IMMABM developed to simulate HIR in a mouse infected with *Salmonella*. The IMMABM described interactions between selected agents as a representation of HIR during *Salmonella* infection and required understanding of key cellular and molecular processes of HIR at the tissue level. Most importantly, the IMMABM was validated through a series of comparisons between simulated results and experimental studies.

Four distinct dynamic patterns (healing response, persistent infection, hyperinflammatory response, and organ dysfunction) were identified during IMMABM simulation. One significant finding from the simulations was that outcomes of HIR were highly correlated to initial *Salmonella* counts. When initial *Salmonella* counts were below 500, hepatic infection had 98% probability to develop into healing response during 100 simulation runs. When initial *Salmonella* counts were between 500 and 1300 counts, outcomes of HIR were uncertain. As initial counts of *Salmonella* increased, HIR had higher probability to end with hyperinflammatory or organ dysfunction responses. Furthermore, *CRP*, *HMGB-1*, *IL-10: TNF- $\alpha$*  ratio, and *CD4+ T cell: CD8+ T cell* ratios emerged as biomarkers during HIR. If *CRP* and *HMGB-1* were persistently elevated, HIR was more likely to end in a hyperinflammatory or organ dysfunction response. If the *IL-10: TNF- $\alpha$*  ratio or *CD4+ T cell: CD8+ T cell* ratio dropped significantly during HIR, a hyperinflammatory or organ dysfunction response would occur.

### 6.5.1 Insights into simulated results

This IMMABM began to capture the essence of adaptive immunity during HIR. T cell activation occurs within 24 hrs of HIR *in vivo* (174). Therefore, we incorporated adaptive immunity, including essential lymphocytes such as  $CD4^+$  and  $CD8^+$  T cells, as well as B cells, into our simulation. We found that incorporation of T cells could be detrimental to hepatic

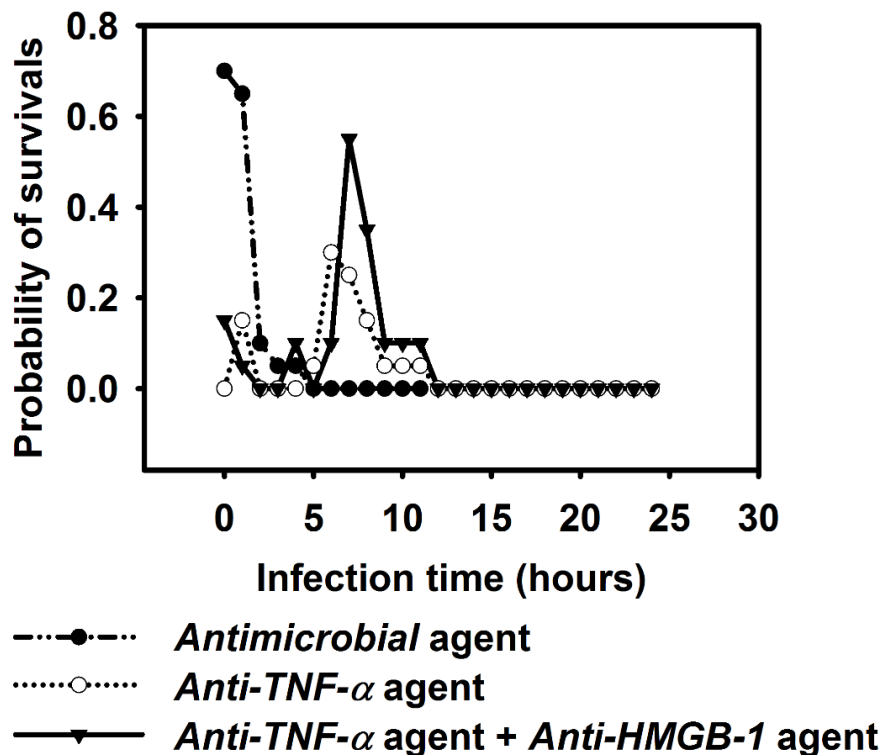
infection because the hyperinflammatory response that we identified in the simulations paralleled observations made in a murine sepsis model (174). In addition, we found that antibodies released during HIR failed to significantly affect organ dysfunction based on the release rate of antibodies and the binding amount of antibody to one *Salmonella* we calibrated (243-245).

It appears that severe hepatocyte damage was mostly caused by a persistent elevation of inflammatory cytokines such as *HMGB-1*. This would indicate that our model is beginning to accurately reflect the biological situations since this parallels the *in vivo* experience (22, 36, 237, 246) where a persistent elevation of *HMGB-1* in patients with severe sepsis and mice with organ damage have high HMGB-1 concentrations.

Strategies for sepsis treatment have been discussed extensively in recent years (2, 29, 32-34, 43, 44, 247), but no general agreement exists regarding efficacy of these strategies. This lack of consensus is due to the complex nature of what causes sepsis to progress, including different clinical and experimental settings, and heterogeneous groups of patients with infections caused by various microorganisms (47). As the IMMABM is constructed now and by future refinements, this tool will allow us to explore various types of treatments to evaluate their possible effectiveness and could help in the design of future preclinical experiments. For example, during IMMABM simulation, we designed an experiment using a hypothetical *antimicrobial* agent (*i.e.* an antibiotic that could kill *Salmonella*), an *anti-TNF- $\alpha$*  agent (*i.e.* an antibody therapy), and a combination of anti-*HMGB-1* agent and anti-*TNF- $\alpha$*  agent. We incorporated these treatments into the IMMABM, and compared the effects of the three hypothetical treatments to the outcomes of HIR. Simulated data showed that the treatment effectiveness was highly correlated with when treatments were started during the simulation in the IMMABM (Fig. 6.19). Specifically, *antimicrobial* agents caused significant improvement in

the survival rates when started during the first hour of HIR. Interestingly, current recommendations are to administer appropriate antibiotics within 1 hour of a diagnosis of severe sepsis or septic shock (43, 44). In contrast, the optimal treatment window for *anti-TNF- $\alpha$*  agents was between 6 hours and 8 hours (Fig 6.19), which may explain why *anti-TNF- $\alpha$*  treatment did not effectively improve survival for patients in some clinical studies (29, 30). The combination of *anti-HMGB-1* and *anti-TNF- $\alpha$*  was more effective in improving the survival rates when treatment was started between 7 hours and 11 hours, compared to using only *anti-TNF- $\alpha$*  (Fig. 6.19).

**Figure 6.19 Assessment of therapy in IMMABM. Hypothetical antimicrobial agents, anti-TNF- $\alpha$  agents, and a combination of anti-TNF- $\alpha$  and anti-HMGB-1 agents were administered to determine their impact in HIR. The “Probability of survival” label represents the probability of HIR ending with a healing response. We assume 1 antimicrobial agent kills 1 CFU Salmonella, 1 anti-TNF- $\alpha$  agent degrades  $2.82 \times 10^{-5}$  pg TNF- $\alpha$ , and 1 anti-HMGB-1 agent degrades  $2.82 \times 10^{-5}$  pg HMGB-1. The administration of the treatment therapies was done one time IMMABM starting at 0 hour to 24 hours (abscissa). 20 simulation replications were conducted for each treatment regimen (1500 simulation replications were conducted for this experiment)**



These findings support contentions that timing of therapy is critical to success (41, 45, 46). Given the consistent outcome between our simulations and existing studies (29, 30, 32, 43, 44), it suggests that our IMMABM is beginning to accurately reflect some aspects of HIR. IMMABM can provide an initial *silico* test for proposed therapeutic agents. Although experimental studies have shown that sepsis in humans is not a model of veterinary sepsis and implementation of an animal sepsis model to human medicine must be further validated (45), IMMABM modeling techniques could be applied to human medicine and the IMMABM can be refined as future human data becomes available in the future.

### ***6.5.2 Model simplification and generalizations***

ABM has been employed to describe complex and nonlinear biological immune processes responding to infection (102). Compared to traditional differential equation models, ABM is more similar to the description and representation of a true biological system because ABM can incorporate stochastic and spatial processes of cell interactions in a host-pathogen system. The IMMABM in this study simulated dynamic patterns of essential indicators in a mouse HIR and captured quantitative changes in dynamic patterns of HIR under various initial levels of *Salmonella*. Furthermore, IMMABM allowed us to simulate distribution of changes in dynamic patterns and provided insights into the probability of those changes.

Although ABMs are advantageous compared to mathematical models (194), they are limited as an “instructive” tool and cannot represent real immune responses in disease progression because they fail in one-to-one mapping of components and processes to biological systems. Since every intermediate biological processes of HIR cannot be simultaneously incorporated into the IMMABM, reasonable assumptions must be made when building an ABM. Moreover, an ABM is built based on simplification of biological responses. For example, in our

IMMABM, we did not model that *Salmonella* replicates within neutrophils even though we know that they are a primary replication site *in vivo* (176). Therefore, this type of *Salmonella* replication could be considered for inclusion in a future model. ABM assumptions can also be more complicated than leaving out some biological responses.

We modeled that *TNF- $\alpha$*  induced apoptosis of hepatocytes because *TNF- $\alpha$*  secretion from activated *Kupffer Cells* induces apoptosis in hepatocytes (15). However, another study showed hepatocyte apoptosis was induced by *TNF- $\alpha$*  only in combination with the transcriptional inhibitor actinomycin D (ActD) (248). Because our model considered a general concept of HIR at the current stage, we modeled that *TNF- $\alpha$*  would induce hepatocyte apoptosis if *TNF- $\alpha$*  were bound to hepatocytes.

Mast cells release many biologically active molecules and chemical substances, such as protease and IL-6, which decrease or increase survival rates of septic patients (249-251). *Salmonella* that bind to mast cells eventually die because of the substances secreted by mast cells. Therefore, in order to simplify our ABM, we considered only some main functions of mast cells during inflammation. For many years, mast cells were believed to phagocytize *Salmonella* (252). However, a recent experiment showed (253) that mast cells bind to *Salmonella*, making them unable to phagocytize *Salmonella*. Therefore, we did not model that mast cells phagocytize *Salmonella*. Instead, we modeled that *Salmonella* binds to mast cells which initiates the release of *TNF- $\alpha$*  from the engaged mast cells.

T cell subpopulations have been reported to express *IL-10* under various conditions (177), making it difficult to estimate *IL-10* production. Because *IL-10* levels released from T cells varies due to the type or concentration of stimuli, we modeled that CD4<sup>+</sup> T cells produce *IL-*

10 and we estimated the average release rate of *IL-10*. We did not differentiate helper T cells to specific types (*e.g.* Th2 or Treg) identified in biological process.

Plasma cells secrete antibody (11), but we did not incorporate this specific B cell population into our ABM. We modeled that B cells released antibody knowing that this does not mimic the real biological system. Likewise, when antibody is released from plasmas cells, T<sub>H</sub> cells define the isotype of the antibody (11). However, we did not model specific antibody isotypes in our model. Furthermore, we ignored the fact that antibody opsonization also induces stimulation of the release of various cytokines and the type of FcR engagement can alter cell function (254, 255). We also did not incorporate that antibody-opsonized *Salmonella* are phagocytized better by neutrophils and macrophages compared to *Salmonella* alone (11).

We did not model natural killer cells in our ABM and we ignored effects of other pro-inflammatory cytokines such as *IL-1*, *IL-12*, and *IL-8*. Also, biological immune responses to infection are recognized as a series of complex processes including intracellular signal transductions (including activation of gene transcription) and intercellular interactions between cells. These biological processes can be developed over time and will evolved as our understanding of these processes becomes more sophisticated (102). Therefore, our IMMABM is still under development and has the potential to incorporate many of the variables that we have left out at the present time.

One final important consideration is that an ABM requires a high level of computational effort in order to simulate the detailed interactions between classes of agents in the HIR. This is particularly true because the ABM is designed to describe the aggregated level of components by simulating individual agent behavior and interactions. These processes are occurring in parallel and require extensive computational effort and high computational efficiency (102). An average

of 18 mins was required to run 300 simulation steps in one replication of IMMABM for a healing and persistent infection response in the IMMABM. The computational time was significantly more for hyperinflammatory or organ dysfunction responses. In those cases, computational efficiency required an average of 10 mins per simulation step (average of 50 hours if run 300 simulation steps, and total 208.3 days (approximation) for 100 replications of simulation). Therefore, one of the factors that limits the number of variables included in an ABM is the computer power available.

## 6.6 Future research

Limitations of current ABMs provide opportunities for future enhancements. A major step forward will include the addition of one or more of the sophisticated cellular and molecular pathways discussed in Section 6.5.

The activation of the coagulation cascade is characteristically seen in patients with sepsis (256). Activated protein C (APC), as an endogenous protein with the ability to modulate coagulation, has currently been approved to be the only pharmacologic therapy in the treatment of severe sepsis (31, 256), highlighting the importance of coagulation and fibrinolysis in sepsis (31). Thus, modeling complement cascades of inflammatory responses and possible progression to coagulation episodes during sepsis would also help the understanding of both inflammation and coagulation and associated therapeutic targets during sepsis progression. An explicit modeling of coagulation cascades such as blood changing from a liquid to a gel needs to incorporate to IMMABM in order to describe hemostasis during sepsis.

Mediator-directed treatments could be incorporated into this IMMABM in order to implement pre-clinical treatment tests *in silico*. Initial *in silico* simulation of IMMABM allowed us to recognize that a combination of anti-TNF- $\alpha$  and anti-HMGB-1 agents could significantly

improve survival rates in HIR. Furthermore, we also observed that the time drugs were administered also impacts HIR outcomes. This not only provides evidence that the core IMMABM is sound, it also provides hope that it can be developed into an effective tool to assist in physicians in their clinical decision-making process.

Current ABMs also require computational resources. For the current  $200 \times 200$  2D grid simulation size, the average simulation implementation time ranged from 10 mins to 2 hrs per replication. Computational time exponentially increased as the number of interactions among agents increased because of the numerous repetitive interactions. Therefore, another future direction of ABM research could be to reduce this computational hurdle by designing new and efficient computational algorithms.



## **Chapter 7 - A novel semi-Markov decision process for clinical decisions related to individuals with sepsis**

Chapter 7 is based on the paper “A Novel Semi-Markov decision process for clinical decisions related to individuals with sepsis” to be submitted to Medical Decision Making.

### **Abstract**

Applications of Markov decision processes (MDPs) to the clinical decision-making process have been widely explored since late 1990s. However, MDP implementation has proven to be challenging because MDPs require a data-intensive estimation step in order to generate reasonable transition models. Therefore, this chapter proposes a novel decision-making framework for clinical decisions that employs generated transition probabilities from agent-based modeling to conventional MDPs, thereby resolving data estimation difficulties of MDPs. A finite-horizon semi-Markov decision process is employed in order to capture the transition time between various states of septic individuals, potentially allowing estimation of changes in infected individuals' states in evolutionary time.

Simulated results of this study demonstrated that the effectiveness of proposed treatment strategies (*antimicrobial* agents, *anti-HMGB-1* agents, or a combination of agents) for septic individuals was correlated to the current states of an infected individual. The conclusion was made that the proposed treatment strategy should be adjusted based on length of required hospitalization. Simulated results also showed that *anti-HMGB-1* agents could negatively impact the treatment of septic individuals and that treatment effectiveness of *anti-HMGB-1* agents was sensitive to the current states of infected individuals.

## 7.1 Introduction

In the absence of analytical decision-making tools, physicians often use heuristic strategies in order to select corresponding patient treatments. Computational and artificial intelligence (AI) techniques are typically applied in order to predict optimal treatments, minimize side effects of drugs, reduce medical errors, and accurately integrate research and practice (55, 56). However, because AI is applicable for clinical decision-making only at single decision points, a decision-making framework is needed in order to extend clinical decision-making from single decision points to a required decision-making time horizon. MDPs have recently become subjects of research interest because they help physicians accurately make difficult clinical decisions on a decision-making time horizon (95, 257, 258). Contemporary health care research has employed MDPs for the purpose of making sequential clinical decisions with multiple objectives. For example, MDPs have been proposed for optimization of sequential treatment strategies in order to improve quality of care in clinics or reduce mortality rates of severe diseases. By implementing MDPs, physicians become aware of rewards or costs associated with a single treatment at specific time epochs. With a calculated probability transition matrix, decision makers (physicians) can predict total reward among various treatment bundles and then be able to recommend optimal treatment strategies.

Compared to MDP applications in domains such as robotics, manufacturing, and inventory control, MDP applications in health care are relatively few (55, 57, 257). This study included review of previous successful applications of MDPs to difficult medical decisions. Lefèvre (259) applied a continuous-time Markov decision model in order to control the spread of infectious disease in a closed population. The model determined optimal strategies that minimized expected discounted costs associated with infected individuals over an infinite

decision horizon. Hu et al. (260) employed a partially observable Markov decision process (POMDP) in order to select appropriate drug infusion plans for anesthesia administration (57). Magni (100) et al. developed an MDP approach that determined optimal intervention time for mild hereditary spherocytosis (HS), a disease identified by chronic destruction of red blood cells. Hauskrecht and Fraser (89) used a POMDP to model and analyze the complex decision process for Ischemic Heart Disease (IHD), and they discussed the advantages of POMDP compared to standard decision formalisms. Alagoz (261) formulated an MDP in order to determine optimal timing of liver transplantation for maximization of patients' quality-adjusted life expectancy. Faissol et al. (262) used an MDP to determine ideal timing for testing and treatment when disease progression is previously unknown. Alterovitz et al. (263) utilized an MDP in order to maximize the probability of image-guided medical needles reaching the desired target. Maillart (264) developed and solved a POMDP in order to evaluate breast cancer screening policies. Shechter et al. (81) presented the first human immunodeficiency virus (HIV) MDP model that addresses the question of optimal time for HIV therapy initiation, with a goal of maximizing the expected lifespan of HIV patients. Denton et al. (265) applied an MDP in order to optimize the start time of statin treatment for cardiovascular risk reduction. Chhatwal et al. (266) proposed an MDP for determination of optimal breast-biopsy decisions for individual patients over a finite decision horizon. Existing MDPs prove that MDPs are valid approaches for clinical decision-making, with potential for development as bedside decision-making tools under certain modeling assumptions.

## 7.2 Background

Sepsis is defined as a systemic inflammatory response syndrome (SIRS) primarily caused by bacterial infection (1). Sepsis accompanied by organ dysfunction, defined as severe sepsis,

can progress with persistently low blood pressure and intravascular coagulation, eventually resulting in septic shock (1). Severe sepsis and septic shock have a mortality rate of approximately 20% to 80% (267); an average of 250,000 deaths per year in the United States (US) are caused by sepsis (4). Sepsis during an infection is a primary cause of death in intensive care settings (3). Among patients in intensive care units (ICUs), sepsis ranks as the second highest cause of mortality (5) and the 10th leading cause of death overall in the United States (6). An average of 750,000 sepsis cases occur annually, and this number continues to increase each year (5). Care of patients with sepsis can cost as much as \$60,000 per patient, resulting in a significant health care burden of nearly \$17 billion annually in the United States (7, 8).

Clinical trials for sepsis treatment have been conducted since 1963, at which time high doses of corticosteroids were shown to be beneficial for infected patients (268). However, subsequent clinical trials failed to show significant benefits for septic patients administered high doses of corticosteroids (269). Tumor necrosis factor-alpha (TNF- $\alpha$ ) is a pro-inflammatory mediator that is released from various types of immune cells in response to an infection (14-20). TNF- $\alpha$  was recognized as a therapeutic target for sepsis because anti-TNF- $\alpha$  agents tested positive in mouse models (27, 270, 271) and two human models with septic shock (33, 34). However, a randomized controlled trial (RCT) failed to identify anti-TNF- $\alpha$  agent effectiveness for improving survival rates for patients with elevated TNF levels upon study entry (29). High-mobility group box 1 protein (HMGB-1), recognized as a late pro-inflammatory mediator, stimulates monocytes to produce TNF- $\alpha$  and other inflammatory proteins (21, 272). Experimental results have shown that inhibition of HMGB-1 production improves survival in experimental models of sepsis (35, 273). Such results make HMGB-1 an especially promising candidate as a target for treatment of septic patients because elevated serum concentration of

HMGB-1 was found in septic patients (22, 41, 237). A recent study discovered that deletion of intracellular HMGB-1 in hepatocytes leads to increased cell death during liver ischemia/reperfusion (I/R) (208). Because inhibition of a single inflammatory component is disappointing in the efficacy of treatment for sepsis, Cross et al. proposed a combination theory in 2003, stating that “A dramatic breakthrough with monotherapy is unlikely. It is now time to test a new paradigm based on an improved understanding of the pathophysiology of the septic process and the recognition that we must step beyond single-agent therapy” (32). Although use of antimicrobials was proposed for sepsis treatment, antimicrobials were found to be insufficient for optimal treatment of patients with sepsis (42). Empiric broad-spectrum antimicrobial agents that target the likely cause of infection have been recommended for immediate initialization for septic treatment (42). A current recommendation is to administer appropriate amount of antimicrobials within 1 hr of severe sepsis or septic shock diagnosis (43, 44). However, identification of the most beneficial time to administer antimicrobials remains unknown because variation in sepsis outcomes has been observed after antimicrobial administration (45).

All evidences have highlighted the need for treatment strategy development for future clinical research. Clinical trials of sepsis treatments have been extensively studied, but only activated protein C (APC) has been approved for treatment of severe sepsis cases (41). Various reasons have contributed to the failure of sepsis treatment in clinical trials. First, monitoring of sepsis development before patient enrollment in clinical trials is difficult, resulting in ineffective use of anti-inflammatory mediators, such as TNF- $\alpha$ , when patients with well-established sepsis enroll. Second, patients with sepsis are highly heterogeneous based on source of infection, site of infection, duration of illness, and current immune status (46); therefore, development of a practical, general treatment strategy suitable for all septic patients is impossible (47). Third,

sepsis development involves numerous biological responses, leading to uncertainty in sepsis progression outcomes. Because clinical trials with single agents have proven to be inadequate and insufficient for sepsis treatment (32), combinations of several agents have been proposed for treatment (32, 46).

### **7.3 Previous MDPs on clinical decision makings for patients with sepsis**

A general application of MDPs to clinical decision-making was reviewed in Section 7.2. This section emphasizes application of MDPs to clinical decision-making for patients with sepsis. In 1998, Rangel-Frausto et al. conducted a 9-month study of 2,527 patients with SIRS (274). Using anti-agent therapy, this study developed Markov modeling in order to predict reduction in organ dysfunction and mortality. On average, the probability of progression from sepsis to severe sepsis was found to be 72%, but with use of an anti-sepsis agent, Markov modeling predicted that the probability of developing severe sepsis would decline to 36%. In 2000, Bäuerle et al. developed a Markov model in order to predict the risk profile of various groups of septic patients in intensive care units (96). In 2007, Kreker proposed a finite-horizon MDP and POMDP that explored hospital discharge strategies for patients with sepsis (97). Kreker used total Sepsis-related Organ Failure Assessment (SOFA) scores to define four patient health states. The MDP suggested that patients in State 1 and State 2 should be discharged from the hospital during the early phase of hospital stays (1 day to 3 days). All other patients (State 3 and State 4) should remain in the hospital for one additional day, compared to the patients in State 1 and State 2. From Days 4 to 6 days of hospital stay, only patients in State 1 (healthiest patients) should be discharged from the hospital; other patients should remain in the hospital for one more day. During Days 7 through 29, all patients, with the exception of the sickest patients (State 4), should be discharged from the hospital. The POMDP model applied the level of a

cytokine in order to define the health states of patients. This POMDP also used a belief variable (probability of a high cytokine level in a cytokine test in accordance with a high level of cytokine the clinician believes prior to the test) to indicate partial observable health-state information of patients. In order to maximize the patient's expected survival in the hospital, the clinician could solve the POMDP and choose to continue patient treatment using standard care without testing, continue patient treatment using standard care and a cytokine test, or discharge the patient from the hospital without testing.

This chapter proposes the first application of a finite-horizon semi-Markov decision process (FHSMDP) in an attempt to address challenges related to current medical decision-making for sepsis treatment. To the best of the author's knowledge, this proposed FHSMDP is also the first application of a finite-horizon semi-Markov decision process (SMDP) to clinical decision-making. In this study, using the developed integrated-mathematical-multi-agent-based model (IMMAB), a probability transition matrix was generated and incorporated into the FHSMDP framework. This novel decision-making framework allows clinicians to optimize a sequence of treatment strategies for infected individuals. Compared to discrete-Markov decision processes, SMDP advantageously calculated the effect of treatments to health states of infected individuals, thereby providing accurate recommendations for treatment strategies. Previous research has indicated that a combination of sepsis treatments could be more effective than a single therapeutic agent during sepsis progression (32, 41, 46). This study tested the effectiveness of a combination of treatments (*antimicrobial* agents and *anti-HMGB-1* agents) for infected individuals and reported the observations in *silico* simulations.

The rest of this chapter is organized as follows. Section 7.4 introduces the model formulation of FHSMDP, and Section 7.5 illustrates the algorithm to solve the FHSMDP. Main

computational results are stated in Section 7.6 and initially compared to clinical studies. Section 7.7 includes the conclusion, and future research is proposed in Section 7.8.

## **7.4 Model Formulation**

### ***7.4.1 Classes of MDPs***

MDPs typically model uncertain dynamic systems and provide decision-making policy for a dynamic system (84). A policy is a set of actions a decision maker chooses in order to optimize (maximize or minimize) a predefined performance criterion (84). MDPs are categorized according to various criteria, including whether the time between decision epochs is continuous or whether a patient's state contains partially observed information. Based on the decision time horizon, each type of MDPs can be further classified as finite or infinite-horizon. Figure 7.1 illustrates the four types of MDPs based on various criteria.

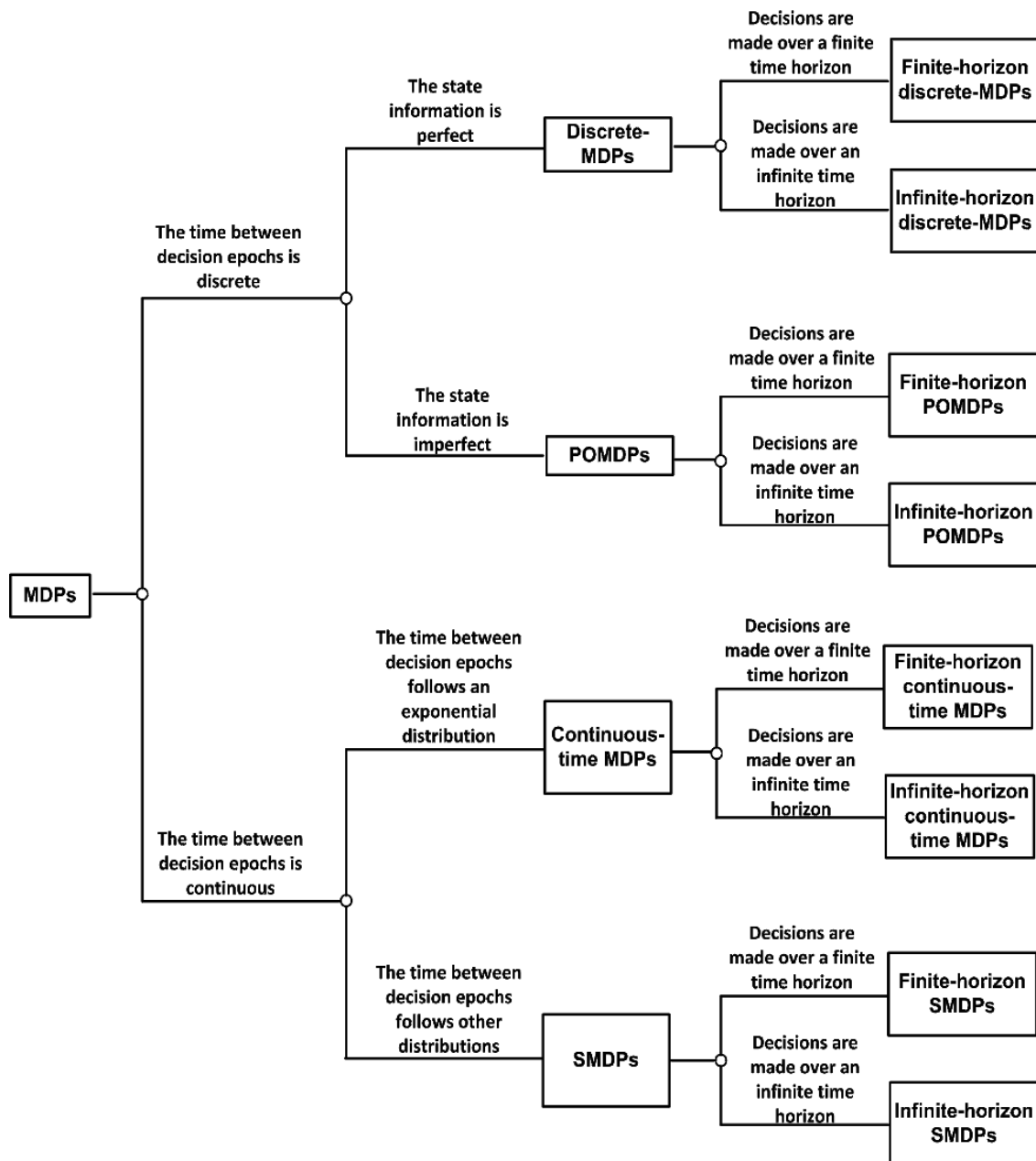
A conventional discrete-time MDP consists of five elements: state, action, transition probability, reward, and decision epoch. Evolution of a typical discrete-time MDP involves several steps. First, the decision maker chooses an action from an action set based on a system's current state when a decision is made. A reward (or a cost) is received when an action is made, and the current state transitions to a new state (or retains the current state) based on a transition probability. The decision maker takes action based on the new state at the time at which the next decision is made. This process continues until the end of the decision time horizon. In MDPs, a decision epoch is a point in time at which a decision is made; decisions are made at discrete time intervals in discrete-time MDPs.

Other types of MDPs can be developed from a discrete-time MDP using various modifications. For example, SMDPs are unique discrete-time MDPs because the time interval



between decision epochs in SMDPs is modeled as a continuous random variable (275). If the random variable follows exponential distribution, an SMDP is regarded as a continuous-time MDP (CTMDP) (84). Sometimes, however, the state of a system is not entirely known or only partially observed by the decision maker, such as uncertainty regarding the underlying disease. This type of MDP with partially observed states is called POMDP.

**Figure 7.1 Classification of MDPs**



POMDPs have been developed for application to clinical decision-making, especially clinical decisions that must be made with unknown patient information (89, 97, 260, 264). Discrete-MDPs and POMDPs must assume that a clinician provides patient treatments at predetermined discrete decision epochs. However, a clinician also must monitor changes in a patient's state and recommend appropriate treatment when the state of the patient changes or a hypothetical death state persists. Compared to a discrete-MDP, an SMDP models a clinical decision-making problem in a more nature way because SMDPs allow clinicians to choose appropriate treatments for patients at randomly selected decision epochs.

#### **7.4.2 Basic elements of SMDP**

In this study, an SMDP was used to develop optimal strategies for treating individuals with sepsis. A patient's state was described as a combination of levels of selected biomarkers during sepsis development. Each selected biomarker had three distinct levels: Low ( $L$ ), Medium ( $M$ ), and High ( $H$ ). A state set ( $S$ ) was comprised of all possible states, and the number of states in a state set was equivalent to the number of biomarkers<sup>3</sup>. A detailed description of a state set is presented in computational results in Appendix C.

Based on the literature review in Section 7.2, *antimicrobial* agents and *anti-HMGB-1* agents were selected as initial therapeutic interventions to treat individuals with sepsis. Computational studies were used to test effects of *antimicrobial* agents on outcomes of septic patients. Effects of a combination of *antimicrobial* agents and *anti-HMGB-1* agents for sepsis treatment were also tested.

The transition probability was formulated as  $p(s_j | s_i, a_{ik})$  to denote the chance of state  $s_i$  transition to state  $s_j$  at the next decision epoch, given that treatment  $a_{ik}$  was chosen at state  $s_i$  (276). Compared to a discrete-time MDP, the probability of time for transiting from state  $s_i$  to

any other states (including state  $s_i$ ) at the next decision epoch within time  $t$  followed a certain distribution function, denoted as  $F(t | s_i, a_{ik}) \cdot Q(s_j | s_i, a_{ik})$ , known as a stochastic kernel in an SMDP, was used to represent the probability of state  $s_i$  transition to state  $s_j$  at the next decision epoch within time  $t$ , given that treatment  $a_{ik}$  was chosen at state  $s_i$ . The stochastic kernel  $Q(s_j | s_i, a_{ik})$  was formulated as follows:

$$Q(t, s_j | s_i, a_{ik}) = F(t | s_i, a_{ik}) P(s_j | s_i, a_{ik}) \quad (7.1)$$

Where,

$$i = 1, \dots, N \text{ and } j = 1, \dots, N \text{ and } k = 1, \dots, M$$

$$N = \text{number of states and } M = \text{number of treatments}$$

Cost in this application was defined as the probability of an infected individual dying from sepsis at state  $s_i$  under treatment  $a_{ik}$ , denoted by  $P(s_i, a_{ik})$ . Cost  $P(s_i, a_{ik})$  measured the risk of an infected individual dying from sepsis, given that treatment  $a_{ik}$  was chosen at state  $s_i$ .

### 7.4.3 Objective function of FHSM DP

The objective of this SMDP was to determine an optimal policy (sequence of treatments) in order to minimize the risk of an infected individual dying from sepsis progression within a certain time window. Because 24 to 51% of patients met severe sepsis criteria within the first 24 hrs of becoming infected (277), the first 24 hrs after hospitalization were considered an initial decision-making time horizon for treating individuals with sepsis. Therefore, the following FHSM DP was formulated to measure accumulated probability of an infected individual dying from sepsis over 24 hrs of hospitalization:

$$V_{n+1}^\pi(s_j, \lambda - t) = P(s_i, a_{ik}) \int_0^\lambda (1 - D(t | s_i, a_{ik})) dt + \sum_{s_j \in S} \int_0^\lambda Q(t, s_j | s_i, a_{ik}) V_n^\pi(s_i, \lambda) \quad (7.2)$$

$$D(t | s_i, a_{ik}) = \sum_{s_j \in S} Q(t, s_j | s_i, a_{ik}), \quad t \in R^+ \quad (7.3)$$

$D(t | s_i, a_{ik})$  in Equation (7.3) represents the probability of an infected individual remains at state  $s_i$  (NOT transition to other states) within time  $t$ , given that an infected individual received a treatment  $a_{ik}$  at state  $s_i$ . The first term,  $P(s_i, a_{ik}) \int_0^\lambda (1 - D(t | s_i, a_{ik})) dt$ , in Equation (7.2) describes the accumulated probability of an infected individual dying from sepsis between the decision epoch  $n$  and the decision epoch  $(n+1)$ , given that the infected individuals stays at state  $s_i$ .  $P(s_i, a_{ik})$  is a cost function to measure the risk of death (probability) for a patient when the patient stays at state  $s_i$  and receive treatment  $a_{ik}$ . The second term,  $\sum_{s_j \in S} \int_0^\lambda Q(t, s_j | s_i, a_{ik}) V_n^\pi(s_i, \lambda)$ , in equation (7.2) calculates the accumulated probability of an infected individual dying from sepsis between the decision epoch  $n$  and the decision epoch  $(n+1)$ , given that the infected individual transits to other states ( $s_j$ ), where  $Q(t, s_j | s_i, a_{ik})$  is a stochastic kernel.  $V_{n+1}^\pi(s_j, \lambda - t)$  is a value function (accumulated risk of death for a patient at state  $s_i$ ), with the left decision-making horizon equal to  $\lambda - t$  (the patient could stay in the hospital for  $(\lambda - t)$  hours).  $\lambda$  is a continuous variable between 0 and 24 hrs.

#### 7.4.4 FHSMDP data sources

Input data to FHSMDP were estimated using IMMABM, a platform developed to simulate *Salmonella* infection in a mouse liver. Based on data over 200 reports and reviews, this IMMABM describes interactions between 23 agents in order to simulate a mouse's hepatic inflammatory response (HIR) in *silico*. By integrating experimental data and mathematical expressions derived from hypothesized kinetics, an attempt was made to quantitatively simulate dynamic patterns of an HIR in IMMABM.

By specifying the infected species, source of infection, and site of infection, the scope of the IMMABM allowed improvement of modeling approach accuracy without loss of generality. Furthermore, IMMABM allows clinicians to observe sepsis development and capture stochastic processes involved in inflammatory responses to an infection. Figure 7.2 and Figure 7.3 shows hypothetical death states (hyperinflammatory response and organ dysfunction) simulated by IMMABM using Netlogo, a software platform employed to conduct IMMABM simulations (73).

**Figure 7.2 Netlogo interface at selected time points (5 - 240 hrs) with hyperinflammatory response**

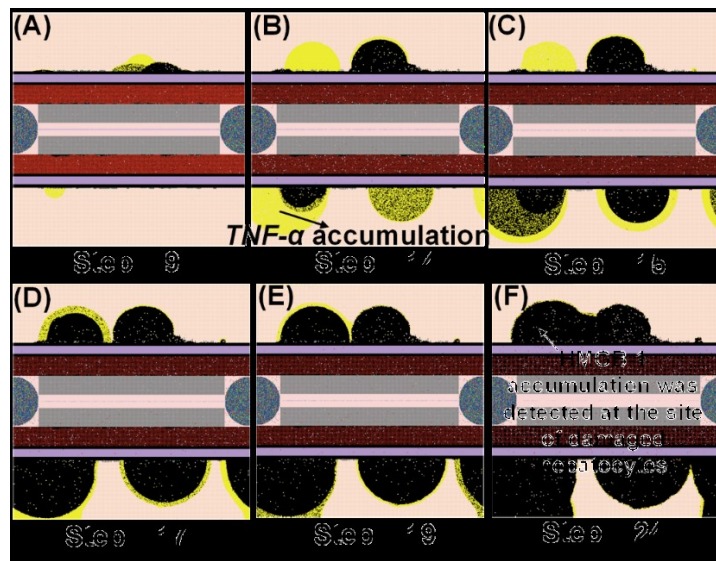
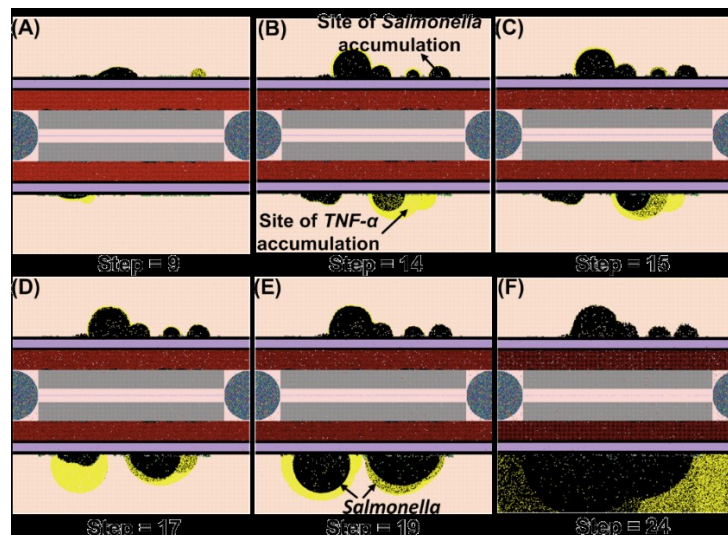


**Figure 7.3 Netlogo interface at selected time points (5 - 240 hrs) with organ dysfunction**



Stochastic kernels and cost functions of the FHSMDP were calculated using IMMABM, but those calculations were based on a veterinary model. Therefore, treatment strategies developed from FHSMDP failed to directly apply to human patients in clinics. However, this FHSMDP framework can be applied for development of treatment strategies for septic patients once human data are available for incorporation into IMMABM.

## 7.5 Solving the FHSMDP

The value iteration algorithm presented in Huang is the basis for solving FHSMDP (278).

The implementation process of a value iteration algorithm is summarized as follows:

- Initialization

When  $k=0$ ,

let  $V_0^*(s_i, \lambda) = 0$  for every  $(s_i, \lambda) \in S \times [0, T]$ ,  $T$  is a planning decision horizon

- Iteration

Compute using the following iterative equation:

$$V_{k+1}^\pi(s_i, \lambda) = P(s_i, a_{ik}) \int_0^\lambda (1 - D(t | s_i, a_{ik})) dt + \sum_{s_j \in S} \int_0^\lambda Q(t, s_j | s_i, a_{ik}) V_k^\pi(s_j, \lambda - t) \quad (7.4)$$

$$D(t | s_i, a_{ik}) = \sum_{s_j \in S} Q(t, s_j | s_i, a_{ik}), \quad t \in R^+$$

- Optimal stopping

If,

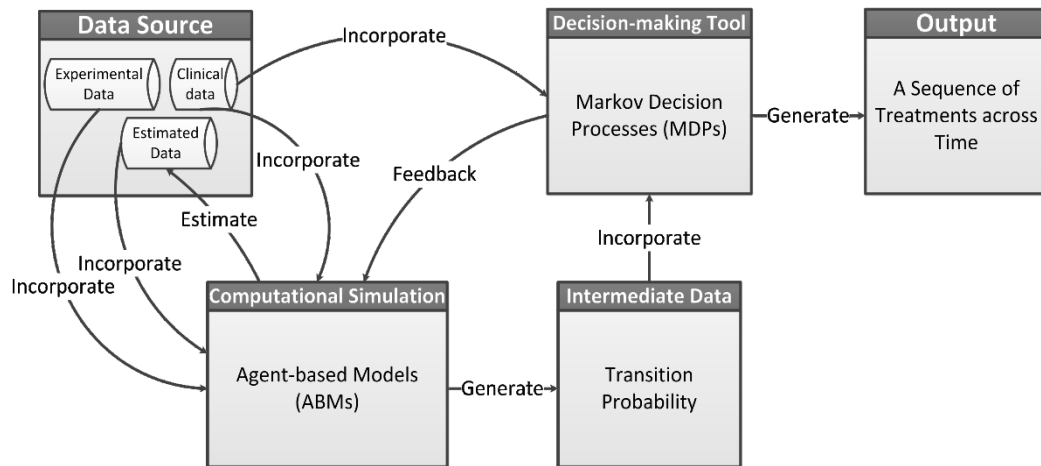
$V_{k+1}^*(s_i, \lambda) - V_k^*(s_i, \lambda) \leq \varepsilon$  for every  $(s_i, \lambda) \in S \times [0, T]$ ,  $T$  is planning decision horizon

Stop. Otherwise, go to Iteration.  $\varepsilon$  is an extreme small number.

In this study, IMMABM was used to propose a novel framework in order to solve FHSMDPs. This framework, broadly structured based on integration of computational simulation driven by real data and analytic decision-making tools, can be applied to general clinical

decision-making. A flow diagram of the proposed framework is shown in Figure 7.4, in which data are summarized (collected) from experimental studies (clinical data).

**Figure 7.4 Proposed decision-making framework**



Unknown data can be estimated in an agent-based model (ABM) through a series of *silico* simulations. By incorporating those data to the ABM, clinicians or physicians can observe and predict changes in a patient’s state as an initial step for development of a treatment strategy.

An ABM can also generate input data to an MDP. Based on generated input data such as transition probabilities, the MDP develops a sequence of treatments for patients. Developed strategies from MDPs can be further validated by the ABM in *silico* through a feedback loop. The ABM and MDP are adjustable based on clinical decision-makings on specific diseases.

## 7.6 Computational results

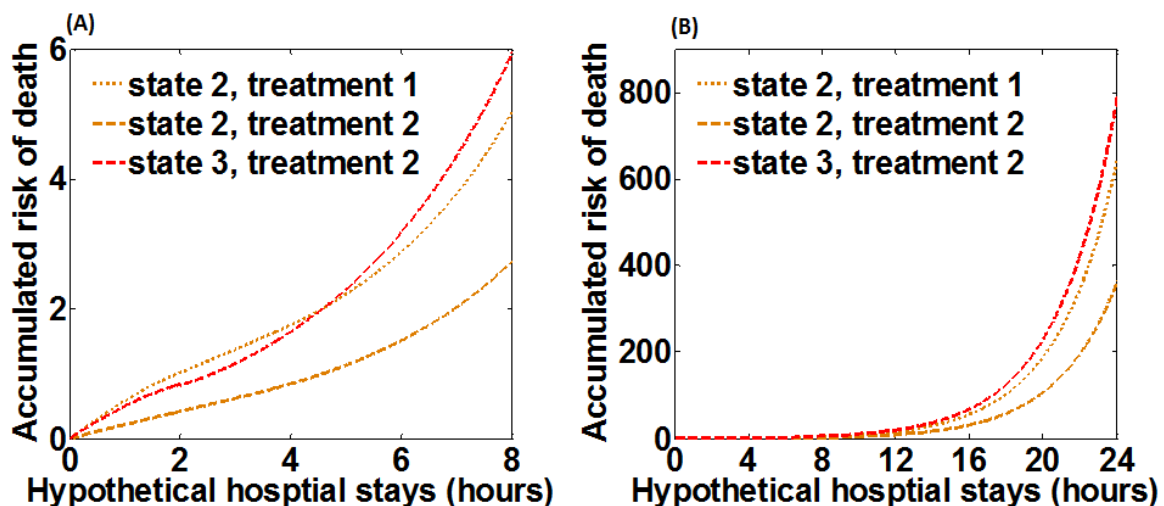
Clinical and experimental data have shown that *antimicrobial* agents and *anti-HMGB-1* agents contribute to improved survival rates of septic individuals (35, 42-44, 273). Computational Study I in this study tested the effects of *antimicrobial* agents on sepsis development in infected individuals. As indicated by Cross, a combination of anti-agent

therapies may be more effective in treating sepsis as compared to a single anti-agent therapy (32). Computational Study II tested the effects of a combination of *antimicrobial* agents and *anti-HMGB-1* agents on sepsis treatment. A detailed description of computational study I and computational study II is provided in Appendix C.

### 7.6.1 Computational study I

Three distinct states of individuals were defined based on the level of *Salmonella*. State 1 represented a low level of *Salmonella* in an individual. An individual was assigned State 2 if a medium level of *Salmonella* was present, and State 3 described a high level of *Salmonella* in an individual. *Antimicrobial* agents were incorporated into the IMMABM whenever a change in the health state of an individual was observed, given that the individual previously had a medium or high level of *Salmonella*. Detailed description of state definitions, model assumptions, and FHSMDP calculation is provided in Appendix C. Objective values obtained from the FHSMDP are shown in Figure 7.5.

**Figure 7.5 (A) Accumulated risk of an infected individual dying from sepsis from 0 - 8 hrs of hospital stays. (B) Accumulated risk of an infected individual dying from sepsis from 0 - 24 hrs of hospital stay. Treatment 1: *antimicrobial* agent, treatment 2: *anti-HMGB-1* agent, treatment 3: a combination of *antimicrobial* agent/*antiHMGB-1* agent**





Simulated results from FHSMDP indicated that *antimicrobial* agents reduced accumulated risk of death for septic individuals with medium levels of *Salmonella* who experienced a long period of hospital stays (8 – 24 hrs). However, infected individuals with high levels of *Salmonella* were more likely to die than individuals with medium levels of *Salmonella* as the length of hospital stay increases. The chance of death significantly increased with increased length of hospitalization, as shown in Figure 7.5 (B).

In Figure 7.5 (A), simulated results imply that *antimicrobial* treatment is more effective for treating infected individuals with high levels of *Salmonella* within (0 – 5 hrs) of hospitalization, indicating that *antimicrobial* treatment should be given to infected individuals with high levels of *Salmonella* within (0 – 5 hrs) of hospitalization. Because the assumption was made that patients began hospitalization immediately after initial infection, the treatment time window for heavily infected individuals was recommended as 0 – 1 hrs after hospitalization, matching with the conclusion in (43, 44). From 5 – 24 hrs of hospitalization, simulated results showed that infected individuals with high levels of initial infection had increased likelihood of achieving a death state, even with antimicrobial treatments, as compared to infected individuals with medium levels of initial infection. From 0 – 24 hrs of hospitalization, simulated results recommended administration of *antimicrobial* agents to infected individuals with medium levels of *Salmonella*.

### **7.6.2 Computational study II**

Computational Study I defined the health state of individuals using a combination of *Salmonella* levels and HMGB-1 levels. Detailed information of state definitions, modeling assumptions, and FHSMDP calculation is provided in Appendix C. Accumulated risks of death generated from FHSMDP are shown in Figures 7.6, 7.7, 7.8, and 7.9.

Figure 7.6 Accumulated risk of infected individuals dying from sepsis (hypothetical death states) at  $s_5$  from 0-24 hrs of hospital stays using various treatment strategies. Treatment 1: antimicrobial agent, treatment 2: anti-HMGB-1 agent, treatment 3: a combination of antimicrobial agent/antiHMGB-1 agent

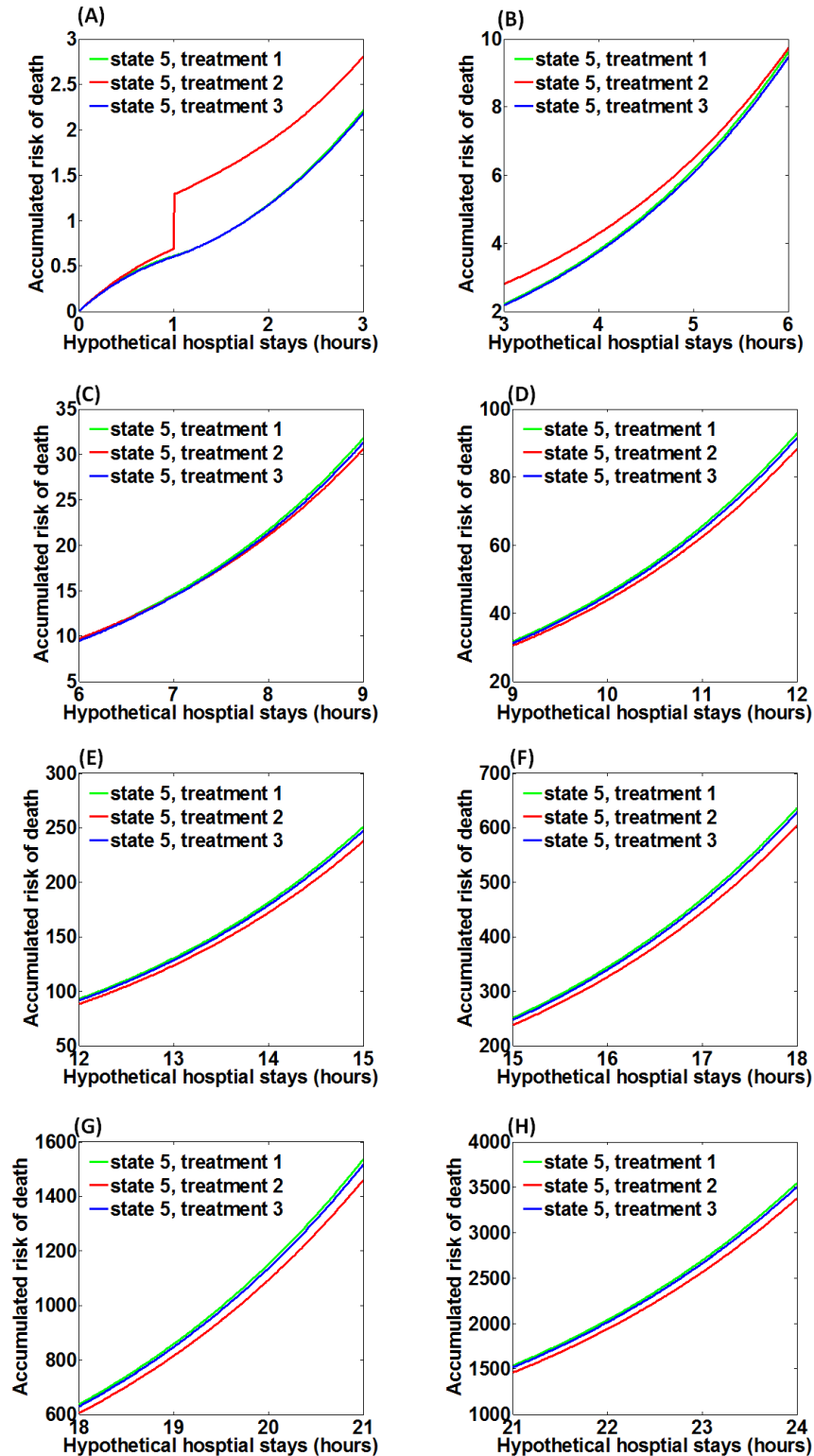
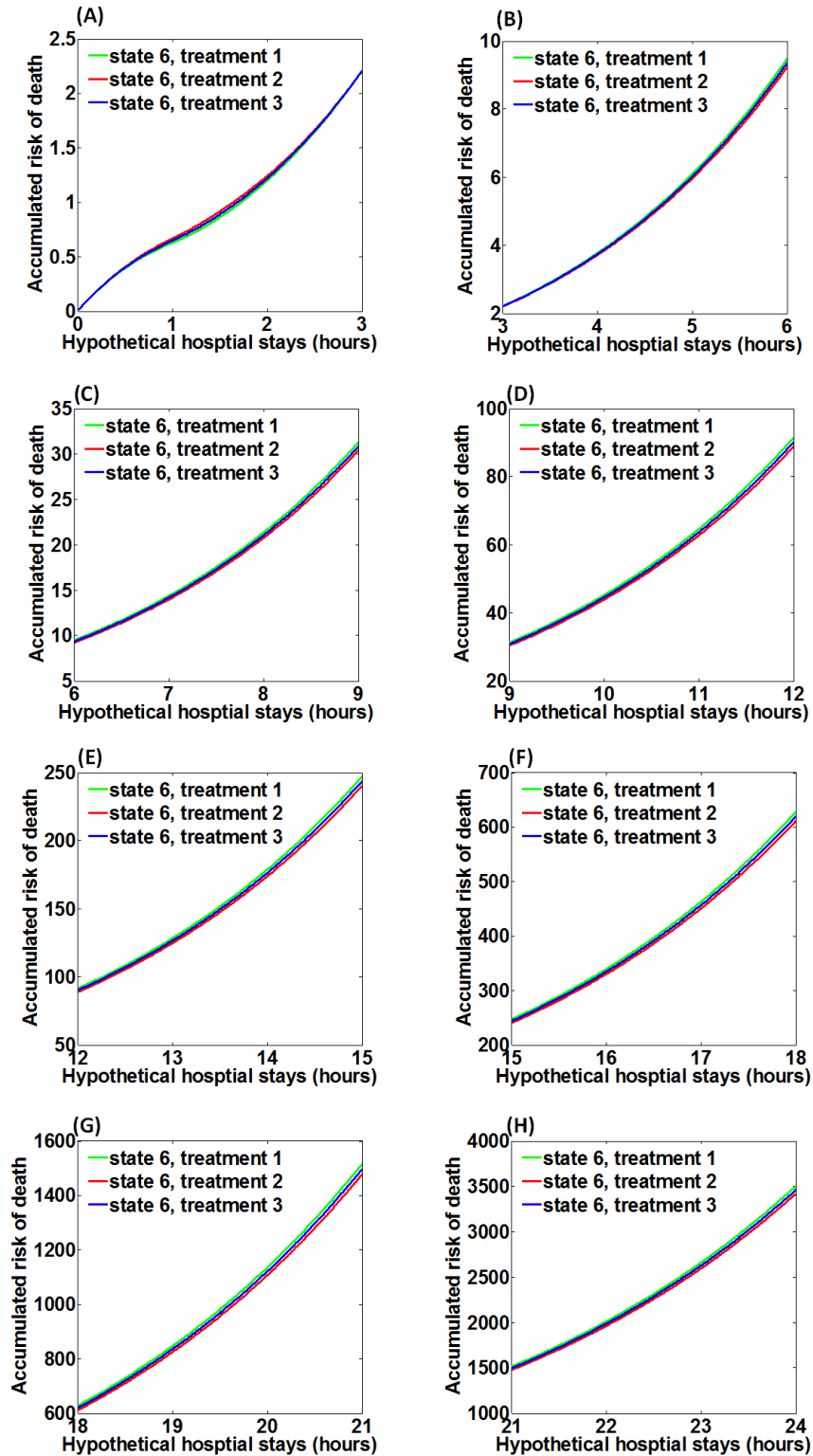


Figure 7.7 Accumulated risk of infected individuals dying from sepsis (hypothetical death states) at  $s_6$  from 0-24 hrs of hospital stays using various treatment strategies. Treatment 1: antimicrobial agent, treatment 2: anti-HMGB-1 agent, treatment 3: a combination of antimicrobial agent/antiHMGB-1 agent



**Figure 7.8** Accumulated risk of infected individuals dying from sepsis (hypothetical death states) at  $s_8$  from 0-24 hrs of hospital stays using various treatment strategies. Treatment 1: *antimicrobial agent*, treatment 2: *anti-HMGB-1 agent*, treatment 3: a combination of *antimicrobial agent/antiHMGB-1 agent*

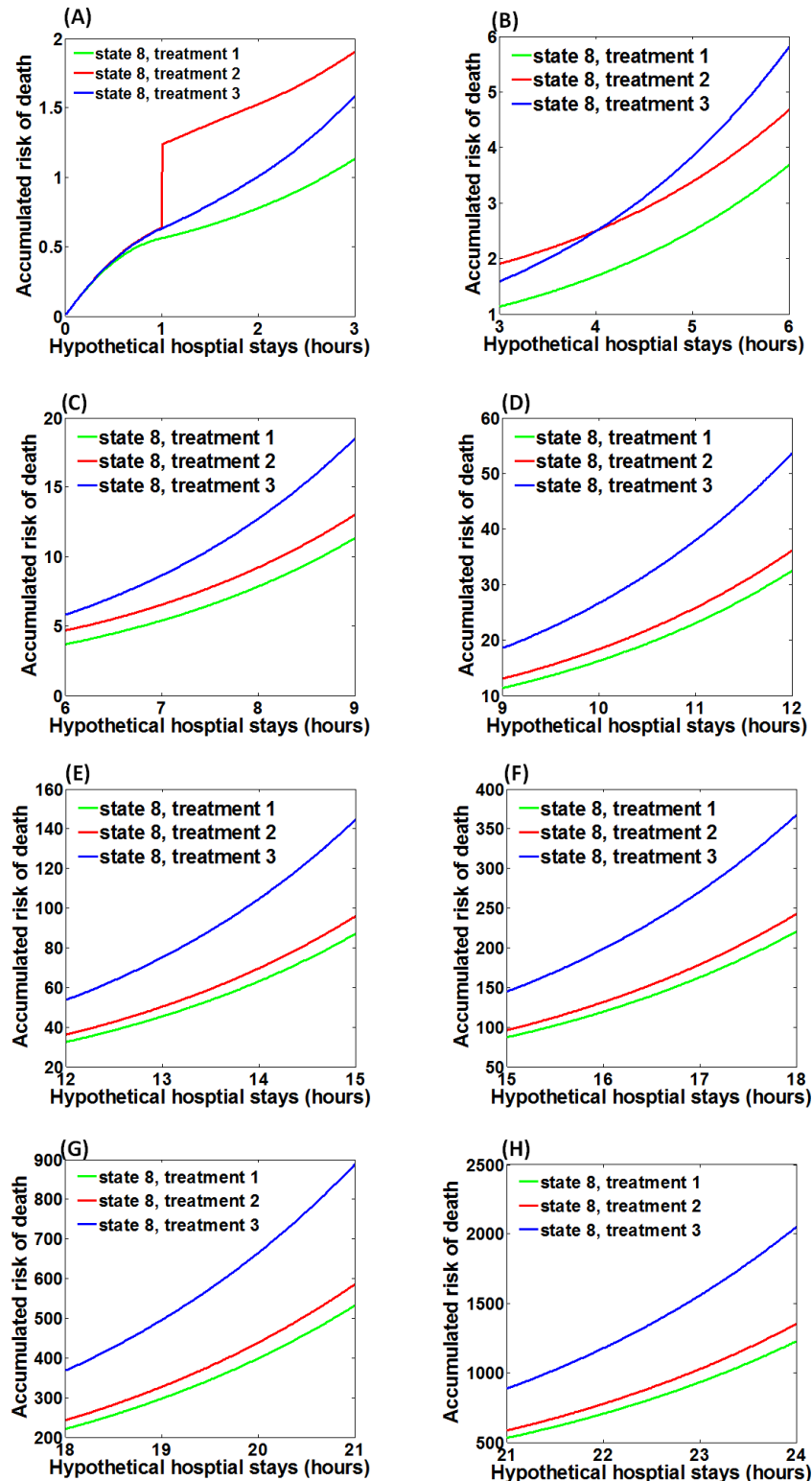
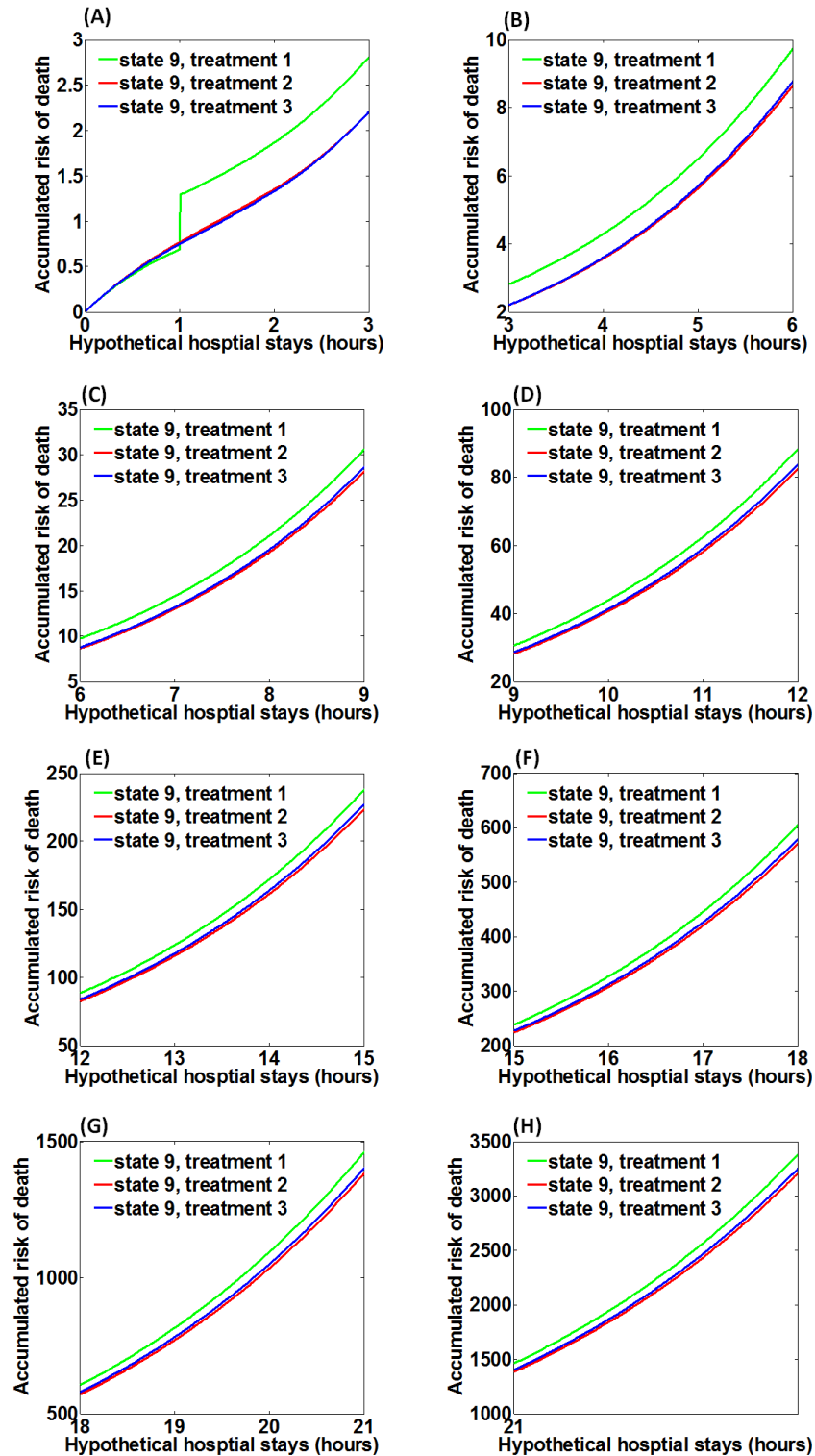


Figure 7.9 Accumulated risk of infected individuals dying from sepsis (hypothetical death states) at  $s_9$  from 0-24 hrs of hospital stays using various treatment strategies. Treatment 1: antimicrobial agent, treatment 2: anti-HMGB-1 agent, treatment 3: a combination of antimicrobial agent/antiHMGB-1 agent



### 7.6.3 Evaluation

Computational studies from FHSMDP showed that the effectiveness of anti-agent treatments was significantly correlated to the length of hospital stay and the health states of infected individuals. The following paragraphs in this section describe the impacts of length of hospital stay on infected individuals and states of infected individuals in relation to clinical decision-making using proposed treatment strategies.

As shown in Figure 7.6, infected individuals at  $s_5$  (medium level of *Salmonella* and medium level of HMGB-1) who received anti-HMGB-1 agents had increased chances of death from 0 to 6 hrs of hospital stay as compared to infected individuals who received antimicrobial agents and infected individuals who received a combination of antimicrobial agents and anti-HMGB-1 agents. As hospital stays extended, simulated results failed to show significance differences in likelihood of death between infected individuals treated with antimicrobial agents, infected individuals treated with anti-HMGB-1 agents, and infected individuals treated with a combination of antimicrobial agents and anti-HMGB-1 agents.

For infected individuals at state  $s_6$  (medium level of *Salmonella* and high level of HMGB-1), simulated results showed no significant differences in survival rates between infected individuals who received *antimicrobial* agents, infected individuals who received *anti-HMGB-1* agents, and infected individuals who received a combination of *antimicrobial* agents and *anti-HMGB-1* agents. Simulated results are shown in Figure 7.7.

As shown in Figure 7.8, treating infected individuals at state  $s_8$  (high level of *Salmonella* and medium level of HMGB-1) using a combination of *antimicrobial* agents and *anti-HMGB-1* agents could be deleterious as compared to treatment using only *antimicrobial* agents during 0 - 24 hrs of hospital stay.

Simulated results in Figure 7.9 show that infected individuals at state  $s_9$  should receive *anti-HMGB-1* agents or a combination of *antimicrobial* agents and *anti-HMGB-1* agents in order to decrease the likelihood of death. The difference in chance of death between infected individuals who received *antimicrobial* agents, infected individuals who received *anti-HMGB-1* agents, and infected individuals who received a combination of *antimicrobial* agents and *anti-HMGB-1* agents decreased as length of hospital stay increased.

HMGB-1, a downstream pro-inflammatory mediator of TNF- $\alpha$  (232), was recognized as a potential therapeutic target for treating sepsis (37, 279). Simulated results from this study showed that use of anti-HMGB-1 agents could be deleterious to septic individuals (Figure 7.8), but use of anti-HMGB-1 agents could effectively treat individuals infected with sepsis (Figure 7.9). A previous experiment (280) reported that pretreatment of anti-HMGB-1 monoclonal antibody significantly enhanced retinal ischemia-reperfusion injury in a rat model, as shown in Figure 7.5 (A) and Figure 7.8 (A). Therefore, observations of the double sword effect of anti-HMGB-1 in this study were assumed to be due to various injection times of anti-HMGB-1 agents to infected individuals at state  $s_5, s_6, s_8$ , and  $s_9$ .

## 7.7 Conclusion and discussion

The ABM, a powerful computational modeling technique, simulates complicated nonlinear dynamic relationships between components and intuitively maps a realistic biological system by incorporating spatial effects and the stochastic nature of the immune response into model construction (76, 195). A recent extensive application of ABMs in order to simulate inflammation (48-52) provided evidence that agent-based modeling is a valid approach for simulating disease progression. The proposed decision-making framework employed transition probabilities generated from an IMMABM as inputs to conventional MDP, thereby reducing the

difficulty of conventional MDPs for calculating transition probabilities (57). Furthermore, an ABM can predict dynamic patterns of disease progression and help initially screen therapeutic targets for disease treatment. Because an ABM is vital for the proposed decision-making process, construction of a rigorous ABM is an essential step for the establishment of the proposed decision-making framework. Although development of a rigorous ABM for simulation of disease progression is challenging due to lack of clinical data incorporation, involvement of intermediate biological responses, and limited understanding of various biological processes (102), this novel decision-making framework allows clinicians to test the effectiveness of a sequence of proposed treatments prior to clinical trials.

The IMMABM in this study simulated HIR progression when *Salmonella* initial loads were 3200 counts (*in silico* equivalent to colony forming units [CFU]). A total of 200 counts *antimicrobial* agents or 800 counts *anti-HMGB-1* agents (*in silico* 1 count of anti-HMGB-1 degrades  $2.82 \times 10^{-5}$  pg HMGB-1) were incorporated into the IMMABM when the states of septic individuals changed. Simulations showed that outcomes of HIR were significantly correlated to *Salmonella* initial counts. The HIR had a higher likelihood of progressing to hypothetical death states (hyperinflammatory response or organ dysfunction) if *Salmonella* initial loads were high. Therefore, the amount of *antimicrobial* agents or *anti-HMGB-1* agents incorporated into the IMMABM should be enhanced if a high initial load of *Salmonella* is detected in septic individuals.

In addition, a fixed amount of *antimicrobial* agents or *anti-HMGB-1* agents were incorporated into the IMMABM at each decision epoch. During IMMABM simulations, averaged 72960 counts of HMGB-1 (*in silico* 1 count of HMGB-1 equivalent to  $2.82 \times 10^{-5}$  pg HMGB-1) was observed when infected individuals were at state  $s_3$ . If 800 anti-HMGB-1 agents



were administered to infected individuals at state  $s_3$ , the probability of transition to a healthy state was approximately 9%. The hypothesis was made that an increased amount of anti-HMGB-1 agents injected at state  $s_3$  could lead to an increased chance of ending with a healthy state. This hypothesis will be tested in future studies.

The IMMABM was constructed to simulate mouse HIR infected by *Salmonella*. As indicated by Hotchkiss et al., “The theory that death from sepsis was attributable to an overstimulated immune system was based on studies in animals that do not seem to reflect the clinical picture in human” (247). An ABM of human inflammatory responses to an infection would help establish accurate prediction of dynamic patterns of human inflammation and provide accurate data incorporation for the decision-making framework for septic patients.

In this study, states of infected individuals were defined based on a boundary rule. For example, maximum levels of *Salmonella* during selected 50 simulation runs were recorded. According to the maximum level of *Salmonella*, the upper limit of low levels of *Salmonella* were defined as equivalent to one-third the maximum level of *Salmonella*; the upper limit of medium levels of *Salmonella* were defined as equivalent to two-thirds the maximum level of *Salmonella*. Detailed descriptions of state definitions are provided in Appendix C.

This study tested the efficacy of incorporating *antimicrobial* agents and a combination of *antimicrobial* agents and *anti-HMGB-1* agents to infected individuals during HIR. *Silico* results showed that a combination of *antimicrobial* agents and *anti-HMGB-1* agents was not significantly effective in reducing accumulated risk of death as compared to administration of only *antimicrobial* agents. HMGB-1 was recognized as a late pro-inflammatory mediator during inflammation; an elevated level of HMGB-1 would be correlated to the death of infected individuals (22, 23, 237). Incorporation of *anti-TNF- $\alpha$*  agents between 6 hrs and 8 hrs of

infection improved survival rates of infected individuals with HIR in multiple simulation runs. However, because computational studies conducted for this study were initial therapeutic tests for treating infected individuals, the effectiveness of additional tests, such as a combination of *anti-TNF- $\alpha$*  agents and *anti-HMGB-1* agents or a combination of *antimicrobial* agents, *anti-TNF- $\alpha$*  agents, and *anti-HMGB-1* agents, for treating septic individuals must be verified in future studies.

## 7.8 Future research

The proposed decision-making framework in this chapter is a general methodology that can be applied in order to develop strategies for treating other diseases, such as cancer. Researchers can formulate their individual decision-making platforms by specifically modifying this decision-making framework.

Future research will pursue several objectives. First, additional therapeutic tests will be conducted using a combination of *antimicrobial* agents and *anti-TNF- $\alpha$*  agents and a combination of *antimicrobial* agents, *anti-TNF- $\alpha$*  agents, and *anti-HMGB-1* agents. The tests will be designed to fully explore the impact of treatment combinations for individuals infected with sepsis, as proposed by Cross et al. (32). A comparative study on proposed treatments could help clinical decision makers, such as clinicians, determine optimal treatment bundle for septic individuals. Second, sensitivity analysis on various *antimicrobial* loads, *anti-TNF- $\alpha$*  agents, or *anti-HMGB-1* injection to infected individuals at various decision epochs will be conducted in order to identify optimal treatment plans for infected individuals. Third, the impact of initial *Salmonella* counts on the effectiveness of treatment combinations will be explored in order to develop appropriate, individualized treatment strategies for each septic patient.

## Chapter 8 - Conclusions and Contributions

### 8.1 Conclusions

In this dissertation, two SDMMs were developed to simulate various dynamic patterns of inflammatory responses to an infection (*Salmonella*). Furthermore, two ABMs were built, with an incorporation of mathematical expressions from SDMMs, to accurately reflect the possible pathogenesis of sepsis based on the host's physiological conditions. Ultimately, a novel decision making framework was developed to apply to a clinical decision making on the treatment for sepsis.

Main conclusions drawn from this dissertation are:

1. Three dynamic patterns, “healing process”, “persistent infection”, and “organ dysfunction”, were identified from developed SDMMs in a quantitative way. Four identifiable patterns were found in IMMABM, including “healing process”, “persistent infection”, “hyperinflammatory response”, and “organ dysfunction”. Specifically, a ***dampened oscillated pattern*** observed in experimental studies was captured using both SDMMs and IMMABM.
2. System parameters such as  $k_{pg}$ ,  $r_{pn}$ ,  $u_n$ ,  $r_{l2max}$ ,  $k_{mkub}$ ,  $u_{mk}$  and  $k_{mk}$  were identified in SDMMs as “key parameters” because the changes in their values impacted the outcomes of inflammatory responses to an infection (*Salmonella*).
3. The 18-equation SDMM showed that CD4+ T cell count, CD8+ T cell count, B cell count, and antibody count were persistently elevated, which contributed to the pathogen clearance during a late stage of sepsis progression.
4. Both SDMMs and ABMs showed that the outcomes of inflammatory responses to an infection (*Salmonella*) were highly correlated with pathogen (*Salmonella*).

initial loads. The chance of death were increased as the pathogen initial loads increased.

5. In IMMABM, outcomes of inflammatory responses to an infection (*Salmonella*) was found to clearly skew toward a “healing response” at *Salmonella* doses less than 500 counts. As the initial *Salmonella* doses increased, the dynamic patterns of inflammation could diverge in the health outcomes (healing response vs. persistent infection vs. hyperinflammatory response vs. organ dysfunction).
6. Biomarkers such as *HMGB-1*, *CRP*, *IL-10: TNF- $\alpha$*  ratios, and *CD4+ T cell: CD8+ T cell* ratios were highly correlated with the outcomes of an HIR in IMMABM. The elevation in *HMGB-1* level, *CRP* level, and a decrease in *IL-10: TNF- $\alpha$*  ratios and *CD4+ T cell: CD8+ T cell* ratios indicated a risk of death (was developing to “hyperinflammatory response” or “organ dysfunction”).
7. The therapy-directed tests in IMMABM showed that *Antimicrobial* agents significantly improved the survival rates during the first hour of HIR. In contrast, the optimal treatment window for *anti-TNF- $\alpha$*  agents was between 6 hours and 8 hours. The combination of *anti-HMGB-1* and *anti-TNF- $\alpha$*  was more effective in improving the survival rates when treatment was started between 7 hours and 11 hours, compared to using only *anti-TNF- $\alpha$* . The therapy-directed *silico* simulations demonstrated that anti-agents impacted the survival rates of septic individuals at various treatment time windows.
8. When infected individuals at  $s_5$  (a medium level of *Salmonella* and a medium level of *HMGB-1* were observed in IMMABM), antimicrobial agent treatment or a combination of antimicrobial agent and *anti-HMGB-1* agent treatment should be

injected to infected individuals from 0 - 6 hours after hospitalization. From 6 - 9 hours after hospitalization, there is no significant difference in the efficacy of the treatment between choosing antimicrobial agent treatment, anti-HMGB-1 agent treatment, and a combination of antimicrobial agent and anti-HMGB-1 agent treatment. From 9 - 24 hours, anti-HMGB-1 agent treatment is more effective in treating infected individuals, compared to antimicrobial agent treatment or a combination of antimicrobial agent and anti-HMGB-1 agent treatment.

9. When infected individuals at  $s_6$  (a medium level of *Salmonella* and a high level of HMGB-1 were observed in IMMABM), there is no significant difference in the efficacy of the treatment between choosing antimicrobial agent treatment, anti-HMGB-1 agent treatment, and a combination of antimicrobial agent and anti-HMGB-1 agent treatment.
10. When infected individuals at  $s_8$  (a high level of *Salmonella* and a medium level of HMGB-1 were observed in IMMABM), antimicrobial agent treatment is the best treatment among antimicrobial agent treatment, anti-HMGB-1 agent treatment, and a combination of antimicrobial agent and anti-HMGB-1 agent treatment from 0 – 24 hours of hospitalization.
11. When infected individuals at  $s_9$  (a high level of *Salmonella* and a high level of HMGB-1 were observed in IMMABM), there is no significant difference in the efficacy of treatment between antimicrobial agent treatment, anti-HMGB-1 agent treatment, and a combination of antimicrobial agent and anti-HMGB-1 agent treatment from 0 hour – 1 hour after hospitalization. From 1 – 24 hours after hospitalization, either anti-HMGB-1 agent treatment or a combination of

antimicrobial agent and anti-HMGB-1 agent treatment had a lower accumulated risk of death over hospitalization, compared to antimicrobial agent treatment.

## 8.2 Contributions

Major contributions of this dissertation to the area of computational modeling, decision making, and clinical research are listed as follows:

1. This research developed a 14-equation SDMM and an 18-equation SDMM to predict various dynamic patterns of inflammatory responses to an infection. Key parameters were identified using stability analysis. Levels of indicators during the development of sepsis was quantitatively simulated over time. Compared to existing mathematical models, the developed SDMMs provided more accurate qualitative estimates.
2. For the first time, this research incorporated extensive experimental data to an agent-based model to simulate a hepatic inflammatory response (HIR) in a mouse infected by *Salmonella*. Relationships between dynamic patterns of inflammatory responses and dynamic patterns of essential biomarkers were studied for the first time in *silico* simulation.
3. This study, for the first time, presented a mapping of probabilities of leading to various dynamic patterns of inflammatory responses to pathogen (*Salmonella*) initial loads. This mapping provided a predictive tool for estimating the mortality rate of an infected individuals, given the pathogen initial loads were measured.
4. This dissertation is the first one to propose a concept of a general decision making framework with application to clinical decision makings. Furthermore, this research developed the first application of a finite-horizon semi-Markov decision

process (FHSMDP) in an attempt to address the challenges in current medical decision makings for the sepsis treatment. This proposed FHSMDP is also the first application of a finite-horizon SMDP to the clinical decision makings. Results obtained in this study would provide recommendations for clinicians to select an optimal sequence of treatments for an infected individual during the hospitalization.

## References

1. R. Bone, R. Balk, F. Cerra, R. Dellinger, A. Fein, W. Knaus, R. Schein, W. Sibbald, Definitions for sepsis and organ failure and guidelines for the use of innovative therapies in sepsis. The American College of Chest Physicians/Society of Critical Care Medicine Consensus Conference Committee. *Chest* **101**, 1644-1655 (1992).
2. M. P. Glauser, Pathophysiologic basis of sepsis: considerations for future strategies of intervention. *Critical care medicine* **28**, S4-S8 (2000).
3. S. Sharma, A. Kumar, Septic shock, multiple organ failure, and acute respiratory distress syndrome. *Current opinion in pulmonary medicine* **9**, 199-209 (2003).
4. D. C. Angus, W. T. Linde-Zwirble, J. Lidicker, G. Clermont, J. Carcillo, M. R. Pinsky, Epidemiology of severe sepsis in the United States: analysis of incidence, outcome, and associated costs of care. *Critical care medicine* **29**, 1303-1310 (2001).
5. J. E. Parrillo, M. M. Parker, C. Natanson, A. F. Suffredini, R. L. Danner, R. E. Cunnion, F. P. Ognibene, Septic shock in humans: advances in the understanding of pathogenesis, cardiovascular dysfunction, and therapy. *Annals of internal medicine* **113**, 227-242 (1990).
6. D. L. Hoyert, E. Arias, B. L. Smith, S. Murphy, K. Kochanek, Deaths: final data for 1999. *National vital statistics report. Hyattsville, Maryland: National Center for Health Statistics* **49**, (1999).
7. T. M. Perl, L. Dvorak, T. Hwang, R. P. Wenzel, Long-term survival and function after suspected gram-negative sepsis. *Jama* **274**, 338-345 (1995).
8. M. S. Rangel-Frausto, D. Pittet, M. Costigan, T. Hwang, C. S. Davis, R. P. Wenzel, The natural history of the systemic inflammatory response syndrome (SIRS): a prospective study. *Jama* **273**, 117-123 (1995).
9. P. Parham, *The immune system*. (Garland Science, 2014).
10. C. A. Janeway, P. Travers, M. Walport, J. D. Capra, *Immunobiology: the immune system in health and disease*. (Current Biology Publications New York, NY;, 1999), vol. 157.
11. T. J. Kindt, R. A. Goldsby, B. A. Osborne, J. Kuby, *Kuby immunology*. (Macmillan, 2007).
12. C. A. Gogos, E. Drosou, H. P. Bassaris, A. Skoutelis, Pro-versus anti-inflammatory cytokine profile in patients with severe sepsis: a marker for prognosis and future therapeutic options. *Journal of Infectious Diseases* **181**, 176-180 (2000).
13. K. R. Walley, N. W. Lukacs, T. J. Standiford, R. M. Strieter, S. L. Kunkel, Balance of inflammatory cytokines related to severity and mortality of murine sepsis. *Infection and immunity* **64**, 4733-4738 (1996).
14. S. H. Gregory, E. J. Wing, Neutrophil-Kupffer cell interaction: a critical component of host defenses to systemic bacterial infections. *Journal of leukocyte biology* **72**, 239-248 (2002).
15. H. Malhi, M. E. Guicciardi, G. J. Gores, Hepatocyte death: a clear and present danger. *Physiological reviews* **90**, 1165-1194 (2010).
16. A. Sindrilaru, T. Peters, S. Wieschalka, C. Baican, A. Baican, H. Peter, A. Hainzl, S. Schatz, Y. Qi, A. Schlecht, An unrestrained proinflammatory M1 macrophage population induced by iron impairs wound healing in humans and mice. *The Journal of clinical investigation* **121**, 985 (2011).



17. V. Kumar, A. Sharma, Neutrophils: Cinderella of innate immune system. *International immunopharmacology* **10**, 1325-1334 (2010).
18. T. Abe, T. Arai, A. Ogawa, T. Hiromatsu, A. Masuda, T. Matsuguchi, Y. Nimura, Y. Yoshikai, Kupffer cell-derived interleukin 10 is responsible for impaired bacterial clearance in bile duct-ligated mice. *Hepatology* **40**, 414-423 (2004).
19. K. A. Bardadin, P. J. Scheuer, Mast cells in acute hepatitis. *The Journal of pathology* **149**, 315-325 (1986).
20. M. Yamashiro, W. Kouda, N. Kono, K. Tsuneyama, O. Matsui, Y. Nakanuma, Distribution of intrahepatic mast cells in various hepatobiliary disorders. *Virchows Archiv* **433**, 471-479 (1998).
21. U. Andersson, H. Wang, K. Palmblad, A.-C. Aveberger, O. Bloom, H. Erlandsson-Harris, A. Janson, R. Kokkola, M. Zhang, H. Yang, High mobility group 1 protein (HMG-1) stimulates proinflammatory cytokine synthesis in human monocytes. *The Journal of experimental medicine* **192**, 565-570 (2000).
22. J. Sundén-Cullberg, A. Norrby-Teglund, A. Rouhiainen, H. Rauvala, G. Herman, K. J. Tracey, M. L. Lee, J. Andersson, L. Tokics, C. J. Treutiger, Persistent elevation of high mobility group box-1 protein (HMGB1) in patients with severe sepsis and septic shock\*. *Critical care medicine* **33**, 564-573 (2005).
23. H. Wang, O. Bloom, M. Zhang, J. M. Vishnubhakat, M. Ombrellino, J. Che, A. Frazier, H. Yang, S. Ivanova, L. Borovikova, HMGB-1 as a late mediator of endotoxin lethality in mice. *Science* **285**, 248-251 (1999).
24. H. Wang, H. Yang, K. Tracey, Extracellular role of HMGB1 in inflammation and sepsis. *Journal of internal medicine* **255**, 320-331 (2004).
25. D. F. Fiorentino, A. Zlotnik, T. Mosmann, M. Howard, A. O'garra, IL-10 inhibits cytokine production by activated macrophages. *The Journal of Immunology* **147**, 3815-3822 (1991).
26. C. S. Chan, A. Ming-Lum, G. B. Golds, S. J. Lee, R. J. Anderson, A. L.-F. Mui, Interleukin-10 Inhibits Lipopolysaccharide-induced Tumor Necrosis Factor- $\alpha$  Translation through a SHIP1-dependent Pathway. *Journal of Biological Chemistry* **287**, 38020-38027 (2012).
27. K. J. Tracey, Y. Fong, D. G. Hesse, K. R. Manogue, A. T. Lee, G. C. Kuo, S. F. Lowry, A. Cerami, Anti-cachectin/TNF monoclonal antibodies prevent septic shock during lethal bacteraemia. *Nature* **330**, 662-664 (1987).
28. F. Zeni, B. Freeman, C. Natanson, Anti-inflammatory therapies to treat sepsis and septic shock: a reassessment. *Critical care medicine* **25**, 1095-1100 (1997).
29. E. Abraham, A. Anzueto, G. Gutierrez, S. Tessler, G. San Pedro, R. Wunderink, A. Dal Nogare, S. Nasraway, S. Berman, R. Cooney, Double-blind randomised controlled trial of monoclonal antibody to human tumour necrosis factor in treatment of septic shock. *The Lancet* **351**, 929-933 (1998).
30. K. Reinhart, W. Karzai, Anti-tumor necrosis factor therapy in sepsis: update on clinical trials and lessons learned. *Critical care medicine* **29**, S121-S125 (2001).
31. C. Morris, Activated protein C in the treatment of sepsis. *Anaesthesia* **57**, 501-521 (2002).
32. A. S. Cross, S. M. Opal, A new paradigm for the treatment of sepsis: is it time to consider combination therapy? *Annals of internal medicine* **138**, 502-505 (2003).

33. E. Abraham, R. Wunderink, H. Silverman, T. M. Perl, S. Nasraway, H. Levy, R. Bone, R. P. Wenzel, R. Balk, R. Allred, Efficacy and safety of monoclonal antibody to human tumor necrosis factor  $\alpha$  in patients with sepsis syndrome: a randomized, controlled, double-blind, multicenter clinical trial. *Jama* **273**, 934-941 (1995).
34. J. Cohen, J. Carlet, INTERSEPT: an international, multicenter, placebo-controlled trial of monoclonal antibody to human tumor necrosis factor-alpha in patients with sepsis. *Critical care medicine* **24**, 1431-1440 (1996).
35. L. Ulloa, M. Ochani, H. Yang, M. Tanovic, D. Halperin, R. Yang, C. J. Czura, M. P. Fink, K. J. Tracey, Ethyl pyruvate prevents lethality in mice with established lethal sepsis and systemic inflammation. *Proceedings of the National Academy of Sciences* **99**, 12351-12356 (2002).
36. H. Yang, M. Ochani, J. Li, X. Qiang, M. Tanovic, H. E. Harris, S. M. Susarla, L. Ulloa, H. Wang, R. DiRaimo, Reversing established sepsis with antagonists of endogenous high-mobility group box 1. *Proceedings of the National Academy of Sciences* **101**, 296-301 (2004).
37. L. L. Mantell, W. R. Parrish, L. Ulloa, Hmgb-1 as a therapeutic target for infectious and inflammatory disorders. *Shock* **25**, 4-11 (2006).
38. S. Qin, H. Wang, R. Yuan, H. Li, M. Ochani, K. Ochani, M. Rosas-Ballina, C. J. Czura, J. M. Huston, E. Miller, Role of HMGB1 in apoptosis-mediated sepsis lethality. *The Journal of experimental medicine* **203**, 1637-1642 (2006).
39. K. Tsukaguchi, B. de Lange, W. H. Boom, Differential Regulation of IFN- $\gamma$ , TNF- $\alpha$ , and IL-10 Production by CD4<sup>+</sup>  $\alpha\beta$ TCR<sup>+</sup> T Cells and V $\delta$ 2<sup>+</sup>  $\gamma\delta$  T Cells in Response to Monocytes Infected with Mycobacterium tuberculosis-H37Ra. *Cellular immunology* **194**, 12-20 (1999).
40. G. E. Bacon, F. M. Kenny, H. V. Murdaugh, C. Richards, Prolonged serum half-life of cortisol in renal failure. *The Johns Hopkins medical journal* **132**, 127 (1973).
41. N. C. Riedemann, R.-F. Guo, P. A. Ward, Novel strategies for the treatment of sepsis. *Nature medicine* **9**, 517-524 (2003).
42. D. Simon, G. Trenholme, Antibiotic selection for patients with septic shock. *Critical care clinics* **16**, 215-231 (2000).
43. R. Daniels, Surviving the first hours in sepsis: getting the basics right (an intensivist's perspective). *Journal of antimicrobial chemotherapy* **66**, ii11-ii23 (2011).
44. R. Ferrer, I. Martin-Loeches, G. Phillips, T. M. Osborn, S. Townsend, R. P. Dellinger, A. Artigas, C. Schorr, M. M. Levy, Empiric Antibiotic Treatment Reduces Mortality in Severe Sepsis and Septic Shock From the First Hour: Results From a Guideline-Based Performance Improvement Program\*. *Critical care medicine* **42**, 1749-1755 (2014).
45. I. Keir, A. E. Dickinson, The role of antimicrobials in the treatment of sepsis and critical illness - related bacterial infections: Examination of the evidence. *Journal of Veterinary Emergency and Critical Care*, (2015).
46. J.-L. Vincent, Q. Sun, M.-J. Dubois, Clinical trials of immunomodulatory therapies in severe sepsis and septic shock. *Clinical infectious diseases* **34**, 1084-1093 (2002).
47. L. Ulloa, M. Brunner, L. Ramos, E. A. Deitch, Scientific and clinical challenges in sepsis. *Current pharmaceutical design* **15**, 1918 (2009).
48. G. An, Agent-based computer simulation and sirs: building a bridge between basic science and clinical trials. *Shock* **16**, 266-273 (2001).

49. G. An, In silico experiments of existing and hypothetical cytokine-directed clinical trials using agent-based modeling\*. *Critical care medicine* **32**, 2050-2060 (2004).
50. X. Dong, P. T. Foteinou, S. E. Calvano, S. F. Lowry, I. P. Androulakis, Agent-based modeling of endotoxin-induced acute inflammatory response in human blood leukocytes. *PloS one* **5**, e9249 (2010).
51. J. Dutta-Moscato, A. Solovyev, Q. Mi, T. Nishikawa, A. Soto-Gutierrez, I. J. Fox, Y. Vodovotz, A multiscale agent-based in silico model of liver fibrosis progression. *Frontiers in bioengineering and biotechnology* **2**, (2014).
52. J. Wu, D. Ben-Arieh, Z. Shi, An Autonomous Multi-Agent Simulation Model for Acute Inflammatory Response. *Investigations Into Living Systems, Artificial Life, and Real-world Solutions*, 218 (2013).
53. A. Reynolds, J. Rubin, G. Clermont, J. Day, Y. Vodovotz, G. B. Ermentrout, A reduced mathematical model of the acute inflammatory response: I. Derivation of model and analysis of anti-inflammation. *Journal of theoretical biology* **242**, 220-236 (2006).
54. R. Kumar, G. Clermont, Y. Vodovotz, C. C. Chow, The dynamics of acute inflammation. *Journal of Theoretical Biology* **230**, 145-155 (2004).
55. C. C. Bennett, K. Hauser, Artificial intelligence framework for simulating clinical decision-making: A Markov decision process approach. *Artificial intelligence in medicine* **57**, 9-19 (2013).
56. V. L. Patel, E. H. Shortliffe, M. Stefanelli, P. Szolovits, M. R. Berthold, R. Bellazzi, A. Abu-Hanna, The coming of age of artificial intelligence in medicine. *Artificial intelligence in medicine* **46**, 5-17 (2009).
57. A. J. Schaefer, M. D. Bailey, S. M. Shechter, M. S. Roberts, in *Operations research and health care*. (Springer, 2004), pp. 593-612.
58. F. Pappalardo, F. Chiacchio, S. Motta, Cancer vaccines: state of the art of the computational modeling approaches. *BioMed research international* **2013**, (2012).
59. B. Hancioglu, D. Swigon, G. Clermont, A dynamical model of human immune response to influenza A virus infection. *Journal of theoretical biology* **246**, 70-86 (2007).
60. A. Atangana, E. F. Doungmo Goufo, Computational Analysis of the Model Describing HIV Infection of CD4<sup>+</sup>T Cells. *BioMed research international* **2014**, (2014).
61. R. M. Axelrod, *The complexity of cooperation: Agent-based models of competition and collaboration*. (Princeton University Press, 1997).
62. J. M. Epstein, R. Axtell, *Growing artificial societies: social science from the bottom up*. (Brookings Institution Press, 1996).
63. A. L. Bauer, C. A. Bauchemin, A. S. Perelson, Agent-based modeling of host-pathogen systems: the successes and challenges. *Information sciences* **179**, 1379-1389 (2009).
64. J. Wu, D. Ben-Arieh, Z. Shi, An Autonomous Multi-Agent Simulation Model for Acute Inflammatory Response. *International Journal of Artificial Life Research* **2**, 105-121 (2011).
65. Q. Mi, B. Rivière, G. Clermont, D. L. Steed, Y. Vodovotz, Agent - based model of inflammation and wound healing: insights into diabetic foot ulcer pathology and the role of transforming growth factor -  $\beta$  1. *Wound Repair and Regeneration* **15**, 671-682 (2007).
66. N. Li, K. Verdolini, G. Clermont, Q. Mi, E. N. Rubinstein, P. A. Hebda, Y. Vodovotz, A patient-specific in silico model of inflammation and healing tested in acute vocal fold injury. *PloS one* **3**, e2789 (2008).

67. G. M. Dancik, D. E. Jones, K. S. Dorman, in *Unifying Themes in Complex Systems*. (Springer, 2008), pp. 243-250.
68. J. B. Seal, J. C. Alverdy, O. Zaborina, G. An, Agent-based dynamic knowledge representation of *Pseudomonas aeruginosa* virulence activation in the stressed gut: Towards characterizing host-pathogen interactions in gut-derived sepsis. *Theor Biol Med Model* **8**, 1742-4682 (2011).
69. Y. Mei, R. Hontecillas, X. Zhang, K. Bisset, S. Eubank, S. Hoops, M. Marathe, J. Bassaganya-Riera, in *Bioinformatics and Biomedicine (BIBM), 2012 IEEE International Conference on*. (IEEE, 2012), pp. 1-5.
70. T. Lux, M. Marchesi, Volatility clustering in financial markets: a microsimulation of interacting agents. *International journal of theoretical and applied finance* **3**, 675-702 (2000).
71. B. LeBaron, Agent-based computational finance: Suggested readings and early research. *Journal of Economic Dynamics and Control* **24**, 679-702 (2000).
72. A. M. El-Sayed, P. Scarborough, L. Seemann, S. Galea, Social network analysis and agent-based modeling in social epidemiology. *Epidemiologic Perspectives & Innovations* **9**, 1 (2012).
73. Netlogo. (<https://ccl.northwestern.edu/netlogo/5.1.0/>, 2014).
74. S. F. Railsback, S. L. Lytinen, S. K. Jackson, Agent-based simulation platforms: Review and development recommendations. *Simulation* **82**, 609-623 (2006).
75. Repast. (<http://repast.sourceforge.net/>, 2015).
76. E. Bonabeau, Agent-based modeling: Methods and techniques for simulating human systems. *Proceedings of the National Academy of Sciences* **99**, 7280-7287 (2002).
77. M. Aziz, A. Jacob, W.-L. Yang, A. Matsuda, P. Wang, Current trends in inflammatory and immunomodulatory mediators in sepsis. *Journal of leukocyte biology* **93**, 329-342 (2013).
78. G. An, Introduction of an agent-based multi-scale modular architecture for dynamic knowledge representation of acute inflammation. *Theoretical Biology and Medical Modelling* **5**, 11 (2008).
79. S. Wendel, C. Dibble, Dynamic agent compression. *Journal of Artificial Societies and Social Simulation* **10**, 9 (2007).
80. L. A. Harris, P. Clancy, A “partitioned leaping” approach for multiscale modeling of chemical reaction dynamics. *The Journal of chemical physics* **125**, 144107 (2006).
81. S. M. Shechter, M. D. Bailey, A. J. Schaefer, M. S. Roberts, The optimal time to initiate HIV therapy under ordered health states. *Operations Research* **56**, 20-33 (2008).
82. M. Mundhenk, J. Goldsmith, C. Lusena, E. Allender, Complexity of finite-horizon Markov decision process problems. *Journal of the ACM (JACM)* **47**, 681-720 (2000).
83. O. Madani, Complexity results for infinite-horizon markov decision processes. (2000).
84. M. L. Puterman, *Markov decision processes: discrete stochastic dynamic programming*. (John Wiley & Sons, 2014).
85. R. Bellman, Dynamic programming and Lagrange multipliers. *Proceedings of the National Academy of Sciences of the United States of America* **42**, 767 (1956).
86. H. S. Chang, J. Hu, M. C. Fu, S. I. Marcus, *Simulation-based algorithms for Markov decision processes*. (Springer Science & Business Media, 2013).
87. G. E. Monahan, State of the art—a survey of partially observable Markov decision processes: theory, models, and algorithms. *Management Science* **28**, 1-16 (1982).

88. C. H. Papadimitriou, J. N. Tsitsiklis, The complexity of Markov decision processes. *Mathematics of operations research* **12**, 441-450 (1987).
89. M. Hauskrecht, Value-function approximations for partially observable Markov decision processes. *Journal of Artificial Intelligence Research*, 33-94 (2000).
90. M. L. Littman, The witness algorithm: Solving partially observable Markov decision processes. *Brown University, Providence, RI*, (1994).
91. T. Smith, R. Simmons, in *Proceedings of the 20th conference on Uncertainty in artificial intelligence*. (AUAI Press, 2004), pp. 520-527.
92. T. Michael, I. Jordan, Reinforcement learning algorithm for partially observable Markov decision problems. *Proceedings of the Advances in Neural Information Processing Systems*, 345-352 (1995).
93. W. S. Lovejoy, A survey of algorithmic methods for partially observed Markov decision processes. *Annals of Operations Research* **28**, 47-65 (1991).
94. E. Pashenkova, I. Rish, R. Dechter, in *AAAI'96: Workshop on Structural Issues in Planning and Temporal Reasoning*. (Citeseer, 1996).
95. J. R. Beck, S. G. Pauker, The Markov process in medical prognosis. *Medical Decision Making* **3**, 419-458 (1983).
96. R. Bäuerle, A. Rücker, T. C. Schmandra, K. Holzer, A. Encke, E. Hanisch, Markov cohort simulation study reveals evidence for sex-based risk difference in intensive care unit patients. *The American Journal of Surgery* **179**, 207-211 (2000).
97. J. E. Kreke, University of Pittsburgh, (2007).
98. J.-L. Vincent, R. Moreno, J. Takala, S. Willatts, A. De Mendonça, H. Bruining, C. Reinhart, P. Suter, L. Thijs, The SOFA (Sepsis-related Organ Failure Assessment) score to describe organ dysfunction/failure. *Intensive care medicine* **22**, 707-710 (1996).
99. M. Weinstein, J. Siegel, M. Gold, M. Kamlet, L. Russell, Cost-effectiveness in health and medicine. *New York: Oxford University* **55**, (1996).
100. P. Magni, S. Quaglini, M. Marchetti, G. Barosi, Deciding when to intervene: a Markov decision process approach. *International Journal of Medical Informatics* **60**, 237-253 (2000).
101. J. Y. Yu, S. Mannor, N. Shimkin, Markov decision processes with arbitrary reward processes. *Mathematics of Operations Research* **34**, 737-757 (2009).
102. Z. Z. Shi, C.-H. Wu, D. Ben-Arieh, Agent-Based Model: A Surging Tool to Simulate Infectious Diseases in the Immune System. *Open Journal of Modelling and Simulation* **2014**, (2014).
103. A. Aderem, R. J. Ulevitch, Toll-like receptors in the induction of the innate immune response. *Nature* **406**, 782-787 (2000).
104. C. A. Janeway Jr, R. Medzhitov, Innate immune recognition. *Annual review of immunology* **20**, 197-216 (2002).
105. M. Bhatia, S. Moochhala, Role of inflammatory mediators in the pathophysiology of acute respiratory distress syndrome. *The Journal of pathology* **202**, 145-156 (2004).
106. S. M. Graham, Salmonellosis in children in developing and developed countries and populations. *Current opinion in infectious diseases* **15**, 507-512 (2002).
107. R. Jotwani, Y. Tanaka, K. Watanabe, K. Tanaka, N. Kato, K. Ueno, Cytokine stimulation during *Salmonella typhimurium* sepsis in Itys mice. *Journal of medical microbiology* **42**, 348-352 (1995).

108. C. R. Beuzón, S. P. Salcedo, D. W. Holden, Growth and killing of a *Salmonella enterica* serovar Typhimurium sifA mutant strain in the cytosol of different host cell lines. *Microbiology* **148**, 2705-2715 (2002).
109. H. K. de Jong, C. M. Parry, T. van der Poll, W. J. Wiersinga, Host-pathogen interaction in invasive salmonellosis. *PLoS pathogens* **8**, e1002933 (2012).
110. R. L. Friedman, R. J. Moon, Hepatic clearance of *Salmonella typhimurium* in silica-treated mice. *Infection and immunity* **16**, 1005-1012 (1977).
111. J. R. Gog, A. Murcia, N. Osterman, O. Restif, T. J. McKinley, M. Sheppard, S. Achouri, B. Wei, P. Mastroeni, J. L. Wood, Dynamics of *Salmonella* infection of macrophages at the single cell level. *Journal of The Royal Society Interface* **9**, 2696-2707 (2012).
112. J. Hess, C. Ladel, D. Miko, S. Kaufmann, *Salmonella typhimurium* aroA-infection in gene-targeted immunodeficient mice: major role of CD4+ TCR-alpha beta cells and IFN-gamma in bacterial clearance independent of intracellular location. *The Journal of Immunology* **156**, 3321-3326 (1996).
113. C. M. Rosenberger, B. B. Finlay, Phagocyte sabotage: disruption of macrophage signalling by bacterial pathogens. *Nature reviews Molecular cell biology* **4**, 385-396 (2003).
114. J.-F. Dhainaut, N. Marin, A. Mignon, C. Vinsonneau, Hepatic response to sepsis: interaction between coagulation and inflammatory processes. *Critical care medicine* **29**, S42-S47 (2001).
115. H. W. Zimmermann, C. Trautwein, F. Tacke, Functional role of monocytes and macrophages for the inflammatory response in acute liver injury. *Frontiers in physiology* **3**, (2012).
116. H. Ishibashi, M. Nakamura, A. Komori, K. Migita, S. Shimoda, in *Seminars in immunopathology*. (Springer, 2009), vol. 31, pp. 399-409.
117. S. H. Gregory, A. J. Sagnimeni, E. J. Wing, Bacteria in the bloodstream are trapped in the liver and killed by immigrating neutrophils. *The Journal of Immunology* **157**, 2514-2520 (1996).
118. D. G. Russell, B. C. VanderVen, S. Glennie, H. Mwandumba, R. S. Heyderman, The macrophage marches on its phagosome: dynamic assays of phagosome function. *Nature Reviews Immunology* **9**, 594-600 (2009).
119. S. P. Otto, T. Day, *A biologist's guide to mathematical modeling in ecology and evolution*. (Princeton University Press, 2007), vol. 13.
120. D. A. Lauffenburger, J. J. Linderman, *Receptors: models for binding, trafficking, and signaling*. (Oxford University Press New York:, 1993), vol. 365.
121. M. Morelock, R. Ingraham, R. Betageri, S. Jakes, Determination of receptor-ligand kinetic and equilibrium binding constants using surface plasmon resonance: application to the lck SH2 domain and phosphotyrosyl peptides. *Journal of medicinal chemistry* **38**, 1309-1318 (1995).
122. R. Gesztelyi, J. Zsuga, A. Kemeny-Beke, B. Varga, B. Juhasz, A. Tosaki, The Hill equation and the origin of quantitative pharmacology. *Archive for history of exact sciences* **66**, 427-438 (2012).
123. M. Diesselhoff-den Dulk, R. Crofton, R. Van Furth, Origin and kinetics of Kupffer cells during an acute inflammatory response. *Immunology* **37**, 7 (1979).
124. M. Naito, G. Hasegawa, Y. Ebe, T. Yamamoto, Differentiation and function of Kupffer cells. *Medical Electron Microscopy* **37**, 16-28 (2004).

125. J. I. Gallin, R. Snyderman, D. T. Fearon, B. F. Haynes, C. Nathan, *Inflammation Basic: Principles and Clinical Correlates*. (Raven Press, New York, 1992).
126. J. A. Hewett, P. A. Jean, S. L. Kunkel, R. A. Roth, Relationship between tumor necrosis factor-alpha and neutrophils in endotoxin-induced liver injury. *American Journal of Physiology-Gastrointestinal and Liver Physiology* **265**, G1011-G1015 (1993).
127. S. K. Ramaiah, H. Jaeschke, Role of neutrophils in the pathogenesis of acute inflammatory liver injury. *Toxicologic pathology* **35**, 757-766 (2007).
128. H. L. Wright, R. J. Moots, R. C. Bucknall, S. W. Edwards, Neutrophil function in inflammation and inflammatory diseases. *Rheumatology* **49**, 1618-1631 (2010).
129. P. Lacy, J. L. Stow, Cytokine release from innate immune cells: association with diverse membrane trafficking pathways. *Blood* **118**, 9-18 (2011).
130. A. C. Stanley, P. Lacy, Pathways for cytokine secretion. *Physiology* **25**, 218-229 (2010).
131. D. L. Nelson, A. L. Lehninger, M. M. Cox, *Lehninger principles of biochemistry*. (Macmillan, 2008).
132. B. Drescher, F. Bai, Neutrophil in viral infections, friend or foe? *Virus research* **171**, 1-7 (2013).
133. A. Ashare, L. S. Powers, N. S. Butler, K. C. Doerschug, M. M. Monick, G. W. Hunninghake, Anti-inflammatory response is associated with mortality and severity of infection in sepsis. *American Journal of Physiology-Lung Cellular and Molecular Physiology* **288**, L633-L640 (2005).
134. H. Jaeschke, Mechanisms of Liver Injury. II. Mechanisms of neutrophil-induced liver cell injury during hepatic ischemia-reperfusion and other acute inflammatory conditions. *American Journal of Physiology-Gastrointestinal and Liver Physiology* **290**, G1083-G1088 (2006).
135. H. Jaeschke, M. A. Fisher, J. A. Lawson, C. A. Simmons, A. Farhood, D. A. Jones, Activation of caspase 3 (CPP32)-like proteases is essential for TNF- $\alpha$ -induced hepatic parenchymal cell apoptosis and neutrophil-mediated necrosis in a murine endotoxin shock model. *The Journal of Immunology* **160**, 3480-3486 (1998).
136. M. Schiraldi, A. Raucci, L. M. Muñoz, E. Livoti, B. Celona, E. Venereau, T. Apuzzo, F. De Marchis, M. Pedotti, A. Bachi, HMGB1 promotes recruitment of inflammatory cells to damaged tissues by forming a complex with CXCL12 and signaling via CXCR4. *The Journal of experimental medicine* **209**, 551-563 (2012).
137. K. R. Karlmark, R. Weiskirchen, H. W. Zimmermann, N. Gassler, F. Ginhoux, C. Weber, M. Merad, T. Luedde, C. Trautwein, F. Tacke, Hepatic recruitment of the inflammatory Gr1<sup>+</sup> monocyte subset upon liver injury promotes hepatic fibrosis. *Hepatology* **50**, 261-274 (2009).
138. F. Tacke, Functional role of intrahepatic monocyte subsets for the progression of liver inflammation and liver fibrosis in vivo. *Fibrogenesis Tissue Repair* **5**, S27 (2012).
139. G. Chen, J. Li, M. Ochani, B. Rendon-Mitchell, X. Qiang, S. Susarla, L. Ulloa, H. Yang, S. Fan, S. M. Goyert, Bacterial endotoxin stimulates macrophages to release HMGB1 partly through CD14- and TNF-dependent mechanisms. *Journal of leukocyte biology* **76**, 994-1001 (2004).
140. S. Willenbrock, O. Braun, J. Baumgart, S. Lange, C. Junghanss, A. Heisterkamp, I. Nolte, J. Bullerdiek, H. M. Escobar, TNF- $\alpha$  induced secretion of HMGB1 from non-immune canine mammary epithelial cells (MTH53A). *Cytokine* **57**, 210-220 (2012).

141. U. Grunwald, X. Fan, R. S. Jack, G. Workalemahu, A. Kallies, F. Stelter, C. Schütt, Monocytes can phagocytose Gram-negative bacteria by a CD14-dependent mechanism. *The Journal of Immunology* **157**, 4119-4125 (1996).
142. J. Savill, A. Wyllie, J. Henson, M. Walport, P. Henson, C. Haslett, Macrophage phagocytosis of aging neutrophils in inflammation. Programmed cell death in the neutrophil leads to its recognition by macrophages. *Journal of Clinical Investigation* **83**, 865 (1989).
143. R. Kokkola, E. Sundberg, A. K. Ulfgren, K. Palmblad, J. Li, H. Wang, L. Ulloa, H. Yang, X. J. Yan, R. Furie, High mobility group box chromosomal protein 1: a novel proinflammatory mediator in synovitis. *Arthritis & Rheumatism* **46**, 2598-2603 (2002).
144. C. Shi, P. Velázquez, T. M. Hohl, I. Leiner, M. L. Dustin, E. G. Pamer, Monocyte trafficking to hepatic sites of bacterial infection is chemokine independent and directed by focal intercellular adhesion molecule-1 expression. *The Journal of immunology* **184**, 6266-6274 (2010).
145. M. Bhatia, M. Brady, S. Shokuhi, S. Christmas, J. P. Neoptolemos, J. Slavin, Inflammatory mediators in acute pancreatitis. *The Journal of pathology* **190**, 117-125 (2000).
146. K. N. Couper, D. G. Blount, E. M. Riley, IL-10: the master regulator of immunity to infection. *The Journal of Immunology* **180**, 5771-5777 (2008).
147. Y. Geng, E. Gulbins, A. Altman, M. Lotz, Monocyte deactivation by interleukin 10 via inhibition of tyrosine kinase activity and the Ras signaling pathway. *Proceedings of the National Academy of Sciences* **91**, 8602-8606 (1994).
148. P. Wang, P. Wu, M. I. Siegel, R. W. Egan, M. M. Billah, IL-10 inhibits transcription of cytokine genes in human peripheral blood mononuclear cells. *The Journal of Immunology* **153**, 811-816 (1994).
149. P. Wang, P. Wu, M. I. Siegel, R. W. Egan, M. M. Billah, Interleukin (IL)-10 Inhibits Nuclear Factor B (NFB) Activation in Human Monocytes IL-10 AND IL-4 SUPPRESS CYTOKINE SYNTHESIS BY DIFFERENT MECHANISMS. *Journal of Biological Chemistry* **270**, 9558-9563 (1995).
150. A. J. Schottelius, M. W. Mayo, R. B. Sartor, A. S. Baldwin, Interleukin-10 signaling blocks inhibitor of  $\kappa$ B kinase activity and nuclear factor  $\kappa$ B DNA binding. *Journal of Biological Chemistry* **274**, 31868-31874 (1999).
151. F. Wan, M. J. Lenardo, Specification of DNA binding activity of NF- $\kappa$ B proteins. *Cold Spring Harbor perspectives in biology* **1**, a000067 (2009).
152. M. Figuera-Losada, P. V. LoGrasso, Enzyme kinetics and interaction studies for human JNK1 $\beta$ 1 and substrates activating transcription factor 2 (ATF2) and c-Jun N-terminal kinase (c-Jun). *Journal of Biological Chemistry* **287**, 13291-13302 (2012).
153. A. Dhooge, W. Govaerts, Y. A. Kuznetsov, in *Computational Science—ICCS 2003*. (Springer, 2003), pp. 701-710.
154. B. Hassard, Y. Wan, Bifurcation formulae derived from center manifold theory. *Journal of Mathematical Analysis and Applications* **63**, 297-312 (1978).
155. T. van der Poll, A. Marchant, W. A. Buurman, L. Berman, C. V. Keogh, D. D. Lazarus, L. Nguyen, M. Goldman, L. L. Moldawer, S. F. Lowry, Endogenous IL-10 protects mice from death during septic peritonitis. *The Journal of immunology* **155**, 5397-5401 (1995).



156. D. G. Remick, S. J. Garg, D. E. Newcomb, G. Wollenberg, T. K. Huie, G. L. Bolgos, Exogenous interleukin-10 fails to decrease the mortality or morbidity of sepsis. *Critical care medicine* **26**, 895-904 (1998).
157. H. Louis, J. L. Van Laethem, W. Wu, E. Quertinmont, C. Degraef, K. Van den Berg, A. Demols, M. Goldman, O. Le Moine, A. Geerts, Interleukin - 10 controls neutrophilic infiltration, hepatocyte proliferation, and liver fibrosis induced by carbon tetrachloride in mice. *Hepatology* **28**, 1607-1615 (1998).
158. D. G. Brooks, M. J. Trifilo, K. H. Edelmann, L. Teyton, D. B. McGavern, M. B. Oldstone, Interleukin-10 determines viral clearance or persistence in vivo. *Nature medicine* **12**, 1301-1309 (2006).
159. M. Kylänpää-Bäck, Definitions for sepsis and organ failure and guidelines for the use of innovative therapies in sepsis. *Crit Care Med* **20**, 864-874 (1992).
160. R. Batrla, M. Linnebacher, W. Rudy, S. Stumm, D. Wallwiener, B. Gückel, CD40-expressing carcinoma cells induce down-regulation of CD40 ligand (CD154) and impair T-cell functions. *Cancer research* **62**, 2052-2057 (2002).
161. W. L. Redmond, C. E. Ruby, A. D. Weinberg, The role of OX40-mediated co-stimulation in T-cell activation and survival. *Critical Reviews™ in Immunology* **29**, (2009).
162. C. J. Workman, L. S. Cauley, I.-J. Kim, M. A. Blackman, D. L. Woodland, D. A. Vignali, Lymphocyte activation gene-3 (CD223) regulates the size of the expanding T cell population following antigen activation in vivo. *The Journal of Immunology* **172**, 5450-5455 (2004).
163. K. C. Howland, L. J. Ausubel, C. A. London, A. K. Abbas, The roles of CD28 and CD40 ligand in T cell activation and tolerance. *The Journal of Immunology* **164**, 4465-4470 (2000).
164. G. J. Bellingan, H. Caldwell, S. Howie, I. Dransfield, C. Haslett, In vivo fate of the inflammatory macrophage during the resolution of inflammation: inflammatory macrophages do not die locally, but emigrate to the draining lymph nodes. *The Journal of Immunology* **157**, 2577-2585 (1996).
165. H. F. Lodish, A. Berk, S. L. Zipursky, P. Matsudaira, D. Baltimore, J. Darnell, *Molecular cell biology*. (WH Freeman New York, 2000), vol. 4.
166. K. R. Kasten, J. Tschöp, S. G. Adediran, D. A. Hildeman, C. C. Caldwell, T cells are potent early mediators of the host response to sepsis. *Shock* **34**, 327-336 (2010).
167. T. Kasahara, J. Hooks, S. Dougherty, J. Oppenheim, Interleukin 2-mediated immune interferon (IFN-gamma) production by human T cells and T cell subsets. *The Journal of Immunology* **130**, 1784-1789 (1983).
168. D. M. Mosser, The many faces of macrophage activation. *Journal of leukocyte biology* **73**, 209-212 (2003).
169. T. K. Held, X. Weihua, L. Yuan, D. V. Kalvakolanu, A. S. Cross, Gamma interferon augments macrophage activation by lipopolysaccharide by two distinct mechanisms, at the signal transduction level and via an autocrine mechanism involving tumor necrosis factor alpha and interleukin-1. *Infection and immunity* **67**, 206-212 (1999).
170. R. R. Ganta, C. Cheng, E. C. Miller, B. L. McGuire, L. Peddireddi, K. R. Sirigireddy, S. K. Chapes, Differential clearance and immune responses to tick cell-derived versus macrophage culture-derived Ehrlichia chaffeensis in mice. *Infection and immunity* **75**, 135-145 (2007).

171. R. Witthaut, A. Farhood, C. W. Smith, H. Jaeschke, Complement and tumor necrosis factor-alpha contribute to Mac-1 (CD11b/CD18) up-regulation and systemic neutrophil activation during endotoxemia in vivo. *Journal of leukocyte biology* **55**, 105-111 (1994).
172. S. W. Lindgren, I. Stojiljkovic, F. Heffron, Macrophage killing is an essential virulence mechanism of Salmonella typhimurium. *Proceedings of the National Academy of Sciences* **93**, 4197-4201 (1996).
173. S. Helaine, J. A. Thompson, K. G. Watson, M. Liu, C. Boyle, D. W. Holden, Dynamics of intracellular bacterial replication at the single cell level. *Proceedings of the National Academy of Sciences* **107**, 3746-3751 (2010).
174. S. M. van Schaik, A. K. Abbas, Role of T cells in a murine model of Escherichia coli sepsis. *European journal of immunology* **37**, 3101-3110 (2007).
175. O. Rigato, S. Ujvari, A. Castelo, R. Salomao, Tumor necrosis factor alpha (TNF- $\alpha$ ) and sepsis: evidence for a role in host defense. *Infection* **24**, 314-318 (1996).
176. N. Nnalue, A. Shnyra, K. Hultenby, A. Lindberg, Salmonella choleraesuis and Salmonella typhimurium associated with liver cells after intravenous inoculation of rats are localized mainly in Kupffer cells and multiply intracellularly. *Infection and immunity* **60**, 2758-2768 (1992).
177. M. Saraiva, A. O'Garra, The regulation of IL-10 production by immune cells. *Nature Reviews Immunology* **10**, 170-181 (2010).
178. W. Wakeland, L. Macovsky, G. An, in *Proceedings of the 2007 spring simulation multiconference-Volume 2*. (Society for Computer Simulation International, 2007), pp. 39-46.
179. Netlogo. (<https://ccl.northwestern.edu/netlogo/4.0.4/>, 2005).
180. V. Bocci, Interleukins. Clinical pharmacokinetics and practical implications. *Clinical Pharmacokinetics* **21**, 274-284 (1991).
181. W. Reyes, S. Brimiouille, J.-L. Vincent, Septic shock without documented infection: an uncommon entity with a high mortality. *Intensive care medicine* **25**, 1267-1270 (1999).
182. J. Branger, B. van den Blink, S. Weijer, J. Madwed, C. L. Bos, A. Gupta, C.-L. Yong, S. H. Polmar, D. P. Olszyna, C. E. Hack, Anti-inflammatory effects of a p38 mitogen-activated protein kinase inhibitor during human endotoxemia. *The journal of immunology* **168**, 4070-4077 (2002).
183. W. S. Spector, Handbook of biological data. *Handbook of biological data.*, (1956).
184. E. O. Wilson, The encyclopedia of life. *Trends in Ecology & Evolution* **18**, 77-80 (2003).
185. A. Coxon, T. Tang, T. N. Mayadas, Cytokine-Activated Endothelial Cells Delay Neutrophil Apoptosis in Vitro and in Vivo A Role for Granulocyte/Macrophage Colony-Stimulating Factor. *The Journal of experimental medicine* **190**, 923-934 (1999).
186. A. C. Fuchs, E. V. Granowitz, L. Shapiro, E. Vannier, G. Lonnemann, J. B. Angel, J. S. Kennedy, A. R. Rabson, E. Radwanski, M. B. Affrime, Clinical, hematologic, and immunologic effects of interleukin-10 in humans. *Journal of clinical immunology* **16**, 291-303 (1996).
187. R. D. Huhn, E. Radwanski, J. Gallo, M. B. Affrime, R. Sabo, G. Gonyo, A. Monge, D. L. Cutler, Pharmacodynamics of subcutaneous recombinant human interleukin - 10 in healthy volunteers. *Clinical Pharmacology & Therapeutics* **62**, 171-180 (1997).
188. B. Eiseman, R. Beart, L. Norton, Multiple organ failure. *Surgery, gynecology & obstetrics* **144**, 323-326 (1977).

189. H. Wang, H. Yang, C. J. CZURA, A. E. Sama, K. J. Tracey, HMGB1 as a late mediator of lethal systemic inflammation. *American Journal of Respiratory and Critical Care Medicine* **164**, 1768-1773 (2001).
190. J. Rello, T. Lisboa, M. Lujan, M. Gallego, C. Kee, I. Kay, D. Lopez, G. W. Waterer, Severity of pneumococcal pneumonia associated with genomic bacterial load. *CHEST Journal* **136**, 832-840 (2009).
191. D. Annane, V. Sébille, C. Charpentier, P.-E. Bollaert, B. François, J.-M. Korach, G. Capellier, Y. Cohen, E. Azoulay, G. Troché, Effect of treatment with low doses of hydrocortisone and fludrocortisone on mortality in patients with septic shock. *Jama* **288**, 862-871 (2002).
192. S. K. Chapes, A. A. Beharka, Salmonella infections in the absence of the major histocompatibility complex II. *Journal of leukocyte biology* **63**, 297-304 (1998).
193. M. L. Hart, D. A. Mosier, S. K. Chapes, Toll-like receptor 4-positive macrophages protect mice from Pasteurella pneumotropica-induced pneumonia. *Infection and immunity* **71**, 663-670 (2003).
194. H. V. D. Parunak, R. Savit, R. L. Riolo, in *Multi-agent systems and agent-based simulation*. (Springer, 1998), pp. 10-25.
195. G. An, Q. Mi, J. Dutta - Moscato, Y. Vodovotz, Agent - based models in translational systems biology. *Wiley Interdisciplinary Reviews: Systems Biology and Medicine* **1**, 159-171 (2009).
196. D. E. Malarkey, K. Johnson, L. Ryan, G. Boorman, R. R. Maronpot, New insights into functional aspects of liver morphology. *Toxicologic Pathology* **33**, 27-34 (2005).
197. D. J. Farrell, J. E. Hines, A. F. Walls, P. J. Kelly, M. K. Bennett, A. D. Burt, Intrahepatic mast cells in chronic liver diseases. *Hepatology* **22**, 1175-1181 (1995).
198. J. W. Conlan, R. J. North, Early pathogenesis of infection in the liver with the facultative intracellular bacteria *Listeria monocytogenes*, *Francisella tularensis*, and *Salmonella typhimurium* involves lysis of infected hepatocytes by leukocytes. *Infection and immunity* **60**, 5164-5171 (1992).
199. A. Richter-Dahlfors, A. M. Buchan, B. B. Finlay, Murine salmonellosis studied by confocal microscopy: *Salmonella typhimurium* resides intracellularly inside macrophages and exerts a cytotoxic effect on phagocytes in vivo. *The Journal of experimental medicine* **186**, 569-580 (1997).
200. J. W. Conlan, Neutrophils prevent extracellular colonization of the liver microvasculature by *Salmonella typhimurium*. *Infection and immunity* **64**, 1043-1047 (1996).
201. J. M. Schlauch, How does the oxidative burst of macrophages kill bacteria? Still an open question. *Molecular microbiology* **80**, 580-583 (2011).
202. M. Nagl, L. Kacani, B. Müllauer, E.-M. Lemberger, H. Stoiber, G. M. Sprinzl, H. Schennach, M. P. Dierich, Phagocytosis and killing of bacteria by professional phagocytes and dendritic cells. *Clinical and diagnostic laboratory immunology* **9**, 1165-1168 (2002).
203. T. W. Du Clos, Function of C-reactive protein. *Annals of medicine* **32**, 274-278 (2000).
204. A. Inatsu, M. Kinoshita, H. Nakashima, J. Shimizu, D. Saitoh, S. Tamai, S. Seki, Novel mechanism of C - reactive protein for enhancing mouse liver innate immunity. *Hepatology* **49**, 2044-2054 (2009).
205. S. Black, I. Kushner, D. Samols, C-reactive protein. *Journal of Biological Chemistry* **279**, 48487-48490 (2004).

206. B. Alberts, D. Bray, J. Lewis, M. Raff, K. Roberts, J. D. Watson, A. Grimstone, Molecular Biology of the Cell (3rd edn). *Trends in Biochemical Sciences* **20**, 210-210 (1995).
207. S. A. D. Santos, D. R. D. Andrade Júnior, D. R. D. Andrade, Tnf- $\alpha$  production and apoptosis in hepatocytes after listeria monocytogenes and salmonella typhimurium invasion. *Revista do Instituto de Medicina Tropical de São Paulo* **53**, 107-112 (2011).
208. H. Huang, G. Nace, K. McDonald, S. Tai, J. Klune, B. Rosborough, Q. Ding, P. Loughran, X. Zhu, D. Beer-Stolz, Hepatocyte specific HMGB1 deletion worsens the injury in liver ischemia/reperfusion: A role for intracellular HMGB1 in cellular protection. *Hepatology (Baltimore, Md.)*, (2013).
209. H. Jaeschke, M. L. Bajt, Intracellular signaling mechanisms of acetaminophen-induced liver cell death. *Toxicological sciences* **89**, 31-41 (2006).
210. H. Jaeschke, C. W. Smith, Mechanisms of neutrophil-induced parenchymal cell injury. *Journal of leukocyte biology* **61**, 647-653 (1997).
211. S. Elmore, Apoptosis: a review of programmed cell death. *Toxicologic pathology* **35**, 495-516 (2007).
212. T. TAKEISHI, K. HIRANO, T. KOBAYASHI, G. HASEGAWA, K. HATAKEYAMA, M. NAITO, The role of Kupffer cells in liver regeneration. *Archives of histology and cytology* **62**, 413-422 (1999).
213. K. R. Kasten, J. T. Muenzer, C. C. Caldwell, Neutrophils are significant producers of IL-10 during sepsis. *Biochemical and biophysical research communications* **393**, 28-31 (2010).
214. V. Papayannopoulos, K. D. Metzler, A. Hakkim, A. Zychlinsky, Neutrophil elastase and myeloperoxidase regulate the formation of neutrophil extracellular traps. *The Journal of cell biology* **191**, 677-691 (2010).
215. V. Brinkmann, U. Reichard, C. Goosmann, B. Fauler, Y. Uhlemann, D. S. Weiss, Y. Weinrauch, A. Zychlinsky, Neutrophil extracellular traps kill bacteria. *science* **303**, 1532-1535 (2004).
216. E. Liaskou, D. V. Wilson, Y. H. Oo, Innate immune cells in liver inflammation. *Mediators of inflammation* **2012**, (2012).
217. P. F. Lalor, P. Shields, A. J. Grant, D. H. Adams, Recruitment of lymphocytes to the human liver. *Immunology and cell biology* **80**, 52-64 (2002).
218. A. Tsung, J. R. Klune, X. Zhang, G. Jeyabalan, Z. Cao, X. Peng, D. B. Stolz, D. A. Geller, M. R. Rosengart, T. R. Billiar, HMGB1 release induced by liver ischemia involves Toll-like receptor 4-dependent reactive oxygen species production and calcium-mediated signaling. *The Journal of experimental medicine* **204**, 2913-2923 (2007).
219. J. Haveman, A. M. Kobold, J. C. Tervaert, A. Van den Berg, J. Tulleken, C. Kallenberg, T. The, The central role of monocytes in the pathogenesis of sepsis: consequences for immunomonitoring and treatment. *The Netherlands journal of medicine* **55**, 132-141 (1999).
220. B. Gao, Hepatoprotective and anti - inflammatory cytokines in alcoholic liver disease. *Journal of gastroenterology and hepatology* **27**, 89-93 (2012).
221. K. K. Yang, B. G. Dorner, U. Merkel, B. Ryffel, C. Schütt, D. Golenbock, M. W. Freeman, R. S. Jack, Neutrophil influx in response to a peritoneal infection with Salmonella is delayed in lipopolysaccharide-binding protein or CD14-deficient mice. *The Journal of Immunology* **169**, 4475-4480 (2002).

222. C. Shi, E. G. Pamer, Monocyte recruitment during infection and inflammation. *Nature Reviews Immunology* **11**, 762-774 (2011).
223. A. R. Schenkel, Z. Mamdouh, W. A. Muller, Locomotion of monocytes on endothelium is a critical step during extravasation. *Nature immunology* **5**, 393-400 (2004).
224. J. I. Steinfeld, J. S. Francisco, W. L. Hase, *Chemical kinetics and dynamics*. (Prentice Hall Englewood Cliffs (New Jersey), 1989), vol. 3.
225. J. C. Tan, S. R. Indelicato, S. K. Narula, P. J. Zavodny, C. Chou, Characterization of interleukin-10 receptors on human and mouse cells. *Journal of Biological Chemistry* **268**, 21053-21059 (1993).
226. D. Bharadwaj, M.-P. Stein, M. Volzer, C. Mold, T. W. Du Clos, The major receptor for C-reactive protein on leukocytes is Fc $\gamma$  receptor II. *The Journal of experimental medicine* **190**, 585-590 (1999).
227. M. Leist, F. Gantner, S. Jilg, A. Wendel, Activation of the 55 kDa TNF receptor is necessary and sufficient for TNF-induced liver failure, hepatocyte apoptosis, and nitrite release. *The Journal of Immunology* **154**, 1307-1316 (1995).
228. V. Brinkmann, A. Zychlinsky, Neutrophil extracellular traps: is immunity the second function of chromatin? *The Journal of cell biology* **198**, 773-783 (2012).
229. Y. Weinrauch, D. Drujan, S. D. Shapiro, J. Weiss, A. Zychlinsky, Neutrophil elastase targets virulence factors of enterobacteria. *Nature* **417**, 91-94 (2002).
230. R. G. Ihaka, Robert. (2014).
231. M. Sheppard, C. Webb, F. Heath, V. Mallows, R. Emilianus, D. Maskell, P. Mastroeni, Dynamics of bacterial growth and distribution within the liver during Salmonella infection. *Cellular microbiology* **5**, 593-600 (2003).
232. C. J. Czura, H. Yang, K. J. Tracey, High mobility group box-1 as a therapeutic target downstream of tumor necrosis factor. *Journal of Infectious Diseases* **187**, S391-S396 (2003).
233. D. C. Lau, B. Dhillon, H. Yan, P. E. Szmitko, S. Verma, Adipokines: molecular links between obesity and atherosclerosis. *American Journal of Physiology-Heart and Circulatory Physiology* **288**, H2031-H2041 (2005).
234. P. Póvoa, C-reactive protein: a valuable marker of sepsis. *Intensive care medicine* **28**, 235-243 (2002).
235. C. S. Xu, Y. Jiang, L. X. Zhang, C. F. Chang, G. P. Wang, R. J. Shi, Y. J. Yang, The role of kupffer cells in rat liver regeneration revealed by cell - specific microarray analysis. *Journal of cellular biochemistry* **113**, 229-237 (2012).
236. M. Theodorakopoulou, N. Skabas, M. Lignos, A. Kandili, S. Ioannidou, E. Kavadia, A. Armaganidis, C-reactive protein as a marker of septic shock and outcome in the intensive care unit. *Critical Care* **9**, 1-1 (2005).
237. D. C. Angus, L. Yang, L. Kong, J. A. Kellum, R. L. Delude, K. J. Tracey, L. Weissfeld, G. Investigators, Circulating high-mobility group box 1 (HMGB1) concentrations are elevated in both uncomplicated pneumonia and pneumonia with severe sepsis\*. *Critical care medicine* **35**, 1061-1067 (2007).
238. B. Goswami, M. Rajappa, V. Mallika, D. K. Shukla, S. Kumar, TNF- $\alpha$ /IL-10 ratio and C-reactive protein as markers of the inflammatory response in CAD-prone North Indian patients with acute myocardial infarction. *Clinica Chimica Acta* **408**, 14-18 (2009).
239. I. Dimopoulou, A. Armaganidis, E. Douka, I. Mavrou, C. Augustatou, P. Kopterides, P. Lyberopoulos, M. Tzanela, S. E. Orfanos, E. Pelekanou, Tumour necrosis factor-alpha

- (TNF $\alpha$ ) and interleukin-10 are crucial mediators in post-operative systemic inflammatory response and determine the occurrence of complications after major abdominal surgery. *Cytokine* **37**, 55-61 (2007).
240. H. Syrjälä, H. M. SURCEL, J. Ilonen, Low CD4/CD8 T lymphocyte ratio in acute myocardial infarction. *Clinical & Experimental Immunology* **83**, 326-328 (1991).
  241. X.-j. Xia, B.-c. Liu, J.-s. Su, H. Pei, H. Chen, L. Li, Y.-f. Liu, Preoperative CD4 count or CD4/CD8 ratio as a useful indicator for postoperative sepsis in HIV-infected patients undergoing abdominal operations. *Journal of Surgical Research* **174**, e25-e30 (2012).
  242. M. Benoit, B. Desnues, J.-L. Mege, Macrophage polarization in bacterial infections. *The Journal of Immunology* **181**, 3733-3739 (2008).
  243. D. R. Blake, R. Allen, Inflammation: Basic Principles and Clinical Correlates. *Annals of the rheumatic diseases* **47**, 792 (1988).
  244. Y. Souwer, A. Griekspoor, T. Jorritsma, J. de Wit, H. Janssen, J. Neeffjes, S. M. van Ham, B cell receptor-mediated internalization of salmonella: a novel pathway for autonomous B cell activation and antibody production. *The journal of immunology* **182**, 7473-7481 (2009).
  245. K.-H. Chung, H.-S. Hwang, K.-Y. Lee, Kinetics of Salmonella typhimurium binding with antibody by immunoassays using a surface plasmon resonance biosensor. *Journal of Industrial and Engineering Chemistry* **16**, 115-118 (2010).
  246. S. Gibot, F. Massin, A. Cravoisy, D. Barraud, L. Nace, B. Levy, P.-E. Bollaert, High-mobility group box 1 protein plasma concentrations during septic shock. *Intensive care medicine* **33**, 1347-1353 (2007).
  247. R. S. Hotchkiss, I. E. Karl, The pathophysiology and treatment of sepsis. *New England Journal of Medicine* **348**, 138-150 (2003).
  248. R. Schlatter, K. Schmich, A. Lutz, J. Trefzger, O. Sawodny, M. Ederer, I. Merfort, Modeling the TNF $\alpha$ -induced apoptosis pathway in hepatocytes. *PloS one* **6**, e18646 (2011).
  249. S. N. Abraham, A. L. S. John, Mast cell-orchestrated immunity to pathogens. *Nature Reviews Immunology* **10**, 440-452 (2010).
  250. M. Maurer, J. Wedemeyer, M. Metz, A. M. Piliponsky, K. Weller, D. Chatterjea, D. E. Clouthier, M. M. Yanagisawa, M. Tsai, S. J. Galli, Mast cells promote homeostasis by limiting endothelin-1-induced toxicity. *Nature* **432**, 512-516 (2004).
  251. J. M. S. Clair, C. T. Pham, S. A. Villalta, G. H. Caughey, P. J. Wolters, Mast cell dipeptidyl peptidase I mediates survival from sepsis. *Journal of Clinical Investigation* **113**, 628 (2004).
  252. S. N. Abraham, R. Malaviya, Mast cells in infection and immunity. *Infection and immunity* **65**, 3501 (1997).
  253. N. Dietrich, M. Rohde, R. Geffers, A. Kröger, H. Hauser, S. Weiss, N. O. Gekara, Mast cells elicit proinflammatory but not type I interferon responses upon activation of TLRs by bacteria. *Proceedings of the National Academy of Sciences* **107**, 8748-8753 (2010).
  254. D. M. Mosser, X. Zhang, Measuring Opsonic Phagocytosis via Fc $\gamma$  Receptors and Complement Receptors on Macrophages. *Current Protocols in Immunology*, 14.27. 11-14.27. 11 (2011).
  255. X. Liu, L. Lu, Z. Yang, S. Palaniyandi, R. Zeng, L.-Y. Gao, D. M. Mosser, D. C. Roopenian, X. Zhu, The neonatal FcR-mediated presentation of immune-complexed

- antigen is associated with endosomal and phagosomal pH and antigen stability in macrophages and dendritic cells. *The Journal of Immunology* **186**, 4674-4686 (2011).
256. L. Wang, J. A. Bastarache, L. B. Ware, The coagulation cascade in sepsis. *Current pharmaceutical design* **14**, 1860-1869 (2008).
  257. O. Alagoz, H. Hsu, A. J. Schaefer, M. S. Roberts, Markov decision processes: a tool for sequential decision making under uncertainty. *Medical Decision Making*, (2009).
  258. F. A. Sonnenberg, J. R. Beck, Markov models in medical decision making a practical guide. *Medical decision making* **13**, 322-338 (1993).
  259. C. Lefèvre, Optimal control of a birth and death epidemic process. *Operations Research* **29**, 971-982 (1981).
  260. C. Hu, W. S. Lovejoy, S. L. Shafer, Comparison of some suboptimal control policies in medical drug therapy. *Operations Research* **44**, 696-709 (1996).
  261. O. Alagoz, L. M. Maillart, A. J. Schaefer, M. S. Roberts, The optimal timing of living-donor liver transplantation. *Management Science* **50**, 1420-1430 (2004).
  262. D. M. Faissol, P. M. Griffin, J. L. Swann, in *INFORMS international meeting*. (2007), pp. 11.
  263. R. Alterovitz, M. Branicky, K. Goldberg, in *Algorithmic Foundation of Robotics VII*. (Springer, 2008), pp. 319-334.
  264. L. M. Maillart, J. S. Ivy, S. Ransom, K. Diehl, Assessing dynamic breast cancer screening policies. *Operations Research* **56**, 1411-1427 (2008).
  265. B. T. Denton, M. Kurt, N. D. Shah, S. C. Bryant, S. A. Smith, Optimizing the start time of statin therapy for patients with diabetes. *Medical Decision Making* **29**, 351-367 (2009).
  266. J. Chhatwal, O. Alagoz, E. S. Burnside, Optimal breast biopsy decision-making based on mammographic features and demographic factors. *Operations research* **58**, 1577-1591 (2010).
  267. G. S. Martin, Sepsis, severe sepsis and septic shock: changes in incidence, pathogens and outcomes. (2012).
  268. C. S. Group, The effectiveness of hydrocortisone in the management of severe infections. *JAMA: The Journal of the American Medical Association* **183**, 462-465 (1963).
  269. R. Lefering, E. A. Neugebauer, Steroid controversy in sepsis and septic shock: a meta-analysis. *Critical care medicine* **23**, 1294-1303 (1995).
  270. B. Beutler, I. Milsark, A. Cerami, Passive immunization against cachectin/tumor necrosis factor protects mice from lethal effect of endotoxin. *Science* **229**, 869-871 (1985).
  271. K. J. Tracey, B. Beutler, S. F. Lowry, J. Merryweather, S. Wolpe, I. W. Milsark, R. J. Hariri, T. J. Fahey, A. Zentella, J. D. Albert, Shock and tissue injury induced by recombinant human cachectin. *Science* **234**, 470-474 (1986).
  272. U. Andersson, H. Wang, K. Palmblad, High mobility group 1 protein stimulates proinflammatory cytokine synthesis in human monocytes. *J Exp Med* **192**, 655-657 (2000).
  273. H. Wang, H. Liao, M. Ochani, M. Justiniani, X. Lin, L. Yang, Y. Al-Abed, H. Wang, C. Metz, E. J. Miller, Cholinergic agonists inhibit HMGB1 release and improve survival in experimental sepsis. *Nature medicine* **10**, 1216-1221 (2004).
  274. M. S. R. Frausto, D. Pittet, T. Hwang, R. F. Woolson, R. P. Wenzel, The dynamics of disease progression in sepsis: Markov modeling describing the natural history and the likely impact of effective antisepsis agents. *Clinical infectious diseases* **27**, 185-190 (1998).

275. R. S. Sutton, D. Precup, S. Singh, Between MDPs and semi-MDPs: A framework for temporal abstraction in reinforcement learning. *Artificial intelligence* **112**, 181-211 (1999).
276. M. Baykal-Gürsoy, K. Gürsoy, SEMI-MARKOV DECISION PROCESSES. *Probability in the Engineering and Informational Sciences* **21**, 635-657 (2007).
277. A. Padkin, C. Goldfrad, A. R. Brady, D. Young, N. Black, K. Rowan, Epidemiology of severe sepsis occurring in the first 24 hrs in intensive care units in England, Wales, and Northern Ireland. *Critical care medicine* **31**, 2332-2338 (2003).
278. Y. Huang, X. Guo, Finite horizon semi-Markov decision processes with application to maintenance systems. *European Journal of Operational Research* **212**, 131-140 (2011).
279. H. Yang, H. Wang, C. J. Czura, K. J. Tracey, HMGB1 as a cytokine and therapeutic target. *Journal of endotoxin research* **8**, 469-472 (2002).
280. S. Yang, K. Hirooka, Y. Liu, T. Fujita, K. Fukuda, T. Nakamura, T. Itano, J. Zhang, M. Nishibori, F. Shiraga, Deleterious role of anti-high mobility group box 1 monoclonal antibody in retinal ischemia-reperfusion injury. *Current eye research* **36**, 1037-1046 (2011).
281. L. Bouwens, M. Baekeland, R. de Zanger, E. Wisse, Quantitation, tissue distribution and proliferation kinetics of Kupffer cells in normal rat liver. *Hepatology* **6**, 718-722 (1986).
282. T. P. Stossel, R. J. Mason, J. Hartwig, M. Vaughan, Quantitative studies of phagocytosis by polymorphonuclear leukocytes: use of emulsions to measure the initial rate of phagocytosis. *Journal of Clinical Investigation* **51**, 615 (1972).
283. M. B. Hampton, M. Vissers, C. C. Winterbourn, A single assay for measuring the rates of phagocytosis and bacterial killing by neutrophils. *Journal of leukocyte biology* **55**, 147-152 (1994).
284. M. Bemelmans, D. Gouma, W. Buurman, Influence of nephrectomy on tumor necrosis factor clearance in a murine model. *The Journal of Immunology* **150**, 2007-2017 (1993).
285. R. Boxio, C. Bossenmeyer-Pourié, N. Steinckwich, C. Dournon, O. Nüße, Mouse bone marrow contains large numbers of functionally competent neutrophils. *Journal of leukocyte biology* **75**, 604-611 (2004).
286. P. K. Lund, E. Namork, S. H. Brorson, Å.-B. Westvik, G. B. Joø, R. Øvstebø, P. Kierulf, The fate of monocytes during 24 h of culture as revealed by flow cytometry and electron microscopy. *Journal of immunological methods* **270**, 63-76 (2002).
287. A. Ahuja, S. M. Anderson, A. Khalil, M. J. Shlomchik, Maintenance of the plasma cell pool is independent of memory B cells. *Proceedings of the National Academy of Sciences* **105**, 4802-4807 (2008).
288. W. A. Langley, S. N. Mueller, R. Ahmed, Memory B cells are required to maintain long-lived plasma cells in mice following viral infections. *The Journal of Immunology* **182**, 132.116 (2009).
289. P. Vieira, K. Rajewsky, The half - lives of serum immunoglobulins in adult mice. *European journal of immunology* **18**, 313-316 (1988).
290. D. M. Underhill, M. Bassetti, A. Rudensky, A. Aderem, Dynamic interactions of macrophages with T cells during antigen presentation. *The Journal of experimental medicine* **190**, 1909-1914 (1999).
291. S. H.-F. Macdonald, E. Woodward, M. M. Coleman, E. R. Dorris, P. Nadarajan, W.-M. Chew, A.-M. McLaughlin, J. Keane, Networked T cell death following macrophage infection by Mycobacterium tuberculosis. *PloS one* **7**, e38488 (2012).



292. B. Benacerraf, M. M. Sebestyen, S. Schlossman, A quantitative study of the kinetics of blood clearance of P32-labelled Escherichia coli and staphylococci by the reticulo-endothelial system. *The Journal of experimental medicine* **110**, 27-48 (1959).
293. P. Lacy, Mechanisms of degranulation in neutrophils. *Allergy Asthma Clin Immunol* **2**, 98-108 (2006).
294. M. A. Kovach, M. N. Ballinger, M. W. Newstead, X. Zeng, U. Bhan, F.-s. Yu, B. B. Moore, R. L. Gallo, T. J. Standiford, Cathelicidin-related antimicrobial peptide is required for effective lung mucosal immunity in Gram-negative bacterial pneumonia. *The Journal of Immunology* **189**, 304-311 (2012).
295. M. Guicciardi, G. Gores, Apoptosis: a mechanism of acute and chronic liver injury. *Gut* **54**, 1024-1033 (2005).
296. H. Neumann, M. Kotter, R. Franklin, Debris clearance by microglia: an essential link between degeneration and regeneration. *Brain* **132**, 288-295 (2009).
297. M. P. Holt, L. Cheng, C. Ju, Identification and characterization of infiltrating macrophages in acetaminophen-induced liver injury. *Journal of leukocyte biology* **84**, 1410-1421 (2008).
298. Z. Bian, Y. Guo, B. Ha, K. Zen, Y. Liu, Regulation of the inflammatory response: enhancing neutrophil infiltration under chronic inflammatory conditions. *The Journal of Immunology* **188**, 844-853 (2012).
299. R. Van Furth, M. M. Diesselhoff-den Dulk, H. Mattie, Quantitative study on the production and kinetics of mononuclear phagocytes during an acute inflammatory reaction. *The Journal of experimental medicine* **138**, 1314-1330 (1973).
300. S. B. Brown, J. Savill, Phagocytosis triggers macrophage release of Fas ligand and induces apoptosis of bystander leukocytes. *The Journal of Immunology* **162**, 480-485 (1999).
301. J. A. Smith, Neutrophils, host defense, and inflammation: a double-edged sword. *Journal of Leukocyte Biology* **56**, 672-686 (1994).
302. G. Cox, J. Crossley, Z. Xing, Macrophage engulfment of apoptotic neutrophils contributes to the resolution of acute pulmonary inflammation in vivo. *American journal of respiratory cell and molecular biology* **12**, 232-237 (1995).
303. J. Savill, C. Haslett, in *Seminars in cell biology*. (Elsevier, 1995), vol. 6, pp. 385-393.
304. M. T. Silva, Macrophage phagocytosis of neutrophils at inflammatory/infectious foci: a cooperative mechanism in the control of infection and infectious inflammation. *Journal of leukocyte biology* **89**, 675-683 (2011).
305. E. Helk, H. Bernin, T. Ernst, H. Ittrich, T. Jacobs, J. Heeren, F. Tacke, E. Tannich, H. Lotter, TNF $\alpha$ -mediated liver destruction by Kupffer cells and Ly6Chi monocytes during *Entamoeba histolytica* infection. *PLoS pathogens* **9**, e1003096 (2013).
306. M. Indramohan, A. N. Sieve, T. J. Break, R. E. Berg, Inflammatory monocyte recruitment is regulated by interleukin-23 during systemic bacterial infection. *Infection and immunity* **80**, 4099-4105 (2012).
307. Y. Zhang, M. J. Morgan, K. Chen, S. Choksi, Z.-g. Liu, Induction of autophagy is essential for monocyte-macrophage differentiation. *Blood* **119**, 2895-2905 (2012).
308. K. Zen, J. Masuda, J. Ogata, Monocyte-derived macrophages prime peripheral T cells to undergo apoptosis by cell-cell contact via ICAM-1/LFA-1-dependent mechanism. *Immunobiology* **195**, 323-333 (1996).

309. S. P. Ballou, G. Lozanski, Induction of inflammatory cytokine release from cultured human monocytes by C-reactive protein. *Cytokine* **4**, 361-368 (1992).
310. R. Crofton, M. M. Diesselhoff-den Dulk, R. v. Furth, The origin, kinetics, and characteristics of the Kupffer cells in the normal steady state. *The Journal of experimental medicine* **148**, 1-17 (1978).
311. I. Klein, J. C. Cornejo, N. K. Polakos, B. John, S. A. Wuensch, D. J. Topham, R. H. Pierce, I. N. Crispe, Kupffer cell heterogeneity: functional properties of bone marrow-derived and sessile hepatic macrophages. *Blood* **110**, 4077-4085 (2007).
312. M.-R. Losser, C. Bernard, J.-L. Beaudoux, C. Pison, D. Payen, Glucose modulates hemodynamic, metabolic, and inflammatory responses to lipopolysaccharide in rabbits. *Journal of Applied Physiology* **83**, 1566-1574 (1997).
313. J. Xaus, M. Comalada, A. F. Villedor, J. Lloberas, F. López-Soriano, J. M. Argilés, C. Bogdan, A. Celada, LPS induces apoptosis in macrophages mostly through the autocrine production of TNF- $\alpha$ . *Blood* **95**, 3823-3831 (2000).
314. N. Y. Spencer, W. Zhou, Q. Li, Y. Zhang, M. Luo, Z. Yan, T. J. Lynch, D. Abbott, B. Banfi, J. F. Engelhardt, Hepatocytes produce TNF- $\alpha$  following hypoxia-reoxygenation and liver ischemia-reperfusion in a NADPH oxidase-and c-Src-dependent manner. *American Journal of Physiology-Gastrointestinal and Liver Physiology* **305**, G84-G94 (2013).
315. S. Gardella, C. Andrei, D. Ferrera, L. V. Lotti, M. R. Torrisi, M. E. Bianchi, A. Rubartelli, The nuclear protein HMGB1 is secreted by monocytes via a non - classical, vesicle - mediated secretory pathway. *EMBO reports* **3**, 995-1001 (2002).
316. S. Yin, H. Wang, O. Park, W. Wei, J. Shen, B. Gao, Enhanced Liver Regeneration in IL-10-Deficient Mice after Partial Hepatectomy via Stimulating Inflammatory Response and Activating Hepatocyte STAT3. *The American journal of pathology* **178**, 1614-1621 (2011).
317. K. Thompson, J. Maltby, J. Fallowfield, M. McAulay, H. Millward - Sadler, N. Sheron, Interleukin - 10 expression and function in experimental murine liver inflammation and fibrosis. *Hepatology* **28**, 1597-1606 (1998).
318. J. Zhong, I. V. Deaciuc, R. Burikhanov, W. J. de Villiers, Lipopolysaccharide-induced liver apoptosis is increased in interleukin-10 knockout mice. *Biochimica et Biophysica Acta (BBA)-Molecular Basis of Disease* **1762**, 468-477 (2006).
319. S. Chensue, P. Terebuh, D. Remick, W. Scales, S. Kunkel, In vivo biologic and immunohistochemical analysis of interleukin-1 alpha, beta and tumor necrosis factor during experimental endotoxemia. Kinetics, Kupffer cell expression, and glucocorticoid effects. *The American journal of pathology* **138**, 395 (1991).
320. A. Sugihara, T. Tsujimura, Y. Fujita, Y. Nakata, N. Terada, Evaluation of role of mast cells in the development of liver fibrosis using mast cell-deficient rats and mice. *Journal of hepatology* **30**, 859-867 (1999).
321. E. J. Seeley, R. E. Sutherland, S. S. Kim, P. J. Wolters, Systemic mast cell degranulation increases mortality during polymicrobial septic peritonitis in mice. *Journal of leukocyte biology* **90**, 591-597 (2011).
322. Y. A. Mekori, D. D. Metcalfe, Mast cell-T cell interactions. *Journal of Allergy and Clinical Immunology* **104**, 517-523 (1999).

323. R. Kew, T. Hyers, R. Webster, Human C-reactive protein inhibits neutrophil chemotaxis in vitro: possible implications for the adult respiratory distress syndrome. *The Journal of laboratory and clinical medicine* **115**, 339-345 (1990).
324. W. Zhong, Q. Zen, J. Tebo, K. Schlottmann, M. Coggeshall, R. F. Mortensen, Effect of human C-reactive protein on chemokine and chemotactic factor-induced neutrophil chemotaxis and signaling. *The Journal of Immunology* **161**, 2533-2540 (1998).
325. M. B. Pepys, G. M. Hirschfield, C-reactive protein: a critical update. *Journal of Clinical Investigation* **111**, 1805 (2003).
326. M. Naito, S. Umeda, T. Yamamoto, H. Moriyama, H. Umezu, G. Hasegawa, H. Usuda, L. D. Shultz, K. Takahashi, Development, differentiation, and phenotypic heterogeneity of murine tissue macrophages. *Journal of leukocyte biology* **59**, 133-138 (1996).
327. S. J. Jenkins, D. Ruckerl, P. C. Cook, L. H. Jones, F. D. Finkelman, N. van Rooijen, A. S. MacDonald, J. E. Allen, Local macrophage proliferation, rather than recruitment from the blood, is a signature of TH2 inflammation. *Science* **332**, 1284-1288 (2011).
328. C. Tkaczyk, Y. Okayama, D. D. Metcalfe, A. M. Gilfillan, Fcγ receptors on mast cells: activatory and inhibitory regulation of mediator release. *International archives of allergy and immunology* **133**, 305-315 (2004).
329. C. Mold, H. D. Gresham, T. W. Du Clos, Serum amyloid P component and C-reactive protein mediate phagocytosis through murine FcγRs. *The journal of Immunology* **166**, 1200-1205 (2001).
330. C. Mold, R. Baca, T. W. Du Clos, Serum amyloid P component and C-reactive protein opsonize apoptotic cells for phagocytosis through Fcγ receptors. *Journal of autoimmunity* **19**, 147-154 (2002).
331. S. Seshadri, Y. Kannan, S. Mitra, J. Parker-Barnes, M. D. Wewers, MAIL regulates human monocyte IL-6 production. *The Journal of Immunology* **183**, 5358-5368 (2009).
332. A. azzaq Belaaouaj, K. S. Kim, S. D. Shapiro, Degradation of outer membrane protein A in Escherichia coli killing by neutrophil elastase. *Science* **289**, 1185-1187 (2000).
333. F. Lajarin, G. Rubio, J. Galvez, P. Garcia-Peñarrubia, Adhesion, invasion and intracellular replication of Salmonella typhimurium in a murine hepatocyte cell line. Effect of cytokines and LPS on antibacterial activity of hepatocytes. *Microbial pathogenesis* **21**, 319-329 (1996).
334. G. Brouckaert, M. Kalai, D. V. Krysko, X. Saelens, D. Vercammen, M. Ndlovu, G. Haegeman, K. D'Herde, P. Vandenabeele, Phagocytosis of necrotic cells by macrophages is phosphatidylserine dependent and does not induce inflammatory cytokine production. *Molecular biology of the cell* **15**, 1089-1100 (2004).
335. S.-T. Ju, H. Cui, D. J. Panka, R. Ettinger, A. Marshak-Rothstein, Participation of target Fas protein in apoptosis pathway induced by CD4<sup>+</sup> Th1 and CD8<sup>+</sup> cytotoxic T cells. *Proceedings of the National Academy of Sciences* **91**, 4185-4189 (1994).
336. J. Nemzek, G. Bolgos, B. Williams, D. Remick, Differences in normal values for murine white blood cell counts and other hematological parameters based on sampling site. *Inflammation research* **50**, 523-527 (2001).
337. S. C. Grubb, T. P. Maddatu, C. J. Bult, M. A. Bogue, Mouse phenome database. *Nucleic acids research* **37**, D720-D730 (2009).
338. K. P. O'Dea, M. R. Wilson, J. O. Dokpesi, K. Wakabayashi, L. Tatton, N. van Rooijen, M. Takata, Mobilization and margination of bone marrow Gr-1high monocytes during

- subclinical endotoxemia predisposes the lungs toward acute injury. *The Journal of Immunology* **182**, 1155-1166 (2009).
339. J. Yang, L. Zhang, C. Yu, X.-F. Yang, H. Wang, Monocyte and macrophage differentiation: circulation inflammatory monocyte as biomarker for inflammatory diseases. *Biomark Res* **2**, 1 (2014).
340. L. Patterson, R. Higginbotham, Mouse C-reactive protein and endotoxin-induced resistance. *Journal of bacteriology* **90**, 1520-1524 (1965).
341. B. G. Harbrecht, T. R. Billiar, R. D. Curran, J. Stadler, R. L. Simmons, Hepatocyte injury by activated neutrophils in vitro is mediated by proteases. *Annals of surgery* **218**, 120 (1993).
342. J. Shi, G. E. Gilbert, Y. Kokubo, T. Ohashi, Role of the liver in regulating numbers of circulating neutrophils. *Blood* **98**, 1226-1230 (2001).
343. P. Noel, S. Nelson, R. Bokulic, G. Bagby, H. Lipton, G. Lipscomb, W. Summer, Pentoxifylline inhibits lipopolysaccharide-induced serum tumor necrosis factor and mortality. *Life sciences* **47**, 1023-1029 (1990).
344. S. B. Inc.
345. PEPROTECH.
346. R. D. SYSTEMS.
347. PROSPEC.
348. L. A. Sklar, V. McNeil, A. Jesaitis, R. Painter, C. Cochrane, A continuous, spectroscopic analysis of the kinetics of elastase secretion by neutrophils. The dependence of secretion upon receptor occupancy. *Journal of Biological Chemistry* **257**, 5471-5475 (1982).
349. T. Calandra, J. Bernhagen, R. A. Mitchell, R. Bucala, The macrophage is an important and previously unrecognized source of macrophage migration inhibitory factor. *The Journal of experimental medicine* **179**, 1895-1902 (1994).
350. A. Liu, H. Fang, O. Dirsch, H. Jin, U. Dahmen, Oxidation of HMGB1 causes attenuation of its pro-inflammatory activity and occurs during liver ischemia and reperfusion. *PloS one* **7**, e35379 (2012).
351. A. M. Piliponsky, C.-C. Chen, M. A. Grimbaldston, S. M. Burns-Guydish, J. Hardy, J. Kalesnikoff, C. H. Contag, M. Tsai, S. J. Galli, Mast cell-derived TNF can exacerbate mortality during severe bacterial infections in C57BL/6-Kit W-sh/W-sh mice. *The American journal of pathology* **176**, 926-938 (2010).
352. E. Bissonnette, J. Enciso, A. Befus, Inhibition of tumour necrosis factor - alpha (TNF -  $\alpha$ ) release from mast cells by the anti - inflammatory drugs, sodium cromoglycate and nedocromil sodium. *Clinical & Experimental Immunology* **102**, 78-84 (1995).
353. C. Schmidt-Weber, S. Alexander, L. Henault, L. James, A. Lichtman, IL-4 enhances IL-10 gene expression in murine Th2 cells in the absence of TCR engagement. *The Journal of Immunology* **162**, 238-244 (1999).

## Appendix A - Supplementary Tables for SDMMs

**Table A.1 Definition of parameters and experimental values in Kupffer local response model**

Parameters	Description	Value	References
$k_{pg}$	<i>Salmonella</i> growth rate	1.2-3.6/h	(108)
$P_{\infty}$	<i>Salmonella</i> carrying capacity	$10^8$ cells	(112)
$r_{pmk}$	Rate at which pathogens are killed by Kupffer cells	0.03/per kupffer cell/h	(110)
$n$	The extent of <i>Salmonella</i> binding to Kupffer cells	2	Estimated
$k_{c1}$	Number of Kupffer cells which phagocytose half of <i>Salmonella</i>	0.03 cells/h	(110)
$k_{mk}$	Proliferation rate of Kupffer cells under inflammation	0.015-2/h	Estimated
$K_{\infty}$	Kupffer cells carrying capacity	$\frac{(16 - 20) \times 10^6 \text{ cells}}{g \text{ liver}}$	(281)
$k_{mkub}$	Unbinding rate of binding Kupffer cells	0.1-0.77/h	(111)
$u_{mk}$	Killing rate of free Kupffer cells induced by binding to pathogens	0.23-0.9/h	(111)

**Table A.2 Definition of parameters and experimental values in neutrophils immune response model**

Parameters	Description	Value	References
$r_{pn}$	Rate at which pathogens are killed by neutrophils	20-100/per neutrophil/h	(282)
$r_{t1max}$	The maximum number of TNF- $\alpha$ being released by Kupffer cells per enzyme molecule per hour	10/h	Estimated
$r_{t2max}$	The maximum number of TNF- $\alpha$ being released by neutrophils per enzyme molecule per hour	1000/h	Estimated
$m_{t1}$	Number of Kupffer cells at which the reaction rate is half of maximal production rate	10000 cells	Estimated
$m_{t2}$	Number of activated neutrophils at which the reaction rate is half of maximal production rate	10000 cells	Estimated

$k_{c2}$	Concentration of neutrophils which phagocytose half of <i>Salmonella</i>	<i>about</i> $1.5 \times 10^{-4}/h$	(283)
$u_t$	Degradation rate of TNF- $\alpha$	0.025-0.5/h (measured in kidney)	(284)
$k_{rd}$	Influx rate of neutrophils into blood vessel	0.1 – 0.72/h	(285)
$N_s$	Maximum amount of neutrophils in liver	$3.5 \times 10^5$	(117)
$\mu_{nr}$	Apoptotic rate of resting neutrophils	0.069-0.12/h	(185)
$\mu_n$	Apoptotic rate of activated neutrophils	0.05/h	(185)
$k_{nub}$	Unbinding rate of activated neutrophils	0.01-0.5/h	Estimated
$k_{r1}$	Auxiliary parameter associated with the activation rate of resting neutrophils	3/h	Estimated
$u_{r1}$	Degradation rate of parameter $r_1$ to maintain a slow-saturation curve	0.003/h	Estimated

**Table A.3 Definition of parameters and experimental values in damaged tissue model**

Parameters	Description	Value	References
$A_\infty$	Number of hepatocytes in liver	$3.2 \times 10^8 \text{ cells}/h$	mouse phenome database
$r_{hn}$	Rate at which activated neutrophils kill apoptotic hepatocytes	9000/per neutrophil/h	Estimated
$k_{c3}$	Concentration of activated neutrophils which phagocytose half of apoptotic hepatocytes	0.04 <i>cells/h</i>	Estimated
$r_{ah}$	Recovery rate of apoptotic hepatocytes	0.5-2/hour	(207)

**Table A.4 Definition of parameters and experimental values in monocytes immune response model**

Parameters	Description	Value	References
$k_{mr}$	Influx rate of monocytes into blood vessel	0.5/h	(285)
$r_{pm}$	Rate at which pathogens are killed by inflammatory monocytes	7/per monocyte/h	(202)
$r_2$	Influx rate of monocytes in liver	80/hours	(144)
$M_s$	Maximum amount of inflammatory monocytes in liver	50000	(125)
$\mu_{mr}$	Apoptotic rate of resting monocytes	0.2	Estimated
$\mu_m$	Apoptotic rate of activated monocytes (monocytes-derived-macrophage)	0.08	(286)

$r_{h1max}$	The maximum number of HMGB-1 being released by monocytes per enzyme molecule per hour	0.001	Estimated
$m_{h1}$	Number of monocytes generate half of maximal HMGB-1 production rate	10000	Estimated
$n$	Hill-type coefficient associated with monocytes	2	Estimated
$k_{cA}$	Number of monocytes which phagocytose half of <i>Salmonella</i>	0.002cells/h	(202)
$k_{umb}$	Unbinding rate of binding activated monocytes	0.4	(36)
$u_h$	Degradation rate of HMGB-1	0.5-3	Estimated
$u_{mn}$	Rate at which activated neutrophils are killed by inflammatory monocytes	200	Estimated

**Table A.5 Definition of parameters and experimental values in anti-inflammatory immune response model**

Parameters	Description	Value	References
$r_{camax}$	The maximum number of IL-10 being released by monocytes per enzyme molecule per hour	10000	Estimated
$C_{Ah}$	Number of monocytes generate half of maximal HMGB-1 production rate	10000	Estimated
$n$	Hill-type coefficient associated with monocytes	2	Estimated
$u_{ca}$	Degradation rate of IL-10	0.02	Estimated

**Table A.6 Definition of parameters and experimental values in full model with adaptive immunity**

Parameters	Description	Value	References
$k_{cd4}$	The influx rate of CD4+ T cells to blood vessel	0.014	(174)
$T_{cd4\infty}$	CD4+ T cell carrying capacity in the blood vessel	$27.4 \times 10^6$	(174)
$u_{cd4}$	Degradation rate of CD4+ T cells	0.00083-0.001	(174)
$k_{cd8}$	The influx rate of CD8+ T cells to blood vessel	0.0625	(174)
$T_{cd8\infty}$	CD8+ T cell carrying capacity in the blood vessel	$5 \times 10^6$	(174)
$u_{cd8}$	Degradation rate of CD8+ T cells	0.00079-0.001	(174)
$k_B$	The influx rate of B cells to blood vessel	0.0122	(174)
$B_\infty$	B cell carrying capacity in the blood vessel	$28.6 \times 10^6$	(174)
$u_B$	Degradation rate of B cells	0.00012-0.00016	(287, 288)


$r_{Abmax}$	The maximum production amount of antibody by B cells	0.00053	(243-245)
$m_{Ab}$	Number of B cells at which the reaction rate is half of maximum production rate	10000	Estimated
$u_{Ab}$	Degradation rate of antibody	0.0035-0.01	(289)
$r_{pAb}$	Rate at which pathogens are killed by antibody	1	Estimated based on (243, 245, 289)
$k_{c5}$	Concentration of antibody which kill half of <i>Salmonella</i>	0.035	Estimated
$r_{pcd4}$	Rate at which pathogens are killed by CD4+ T cells	8	(176, 202, 290)
$k_{c6}$	Concentration of CD4+ T cells which kill half of <i>Salmonella</i>	0.0015	Estimated
$r_{Mkbc8}$	Rate at which binding Kupffer Cells are killed by CD8+ T cells	0.25	(290)
$k_{c7}$	Concentration of CD8+ T cells which kill half of binding antigen presenting cells	0.0015	Estimated
$r_{Nbcd8}$	Rate at which binding activated neutrophils are killed by CD8+ T cells	0.25	(290)
$r_{Mbcd8}$	Rate at which binding activated monocytes are killed by CD8+ T cells	0.25	(290)
$r_{cd4Mb}$	Rate at which CD4+ T cells bind to activated monocytes	4	(290)
$r_{cd8Mb}$	Rate at which CD8+ T cells bind to activated monocytes	4	(290)
$k_{c8}$	Activated monocyte concentration produce half occupation on T cells	0.0075	Estimated
$r_{Bt}$	Rate at which B cells bind to T cells	1-10	Estimated
$k_{c9}$	B cell concentration produce half occupation on T cells	0.045	Estimated
$k_{cd4M}$	Rate at which binding CD4+ T cells are killed by activated monocytes	0.73-2	(291)
$k_{cd8M}$	Rate at which binding CD8+ T cells are killed by activated monocytes	0.73-2	(291)
$k_{c10}$	Concentration of activated monocytes which kill half of binding T cells	0.018	Estimated




## Appendix B - Supplementary Materials for IMMABM



**Table B.7 Agent Types and Agent Behaviors in IMMABM Based on Biological Behaviors (Agent types in “Agent Behavior(s)” are highlighted in *Italic* format, except terminology *Salmonella enterica serovar Typhimurium (Salmonella)* is *Italic* format in both “Biological Behavior(s)” and “Agent Behavior(s)”**


Note: biological behaviors that are lack of references (citations) indicate that the behaviors are implied from the literature in general.



Agent Type (Biological Indicator)	Shape (s) in IMMABM	Biological Behavior(s) (BB)	Agent Behavior(s) (Netlogo process)	Agent Type(s) that the specific agent type interacts with
<i>Salmonella</i> ( <i>Salmonella</i> )		<ol style="list-style-type: none"> <li>1. <i>Samonella</i> are phagocytized by Kupffer Cells (198, 292).</li> <li>2. <i>Salmonella</i> are killed by Kupffer Cells (198, 292).</li> <li>3. <i>Salmonella</i> replicate within apoptotic Kupffer Cells (172, 173).</li> <li>4. <i>Salmonella</i> escape from apoptotic Kupffer Cells.</li> <li>5. <i>Salmonella</i> infect SECs and replicate within SECs (176) .</li> <li>6. <i>Salmonella</i> released from infected SECs persistently infect and replicate within neighboring cells.</li> <li>7. Released <i>Salmonella</i> infect healthy hepatocytes (176, 199).</li> <li>8. <i>Salmonella</i> replicate within infected hepatocytes (176, 199).</li> <li>9. <i>Salmonella</i> escape from apoptotic hepatocytes (200).</li> <li>10. <i>Salmonella</i> released from infected hepatocytes and persistently infect and replicate within liver tissue.</li> <li>11. Released <i>Salmonella</i> are phagocytized by neutrophils (198, 200).</li> <li>12. <i>Salmonella</i> are killed by neutrophils (198, 200).</li> <li>13. Escaped <i>Salmonella</i></li> </ol>	<ol style="list-style-type: none"> <li>1. salmonellaPhagocytizeByKupfferCellSubRoutine [BB.1]</li> <li>2. salmonellaKillByKupfferCellSubRoutine [BB.2]</li> <li>3. salmonellaReplicateWithinKupfferCellSubRoutine [BB.3]</li> <li>4. salmonellaReplicateWithinSECsSubRoutine [BB. 5]</li> <li>5. salmonellaReplicateWithinHepatocyteSubRoutine [BB.7, BB.8]</li> <li>6. salmonellaPhagocytizeByActivatedNeutrophilSubRoutine [BB. 11, BB. 12]</li> <li>7. salmonellaPhagocytizeByMDMISubRoutine [BB. 13, BB.14]</li> <li>8. salmonellaReplicateWithinMDMISubRoutine [BB. 15]</li> <li>9. newlyReleasedSalmonellaFromApoptoticCellsInteractWithSECsOrHepatocyteOrMastCellSubRoutine [BB. 4, BB.6, BB.9, BB. 10, BB. 17]</li> <li>10. salmonellaGetTrappedByNETsSubRoutine [BB. 16]</li> <li>11. For BB. 18, see CRP Behaviors(s). 3</li> <li>12. For BB. 19, see CRP Behaviors(s). 4</li> <li>13. For BB. 20, see CRP Behaviors(s). 5</li> <li>14. For BB. 21, see CRP Behaviors(s). 6 and 7</li> <li>15. For BB. 22, see Antibody Behaviors(s). 4</li> <li>16. For BB. 23, see Antibody Behaviors(s). 5</li> <li>17. For BB. 24, see Antibody Behaviors(s). 6</li> <li>18. For BB. 25, see Antibody Behaviors(s). 7 and 8</li> <li>19. salmonellaDieBecauseOtherChemicalsReleaseByMastCellSubRoutine [BB. 26]</li> </ol>	<ol style="list-style-type: none"> <li>1. KupfferCell</li> <li>2. Hepatocyte</li> <li>3. SEC</li> <li>4. ActivatedNeutrophil</li> <li>5. NET</li> <li>6. MDMI</li> <li>7. MastCell</li> <li>8. Antibody</li> <li>9. CRP</li> </ol>

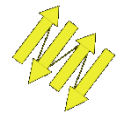

		<p>are phagocytized by monocyte-derived-macrophage type I (MDMI) (172, 201).</p> <ol style="list-style-type: none"> <li>14. <i>Salmonella</i> are killed by monocyte-derived-macrophage type I (172, 201).</li> <li>15. <i>Salmonella</i> replicate within monocyte-derived-macrophage type I (216).</li> <li>16. <i>Salmonella</i> are trapped and killed by neutrophil extracellular traps (NETs) as a complex of Myeloperoxidase (MPO) and neutrophil elastase (NE). MPO and NE are released from neutrophil degranulation (214, 215, 293).</li> <li>17. <i>Salmonella</i> bind to mast cells (252, 253).</li> <li>18. <i>Salmonella</i> that bind CRP are killed by Kupffer Cells (205).</li> <li>19. <i>Salmonella</i> that bind CRP are killed by mast cells (205).</li> <li>20. <i>Salmonella</i> that bind CRP are killed by neutrophils (205).</li> <li>21. <i>Salmonella</i> that bind CRP are killed by macrophages (205).</li> <li>22. <i>Salmonella</i> that bind by antibody are killed by Kupffer Cells (10).</li> <li>23. <i>Salmonella</i> that bind by antibody are killed by mast cells (10).</li> <li>24. <i>Salmonella</i> that bind by antibody are killed by neutrophils (10).</li> <li>25. <i>Salmonella</i> that bind by antibody are killed by macrophages (10).</li> <li>26. <i>Salmonella</i> growth is inhibited by other undefined mechanism (294).</li> </ol>		
<p><b>Hepatocyte (Hepatocyte)</b></p>		<ol style="list-style-type: none"> <li>1. Hepatocytes are infected by <i>Salmonella</i> and undergo apoptosis (176, 198). Apoptotic hepatocytes become hepatocyte debris.</li> </ol>	<ol style="list-style-type: none"> <li>1. hepatocyteBecomeHepatocyteDebrisInducedBySalmonellaSubRoutine [BB. 1]</li> <li>2. hepatocyteBecomeHepatocyteDebrisInducedByTNFAlphaSubRoutine [BB. 2]</li> <li>3. hepatocyteReleaseCRPIfAnyMDMIWasDetectedSubRoutine [BB. 3]</li> <li>4. apoptoticHepatocyteKillByNeutrophilSubR</li> </ol>	<ol style="list-style-type: none"> <li>1. <i>Salmonella</i></li> <li>2. <i>TNF-α</i></li> <li>3. <i>ActivatedNeutrophil</i></li> </ol>



		<ol style="list-style-type: none"> <li>Hepatocytes are activated with TNF-<math>\alpha</math> and become apoptotic (15). Apoptotic hepatocytes become hepatocyte debris.</li> <li>CRP is released by hepatocytes in response to IL-6 released by macrophages (203, 204).</li> <li><i>Salmonella</i>-infected hepatocytes interact with activated neutrophils which accelerates the apoptosis (127, 209, 210).</li> <li>Apoptotic hepatocytes release TNF-<math>\alpha</math> (207).</li> <li>Apoptotic hepatocytes release HMGB1 (208).</li> <li>Hepatocytes regenerate (295).</li> </ol>	<ol style="list-style-type: none"> <li>apoptoticHepatocyteProduceTNFAlphaSubRoutine [BB. 4]</li> <li>apoptoticHepatocyteProduceHMGB1SubRoutine [BB. 5]</li> <li>hepatocyteRegenerateSubRoutine [BB. 7]</li> </ol>	
<b>HepatocyteDebris (Hepatocyte debris)</b>		<ol style="list-style-type: none"> <li>Hepatocyte debris is phagocytized by Kupffer Cells (15).</li> <li>Hepatocyte debris is phagocytized by mast cells.</li> <li>Hepatocyte debris can also be phagocytized by neutrophils (127).</li> <li>Hepatocyte debris can also be phagocytized by monocyte-derived-macrophage type I (296, 297).</li> <li>Hepatocyte debris can also be phagocytized by monocyte-Derived-Macrophage Type II (MDMII) (296, 297).</li> <li>Hepatocyte debris bind to CRP (205).</li> <li>Hepatocyte debris binding to CRP are phagocytized by inflammatory cells including Kupffer Cells, neutrophils, mast cells, MDMI, and MDMII (205).</li> <li>Hepatocyte debris undergo natural degradation.</li> </ol>	<ol style="list-style-type: none"> <li>hepatocyteDebrisPhagocytizeByInflammatoryCellSubRoutine [BB. 1, BB.2, BB. 3, BB. 4, and BB. 5]</li> <li>For BB. 6, see CRP Behaviors(s). 14</li> <li>For BB. 7, see CRP Behaviors(s). 15, 16, 17, 18, and 19</li> <li>hepatocyteDebrisDieByNatureSubRoutine [BB. 8]</li> </ol>	<ol style="list-style-type: none"> <li>KupfferCell</li> <li>MastCell</li> <li>ActivatedNeutrophil</li> <li>MDMI</li> <li>MDMII</li> <li>CRP</li> </ol>
<b>RestingNeutr</b>		<ol style="list-style-type: none"> <li>Circulating neutrophil</li> </ol>	<ol style="list-style-type: none"> <li>restingNeutrophilInfluxToLiverSinusoidFro</li> </ol>	SEC

<p><b>ophil</b> (Circulating neutrophil)</p>		<p>numbers increase after infection (298).</p> <ol style="list-style-type: none"> <li>2. Circulating neutrophils roll along sinusoidal endothelial cells (216, 299).</li> <li>3. Circulating neutrophils get signals from sinusoidal endothelial cells (216, 299).</li> <li>4. Circulating neutrophils are activated by TNF-<math>\alpha</math>, <i>Salmonella</i>, and HMGB-1 (24, 127, 171, 206, 221).</li> <li>5. Circulating neutrophils undergo aging and undergo apoptosis (300).</li> </ol>	<p>mBoneMarrowSubRoutine [BB. 1]</p> <ol style="list-style-type: none"> <li>2. restingNeutrophilMoveToSECsFollowingSignalSentFromCytokineAndGetActivatedSubRoutine [BB. 2, BB. 3, and BB. 4]</li> <li>3. restingNeutrophilUndergoAgingByNatureSubRoutine [BB. 5]</li> </ol>	
<p><b>ActivatedNeutrophil</b> (Activated neutrophil)</p>		<ol style="list-style-type: none"> <li>1. Activated circulating neutrophils adhere to sinusoidal endothelial cells (216, 299).</li> <li>2. Activated neutrophils migrate to liver Kupffer Cells (14).</li> <li>3. Activated neutrophils interact with <i>Salmonella</i> (14, 200, 301).</li> <li>4. Activated neutrophils migrate to apoptotic hepatocytes which are infected by <i>Salmonella</i> (200).</li> <li>5. Activated neutrophils undergo natural aging (302, 303).</li> <li>6. Apoptotic neutrophils interact with CRP (205).</li> <li>7. Apoptotic neutrophils interact with CRP are phagocytized by inflammatory cells (205). Apoptotic neutrophils die after phagocytosis.</li> <li>8. Activated neutrophils inhibit neutrophil movement to the site of infection by taking up CRP that has bound to cell debris [see CRP 1].</li> <li>9. Apoptotic neutrophils are engulfed by MDMII (216).</li> </ol>	<ol style="list-style-type: none"> <li>1. restingNeutrophilMoveToSECsFollowingSignalSentFromCytokineAndGetActivatedSubRoutine [BB. 1, BB. 8]</li> <li>2. activatedNeutrophilInteractWithKupfferCellsSubRoutine [BB. 2]</li> <li>3. activatedNeutrophilPhagocytizeByKupfferCellSubRoutine [BB. 2]</li> <li>4. activatedNeutrophilMoveToSiteOfSalmonellaSubRoutine [BB. 3]</li> <li>5. activatedNeutrophilMoveToSiteOfApoptoticHepatocyteSubRoutine [BB. 4]</li> <li>6. activatedNeutrophilUndergoAgingByNatureSubRoutine [BB. 5]</li> <li>7. For BB. 6, see CRP Behaviors(s). 20</li> <li>8. For BB. 7, see CRP Behaviors(s). 21, 22, 23, 24, and 25</li> <li>9. apoptoticActivatedNeutrophilPhagocytizeByMDMII [BB. 9]</li> <li>10. activatedNeutrophilProduceTNFAlphaSubRoutine [BB. 10]</li> <li>11. activatedNeutrophilProduceIL10SubRoutine [BB. 11]</li> <li>12. activatedNeutrophilProduceNETsSubRoutine [BB. 12]</li> <li>13. For BB. 13, see IL-10 Behavior(s). 4 and 5</li> <li>14. activatedNeutrophilWhoPhagocytizeSalmonellaUndergoApoptosisByInteractWithCD8TCellSubRoutine [BB. 14]</li> </ol>	<ol style="list-style-type: none"> <li>1. SEC</li> <li>2. KupfferCell</li> <li>3. Salmonella</li> <li>4. Hepatocyte</li> <li>5. CRP</li> <li>6. IL-10</li> <li>7. MDMI</li> <li>8. MDMII</li> <li>9. MastCell</li> <li>10. ActivatedNeutrophil</li> </ol>


		<ol style="list-style-type: none"> <li>10. Activated neutrophils release cytokines such as TNF-<math>\alpha</math> and IL-10 after neutrophil simulation by bacterial LPS (17, 77, 213).</li> <li>11. Activated neutrophils undergo degranulation and release MPO and NE after neutrophils simulation by bacterial LPS (293).</li> <li>12. Activated neutrophils release NETs (214).</li> <li>13. Activated neutrophils bind to IL-10 (220) [see model assumption 16].</li> <li>14. Activated neutrophils that phagocytize Salmonella undergo apoptosis if bind to CD8<sup>+</sup> T cells (10).</li> </ol>		
<b>Resting Monocyte (Circulating monocyte)</b>		<ol style="list-style-type: none"> <li>1. Circulating monocytes are released after infection (111).</li> <li>2. Circulating monocytes roll in the blood vessel (216, 222).</li> <li>3. Circulating monocytes get signals and are activated to adhere to endothelial cells (216, 222, 223).</li> <li>4. Circulating monocytes are activated by TNF-<math>\alpha</math>, Salmonella, HMGB-1, and T<sub>H</sub>1 effector cells and apoptotic activated neutrophils (14, 24, 142, 144, 216, 222, 298, 304-306).</li> <li>5. Monocytes become MDMI when they encounter Salmonella or TNF-<math>\alpha</math> (16, 216).</li> <li>6. Monocytes become MDMI when they encounter apoptotic activated neutrophils (16, 216).</li> <li>7. Circulating monocytes undergo aging and undergo apoptosis (307).</li> </ol>	<ol style="list-style-type: none"> <li>1. restingMonocyteInfluxToLiverSinusoidFromBoneMarrowSubRoutine [BB. 1]</li> <li>2. restingMonocyteMoveToSECSFollowingSignalSentFromCytokineAndGetActivatedSubRoutine [BB. 2, BB. 3, and BB. 4]</li> <li>3. restingMonocyteBecomeMDMIOrMDMIIByInteractWithCorrespondingCellOrCytokineSubRoutine [BB. 5, BB. 6]</li> <li>4. restingMonocyteUndergoAgingByNatureSubRoutine [BB. 7]</li> </ol>	<ol style="list-style-type: none"> <li>1. Salmonella</li> <li>2. TNF-<math>\alpha</math></li> <li>3. Activated Neutrophil</li> <li>4. SEC</li> </ol>
<b>MDMI</b>		<ol style="list-style-type: none"> <li>1. MDMI migrate to</li> </ol>	<ol style="list-style-type: none"> <li>1. restingMonocyteBecomeMDMIOrMDMIIB</li> </ol>	<ol style="list-style-type: none"> <li>1. Salmonella</li> </ol>




<p><b>(monocyte-Derived-Macrophage Type I)</b></p>		<p>the site of <i>Salmonella</i> (16, 216).</p> <ol style="list-style-type: none"> <li>2. MDMIs phagocytize (kill) <i>Salmonella</i> at certain rate(16, 216).</li> <li>3. MDMIs release TNF-<math>\alpha</math> (216).</li> <li>4. MDMIs are killed by <i>Salmonella</i> (172, 201).</li> <li>5. MDMIs undergo natural aging (308).</li> <li>6. Aging MDMIs interact with CRP (205).</li> <li>7. Aging MDMIs interacted with CRP are phagocytized by inflammatory cells (205).</li> <li>8. MDMIs phagocytize CRP bound to cell debris and release cytokines such as TNF-<math>\alpha</math> (205, 309).</li> <li>9. MDMIs (partially) transform to Kupffer Cells (123, 310, 311).</li> <li>10. MDMIs bind to IL-10 [See model assumption 16].</li> <li>11. MDMIs, as APCs, attract T cells from lymph node to the site of infection (164).</li> <li>12. MDMIs phagocytize apoptotic T cells (166).</li> <li>13. MDMIs release IL-10 by phagocytizing apoptotic T cells (166).</li> <li>14. MDMIs that phagocytize <i>Salmonella</i> undergo apoptosis if they bind to CD8<sup>+</sup> T cells (10).</li> </ol>	<p>yInteractWithCorrespondingCellOrCytokineSubRoutine [BB. 1]</p> <ol style="list-style-type: none"> <li>2. MDMIPhagocytizeSalmonellaSubRoutine [BB. 2]</li> <li>3. MDMIProduceTNFAlphaByPhagocytizeSalmonellaOrCRPTypeComplexSubRoutine [BB. 3, BB. 8]</li> <li>4. MDMIKillBySalmonellaSubRoutine [BB. 4]</li> <li>5. MDMIUndergoAgingByNatureSubRoutine [BB. 5]</li> <li>6. For BB. 6, see CRP Behavior(s). 26</li> <li>7. For BB. 7, see CRP Behavior(s). 27, 28, 29, 30, and 31</li> <li>8. MDMITransformToKupfferCellSubRoutine [BB. 9]</li> <li>9. For BB. 10, see IL-10 Behavior (s). 4 and 5</li> <li>10. For BB. 11, see CD4TCellBehavior(s). 1 and CD8TCellBehavior (s). 1</li> <li>11. For BB. 12, see CD4TCellBehavior(s). 4 and CD8TCellBehavior (s). 3</li> <li>12. MDMIProduceIL10ByPhagocytizeApoptoticCD4TCellOrCD8TCellSubRoutine [BB. 13]</li> <li>13. MDMIWhoPhagocytizeSalmonellaUndergoApoptosisByInteractWithCD8TCellSubRoutine [BB. 14]</li> </ol>	<ol style="list-style-type: none"> <li>2. CRP</li> <li>3. IL-10</li> <li>4. KupfferCell</li> <li>5. ActivatedNeutrophil</li> <li>6. MastCell</li> <li>7. MDMI</li> <li>8. MDMII</li> <li>9. CD8TCell</li> <li>10. Hepatocyte</li> </ol>
<p><b>MDMII (monocyte-Derived-Macrophage Type II)</b></p>		<ol style="list-style-type: none"> <li>1. MDMII migrate to apoptotic activated neutrophils (142, 216, 304).</li> <li>2. MDMII phagocytize apoptotic activated neutrophils (142, 216, 304).</li> <li>3. MDMII release HMGB-1 after phagocytizing apoptotic activated neutrophils (216).</li> <li>4. MDMII release IL-10 after phagocytizing apoptotic activated neutrophils (216).</li> <li>5. MDMII phagocytize apoptotic T cells</li> </ol>	<ol style="list-style-type: none"> <li>1. restingMonocyteBecomeMDMIOrMDMIIByInteractWithCorrespondingCellOrCytokineSubRoutine [BB. 1]</li> <li>2. MDMIIPhagocytizeApoptoticNeutrophilSubRoutine [BB. 2]</li> <li>3. MDMIIProduceHMGB1ByPhagocytizeApoptoticNeutrophilSubRoutine [BB. 3]</li> <li>4. MDMIIProduceIL10ByPhagocytizeApoptoticNeutrophilOrApoptoticTCellSubRoutine [BB. 4, BB. 6]</li> <li>5. For BB. 5, see CD4TCellBehavior(s). 4 and CD8TCellBehavior(s). 3</li> <li>6. MDMIIUndergoAgingByNatureSubRoutine [BB. 7]</li> <li>7. For BB. 8, see CRP Behavior(s). 32</li> <li>8. For BB. 9, see CRP Behavior(s). 33, 34, 35, 36 and 37</li> <li>9. For BB. 10, see CRP Behavior(s). 7</li> </ol>	<ol style="list-style-type: none"> <li>1. ActivatedNeutrophil</li> <li>2. CRP</li> <li>3. IL-10</li> <li>4. CD4TCell</li> <li>5. CD8TCell</li> <li>6. KupfferCell</li> <li>7. MastCell</li> <li>8. MDMI</li> <li>9. MDMII</li> </ol>



		<p>(166).</p> <ol style="list-style-type: none"> <li>MDMIIIs release IL-10 after phagocytizing apoptotic T cells (166).</li> <li>MDMIIIs undergo natural aging (308).</li> <li>Aging MDMIIIs bind CRP (205).</li> <li>Aging MDMIIIs that bind CRP are phagocytized by inflammatory cells (205).</li> <li>MDMIIIs phagocytize CRP bound to cell debris and release cytokines (205).</li> <li>MDMIIIs (partially) transform to Kupffer Cells (123, 310, 311).</li> <li>MDMIIIs <i>bind</i> IL-10 [See model assumption 16].</li> <li>MDMIIIs, as APCs, attract T cells from lymph node to the site of infection (164).</li> </ol>	<ol style="list-style-type: none"> <li>MDMIITransformToKupfferCellSubRoutine [BB. 11]</li> <li>For BB. 12, see IL-10 Behavior(s). 4 and 5</li> <li>For BB. 13, see CD4TCellBehavior(s). 1 and CD8TCellBehavior(s). 1</li> </ol>	10. <i>Hepatocyte</i>
<p><b>TNF-<math>\alpha</math></b> (Tumor necrosis factor alpha)</p>		<ol style="list-style-type: none"> <li>TNF-<math>\alpha</math> is released by Kupffer Cells upon interacting with <i>Salmonella</i> (14).</li> <li>TNF-<math>\alpha</math> is released by Kupffer Cells upon interacting with hepatocyte debris (15).</li> <li>TNF-<math>\alpha</math> is released by Kupffer Cells upon interacting with activated neutrophils (14).</li> <li>TNF-<math>\alpha</math> is released by MDMIIIs (16, 216).</li> <li>TNF-<math>\alpha</math> is released by activated neutrophils (17).</li> <li>TNF-<math>\alpha</math> is released by apoptotic hepatocytes (18).</li> <li>TNF-<math>\alpha</math> is released by mast cells (19, 20).</li> <li>TNF- <math>\alpha</math> migrates to hepatocytes (15).</li> <li>TNF- <math>\alpha</math> damages healthy hepatocytes (15).</li> <li>TNF-<math>\alpha</math> undergoes natural catabolism (312-314).</li> </ol>	<ol style="list-style-type: none"> <li>For BB. 1, see KupfferCell Behavior(s). 2</li> <li>For BB. 2, see KupfferCell Behavior(s). 2</li> <li>For BB. 3, see KupfferCell Behavior(s). 2</li> <li>For BB. 4, see MDMI Behavior(s). 3</li> <li>For BB. 5, see ActivatedNeutrophil Behavior(s). 10</li> <li>For BB. 6, see Hepatocyte Behavior(s). 5</li> <li>For BB. 7, see MastCell Behavior(s). 3 and 4</li> <li>For BB. 8, see Hepatocyte Behavior(s). 2</li> <li>For BB. 9, see Hepatocyte Behavior(s). 2</li> <li>TNFAlphaUndergoCatabolismByNatureSubRoutine [BB. 10]</li> </ol>	<i>Hepatocyte</i>
<p><b>HMGB-1</b> (High mobility group)</p>		<ol style="list-style-type: none"> <li>HMGB-1 is released by MDMIIIs in response to apoptotic neutrophils (139, 218).</li> </ol>	<ol style="list-style-type: none"> <li>For BB. 1, see MDMI Behavior(s). 3</li> <li>For BB. 2, see Hepatocyte Behavior(s). 6</li> <li>HMGB1UndergoCatabolismByNatureSubRoutine [BB. 3]</li> </ol>	

protein B1)		<ol style="list-style-type: none"> <li>HMGB-1 is released by apoptotic hepatocytes (24).</li> <li>HMGB-1 undergoes natural catabolism (38, 219, 315).</li> </ol>		
<b>IL-10</b> (Interleukin 10)		<ol style="list-style-type: none"> <li>IL-10 is produced by MDMIs (16, 216, 219).</li> <li>IL-10 is released by activated neutrophils (77, 213).</li> <li>IL-10 is produced by T cells (206).</li> <li>IL-10 diffuses to the site of Kupffer Cells and inhibits the release of TNF-<math>\alpha</math>.</li> <li>IL-10 diffuses to the site of activated neutrophils and inhibits the release of TNF-<math>\alpha</math> (220).</li> <li>IL-10 diffuses to the site of MDMIs and inhibits the release of TNF-<math>\alpha</math> (219).</li> <li>IL-10 diffuses to the site of MDMIs and inhibits the release of HMGB-1 (147-150).</li> <li>IL-10 diffuses to the site of MDMIs and inhibits the release of IL-10 (147-150).</li> <li>IL-10 diffuses to the site of mast cells and inhibits the release of TNF-<math>\alpha</math> [see model assumption 16].</li> <li>IL-10 undergoes natural catabolism (316-318).</li> </ol>	<ol style="list-style-type: none"> <li>For <b>BB. 1</b>, see <b>MDMI Behavior(s). 4</b></li> <li>For <b>BB. 2</b>, see <b>ActivatedNeutrophil Behavior(s). 11</b></li> <li>For <b>BB. 3</b>, see <b>CD4TCell Behavior(s). 3</b></li> <li>IL10InteractWithInflammatoryCellsSubRoutine [<b>BB. 4, BB. 5, BB. 6, BB. 7, BB. 8, and BB. 9</b>]</li> <li>IL10BindToInflammatoryCellsSubRoutine [<b>BB. 4, BB. 5, BB. 6, BB. 7, BB. 8, and BB. 9</b>]</li> <li>IL10UndergoCatabolismByNatureSubRoutine [<b>BB. 10</b>]</li> </ol>	<ol style="list-style-type: none"> <li><i>KupfferCell</i></li> <li><i>MDMI</i></li> <li><i>MDMI</i></li> <li><i>ActivatedNeutrophil</i></li> <li><i>MastCell</i></li> </ol>
<b>KupfferCell</b> (Kupffer Cell)		<ol style="list-style-type: none"> <li>Kupffer Cells are killed by Salmonella (172, 173).</li> <li>Kupffer Cells release TNF-<math>\alpha</math> after interacting with <i>Salmonella</i> (319).</li> <li>Kupffer Cells release TNF-<math>\alpha</math> after phagocytizing hepatocyte debris (15).</li> <li>Kupffer Cells release TNF-<math>\alpha</math> after interacting with activated neutrophils (14, 126).</li> <li>Kupffer Cells bind to IL-10 (147)[See model assumption</li> </ol>	<ol style="list-style-type: none"> <li>kupfferCellKillBySalmonellaSubRoutine [<b>BB. 1</b>]</li> <li>kupfferCellProduceTNFAlphaInteractWithSalmonellaOrHepatocyteDebrisOrActivatedNeutrophilSubRoutine [<b>BB. 2, BB. 3, and BB. 4</b>]</li> <li>For <b>BB. 5</b>, see <b>IL-10 Behavior(s). 4 and 5</b></li> <li>For <b>BB. 6</b>, see <b>MDMI Behavior(s). 8 and MDMI Behavior(s). 10</b></li> <li>kupfferCellUndergoAgingByNature [<b>BB. 7</b>]</li> <li>For <b>BB. 8</b>, see <b>CRP Behavior(s). 8</b></li> <li>For <b>BB. 9</b>, see <b>CRP Behavior(s). 9, 10, 11, 12, and 13</b></li> <li>For <b>BB. 10</b>, see <b>KupfferCell Behavior(s). 2</b></li> <li>kupfferCellWhoPhagocytizeSalmonellaUndergoApoptosisByInteractWithCD8TCellSubRoutine [<b>BB. 11</b>]</li> <li>kupfferCellProduceIL10ByIngestApoptoticHepatocyteSubRoutine [<b>BB. 12</b>]</li> </ol>	<ol style="list-style-type: none"> <li><i>Salmonella</i></li> <li><i>HepatocyteDebris</i></li> <li><i>Hepatocyte</i></li> <li><i>ActivatedNeutrophil</i></li> <li><i>IL-10</i></li> <li><i>CRP</i></li> <li><i>KupfferCell</i></li> <li><i>MastCell</i></li> <li><i>MDMI</i></li> </ol>

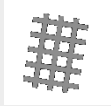





		<p>16].</p> <ol style="list-style-type: none"> <li>6. Kupffer Cells are replaced by monocyte-Derived MDMs/MDMIs (123, 310, 311).</li> <li>7. Kupffer Cells undergo natural apoptosis (310, 311).</li> <li>8. Apoptotic Kupffer Cells interact with CRP (205).</li> <li>9. Apoptotic Kupffer Cells decorated with CRP are phagocytized by inflammatory cells (205). Apoptotic Kupffer Cells die after phagocytosis.</li> <li>10. Kupffer Cells phagocytize CRP-opsonized cell debris and inhibit the production of TNF-<math>\alpha</math>. The phagocytic ability of Kupffer Cells is enhanced by CRP-opsonized particles (205)[see model assumption 21].</li> <li>11. Kupffer Cells that phagocytize Salmonella undergo apoptosis if they bind to CD8<sup>+</sup> T cells (10).</li> <li>12. Kupffer Cells Release IL-10 (204).</li> </ol>		<ol style="list-style-type: none"> <li>10. <i>MDMI</i></li> <li>11. <i>CD8TCell</i></li> </ol>
<p><b>MastCell</b> (Mast cell)</p>		<ol style="list-style-type: none"> <li>1. Mast cells self-renewal (252, 320).</li> <li>2. Mast cell degranulation is activated by interacting with a complex of antibody and <i>Salmonella</i> (249).</li> <li>3. Mast cells release histamine by degranulation (249, 321).</li> <li>4. Mast cells binding to <i>Salmonella</i> release TNF-<math>\alpha</math> (249).</li> <li>5. Mast cells release TNF-<math>\alpha</math> upon interacting with antibody-opsonized <i>Salmonella</i> (19, 20).</li> <li>6. TNF-<math>\alpha</math> and histamine help to recruit T cells from lymph node to the site of infection (249, 322).</li> <li>7. Mast cells bind to IL-10 and fail to release TNF-<math>\alpha</math> [see model</li> </ol>	<ol style="list-style-type: none"> <li>1. mastCellProliferateSubRoutine [BB. 1]</li> <li>2. mastCellProduceHistamineByInteractWithAntibodySalmonellaComplexSubRoutine [BB. 2, BB. 3]</li> <li>3. mastCellProduceTNFAlphaByBindingToSalmonellaSubRoutine [BB. 4]</li> <li>4. mastCellProduceTNFAlphaByInteractWithAntibodySalmonellaComplexSubRoutine [BB. 5]</li> <li>5. For BB. 6, see CD4TCell Behavior(s). 1 and CD8TCellBehavior (s). 2</li> <li>6. For BB. 7, see IL-10 Behavior(s). 4 and 5</li> <li>7. mastCellUndergoApoptosisByNatureSubRoutine [BB. 8]</li> </ol>	<ol style="list-style-type: none"> <li>1. <i>Salmonella</i></li> <li>2. <i>Antibody</i></li> <li>3. <i>ActivatedNeutrophil</i></li> <li>4. <i>Hepatocyte</i></li> <li>5. <i>MastCell</i></li> <li>6. <i>MDMI</i></li> <li>7. <i>MDMII</i></li> <li>8. <i>CD4Tcell</i></li> <li>9. <i>CD8Tcell</i></li> </ol>

		<p>assumption 16].</p> <ol style="list-style-type: none"> <li>Mast cells undergo natural aging (10).</li> </ol>		
<p><b>CD4TCell</b> (CD4 T cell)</p>		<ol style="list-style-type: none"> <li>CD4<sup>+</sup> T cells in lymph node (10).</li> <li>CD4<sup>+</sup> T cells are activated by APCs to proliferate and differentiate into T<sub>H</sub>1 effector cells to release TNF-α (166, 206).</li> <li>CD4<sup>+</sup> T cells are activated by APCs to proliferate and differentiate into T<sub>H</sub>2 effector cells to release IL-10 (206).</li> <li>T<sub>H</sub>1 effector cells activate infected Kupffer Cells to kill <i>Salmonella</i> (206).</li> <li>T<sub>H</sub>1 effector cells activate infected macrophages to kill <i>Salmonella</i> (206).</li> <li>Apoptotic CD4<sup>+</sup> T cells are phagocytized by MDMIIIs (164).</li> <li>CD4<sup>+</sup> T cells (fails to bind to APCs) undergo apoptosis (206).</li> </ol>	<ol style="list-style-type: none"> <li>CD4TCellMigrateFromPortalTriadToLiverSinusoidSubRoutine [BB. 1]</li> <li>CD4TCellProduceTNFAlphaByInteractWithAPCsSubRoutine [BB. 2, BB. 4, and BB. 5]</li> <li>CD4TCellProduceIL10ByInteractWithAPCsSubRoutine [BB. 3]</li> <li>apoptoticCD4TCellPhagocytizeByMDMIOrMDMIISubRoutine [BB. 6]</li> <li>CD4TCellUndergoAgingByNatureSubRoutine [BB. 7]</li> </ol>	<ol style="list-style-type: none"> <li>MastCell</li> <li>ActivatedNeutrophil</li> <li>KupfferCell</li> <li>MDMII</li> </ol>
<p><b>CD8TCell</b> (CD8 T cell)</p>		<ol style="list-style-type: none"> <li>CD8<sup>+</sup> T cells in lymph node (10).</li> <li>CD8<sup>+</sup> T cells induce the apoptosis of infected cells (infected cells are the inflammatory cells that <i>Salmonella</i> inhabit) (10, 166, 206).</li> <li>Apoptotic CD8<sup>+</sup> T cells are phagocytized by MDMIIIs (164).</li> <li>CD8<sup>+</sup> T cells (fails to bind to APCs) undergo apoptosis (206).</li> </ol>	<ol style="list-style-type: none"> <li>CD8TCellMigrateFromPortalTriadToLiverSinusoidSubRoutine [BB. 1]</li> <li>CD8TCellInduceApoptosisOfKupfferCellOrNeutrophilOrMDMIWhoPhagocytizeSalmonellaSubRoutine [BB. 2]</li> <li>apoptoticCD8TCellPhagocytizeByMDMIOrMDMIISubRoutine [BB. 3]</li> <li>CD8TCellUndergoAgingByNatureSubRoutine [BB. 4]</li> </ol>	<ol style="list-style-type: none"> <li>MastCell</li> <li>ActivatedNeutrophil</li> <li>KupfferCell</li> <li>MDMII</li> </ol>
<p><b>BCell</b> (B cell)</p>		<ol style="list-style-type: none"> <li>B cells in lymph node (11).</li> <li>B cells are activated by T<sub>H</sub>1 or T<sub>H</sub>2 cells to proliferate and release antibody (206).</li> <li>B cell (fails to bind to T helper cells or antigen) undergo apoptosis (206).</li> </ol>	<ol style="list-style-type: none"> <li>BCellMigrateFromPortalTriadToLiverSinusoidSubRoutine [BB. 1]</li> <li>BCellProduceAntibodySubRoutine [BB. 2]</li> <li>BCellUndergoAgingByNatureSubRoutine [BB. 3]</li> </ol>	<ol style="list-style-type: none"> <li>CD4TCell</li> </ol>
<p><b>Antibody</b></p>		<ol style="list-style-type: none"> <li>Antibody is released</li> </ol>	<ol style="list-style-type: none"> <li>For BB. 1, see BCell Behavior(s). 2</li> </ol>	<ol style="list-style-type: none"> <li>MastCell</li> </ol>

(Antibody)		<p>from activated B cells (206).</p> <ol style="list-style-type: none"> <li>2. Antibody Interacts with <i>Salmonella</i> (multiple antibodies to one <i>Salmonella</i>) (10).</li> <li>3. Antibody-opsonized <i>Salmonella</i> interacts with mast cells and initiates the degranulation of mast cells (249).</li> <li>4. Antibody-bound to <i>Salmonella</i> is phagocytized by Kupffer Cells (higher phagocytosis rate here). This process refers to opsonization (10).</li> <li>5. Antibody-bound to <i>Salmonella</i> is phagocytized by mast cells (higher phagocytosis rate here). This process refers to opsonization (10).</li> <li>6. Antibody-bound to <i>Salmonella</i> is phagocytized by neutrophils (higher phagocytosis rate here) (10).</li> <li>7. Antibody-bound to <i>Salmonella</i> is phagocytized by macrophage-derived-macrophage type I (higher phagocytosis rate here) (10).</li> <li>8. Antibody-bound by <i>Salmonella</i> is phagocytized by macrophage-derived-macrophage type II (higher phagocytosis rate here) (10).</li> </ol>	<ol style="list-style-type: none"> <li>2. antibodyInteractWithSalmonellaSubRoutine [BB. 2]</li> <li>3. For BB. 3, see <b>MastCell Behavior(s). 4</b></li> <li>4. antibodySalmonellaComplexPhagocytizeByKupfferCellSubRoutine [BB. 4]</li> <li>5. antibodySalmonellaComplexPhagocytizeByMastCellSubRoutine [BB. 5]</li> <li>6. antibodySalmonellaComplexPhagocytizeByNeutrophilSubRoutine [BB. 6]</li> <li>7. antibodySalmonellaComplexPhagocytizeByMDMISubRoutine [BB. 7]</li> <li>8. antibodySalmonellaComplexPhagocytizeByMDMIISubRoutine [BB. 8]</li> </ol>	<ol style="list-style-type: none"> <li>2. <i>Salmonella</i></li> <li>3. <i>KupfferCell</i></li> <li>4. <i>ActivatedNeutrophil</i></li> <li>5. <i>MDMI</i></li> <li>6. <i>MDMI</i></li> </ol>
CRP (C-reactive protein)		<ol style="list-style-type: none"> <li>1. CRP inhibits neutrophil movement to the site of infection in a human model with adult respiratory distress syndrome (323, 324).</li> <li>2. CRP is released by hepatocytes in response to IL-6 released by macrophages (203, 204).</li> <li>3. CRP-bound</li> </ol>	<ol style="list-style-type: none"> <li>1. For BB. 1, see <b>RestingNeutrophil Behavior(s). 2</b></li> <li>2. For BB. 2, see <b>Hepatocyte Behavior(s). 3</b></li> <li>3. CRPSalmonellaComplexPhagocytizeByKupfferCellSubRoutine [BB. 3]</li> <li>4. CRPSalmonellaComplexPhagocytizeByMastCellSubRoutine [BB. 4]</li> <li>5. CRPSalmonellaComplexPhagocytizeByNeutrophilSubRoutine [BB. 5]</li> <li>6. CRPSalmonellaComplexPhagocytizeByMDMISubRoutine [BB. 6]</li> <li>7. CRPSalmonellaComplexPhagocytizeByMDMIISubRoutine [BB. 7]</li> <li>8. CRPBindToApoptoticKupfferCellSubRoutine [BB. 8]</li> <li>9. CRPOpsionizedApoptoticKupfferCellPhagoc</li> </ol>	<ol style="list-style-type: none"> <li>1. <i>Salmonella</i></li> <li>2. <i>ActivatedNeutrophil</i></li> <li>3. <i>KupfferCell</i></li> <li>4. <i>MDMI</i></li> <li>5. <i>MDMI</i></li> <li>6. <i>MastCell</i></li> <li>7. <i>HepatocyteDeb</i></li> </ol>

		<p><i>Salmonella</i> are phagocytized by Kupffer Cells (205).</p> <p>4. CRP-bound <i>Salmonella</i> are phagocytized by mast cells (205).</p> <p>5. CRP-bound <i>Salmonella</i> are phagocytized by neutrophils (205).</p> <p>6. CRP-bound <i>Salmonella</i> are phagocytized by MDMLs (205).</p> <p>7. CRP-bound <i>Salmonella</i> are phagocytized by MDMLs (205).</p> <p>8. CRP binds to apoptotic Kupffer Cells (205).</p> <p>9. CRP-bound apoptotic Kupffer Cells are phagocytized by inflammatory cells (205).</p> <p>10. CRP binds to apoptotic hepatocytes (205).</p> <p>11. CRP-bound apoptotic hepatocytes are phagocytized by inflammatory cells (205).</p> <p>12. CRP binds to apoptotic neutrophils (205).</p> <p>13. CRP-bound apoptotic neutrophils are phagocytized by inflammatory cells (205).</p> <p>14. CRP binds to apoptotic monocyte-derived-macrophage type I (205).</p> <p>15. CRP-bound apoptotic monocyte-derived-macrophage type I are phagocytized by inflammatory cells (205).</p> <p>16. CRP binds to apoptotic monocyte-derived-macrophage type II (205).</p> <p>17. CRP-bound apoptotic monocyte-derived-macrophage type II are phagocytized by inflammatory cells (205).</p> <p>18. CRP undergo natural</p>	<p>ytizeByKupfferCellSubRoutine [BB. 9]</p> <p>10. CRPOpsionizedApoptoticKupfferCellPhagocytizeByMastCellSubRoutine [BB. 9]</p> <p>11. CRPOpsionizedApoptoticKupfferCellPhagocytizeByNeutrophilSubRoutine [BB. 9]</p> <p>12. CRPOpsionizedApoptoticKupfferCellPhagocytizeByMDMLSubRoutine [BB. 9]</p> <p>13. CRPOpsionizedApoptoticKupfferCellPhagocytizeByMDMLSubRoutine [BB. 9]</p> <p>14. CRPBindToHepatocyteDebrisSubRoutine [BB. 10]</p> <p>15. CRPOpsionizedHepatocyteDebrisPhagocytizeByKupfferCellSubRoutine [BB. 11]</p> <p>16. CRPOpsionizedHepatocyteDebrisPhagocytizeByMastCellSubRoutine [BB. 11]</p> <p>17. CRPOpsionizedHepatocyteDebrisPhagocytizeByNeutrophilSubRoutine [BB. 11]</p> <p>18. CRPOpsionizedHepatocyteDebrisPhagocytizeByMDMLSubRoutine [BB. 11]</p> <p>19. CRPOpsionizedHepatocyteDebrisPhagocytizeByMDMLSubRoutine [BB. 11]</p> <p>20. CRPBindToApoptoticNeutrophilSubRoutine [BB. 12]</p> <p>21. CRPOpsionizedApoptoticNeutrophilPhagocytizeByKupfferCellSubRoutine [BB. 13]</p> <p>22. CRPOpsionizedApoptoticNeutrophilPhagocytizeByMastCellSubRoutine [BB. 13]</p> <p>23. CRPOpsionizedApoptoticNeutrophilPhagocytizeByNeutrophilSubRoutine [BB. 13]</p> <p>24. CRPOpsionizedApoptoticNeutrophilPhagocytizeByMDMLSubRoutine [BB. 13]</p> <p>25. CRPOpsionizedApoptoticNeutrophilPhagocytizeByMDMLSubRoutine [BB. 13]</p> <p>26. CRPBindToApoptoticMDMLSubRoutine [BB. 14]</p> <p>27. CRPOpsionizedApoptoticMDMLPhagocytizeByKupfferCellSubRoutine [BB. 15]</p> <p>28. CRPOpsionizedApoptoticMDMLPhagocytizeByMastCellSubRoutine [BB. 15]</p> <p>29. CRPOpsionizedApoptoticMDMLPhagocytizeByNeutrophilSubRoutine [BB. 15]</p> <p>30. CRPOpsionizedApoptoticMDMLPhagocytizeByMDMLSubRoutine [BB. 15]</p> <p>31. CRPOpsionizedApoptoticMDMLPhagocytizeByMDMLSubRoutine [BB. 15]</p> <p>32. CRPBindToApoptoticMDMLSubRoutine [BB. 16]</p> <p>33. CRPOpsionizedApoptoticMDMLPhagocytizeByKupfferCellSubRoutine [BB. 17]</p> <p>34. CRPOpsionizedApoptoticMDMLPhagocytizeByMastCellSubRoutine [BB. 17]</p> <p>35. CRPOpsionizedApoptoticMDMLPhagocytizeByNeutrophilSubRoutine [BB. 17]</p> <p>36. CRPOpsionizedApoptoticMDMLPhagocytizeByMDMLSubRoutine [BB. 17]</p> <p>37. CRPOpsionizedApoptoticMDMLPhagocytizeByMDMLSubRoutine [BB. 17]</p> <p>38. CRPUndergoCatabolismByNatureSubRoutine [BB. 18]</p>	ris
--	--	---	--	-----

		catabolism (325).		
<b>NETs</b> (Neutrophil extracellular traps)		<ol style="list-style-type: none"> <li>NETs are released by neutrophils (214).</li> <li>NETs interact with <i>Salmonella</i> (214, 215, 293).</li> <li>NET undergoes natural catabolism.</li> </ol>	<ol style="list-style-type: none"> <li>For <b>BB. 1</b>, see <b>ActivatedNeutrophil Behavior(s). 12</b></li> <li>NETTrappSalmonellaSubRoutine [<b>BB. 2</b>]</li> <li>NETUndergoApoptosisByNatureSubRoutine [<b>BB.3</b>]</li> </ol>	<i>Salmonella</i>
<b>SECs</b> (Sinusoid endothelial cells)		<ol style="list-style-type: none"> <li>SECs are infected by <i>Salmonella</i> (176).</li> </ol>	<ol style="list-style-type: none"> <li>For <b>BB. 1</b>, see <b>Salmonella Behavior(s). 9</b></li> </ol>	<i>Salmonella</i>
<b>Signals</b> (Signal)		<ol style="list-style-type: none"> <li>Signals are sent by <i>Salmonella</i>, cytokines such as TNF-<math>\alpha</math> and HMGB-1, or cells such as activated neutrophils and CD4<sup>+</sup> T cells to recruit circulating neutrophil or circulating monocytes to the site of infection.</li> </ol>	<ol style="list-style-type: none"> <li>For <b>BB. 1</b>, see <b>RestingNeutrophil Behavior(s). 2</b> and <b>RestingMonocyte Behavior(s). 2</b></li> </ol>	<i>RestingNeutrophil</i>  <i>RestingMonocyte</i>
<b>AntiSignals</b> (Anti-signal)		<ol style="list-style-type: none"> <li>Anti-Signals are sent by activated neutrophils bind to CRP (323)[89, 90].</li> </ol>	<ol style="list-style-type: none"> <li>For <b>BB. 1</b>, see <b>ActivatedNeutrophil Behavior(s). 2</b></li> </ol>	<i>RestingNeutrophil</i>  <i>RestingMonocyte</i>

### Model Assumption:

- We assume that resting neutrophils (circulating neutrophils) proliferate in the bone marrow and traffic to the vessel near the site of infection when the infection occurs. This assumption is based on observations in a study (298) which showed massive neutrophil infiltration into peritoneum after 2 hrs of infection.
- We assume MDMI and MDMII will conduct some similar functions such as phagocytosis of apoptotic T cells (166). Some observations failed to differentiate the behaviors of MDMI and MDMII (166).
- We assume that HMGB-1 contributes to activation of neutrophils and monocytes. This assumption is based on recent identified biological activities of HMGB-1 including upregulation of endothelial adhesion molecules during the infection (24).
- We assume that resting monocytes (circulating monocytes) develop in the bone marrow and are circulating in the vessel near the site of infection when the infection occurs. This assumption is based on observations in a study (216) which showed massive monocyte infiltration following neutrophil infiltration.

5. We assume that activated neutrophils produce IL-10 after their interaction with *Salmonella* because it was observed that a rapid IL-10 production occurred during the early stages of sepsis (213).
6. We assume the level of apoptotic activated neutrophils contributes to the activation process of resting monocytes (circulating monocytes) based on studies (14, 142, 304) which showed activated macrophages phagocytize and ingest apoptotic neutrophils during infection.
7. We assume that TNF- $\alpha$  contributes to activation of neutrophils and monocytes. This assumption is based on recent identified biological evidence that TNF- $\alpha$  up-regulates endothelial adhesion molecules during the infection (298) and improved endothelial adhesion to induce monocyte trafficking to hepatic sites of Gram-positive bacterial infection (144). Other studies supporting this assumption are cited (222, 305, 306).
8. We assume that *Salmonella* contributes to activation of monocytes. This assumption is based on evidence showing that monocyte-derived-macrophages phagocytize Gram-negative bacteria (16).
9. We assume resting monocytes (circulating monocytes) undergo a constant basal level of apoptosis (a constant decay rate per hr). This assumption is based on data showing that circulating monocytes are programmed to undergo apoptosis in the absence of stimulation (307).
10. We assume TNF- $\alpha$  undergoes a degradation process. Experimental studies (various biological models) demonstrated TNF- $\alpha$  has a decay rate during infection (312-314).
11. We assume HMGB-1 undergoes a degradation process. Experimental studies (various biological models) demonstrated HMGB-1 has a decay rate during infection (38, 219, 315).
12. We assume IL-10 production inhibits the secretion of inflammatory cytokines (including TNF- $\alpha$ , HMGB-1 and IL-10) in our model. This assumption is based on biological evidence showing that IL-10 production inhibited the secretion of inflammatory cytokines (147-150).
13. We assume IL-10 undergo a natural catabolism since experimental studies demonstrated IL-10 had a decay rate during infection (316-318).
14. We assume each agent type has an equal chance of interacting with other agent types by following the agent rule.
15. We assume activated neutrophils can phagocytize multiple *Salmonella* (one ligand to multiple receptor mechanisms) at a time. However, *Salmonella* can't interact with multiple activated neutrophils at a time. Similarly, MDMLs can phagocytize multiple *Salmonella* at a time. However, *Salmonella* can't interact with multiple MDMLs at a time.
16. There is controversy about the replenishment of Kupffer Cells (123, 310, 326, 327); however, we assume Kupffer Cells are only replaced by bone marrow-derived macrophages due to the fact only bone marrow-derived KCs engaged in inflammatory responses (311).
17. We assume Kupffer Cells, mast cells, neutrophils, monocyte-derived-macrophage type I, and monocyte-derived-macrophage type II, interact with IL-10 since we assume IL-10 inhibits the production of pro-inflammatory cytokines in assumption 12.
18. We assume Kupffer Cells undergo apoptosis in the context of Kupffer cell turnover being observed (310, 311).
19. We assume one MDMLII can phagocytize more than one apoptotic activated neutrophil as observed previously (302).

20. We model T cell progenitors and B cell progenitors in the lymph node instead of thymus to generate mature CD4<sup>+</sup> T cells, CD8<sup>+</sup> T cells and B cells in our agent-based model.
21. We assume Kupffer Cells stop producing TNF- $\alpha$  by phagocytizing CRP-opsonized particles based on observations that synthetic CRP greatly decreased the production of TNF- $\alpha$  in a mouse model stimulated with *E.coli* (204).
22. Mast cells were observed to present high-affinity Fc $\gamma$ R receptor (328). We assume mast cells can phagocytize CRP-opsonized particles based on phagocytosis of CRP-opsonized particles proceeds through Fc $\gamma$ RI in a mouse model (329, 330).
23. We determined NETs secretion from neutrophil degranulation is dependent on the quantity of secreted neutrophil elastase (NE) from neutrophil degranulation. This assumption is based on the observation that NETs is a complex of NE (214). Since we failed to directly find a quantitation of NETs secretion from neutrophils, we believe that using secreted NE level to represent secreted NETs could be a reasonable assumption.
24. The activation of macrophages is related to IFN-gamma released by T cells (167-169). Since we didn't calibrate IFN- $\gamma$  in our model, we simplify to calculate macrophage activation process using CD4<sup>+</sup> T cell and CD8<sup>+</sup> T cell count in our model instead of IFN- $\gamma$  count.  
Since we didn't incorporate IL-6 in our model, we assume that CRP is released by hepatocytes (233) in response to monocyte infiltration because data show that monocytes are the main producer for IL-6 (331).

### **Table B.8 Agent Behaviors and Agent Update Rules in IMMABM**

NOTE: DATA IN THE AGENT RULE SECTION ARE FROM TABLE B. 9

<b>WORLD</b>
The world is a 200 units x 200 units square.
<p><b>Initialization (The initialization is setup under normal conditions)</b></p> <ol style="list-style-type: none"> <li>1. Hepatocytes are created. The initial number of hepatocytes is 80,200.</li> <li>2. Sinusoidal endothelial cells (SECs) are created and parallel arrangement in a two-dimensional world. They are structural agents which model the boundary of the liver sinusoid. The initial number of SECs is 26,466, which is approximately 1/3 of hepatocyte population.</li> <li>3. The liver sinusoid is created. They are modeled as “patches” with boundary lined by SECs. Liver sinusoid is separated from the hepatocytes by the space of Disse.</li> <li>4. The space of Disse is created as “patches” to model locations between hepatocytes and the liver sinusoid.</li> <li>5. Kupffer Cells are created adherent to SECs in the liver sinusoid. The initial number of Kupffer Cells is 20,160, which is approximately 1/4 of the hepatocyte population. Kupffer Cells are in a parallel arrangement in a two-dimensional world.</li> <li>6. Mast cells are placed in the space of Disse. The initial number of mast cells is 10,426, which is approximately 1/8 of the hepatocyte population. Mast cells are in a parallel arrangement in a two-dimensional world.</li> <li>7. Circulating neutrophils are created in the liver sinusoid, which take the place of</li> </ol>

being normally formed in the bone marrow. The initial number of circulating neutrophils is 1000. Circulating neutrophils are circle shaped with “multi-lobed nuclei” inside.

8. Circulating monocytes are created in the liver sinusoid, which take the place of being normally formed in the bone marrow. The initial number of circulating monocytes is 1000. Circulating monocytes are by circle shaped with “circle-shaped nuclei” inside.
9. The portal triad is represented as “patches” to model the site of T cells and B cell generation.
10. Circulating CD4<sup>+</sup> T cells are created in portal triad. The initial number of circulating CD4<sup>+</sup> T cells is 739, which is approximately 14% of total lymphocytes in the lymph node. CD4<sup>+</sup> T cells are represented as yellow circles in the portal triad.
11. Circulating CD8<sup>+</sup> T cells are created in portal triad. The initial number of circulating CD8<sup>+</sup> T cells is 482, which is approximately 9% of total lymphocytes in the lymph node. CD8<sup>+</sup> T cells are represented as green circles in portal triad.
12. Circulating B cells are created in portal triad. The initial number of circulating B cells is 3,235, which is approximately 60% of total lymphocytes in the lymph node. B cells are represented as blue circles in the portal triad.

#### ABM RULES (1 TICK REPRESENTS 1 HR DURING SIMULATION)

#### AGENTS

##### Kupffer Cell. (Called *KupfferCell* in the ABM.)

1. Phagocytose 90 ~ 95% *Salmonella* over 6 ticks.
2. 5% ~ 10% of the Kupffer Cells are killed by *Salmonella* from 4 tick - 6 ticks. [Active] Kupffer Cells are killed by *Salmonella*. [Inactive] Kupffer Cells are killed by *Salmonella* if interact with CD4<sup>+</sup> T cells.
3. Phagocytose hepatocyte debris.
4. Phagocytose activated circulating neutrophils in the liver sinusoid. 5% of the activated circulating neutrophils are phagocytosed by Kupffer Cells per tick. Activated circulating neutrophils are defined as circulating neutrophils that are attracted to SECs.
5. [Inactive] Secrete TNF- $\alpha$ . Activated if it interacts with *Salmonella*, hepatocyte debris, or activated circulating neutrophils. Rate of TNF- $\alpha$  released from Kupffer cells is  $2.09 \times 10^{-5} \sim 2.30 \times 10^{-4}$  pg/Kupffer Cell/tick. TNF production is computed with Michaelis-Menten Kinetics:  

$$\text{TNF-}\alpha \text{ [new]} = \frac{(\text{maximum production rate} * \text{Kupffer Cell [who release TNF-}\alpha\text{]})}{(\text{Kupffer Cell count at which the reaction rate is half of maximum production rate} + \text{Kupffer Cell [who release TNF-}\alpha\text{]})} \times \text{Kupffer Cell [who release TNF-}\alpha\text{]}$$
 Maximum production rate is equivalent to  $2.30 \times 10^{-4}$  pg/Kupffer Cell/tick.
6. [With 14.3% probability] Bind to IL-10. [Inactive] Produce TNF- $\alpha$ .
7. Kupffer Cells are replenished at a rate of 0.63% ~ 0.79% of monocyte-derived-



macrophage type I or monocyte-derived-macrophage type II per tick.

8. [Inactive] Secretes IL-10. Activated if they ingest apoptotic hepatocytes. Rate of IL-10 released from Kupffer Cells is  $4.98 \times 10^{-6}$  pg/Kupffer Cell/tick. IL-10 production is computed with Michaelis-Menten Kinetics:

$IL-10 [new] = ((\text{maximum production rate} * \text{Kupffer Cell [who release IL-10]}) / (\text{Kupffer Cell$

count at which the reaction rate is half of maximum production rate + Kupffer Cell [who release

IL-10]))  $\times$  Kupffer Cell [who release IL-10]. Maximum production rate is equivalent to  $4.98 \times 10^{-6}$

pg/Kupffer Cell/tick.

9. [With 16.7% probability] Apoptotic Kupffer cells interact with CRP.
10. [With 20% probability ] CRP-opsonized apoptotic Kupffer cells are phagocytized by Kupffer cells, or mast cells, or monocyte-derived-macrophage type I, or monocyte-derived-macrophage type II, or neutrophils.
- If CRP-opsonized apoptotic Kupffer Cells are phagocytized by Kupffer Cells, [Inactive] secretes TNF- $\alpha$ . [Increase] phagocytic rate.
  - If CRP-opsonized apoptotic Kupffer Cells are phagocytized by monocyte-derived-macrophage type I, [Active] secretes TNF- $\alpha$ . [Increase] phagocytic rate.
  - If CRP-opsonized apoptotic Kupffer Cells are phagocytized by neutrophils, [Inactive] neutrophil adhere to SECs.
11. CRP-opsonized apoptotic Kupffer Cells die if the number of ticks is higher than 1 tick, the lifespan of apoptotic cells. Reset states of interacted agents.
12. [With 20% probability] Kupffer Cells phagocytize CRP-opsonized *Salmonella*, CRP-opsonized apoptotic mast cells, CRP-opsonized apoptotic monocyte-derived-macrophage type I, CRP-opsonized apoptotic monocyte-derived-macrophage type II, CRP-opsonized apoptotic neutrophils, or CRP-opsonized apoptotic hepatocytes. [Inactive] secretes TNF- $\alpha$ . [Increase] phagocytic rate.
13. [Inactive] Kupffer Cells which phagocytose *Salmonella* undergo apoptosis. [Active] If they interact with CD8<sup>+</sup> T cells. Kupffer Cells die if the number of ticks is higher than 4.

*Salmonella*. (Called *Salmonella* in the ABM.)

- [Inactive] 90 ~ 95% *Salmonella* are phagocytized by Kupffer Cells over 6 ticks. [Active] if they interact with Kupffer Cells.
- Phagocytosed *Salmonella* are killed by Kupffer Cells if the total number of ticks is higher than the lifespan of *Salmonella* in Kupffer Cells. The lifespan of *Salmonella* in Kupffer Cells is generated from a random-generator with a uniform distribution from 0 to 6 ticks.
- Salmonella* survive and replicate within apoptotic Kupffer Cells. The maximum number of *Salmonella* in one Kupffer Cell is 50. The replication rate is 0.42 ~ 1.04/tick. *Salmonella* population is computed with the logistic equation:  $Salmonella [new] = \text{replication rate} * Salmonella [old] * (1 - Salmonella [old] / Salmonella \text{ carrying capacity in Kupffer Cells})$ . *Salmonella* carrying capacity in Kupffer Cells = 4558000.
- Apoptotic Kupffer Cells die and release *Salmonella*. Released *Salmonella* interact with SECs, hepatocytes, NETs, antibody, CRP or normal inflammatory cells (including Kupffer Cells, mast cells, neutrophils, monocyte-derived-macrophage

- type I). The chance of interaction is dependent on the random movement of the *Salmonella* agent.
5. [Inactive] Released *Salmonella* infect SECs. [Active] if they interact with SECs. The replication rate is 0.32/tick. The maximum number of *Salmonella* in one SEC is 3. The *Salmonella* population is computed with a logistic equation:  
 $Salmonella [new] = replication\ rate * Salmonella [old] * (1 - Salmonella [old] / Salmonella\ carrying\ capacity\ in\ SECs)$ . *Salmonella* carrying capacity in SECs=67000.
  6. [Inactive] Released *Salmonella* from killed (dead) SECs move to mast cells, hepatocytes or interact with nearby inflammatory cells (including neutrophils and MDMs). [Active] if SECs die. Infected SECs die after 1 tick.
  7. [Inactive] Released *Salmonella* infect and replicate within healthy hepatocytes. [Active] if released *Salmonella* interact with hepatocytes. Replication rate is 0.05 ~ 0.26/tick. State variable named “hepatocyteInteractWith*Salmonella*” is updated from 0 to 1. The maximum number of *Salmonella* in one hepatocyte is 3. *Salmonella* population is computed with a logistic equation:  
 $Salmonella [new] = replication\ rate * Salmonella [old] * (1 - Salmonella [old] / Salmonella\ carrying\ capacity\ in\ hepatocytes)$ . *Salmonella* carrying capacity in hepatocytes=817000.
  8. *Salmonella* are released from apoptotic hepatocytes and infect nearest hepatocytes. The chance of interaction is dependent on the random movement of the *Salmonella* agent.
  9. [Inactive] Released *Salmonella* are phagocytosed by neutrophils. [Active] if interact with neutrophils. Phagocytic rate of *Salmonella* by neutrophils is 2.94 ~ 12.94 *Salmonella*/neutrophil/tick. The maximum number of *Salmonella* interactions with an activated neutrophil is 17.
  10. Phagocytized *Salmonella* are killed by neutrophils if the total number of ticks is higher than 2 ticks.
  11. [Inactive] Released *Salmonella* are phagocytosed by monocyte-derived-macrophage type I. [Active] if interact with monocyte-derived-macrophage type I. Phagocytic rate of *Salmonella* by monocyte-derived-macrophage type I is 1.18 ~ 6.74 *Salmonella*/macrophage/tick.
  12. Phagocytosed *Salmonella* are killed by monocyte-derived-macrophage type I if the total number of ticks is higher than 2 ticks.
  13. *Salmonella* survive and replicate within apoptotic monocyte-derived-macrophage type I. The replication rate is 0.9 ~ 10.9/tick. The *Salmonella* population is computed with a logistic equation:  
 $Salmonella [new] = replication\ rate * Salmonella [old] * (1 - Salmonella [old] / Salmonella\ carrying\ capacity\ in\ macrophages)$ . *Salmonella* carrying capacity in macrophages =4558000.
  14. [Inactive] Released *Salmonella* are killed by neutrophil extracellular traps (NETs). [Active] if they interact with NETs. The NETs is a complex of Myeloperoxidase (MPO) and neutrophil elastase (NE). 22.79% of *Salmonella* are trapped and killed by 1 $\mu$ M NETs per tick.
  15. [Inactive] Released *Salmonella* bind to mast cells. [Active] if they interact with mast cells. The chance of an interaction is determined by an estimated

probability.

16. [With 20% probability] CRP-opsonized *Salmonella* are phagocytosed by phagocytic cells (Kupffer Cells, or mast cells, or neutrophils, or monocyte-derived-macrophage type I, or monocyte-derived-macrophage-type II). [Update] phagocytosis rate.
17. CRP-opsonized *Salmonella* die if the number of ticks is higher than 1 tick, the lifespan of *Salmonella*. Reset states of interacted agents.
18. [With 20% probability] Antibody-opsonized *Salmonella* are phagocytosed by phagocytic cells (Kupffer Cells, or mast cells, or neutrophils, or monocyte-derived-macrophage type I, or monocyte-derived-macrophage type II). [Update] phagocytosis rate.
19. [With 20% probability] Antibody-opsonized *Salmonella* die if the number of ticks is higher than 1 tick, the lifespan of *Salmonella*. Reset states of interacted agents.
20. [Inactive] *Salmonella* undergo apoptosis by other factors. [Active] if they bind to mast cells. Apoptosis rate is estimated.

Hepatocyte. (Called *Hepatocyte* in the ABM.)

1. [Inactive] Hepatocytes are infected by *Salmonella* and become apoptotic. [Active] if they interact with *Salmonella*. The chance of interaction is dependent on the random movement of *Salmonella*.
2. [Inactive] Hepatocytes become apoptotic by interacting with TNF- $\alpha$ . [Active] if they interact with TNF- $\alpha$ . The interaction between TNF- $\alpha$  and hepatocytes is dependent on the random diffusion of TNF- $\alpha$ .
3. [Inactive] Produce CRP. [Active] if monocyte infiltration is detected. The rate is 0.2pg/hepatocyte/tick. CRP production is computed with Michaelis-Menten Kinetics:

$$\text{CRP [new]} = ((\text{maximum production rate} * \text{Hepatocyte [old]}) / (\text{Hepatocyte count at which the reaction rate is half of maximum production rate} + \text{Hepatocyte [old]})) \times \text{Hepatocyte [old]}.$$

Maximum production rate is equivalent to 0.2pg/hepatocyte/tick.

4. [Inactive] Apoptotic hepatocytes are cleaned up by neutrophils. [Active] if they interact with neutrophils. The phagocytosis rate of hepatocytes by neutrophils is 0.05 ~ 0.2 hepatocytes/neutrophil/tick.
5. Apoptotic hepatocytes become hepatocyte debris if the total number of ticks is higher than 2 or 3 ticks (2 or 3 is randomly assigned by a random generator).
6. Apoptotic hepatocytes release HMGB-1. The rate is  $6.25 \times 10^{-5}$  pg/hepatocyte/tick. HMGB-1 production is computed with Michaelis-Menten Kinetics:

$$\text{HMGB-1[new]} = ((\text{maximum production rate} * \text{Hepatocyte [apoptotic]}) / (\text{Hepatocyte count at which the reaction rate is half of maximum production rate} + \text{Hepatocyte [apoptotic]})) \times$$

Hepatocyte [apoptotic]. Maximum production rate is equivalent to  $6.25 \times 10^{-5}$  pg/hepatocyte/tick.

7. Apoptotic hepatocytes release TNF- $\alpha$ . The rate is  $7.14 \times 10^{-5}$  -  $9.18 \times 10^{-5}$  pg/apoptotic hepatocyte/tick. TNF- $\alpha$  production is computed with Michaelis-Menten Kinetics:

$TNF-\alpha_{[new]} = ((\text{maximum production rate} * \text{Hepatocyte [apoptotic]}) / (\text{Hepatocyte count at which the reaction rate is half of maximum production rate} + \text{Hepatocyte [apoptotic]})) \times \text{Hepatocyte [apoptotic]}$ . Maximum production rate is equivalent to  $9.18 \times 10^{-5}$  pg/apoptotic hepatocyte/tick.

- Hepatocytes regenerate. The replication rate is  $1.32 \times 10^{-3} \sim 6.80 \times 10^{-3}$  /tick. The hepatocyte population is computed with a logistic equation:  
 $\text{Hepatocyte [new]} = \text{replication rate} * \text{Hepatocyte [old]} * (1 - \text{Hepatocyte [old]} / \text{hepatocyte carrying capacity})$ . Hepatocyte carrying capacity = the initial number of hepatocytes

Hepatocyte debris. (Called *HepatocyteDebris* in the ABM.)

- Hepatocyte debris is phagocytosed by phagocytic cells including Kupffer Cells, mast cells, neutrophils, monocyte-derived-macrophage type I, and monocyte-derived-macrophage type II. The phagocytic rate is dependent on random dispersion of hepatocyte debris. The radius of random dispersion is patch-size.
- [With 20% probability] CRP interacts with hepatocyte debris. CRP-opsonized hepatocyte debris is phagocytosed by phagocytic cells including Kupffer Cells, mast cells, neutrophils, monocyte-derived-macrophage type I, and monocyte-derived-macrophage type II. The phagocytic rate is dependent on random movement of phagocytic cells.
- Hepatocyte debris degrades naturally. The degradation rate of is estimated.

Resting neutrophil. (Called *RestingNeutrophil* in the ABM.)

- Resting neutrophil migrate to the liver sinusoid from bone marrow upon infection. The influx rate to the liver sinusoid is  $0.125 \sim 14$ /tick. The resting neutrophil population is computed with a logistic equation:  
 $\text{Resting neutrophil [new]} = \text{influx rate} * \text{Resting neutrophil [old]} * (1 - \text{Resting neutrophil [old]} / \text{resting neutrophil carrying capacity})$ . Resting neutrophil carrying capacity =  $6.9 \times 10^3$ .
- [Inactive] Resting neutrophils get signals and move to SECs. [Active] if *Salmonella*,  $TNF-\alpha$ , and HMGB-1 are detected after 2 ticks. [Set breed] Activated neutrophils. Activation rate is  $0.09 \sim 0.46$ /hrs. Activated neutrophil population is computed with law of mass-action:  
 $\text{Activated neutrophil [new]} = \text{activation rate} * \text{Resting neutrophil population} * (\text{Salmonella population} + \text{TNF-}\alpha + \text{HMGB-1}) / \text{Total population}$ . Total population =  
 $\text{hepatocyteInitialNumber} + \text{mastCellInitialNumber} + \text{kupfferCellInitialNumber} + \text{SECsInitialNumber}$ .
- Resting neutrophils undergo aging and apoptosis. The rate of apoptosis is  $0.05 \sim 0.092$ /tick.

Activated neutrophil. (Called *ActivatedNeutrophil* in the ABM.)

1. Activated neutrophils move towards the site of Kupffer Cells, or apoptotic hepatocytes or *Salmonella*.
2. Activated neutrophils undergo aging. State variable named “activatedNeutrophilBecomeApoptotic” is updated from 0 to 1 if apoptosis starts. The rate of apoptosis is 0.098/tick.
3. Apoptotic neutrophils interact with CRP.
4. [With 20% probability ] CRP-opsonized apoptotic activated neutrophils are phagocytized by Kupffer Cells, or mast cells, or monocyte-derived-macrophage type I, or monocyte-derived-macrophage type II, or neutrophils.
  - a. If CRP-opsonized apoptotic activated neutrophils are phagocytosed by Kupffer Cells, [Inactive] secretes TNF- $\alpha$ . [Increase] phagocytic rate.
  - b. If CRP-opsonized apoptotic activated neutrophils are phagocytosed by monocyte-derived-macrophage type I, [Active] secretes TNF- $\alpha$ . [Increase] phagocytic rate.
  - c. If CRP-opsonized apoptotic activated neutrophils are phagocytosed by neutrophils, [Inactive] neutrophil adhere to SECs.
5. CRP-opsonized apoptotic activated neutrophils die if the number of ticks is higher than 1 tick, the lifespan of apoptotic activated neutrophils. Reset states of interacted agents.
6. [Inactive] Apoptotic neutrophils are ingested by monocyte-derived-macrophage type II. [Active] if neutrophils interact with monocyte-derived-macrophage type II. Apoptotic neutrophils die after 1 tick.
7. [Inactive] Activated neutrophils produce TNF- $\alpha$ . [Active] if they interact with *Salmonella*. The rate is 0.19 ~ 2.00 pg/neutrophil/tick. TNF- $\alpha$  production is computed with Michaelis-Menten Kinetics:

$$\text{TNF-}\alpha \text{ [new]} = \left( \frac{\text{maximum production rate} * \text{Activated neutrophil [interact with } \textit{Salmonella}]}{\text{Activated neutrophil count at which the reaction rate is half of maximum production rate} + \text{Activated neutrophil [interact with } \textit{Salmonella}]} \right) * \text{Activated neutrophil [interact with } \textit{Salmonella}]$$
 Maximum production rate is equivalent to 2.00 pg/neutrophil/tick.

8. [Inactive] Activated neutrophils produce IL-10. [Active] if interact with *Salmonella*. The rate is  $8.44 \times 10^{-5} \sim 1.03 \times 10^{-4}$  pg/neutrophil/tick. IL-10 production is computed with Michaelis-Menten Kinetics:

$$\text{IL-10 [new]} = \left( \frac{\text{maximum production rate} * \text{Activated neutrophil [interact with } \textit{Salmonella}]}{\text{Activated neutrophil count at which the reaction rate is half of maximum production rate} + \text{Activated neutrophil [interact with } \textit{Salmonella}]} \right) * \text{Activated neutrophil [interact with } \textit{Salmonella}]$$
 Maximum production rate is equivalent to  $1.03 \times 10^{-4}$  pg/neutrophil/tick.

9. [Inactive] Activated neutrophils release MPO, NE, and NETs by degranulation. [Active] if interact with *Salmonella*. New values are computed with the equation: NETs [new] = MPO [new] = NE [new] (NETs is a complex agent of MPO and NE)
10. [With 20% probability] Bind to IL-10. [Inactive] Produce TNF- $\alpha$  or IL-10.

11. [Inactive] Activated neutrophils that phagocytose *Salmonella* undergo apoptosis. [Active] If neutrophils interact with CD8<sup>+</sup> T cells. Activated neutrophils die if the number of ticks is higher than 4 ticks.

Resting monocyte. (Called *RestingMonocyte* in the ABM.)

1. [Inactive] Resting monocytes migrate to the liver sinusoid from bone marrow upon infection. [Active] After 2 ticks. Influx rate to the liver sinusoid is 1 ~ 1.75/tick. The resting monocyte population is computed with a logistic equation: Resting monocyte [new] =influx rate \* Resting monocyte [old] \*(1-Resting monocyte [old]/ resting monocyte carrying capacity). Resting monocyte carrying capacity = 1.4×10<sup>3</sup>.
2. [Inactive] Resting monocytes get a signal and move to SECs. [Active] if *Salmonella*, TNF-α, HMGB-1, and apoptotic neutrophils are detected. [Set breed] monocyte-derived-macrophage type I if interact with *Salmonella*. [Set breed] monocyte-derived-macrophage type II if interact with apoptotic neutrophils. Activation rate is 0.25~4.82/hrs. New population is computed with law of mass-action:  
(Monocyte-derived-macrophage type I [new] + monocyte-derived-macrophage type II [New])=activation rate \* Resting monocyte population \* (*Salmonella* population + TNF-α + HMGB-1 + apoptotic neutrophils) / Total population. Total population = hepatocyteInitialNumber + mastCellInitialNumber + kupfferCellInitialNumber + SECsInitialNumber.
3. Resting monocytes age and undergo apoptosis. The rate of apoptosis is 6.90×10<sup>-3</sup> ~ 2.10×10<sup>-2</sup>/tick.

Monocyte-derived-macrophage type I. (Called *MDMI* in the ABM.)

1. Phagocytose *Salmonella* [See *Salmonella* 11].
2. [Inactive] Monocyte-derived-macrophage type I produce TNF-α. [Active] if they phagocytose *Salmonella*. The rate is 1.70×10<sup>-4</sup> pg/macrophage/tick. TNF-α production is computed with Michaelis-Menten Kinetics:  
TNF-α [new] = ((maximum production rate \* Monocyte-derived-macrophage type I [interact with *Salmonella*])/(Monocyte-derived-macrophage type I count at which the reaction rate is half of maximum production rate + Monocyte-derived-macrophage type I [interact with *Salmonella*])) × Monocyte-derived-macrophage type I [interact with *Salmonella*]. Maximum production rate is equivalent to 1.70×10<sup>-4</sup> pg/macrophage/tick.
3. [Inactive] Produce IL-10. [Active] if they phagocytose apoptotic T cells. The rate is 2.02×10<sup>-5</sup> pg/monocyte-derived-macrophage type I/tick. IL-10 production is computed with Michaelis-Menten Kinetics:  
IL-10 [new] = ((maximum production rate \* Monocyte-derived-macrophage type I [interact with

apoptotic T cells)]/(Monocyte-derived-macrophage type I count at which the reaction rate is half of maximum production rate + Monocyte-derived-macrophage type I [interact with apoptotic T cells])) × Monocyte-derived-macrophage type I [interact with apoptotic T cells]. Maximum production rate is equivalent to is  $2.02 \times 10^{-5}$  pg/monocyte-derived-macrophage type I/tick.

4. Monocyte-derived-macrophage type I are killed by *Salmonella*. The killing rate is estimated. [Active] Monocyte-derived-macrophage type I are killed by *Salmonella*. [Inactive] Monocyte-derived-macrophage type I are killed by *Salmonella* if they interact with CD4<sup>+</sup> T cells.
5. Monocyte-derived-macrophage type I undergo aging. The rate needs to be estimated. State variable named “MDMIBecomeApoptotic” is updated from 0 to 1.
6. [With 20% probability ] CRP-opsonized apoptotic monocyte-derived-macrophage type I are phagocytosed by Kupffer Cells, or mast cells, or monocyte-derived-macrophage type I, or monocyte-derived-macrophage type II, or neutrophils.
  - a. If CRP-opsonized apoptotic monocyte-derived-macrophage type I are phagocytosed by Kupffer Cells, [Inactive] they secrete TNF- $\alpha$ . [Increase] phagocytic rate.
  - b. If CRP-opsonized apoptotic monocyte-derived-macrophage type I are phagocytosed by monocyte-derived-macrophage type I, [Active] secretes TNF- $\alpha$ . [Increase] phagocytic rate.
  - c. If CRP-opsonized apoptotic monocyte-derived-macrophage type I are phagocytosed by neutrophils, [Inactive] the neutrophils adhere to SECs.
7. CRP-opsonized apoptotic monocyte-derived-macrophage type I die if the number of ticks is higher than 1 tick, the lifespan of apoptotic monocyte-derived-macrophage type I. Reset states of interacted agents.
8. [With 20% probability] Monocyte-derived-macrophage type I phagocytose CRP-opsonized *Salmonella*, CRP-opsonized apoptotic mast cells, CRP-opsonized apoptotic monocyte-derived-macrophage type I, CRP-opsonized apoptotic monocyte-derived-macrophage type II, CRP-opsonized apoptotic neutrophils, or CRP-opsonized apoptotic hepatocytes. [Active] secretes TNF- $\alpha$ . [Increase] phagocytic rate.
9. 0.63% ~ 0.79% of monocyte-derived-macrophage type I transform to Kupffer Cells every tick. [set breed] Kupffer Cells [See Kupffer Cell 7].
10. [With 20% probability] Bind to IL-10. [Inactive] Produce TNF- $\alpha$ .
11. Monocyte-derived-macrophage type I activate T cell activation.
12. [Inactive] Monocyte-derived-macrophage type I who phagocytose *Salmonella* undergo apoptosis. [Active] If interact with CD8<sup>+</sup> T cells. Monocyte-derived-macrophage type I die if the number of ticks is greater than 4 ticks.

Monocyte-derived-monocytes type II. (Called *MDMII* in the ABM.)

1. Phagocytose apoptotic neutrophils [See Activated neutrophil 6].
2. [Inactive] Produce HMGB-1. [Active] if phagocytosing apoptotic neutrophils. The rate is  $9.38 \times 10^{-3} \sim 4.97 \times 10^{-1}$  pg/monocyte-derived-macrophage type II/tick. HMGB-1 production is computed with Michaelis-Menten Kinetics: HMGB-1 [new] = ((maximum production rate \* Monocyte-derived-macrophage type II [interact

with apoptotic neutrophils)]/(Monocyte-derived-macrophage type II count at which the reaction rate is half of maximum production rate + Monocyte-derived-macrophage type II [interact with apoptotic neutrophils])) × Monocyte-derived-macrophage type II [interact with apoptotic neutrophils]. Maximum production rate is equivalent to  $4.97 \times 10^{-1}$  pg/monocyte-derived-macrophage type II/tick.

3. [Inactive] Produce IL-10. [Active] if phagocytosing apoptotic neutrophils or phagocytosing apoptotic T cells. The rate is  $2.02 \times 10^{-5}$  pg/monocyte-derived-macrophage type II/tick. Assume they produce the same rate of IL-10 under both conditions. IL-10 production is computed with Michaelis-Menten Kinetics: IL-10 [new] = ((maximum production rate \* Monocyte-derived-macrophage type II [interact with apoptotic neutrophils or apoptotic T cells)]/(Monocyte-derived-macrophage type II count at which the reaction rate is half of maximum production rate + Monocyte-derived-macrophage type II [interact with apoptotic neutrophils or apoptotic T cells])) × Monocyte-derived-macrophage type II [interact with apoptotic neutrophils or apoptotic T cells]. Maximum production rate is equivalent to is  $2.02 \times 10^{-5}$  pg/monocyte-derived-macrophage type II/tick.
4. Phagocytose apoptotic T cells.
5. Undergo natural aging. The rate needs to be estimated. State variable named “MDMIIBecomeApoptotic” is updated from 0 to 1.
6. [With 20% probability ] CRP-opsonized apoptotic monocyte-derived-macrophage type II are phagocytosed by Kupffer Cells, or mast cells, or monocyte-derived-macrophage type I, or monocyte-derived-macrophage type II, or neutrophils.
  - a. If CRP-opsonized apoptotic monocyte-derived-macrophage type II are phagocytosed by Kupffer Cells, [Inactive] secretes TNF- $\alpha$ . [Increase] phagocytic rate.
  - b. If CRP-opsonized apoptotic monocyte-derived-macrophage type II are phagocytosed by monocyte-derived-macrophage type I, [Active] secretes TNF- $\alpha$ . [Increase] phagocytic rate.
  - c. If CRP-opsonized apoptotic monocyte-derived-macrophage type II are phagocytosed by neutrophils, [Inactive] the neutrophils adhere to SECs.
7. CRP-opsonized apoptotic monocyte-derived-macrophage type II die if the number of ticks is higher than 1 tick, the lifespan of apoptotic monocyte-derived-macrophage type II. Reset states of interacted agents.
8. [With 20% probability] Monocyte-derived-macrophage type II phagocytose CRP-opsonized *Salmonella*, CRP-opsonized apoptotic mast cells, CRP-opsonized apoptotic monocyte-derived-macrophage type I, CRP-opsonized apoptotic monocyte-derived-macrophage type II, CRP-opsonized apoptotic neutrophils, or CRP-opsonized apoptotic hepatocytes. [Active] secretes TNF- $\alpha$ . [Increase] phagocytic rate.
9. 0.63% ~ 0.79% of monocyte-derived-macrophage type II transform to Kupffer Cells every tick. [set breed] Kupffer Cells [See Kupffer Cell 7].
10. [With 20% probability] Bind to IL-10. [Inactive] Produce HMGB-1.



11. Monocyte-derived-macrophage type II activate T cell activation.  
Mast cell. (Called *MastCell* in the ABM.)

1. Proliferate at a rate of  $9.45 \times 10^{-4} \sim 1.37 \times 10^{-2}$ /tick.
2. [Inactive] Produce histamine. [Active] If interact with antibody-opsonized *Salmonella*. The rate is 0.12-0.18 pg /mast cell/tick. Histamine production is computed with Michaelis-Menten Kinetics:  
Histamine [new] = ((maximum production rate \* Mast cell [interact with antibody-opsonized *Salmonella*]) / (Mast cell count at which the reaction rate is half of maximum production rate + Mast cell [interact with antibody-opsonized *Salmonella*])) × Mast cell [interact with antibody-opsonized *Salmonella*]. Maximum production rate is equivalent to 0.18 pg /mast cell/tick.
3. [Inactive] Produce TNF- $\alpha$ . [Active] if bind to *Salmonella* or bind to antibody-opsonized *Salmonella* [See *Salmonella* 15]. The rate is  $1.33 \times 10^{-7} \sim 1.52 \times 10^{-7}$  pg/mast cell/tick. TNF- $\alpha$  production is computed with Michaelis-Menten Kinetics:  
TNF- $\alpha$  [new] = ((maximum production rate \* Mast cell [bind to *Salmonella*]) / (Mast cell count at which the reaction rate is half of maximum production rate + Mast cell [bind to *Salmonella*])) × Mast cell [bind to *Salmonella*]. Maximum production rate is equivalent to is  $1.52 \times 10^{-7}$  pg/mast cell/tick.
4. [Inactive] Recruit T cells to liver sinusoid. [Active] If both histamine and TNF- $\alpha$  are detected.
5. [With 20% probability] Bind to IL-10. [Inactive] Produce TNF- $\alpha$ .
6. [With 20% probability] Mast cells phagocytose CRP-opsonized *Salmonella*, CRP-opsonized apoptotic Kupffer Cells, CRP-opsonized apoptotic hepatocyte debris, CRP-opsonized apoptotic neutrophils, CRP-opsonized monocyte-derived-macrophage type I, or CRP-opsonized monocyte-derived-macrophage type II.
7. Undergo natural aging. The apoptotic rate needs to be estimated.

CD4 T cell. (Called *CD4TCell* in the ABM.)

1. [Inactive] Migrate from the portal triad to the liver sinusoid. [Active] if MDMIIs or MDMIIIs or both histamine and TNF- $\alpha$  are detected. The migration rate is  $1.24 \times 10^{-3} \sim 2.75 \times 10^{-2}$ /hrs. CD4<sup>+</sup> T cell population is computed with a logistic equation:  
CD4<sup>+</sup> T cell [new] =influx rate \* CD4<sup>+</sup> T cell [old] \*(1-CD4<sup>+</sup> T cell [old]/ CD4<sup>+</sup> T cell carrying capacity). CD4<sup>+</sup> T cell carrying capacity = 1373425.
8. [Inactive] Produce TNF- $\alpha$ . [Active] If interact with APCs including Kupffer Cells, neutrophils, or monocyte-derived-macrophage type I. The rate is  $6.94 \times 10^{-7}$  pg/T cell/hrs. TNF- $\alpha$  production is computed with Michaelis-Menten Kinetics:  
TNF- $\alpha$  [new] = ((maximum production rate \* CD4<sup>+</sup> T cell [bind to APCs]) / (CD4<sup>+</sup> T cell count

at which the reaction rate is half of maximum production rate + CD4<sup>+</sup> T cell [bind to APCs])) × CD4<sup>+</sup> T cell [bind to APCs]. Maximum production rate is equivalent to is  $6.94 \times 10^{-7}$  pg/CD4<sup>+</sup> T cell /tick.

9. [Inactive] Produce IL-10. [Active] If interact with APCs including Kupffer Cells, neutrophils, or monocyte-derived-macrophage type I. The rate is  $8.33 \times 10^{-7}$ - $9.69 \times 10^{-7}$  pg/T cell/hrs. IL-10 production is computed with Michaelis-Menten Kinetics:

IL-10 [new] = ((maximum production rate \* CD4<sup>+</sup> T cell [bind to APCs]) / (CD4<sup>+</sup> T cell count at which the reaction rate is half of maximum production rate + CD4<sup>+</sup> T cell [bind to APCs])) ×

CD4<sup>+</sup> T cell [bind to APCs]. Maximum production rate is equivalent to is  $9.69 \times 10^{-7}$  pg/CD4<sup>+</sup> T cell /tick.

2. [Inactive] Apoptotic CD4<sup>+</sup> T cells are phagocytosed by monocyte-derived-macrophage type I or monocyte-derived-macrophage type II. [Active] If they interact with monocyte-derived-macrophage type I or monocyte-derived-macrophage type II.

3. Undergo natural aging. The apoptotic rate needs to be estimated.

CD8 T cell. (Called *CD8TCell* in the ABM.)

1. [Inactive] Migrate from the portal triad to the liver sinusoid. [Active] if MDMIs or MDMIIIs or both histamine and TNF-α are detected. The migration rate is  $6.25 \times 10^{-2}$ /hrs. CD8<sup>+</sup> T cell population is computed with a logistic equation:

CD8<sup>+</sup> T cell [new] =influx rate \* CD8<sup>+</sup> T cell [old] \*(1- CD8<sup>+</sup> T cell [old]/ CD8<sup>+</sup> T cell carrying capacity). CD8<sup>+</sup> T cell carrying capacity = 250625.

2. [Inactivate] Apoptosis of Kupffer Cells, neutrophils, and monocyte-derived-macrophage type I who phagocytose *Salmonella*. [Active] If interact with APCs including Kupffer Cells, neutrophils, and monocyte-derived-macrophage type I.

3. [Inactive] Apoptotic CD8<sup>+</sup> T cells are phagocytosed by monocyte-derived-macrophage type I or monocyte-derived-macrophage type II. [Active] If interact with monocyte-derived-macrophage type I or monocyte-derived-macrophage type II.

4. Undergo natural aging. The apoptotic rate needs to be estimated.

B cell. (Called *BCell* in the ABM.)

1. [Inactive] Migrate from the portal triad to the liver sinusoid. [Active] if MDMIs are detected. The migration rate is  $4.30 \times 10^{-4}$ - $2.40 \times 10^{-2}$ /hr. The B cell population is computed with a logistic equation:

B cell [new] =influx rate \* B cell [old] \*(1-B cell [old]/ B cell carrying capacity). B cell carrying capacity = 1433575.

2. [Inactivate] Produce antibody. [Activate] if they interact with CD4<sup>+</sup> T cells. The rate is  $4.88 \times 10^{-4}$ - $2.81 \times 10^{-3}$  pg/B cell/hr.

3. Undergo natural aging. The apoptotic rate needs to be estimated.  
Antibody. (Called *Antibody* in the ABM.)

1. Antibodies are produced by B cells [See B cell 2].
2. Interact with *Salmonella* to form antibody-opsonized *Salmonella*. The average amount of antibody binding to one *Salmonella* is 5.31 pg.
3. [With 20% probability] Antibody-opsonized *Salmonella* interact with mast cells [See Mast cell 2].
4. [With 20% probability] Antibody-opsonized *Salmonella* interact with phagocytic cells including Kupffer Cells, or mast cells, or neutrophils, or monocyte-derived-macrophage type I, or monocyte-derived-macrophage type II. [Increase] Phagocytosis rate of if interaction with phagocytic cells is detected. [Set] Antibody decays if the interaction with phagocytic cells is detected.

CRP. (Called *CRP* in the ABM.)

1. [Inactive] Inhibits resting neutrophil recruitment. [Active] if CRP-opsonized apoptotic Kupffer Cells, CRP-opsonized apoptotic activated neutrophils, CRP-opsonized apoptotic MDMIs, or CRP-opsonized apoptotic MDMIIIs.
2. CRP is released by hepatocytes [See Hepatocyte 3].
3. [With 16.7% probability] CRP binds to *Salmonella*.
4. [With 20% probability] CRP-opsonized *Salmonella* are phagocytosed by phagocytic cells [See *Salmonella* 16]
5. [With 20% probability] CRP-opsonized apoptotic Kupffer Cells are phagocytosed by phagocytic cells [See Kupffer Cell 12].
6. [With 20% probability] CRP-opsonized hepatocyte debris are phagocytosed by phagocytic cells [See Hepatocyte debris 2].
7. [With 20% probability] CRP-opsonized apoptotic neutrophils are phagocytosed by phagocytic cells [See Activated neutrophil 4]
8. [With 20% probability] CRP-opsonized apoptotic monocyte-derived-macrophage type I are phagocytosed by phagocytic cells [See monocyte-derived-macrophage type I 6]
9. CRP-opsonized apoptotic monocyte-derived-macrophage type II are phagocytosed by phagocytic cells [See monocyte-derived-macrophage type II 6]
10. Undergo natural catabolism. The rate is 0.26/tick.

TNF- $\alpha$ . (Called *TNF- $\alpha$*  in the ABM.)

1. [See Kupffer Cell 5]
2. [See Monocyte-derived-macrophage type I 2]
3. [See Activated neutrophil 7]
4. [See Hepatocyte 7]
5. [See Mast cell 3]
6. Migrate to the nearest hepatocytes by random migration.
7. [See Hepatocyte 2]
8. Undergo natural catabolism. The catabolism rate needs to be estimated.

HMGB-1. (Called *HMGB-1* in the ABM.)

1. [See Monocyte-derived-macrophage type II 2]

2. [See Hepatocyte 6]
  3. Undergo natural catabolism. The catabolism rate needs to be estimated.
- IL-10. (Called *IL-10* in the ABM.)

1. [See Monocyte-derived-macrophage type II 3]
  2. [See Activated neutrophil 8]
  3. [See T cell 3]
  4. [See Kupffer Cell 6, Activated neutrophil 10, Monocyte-derived-macrophage type I 10, Monocyte-derived-macrophage type II 10, Mast cell 5]
  5. Undergo natural catabolism. The catabolism rate needs to be estimated.
- Histamine. (Called *Histamine* in the ABM.)

[See Mast cell 2]

NETs. (Called *NETs* in the ABM.)

[See Activated neutrophil 9]

Sinusoid Endothelial Cell. (Called *SEC* in the model files.)

A auxiliary agent type which models edges of liver sinusoid. A boundary agent has a thin rectangular shape. *Salmonella* infect sinusoid endothelial cells with certain probability. The probability is determined by random movement of the *Salmonella* agent. SECs are infected by *Salmonella* [See *Salmonella* 5]

Signals. (Called *Signal* in the model files.)

An auxiliary agent type that help to recruit resting neutrophils or resting monocytes in the liver sinusoid. This represents all other factors not specifically represented in the model.

Anti-Signals. (Called *AntiSignal* in the model files.)

An auxiliary agent type that inhibit resting neutrophils or resting monocytes adhere to SECs. This represents all other factors not specifically represented in the model.

**Table B.9 Experimental data and value of system parameters in IMMABM**

Agent Type (Biological Indicator)	Experimental Data [ED]	System Parameter Value in IMMAB
<b>Salmonella</b> <b>(Salmonella)</b>	<ol style="list-style-type: none"> <li>1. <i>Salmonella</i> carrying capacity in Kupffer Cells is 4,558,000 bacteria in a rat model (176).</li> <li>2. <i>Salmonella</i> carrying capacity in hepatocytes is 817,000 bacteria in a rat model (176).</li> <li>3. <i>Salmonella</i> carrying capacity in liver endothelial cells is 67,000 bacteria in a rat model (176).</li> <li>4. <i>Salmonella</i> carrying capacity in macrophages is 4,558,000 bacteria in a rat model [an estimate based on <i>Salmonella</i> carrying capacity in Kupffer Cells].</li> <li>5. <i>Salmonella</i> growth rate in macrophages is 0.9 fold/hr from 0 to 10hrs, and 10.9 fold/hr from 10 to 16 hrs, and 2.7 fold/hr from 16 to 25 hrs (measured in the spleen of mice) (108).</li> <li>6. <i>Salmonella</i> growth rate in epithelial cells is 0.32 fold/hr from 48 to 72 hrs (measured in the liver of rat) (176).</li> <li>7. <i>Salmonella</i> growth rate in Kupffer Cells is 0.42-1.04 fold/hr in rat model (176).</li> <li>8. <i>Salmonella</i> growth rate in hepatocytes is 0.05-0.26 fold/hr in rat model (207).</li> <li>9. 22.79% of <i>E. coli</i> (Gram-negative bacteria) are killed by 1<math>\mu</math>M neutrophil elastase (NE) per hour (332). The rate at which <i>Salmonella</i> are trapped by NETs is not available (229). Since the NETs were a complex of</li> </ol>	<ol style="list-style-type: none"> <li>1. salmonellaCarryCapacityInKupfferCell = 4558000</li> <li>2. salmonellaCarryCapacityInHepatocyte =817000</li> <li>3. salmonellaCarryCapacityInSECs = 67000</li> <li>4. salmonellaCarryCapacityInMDMI = 4558000</li> <li>5. <ol style="list-style-type: none"> <li>a) salmonellaReplicationRateInMDMI From0To10 = 0.9</li> <li>b) salmonellaReplicationRateInMDMI From10To16 = 10.9</li> <li>c) salmonellaReplicationRateInMDMI From16To25 = 2.7</li> </ol> </li> <li>6. salmonellaReplicationRateInSECsPerHour = 0.32</li> <li>7. <ol style="list-style-type: none"> <li>a) salmonellaReplicationRateInKupfferCellLowerLevelPerHour =0.42</li> <li>b) salmonellaReplicationRateInKupfferCellUpperLevelPerHour =1.04</li> </ol> </li> <li>8. <ol style="list-style-type: none"> <li>a) salmonellaReplicationRateInHepatocyteLowerLevelPerHour = 0.05</li> <li>b) salmonellaReplicationRateInHepatocyteUpperLevelPerHour = 0.26</li> </ol> </li> <li>9. percentageOfSalmonellaBeingTrappedByNETPerHour = 0.2279</li> <li>10. <ol style="list-style-type: none"> <li>a) percentageOfSalmonellaPhagocytizeByKupfferCellLowerLevel = 0.90</li> <li>b) percentageOfSalmonellaPhagocytizeByKupfferCellUpperLevel = 0.95</li> <li>c) timeOfSalmonellaKillByKupfferCell = 6</li> </ol> </li> <li>11. <ol style="list-style-type: none"> <li>a) timeOfSalmonellaDieInduceByNeutrophil = 2</li> <li>b) timeOfSalmonellaDieInduceByMDMI = 2</li> </ol> </li> <li>12. maximumNumberOfSalmonellaBeingKilledByNeutrophil = 17</li> </ol>

	<p>Myeloperoxidase (MPO) and NE, we extrapolated the data above to estimate the rate of <i>Salmonella</i> killed by NETs.</p> <p>10. There are controversial observations about whether <i>Salmonella</i> replicates within neutrophils. One study (198) stated that <i>Salmonella</i> were rarely found inside neutrophils in control mice. However, others (199) made an argument that neutrophils and macrophages were at the main site for <i>Salmonella</i> proliferation in the mouse because they found &gt;95% of the <i>Salmonella</i> colocalized to the neutrophils and macrophages at any time point examined. My model reflects that <i>Salmonella</i> replication rarely occurs within neutrophils because I failed to find any appropriate papers to support the concept that <i>Salmonella</i> replicates within neutrophils.</p> <p>11. The Phagocytosis rate of <i>Salmonella</i> by Kupffer Cells is 90-95% of <i>Salmonella</i> (90-95% <i>Salmonella</i> are ingested by Kupffer Cells within first 6 hrs by phagocytosis) (198).</p> <p>12. Phagocytosis by macrophages stimulated with LPS takes approximately 2.5 hrs (90min for phagosome maturation + 60 min for engulfing process) (118).</p> <p>13. The maximum number of</p>	<p>13. maximumNumberOfSalmonellaBeingKilledByMDMI = 30</p> <p>14. maximumNumberOfSalmonellaBeingKilledByKupfferCell = 50</p> <p>15. maximumNumberOfSalmonellaResideWithinSECs = 3</p> <p>16. maximumNumberOfSalmonellaResideWithinHepatocyte = 15</p> <p>17. timeOfSalmonellaCRPComplexDie = 1</p>
--	---	--

	<p><i>Salmonella</i> phagocytized by one neutrophil is 17 (202).</p> <p>14. The maximum number of <i>Salmonella</i> phagocytized by one monocyte-derived macrophage is 30 (202).</p> <p>15. The maximum number of <i>Salmonella</i> phagocytized by one Kupffer Cell is 50 (176).</p> <p>16. The maximum number of <i>Salmonella</i> resides within one SEC is 3 (176).</p> <p>17. The maximum number of <i>Salmonella</i> resides within one hepatocyte is 15 (333).</p> <p>18. Phagocytosis of apoptotic cells by macrophages takes approximately 1 hr (on average), and the phagocytosis of necrotic cells by macrophages takes approximately 3 hrs (on average) (334).</p>	
<p><b>KupfferCell</b> <b>(Kupffer cell)</b></p>	<p>1. Kupffer Cell machinery is disrupted and cells die 6-14 hrs after <i>Salmonella</i> infection (172) .</p> <p>2. By direct cell contact with target cells, T cells could deliver a cytotoxic signal that induces apoptosis in target cells in approximately 4 hrs (on average)(335).</p> <p>3.</p> <p>a) Rate of TNF-<math>\alpha</math> secreted by Kupffer Cells in Sham-operated mice upon injection of <i>E.coli</i> is <math>2.16 \times 10^{-4}</math>-<math>2.30 \times 10^{-4}</math> pg/Kupffer Cell/hr from 0-3 hrs (18).</p> <p>b) Rate of TNF-<math>\alpha</math> secreted by Kupffer Cells in Sham-operated mice upon injection of <i>E.coli</i> is <math>4.88 \times 10^{-5}</math>-<math>8.36 \times 10^{-5}</math> pg/Kupffer Cell/hr from</p>	<p>1.</p> <p>a) lowerTimeOfKupfferCellKillBySalmonella = 6</p> <p>b) upperTimeOfKupfferCellKillBySalmonella = 14</p> <p>2. timeOfKupfferCellWhoPhagocytizeSalmonellaDieByInteractWithCD8TCell = 4</p> <p>3.</p> <p>a) maximumReleaseRateOfTNFAlphaFromKupfferCellPerHourFrom0To3 = <math>2.30 \times 10^{-4}</math></p> <p>b) maximumReleaseRateOfTNFAlphaFromKupfferCellPerHourFrom3To6 = <math>8.36 \times 10^{-5}</math></p> <p>c) maximumReleaseRateOfTNFAlphaFromKupfferCellPerHourFrom6To10 = <math>2.09 \times 10^{-5}</math></p> <p>4. amountOfTNFAlphaBeingRepresentedByOneAgent = <math>2.82 \times 10^{-5}</math></p> <p>5. maximumReleaseRateOfIL10ByKupfferCellPerHour = <math>7.38 \times 10^{-4}</math></p> <p>6. amountOfIL10BeingRepresentedByOneAgent = <math>1.23 \times 10^{-5}</math></p> <p>7. timeOfApoptoticKupfferCellCRPCo</p>

	<p>3-6 hrs (18).</p> <p>c) Rate of TNF-<math>\alpha</math> secreted by Kupffer Cells in Sham-operated mice upon injection of <i>E.coli</i> is <math>2.09 \times 10^{-5}</math> pg/Kupffer Cell/hr from 6-10 hrs (18).</p> <p>4. The average amount of TNF-<math>\alpha</math> damage one hepatocyte is <math>2.82 \times 10^{-5}</math> pg in a mouse model (227).</p> <p>5. Rate of IL-10 secretion by Kupffer Cells is <math>6.15 \times 10^{-4}</math> - <math>7.38 \times 10^{-4}</math> pg/Kupffer Cell/hr in a mouse model injected with <i>E.coli</i> (18).</p> <p>6. The binding rate of IL-10 to one cell is approximately <math>1.23 \times 10^{-5}</math> pg/cell (225).</p> <p>7. Phagocytosis of apoptotic cells by macrophages takes approximately 1 hr (on average), and the phagocytosis of necrotic cells by macrophages takes approximately 3 hrs (on average) (334).</p>	<p>mplexDie = 1</p>
<p><b>RestingNeutrophil (Circulating neutrophil)</b></p>	<p>1. The neutrophil influx into blood vessels from bone marrow stores starts at approximately 1 hr (243).</p> <p>2. Neutrophil influx rates from bone marrow to blood vessel in a human model (243).</p> <p>a. Neutrophil influx rate from bone marrow into blood vessel is 14 fold/hr over a period of 1-1.5 hrs.</p> <p>b. Neutrophil influx rate from bone marrow into blood vessel is 0.39 fold/hr over a period of 1.5-4 hrs.</p> <p>c. Neutrophil influx rate from bone marrow into</p>	<p>1. timeOfNeutrophilStartToInfluxIntoLiverSinusoid = 1</p> <p>2.</p> <p>a) influxRateOfRestingNeutrophilToLiverSinusoidFrom0To2 = 14</p> <p>b) influxRateOfRestingNeutrophilToLiverSinusoidFrom2To4 = 0.39</p> <p>c) influxRateOfRestingNeutrophilToLiverSinusoidFrom4ToEnd = 0.125</p> <p>3. restingNeutrophilCarryCapacityInLiverSinusoid = 6900</p> <p>4.</p> <p>d) rateOfRestingNeutrophilUndergoAgingPerHourLowerLevel = 0.05</p> <p>e) rateOfRestingNeutrophilUndergoAgingPerHourLowerLevel = 0.095</p>



	<p>blood vessel is 0.125 fold/hr over a period of 4-6 hrs.</p> <ol style="list-style-type: none"> <li>Neutrophil counts in blood vessels in a mouse model anesthetized with ketamine and xylazine was <math>6.9 \times 10^3</math> cells/ul (336, 337)</li> <li>Circulating neutrophils undergo apoptosis at a rate of 0.05-0.092 fold/hr (half-life is 6-10 hrs) (185, 285)</li> </ol>	
<b>Resting Monocyte (Circulating monocyte)</b>	<ol style="list-style-type: none"> <li>Monocytes infiltration into blood vessels begins at approximately 2 hrs after infection in a mouse lung model infected with <i>Escherichia coli</i> (338).</li> <li>Influx rate of monocytes into blood vessels in a mouse lung model infected with <i>Escherichia coli</i> is 1-1.75 fold/hr (338).</li> <li>Monocyte carrying capacity in blood vessel was <math>1.4 \times 10^3</math> cells/ul (336, 337).</li> <li>The influx rate of Ly6C<sup>high</sup> monocytes into the liver in a rat infected with <i>L. monocytogenes</i> (Gram-positive bacteria) is 0.25-4.82 fold/hr (144).</li> <li>Circulating monocytes undergo apoptosis at a rate of <math>6.90 \times 10^{-3}</math> - <math>2.10 \times 10^{-2}</math> fold/hr (this is based on data showing circulating monocytes have a half-life about one to three days) (339).</li> </ol>	<ol style="list-style-type: none"> <li>timeOfRestingMonocyteInfluxIntoLiverSinusoid = 2</li> <li> <ol style="list-style-type: none"> <li>influxRateOfRestingMonocyteToLiverSinusoidPerHourLowerLevel = 1</li> <li>influxRateOfRestingMonocyteToLiverSinusoidPerHourUpperLevel = 1.75</li> </ol> </li> <li>restingMonocyteCarryCapacityInLiverSinusoid = 1400</li> <li> <ol style="list-style-type: none"> <li>activationRateOfRestingMonocytePerHourLowerLevel = 0.25</li> <li>activationRateOfRestingMonocytePerHourUpperLevel = 4.82</li> </ol> </li> <li> <ol style="list-style-type: none"> <li>apoptoticRateOfRestingMonocyteByAgingPerHourLowerLevel = 0.0069</li> <li>apoptoticRateOfRestingMonocyteByAgingPerHourUpperLevel = 0.021</li> </ol> </li> </ol>
<b>Hepatocyte (Hepatocyte)</b>	<ol style="list-style-type: none"> <li>Hepatocyte replication rates after partial hepatectomy (212). <ol style="list-style-type: none"> <li>Hepatocyte replication rate is <math>2.65 \times 10^{-3}</math> - <math>3.17 \times 10^{-3}</math> fold/hr over a period of 0-98 hrs.</li> <li>Hepatocyte replication</li> </ol> </li> </ol>	<ol style="list-style-type: none"> <li> <ol style="list-style-type: none"> <li>hepatocyteReplicationRatePerHourFrom0To98LowerLevel = <math>2.65E-3</math></li> <li>hepatocyteReplicationRatePerHourFrom0To98UpperLevel = <math>3.17E-3</math></li> <li>hepatocyteReplicationRatePer</li> </ol> </li> </ol>

	<p>rate is <math>4.08 \times 10^{-3}</math> - <math>6.80 \times 10^{-3}</math> fold/hr over a period of 98-135 hrs.</p> <p>c. Hepatocyte replication rate is <math>1.32 \times 10^{-3}</math> - <math>3.95 \times 10^{-3}</math> fold/hr over a period of 135-173 hrs.</p> <p>d. Hepatocyte replication rate is <math>4.08 \times 10^{-3}</math> - <math>5.27 \times 10^{-3}</math> fold/hr over a period of 173-247 hrs.</p> <p>e. Hepatocyte replication rate is <math>2.12 \times 10^{-3}</math> - <math>2.65 \times 10^{-3}</math> fold/hr over a period of 247-336 hrs.</p> <p>2. Hepatocyte are infected by <i>Salmonella</i> at an infected rate is 0.003 <i>Salmonella</i>/hepatocyte/hr (333).</p> <p>3. The time from initiation of apoptosis by hepatocytes to completion ranges from 2-3 hrs. These data were inferred from a general model that didn't specify apoptosis rates for various organs (211).</p> <p>4. Mouse circulating CRP level increases from 0.3mg/ml to 6 mg/ml by 24 hrs after endotoxin injection (340). The rate of CRP released from hepatocytes is approximately <math>2 \times 10^{-7}</math> <math>\mu\text{g}</math>/hepatocyte/hr (337, 340). This is the only paper that I could find that measured circulating CRP levels in mice. Most of CRP levels are measured in human models.</p> <p>5. The binding rate of CRP to one phagocytic cell is approximately <math>1.25 \times 10^{-5}</math> <math>\mu\text{g}</math>/cell (226).</p> <p>6. Rate of TNF-<math>\alpha</math> secreted by hepatocytes infected with</p>	<p>HourFrom98To135LowerLevel = <math>4.08\text{E-}3</math></p> <p>d) hepatocyteReplicationRatePerHourFrom98To135UpperLevel = <math>6.8\text{E-}3</math></p> <p>e) hepatocyteReplicationRatePerHourFrom135To173LowerLevel = <math>1.32\text{E-}3</math></p> <p>f) hepatocyteReplicationRatePerHourFrom135To173UpperLevel = <math>3.95\text{E-}3</math></p> <p>g) hepatocyteReplicationRatePerHourFrom173To247LowerLevel = <math>4.08\text{E-}3</math></p> <p>h) hepatocyteReplicationRatePerHourFrom173To247UpperLevel = <math>5.27\text{E-}3</math></p> <p>i) hepatocyteReplicationRatePerHourFrom247ToEndLowerLevel = <math>2.12\text{E-}3</math></p> <p>j) hepatocyteReplicationRatePerHourFrom247ToEndUpperLevel = <math>2.65\text{E-}3</math></p> <p>2. rateOfHepatocyteBeingInfectedBySalmonellaPerHour = 0.003</p> <p>3.</p> <p>a) timeOfHepatocyteBecomeDebrisLowerLevel = 2</p> <p>b) timeOfHepatocyteBecomeDebrisUpperLevel = 3</p> <p>4. maximumReleaseRateOfCRPByHepatocytePerHour = <math>2.00\text{E-}7</math></p> <p>5. amountOfCRPBeingRepresentedByOneAgent = <math>1.25\text{E-}5</math></p> <p>6. maximumReleaseRateOfTNFAlphaByApoptoticHepatocytePerHour = <math>9.18\text{E-}5</math></p> <p>7. maximumReleaseRateOfHMGB1ByApoptoticHepatocytePerHour = <math>6.25\text{E-}5</math></p>
--	---	--

	<p><i>Salmonella</i> is <math>7.14 \times 10^{-5}</math> - <math>9.18 \times 10^{-5}</math> pg/hepatocyte/hr (207).</p> <p>7. Rate of HMGB-1 secretion by apoptotic hepatocytes in Sham-operated mice is approximately <math>6.25 \times 10^{-5}</math> pg/hepatocyte/hr (208, 337).</p>	
<b>HepatocyteDebris (Hepatocyte Debris)</b>	<p>1. Phagocytosis of apoptotic cells by macrophages takes approximately 1 hr (on average), and the phagocytosis of necrotic cells by macrophages takes approximately 3 hrs (on average) (334).</p>	<p>1. timeOfHepatocyteDebrisCRPComplexDie = 1</p>
<b>ActivatedNeutrophil (Activated neutrophil, mostly focus on neutrophils at the site of infection)</b>	<p>1. Influx rate of circulating neutrophils in a rat model of acute pulmonary inflammation stimulated with LPS of <i>Escherichia coli</i> is 0.21-0.46 fold/hr (302). Another study (221) showed that activated neutrophils infiltrate into the site of infection at a rate of 0.09-0.16 fold/hr (influx rate is measured as the influx rate of neutrophils into the peritoneum).</p> <p>2. Massive neutrophils infiltration into the peritoneum occurred after 2 hrs (298). Activated neutrophils infiltrate into the site of infection by 2 hrs after infection in mice infected in the peritoneum with <i>Salmonella</i> (221).</p> <p>3. Killing rate of <i>Escherichia coli</i> (<i>E. coli</i> is recognized as a Gram-negative bacteria) by neutrophils is 2.94-12.94 <i>E.coli</i>/neutrophil/hr (202).</p> <p>4. It takes 5-20 neutrophils to injury one hepatocyte by</p>	<p>1.</p> <p>a) activationRateOfRestingNeutrophilPerHourLowerLevel = 0.09</p> <p>b) activationRateOfRestingNeutrophilPerHourUpperLevel = 0.46</p> <p>2. timeOfNeutrophilStartToInfluxIntoSiteOfInfection = 2</p> <p>3.</p> <p>a) phagocytizeRateOfSalmonellaByActivatedNeutrophilPerHourLowerLevel = 2.94</p> <p>b) phagocytizeRateOfSalmonellaByActivatedNeutrophilPerHourUpperLevel = 12.94</p> <p>4.</p> <p>a) killingRateOfApoptoticHepatocyteByNeutrophilPerHourLowerLevel = 0.05</p> <p>b) killingRateOfApoptoticHepatocyteByNeutrophilPerHourUpperLevel = 0.2</p> <p>5. percentageOfNeutrophilBeingKilledByKupfferCell = 0.05</p> <p>6. apoptoticRateOfActivatedNeutrophilByNaturePerHour = 0.098</p> <p>7. timeOfActivatedNeutrophilWhoPhagocytizeSalmonellaDieByInteractWithCD8TCell = 4</p> <p>8. maximumReleaseRateOfIL10ByNeutrophilPerHour = <math>1.03E-4</math></p> <p>9.</p>

	<p>cell-cell contact (210, 341). Also, activated neutrophils accelerate the killing process of apoptotic hepatocytes (134).</p> <ol style="list-style-type: none"> <li>5. 30% of circulating activated neutrophils are phagocytized by Kupffer Cells in a mouse model by 6 hrs after LPS injection (342).</li> <li>6. Activated neutrophils undergo apoptosis at a rate of 0.098 fold/hr (assuming a constant decrease)(the apoptosis was based on mice with meningitis)(185).</li> <li>7. By direct cell contact with target cells, T cells could deliver a cytotoxic signal that induces apoptosis in target cells in approximately 4 hrs (on average) (335).</li> <li>8. Rate of IL-10 secretion by neutrophils in septic mice upon CLP is <math>8.44 \times 10^{-5}</math>-<math>1.03 \times 10^{-4}</math> pg/neutrophil/hr (213).</li> <li>9. <ol style="list-style-type: none"> <li>a) Rate of TNF-<math>\alpha</math> secretion by neutrophils in a mouse model injected with <i>E.coli</i> LPS is 0.19-0.27pg/neutrophil/hr over a period of 0-1 hr (343-347).</li> <li>b) Rate of TNF-<math>\alpha</math> secretion by neutrophils in a mouse model injected with <i>E.coli</i> LPS is 1.47-2.00 pg/neutrophil/hr over a period of 1-1.5 hrs (343-347).</li> </ol> </li> <li>10. Phagocytosis of apoptotic cells by macrophages takes approximately 1 hr (on average), and the phagocytosis of necrotic</li> </ol>	<ol style="list-style-type: none"> <li>a) maximumReleaseRateOfTNFAlphaByNeutrophilFrom0To1 = 0.27</li> <li>b) maximumReleaseRateOfTNFAlphaByNeutrophilFrom1ToEnd = 2</li> <li>10. timeOfApoptoticNeutrophilCRPCo mplexDie = 1</li> <li>11. timeOfNeutrophilKillByKupfferCell = 2</li> <li>12. timeOfApoptoticNeutrophilKillByMDMII = 1</li> </ol>
--	--	---

	<p>cells by macrophages takes approximately 3 hrs (on average) (334).</p> <p>11. Phagocytosis by macrophages stimulated with LPS takes approximately 2.5 hrs (90min for phagosome maturation + 60 min for engulfing process) (118).</p> <p>12. Phagocytosis of apoptotic cells by macrophages takes approximately 1 hr (on average), and the phagocytosis of necrotic cells by macrophages takes approximately 3 hrs (on average) (334).</p>	
<b>NET (NET)</b>	<p>1. Rate of NE secretion by neutrophils was <math>3.2 \times 10^{-7}</math> <math>\mu\text{M}</math> /neutrophil during the first 1 hr, and the stopped (348).</p>	<p>1. amountOfNETBeingRepresentedByOneAgent = 3.2E-7</p>
<b>MDMI (monocyte-Derived-Macrophage Type I)</b>	<p>1. Ly6C<sup>high</sup> monocytes are recruited to the liver in a rat model by 6 hrs after infection with <i>L. monocytogenes</i> (Gram-positive bacteria) (144). Also, monocyte infiltration to peritoneum was detected to increase at 6 hrs after infection in a mouse model with Zymosan-induced peritonitis (298).</p> <p>2. Kupffer Cells are replenished hourly by 0.63 - 0.79% of monocyte-derived-macrophage type I or monocyte-derived-macrophage type II upon zymosan injection in the mouse model (123).</p> <p>3. By direct cell contact with target cells, T cells could deliver a cytotoxic signal</p>	<p>1. timeOfMonocyteInfluxIntoSiteOfInfection = 6</p> <p>2.</p> <p>a) rateOfMDMITransformToKupfferCellLowerLevel = 0.0063</p> <p>b) rateOfMDMITransformToKupfferCellUpperLevel = 0.0079</p> <p>3. timeOfMDMIWhoPhagocytizeSalmonellaDieByInteractWithCD8TCell = 4</p> <p>4. maximumReleaseRateOfTNFAlphaByMDMIPerHour = 1.7E-4</p> <p>5. maximumReleaseRateOfIL10ByMDMIPerHour = 2.02E-5</p> <p>6. timeOfApoptoticMDMICRComplexDie = 1</p>

	<p>that induces apoptosis in target cells in approximately 4 hrs (on average) (335).</p> <ol style="list-style-type: none"> <li>4. Rate of TNF-<math>\alpha</math> secretion by peritoneal macrophages in Sham-operated mice upon injection of <i>E.coli</i> is <math>1.70 \times 10^{-4}</math> pg/ peritoneal macrophage/hr over a period of 0-3 hrs (18).</li> <li>5. Rate of IL-10 secretion by peritoneal macrophages in Sham-operated mice upon injection of <i>E.coli</i> is <math>2.02 \times 10^{-5}</math> pg/ peritoneal macrophage /hr over a period of 0-3 hrs (18).</li> <li>6. Phagocytosis of apoptotic cells by macrophages takes approximately 1 hr (on average), and the phagocytosis of necrotic cells by macrophages takes approximately 3 hrs (on average) (334).</li> </ol>	
<p><b>MDMII (monocyte-Derived-Macrophage Type II)</b></p>	<ol style="list-style-type: none"> <li>1. Kupffer Cells are hourly replenished by 0.63% - 0.79% of monocyte-derived-macrophage type I or monocyte-derived-macrophage type II upon zymosan injection in mice model (123).</li> <li>2. Rate of IL-10 secretion by peritoneal macrophages in Sham-operated mice upon injection of <i>E.coli</i> is <math>2.02 \times 10^{-5}</math> pg/ peritoneal macrophage/hr over a period of 0-3 hrs (18).</li> <li>3. <ol style="list-style-type: none"> <li>a) Rate of HMGB-1 secretion by peritoneal macrophages in a rat model is <math>9.38 \times 10^{-3}</math>-<math>3.8 \times 10^{-2}</math> pg/peritoneal macrophage/hr over a</li> </ol> </li> </ol>	<ol style="list-style-type: none"> <li>1. <ol style="list-style-type: none"> <li>a) rateOfMDMIITransformToKupfferCellLowerLevel = 0.0063</li> <li>b) rateOfMDMIITransformToKupfferCellUpperLevel = 0.0079</li> </ol> </li> <li>2. maximumReleaseRateOfIL10ByMDMIIPerHour = 2.02E-5</li> <li>3. <ol style="list-style-type: none"> <li>a) maximumReleaseRateOfHMGB1ByMDMIIFrom8To12 = 3.8E-2</li> <li>b) maximumReleaseRateOfHMGB1ByMDMIIFrom12To16 = 1.69E-1</li> <li>c) maximumReleaseRateOfHMGB1ByMDMIIFrom16ToEnd = 4.97E-1</li> </ol> </li> <li>4. timeOfApoptoticMDMIICRPComplexDie = 1</li> </ol>

	<p>period of 8-12 hrs (349, 350).</p> <p>b) Rate of HMGB-1 secretion by peritoneal macrophages in a rat model is <math>1.03 \times 10^{-1}</math>-<math>1.69 \times 10^{-1}</math> pg/peritoneal macrophage/hr over a period of 12-16 hrs (349, 350).</p> <p>c) Rate of HMGB-1 secretion by peritoneal macrophages in a rat model is <math>2.72 \times 10^{-1}</math>-<math>4.97 \times 10^{-1}</math> pg/peritoneal macrophage/hr over a period of 16-24 hrs (349, 350).</p> <p>4. Phagocytosis of apoptotic cells by macrophages takes approximately 1 hr (on average), and the phagocytosis of necrotic cells by macrophages takes approximately 3 hrs (on average) (334).</p>	
<p><b>MastCell (Mast cell)</b></p>	<p>1. Mast cells undergo self-renewal after <math>\text{CCl}_4</math> injection in a rat model, the proliferation rate is <math>9.45 \times 10^{-4}</math>-<math>3.10 \times 10^{-3}</math> /hr (320).</p> <p>2. Rate of TNF-<math>\alpha</math> secretion by mast cells in a mouse model injected with CLP ranges from <math>1.33 \times 10^{-7}</math> to <math>1.52 \times 10^{-7}</math> pg/mast cell/hr (351).</p> <p>3. Rate of TNF-<math>\alpha</math> secretion by peritoneal mast cells stimulated with antigen (a collection of soluble excretory and secretory products of adult <i>N. brasiliensis</i>) was <math>1.48 \times 10^{-4}</math>-<math>1.76 \times 10^{-4}</math> pg/mast cell/hr (352). We use these rates to estimate the rates of TNF-<math>\alpha</math> secretion by mast cells</p>	<p>1.</p> <p>a) proliferateRateOfMastCellPerHourLowerLevel = <math>9.45 \times 10^{-4}</math></p> <p>b) proliferateRateOfMastCellPerHourUpperLevel = <math>0.0031</math></p> <p>2. maximumReleaseRateOfTNFAlphaByMastCellPerHour = <math>1.52 \times 10^{-7}</math></p> <p>3. maximumReleaseRateOfTNFAlphaByMastCellIfInteractWithAntibodySalmonellaComplexPerHour = <math>1.76 \times 10^{-4}</math></p> <p>4. maximumReleaseRateOfHistamineByMastCellIfInteractWithAntibodySalmonellaComplexPerHour = <math>0.18</math></p>

	<p>during degranulation in IMMAB.</p> <p>4. Mast cells release histamine during systemic degranulation induced by polymicrobial septic peritonitis in a mouse model. The rate of histamine release by mast cells is 0.12-0.18 pg /mast cell/hr (321, 337).</p>	
<b>CD4TCell (CD4 T cell)</b>	<p>1. The activation rate of CD4 T cells in the spleen of mice injected with <i>E. coli</i> ranges from <math>1.24 \times 10^{-3}</math> to <math>2.75 \times 10^{-2}</math> fold/hr (174).</p> <p>2. The CD4 T cells carrying capacity is approximately <math>27.4 \times 10^6</math> cells in the first 7 days after infection (174).</p> <p>3. Rate of IL-10 secretion by Th2 cells stimulated with IL-4 is <math>8.33 \times 10^{-7}</math>-<math>9.69 \times 10^{-7}</math> pg/Th2 cell/hr (353).</p> <p>4. Rate of TNF-<math>\alpha</math> secretion by T cells in a mouse model infected with <i>E. coli</i> was <math>6.94 \times 10^{-7}</math> pg/T cell/hr (174).</p>	<p>1.</p> <p>a) <code>influxRateOfCD4TCellToLiverSinusoidPerHourLowerLevel = 1.24E-3</code></p> <p>b) <code>influxRateOfCD4TCellToLiverSinusoidPerHourUpperLevel = 2.75E-2</code></p> <p>2. <code>CD4TCellCarryCapacityInLiverSinusoid = 27.4E6</code></p> <p>3. <code>maximumReleaseRateOfIL10ByCD4TCellPerHour = 9.69E-7</code></p> <p>4. <code>maximumReleaseRateOfTNFAlphaByCD4TCellPerHour = 6.94E-7</code></p>
<b>CD8TCell (CD8 T cell)</b>	<p>1. The activation rate of CD8 T cells in the spleen of mice injected with <i>E. coli</i> is approximately <math>6.25 \times 10^{-2}</math> fold/hr (174).</p> <p>2. The CD8 T cells carrying capacity is approximately <math>5 \times 10^6</math> cells in the first 7 days after infection (174).</p>	<p>1. <code>InfluxRateOfCD8TCellToLiverSinusoidPerHour = 6.25E-2</code></p> <p>2. <code>CD8TCellCarryCapacityInLiverSinusoid = 5000000</code></p>
<b>BCell (B cell)</b>	<p>1. The activation rate of B cells in the spleen of mice injected with <i>E. coli</i> ranges from <math>4.30 \times 10^{-4}</math> to <math>2.40 \times 10^{-2}</math> fold/hr (174).</p> <p>2. The B cells carrying capacity is approximately <math>28.6 \times 10^6</math> in the first 7 days after infection (174).</p>	<p>1.</p> <p>a) <code>influxRateOfBCellToLiverSinusoidPerHourLowerLevel = 4.3E-4</code></p> <p>b) <code>influxRateOfBCellToLiverSinusoidPerHourUpperLevel = 2.4E-2</code></p> <p>2. <code>BCellCarryCapacityInLiverSinusoid = 28600000</code></p>
<b>TNFAlpha (Tumor)</b>	<p>1. Kupffer Cells secrete TNF-<math>\alpha</math></p> <p>a) Rate of TNF-<math>\alpha</math> secreted</p>	<p>1.</p> <p>a) <code>maximumReleaseRateOfTNFAI</code></p>



<p><b>necrosis factor alpha)</b></p>	<p>by Kupffer Cells in Sham-operated mice upon injection of <i>E.coli</i> is <math>2.16 \times 10^{-4}</math>-<math>2.30 \times 10^{-4}</math> pg/Kupffer Cell/hr from 0-3 hrs (18).</p> <p>b) Rate of TNF-<math>\alpha</math> secreted by Kupffer Cells in Sham-operated mice upon injection of <i>E.coli</i> is <math>4.88 \times 10^{-5}</math>-<math>8.36 \times 10^{-5}</math> pg/Kupffer Cell/hr from 3-6 hrs (18).</p> <p>c) Rate of TNF-<math>\alpha</math> secreted by Kupffer Cells in Sham-operated mice upon injection of <i>E.coli</i> is <math>2.09 \times 10^{-5}</math> pg/Kupffer Cell/hr from 6-10 hrs (18).</p> <p>2.</p> <p>a) Rate of TNF-<math>\alpha</math> secretion by neutrophils in a mouse model injected with <i>E.coli</i> LPS is 0.19-0.27 pg/neutrophil/hr over a period of 0-1 hr (343-347).</p> <p>b) Rate of TNF-<math>\alpha</math> secretion by neutrophils in a mouse model injected with <i>E.coli</i> LPS is 1.47-2.00 pg/neutrophil/hr over a period of 1-1.5 hrs (343-347).</p> <p>3. Rate of TNF-<math>\alpha</math> secretion by peritoneal macrophages in Sham-operated mice upon injection of <i>E.coli</i> is <math>1.70 \times 10^{-4}</math> pg/ peritoneal macrophage/hr over a period of 0-3 hrs (18).</p> <p>4. Rate of TNF-<math>\alpha</math> secretion by mast cells in a mouse model injected with CLP ranges from <math>1.33 \times 10^{-7}</math> to <math>1.52 \times 10^{-7}</math> pg/mast cell/hr (351).</p> <p>5. Rate of TNF-<math>\alpha</math> secretion by</p>	<p>phaFromKupfferCellPerHourFrom0To3 = <math>2.30 \times 10^{-4}</math></p> <p>b) maximumReleaseRateOfTNFAIphaFromKupfferCellPerHourFrom3To6 = <math>8.36 \times 10^{-5}</math></p> <p>c) maximumReleaseRateOfTNFAIphaFromKupfferCellPerHourFrom6To10 = <math>2.09 \times 10^{-5}</math></p> <p>2.</p> <p>a) maximumReleaseRateOfTNFAIphaByNeutrophilFrom0To1 = 0.27</p> <p>b) maximumReleaseRateOfTNFAIphaByNeutrophilFrom1ToEnd = 2</p> <p>3. maximumReleaseRateOfTNFAIphaByMDMIPerHour = <math>1.7 \times 10^{-4}</math></p> <p>4. maximumReleaseRateOfTNFAIphaByMastCellPerHour = <math>1.52 \times 10^{-7}</math></p> <p>5. maximumReleaseRateOfTNFAIphaByMastCellIfInteractWithAntibodySalmonellaComplexPerHour = <math>1.76 \times 10^{-4}</math></p> <p>6. maximumReleaseRateOfTNFAIphaByCD4TCellPerHour = <math>6.94 \times 10^{-7}</math></p>
--------------------------------------	---	---

	<p>peritoneal mast cells stimulated with antigen (a collection of soluble excretory and secretory products of adult <i>N. brasiliensis</i>) was <math>1.48 \times 10^{-4}</math>-<math>1.76 \times 10^{-4}</math> pg/mast cell/hr (352). We use these rates to estimate the rates of TNF-<math>\alpha</math> secretion by mast cells during degranulation in IMMAB.</p> <p>6. Rate of TNF-<math>\alpha</math> secretion by T cells in a mouse model infected with <i>E. coli</i> was <math>6.94 \times 10^{-7}</math> pg/T cell/hr (174).</p>	
<b>HMGB1 (High-Mobility Group Box 1)</b>	<p>1. Rate of HMGB-1 secretion by apoptotic hepatocytes in Sham-operated mice is approximately <math>6.25 \times 10^{-5}</math> pg/hepatocyte/hr (208, 337).</p> <p>2.</p> <p>a) Rate of HMGB-1 secretion by peritoneal macrophages in a rat model is <math>9.38 \times 10^{-3}</math>-<math>3.8 \times 10^{-2}</math> pg/peritoneal macrophage/hr over a period of 8-12 hrs (349, 350).</p> <p>b) Rate of HMGB-1 secretion by peritoneal macrophages in a rat model is <math>1.03 \times 10^{-1}</math>-<math>1.69 \times 10^{-1}</math> pg/peritoneal macrophage/hr over a period of 12-16 hrs (349, 350).</p> <p>c) Rate of HMGB-1 secretion by peritoneal macrophages in a rat model is <math>2.72 \times 10^{-1}</math>-<math>4.97 \times 10^{-1}</math> pg/peritoneal macrophage/hr over a period of 16-24 hrs (349, 350).</p>	<p>1. maximumReleaseRateOfHMGB1By ApoptoticHepatocytePerHour = <math>6.25E-5</math></p> <p>2.</p> <p>a) SD maximumReleaseRateOfHMGB1ByMDMIIFrom8To12 = <math>3.8E-2</math></p> <p>b) maximumReleaseRateOfHMGB1ByMDMIIFrom12To16 = <math>1.69E-1</math></p> <p>c) maximumReleaseRateOfHMGB1ByMDMIIFrom16ToEnd = <math>4.97E-1</math></p>
<b>IL10</b>	<p>1. Rate of IL-10 secretion by</p>	<p>1. maximumReleaseRateOfIL10ByKup</p>

<p><b>(Interleukin 10)</b></p>	<p>Kupffer Cells is <math>6.15 \times 10^{-4}</math> - <math>7.38 \times 10^{-4}</math> pg/Kupffer Cell/hr in a mouse model injected with <i>E.coli</i> (18).</p> <p>2. Rate of IL-10 secretion by neutrophils in septic mice upon CLP is <math>8.44 \times 10^{-5}</math> - <math>1.03 \times 10^{-4}</math> pg/neutrophil/hr (213).</p> <p>3. Rate of IL-10 secretion by peritoneal macrophages in Sham-operated mice upon injection of <i>E.coli</i> is <math>2.02 \times 10^{-5}</math> pg/ peritoneal macrophage /hr over a period of 0-3 hrs (18).</p> <p>4. Rate of IL-10 secretion by peritoneal macrophages in Sham-operated mice upon injection of <i>E.coli</i> is <math>2.02 \times 10^{-5}</math> pg/ peritoneal macrophage/hr over a period of 0-3 hrs (18).</p> <p>5. Rate of IL-10 secretion by Th2 cells stimulated with IL-4 is <math>8.33 \times 10^{-7}</math> - <math>9.69 \times 10^{-7}</math> pg/Th2 cell/hr (353).</p>	<p>fferCellPerHour = <math>7.38 \times 10^{-4}</math></p> <p>2. maximumReleaseRateOfIL10ByNeutrophilPerHour = <math>1.03 \times 10^{-4}</math></p> <p>3. maximumReleaseRateOfIL10ByMDMIPerHour = <math>2.02 \times 10^{-5}</math></p> <p>4. maximumReleaseRateOfIL10ByMDMIIPerHour = <math>2.02 \times 10^{-5}</math></p> <p>5. maximumReleaseRateOfIL10ByCD4TCellPerHour = <math>9.69 \times 10^{-7}</math></p>
<p><b>CRP (C-reactive protein)</b></p>	<p>1. CRP undergoes degradation at an estimated rate of 0.26 fold/hr (Plasma half-life of CRP is about 19 hrs and is constant under all conditions of health and disease, this data was extrapolated from a human model) (325).</p>	
<p><b>Antibody (antibody)</b></p>	<p>1. The antibody production amount by one B cell in a human model infected by <i>Salmonella</i> is <math>4.88 \times 10^{-4}</math> - <math>2.81 \times 10^{-3}</math> pg/B cell/hr (244).</p> <p>2. The binding amount of antibody to one <i>Salmonella</i> is 5.31 pg/<i>Salmonella</i> (243, 245).</p>	

### **Data assumptions:**

1. Hepatocytes account for 60% of liver cells, Kupffer Cells account for 15% of liver cells, SECs account for 20% of liver cells (196), and mast cells account for 7.5% of liver cells (197).
2. In general, we assume the change in rate is constant because we observed changes in data of interests in most of experimental studies following linear curves.
3. For some experimental data, we used multiple rates of synthesis or secretion. These multiple rates are explained in our experimental data table above.
4. Some experimental data is comprised of multiple linear segments, and therefore we calibrated rates for each linear segment to measure various rates for multiple responding time periods.
5. The release/secretion rates of various cytokines (TNF- $\alpha$ , HMGB-1 and IL-10) by inflammatory cells such as neutrophils, Kupffer Cells and monocyte-derived-macrophages are described as a function of time, by possibly incorporating the effect of decay/catabolism.
6. Experimental data are integrated into our agent-based model as inputs by ignoring different experimental conditions/settings such as different initial loads of bacteria injection, different bacteria strains, different animal models, etc. This limitation could be reduced by additional experiments done under the same experimental conditions/settings.
7. It was not possible to extrapolate the data for our agent-based model from one simple experimental model. The strategy we used was to focus on mouse Salmonella infection studies that were published in papers available in the NCBI. When necessary, we used data from broader systems such as Gram-negative infections (i.e. E. coli) or even Gram positive bacterial infections. Therefore, we are aware that some of these assumptions may not be correct.

## Appendix C - Supplementary Material for FHSMDP

### Computational Study I

#### *Notation and SMDP formulation*

##### *State set:*

$$s_1 = [0, 1152) \quad s_2 = [1152, 2304) \quad s_3 = [2304, \infty)$$

$s_1$ : *Salmonella* loads fall into the range [0, 1152)

$s_2$ : *Salmonella* loads fall into the range [1152, 2304)

$s_3$ : *Salmonella* loads fall into the range [2304,  $\infty$ )

##### *Action set:*

$$A : \{a_1 = \text{No action}, a_2 = \text{Antimicrobials}\}$$

##### *Planning decision horizon:*

$\lambda = 0 - 24$  hrs, and  $\lambda$  is a continuous variable

##### *The following notations are used:*

$P(s_j | s_i, a_{ik})$ : The probability that the current state  $s_i$  transits to state  $s_j$  at the next decision epoch, given action  $a_{ik}$  made at state  $s_i$ .

$F(t | s_i, a_{ik})$ : The probability that the next decision epoch occurs within time  $t$ , given action  $a_{ik}$  made at the current state  $s_i$ .

$P(s_i, a_{ik})$ : The probability of an infected individual ending with “hyperinflammatory response” or “organ dysfunction”, given  $a_{ik}$  made at the current state  $s_i$ .

$Q(t, s_j | s_i, a_{ik})$ : The probability that the current state  $s_i$  transits to the state  $s_j$  at the next decision epoch within time  $t$ , given  $a_{ik}$  made at the current state  $s_i$ .

$D(t | s_i, a_{ik})$ : The probability that current state  $s_i$  transits to other states at the next decision epoch within  $t$ , given  $a_{ik}$  made at the current state  $s_i$ .

### ***Modeling assumptions***

- a. Decision epochs occur whenever the state changes, and a decision epoch occurs if the state remains at  $s_3$  for 5 hrs.
- b. The range of indicator counts are dependent on the initial loads of *Salmonella*. In this numerical example, the initial load of *Salmonella* was set to 3200.
- c. If taking an action  $a_2$ , 50 counts antimicrobial agents (1 agent count *in silico* responds to 1 colony forming unit (CFU) of *Salmonella*) were added to the *silico* experiment each time at decision epoch.
- d. There is no decision epoch when the system remains at  $s_1$ .
- e. We calculated  $P(s_j | s_i, a_{ik})$  and  $F(t | s_i, a_{ik})$  by observing the changes in the number of indicators (states) for 30 simulation runs.

### ***Compute inputs of value iteration algorithm using IMMABM***

#### **Derive $F(t | s_i, a_{ik})$**

Firstly, calculate  $P(t | s_i, a_{ik})$  using the following mathematical formulation:

$$P(t | s_i, a_{ik}) = \frac{\text{No. of the next decision epoch occurs within time } t, \text{ given action } a_{ik} \text{ made at the current state } s_i}{\text{the total number of simulation runs}}$$

Secondly, estimate  $F(t | s_i, a_{ik})$  using calibrated  $P(t | s_i, a_{ik})$ , as shown in Figure C.1:

We calibrated  $P(t | s_i, a_{ik})$  using simulated data from IMMABM, and estimated  $F(t | s_i, a_{ik})$  using obtained  $P(t | s_i, a_{ik})$ . We assumed the line segments between calibrated data

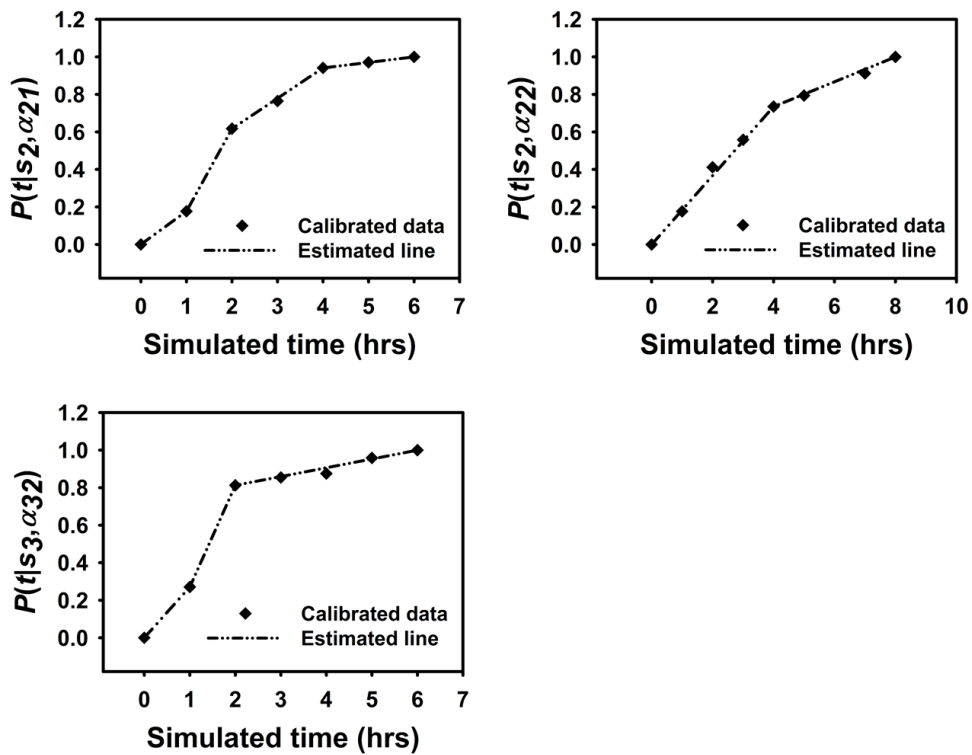
follows a linear relationship in order to simply the calculation, the functions of estimated lines are shown as follows:

$$F(t|s_2, a_{21}) = \begin{cases} \frac{6}{34}t, & 0 \leq t \leq 1 \\ \frac{15}{34}t - \frac{9}{34}, & 1 < t \leq 2 \\ \frac{11}{68}t + \frac{5}{17}, & 2 < t \leq 4 \\ \frac{1}{34}t + \frac{14}{17}, & 4 < t \leq 6 \\ 1, & t > 6 \end{cases}$$

$$F(t|s_2, a_{22}) = \begin{cases} \frac{25}{136}t, & 0 \leq t \leq 4 \\ \frac{9}{136}t + \frac{8}{17}, & 4 < t \leq 8 \\ 1, & t > 8 \end{cases}$$

$$F(t|s_3, a_{32}) = \begin{cases} \frac{13}{48}t, & 0 \leq t \leq 1 \\ \frac{13}{24}t - \frac{13}{48}, & 1 < t \leq 2 \\ \frac{9}{192}t + \frac{23}{32}, & 2 < t \leq 6 \\ 1, & t > 6 \end{cases}$$

Figure 8.1 Calibrated  $P(t|s_i, a_{ik})$  from IMMABM and estimated lines for  $F(t|s_i, a_{ik})$



Calculate  $P(s_j | s_i, a_{ik})$  using the following mathematical formulation:

$$P(s_j | s_i, a_{ik}) = \frac{\text{No. of current state } s_i \text{ transits to state } s_j \text{ at next decision epoch, under action } a_{ik} \text{ at state } s_i}{\text{the total number of simulation runs}}$$

Using IMMABM,  $P(s_j | s_i, a_{ik})$  is obtained as follows:

(state $s_i$ , action $a_{ik}$ )	No. of transitions to ( $s_j$ )	$P(s_j   s_i, a_{ik})$
<b>(<math>s_2, a_{21}</math>)</b>	17 ( $s_1$ )	$P(s_1   s_2, a_{21}) = 17/30$
	0 ( $s_2$ )	$P(s_2   s_2, a_{21}) = 0$
	13 ( $s_3$ )	$P(s_3   s_2, a_{21}) = 13/30$
<b>(<math>s_2, a_{22}</math>)</b>	21 ( $s_1$ )	$P(s_1   s_2, a_{22}) = 21/30$
	0 ( $s_2$ )	$P(s_2   s_2, a_{22}) = 0$
	9 ( $s_3$ )	$P(s_3   s_2, a_{22}) = 9/30$
<b>(<math>s_3, a_{32}</math>)</b>	0 ( $s_1$ )	$P(s_1   s_3, a_{32}) = 0/30$
	29 ( $s_2$ )	$P(s_2   s_3, a_{32}) = 29/30$
	1 ( $s_3$ )	$P(s_3   s_3, a_{32}) = 1/30$

Calculate  $Q(t, s_j | s_i, a_{ik})$  using the following mathematical formulation:

$$Q(t, s_j | s_i, a_{ik}) = P(s_j | s_i, a_{ik}) F(t | s_i, a_{ik})$$

$$Q(t, s_1 | s_2, a_{21}) = P(s_1 | s_2, a_{21}) F(t | s_2, a_{21}) = \begin{cases} \frac{1}{10}t, & 0 \leq t \leq 1 \\ \frac{17}{68}t - \frac{51}{340}, & 1 < t \leq 2 \\ \frac{11}{120}t + \frac{1}{6}, & 2 < t \leq 4 \\ \frac{1}{60}t + \frac{7}{15}, & 4 < t \leq 6 \\ \frac{17}{30}, & t > 6 \end{cases}$$

$$Q(t, s_2 | s_2, a_{21}) = P(s_2 | s_2, a_{21}) F(t | s_2, a_{21}) = 0, \quad t \in R^+$$



$$Q(t, s_3 | s_2, a_{21}) = P(s_3 | s_2, a_{21}) F(t | s_2, a_{21}) = \begin{cases} \frac{13}{170}t, & 0 \leq t \leq 1 \\ \frac{13}{68}t - \frac{39}{340}, & 1 < t \leq 2 \\ \frac{143}{2040}t + \frac{13}{102}, & 2 < t \leq 4 \\ \frac{13}{1020}t + \frac{91}{255}, & 4 < t \leq 6 \\ \frac{13}{30}, & t > 6 \end{cases}$$

$$Q(t, s_1 | s_2, a_{22}) = P(s_1 | s_2, a_{22}) F(t | s_2, a_{22}) = \begin{cases} \frac{35}{272}t, & 0 \leq t \leq 4 \\ \frac{63}{1360}t + \frac{28}{85}, & 4 < t \leq 8 \\ \frac{7}{10}, & t > 8 \end{cases}$$

$$Q(t, s_2 | s_2, a_{22}) = P(s_2 | s_2, a_{22}) F(t | s_2, a_{22}) = 0, \quad t \in R^+$$

$$Q(t, s_3 | s_2, a_{22}) = P(s_3 | s_2, a_{22}) F(t | s_2, a_{22}) = \begin{cases} \frac{15}{272}t, & 0 \leq t \leq 4 \\ \frac{27}{1360}t + \frac{12}{85}, & 4 < t \leq 8 \\ \frac{3}{10}, & t > 8 \end{cases}$$

$$Q(t, s_1 | s_3, a_{32}) = P(s_1 | s_3, a_{32}) F(t | s_3, a_{32}) = 0, \quad t \in R^+$$

$$Q(t, s_2 | s_3, a_{32}) = P(s_2 | s_3, a_{32}) F(t | s_3, a_{32}) = \begin{cases} \frac{377}{1440}t, & 0 \leq t \leq 1 \\ \frac{377}{720}t - \frac{377}{1440}, & 1 < t \leq 2 \\ \frac{87}{1920}t + \frac{667}{960}, & 2 < t \leq 6 \\ \frac{29}{30}, & t > 6 \end{cases}$$

$$Q(t, s_3 | s_3, a_{32}) = P(s_3 | s_3, a_{32}) F(t | s_3, a_{32}) = \begin{cases} \frac{13}{1440}t, & 0 \leq t \leq 1 \\ \frac{13}{720}t - \frac{13}{1440}, & 1 < t \leq 2 \\ \frac{1}{5760}t + \frac{23}{960}, & 2 < t \leq 6 \\ \frac{1}{30}, & t > 6 \end{cases}$$

Calculate  $D(t | s_i, a_{ik})$  using the following mathematical formulation:

$$D(t | s_i, a_{ik}) = \sum_{s_j \in S} Q(t, s_j | s_i, a_{ik})$$

$$D(t | s_2, a_{21}) = \begin{cases} \frac{3}{17}t, & 0 \leq t \leq 1 \\ \frac{15}{34}t - \frac{9}{34}, & 1 < t \leq 2 \\ \frac{11}{68}t + \frac{5}{17}, & 2 < t \leq 4 \\ \frac{1}{34}t + \frac{14}{17}, & 4 < t \leq 6 \\ 1, & t > 6 \end{cases} \quad D(t | s_2, a_{22}) = \begin{cases} \frac{25}{136}t, & 0 \leq t \leq 4 \\ \frac{9}{136}t + \frac{8}{17}, & 4 < t \leq 8 \\ 1, & t > 8 \end{cases}$$

$$D(t | s_3, a_{32}) = \begin{cases} \frac{13}{48}t, & 0 \leq t \leq 1 \\ \frac{13}{24}t - \frac{13}{48}, & 1 < t \leq 2 \\ \frac{3}{64}t + \frac{23}{32}, & 2 < t \leq 6 \\ 1, & t > 6 \end{cases}$$

Calculate  $P(s_i, a_{ik})$  using the following mathematical formulation:

$$P(s_i, a_{ik}) = \frac{\text{No. of infected individuals ending with hyperinflammatory response} + \text{No. of infected individuals ending with organ dysfunction}}{\text{the total number of simulation runs}}$$

$$P(s_2, a_{21}) = 19/30 \quad P(s_2, a_{22}) = 7/30 \quad P(s_3, a_{32}) = 17/30$$

## Computation Study II

### *Notation and SMDP formulation*

#### ***State set:***

$$s_1 = [S_l, H_l]$$

$$s_2 = [S_l, H_m]$$

$$s_3 = [S_l, H_h]$$

$$s_4 = [S_m, H_l]$$

$$s_5 = [S_m, H_m]$$

$$s_6 = [S_m, H_h]$$

$$s_7 = [S_h, H_l]$$

$$s_8 = [S_h, H_m]$$

$$s_9 = [S_h, H_h]$$

$S_l$ : *Salmonella* loads fall into the range [0, 1152)

$S_m$ : *Salmonella* loads fall into the range [1152, 2304)

$S_h$ : *Salmonella* loads fall into the range [2304,  $\infty$ )

$H_l$ : HMGB-1 levels fall into the range [0, 400)

$H_m$ : HMGB-1 levels fall into the range [400, 800)

$H_h$ : HMGB-1 levels fall into the range [800,  $\infty$ )

#### ***Action set:***

$A : \{a_1 = \text{Antimicrobials}, a_2 = \text{Anti-HMGB-1s}, a_3 = \text{Antimicrobials and Anti-HMGB-1s} \}$

#### ***Planning decision horizon:***

$\lambda = 0 - 24$  hrs, and  $\lambda$  is a continuous variable

#### ***The following notations are used:***

$P(s_j | s_i, a_{ik})$ : The probability that the current state  $s_i$  transits to state  $s_j$  at the next decision epoch, given action  $a_{ik}$  made at state  $s_i$ .

$F(t | s_i, a_{ik})$ : The probability that the next decision epoch occurs within time  $t$ , given action  $a_{ik}$  made at the current state  $s_i$ .

$P(s_i, a_{ik})$ : The probability of an infected individual ending with “hyperinflammatory response” or “organ dysfunction”, given  $a_{ik}$  made at the current state  $s_i$ .

$Q(t, s_j | s_i, a_{ik})$ : The probability that the current state  $s_i$  transits to the state  $s_j$  at the next decision epoch within time  $t$ , given  $a_{ik}$  made at the current state  $s_i$ .

$D(t | s_i, a_{ik})$ : The probability that current state  $s_i$  transits to other states at the next decision epoch within  $t$ , given  $a_{ik}$  made at the current state  $s_i$ .

### ***Modeling assumptions***

a. Decision epochs occur whenever the state changes, and a decision epoch occurs if the state remains at  $s_3$  for 5 hrs or the state remains at  $s_3, s_6, s_9$  for 2 hrs.

b. The range of indicator counts are dependent on the initial loads of *Salmonella*. In this numerical example, the initial load of *Salmonella* was set to 3200.

c. If taking an action  $a_1$ , 50 counts antimicrobial agents (1 agent count *in silico* responds to 1 colony forming unit (CFU) of *Salmonella*) were added to the *silico* experiment each time at decision epoch.

d. If taking an action  $a_2$ , 400 counts anti-HMGB-1 agents (1 agent count *in silico* responds to 1 unit of HMGB-1, equivalent to  $2.82 \times 10^{-5}$  pg) were added to the *silico* experiment when HMGB-1 levels fall into  $H_m$ , and 800 counts anti-HMGB-1 agents were added to the *silico* experiment when HMGB-1 levels fall into  $H_l$ .

e. If taking an action  $a_3$ , follow c and d.

f. There is no decision epoch when the system remains at  $s_1$ .

g. We calculated  $P(s_j | s_i, a_{ik})$  and  $F(t | s_i, a_{ik})$  by observing the changes in the number of indicators (states) for 20 simulation runs.

*Compute inputs of value iteration algorithm using IMMABM*

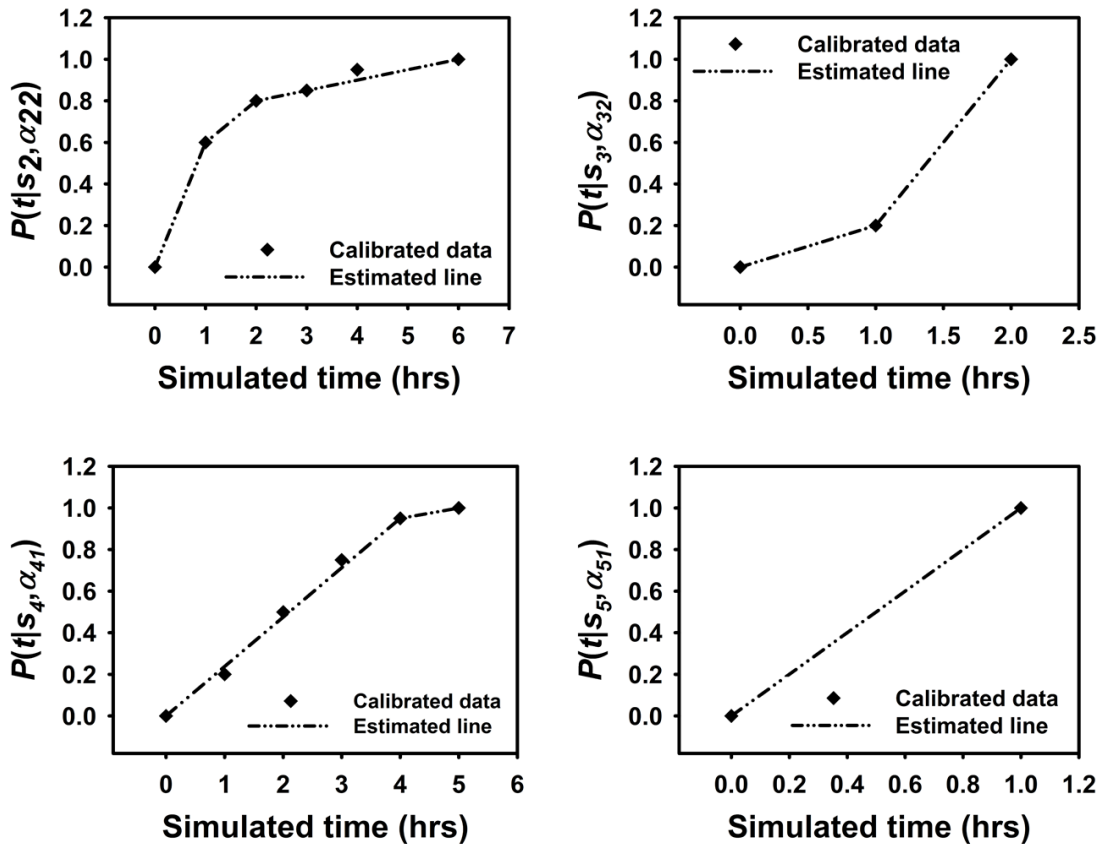
Derive  $F(t | s_i, a_{ik})$

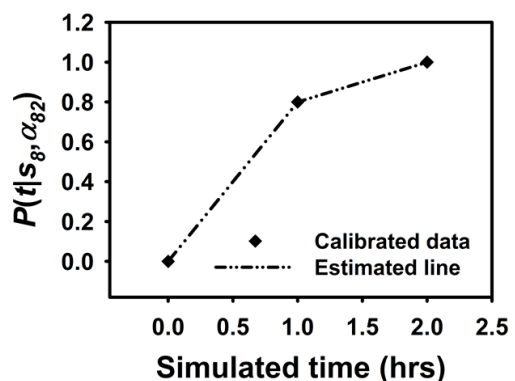
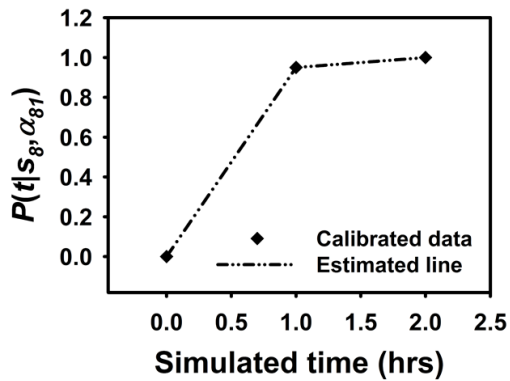
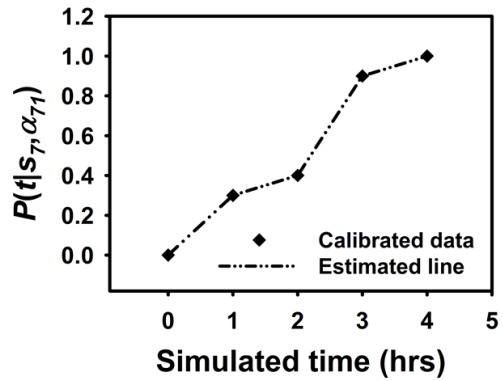
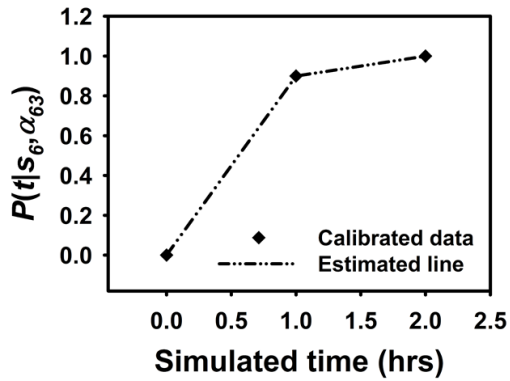
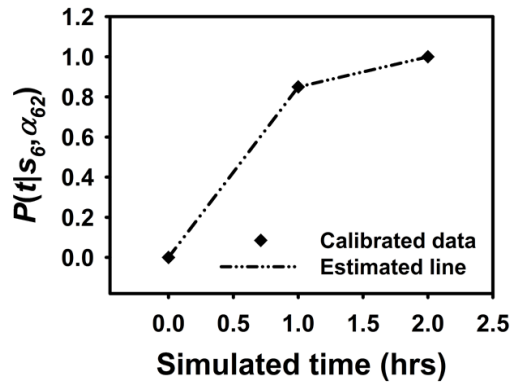
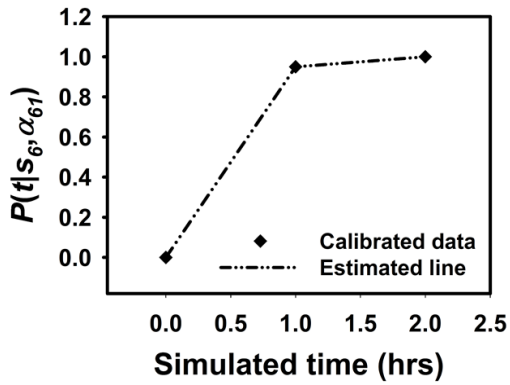
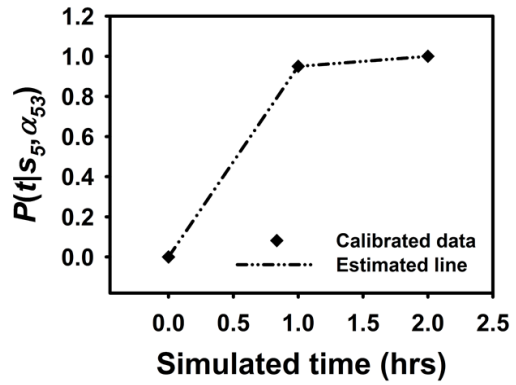
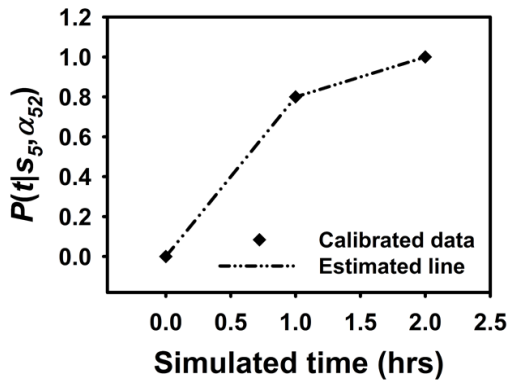
Firstly, calculate  $P(t | s_i, a_{ik})$  using the following mathematical formulation:

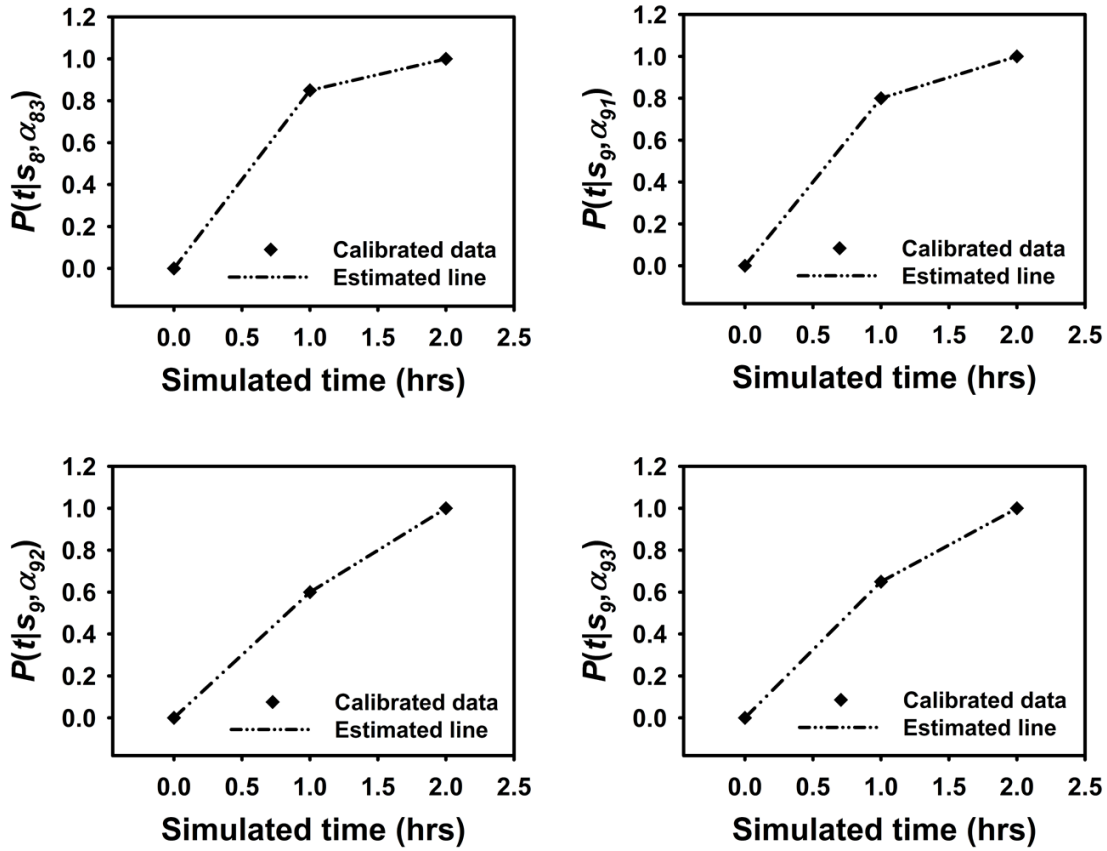
$$P(t | s_i, a_{ik}) = \frac{\text{No. of the next decision epoch occurs within time } t, \text{ given action } a_{ik} \text{ made at the current state } s_i}{\text{the total number of simulation runs}}$$

Secondly, estimate  $F(t | s_i, a_{ik})$  using calibrated  $P(t | s_i, a_{ik})$ , as shown in Fig. C.2:

**Figure 8.2** Calibrated  $P(t | s_i, a_{ik})$  from IMMABM and estimated lines for  $F(t | s_i, a_{ik})$







We calibrated  $P(t|s_i, a_{ik})$  using simulated data from IMMABM, and estimated  $F(t|s_i, a_{ik})$  using obtained  $P(t|s_i, a_{ik})$ . We assumed the line segments between calibrated data follows a linear relationship in order to simply the calculation, the functions of estimated lines are shown as follows:

$$F(t|s_2, a_{22}) = \begin{cases} \frac{3}{5}t, & 0 \leq t \leq 1 \\ \frac{1}{5}t + \frac{2}{5}, & 1 < t \leq 2 \\ \frac{1}{20}t + \frac{7}{10}, & 2 < t \leq 6 \\ 1, & t > 6 \end{cases} \quad F(t|s_3, a_{32}) = \begin{cases} \frac{1}{5}t, & 0 \leq t \leq 1 \\ \frac{4}{5}t - \frac{3}{5}, & 1 < t \leq 2 \\ 1, & t > 2 \end{cases}$$

$$F(t|s_4, a_{41}) = \begin{cases} \frac{19}{80}t, & 0 \leq t \leq 4 \\ \frac{1}{20}t + \frac{3}{4}, & 4 < t \leq 5 \\ 1, & t > 5 \end{cases}$$

$$F(t|s_5, a_{51}) = \begin{cases} t, & 0 \leq t \leq 1 \\ 1, & t > 1 \end{cases}$$

$$F(t|s_5, a_{52}) = \begin{cases} \frac{4}{5}t, & 0 \leq t \leq 1 \\ \frac{1}{5}t + \frac{3}{5}, & 1 < t \leq 2 \\ 1, & t > 2 \end{cases}$$

$$F(t|s_5, a_{53}) = \begin{cases} \frac{19}{20}t, & 0 \leq t \leq 1 \\ \frac{1}{20}t + \frac{9}{10}, & 1 < t \leq 2 \\ 1, & t > 2 \end{cases}$$

$$F(t|s_6, a_{61}) = \begin{cases} \frac{19}{20}t, & 0 \leq t \leq 1 \\ \frac{1}{20}t + \frac{9}{10}, & 1 < t \leq 2 \\ 1, & t > 2 \end{cases}$$

$$F(t|s_6, a_{62}) = \begin{cases} \frac{17}{20}t, & 0 \leq t \leq 1 \\ \frac{3}{20}t + \frac{7}{10}, & 1 < t \leq 2 \\ 1, & t > 2 \end{cases}$$

$$F(t|s_6, a_{63}) = \begin{cases} \frac{9}{10}t, & 0 \leq t \leq 1 \\ \frac{1}{10}t + \frac{4}{5}, & 1 < t \leq 2 \\ 1, & t > 2 \end{cases}$$

$$F(t|s_7, a_{71}) = \begin{cases} \frac{3}{10}t, & 0 \leq t \leq 1 \\ \frac{1}{10}t + \frac{1}{5}, & 1 < t \leq 2 \\ \frac{1}{2}t - \frac{3}{5}, & 2 < t \leq 3 \\ \frac{1}{10}t + \frac{3}{5}, & 3 < t \leq 4 \\ 1, & t > 4 \end{cases}$$

$$F(t|s_8, a_{81}) = \begin{cases} \frac{19}{20}t, & 0 \leq t \leq 1 \\ \frac{1}{20}t + \frac{9}{10}, & 1 < t \leq 2 \\ 1, & t > 2 \end{cases}$$

$$F(t|s_8, a_{82}) = \begin{cases} \frac{4}{5}t, & 0 \leq t \leq 1 \\ \frac{1}{5}t + \frac{3}{5}, & 1 < t \leq 2 \\ 1, & t > 2 \end{cases}$$



$$F(t | s_8, a_{83}) = \begin{cases} \frac{17}{20}t, & 0 \leq t \leq 1 \\ \frac{3}{20}t + \frac{7}{10}, & 1 < t \leq 2 \\ 1, & t > 2 \end{cases}$$

$$F(t | s_9, a_{91}) = \begin{cases} \frac{4}{5}t, & 0 \leq t \leq 1 \\ \frac{1}{5}t + \frac{3}{5}, & 1 < t \leq 2 \\ 1, & t > 2 \end{cases}$$

$$F(t | s_9, a_{92}) = \begin{cases} \frac{3}{5}t, & 0 \leq t \leq 1 \\ \frac{2}{5}t + \frac{1}{5}, & 1 < t \leq 2 \\ 1, & t > 2 \end{cases}$$

$$F(t | s_9, a_{93}) = \begin{cases} \frac{13}{20}t, & 0 \leq t \leq 1 \\ \frac{7}{20}t + \frac{3}{10}, & 1 < t \leq 2 \\ 1, & t > 2 \end{cases}$$

Calculate  $P(s_j | s_i, a_{ik})$  using the following mathematical formulation:

$$P(s_j | s_i, a_{ik}) = \frac{\text{No. of current state } s_i \text{ transits to state } s_j \text{ at next decision epoch, under action } a_{ik} \text{ at state } s_i}{\text{the total number of simulation runs}}$$

Using IMMABM,  $P(s_j | s_i, a_{ik})$  is obtained as follows:

(state $s_i$ , action $a_{ik}$ )	No. of transitions to ( $s_j$ )	$P(s_j   s_i, a_{ik})$
<b>(<math>s_2, a_{22}</math>)</b>	7 ( $s_1$ )	$P(s_1   s_2, a_{22}) = 7/20$
	13 ( $s_3$ )	$P(s_3   s_2, a_{22}) = 13/20$
<b>(<math>s_3, a_{32}</math>)</b>	5 ( $s_2$ )	$P(s_2   s_3, a_{32}) = 5/20$
	15 ( $s_3$ )	$P(s_3   s_3, a_{32}) = 15/20$
<b>(<math>s_4, a_{41}</math>)</b>	3 ( $s_1$ )	$P(s_1   s_4, a_{41}) = 3/20$
	1 ( $s_2$ )	$P(s_2   s_4, a_{41}) = 1/20$
	3 ( $s_3$ )	$P(s_3   s_4, a_{41}) = 3/20$
	3 ( $s_5$ )	$P(s_5   s_4, a_{41}) = 3/20$
	1 ( $s_6$ )	$P(s_6   s_4, a_{41}) = 1/20$
	7 ( $s_7$ )	$P(s_7   s_4, a_{41}) = 7/20$

	2 ( $s_8$ )	$P(s_8 s_4, a_{41})=2/20$
<b>(<math>s_5, a_{51}</math>)</b>	15 ( $s_3$ )	$P(s_3 s_5, a_{51})=15/20$
	5 ( $s_6$ )	$P(s_6 s_5, a_{51})=5/20$
<b>(<math>s_5, a_{52}</math>)</b>	1 ( $s_2$ )	$P(s_2 s_5, a_{52})=1/20$
	13 ( $s_3$ )	$P(s_3 s_5, a_{52})=13/20$
	1 ( $s_4$ )	$P(s_4 s_5, a_{52})=1/20$
	4 ( $s_6$ )	$P(s_6 s_5, a_{52})=4/20$
	1 ( $s_8$ )	$P(s_8 s_5, a_{52})=1/20$
<b>(<math>s_5, a_{53}</math>)</b>	3 ( $s_2$ )	$P(s_2 s_5, a_{53})=3/20$
	12 ( $s_3$ )	$P(s_3 s_5, a_{53})=12/20$
	5 ( $s_6$ )	$P(s_6 s_5, a_{53})=5/20$
<b>(<math>s_6, a_{61}</math>)</b>	20 ( $s_3$ )	$P(s_3 s_6, a_{61})=20/20$
<b>(<math>s_6, a_{62}</math>)</b>	1 ( $s_2$ )	$P(s_2 s_6, a_{62})=1/20$
	18 ( $s_3$ )	$P(s_3 s_6, a_{62})=18/20$
	1 ( $s_6$ )	$P(s_6 s_6, a_{62})=1/20$
<b>(<math>s_6, a_{63}</math>)</b>	2 ( $s_1$ )	$P(s_1 s_6, a_{63})=2/20$
	18 ( $s_3$ )	$P(s_3 s_6, a_{63})=18/20$
<b>(<math>s_7, a_{71}</math>)</b>	5 ( $s_4$ )	$P(s_4 s_7, a_{71})=5/20$
	1 ( $s_5$ )	$P(s_5 s_7, a_{71})=1/20$
	3 ( $s_8$ )	$P(s_8 s_7, a_{71})=3/20$
	11 ( $s_9$ )	$P(s_9 s_7, a_{71})=11/20$
<b>(<math>s_8, a_{81}</math>)</b>	1 ( $s_3$ )	$P(s_3 s_8, a_{81})=1/20$
	6 ( $s_6$ )	$P(s_6 s_8, a_{81})=6/20$
	13 ( $s_9$ )	$P(s_9 s_8, a_{81})=13/20$

$(s_8, a_{82})$	2 ( $s_3$ )	$P(s_3 s_8, a_{82})=2/20$
	1 ( $s_5$ )	$P(s_5 s_8, a_{82})=1/20$
	5 ( $s_6$ )	$P(s_6 s_8, a_{82})=5/20$
	12 ( $s_9$ )	$P(s_9 s_8, a_{82})=12/20$
$(s_8, a_{83})$	1 ( $s_2$ )	$P(s_2 s_8, a_{83})=1/20$
	9 ( $s_3$ )	$P(s_3 s_8, a_{83})=9/20$
	2 ( $s_6$ )	$P(s_6 s_8, a_{83})=2/20$
	8 ( $s_9$ )	$P(s_9 s_8, a_{83})=8/20$
$(s_9, a_{91})$	3 ( $s_3$ )	$P(s_3 s_9, a_{91})=3/20$
	15 ( $s_6$ )	$P(s_6 s_9, a_{91})=15/20$
	2 ( $s_8$ )	$P(s_8 s_9, a_{91})=2/20$
$(s_9, a_{92})$	6 ( $s_3$ )	$P(s_3 s_9, a_{92})=6/20$
	1 ( $s_4$ )	$P(s_4 s_9, a_{92})=1/20$
	13 ( $s_6$ )	$P(s_6 s_9, a_{92})=13/20$
$(s_9, a_{93})$	4 ( $s_3$ )	$P(s_3 s_9, a_{93})=4/20$
	13 ( $s_6$ )	$P(s_6 s_9, a_{93})=13/20$
	3 ( $s_8$ )	$P(s_8 s_9, a_{93})=3/20$

Calculate  $Q(t, s_j | s_i, a_{ik})$  using the following mathematical formulation:

$$Q(t, s_j | s_i, a_{ik}) = P(s_j | s_i, a_{ik}) F(t | s_i, a_{ik})$$

$$Q(t, s_1 | s_2, a_{22}) = P(s_1 | s_2, a_{22}) F(t | s_2, a_{22}) = \begin{cases} \frac{21}{100}t, & 0 \leq t \leq 1 \\ \frac{7}{100}t + \frac{7}{50}, & 1 < t \leq 2 \\ \frac{7}{400}t + \frac{49}{200}, & 2 < t \leq 6 \\ \frac{7}{20}, & t > 6 \end{cases}$$

$$Q(t, s_3 | s_2, a_{22}) = P(s_3 | s_2, a_{22}) F(t | s_2, a_{22}) = \begin{cases} \frac{39}{100}t, & 0 \leq t \leq 1 \\ \frac{13}{100}t + \frac{13}{50}, & 1 < t \leq 2 \\ \frac{13}{400}t + \frac{91}{200}, & 2 < t \leq 6 \\ \frac{13}{20}, & t > 6 \end{cases}$$

$$Q(t, s_j | s_2, a_{22}) = P(s_j | s_2, a_{22}) F(t | s_2, a_{22}) = 0, \quad t \in R^+, \quad j = 2, 4, 5, 6, 7, 8, 9$$

$$Q(t, s_2 | s_3, a_{32}) = P(s_2 | s_3, a_{32}) F(t | s_3, a_{32}) = \begin{cases} \frac{1}{20}t, & 0 \leq t \leq 1 \\ \frac{1}{5}t - \frac{3}{20}, & 1 < t \leq 2 \\ \frac{1}{4}, & t > 2 \end{cases}$$

$$Q(t, s_3 | s_3, a_{32}) = P(s_3 | s_3, a_{32}) F(t | s_3, a_{32}) = \begin{cases} \frac{3}{20}t, & 0 \leq t \leq 1 \\ \frac{3}{5}t - \frac{9}{20}, & 1 < t \leq 2 \\ \frac{3}{4}, & t > 2 \end{cases}$$

$$Q(t, s_j | s_3, a_{32}) = P(s_j | s_3, a_{32}) F(t | s_3, a_{32}) = 0, \quad t \in R^+, \quad j = 1, 4, 5, 6, 7, 8, 9$$

$$Q(t, s_1 | s_4, a_{41}) = P(s_1 | s_4, a_{41}) F(t | s_4, a_{41}) = \begin{cases} \frac{57}{1600}t, & 0 \leq t \leq 4 \\ \frac{3}{400}t + \frac{9}{80}, & 4 < t \leq 5 \\ \frac{3}{20}, & t > 5 \end{cases}$$

$$Q(t, s_2 | s_4, a_{41}) = P(s_2 | s_4, a_{41}) F(t | s_4, a_{41}) = \begin{cases} \frac{19}{1600}t, & 0 \leq t \leq 4 \\ \frac{1}{400}t + \frac{3}{80}, & 4 < t \leq 5 \\ \frac{1}{20}, & t > 5 \end{cases}$$

$$Q(t, s_3 | s_4, a_{41}) = P(s_3 | s_4, a_{41}) F(t | s_4, a_{41}) = \begin{cases} \frac{57}{1600}t, & 0 \leq t \leq 4 \\ \frac{3}{400}t + \frac{9}{80}, & 4 < t \leq 5 \\ \frac{3}{20}, & t > 5 \end{cases}$$

$$Q(t, s_5 | s_4, a_{41}) = P(s_5 | s_4, a_{41}) F(t | s_4, a_{41}) = \begin{cases} \frac{57}{1600}t, & 0 \leq t \leq 4 \\ \frac{3}{400}t + \frac{9}{80}, & 4 < t \leq 5 \\ \frac{3}{20}, & t > 5 \end{cases}$$

$$Q(t, s_6 | s_4, a_{41}) = P(s_6 | s_4, a_{41}) F(t | s_4, a_{41}) = \begin{cases} \frac{19}{1600}t, & 0 \leq t \leq 4 \\ \frac{1}{400}t + \frac{3}{80}, & 4 < t \leq 5 \\ \frac{1}{20}, & t > 5 \end{cases}$$

$$Q(t, s_7 | s_4, a_{41}) = P(s_7 | s_4, a_{41}) F(t | s_4, a_{41}) = \begin{cases} \frac{133}{1600}t, & 0 \leq t \leq 4 \\ \frac{7}{400}t + \frac{21}{80}, & 4 < t \leq 5 \\ \frac{7}{20}, & t > 5 \end{cases}$$

$$Q(t, s_8 | s_4, a_{41}) = P(s_8 | s_4, a_{41}) F(t | s_4, a_{41}) = \begin{cases} \frac{19}{800}t, & 0 \leq t \leq 4 \\ \frac{1}{200}t + \frac{3}{40}, & 4 < t \leq 5 \\ \frac{1}{10}, & t > 5 \end{cases}$$

$$Q(t, s_j | s_4, a_{41}) = P(s_j | s_4, a_{41}) F(t | s_4, a_{41}) = 0, \quad t \in R^+, \quad j = 4, 9$$

$$Q(t, s_3 | s_5, a_{51}) = P(s_3 | s_5, a_{51}) F(t | s_5, a_{51}) = \begin{cases} \frac{3}{4}t, & 0 \leq t \leq 1 \\ \frac{3}{4}, & t > 1 \end{cases}$$

$$Q(t, s_6 | s_5, a_{51}) = P(s_6 | s_5, a_{51}) F(t | s_5, a_{51}) = \begin{cases} \frac{1}{4}t, & 0 \leq t \leq 1 \\ \frac{1}{4}, & t > 1 \end{cases}$$

$$Q(t, s_j | s_5, a_{51}) = P(s_j | s_5, a_{51}) F(t | s_5, a_{51}) = 0, \quad t \in R^+, \quad j = 1, 2, 4, 5, 7, 8, 9$$

$$Q(t, s_2 | s_5, a_{52}) = P(s_2 | s_5, a_{52}) F(t | s_5, a_{52}) = \begin{cases} \frac{1}{25}t, & 0 \leq t \leq 1 \\ \frac{1}{100}t + \frac{3}{100}, & 1 < t \leq 2 \\ \frac{1}{20}, & t > 2 \end{cases}$$

$$Q(t, s_3 | s_5, a_{52}) = P(s_3 | s_5, a_{52}) F(t | s_5, a_{52}) = \begin{cases} \frac{13}{25}t, & 0 \leq t \leq 1 \\ \frac{13}{100}t + \frac{39}{100}, & 1 < t \leq 2 \\ \frac{13}{20}, & t > 2 \end{cases}$$

$$Q(t, s_4 | s_5, a_{52}) = P(s_4 | s_5, a_{52}) F(t | s_5, a_{52}) = \begin{cases} \frac{1}{25}t, & 0 \leq t \leq 1 \\ \frac{1}{100}t + \frac{3}{100}, & 1 < t \leq 2 \\ \frac{1}{20}, & t > 2 \end{cases}$$

$$Q(t, s_6 | s_5, a_{52}) = P(s_6 | s_5, a_{52}) F(t | s_5, a_{52}) = \begin{cases} \frac{4}{25}t, & 0 \leq t \leq 1 \\ \frac{1}{25}t + \frac{3}{25}, & 1 < t \leq 2 \\ \frac{1}{5}, & t > 2 \end{cases}$$

$$Q(t, s_8 | s_5, a_{52}) = P(s_8 | s_5, a_{52}) F(t | s_5, a_{52}) = \begin{cases} \frac{1}{25}t, & 0 \leq t \leq 1 \\ \frac{1}{100}t + \frac{3}{100}, & 1 < t \leq 2 \\ \frac{1}{20}, & t > 2 \end{cases}$$

$$Q(t, s_j | s_5, a_{52}) = P(s_j | s_5, a_{52}) F(t | s_5, a_{52}) = 0, \quad t \in R^+, \quad j = 1, 5, 7, 9$$

$$Q(t, s_2 | s_5, a_{53}) = P(s_2 | s_5, a_{53}) F(t | s_5, a_{53}) = \begin{cases} \frac{57}{400}t, & 0 \leq t \leq 1 \\ \frac{3}{400}t + \frac{27}{200}, & 1 < t \leq 2 \\ \frac{3}{20}, & t > 2 \end{cases}$$

$$Q(t, s_3 | s_5, a_{53}) = P(s_3 | s_5, a_{53}) F(t | s_5, a_{53}) = \begin{cases} \frac{57}{100}t, & 0 \leq t \leq 1 \\ \frac{3}{100}t + \frac{27}{50}, & 1 < t \leq 2 \\ \frac{3}{5}, & t > 2 \end{cases}$$

$$Q(t, s_6 | s_5, a_{53}) = P(s_6 | s_5, a_{53}) F(t | s_5, a_{53}) = \begin{cases} \frac{19}{80}t, & 0 \leq t \leq 1 \\ \frac{1}{80}t + \frac{9}{40}, & 1 < t \leq 2 \\ \frac{1}{4}, & t > 2 \end{cases}$$

$$Q(t, s_j | s_5, a_{53}) = P(s_j | s_5, a_{53}) F(t | s_5, a_{53}) = 0, \quad t \in R^+, \quad j = 1, 4, 5, 7, 8, 9$$

$$Q(t, s_3 | s_6, a_{61}) = P(s_3 | s_6, a_{61}) F(t | s_6, a_{61}) = \begin{cases} \frac{19}{20}t, & 0 \leq t \leq 1 \\ \frac{1}{20}t + \frac{9}{10}, & 1 < t \leq 2 \\ 1, & t > 2 \end{cases}$$

$$Q(t, s_j | s_6, a_{61}) = P(s_j | s_6, a_{61}) F(t | s_6, a_{61}) = 0, \quad t \in R^+, \quad j = 1, 2, 4, 5, 6, 7, 8, 9$$

$$Q(t, s_2 | s_6, a_{62}) = P(s_2 | s_6, a_{62}) F(t | s_6, a_{62}) = \begin{cases} \frac{17}{400}t, & 0 \leq t \leq 1 \\ \frac{3}{400}t + \frac{7}{200}, & 1 < t \leq 2 \\ \frac{1}{20}, & t > 2 \end{cases}$$

$$Q(t, s_3 | s_6, a_{62}) = P(s_3 | s_6, a_{62}) F(t | s_6, a_{62}) = \begin{cases} \frac{153}{200}t, & 0 \leq t \leq 1 \\ \frac{27}{200}t + \frac{63}{100}, & 1 < t \leq 2 \\ \frac{9}{10}, & t > 2 \end{cases}$$

$$Q(t, s_6 | s_6, a_{62}) = P(s_6 | s_6, a_{62}) F(t | s_6, a_{62}) = \begin{cases} \frac{17}{400}t, & 0 \leq t \leq 1 \\ \frac{3}{400}t + \frac{7}{200}, & 1 < t \leq 2 \\ \frac{1}{20}, & t > 2 \end{cases}$$

$$Q(t, s_j | s_6, a_{62}) = P(s_j | s_6, a_{62}) F(t | s_6, a_{62}) = 0, \quad t \in R^+, \quad j = 1, 4, 5, 7, 8, 9$$

$$Q(t, s_1 | s_6, a_{63}) = P(s_1 | s_6, a_{63}) F(t | s_6, a_{63}) = \begin{cases} \frac{9}{100}t, & 0 \leq t \leq 1 \\ \frac{1}{100}t + \frac{2}{25}, & 1 < t \leq 2 \\ \frac{1}{10}, & t > 2 \end{cases}$$

$$Q(t, s_3 | s_6, a_{63}) = P(s_3 | s_6, a_{63}) F(t | s_6, a_{63}) = \begin{cases} \frac{81}{100}t, & 0 \leq t \leq 1 \\ \frac{9}{100}t + \frac{18}{25}, & 1 < t \leq 2 \\ \frac{9}{10}, & t > 2 \end{cases}$$

$$Q(t, s_j | s_6, a_{63}) = P(s_j | s_6, a_{63}) F(t | s_6, a_{63}) = 0, \quad t \in R^+, \quad j = 2, 4, 5, 6, 7, 8, 9$$



$$Q(t, s_4 | s_7, a_{71}) = P(s_4 | s_7, a_{71}) F(t | s_7, a_{71}) = \begin{cases} \frac{3}{40}t, & 0 \leq t \leq 1 \\ \frac{1}{40}t + \frac{1}{20}, & 1 < t \leq 2 \\ \frac{1}{8}t - \frac{3}{20}, & 2 < t \leq 3 \\ \frac{1}{40}t + \frac{3}{20}, & 3 < t \leq 4 \\ \frac{1}{4}, & t > 4 \end{cases}$$

$$Q(t, s_5 | s_7, a_{71}) = P(s_5 | s_7, a_{71}) F(t | s_7, a_{71}) = \begin{cases} \frac{3}{200}t, & 0 \leq t \leq 1 \\ \frac{1}{200}t + \frac{1}{100}, & 1 < t \leq 2 \\ \frac{1}{40}t - \frac{3}{100}, & 2 < t \leq 3 \\ \frac{1}{200}t + \frac{3}{100}, & 3 < t \leq 4 \\ \frac{1}{20}, & t > 4 \end{cases}$$

$$Q(t, s_8 | s_7, a_{71}) = P(s_8 | s_7, a_{71}) F(t | s_7, a_{71}) = \begin{cases} \frac{9}{200}t, & 0 \leq t \leq 1 \\ \frac{3}{200}t + \frac{3}{100}, & 1 < t \leq 2 \\ \frac{3}{40}t - \frac{9}{100}, & 2 < t \leq 3 \\ \frac{3}{200}t + \frac{9}{100}, & 3 < t \leq 4 \\ \frac{3}{20}, & t > 4 \end{cases}$$

$$Q(t, s_9 | s_7, a_{71}) = P(s_9 | s_7, a_{71}) F(t | s_7, a_{71}) = \begin{cases} \frac{33}{200}t, & 0 \leq t \leq 1 \\ \frac{11}{200}t + \frac{11}{100}, & 1 < t \leq 2 \\ \frac{11}{40}t - \frac{33}{100}, & 2 < t \leq 3 \\ \frac{11}{200}t + \frac{33}{100}, & 3 < t \leq 4 \\ \frac{11}{20}, & t > 4 \end{cases}$$

$$Q(t, s_j | s_7, a_{71}) = P(s_j | s_7, a_{71}) F(t | s_7, a_{71}) = 0, \quad t \in R^+, \quad j = 1, 2, 3, 6, 7$$

$$Q(t, s_3 | s_8, a_{81}) = P(s_3 | s_8, a_{81}) F(t | s_8, a_{81}) = \begin{cases} \frac{19}{400}t, & 0 \leq t \leq 1 \\ \frac{1}{400}t + \frac{9}{200}, & 1 < t \leq 2 \\ \frac{1}{20}, & t > 2 \end{cases}$$

$$Q(t, s_6 | s_8, a_{81}) = P(s_6 | s_8, a_{81}) F(t | s_8, a_{81}) = \begin{cases} \frac{57}{200}t, & 0 \leq t \leq 1 \\ \frac{3}{200}t + \frac{27}{100}, & 1 < t \leq 2 \\ \frac{3}{10}, & t > 2 \end{cases}$$

$$Q(t, s_9 | s_8, a_{81}) = P(s_9 | s_8, a_{81}) F(t | s_8, a_{81}) = \begin{cases} \frac{247}{400}t, & 0 \leq t \leq 1 \\ \frac{13}{400}t + \frac{117}{200}, & 1 < t \leq 2 \\ \frac{13}{20}, & t > 2 \end{cases}$$

$$Q(t, s_j | s_8, a_{81}) = P(s_j | s_8, a_{81}) F(t | s_8, a_{81}) = 0, \quad t \in R^+, \quad j = 1, 2, 4, 5, 7, 8$$

$$Q(t, s_3 | s_8, a_{82}) = P(s_3 | s_8, a_{82}) F(t | s_8, a_{82}) = \begin{cases} \frac{2}{25}t, & 0 \leq t \leq 1 \\ \frac{1}{50}t + \frac{3}{50}, & 1 < t \leq 2 \\ \frac{1}{10}, & t > 2 \end{cases}$$

$$Q(t, s_5 | s_8, a_{82}) = P(s_5 | s_8, a_{82}) F(t | s_8, a_{82}) = \begin{cases} \frac{1}{25}t, & 0 \leq t \leq 1 \\ \frac{1}{100}t + \frac{3}{100}, & 1 < t \leq 2 \\ \frac{1}{20}, & t > 2 \end{cases}$$

$$Q(t, s_6 | s_8, a_{82}) = P(s_6 | s_8, a_{82}) F(t | s_8, a_{82}) = \begin{cases} \frac{1}{5}t, & 0 \leq t \leq 1 \\ \frac{1}{20}t + \frac{3}{20}, & 1 < t \leq 2 \\ \frac{1}{4}, & t > 2 \end{cases}$$

$$Q(t, s_9 | s_8, a_{82}) = P(s_9 | s_8, a_{82}) F(t | s_8, a_{82}) = \begin{cases} \frac{12}{25}t, & 0 \leq t \leq 1 \\ \frac{3}{25}t + \frac{9}{25}, & 1 < t \leq 2 \\ \frac{3}{5}, & t > 2 \end{cases}$$

$$Q(t, s_j | s_8, a_{82}) = P(s_j | s_8, a_{82}) F(t | s_8, a_{82}) = 0, \quad t \in R^+, \quad j=1,2,4,7,8$$

$$Q(t, s_2 | s_8, a_{83}) = P(s_2 | s_8, a_{83}) F(t | s_8, a_{83}) = \begin{cases} \frac{17}{400}t, & 0 \leq t \leq 1 \\ \frac{3}{400}t + \frac{7}{200}, & 1 < t \leq 2 \\ \frac{1}{20}, & t > 2 \end{cases}$$

$$Q(t, s_3 | s_8, a_{83}) = P(s_3 | s_8, a_{83}) F(t | s_8, a_{83}) = \begin{cases} \frac{153}{400}t, & 0 \leq t \leq 1 \\ \frac{27}{400}t + \frac{63}{200}, & 1 < t \leq 2 \\ \frac{9}{20}, & t > 2 \end{cases}$$

$$Q(t, s_6 | s_8, a_{83}) = P(s_6 | s_8, a_{83}) F(t | s_8, a_{83}) = \begin{cases} \frac{17}{200}t, & 0 \leq t \leq 1 \\ \frac{3}{200}t + \frac{7}{100}, & 1 < t \leq 2 \\ \frac{1}{10}, & t > 2 \end{cases}$$

$$Q(t, s_9 | s_8, a_{83}) = P(s_9 | s_8, a_{83}) F(t | s_8, a_{83}) = \begin{cases} \frac{17}{50}t, & 0 \leq t \leq 1 \\ \frac{3}{50}t + \frac{7}{25}, & 1 < t \leq 2 \\ \frac{2}{5}, & t > 2 \end{cases}$$

$$Q(t, s_j | s_8, a_{83}) = P(s_j | s_8, a_{83}) F(t | s_8, a_{83}) = 0, \quad t \in R^+, \quad j = 1, 4, 5, 7, 8$$

$$Q(t, s_3 | s_9, a_{91}) = P(s_3 | s_9, a_{91}) F(t | s_9, a_{91}) = \begin{cases} \frac{3}{25}t, & 0 \leq t \leq 1 \\ \frac{3}{100}t + \frac{9}{100}, & 1 < t \leq 2 \\ \frac{3}{20}, & t > 2 \end{cases}$$

$$Q(t, s_6 | s_9, a_{91}) = P(s_6 | s_9, a_{91}) F(t | s_9, a_{91}) = \begin{cases} \frac{3}{5}t, & 0 \leq t \leq 1 \\ \frac{3}{20}t + \frac{9}{20}, & 1 < t \leq 2 \\ \frac{3}{4}, & t > 2 \end{cases}$$

$$Q(t, s_8 | s_9, a_{91}) = P(s_8 | s_9, a_{91}) F(t | s_9, a_{91}) = \begin{cases} \frac{2}{25}t, & 0 \leq t \leq 1 \\ \frac{1}{50}t + \frac{3}{50}, & 1 < t \leq 2 \\ \frac{1}{10}, & t > 2 \end{cases}$$

$$Q(t, s_j | s_9, a_{91}) = P(s_j | s_9, a_{91}) F(t | s_9, a_{91}) = 0, \quad t \in R^+, \quad j = 1, 2, 4, 5, 7, 9$$

$$Q(t, s_3 | s_9, a_{92}) = P(s_3 | s_9, a_{92}) F(t | s_9, a_{92}) = \begin{cases} \frac{9}{50}t, & 0 \leq t \leq 1 \\ \frac{3}{25}t + \frac{3}{50}, & 1 < t \leq 2 \\ \frac{3}{10}, & t > 2 \end{cases}$$

$$Q(t, s_4 | s_9, a_{92}) = P(s_4 | s_9, a_{92}) F(t | s_9, a_{92}) = \begin{cases} \frac{3}{100}t, & 0 \leq t \leq 1 \\ \frac{1}{50}t + \frac{1}{100}, & 1 < t \leq 2 \\ \frac{1}{20}, & t > 2 \end{cases}$$

$$Q(t, s_6 | s_9, a_{92}) = P(s_6 | s_9, a_{92}) F(t | s_9, a_{92}) = \begin{cases} \frac{39}{100}t, & 0 \leq t \leq 1 \\ \frac{13}{50}t + \frac{13}{100}, & 1 < t \leq 2 \\ \frac{13}{20}, & t > 2 \end{cases}$$

$$Q(t, s_j | s_9, a_{92}) = P(s_j | s_9, a_{92}) F(t | s_9, a_{92}) = 0, \quad t \in R^+, \quad j = 1, 2, 5, 7, 8, 9$$

$$Q(t, s_3 | s_9, a_{93}) = P(s_3 | s_9, a_{93}) F(t | s_9, a_{93}) = \begin{cases} \frac{13}{100}t, & 0 \leq t \leq 1 \\ \frac{7}{100}t + \frac{3}{50}, & 1 < t \leq 2 \\ \frac{1}{5}, & t > 2 \end{cases}$$

$$Q(t, s_6 | s_9, a_{93}) = P(s_6 | s_9, a_{93}) F(t | s_9, a_{93}) = \begin{cases} \frac{169}{400}t, & 0 \leq t \leq 1 \\ \frac{91}{400}t + \frac{39}{200}, & 1 < t \leq 2 \\ \frac{13}{20}, & t > 2 \end{cases}$$

$$Q(t, s_8 | s_9, a_{93}) = P(s_8 | s_9, a_{93}) F(t | s_9, a_{93}) = \begin{cases} \frac{39}{400}t, & 0 \leq t \leq 1 \\ \frac{21}{400}t + \frac{9}{200}, & 1 < t \leq 2 \\ \frac{3}{20}, & t > 2 \end{cases}$$

$$Q(t, s_j | s_9, a_{93}) = P(s_j | s_9, a_{93}) F(t | s_9, a_{93}) = 0, \quad t \in R^+, \quad j = 1, 2, 4, 5, 7, 9$$

Calculate  $D(t|s_i, a_{ik})$  using the following mathematical formulation:

$$D(t|s_i, a_{ik}) = \sum_{s_j \in S} Q(t, s_j | s_i, a_{ik})$$

$$D(t|s_2, a_{22}) = \begin{cases} \frac{3}{5}t, & 0 \leq t \leq 1 \\ \frac{1}{5}t + \frac{2}{5}, & 1 < t \leq 2 \\ \frac{1}{20}t + \frac{7}{10}, & 2 < t \leq 6 \\ 1, & t > 6 \end{cases}$$

$$D(t|s_3, a_{32}) = \begin{cases} \frac{1}{5}t, & 0 \leq t \leq 1 \\ \frac{4}{5}t - \frac{3}{5}, & 1 < t \leq 2 \\ 1, & t > 2 \end{cases}$$

$$D(t|s_4, a_{41}) = \begin{cases} \frac{19}{80}t, & 0 \leq t \leq 4 \\ \frac{1}{20}t + \frac{3}{4}, & 4 < t \leq 5 \\ 1, & t > 5 \end{cases}$$

$$D(t|s_5, a_{51}) = \begin{cases} t, & 0 \leq t \leq 1 \\ 1, & t > 1 \end{cases}$$

$$D(t|s_5, a_{52}) = \begin{cases} \frac{4}{5}t, & 0 \leq t \leq 1 \\ \frac{1}{5}t + \frac{3}{5}, & 1 < t \leq 2 \\ 1, & t > 2 \end{cases}$$

$$D(t|s_5, a_{53}) = \begin{cases} \frac{19}{20}t, & 0 \leq t \leq 1 \\ \frac{1}{20}t + \frac{9}{10}, & 1 < t \leq 2 \\ 1, & t > 2 \end{cases}$$

$$D(t|s_6, a_{61}) = \begin{cases} \frac{19}{20}t, & 0 \leq t \leq 1 \\ \frac{1}{20}t + \frac{9}{10}, & 1 < t \leq 2 \\ 1, & t > 2 \end{cases}$$

$$D(t|s_6, a_{62}) = \begin{cases} \frac{17}{20}t, & 0 \leq t \leq 1 \\ \frac{3}{20}t + \frac{7}{10}, & 1 < t \leq 2 \\ 1, & t > 2 \end{cases}$$

$$D(t|s_6, a_{63}) = \begin{cases} \frac{9}{10}t, & 0 \leq t \leq 1 \\ \frac{1}{10}t + \frac{4}{5}, & 1 < t \leq 2 \\ 1, & t > 2 \end{cases}$$

$$D(t|s_7, a_{71}) = \begin{cases} \frac{3}{10}t, & 0 \leq t \leq 1 \\ \frac{1}{10}t + \frac{1}{5}, & 1 < t \leq 2 \\ \frac{1}{2}t - \frac{3}{5}, & 2 < t \leq 3 \\ \frac{1}{10}t + \frac{3}{5}, & 3 < t \leq 4 \\ 1, & t > 4 \end{cases}$$

$$D(t|s_8, a_{81}) = \begin{cases} \frac{19}{20}t, & 0 \leq t \leq 1 \\ \frac{1}{20}t + \frac{9}{10}, & 1 < t \leq 2 \\ 1, & t > 2 \end{cases}$$

$$D(t|s_8, a_{82}) = \begin{cases} \frac{4}{5}t, & 0 \leq t \leq 1 \\ \frac{1}{5}t + \frac{3}{5}, & 1 < t \leq 2 \\ 1, & t > 2 \end{cases}$$

$$D(t|s_8, a_{83}) = \begin{cases} \frac{17}{20}t, & 0 \leq t \leq 1 \\ \frac{3}{20}t + \frac{7}{10}, & 1 < t \leq 2 \\ 1, & t > 2 \end{cases}$$

$$D(t|s_9, a_{91}) = \begin{cases} \frac{4}{5}t, & 0 \leq t \leq 1 \\ \frac{1}{5}t + \frac{3}{5}, & 1 < t \leq 2 \\ 1, & t > 2 \end{cases}$$

$$D(t|s_9, a_{92}) = \begin{cases} \frac{3}{5}t, & 0 \leq t \leq 1 \\ \frac{2}{5}t + \frac{1}{5}, & 1 < t \leq 2 \\ 1, & t > 2 \end{cases}$$

$$D(t|s_9, a_{93}) = \begin{cases} \frac{13}{20}t, & 0 \leq t \leq 1 \\ \frac{7}{20}t + \frac{3}{10}, & 1 < t \leq 2 \\ 1, & t > 2 \end{cases}$$

**Calculate  $P(s_i, a_i)$  using the following mathematical formulation:**

$$P(s_i, a_i) = \frac{\text{No. of infected individuals ending with hyperinflammatory response} + \text{No. of infected individuals ending with organ dysfunction}}{\text{the total number of simulation runs}}$$

$P(s_2, a_{22}) = 16/20$	$P(s_3, a_{32}) = 18/20$	$P(s_4, a_{41}) = 19/20$	$P(s_5, a_{51}) = 20/20$
$P(s_5, a_{52}) = 20/20$	$P(s_5, a_{53}) = 19/20$	$P(s_6, a_{61}) = 20/20$	$P(s_6, a_{62}) = 20/20$
$P(s_6, a_{63}) = 20/20$	$P(s_7, a_{71}) = 20/20$	$P(s_8, a_{81}) = 20/20$	$P(s_8, a_{82}) = 20/20$
$P(s_8, a_{83}) = 20/20$	$P(s_9, a_{91}) = 20/20$	$P(s_9, a_{92}) = 20/20$	$P(s_9, a_{93}) = 20/20$